Civil Engineering and Applied Solutions

Research Article

journal homepage: ceas.journals.umz.ac.ir

CEAS Civil Engineering and Applied Solutions

A Data-Driven Seismic Design Framework for RC Frames Using Wavelet Transforms and Machine Learning

Sina Farahani [a*]

[a] *Department of Civil Engineering, Faculty of Civil Engineering and Architecture, Shahid Chamran University of Ahvaz, Ahvaz, Iran*

A R T I C L E I N F O

Article history:

Received 12 January 2026

Revised 13 February 2026

Accepted 07 May 2026

Available online 01 January 2027

Keywords:

Reinforced concrete moment resisting frame

Wavelet transform

Machine learning-based method

Seismic behavior

Dynamic analysis

A B S T R A C T

Nowadays, reinforced concrete (RC) frames are one of the most well-developed lateral load-resisting systems used around the world. However, the complex nonlinear behavior of the composite material system, which combines steel and concrete, makes precise seismic analysis and design particularly challenging. Established methods, such as modal response history analysis and time history analysis, are often difficult to apply. This challenge is compounded when significant soil-structure interaction alters the structural response through higher mode effects. Consequently, the development of innovative analytical methods that are both simplified and robust remains a primary challenge in advancing the design of these structural systems. This study presents a novel wavelet transform-based machine learning method (WTMLM) for the seismic design of RC frames. The method incorporates soil-structure interaction (SSI) effects and formulates the dynamic equilibrium of the system. The proposed WTMLM is used to design five RC frames with varying story heights on two different soil types. The performance is evaluated using nonlinear time-history analyses (NTHA) under real ground motions. Finally, a new equation for predicting displacement distribution is developed based on machine learning and median NTHA results. The findings indicate the WTMLM is an effective method for controlling the seismic performance of RC structures.

How to cite this article: Farahani, S. A Data-Driven Seismic Design Framework for RC Frames Using Wavelet Transforms and Machine Learning. Civil Engineering and Applied Solutions. 2027; 3(1): 1–24. doi:10.22080/ceas.2026.30950.1073.

1. Introduction

The global impact of earthquakes presents a profound risk to human safety, critical infrastructure, and economic systems. These seismic events induce vibrations that generate internal forces and displacements in reinforced concrete (RC) structures. Crucially, at the ultimate nonlinear performance level, the resulting structural damage is a function of the displacement history at each degree of freedom (DOF). Determining this damage precisely requires solving the structural response via exact dynamic equilibrium equations, which in turn necessitates a complete time history of the ground motion-induced forces. However, the vibration characteristics of earthquake signals are non-harmonic and highly unpredictable, making such a precise analysis challenging. Furthermore, employing exact methods such as nonlinear time-history analysis (NTHA) and modal response history analysis (MRHA) in the initial design phase is complex and time-consuming. Moreover, incorporating soil-structure interaction (SSI) into the analysis introduces additional degrees of freedom and leads to a more complex formulation of the coupled equations of motion. This added complexity further exacerbates the challenges of precise seismic assessment. Consequently, major design codes, such as ASCE 7-22 [1], Eurocode 8 [2], and the Iranian Standard 2800 [3], provide simplified methods like the Equivalent Lateral Force (ELF) procedure. Although the ELF procedure simplifies the design process by primarily considering the fundamental mode of vibration, it omits the time-dependent characteristics of seismic motion and the complexities introduced by SSI. This simplification

* Corresponding author.

E-mail addresses: s.farahani@scu.ac.ir (S. Farahani).

https://doi.org/10.22080/ceas.2026.30950.1073

ISSN: 3092-7749/© 2027 The Author(s). Published by University of Mazandaran.

can lead to an underestimation of story shears, particularly in the upper levels of a structure, due to the influence of higher-mode effects.

Conversely, solving the equation of motion is significantly simplified when the excitation can be represented by a periodic harmonic force, as this permits a precise analytical solution [4]. Furthermore, research has demonstrated that displacement has a greater influence on structural performance than resistance during seismic events [4-7]. Consequently, displacement can be considered a critical parameter for controlling structural damage. This understanding has led the field of seismic design to increasingly adopt displacement-based methods. Within this framework, the accurate estimation of seismic-induced damage is achieved by treating displacement as a fundamental performance parameter. In essence, a method that successfully incorporates displacement as a key parameter and represents the seismic excitation with an equivalent periodic harmonic force would yield a more efficient solution to the dynamic equation of motion and a more accurate prediction of the structural response [8, 9].

Recently, robust signal processing methods, such as those based on wavelet transform and machine learning (ML), have been applied to predict seismic performance corresponding to equivalent forces in practical applications. Imam et al. [10] demonstrated the practical application of machine learning for seismic performance prediction of steel frames. By training models like Random Forest and XGBoost on a large dataset generated from nonlinear dynamic analyses, they achieved highly accurate predictions of maximum inter-story drift and corresponding damages. Demir et al. [11] highlighted a critical success factor for ML in engineering, demonstrating that feature selection and data cleaning significantly enhance model performance, with Random Forest consistently emerging as the most robust predictor. Farahani and Barari [12] developed an ML-based model using the Group Method of Data Handling (GMDH) that accounts for the complex interplay of multiple displacement properties in offshore structures. The wavelet transforms have been successfully applied to various challenges in structural engineering, including signal processing of ground motions, damage detection, and simplifying complex dynamic analyses. The potential of wavelet transforms to tackle computational cost in seismic design was recognized early on. For instance, Salajegheh et al. [13] demonstrated over a decade ago that the Discrete Wavelet Transform could drastically reduce the number of points in an earthquake record, enabling a much faster optimization process for structural weight. Kamgar et al. [14] provided a crucial insight into the practicality of wavelet transforms, establishing that the first-level approximation of a decomposed seismic signal could predict key SSI response parameters with over 90% accuracy, offering a compelling balance between computational efficiency and precision. Dadkhah et al. [15] quantified a highly favorable trade-off between efficiency and precision in seismic analysis. Their work showed that applying DWT to filter ground motions for IDA slashes computational effort by nearly 87% while maintaining a maximum error below 8%, a compromise that is acceptable for many engineering applications. A compelling precedent for using signal processing to simplify complex analyses was set by Kamgar et al. [16], who demonstrated that the Discrete Wavelet Transform (DWT) could reduce the computational time of nonlinear dynamic analysis while maintaining acceptable accuracy. Yang et al. [17] used experiments to prove that wavelet analysis works for soil-structure interaction problems. Their real-world test results provide a strong foundation for data-driven models like the one in this study. The trend toward intelligent, self-adjusting structural systems is exemplified by the work of Zhang et al. [18]. They created a semi-active damper that uses an LSTM-Wavelet algorithm to dynamically retune itself, proving highly effective for retrofitting aging structures with degraded stiffness.

In parallel with the development of signal-based seismic design methodologies, significant advances have been made in modeling soil and foundation response under dynamic loading. Asgari and Bagheripour [19] employed the Hybrid Frequency Time Domain (HFTD) approach to evaluate nonlinear ground response. They demonstrated that iterative frequency–time domain coupling can efficiently capture strain-dependent soil behavior, a concept relevant to the equivalent linear soil representation adopted in the present study. The influence of soil liquefaction and multi-hazard loading on pile-supported systems has also been extensively investigated. Akbarzadeh et al. [20] examined offshore wind turbines on liquefiable soils, while Asgari et al. [21] studied pile groups in laterally spreading soils. Both studies highlighted the critical role of soil–structure interaction, frequency content, and pile configuration in overall system performance. More recently, Asgari and Ahmadtabar Sorkhi [22] developed parameterized fragility and sensitivity frameworks that quantify the influence of uncertain mechanical and geotechnical parameters on structural vulnerability. Their work emphasizes the need for data-driven approaches that can account for such uncertainties. While the present study focuses on wavelet-based pulse generation and machine learning-assisted design, the broader body of research on nonlinear soil response, SSI, and uncertainty quantification provides both theoretical grounding and motivation for the proposed WTMLM framework. Regarding the choice of time–frequency analysis tool, the wavelet transform was selected for its well-established capability to capture non-stationary frequency content of earthquake records while maintaining temporal localization. However, alternative transforms such as the Stockwell Transform offer distinct advantages, including absolute phase preservation and frequency-dependent spectral localization, which can enhance interpretability and stability for certain classes of seismic signals [21, 22]. A comparative evaluation of wavelet-based and S-Transform-based pulse generation within the WTMLM framework is beyond the scope of the present study, but is acknowledged as a valuable direction for future refinement.

This study introduces a novel Wavelet Transform-based Machine Learning Method (WTMLM) for the seismic design of reinforced concrete (RC) frames. The primary innovation of this study lies in the novel integration of wavelet transforms and machine learning to generate equivalent pulse functions directly from recorded ground motions. This represents a departure from existing methods that rely on idealized pulse shapes or equivalent oscillators. The proposed approach preserves the non-stationary frequency content of real earthquakes and, for the first time, embeds SSI effects within a data-driven design framework validated through rigorous nonlinear analysis. The proposed methodology begins by utilizing the wavelet transform to decompose a selected set of ground motions into two distinct levels. The WTMLM is subsequently developed by employing a shear beam model, formulating the dynamic equilibrium of the structure, and correcting the mass, stiffness, and damping matrices. A key innovation of this approach is the replacement of the force term in the equation of motion with an equivalent pulse function. To achieve this, the study proposes a new solution that converts real earthquake records into a representative pulse function using wavelet transformation. This process introduces a pulsed sine function to generate equivalent seismic forces by filtering out frequency content that falls outside the critical design range. Subsequently, the WTMLM is applied to design five RC frames of 3, 6, 9, 12, and 15 stories, considering two different soil conditions. The seismic performance of these designed frames is then rigorously evaluated using Nonlinear Time History Analysis (NTHA) to verify that they achieve the target performance level. Finally, leveraging the median maximum-story displacements derived from the NTHA results, a machine learning-based predictive equation is formulated for the displacement prediction of RC frames, explicitly accounting for soil-structure interaction (SSI) effects.

2. Development of wavelet transform-based machine learning method (WTMLM)

2.1. Equivalent SDOF system substitution

In the initial step, the main structure is idealized as a single-degree-of-freedom (SDOF) system characterized by an equivalent mass and an effective height. Based on a target performance level and the corresponding demand displacement, the displacement prediction formula of the RC structure is determined using Eq. 4 [4, 5]. Once the demand displacement is established, the effective period of the structure is obtained from the displacement response spectrum of the seismic-prone area for the considered earthquake scenario. Using this effective period, Eqs. 1 to 3 are subsequently applied to calculate the effective stiffness, the base shear, and the distribution of lateral forces over the height of the structure.

$$K_e = 4\pi^2 \frac{m_e}{T_e^2} \tag{1}$$

$$V_b = K_e\Delta_d + C\frac{m_e g\Delta_d}{H_e} \tag{2}$$

$$F_i = \frac{m_i\Delta_i}{\sum m_i\Delta_i}V_b \tag{3}$$

In Eq. 2, the second term accounts for the P-Delta effect. The effective height H_e, effective mass m_e, and demand displacement Δ_d in the equations above are determined by Eqs. 4 to 6 as follows:

$$\Delta_d = \frac{\sum m_i{\Delta_i}^2}{\sum m_i\Delta_i} \tag{4}$$

$$m_e = \frac{\sum m_i\Delta_i}{\Delta_d} \tag{5}$$

$$H_e = \frac{\sum m_i\Delta_i\, h_i}{\sum m_i\Delta_i} \tag{6}$$

Which are in Eqs. 4 to 6, Δ_i, m_i and h_i, the design displacement of RC structures, seismic mass, and height in the i level, respectively.

2.2. The formulation of the model includes degrees of freedom representative of SSI

The shear beam model, originally proposed by Idriss Izzat and Seed [23] for multilayer soil, is adopted in this study to develop the WTMLM. This formulation focuses on the translational degrees of freedom of the soil-structure system. While this approach captures the essential coupling between soil flexibility and structural lateral response, it intentionally excludes the rocking degree of freedom of the foundation. This simplification is justified for the scope of this study, which involves low- to mid-rise RC frames with squat configurations on relatively stiff soil, where translational SSI effects dominate the global seismic response [4, 9]. As depicted in Fig. 1, this model idealizes the soil as an n-degree-of-freedom (DOF) system, where each DOF possesses unique stiffness and damping properties. This multi-layered representation is well-suited for evaluating the realistic behavior of soil. Each soil layer is substituted with a concentrated mass m_i and stiffness K_i, according to Eqs. 7 and 8.

$$m_i = \frac{\gamma_{i-1}h_{i-1} + \gamma_i h_i}{g} \tag{7}$$

$$K_i = {}^{G_i}\!/_{2h_i} \tag{8}$$

In Eqs. 7 and 8, G_i is the shear modulus of the soil layer. Also h_i and h_{i-1} are the half-thicknesses of soil layers i and $i-1$, respectively. However, m_1 is a lumped mass placed at the top of soil layer 1, which is calculated just using the half thickness of soil layer $1(h_1)$.

Moreover, the initial slope correction method is used to evaluate the effects of the material nonlinearity of soil [24]. Based on this method, the non-linear behavior of the real soil is replaced by an equivalent linear model. This linear model will be used to solve the dynamic equilibrium equation by the MODAL method in section 5. As shown in Fig. 2, in the slope correction method, the initial slope G_0 of the shear stress-shear strain curve in the linear region will be modified by the use of a decreasing factor, namely, the seismic hazard area coefficient N_0, for evaluating nonlinear effects. In Eq. 9, the coefficient N_0 is obtained from FEMA440 [24] illustrated in Table 1. Hence, by the use of this approach, the nonlinear effects of the soil can be obtained in an equivalent linear way employing Eqs. 9 and 10 as follows:

$$G_i = N_0 G_0 (\mathrm{ton}/_{\mathrm{m}^2}) \tag{9}$$

$$G_0 = \frac{\gamma}{g} V_s^{\,2} (\mathrm{ton}/_{\mathrm{m}^2}) \tag{10}$$

In Eq. 10, γ and V_s are the specific weight and shear wave velocity of the soil layer, respectively.

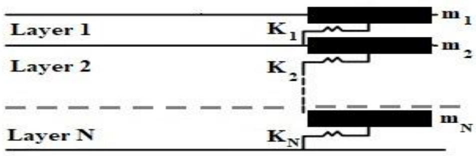

Fig. 1. Conceptual shear beam model for multi-layered soil.

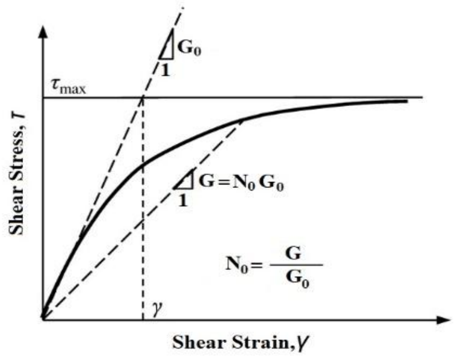

Fig. 2. Modified soil behavior model.

Table 1. The values of the shear modulus ratio [24].

PGA(g)	$\leq 0 \cdot 10$	$0 \cdot 15$	$0 \cdot 20$	$\geq 0 \cdot 30$
Value of $N_0 = G/G_0$	0.81	0.64	0.49	0.42

2.3. Displacement profile of RC frame

The displacement profile of the moment-resistant RC frame is obtained by Eq. 11, taking into account its ideal mechanism, defined as plastic hinges formed at the end of the beams and base of the columns using the strong column-weak beam concept [7]:

$$\Delta_{i.RC} = \theta_c h_i \left[\frac{4h_n - h_i}{4h_n - h_1}\right] \tag{11}$$

In the above equation, θ_c is drift ratio is calculated with regard to the performance level based on the damage to the structural or non-structural members. Moreover, the design displacement profile of the RC frame is modified upon Eq. 12, given as follows:

$$\Delta_{i.SYS} = \omega_\theta (\theta_c h_i \left[\frac{4h_n - h_i}{4h_n - h_1}\right]) \tag{12}$$

The coefficient ω_θ is a modification factor of the higher mode effects obtained by Eq. 13 [7]:

$$\omega_\theta = 1 \cdot 15 - 0 \cdot 0034 h_n \leq 1 \tag{13}$$

2.4. Final characteristics of the SDOF system

In the following, the characteristics of the equivalent SDOF system are calculated:

$$\Delta_d = \frac{\sum_{i=1}^{n}(m_i \cdot \Delta_{i.SYS}{}^2)}{\sum_{i=1}^{n}(m_i \cdot \Delta_{i.SYS})} \tag{14}$$

$$H_e = \frac{\sum_{i=1}^{n}(m_i \cdot \Delta_{i.SYS} \cdot h_i)}{\sum_{i=1}^{n}(m_i \cdot \Delta_{i.SYS})} \tag{15}$$

$$m_e = \frac{\sum_{i=1}^{n}(m_i \cdot \Delta_{i.SYS})}{\Delta_d} \tag{16}$$

In these equations, the characteristics of the SDOF system are Δ_d H_e, m_e named as displacement demand, effective height, and effective mass, respectively. To modify the displacement design profile for the desired damping level, the yield displacement of the RC frame system ($\Delta_{y.RC}$) is first obtained from Eqs. 17 to 19 [5].

$$\Delta_{y.RC} = \theta_{y.RC} \cdot H_e \tag{17}$$

$$\theta_{y.RC} = 0 \cdot 5 \cdot \varepsilon_y \cdot \frac{L_b}{h_b} \tag{18}$$

$$\Delta_{y.RC-system} = [0 \cdot 5 \cdot \varepsilon_y \cdot \frac{L_b}{h_b} \cdot H_e] \tag{19}$$

In the equations above, $\theta_{y.RC}$, L_b, and h_b represent the yield drift ratio, span length, and depth of the beam, respectively. At this stage, with both Δ_d and $\Delta_{y.RC}$ known, Eq. 20 is used to determine the demand ductility:

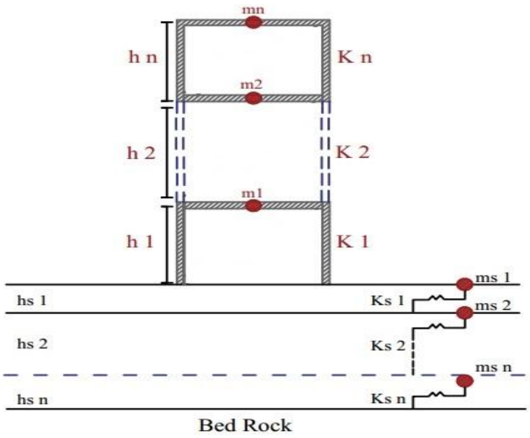

Fig. 3. Numerical model developed in this study.

$$\mu_{RC} = \frac{\Delta_d}{\Delta_{y.RC-system}} \tag{20}$$

The equivalent viscous damping of the system is calculated using Eq. 21.

$$\xi_{eq.RC} = 0 \cdot 05 + 0 \cdot 565 (\frac{\mu_{RC} - 1}{\mu_{RC} \cdot \pi}) \tag{21}$$

In the next step, Eq. 22 is used to determine the modification damping factor of the displacement profile.

$$R_\xi = (\frac{0 \cdot 07}{0 \cdot 02 + \xi_{eq.RC}})^{0 \cdot 5} \tag{22}$$

Moreover, Eq. 23 is proposed to obtain the viscous damping coefficient.

$$C_e = 2 \cdot \xi_{eq.RC} \cdot (\frac{2\pi}{T_e})^2 \tag{23}$$

2.5. Development of a three-degree-of-freedom system

This stage involves extending the SDOF equivalent system from subsection 2.1 to a multi-degree-of-freedom (MDOF) system. The proposed MDOF model, illustrated in Fig. 3, represents an N-degree-of-freedom system that integrates both the N-story structure and the different soil layers. The dynamic equilibrium equation for a multi-degree-of-freedom (MDOF) system excited by external vibration forces P(t) is typically presented in the following form [8]:

$$[M]\{\ddot{u}\} + [C]\{\dot{u}\} + [K]\{u\} = \{P(t)\} \tag{24}$$

Prior to composing and solving the equilibrium Eq. 24, the constituent matrices, including the mass, stiffness, and damping matrices and the force vector, must be extended to include SSI effects. In this study, the shear beam model of SSI with two distinct soil layers is utilized to extend the matrices of the dynamic equilibrium equation. To this end, the SDOF equivalent system is first modified into a three-degree-of-freedom (3DOF) system by incorporating two additional DOFs representing the two soil layers, as illustrated in Fig. 4. The mass, stiffness, and damping matrices for the proposed three-degree-of-freedom equivalent system are developed using Eqs. 25 through 27. These matrices are three-by-three square matrices. The first degree of freedom corresponds to the equivalent SDOF of the structure, characterized by its effective mass (m_e), effective damping (C_e), and effective stiffness (K_e).

The remaining two degrees of freedom are assigned to the soil layers, each characterized by its mass, damping, and stiffness (m_{si}, C_{si}, and K_{si}), where i denotes the layer number. As illustrated in these equations, the matrix components in the present formulation are fundamentally different from those extended in Lu et al. [25]. For instance, unlike their formulation, the mass matrix in Eq. 25 does not incorporate rotational inertia. Furthermore, the equivalent structural mass (m_e) is determined using Eq. 16, while the concentrated soil masses ($m_{s1}.m_{s2}$) are calculated for each layer using Eq. 7. Similar to the impedance model in Lu et al. [25], the proposed stiffness matrix in Eq. 26 differs by excluding a rotational stiffness term. Furthermore, its components are ordered according to the stiffness of each respective soil layer. The matrix components for the soil layers and the superstructure are calculated using Eqs. 1 and 8, respectively. For the damping matrix in Eq. 27, the equivalent structural damping is determined from Eq. 23, while the damping terms for the soil layers are modeled using the Rayleigh damping method. In general, as depicted in Fig. 4, this proposed three-degree-of-freedom system provides a more accurate numerical model than an SDOF system.

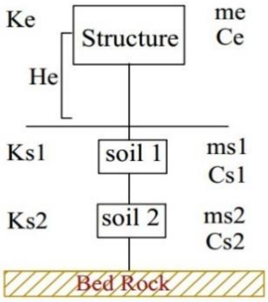

Fig. 4. Proposed 3-degree-of-freedom model in the current study.

$$[M] = \begin{bmatrix} m_e & 0 & 0 \\ 0 & m_{s1} & 0 \\ 0 & 0 & m_{s2} \end{bmatrix} \tag{25}$$

$$[k] = \begin{bmatrix} \mathrm{K_e} & -\mathrm{K_e} & 0 \\ -\mathrm{K_e} & \mathrm{K_{s1}} + \mathrm{K_e} & -\mathrm{K_{s1}} \\ 0 & -\mathrm{K_{s1}} & \mathrm{K_{s1}} + \mathrm{K_{s2}} \end{bmatrix} \tag{26}$$

$$[c] = \begin{bmatrix} C_e & -C_e & 0 \\ -C_e & C_{s1} + C_e & -C_{s1} \\ 0 & -C_{s1} & C_{s1} + C_{s2} \end{bmatrix} \tag{27}$$

Finally, the dynamic equilibrium equation of the proposed 3-degree-of-freedom system is presented as follows:

$$\begin{bmatrix} m_e & 0 & 0 \\ 0 & m_{s1} & 0 \\ 0 & 0 & m_{s2} \end{bmatrix}\{\ddot{u}\} + \begin{bmatrix} C_e & -C_e & 0 \\ -C_e & C_{s1} + C_e & -C_{s1} \\ 0 & -C_{s1} & C_{s1} + C_{s2} \end{bmatrix}\{\dot{u}\} + \begin{bmatrix} \mathrm{K_e} & -\mathrm{K_e} & 0 \\ -\mathrm{K_e} & \mathrm{K_{s1}} + \mathrm{K_e} & -\mathrm{K_{s1}} \\ 0 & -\mathrm{K_{s1}} & \mathrm{K_{s1}} + \mathrm{K_{s2}} \end{bmatrix}\{u\} = \{P(t)\} \tag{28}$$

It is important to note that this study aims to generate a closed-form equation by theoretically solving the dynamic equilibrium equation (i.e., Eq. 28). Consequently, the force vector {P(t)} on the right-hand side of Eq. 28 must be replaced with equivalent force functions to facilitate modal analysis and solve the system of equations, leading to the development of uncoupled equations of motion. To this end, the WTMLM is proposed in the next subsection to generate the required equivalent force function.

2.6. Frequency band separation and equivalent force generation via WTMLM

Seismic data from past earthquakes are typically available as acceleration time histories. However, these records are often of short duration and exhibit significant dispersion, making them unsuitable for deriving theoretical, closed-form solutions required for seismic analysis of the system. While solving the dynamic equilibrium equation is essential for this derivation, the irregular nature of real ground motions complicates analysis and prevents a closed-form solution. Similarly, MRHA is also inadequate, as it does not yield a closed-form solution [8]. As an alternative, this study proposes the use of an equivalent pulse signal, generated via WTMLM, to replace the real earthquake record in the analytical development. These equivalent pulse signals are well-defined mathematical functions. Consequently, they can be substituted for the force vector {P(t)} on the right-hand side of the dynamic equilibrium equation, enabling a theoretical solution. Previous studies indicate that earthquake records comprise distinct high- and low-frequency bands. While the high-frequency components often contain the peak accelerations, their most significant impact occurs near the structure's fundamental period due to resonance. Consequently, an equivalent pulse function can be suitable for developing theoretical equations, provided it is defined to accurately represent these influential frequency bands. This approach of substituting real seismic signals with equivalent pulses has gained scholarly interest in recent decades. For instance, Agrawal and He [26] proposed Eq. 29, which models the equivalent pulse using a decaying sinusoidal function.

$$\dot{u}_g = s \times e^{-\zeta_p \omega_p t} \sin\left(\omega_p \sqrt{1 - {\zeta_p}^2} \cdot t\right) \tag{29}$$

This equation was derived by fitting a curve to the approximate maximum velocity response in the velocity-time history of the earthquake. The corresponding acceleration signal is subsequently obtained by differentiating Eq. 29. Similarly, Makris and Black [27] introduced two functions, presented as Eqs. 30 and 31 and designated Type A and Type B, respectively, to model equivalent pulses. These functions calculate the acceleration signal using sine and cosine formulations. In both equations, the amplitude parameter (v_p) represents the maximum pulse velocity, determined by fitting the velocity functions to their peak value.

$$\ddot{u}_g = \omega_p \frac{v_p}{2} sin\,(\omega_p t) \tag{30}$$

$$\ddot{u}_g = \omega_p v_p cos\,(\omega_p t) \tag{31}$$

Amiri et al. [28] evaluated the three pulse functions defined by Eqs. 29 to 31. Their findings indicate that while Eqs. 29 and 30 yield more accurate results than Eq. 31; time-history analyses reveal significant discrepancies between the responses from these equivalent pulses and those from real earthquake records. This inherent variability constitutes a major drawback, reducing the precision of numerical simulations. To overcome these limitations, the current study introduces a novel method for generating a pulse function from a real earthquake record by employing the wavelet transform. The wavelet transform is uniquely suited for this task because it can accurately capture the time-varying frequency content of seismic signals. It is a highly efficient mathematical tool for signal processing, developed to overcome the limitations of the Fourier transform. While knowledge of a signal's frequency content can reduce error in the structural response, the Fourier transform is restricted by its use of constant-duration time windows, which limit its analysis of transient signals. In contrast, the wavelet transform employs variable time windows, allowing it to adaptively resolve frequency components at any point in time [29]. This provides a more accurate representation of non-stationary signals like earthquake records. The current study employs the wavelet transform to generate an equivalent pulse signal for earthquakes, as it effectively captures their time-varying frequency content. This is achieved by isolating the critical frequency bands within the hazardous range of the real seismic signals. As illustrated in Fig. 5a, the original signal is decomposed into wavelets across variable frequency bands. Using an ML-based algorithm in MATLAB, each earthquake record is decomposed into approximate (low-frequency) and detail (high-frequency) wavelet components. Indeed, an ML-based algorithm is applied to each decomposed wavelet component. A candidate pool of pulse functions, including sinusoidal, exponentially damped, and wavelet-based analytical forms, is evaluated against the reconstructed signal segment. The algorithm selects the function and optimizes its parameters, such as amplitude, frequency, and phase shift, to minimize the Square-Root-of-Sum-of-Squares (SRSS) error between the fitted pulse and the target wavelet. This process is repeated across all significant duration segments, and the optimal pulse family is retained for each ground motion. The training data for this phase consist of the decomposed wavelet coefficients themselves, and no separate validation set is required as the error metric is computed directly on the signal being modeled.

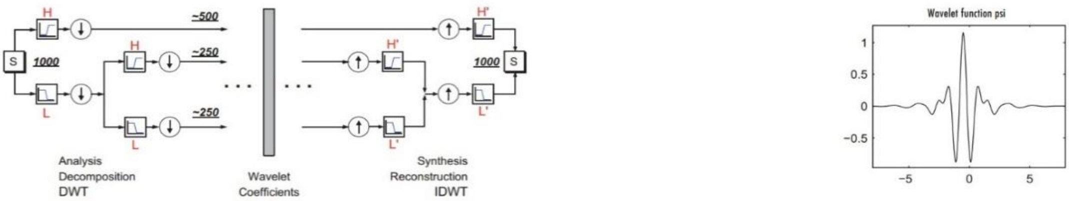

(a) **(b)**

Fig. 5. Wavelet transform of the primary signal: (a) wavelet decomposition and reconstruction steps, (b) Meyer wavelet function [29].

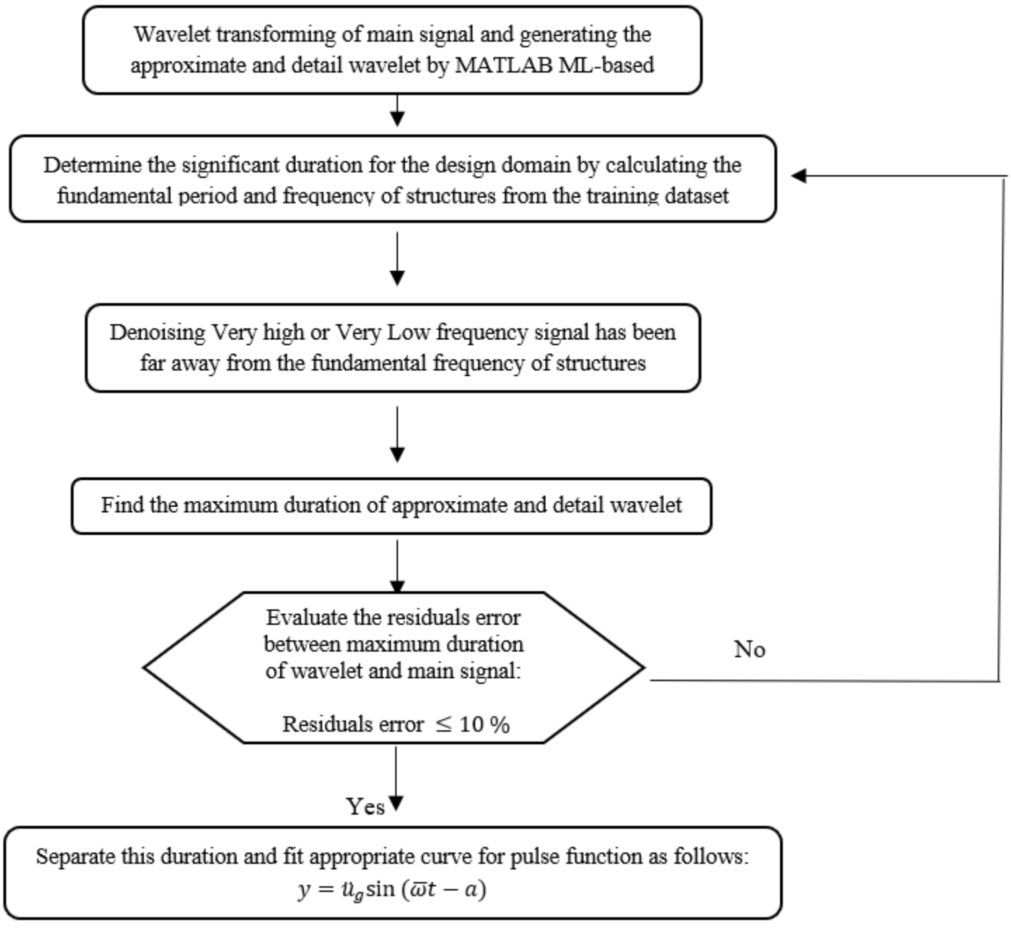

Fig. 6. Flowchart of equivalent pulse generation by WTMLM.

This decomposition is iterated until the transformed signal's characteristics converge with those of the selected base wavelet, namely the Meyer wavelet [29], chosen for its similarity to real seismic signals (Fig. 5b). The final transform is obtained by filtering out frequency content outside the structure's design frequency range. Fig. 6 presents the flowchart of the proposed method. As shown, fitting functions for both the approximate and detail wavelets are derived using the sinusoidal function $y = \ddot{u}_g \sin(\varpi t - a)$, where $\ddot{u}_g$ is the pulse acceleration amplitude, ϖ represents the frequency, and a denotes the phase difference.

2.7. Solution of the dynamic equilibrium equation

As previously stated, the data complexity of real earthquake records prevents the development of a theoretical closed-form solution for Eq. 28. To resolve this, the force function on the right-hand side of Eq. 28 is replaced with the proposed equivalent force function as follows:

$$P_{eq}(\mathrm{t}) = -[M]\{I\}(\ddot{u}) = -[M]\{I\}\ddot{u}_g \sin(\varpi t - a) \tag{32}$$

Here, $\ddot{u}_g \sin(\varpi t - a)$ is the fitted acceleration function for the main earthquake record, generated using the proposed WTMLM as explained in the previous subsection (see Fig. 6). Finally, by substituting Eqs. 25 through 27 into Eq. 32, the resulting dynamic equilibrium equation is formulated as follows:

$$\begin{aligned}&\begin{bmatrix} \frac{\sum_{i=1}^{n}(m_i \cdot \Delta_{i.SYS})}{\Delta_d} & 0 & 0 \\ 0 & \frac{\gamma_{i-1}h_{i-1} + \gamma_i h_i}{g} & 0 \\ 0 & 0 & \frac{\gamma_{i-1}h_{i-1} + \gamma_i h_i}{g} \end{bmatrix} \begin{Bmatrix} \ddot{u}_{st} \\ \ddot{u}_{s1} \\ \ddot{u}_{s2} \end{Bmatrix} + \begin{bmatrix} 2 \cdot \xi_{eq.RC} \cdot (\frac{2\pi}{T_e})^2 & -2 \cdot \xi_{eq.RC} \cdot (\frac{2\pi}{T_e})^2 & 0 \\ -2 \cdot \xi_{eq.RC} \cdot (\frac{2\pi}{T_e})^2 & C_{s1} + 2 \cdot \xi_{eq.RC} \cdot (\frac{2\pi}{T_e})^2 & -C_{s1} \\ 0 & -C_{s1} & C_{s1} + C_{s2} \end{bmatrix} \begin{Bmatrix} \dot{u}_{st} \\ \dot{u}_{s1} \\ \dot{u}_{s2} \end{Bmatrix} \\ &+ \begin{bmatrix} K_e & -K_e & 0 \\ -K_e & \frac{G_{s1}}{2h_{s1}} + K_e & -\frac{G_{s1}}{2h_{s1}} \\ 0 & -\frac{G_{s1}}{2h_{s1}} & \frac{G_{s1}}{2h_{s1}} + \frac{G_{s2}}{2h_{s2}} \end{bmatrix} \begin{Bmatrix} u_{st} \\ u_{s1} \\ u_{s2} \end{Bmatrix} \\ &= -\begin{bmatrix} \frac{\sum_{i=1}^{n}(m_i \cdot \Delta_{i.SYS})}{\Delta_d} & 0 & 0 \\ 0 & \frac{\gamma_{i-1}h_{i-1} + \gamma_i h_i}{g} & 0 \\ 0 & 0 & \frac{\gamma_{i-1}h_{i-1} + \gamma_i h_i}{g} \end{bmatrix} \{\mathrm{I}\}\ddot{u}_g \sin(\varpi t - a)\end{aligned} \tag{33}$$

The dynamic equilibrium equation is solved using the characteristic equation method. This approach is valid because the equivalent stiffness, as defined by Eqs. 1 and 9, is treated as a linear parameter. This linearization permits the correct application of modal analysis. The eigenvalues obtained from solving the characteristic equation yield the system's natural frequencies, ω_n, which are then assembled into the modal matrix $[\phi]$ as follows:

$$\left\| \begin{bmatrix} K_e & -K_e & 0 \\ -K_e & \frac{G_{s1}}{2h_{s1}} + K_e & -\frac{G_{s1}}{2h_{s1}} \\ 0 & -\frac{G_{s1}}{2h_{s1}} & \frac{G_{s1}}{2h_{s1}} + \frac{G_{s2}}{2h_{s2}} \end{bmatrix} - \omega_n{}^2 \begin{bmatrix} \frac{\sum_{i=1}^{n}(m_i \cdot \Delta_{i.SYS})}{\Delta_d} & 0 & 0 \\ 0 & \frac{\gamma_{i-1}h_{i-1} + \gamma_i h_i}{g} & 0 \\ 0 & 0 & \frac{\gamma_{i-1}h_{i-1} + \gamma_i h_i}{g} \end{bmatrix} \right\| = 0 \tag{34}$$

$$[\omega_n] = \begin{bmatrix} \omega_1 \\ \omega_2 \\ \omega_3 \end{bmatrix} \tag{35}$$

By using the obtained natural frequencies, the modal matrix could be calculated as follows:

$$[\phi_n] = \begin{bmatrix} \phi_{11} & \phi_{12} & \phi_{13} \\ \phi_{21} & \phi_{22} & \phi_{23} \\ \phi_{31} & \phi_{32} & \phi_{33} \end{bmatrix} \tag{36}$$

The displacement vector {u} is expressed in terms of its modal contributions as follows:

$$u(t) = \sum_{n=1}^{N} \phi_{\mathrm{n}} y_n(t) \tag{37}$$

Substituting Eq. 37 in Eq. 24 gives:

$$\sum_{n=1}^{N} m\phi_{\mathrm{n}}\ddot{y}_n(t) + \sum_{n=1}^{N} c\phi_{\mathrm{n}}\dot{y}_n(t) + \sum_{n=1}^{N} k\phi_{\mathrm{n}} y_n(t) = P(t) \tag{38}$$

By multiplying ϕ_n^T, the uncoupled form of Eq. 38 can be rewritten as follows [8]:

$$\sum_{n=1}^{N}\phi_n^T m\phi_\mathrm{n}\ddot{y}_n(t)+\sum_{n=1}^{N}\phi_n^T c\phi_\mathrm{n}\dot{y}_n(t)+\sum_{n=1}^{N}\phi_n^T k\phi_\mathrm{n}y_n(t)=\phi_n^T P(t) \tag{39}$$

According to orthogonality relations, the Eq. 39 can be formed as Eq. 40.

$$\mathrm{M}_n\ddot{y}_n(t)+\mathrm{C}_n\dot{y}_n(t)+\mathrm{K}_n y_n(t)=P_n(t) \tag{40}$$

Where $\mathrm{M}_n=\phi_n^T m\phi_\mathrm{n}$, $\mathrm{C}_n=\phi_n^T c\phi_\mathrm{n}$, $\mathrm{K}_n=\phi_n^T k\phi_\mathrm{n}$ and $P_n(t)=\phi_n^T P(t)$

Analogous to a SDOF system under a harmonic force $P_n(t)$, the steady-state solution for each modal degree of freedom n is given by:

$$y_n(t)=\frac{P_{nt}}{\mathrm{K}_n}\cdot\frac{1}{\sqrt{\left(1-(\overline{\omega}/\omega_n)^2\right)^2+\left(2\xi_n(\overline{\omega}/\omega_n)\right)^2}} \tag{41}$$

Considering the proposed equivalent force function of Eq. 32 and Eq. 40, the P_{nt} is defined as follows:

$$P_{nt}=\phi_n^T P(t)=\phi_n^T\begin{Bmatrix}m_e\\m_{s1}\\m_{s2}\end{Bmatrix}\ddot{u}_g\sin(\overline{\omega}t-a) \tag{42}$$

Also, $\mathrm{K}_n=\phi_n^T k\phi_\mathrm{n}$ for each degree of freedom n. Since $-1\le\sin(x)\le 1$, The maximum final response of the system is calculated as follows:

$$y_{max.n}=\frac{\phi_n^T\left(\frac{\sum_{i=1}^{n}(m_i\cdot\Delta_{i.SYS})}{\Delta_d}+\frac{\gamma_{i-1}h_{i-1}+\gamma_i h_i}{g}+\frac{\gamma_{i-1}h_{i-1}+\gamma_i h_i}{g}\right)\cdot\ddot{u}_g/K_n}{\sqrt{\left(1-(\overline{\omega}/\omega_n)^2\right)^2+\left(2\xi_n(\overline{\omega}/\omega_n)\right)^2}} \tag{43}$$

The equivalent system of this study has three DOFs, including structural component, soil layer 1, and 2, as shown in Fig. 4. The solutions of each DOF are called y_{st}, y_{s1}, and y_{s2} obtained by Eq. 44.

$$\begin{aligned}
y_{st}&=\frac{\left(\frac{\sum_{i=1}^{n}(m_i\cdot\Delta_{i.SYS})}{\Delta_d}\phi_{11}+\frac{\gamma_1 h_1}{g}\phi_{21}+\frac{\gamma_1 h_1+\gamma_2 h_2}{g}\phi_{31}\right)\cdot\ddot{u}_g/K_1}{\sqrt{\left(1-(\overline{\omega}/\omega_1)^2\right)^2+\left(2\xi_n(\overline{\omega}/\omega_1)\right)^2}}\\
y_{s1}&=\frac{\left(\frac{\sum_{i=1}^{n}(m_i\cdot\Delta_{i.SYS})}{\Delta_d}\phi_{12}+\frac{\gamma_1 h_1}{g}\phi_{22}+\frac{\gamma_1 h_1+\gamma_2 h_2}{g}\phi_{32}\right)\cdot\ddot{u}_g/K_2}{\sqrt{\left(1-(\overline{\omega}/\omega_2)^2\right)^2+\left(2\xi_n(\overline{\omega}/\omega_2)\right)^2}}\\
y_{s2}&=\frac{\left(\frac{\sum_{i=1}^{n}(m_i\cdot\Delta_{i.SYS})}{\Delta_d}\phi_{13}+\frac{\gamma_1 h_1}{g}\phi_{23}+\frac{\gamma_1 h_1+\gamma_2 h_2}{g}\phi_{33}\right)\cdot\ddot{u}_g/K_3}{\sqrt{\left(1-(\overline{\omega}/\omega_3)^2\right)^2+\left(2\xi_n(\overline{\omega}/\omega_3)\right)^2}}
\end{aligned} \tag{44}$$

Where, the h_1 and h_2 are the half thickness of soil layers 1 and 2, respectively. Using Eqs. 37 and 44, the displacements of each DOF are calculated as Eq. 45. Furthermore, the Square-Root-of-Sum-of-Squares (SRSS) method has been used to obtain the maximum responses.

$$\begin{Bmatrix}u_{st}=\sqrt{(\varphi_{11}y_{st})^2+(\varphi_{12}y_{s1})^2+(\varphi_{13}y_{s2})^2}\\u_{s1}=\sqrt{(\varphi_{21}y_{st})^2+(\varphi_{22}y_{s1})^2+(\varphi_{23}y_{s2})^2}\\u_{s2}=\sqrt{(\varphi_{31}y_{st})^2+(\varphi_{32}y_{s1})^2+(\varphi_{33}y_{s2})^2}\end{Bmatrix} \tag{45}$$

Hence, the drift ratio of the structure with the SSI effect is calculated.

$$\theta_{st-SSI}=\frac{u_{st}-u_{s1}}{h_e} \tag{46}$$

The modified demand displacement with the SSI effect is also obtained.

$$\Delta_{st-SSI}=\theta_{st-SSI}\cdot h_e \tag{47}$$

The modified period is then derived from the modified displacement response spectrum using Eq. 47. Subsequently, the modified stiffness and base shear of the structure, accounting for SSI effects, are calculated as follows:

$$K_{e.st-SSI}=\frac{4\pi^2 m_e}{T_{e.st-SSI}^2} \tag{48}$$

$$V_{st-SSI}=\Delta_{st-SSI}\cdot K_{e.st-SSI} \tag{49}$$

Finally, the modified base shear, which accounts for SSI effects, is distributed over the height of the structure to determine the lateral force at each story level i as follows:

$$F_{i.total} = \frac{m_i \Delta_i}{\sum_{i=1}^{n} m_i \Delta_i} V_{st-SSI} \tag{50}$$

3. Summary of proposed method

The design process for the proposed Wavelet Transform-based Machine Learning Method (WTMLM) for RC frames with SSI effects is summarized in the flowchart in Fig. 7, which is based on the equations developed in the preceding sections. Given that the equivalent stiffness depends on the components of the stiffness matrix, the design procedure is iterative. As illustrated in Fig. 7, the procedure begins by defining the target performance level, geometric parameters, and material properties of the soil and structure. Subsequently, the characteristics of the equivalent SDOF system and the effective structural stiffness are calculated. The seismic input is then transformed into an equivalent pulse function using the proposed WTMLM for use as the force function on the right-hand side of the dynamic equilibrium equation. Next, the dynamic equilibrium equation for the structure with SSI effects is formulated using the mass, stiffness, and damping matrices. This equation is solved to obtain the final displacement response, from which the modified demand displacement incorporating SSI effects is determined. The effective period of the system is then derived using this modified displacement. The resulting modified structural stiffness is calculated and compared with the effective stiffness from the initial step. The equivalent stiffness is updated iteratively until convergence is achieved between successive stiffness values. Upon convergence, the final design base shear is computed. This base shear is then distributed over the height of the structure, enabling the final frame design according to the ACI 318 code [30]. Furthermore, the procedural steps of the proposed WTMLM are detailed in Fig. 8.

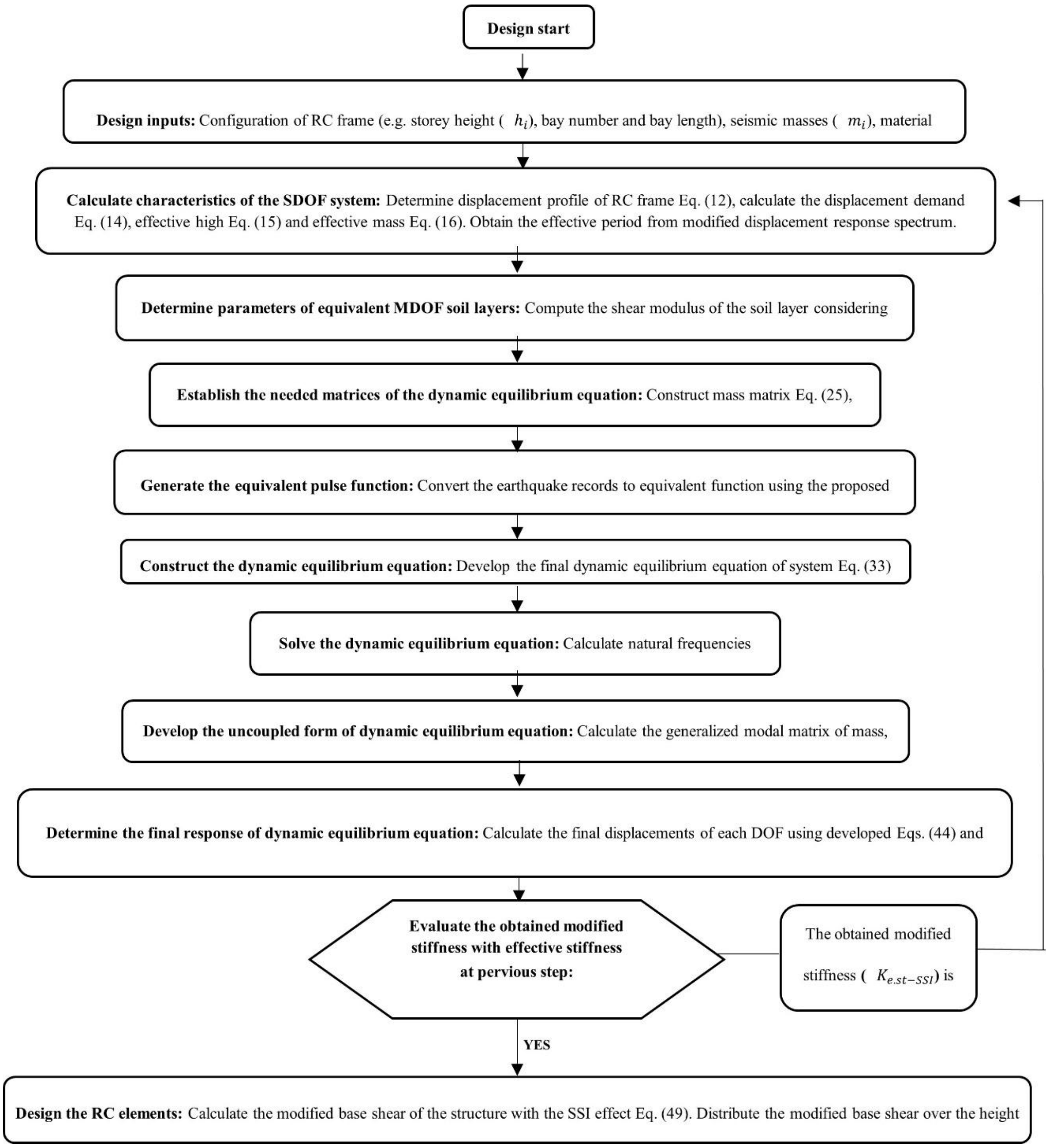

Fig. 7. Flowchart of proposed wavelet transform-based machine learning method (WTMLM).

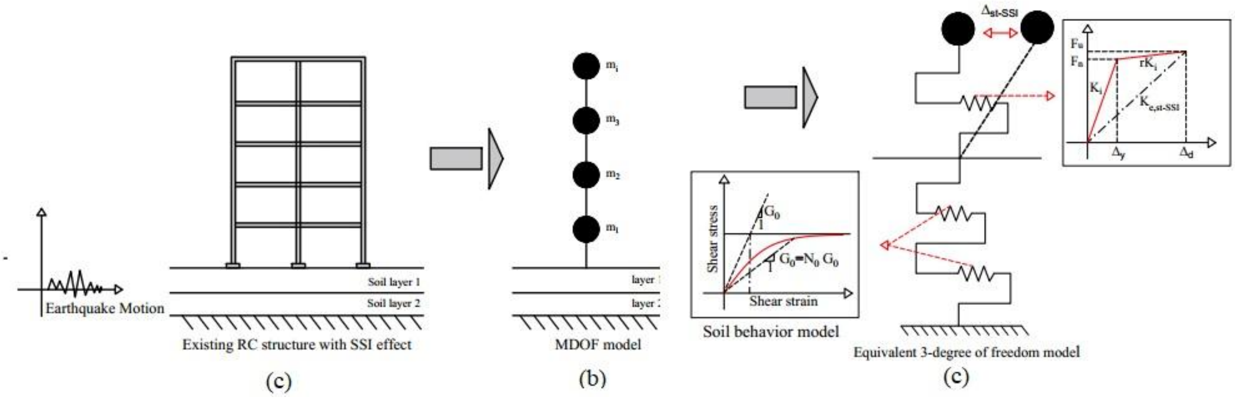

Fig. 8. Framework of WTMLM: (a) Existing RC frame with two layers of soil (b) MDOF model (c) Proposed equivalent three-degree-of-freedom model.

4. Application of the proposed WTMLM to case study, models

4.1. Seismic ground motion inputs

A set of seven real ground motions was selected from the PEER NGA-West2 database to design the case study structures, as listed in Table 2. Fig. 9 shows that the spectral accelerations of these records were scaled to match the design spectrum for site class B, as specified in ASCE/SEI 7-22 [1]. Amplitude scaling was adopted in accordance with ASCE 7-22 [1], with each record scaled individually so that its 5% damped response spectrum, averaged over the period range from 0.2T to 1.5T, does not fall below the corresponding design spectrum. For the 3- storey case study frames, this period range spans approximately 0.076 s to 0.574 s, as shown in Fig. 9. No spectral matching was employed, ensuring the preservation of the original frequency content and non-stationary characteristics of the ground motions. Following the procedure in the flowchart of Fig. 6, the seven earthquake records were converted into seven pairs of approximate and detail functions. For instance, Figs. 10 and 11 display the approximate and detail wavelets for the R4 and R6 signals alongside their equivalent pulse functions. The equivalent pulses generated with WTMLM for the remaining signals are provided in Table 3. It should be noted that all generated pulse signals are used in the following subsection to formulate the dynamic equilibrium equations for the case study structures, including SSI effects.

Table 2. Details of earthquake signals.

No.	Earthquake name	Station	PGA (m/s^2)
R1	Cape Mendocino, 1992	89324 Rio Dell Overpass-FF	0.385
R2	Chi-Chi, Taiwan, 1999	TCU045	0.474
R3	Kocaeli, Turkey, 1999	Arcelik	0.149
R4	Landers, 1992	23 Coolwater	0.283
R5	Loma Prieta, 1989	1652 Anderson Dam	0.240
R6	Northridge, 1994	24688 LA –UCL Grounds	0.278
R7	San Fernando, 1971	128 Lake Hughes	0.283

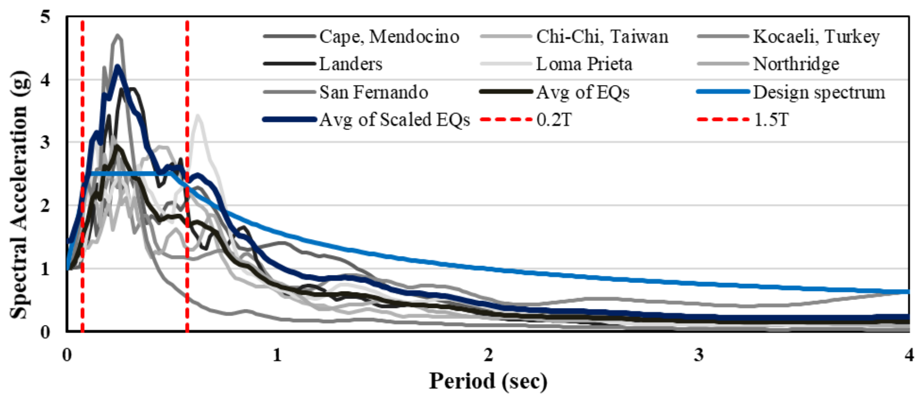

Fig. 9. Response spectra of the scaled records and the design spectrum for 3-storey structure.

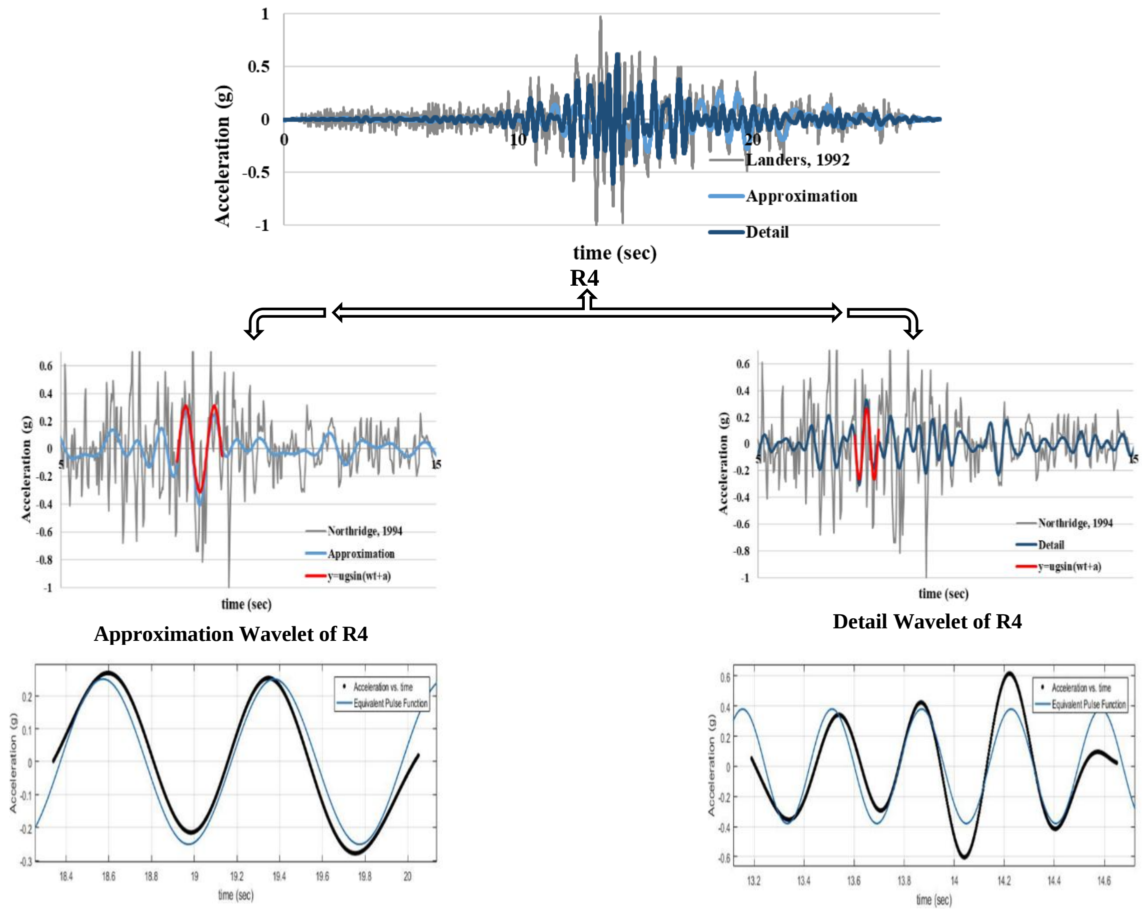

Equivalent Pulse Function:
$y = 0 \cdot 2511 sin(7 \cdot 844t - 12 \cdot 17)$

Equivalent Pulse Function:
$y = 0 \cdot 38 sin(17 \cdot 56t - 3 \cdot 229)$

Fig. 10.WTMLM flowchart for equivalent pulse signal generation (example: record R4).

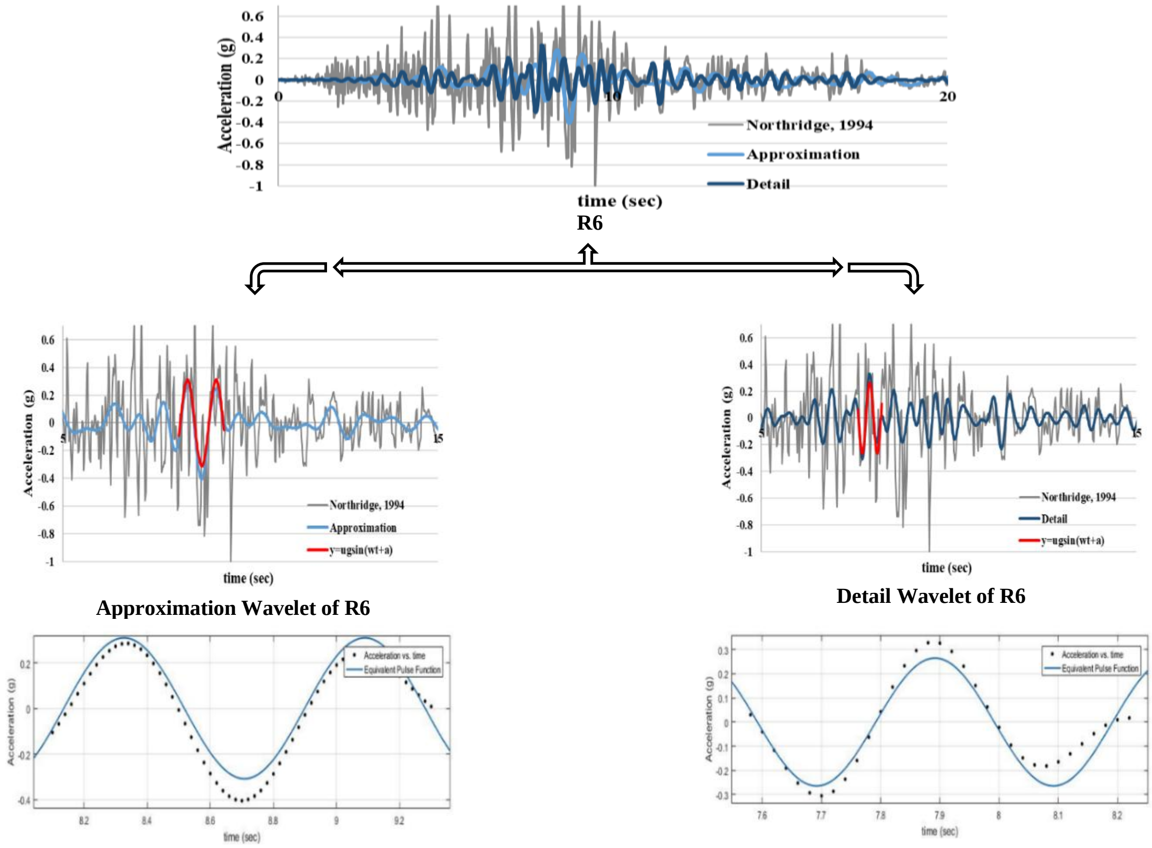

Equivalent Pulse Function:
$y = 0 \cdot 3095 sin(8 \cdot 234t - 23 \cdot 01)$

Equivalent Pulse Function:
$y = 0 \cdot 265 sin(15 \cdot 7t + 28 \cdot 43)$

Fig. 11. WTMLM flowchart for equivalent pulse signal generation (example: record R6).

Table 3. Characteristics of equivalent pulse function.

Signal Names	Equivalent Pulse Function From Approximation Wavelet	Equivalent Pulse Function From Detail Wavelet
R1	$y = 0 \cdot 189sin(4 \cdot 21t + 0 \cdot 47)$	$y = 0 \cdot 3941sin(7 \cdot 98t - 14 \cdot 41)$
R2	$y = 0 \cdot 1541sin(4 \cdot 44t + 84 \cdot 05)$	$y = 0 \cdot 6713sin(13 \cdot 12t - 5 \cdot 90)$
R3	$y = 0 \cdot 2991sin(1 \cdot 67t + 0 \cdot 86)$	$y = 0 \cdot 3041sin(16 \cdot 03t - 79 \cdot 06)$
R4	$y = 0 \cdot 2511sin(7 \cdot 84t - 12 \cdot 17)$	$y = 0 \cdot 38sin(17 \cdot 56t - 3 \cdot 23)$
R5	$y = 0 \cdot 4159sin(9 \cdot 21t - 24 \cdot 51)$	$y = 0 \cdot 4414sin(13 \cdot 81t - 15 \cdot 82)$
R6	$y = 0 \cdot 3095sin(8 \cdot 23t - 23 \cdot 01)$	$y = 0 \cdot 265sin(15 \cdot 70t + 28 \cdot 43)$
R7	$y = 0 \cdot 1322sin(13 \cdot 88t - 7 \cdot 51)$	$y = 0 \cdot 8154sin(25 \cdot 80t - 3 \cdot 30)$

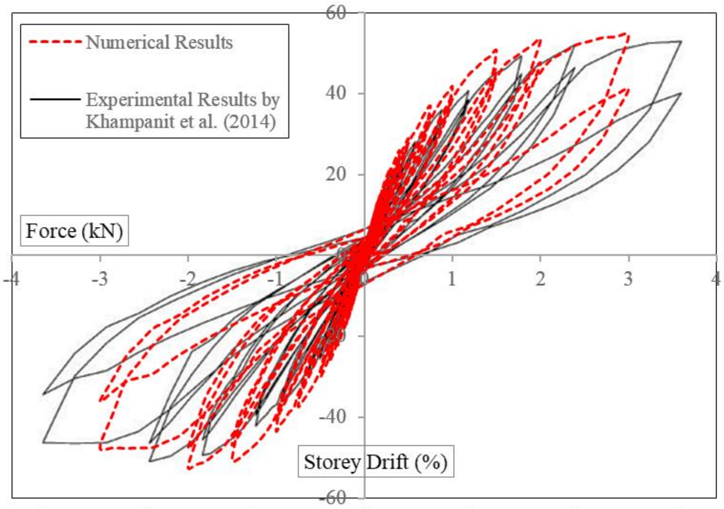

Fig. 12. Comparison of load-displacement responses from the numerical model and the experimental test by Khampanit et al. [31].

4.2. Validation of RC frame numerical modeling

To validate the modeling approach, the numerical model of the RC frame was verified against an experimental test. This study utilizes OpenSees, an open-source software, to perform all numerical analyses. The experimental benchmark is based on the work of Khampanit et al. [31]. Further details on the specifications and dimensions of the experimental RC frame model sections tested under cyclic loading can be found in Khampanit et al. [31]. For the numerical modeling, unconfined and confined concrete were modeled using the *Concrete01* material model, while reinforcing steel was modeled with *Steel02*. The effects of concrete confinement were considered by modeling closed stirrups at specified intervals and defining a separate concrete cover region. The fiber section method was employed to model the beam-column elements. A comparison of the load-displacement responses from the numerical and experimental analyses is presented in Fig. 12. The close agreement between the two results confirms the accuracy of the numerical modeling technique.

4.3. Design of case study structures

Five RC frame structures on two-layer soil profiles were designed using the WTMLM, as illustrated in Fig. 13. As shown in Fig. 14, the structures have a regular plan with moment-resisting connections. The frames are 3, 6, 9, 12, and 15 stories tall, respectively, with a story height of 3.2 m and a two-bay length of 5 m per bay. Uniform dead and live loads of 5 kN/m² and 2 kN/m², respectively, were applied to all floors. The seismic weight for each story was calculated based on the tributary area of the gravity columns. The structural models are founded on two distinct soil layers, whose properties are detailed in Table 4.

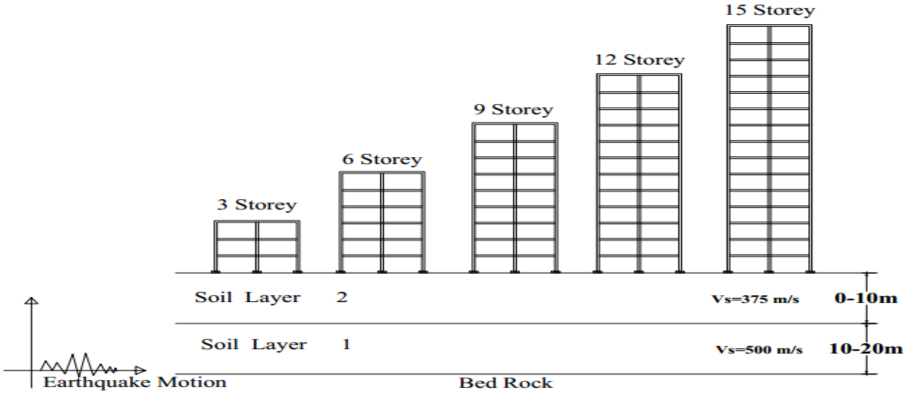

Fig. 13. Structural models of 3, 6, 9, 12 and 15 stories with two soil layers.

The target performance level was set at a 2% drift ratio, corresponding to a repairable damage state [7]. According to Table 4, the shear wave velocities at the bedrock for the first and second soil layers are 375 m/s and 500 m/s, respectively. For each case study, the dynamic equilibrium equation was formulated and solved following the WTMLM outlined in Fig. 6. This analysis was repeated for each ground motion record, and the maximum responses were used to compute the final design base shear. The characteristics of the proposed equivalent three-degree-of-freedom (3DOF) system, including demand displacement, equivalent mass, and effective height, are summarized in Table 5.

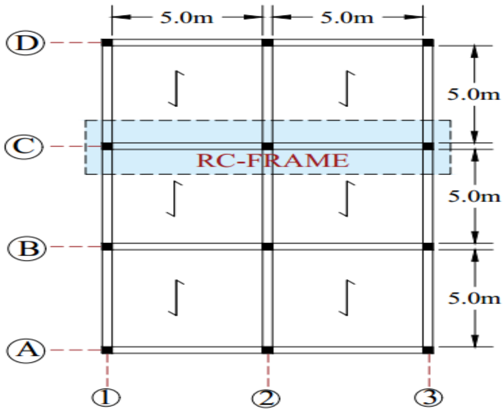

Fig. 14. Plan of Structures.

Table 4. Characteristics of soil layers.

Layer	height (m)	V_s (m/s)	Damping (%)	γ ($^{t}/_{m^3}$)	G_0 ($^{ton}/_{m^2}$)	G ($^{ton}/_{m^2}$)	K_i ($^{ton}/_{m}$)	m_i (ton)
1	0-10	375	5	1.6	22936	9633	963.3	0.815
2	10-20	500	5	2	50968	21407	2140.7	1.83

Table 5. Design results of WTMLM.

Story	Δ_{d-SSI} (m)	m_e (T)	H_e (m)	μ	T_{e-SSI} (s)	V_{st-SSI} (kN)
3	0.0148	201.84	7.28	1.60	0.333	1063.8
6	0.0062	381.61	13.50	1.51	0.213	2059.1
9	0.0133	559.53	19.74	1.45	0.309	3074.2
12	0.0327	736.94	25.98	1.40	0.481	4123.3
15	0.0502	914.15	32.21	1.35	0.641	4420.4

Table 6. Final results of lateral loads.

Level	Lateral Forces of WTMLM (kN)				
	3-storey frame	6-storey frame	9-storey frame	12-storey frame	15-storey frame
1	201.75	114.67	80.59	62.64	43.75
2	366.82	219.37	156.58	122.60	86.03
3	495.20	314.09	227.96	179.91	126.82
4		398.85	294.74	234.55	166.14
5		473.63	356.92	286.52	203.96
6		538.45	414.48	335.83	240.30
7			467.44	382.47	275.16
8			515.80	426.45	220.36
9			559.55	467.77	308.53
10				506.42	370.83
11				542.40	399.76
12				575.72	427.20
13					453.16
14					477.63
15					500.62

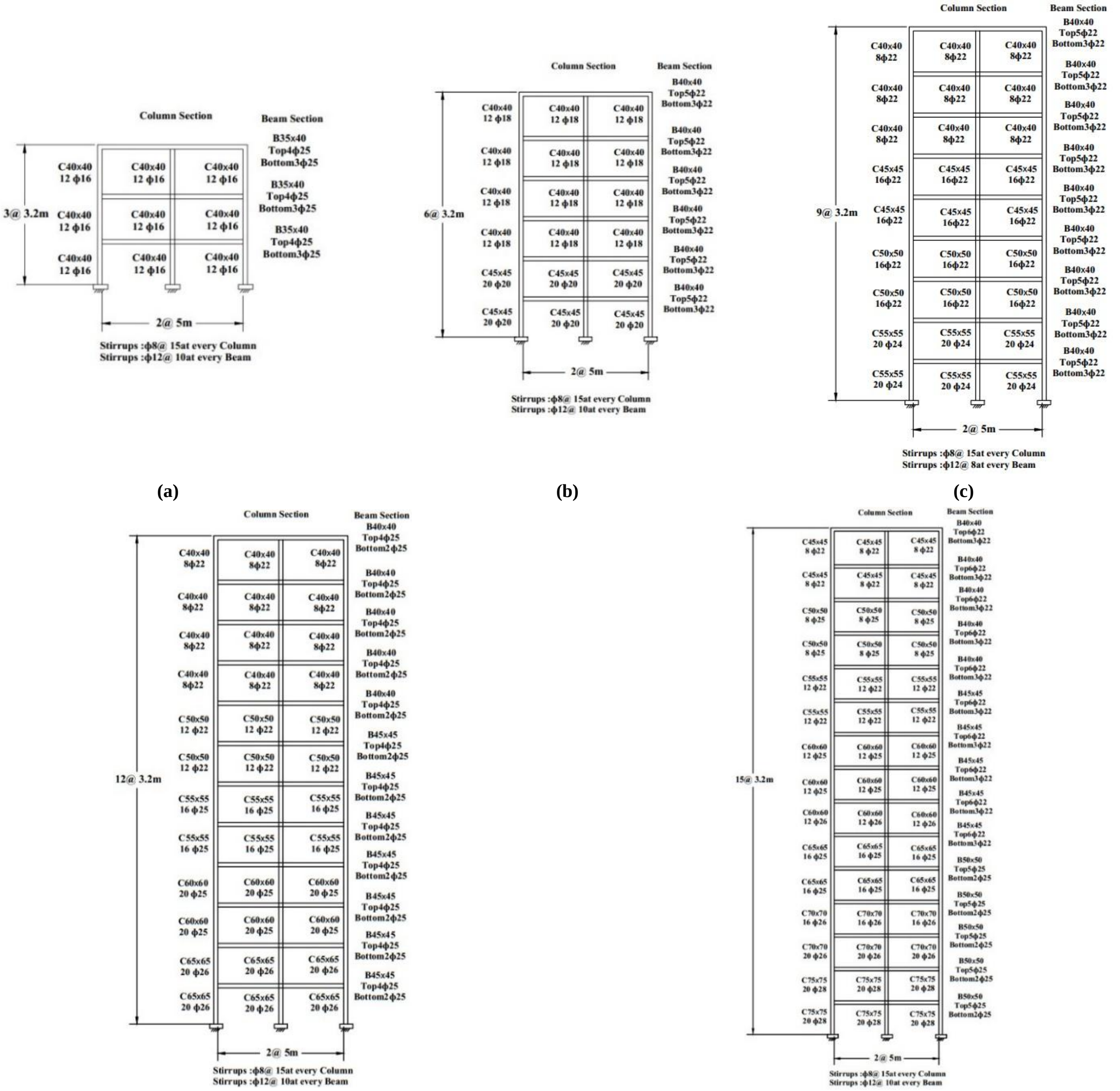

(a) (b) (c)

(d) (e)

Fig. 15. Final design section results: a) 3-storey, b) 6-storey, c) 9-storey, d) 12-storey, e) 15-storey.

The final design base shear, calculated using Eq. 49, is presented in the last column of Table 5. Table 6 shows the resulting lateral forces distributed over the height of each frame. These forces are used to determine the design forces and moments for the structural members. All members are designed based on structural analysis, following the strong column-weak beam principle to ensure plastic hinges form at the beam ends [30]. The final cross-sections of the designed RC frames are shown in Fig. 15.

5. Nonlinear time-history analysis (NTHA) results

To validate the proposed WTMLM, all designed frames are evaluated using nonlinear time-history analysis (NTHA) with real earthquake records. The NTHA employs a two-dimensional model constrained against out-of-plane deformation. All analyses are performed using the open-source software OpenSees. The Concrete01 and Steel02 material models are used for concrete and reinforcing steel, respectively. Concrete confinement is modeled by specifying closed stirrups at appropriate intervals and defining a separate concrete cover. Beam-column sections are modeled using the fiber method. Gravity loads are applied as distributed loads on the beams using the eleLoad command, while seismic masses are assigned to nodes using the mass command. Geometric nonlinearity and P-Delta effects are incorporated using the geomTransf PDelta command for column elements. All NTHAs are performed using the Newmark integration method with $\gamma = 0.5$ and $\beta = 0.25$. The analysis time step is defined by the original earthquake record. A tangent stiffness-proportional Rayleigh damping model with 5% viscous damping is assigned to the numerical models.

Soil layers are modeled using shear beam theory; each layer is represented by a concentrated mass and springs, as illustrated in Fig. 1. To validate the proposed WTMLM, NTHAs were performed on all five frames using the seven real ground motion records. The inter-story drift ratios and displacement profiles for each frame are presented in the following figures. Figs. 16 to 18 show the inter-story drift distributions from the analyses. The drift profile indicates that the drift ratio is lowest at the first story, increases to a maximum at approximately mid-height, and then decreases toward the top of the frame. In these profiles, the horizontal axis represents the drift ratio (in percent), and the vertical axis represents the story level. The target performance level is marked by a vertical dashed line at 2% drift, corresponding to the repairable damage state. Fig. 16a presents the inter-story drift ratio diagram for the three-story RC frame designed without SSI effects, while Fig. 16b shows the same diagram including SSI effects. A design capacity line, representing the minimum capacity of structural and non-structural members for the repairable damage level, is also included. As shown in both figures, the average inter-story drift across the seven earthquake records remains below this capacity line. This confirms that the WTMLM accurately achieves the target performance level.

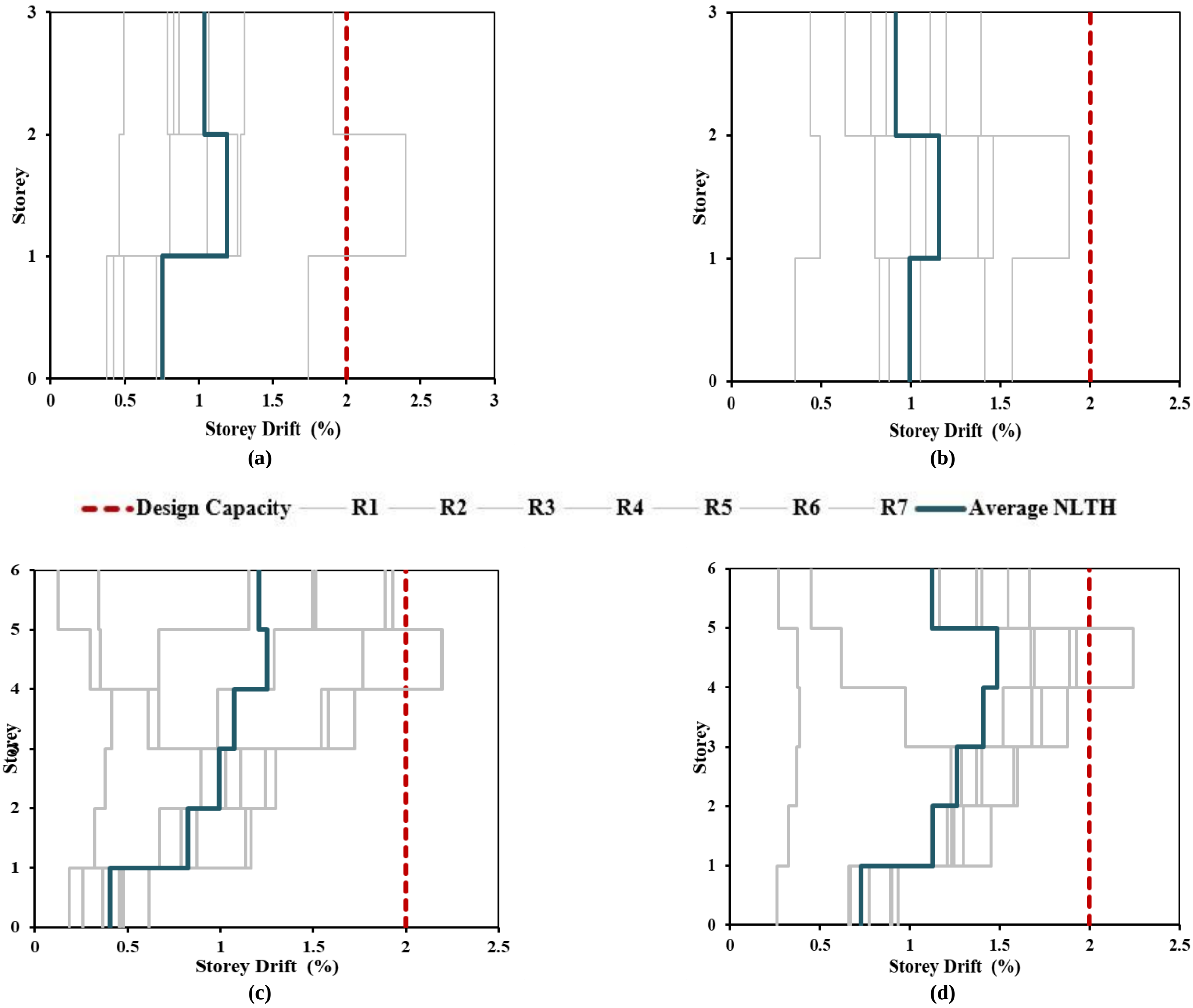

Fig. 16. The interstorey drift profiles obtained by NTHA of frames designed by WTMLM: (a) 3-storey frame without SSI effect, (b) 3-storey frame with SSI effect, (c) 6-storey frame without SSI effect, (d) 6-storey frame with SSI effect.

The results for the 6-story frame are shown in Figs. 16c and 16d, while those for the 9- and 12-story frames are presented in Figs. 17a to 17d. The behavior of these frames is similar to that observed in the 3-story RC frame. However, as shown in Figs. 18a and 18b, the average inter-story drift ratio profile for the 15-story RC frame exceeds the capacity corresponding to the repairable damage performance level, particularly from the 6th to the 10th stories. While this exceeds the repairable limit, the results still satisfy the life safety performance level. The displacement profile was modified according to Eq. 12 to account for higher-mode effects. Nonetheless, the results for the 15-story frame indicate that this modification needs to be intensified for structures of 15 stories or more, likely requiring an increased design base shear. Fig. 19 illustrates the roof displacement time history for all RC frames subjected to the Landers 1992 (R7) earthquake. The plot confirms that the maximum roof displacement in all models is below the acceptable limit, taken as 2% of the structure's height. These results further demonstrate that the proposed WTMLM provides adequate precision in controlling the displacement of the designed structures. It is worth noting that the proposed WTMLM demonstrates accurate prediction of seismic demands and effective capture of ground motion frequency content across multiple RC frame case studies. However, a direct quantitative comparison with existing pulse-based excitation models and SSI replacement oscillator approaches is not included in the present study. This is primarily because no comparable wavelet-based pulse generation methodology currently exists in the literature. Nevertheless, benchmarking against established code-based procedures, evaluating key performance metrics such as displacement error, drift accuracy, and computational efficiency, is essential to further establish the practical advantages of the framework. This critical comparison is identified as a priority for future research.

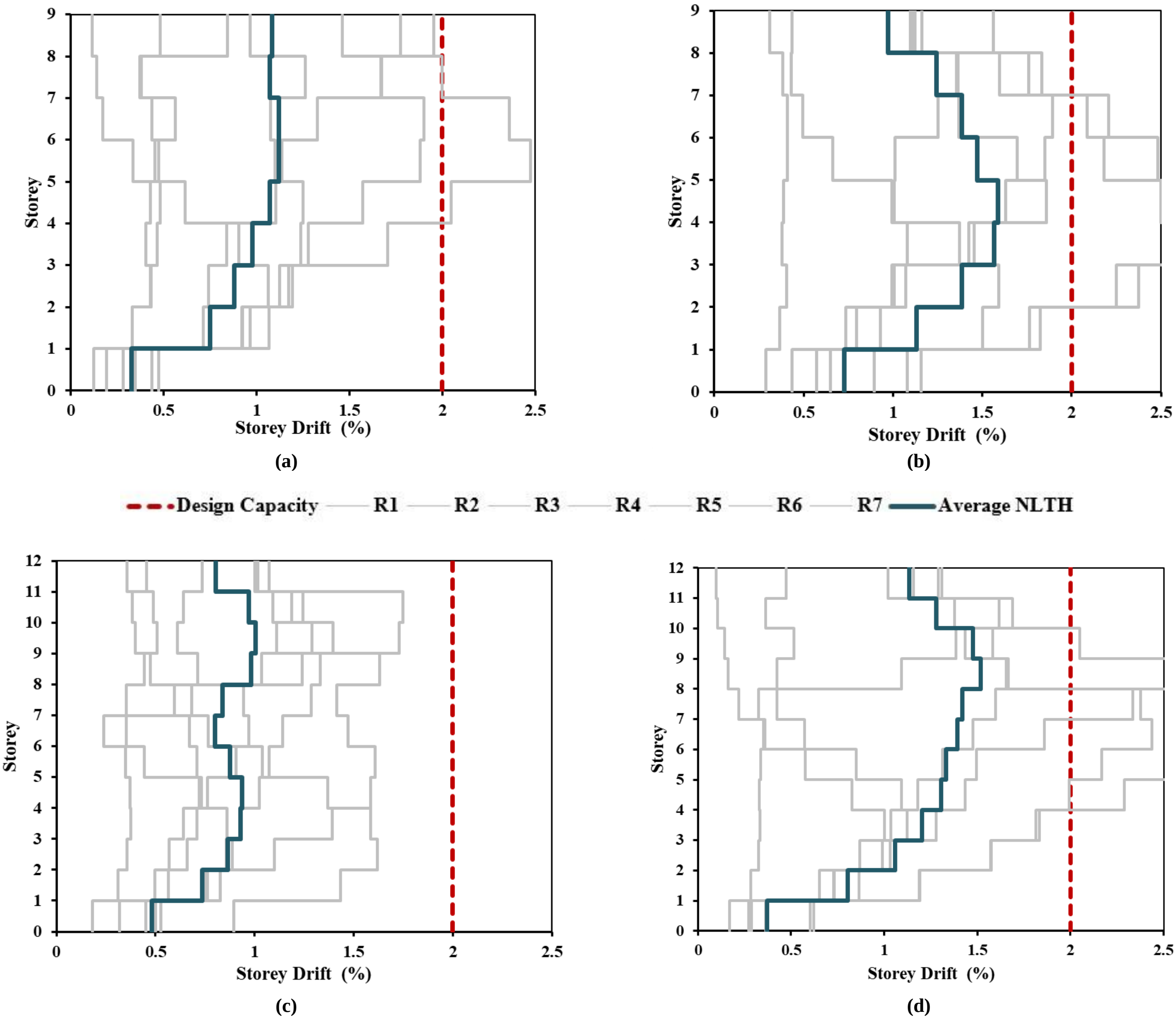

Fig. 17. The interstorey drift profiles obtained by NTHA of frames designed by WTMLM: (a) 9-storey frame without SSI effect, (b) 9-storey frame with SSI effect, (c) 12-storey frame without SSI effect, (d) 12-storey frame with SSI effect.

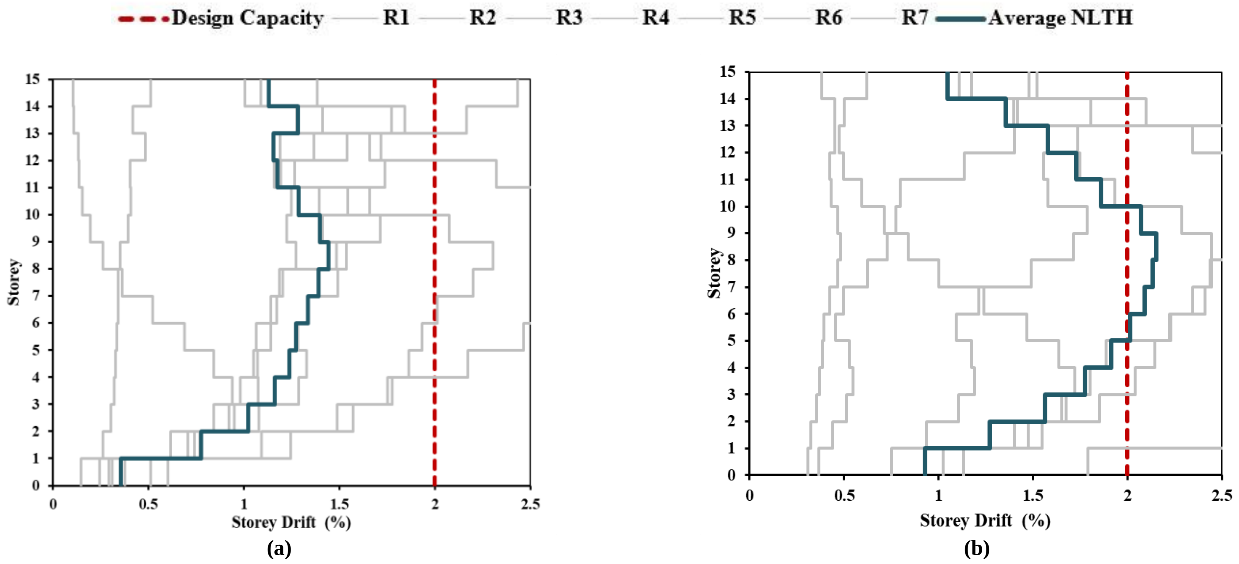

Fig. 18. The interstorey drift profiles obtained by NTHA of frames designed by WTMLM: (a) 15-storey frame without SSI effect, (b) 15-storey frame with SSI effect.

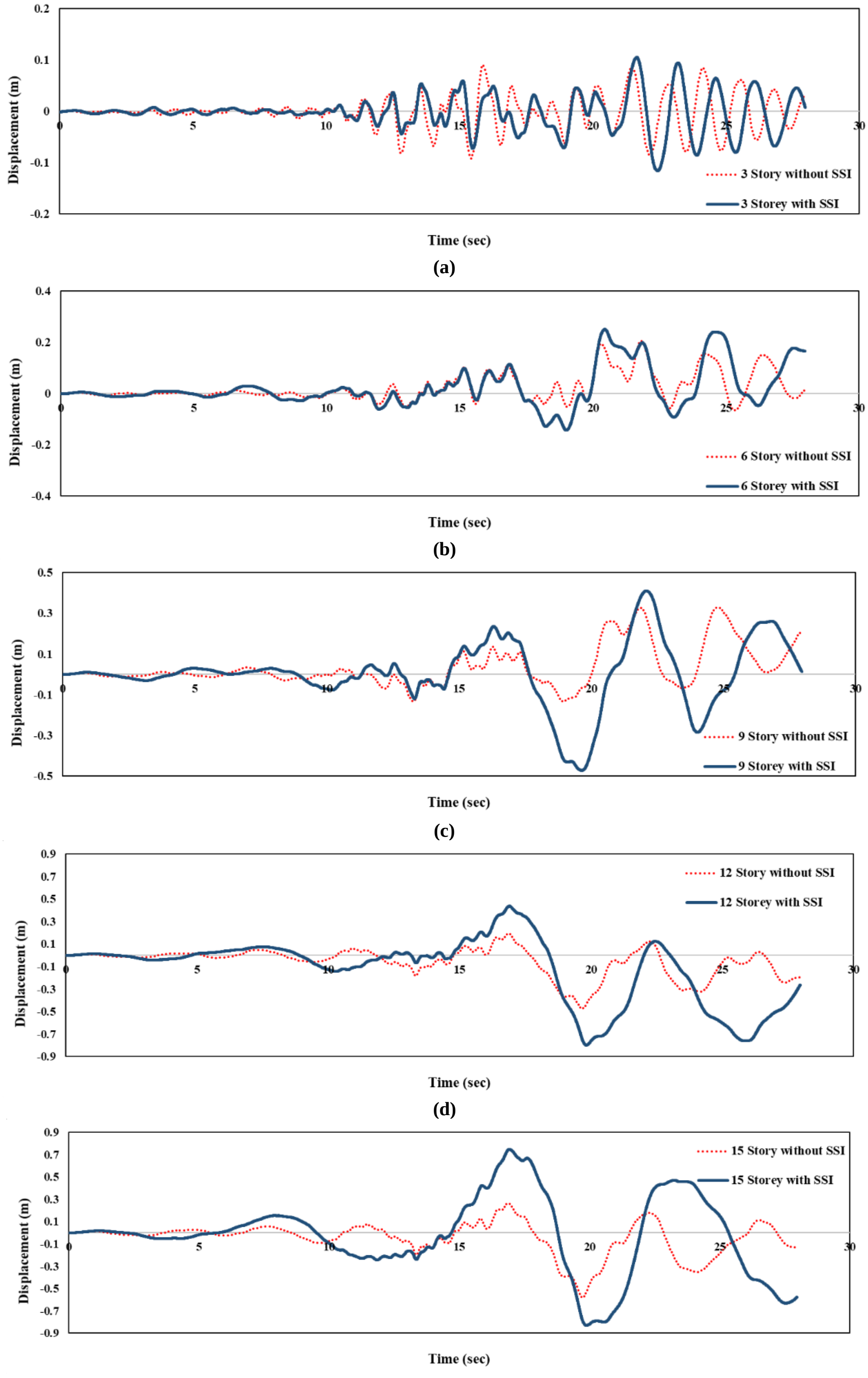

Fig. 19. Comparison of the roof displacement time history of frames designed by WTMLM under the Landers, 1992 (R7) Earthquake with and without the SSI Effect: (a) 3-storey Frame, (b) 6-storey Frame, (c) 9-storey Frame, (d) 12-storey Frame,(e) 15-storey Frame.

The average maximum lateral displacement profiles from the NTHA are presented in Figs. 20 to 24. These figures illustrate the maximum displacement response for each case study structure. For all cases, the average displacement of the RC frames from the NTHA is less than the design capacity displacement. The satisfactory performance of each frame, as evidenced by these results, demonstrates that the proposed WTMLM is a robust method for the seismic design of RC frames incorporating SSI effects. While the proposed WTMLM framework demonstrates promising performance for SSI-inclusive seismic design of RC frames, a systematic comparison with simplified code-based procedures (e.g., ASCE 7 [1] and BHRC-2800 [3]) remains necessary to fully establish its practical advantages. Such a comparative assessment is recommended as a focus of future work. It is noted that prior research by the Farahani et al. [4], has already examined direct displacement-based design incorporating SSI effects using detailed finite element modeling, providing a benchmark for subsequent extensions of the WTMLM framework.

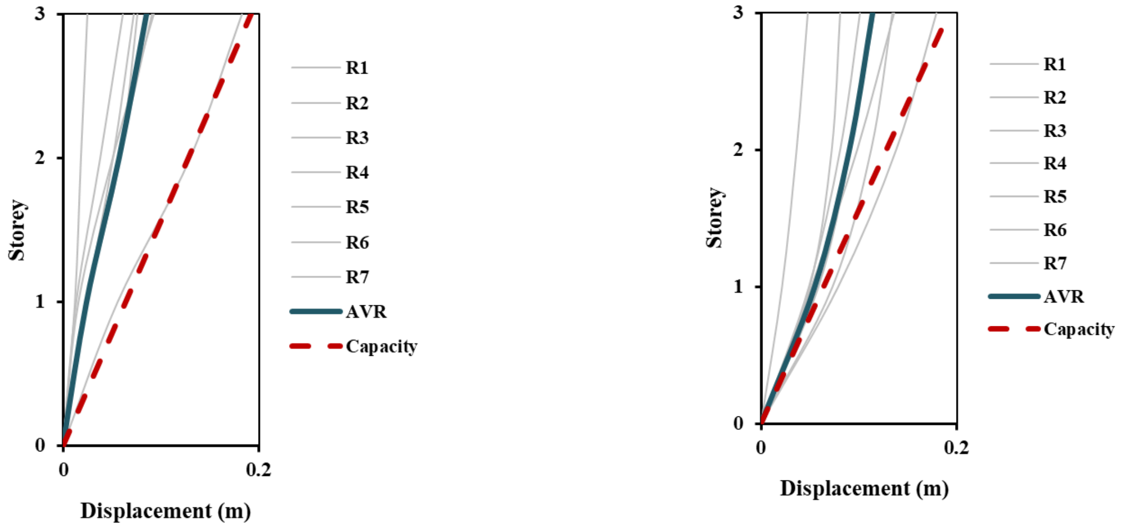

(a) (b)

Fig. 20. The displacement profiles obtained by NTHA of frames designed by WTMLM: (a) 3-storey frame without SSI effect, (b) 3-storey frame with SSI effect.

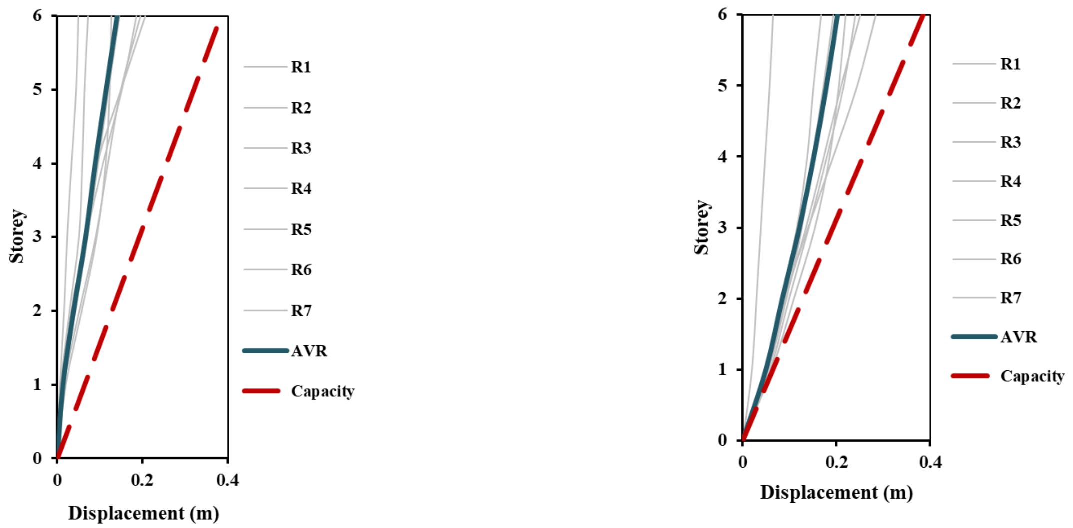

(a) (b)

Fig. 21. The displacement profiles obtained by NTHA of frames designed by WTMLM: (a) 6-storey frame without SSI effect, (b) 6-storey frame with SSI effect.

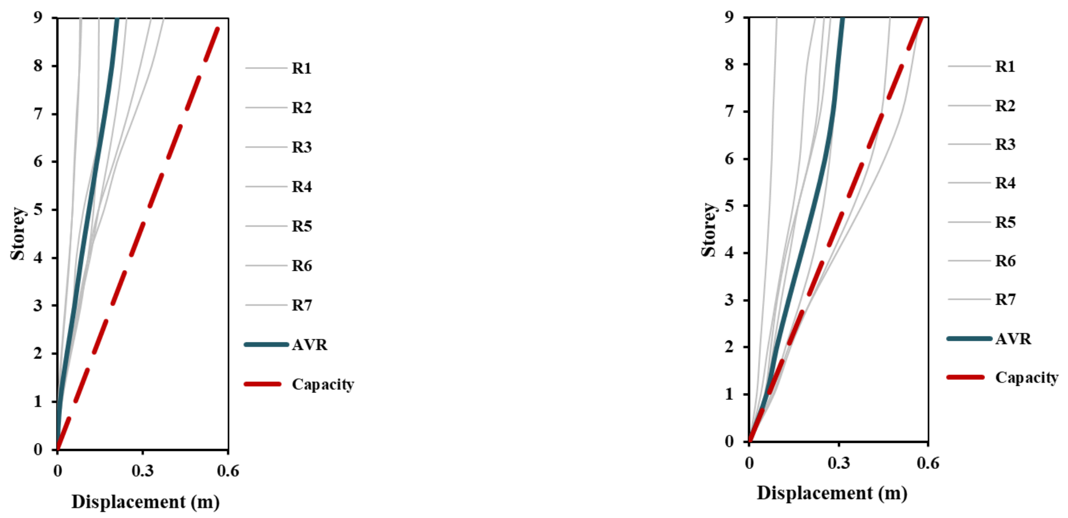

(a) (b)

Fig. 22. The displacement profiles obtained by NTHA of frames designed by WTMLM: (a) 9-storey frame without SSI effect, (b) 9-storey frame with SSI effect.

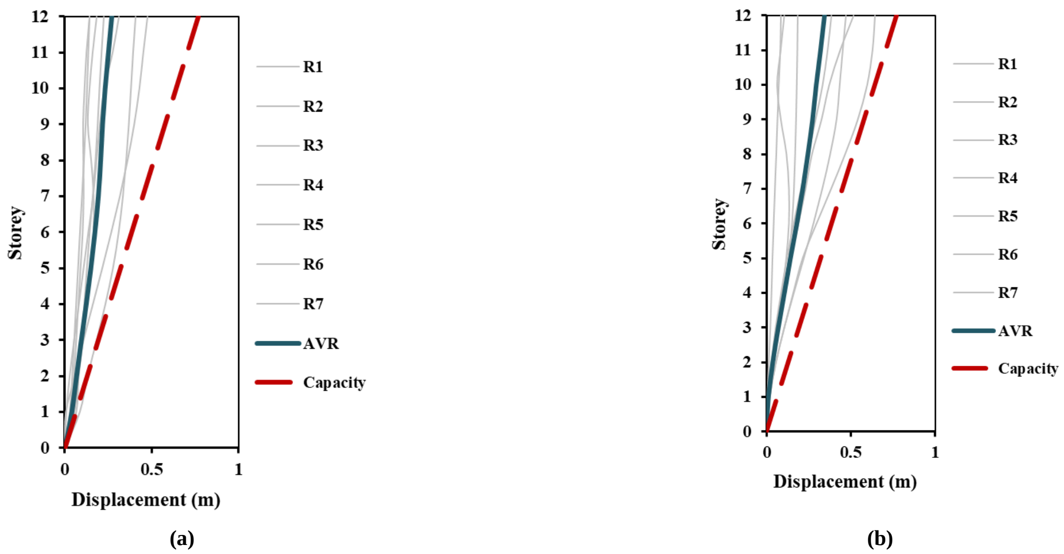

Fig. 23. The displacement profiles obtained by NTHA of frames designed by WTMLM: (a) 12-storey frame without SSI effect, (b) 12-storey frame with SSI effect.

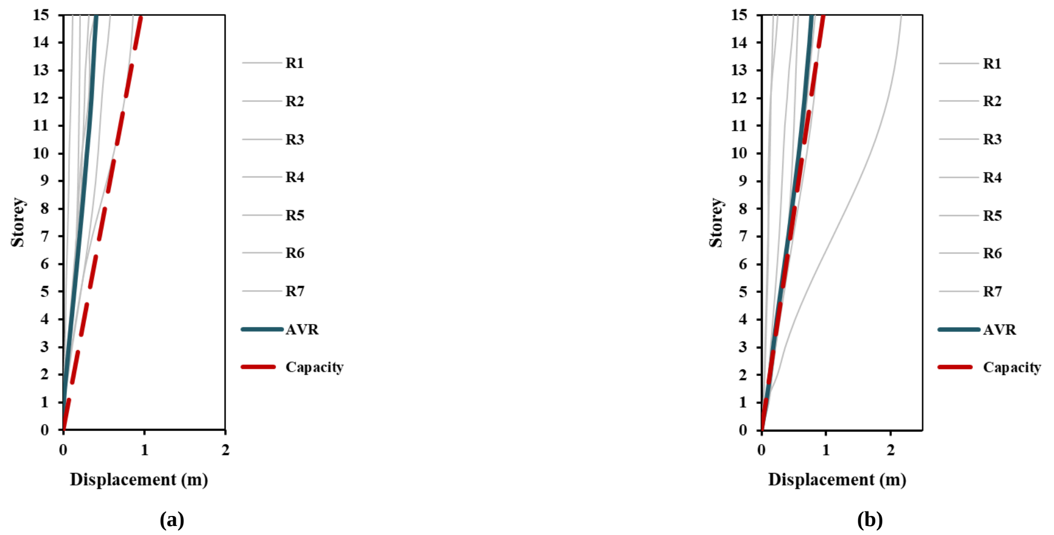

Fig. 24. The displacement profiles obtained by NTHA of frames designed by WTMLM: (a) 15-storey frame without SSI effect, (b) 15-storey frame with SSI effect.

In addition, the WTMLM framework employs equivalent linear soil modeling and linear modal analysis during the design phase to enable efficient pulse generation and system formulation. Seismic performance assessment is conducted exclusively through nonlinear time-history analysis, which fully captures material yielding and geometric nonlinearity of RC frames. The method is applicable to sites where equivalent linear soil representation is valid and for seismic intensities consistent with the employed design spectrum. Extension to strongly nonlinear soil conditions, significant structural yielding, or very high intensity levels requires further refinement and is identified as a priority for future research.

6. An ML-based formula for displacement prediction in RC frame structures

As per Eq. 12, the displacement profile for RC frames proposed by Sullivan et al. [7] is based on a first-mode shape, implying that the inter-story drift ratio decreases with height. This profile essentially represents an inelastic mode shape by treating the structure as an equivalent elastic system. For structures with SSI effects, however, the appropriate displacement profile differs fundamentally, as higher-mode effects become more significant. Consequently, a modified expression for the displacement profile is required. The original formulation inherently assumes that the elastic first-mode shape is approximately linear with height, a premise based solely on elastic behavior. To develop a modified profile, the median displacement profiles obtained from the RC frames with SSI effects (Figs. 20 to 24) were combined. A machine learning (ML)-based curve-fitting procedure [12] was implemented in MATLAB to derive an enhanced displacement profile equation for an n-story frame with SSI effects. Indeed, a supervised machine learning model was developed to predict the seismic displacement distribution of RC frames incorporating SSI effects. The model is trained on a dataset derived from median nonlinear time-history analysis results of frame configurations subjected to seven scaled ground motions on two soil types. The output is the normalized peak inter-story displacement profile.

$$\Delta_{i.RC\_SSI} = C_1\theta_c\left(\frac{H_i}{H_n}\right)\left(1-\frac{1}{C_2}\left(\frac{H_i}{H_n}\right)\right) \quad . \qquad n \le 6$$
$$\Delta_{i.RC\_SSI} = C_3\theta_c\left(\frac{H_i}{H_n}\right)\left(1-\frac{1}{C_4}\left(\frac{H_i}{H_n}\right)+\frac{1}{C_5}\left(\frac{H_i}{H_n}\right)^2\right) \quad . \qquad 6 < n \le 12 \tag{51}$$
$$\Delta_{i.RC\_SSI} = C_6\theta_c\left(\frac{H_i}{H_n}\right)\left(1+\frac{1}{C_7}\left(\frac{H_i}{H_n}\right)-\frac{1}{C_8}\left(\frac{H_i}{H_n}\right)^2\right) \quad . \qquad n > 12$$

Table 7. Coefficients of Eq. 51.

The RC frame with SSI Effect	C_1	C_2	C_3	C_4	C_5	C_6	C_7	C_8
Coefficients	13.3	2.6	24.0	2.8	32.0	42.5	4.7	3.3

The coefficients for Eq. 51 are provided in Table 7. Figs. 25 to 29 compare the displacement response profiles calculated using Eq. 12 and the proposed Eq. 51 against the median response profiles from the NTHA of RC frames with SSI effects. In these figures, the horizontal axis represents the displacement from the NTHA, while the vertical axis represents the displacement calculated from the equations. For clarity, results from Eq. 12 are marked with red triangles, and results from the proposed Eq. 51 are marked with blue squares. A 1:1 line (error estimation line) is also plotted; points closer to this line indicate a more accurate prediction from the corresponding equation. As shown in Fig. 25, Eq. 12 provides a reasonable estimate for the three-story frame, as its results align more closely with the 1:1 line than those of Eq. 51. However, for the six-story frame (Fig. 26), the proposed Eq. 51 yields a better prediction. This improved accuracy is attributed to the increasing influence of SSI effects, which amplify higher-mode responses. In general, as the number of stories increases, SSI effects more significantly alter the fundamental vibration mode through higher-mode participation. Consequently, unlike the proposed Eq. 51, Eq. 12 becomes increasingly inaccurate for taller frames due to its inability to account for these effects, as demonstrated for the 9-, 12-, and 15-story frames in Figs. 27, 28, and 29, respectively. Furthermore, the coefficient of determination (R^2) for the proposed equation, presented in Table 8, confirms that Eq. 55 accurately predicts displacements for RC frames with SSI effects. These results validate that the proposed Eq. 55 is a suitable replacement for Eq. 12 for predicting the displacement of RC frames incorporating SSI.

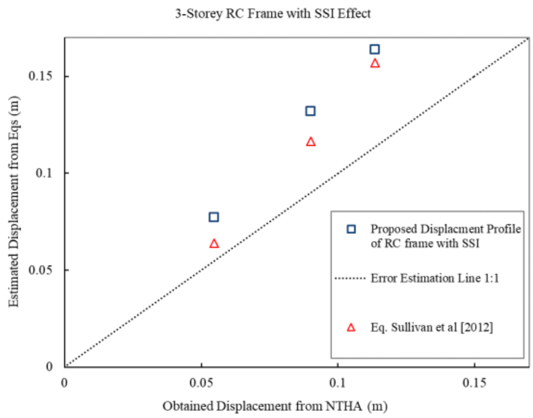

Fig. 25. Comparison of NTHA results with displacement profiles estimated by Sullivan et al. [7] (Eq. 12) and the proposed Eq. 51 for the 3-story RC frame with SSI effects.

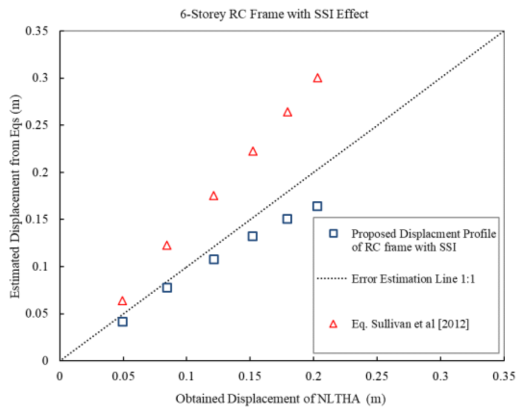

Fig. 26. Comparison of NTHA results with displacement profiles estimated by Sullivan et al. [7] (Eq. 12) and the proposed Eq.51 for the 6-story RC frame with SSI effects.

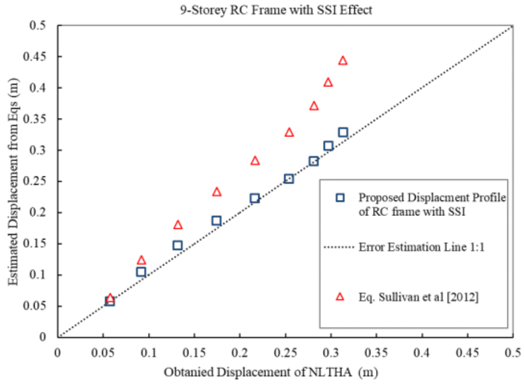

Fig. 27. Comparison of NTHA results with displacement profiles estimated by Sullivan et al. [7] (Eq. 12) and the proposed Eq. 51 for the 9-story RC frame with SSI effects.

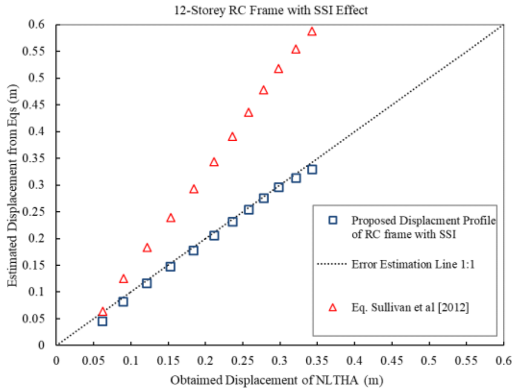

Fig. 28. Comparison of NTHA results with displacement profiles estimated by Sullivan et al. [7] (Eq. 12) and the proposed Eq. 51 for the 12-story RC frame with SSI effects.

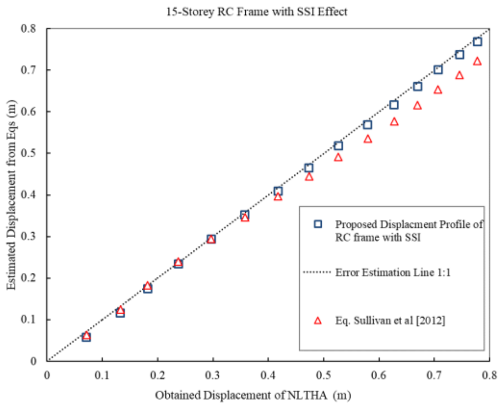

Fig. 29. Comparison of NTHA results with displacement profiles estimated by Sullivan et al. [7] (Eq. 12) and the proposed Eq. 51 for the 15-story RC frame with SSI effects.

Table 8. Coefficient of determination R2 of the proposed equation.

Proposed Equation	ML-Based formula for displacement prediction		
	Eq. 51 $n \leq 6$	**Eq. 51** $6 < n \leq 12$	**Eq. 51** $n > 12$
R^2 (%)	82	98	99

7. Summary and conclusion

This study proposes a novel Wavelet Transform-based Machine Learning Method (WTMLM) for the seismic design of reinforced concrete (RC) frames, explicitly incorporating soil-structure interaction (SSI) effects. The methodology introduces an equivalent three-degree-of-freedom (3DOF) system, solving the dynamic equilibrium equations to account for SSI. A new wavelet transform technique was developed to generate equivalent pulse-type excitation models. Consequently, new equations for demand displacement and stiffness were formulated, along with a novel design displacement profile capable of predicting the higher-mode amplifications induced by SSI. To validate the proposed method, five RC frames (3, 6, 9, 12, and 15 stories) were designed for a repairable damage performance level and subsequently analyzed using nonlinear time-history analysis (NTHA) under seven scaled earthquake records. The results, based on an evaluation of displacement and inter-story drift ratio profiles, are summarized as follows:

- The proposed wavelet transform method effectively generates pulse-type functions by directly processing the primary earthquake acceleration while preserving the fundamental design frequencies. This approach is more practical than previous velocity-based methods, which often retain non-essential frequency content.
- The shear beam SSI model outperforms the cone model due to its detailed multi-layered representation of soil, which provides a more realistic basis for the design process.
- The NTHA results confirm that all RC frames designed using the WTMLM, except the 15-story frame, satisfied the 2% inter-story drift limit for the repairable damage performance level, demonstrating the method's success for low- to mid-rise structures with SSI.
- The drift profile of the 15-story frame with SSI exceeded the repairable limit, particularly between the 6th and 10th stories. This indicates that the higher mode effect coefficient may require modification to account for intensified higher-mode effects in taller structures, a subject for future research.
- For the 15-story frame with SSI, the NTHA results indicate that while the average drift in some stories exceeded the repairable limit (2%), it remained below the life safety limit (2.5%), thus still meeting code requirements.
- The results confirm that the proposed ML-based formula is a suitable and more accurate replacement for the available equation in the design of RC frames with SSI effects. Future work should focus on refining this profile for a broader range of structural configurations and soil parameters.

A key limitation of the current model is the exclusion of the foundation's rocking degree of freedom. This assumption is valid for the investigated regular RC structures but may require extension for taller buildings or softer soil conditions where rocking becomes a dominant response mechanism. Additionally, the validation is limited to regular RC frames on two-layer stiff soil profiles. Future research will focus on enriching the WTMLM framework by integrating rotational soil springs and exploring its applicability to structures founded on softer soils and taller building configurations.

Statements & Declarations

Author contributions

Sina Farahani: Investigation, Formal analysis, Data curation, Software, Writing - Original Draft.

Funding

The authors received no financial support for the research, authorship, and/or publication of this article.

Data availability

The data presented in this study will be available on request from the corresponding author.

Declarations

The authors declare no conflict of interest.

References

[1] American Society of Civil Engineers (ASCE). ASCE/SEI 7-16: Minimum Design Loads and Associated Criteria for Buildings and Other Structures. Reston (VA): ASCE; 2017.

[2] British Standards Institution. CEN EN 1998-1: Eurocode 8: Design of structures for earthquake resistance. Ispra (IT): EN; 1998.

[3] Building and Housing Research Center. Standard No. 2800: Iranian code of practice for seismic resistant design of buildings. Tehran (IR): 2800; 2015.

[4] Farahani, S., Akhaveissy, A. H., Damkilde, L. Towards a modified displacement-based seismic design of braced reinforced concrete frame structures considering soil structure interaction. Structures, 2025; 75: 108443. doi:10.1016/j.istruc.2025.108443.

[5] Priestley, M., Calvi, G., Kowalsky, M. Displacement-based seismic design of structures. 1st ed. Rome (IT): IUSS Press; 2007. doi:10.1002/EQE.807.

[6] Sullivan, T. J. Highlighting Differences between Force-Based and Displacement-Based Design Solutions for Reinforced Concrete Frame Structures. Structural Engineering International, 2013; 23: 122-131. doi:10.2749/101686613X13439149156958.

[7] Sullivan, T. J., Priestley, M. J. N., Calvi, G. M. A Model Code for the Displacement-Based Seismic Design of Structures. 1st ed. Rome (IT): IUSS Press; 2012.

[8] Chopra, A. K. Dynamics of structures: theory and applications to earthquake engineering. 1st ed. Prentice Hall (NJ): Upper Saddle River; 2007.

[9] Nazarimofrad, E., Farahani, S., Zahrai, S. M. Multiobjective optimal placement of active tendons to control irregular multistory buildings with soil–structure interaction. The Structural Design of Tall and Special Buildings, 2019; 28: e1581. doi:10.1002/tal.1581.

[10] Imam, M. H., Mohiuddin, M., Shuman, N. M., Oyshi, T. I., Debnath, B., Liham, M. I. M. H. Prediction of seismic performance of steel frame structures: A machine learning approach. Structures, 2024; 69: 107547. doi:10.1016/j.istruc.2024.107547.

[11] Demir, A., Sahin, E. K., Demir, S. Advanced tree-based machine learning methods for predicting the seismic response of regular and irregular RC frames. Structures, 2024; 64: 106524. doi:10.1016/j.istruc.2024.106524.

[12] Farahani, S., Barari, A. A simplified procedure for the prediction of liquefaction-induced settlement of offshore wind turbines supported by suction caisson foundation based on effective stress analyses and an ML-based group method of data handling. Earthquake Engineering & Structural Dynamics, 2023; 52: 5072-5098. doi:10.1002/eqe.4000.

[13] Salajegheh, E., Heidari, A., Saryazdi, S. Optimum design of structures against earthquake by discrete wavelet transform. International Journal for Numerical Methods in Engineering, 2005; 62: 2178-2192. doi:10.1002/nme.1279.

[14] Kamgar, R., Tavakoli, R., Rahgozar, P., Jankowski, R. Application of discrete wavelet transform in seismic nonlinear analysis of soil–structure interaction problems. Earthquake Spectra, 2021; 37: 1980-2012. doi:10.1177/8755293020988027.

[15] Dadkhah, M., Kamgar, R., Heidarzadeh, H. Reducing the Cost of Calculations for Incremental Dynamic Analysis of Building Structures Using the Discrete Wavelet Transform. Journal of Earthquake Engineering, 2022; 26: 3317-3342. doi:10.1080/13632469.2020.1798830.

[16] Kamgar, R., Dadkhah, M., Naderpour, H. Earthquake-induced nonlinear dynamic response assessment of structures in terms of discrete wavelet transform. Structures, 2022; 39: 821-847. doi:10.1016/j.istruc.2022.03.060.

[17] Yang, J., Li, F., Zhou, J., Zhang, Y., Li, P., Henry, R. S. Experimental Investigation of Seismic Damage in RC Frame Structures With Soil-Structure Interaction Using Wavelet Packet Transformation. Earthquake Engineering and Resilience, 2025; 4: 379-399. doi:10.1002/eer2.70018.

[18] Zhang, H., Wang, L., Shi, W. Seismic intelligent retrofitting of aging steel structure using semi-active TMD with LSTM prediction and wavelet transform combined algorithm. Thin-Walled Structures, 2025; 214: 113431. doi:10.1016/j.tws.2025.113431.

[19] Asgari, A., Bagheripour, M. H. Earthquake Response Analysis of Soil Layers Using HFTD Approach. Soil Dynamics and Earthquake Engineering. 2012. p. 320-325. doi:10.1061/41102(375)39.

[20] Akbarzadeh, M. R., Naeim, B., Asgari, A., Estekanchi, H. E. Framework for multi-hazard parameterized fragility based uncertainty quantification and sensitivity analysis of offshore wind turbines. Soil Dynamics and Earthquake Engineering, 2026; 201: 109963. doi:10.1016/j.soildyn.2025.109963.

[21] Asgari, A., Ranjbar, F., Bagheri, M. Seismic resilience of pile groups to lateral spreading in liquefiable soils: 3D parallel finite element modeling. Structures, 2025; 74: 108578. doi:10.1016/j.istruc.2025.108578.

[22] Asgari, A., Ahmadtabar Sorkhi, S. F. Wind turbine performance under multi-hazard loads: Wave, wind, and earthquake effects on liquefiable soil. Results in Engineering, 2025; 26: 104647. doi:10.1016/j.rineng.2025.104647.

[23] Idriss Izzat, M., Seed, H. B. Seismic Response of Horizontal Soil Layers. Journal of the Soil Mechanics and Foundations Division, 1968; 94: 1003-1031. doi:10.1061/JSFEAQ.0001163.

[24] Federal Emergency Management Agency (FEMA). Improvement of nonlinear static seismic analysis procedures. Washington, D.C. (US): FEMA; 2005.

[25] Lu, Y., Hajirasouliha, I., Marshall, A. M. An improved replacement oscillator approach for soil-structure interaction analysis considering soft soils. Engineering Structures, 2018; 167: 26-38. doi:10.1016/j.engstruct.2018.04.005.

[26] Agrawal, A. K., He, W. L. A closed-form approximation of near-fault ground motion pulses for flexible structures. In: Engineering Mechanics: Proceedings of the 11th Conference; 1996 May 19-22; Fort Lauderdale, Florida. p. 11-24.

[27] Makris, N., Black, C. J. Dimensional Analysis of Inelastic Structures Subjected to Near Fault Ground Motions. Berkeley (CA): Earthquake Engineering Research Center, University of California; 2003. Report No.: UCB/EERC 2003-05.

[28] Amiri, J. V., Davoodi, M. R., Sahafi, A. Simulation of Near-Fault Ground Motions With Equivalent Pulses & Compare Their Effects on MRF Structures. In: Proceedings of the 14th World Conference on Earthquake Engineering; 2008 Oct 12-17; Beijing, China. p. 1-19.

[29] Misiti M, M. Y., Oppenheim G, Poggi JM Wavelet toolbox reference. 1st ed. Natick (MA): The MathWorks; 213.

[30] American Concrete Institute. ACI 318-14: Building code requirements for structural concrete (ACI 318-14). Farmington Hills (MI): ACI; 2014.

[31] Khampanit, A., Leelataviwat, S., Kochanin, J., Warnitchai, P. Energy-based seismic strengthening design of non-ductile reinforced concrete frames using buckling-restrained braces. Engineering Structures, 2014; 81: 110-122. doi:10.1016/j.engstruct.2014.09.033.

Civil Engineering and Applied Solutions

Research Article

journal homepage: ceas.journals.umz.ac.ir

CEAS Civil Engineering and Applied Solutions

Data-Driven Predictive Formulation for FRP-Confined Circular Concrete Columns

Sajjad Shayanfar [a], Meysam Ghasemi Naghibdehi [a], Javad Shayanfar [b*]

[a] *Department of Civil Engineering, Qaemshahr Branch, Islamic Azad University, Qaemshahr, Iran*
[b] *Department of Civil Engineering, University of Minho, Azurém, Guimarães 4800-058, Portugal*

A R T I C L E I N F O

Article history:

Received 10 December 2025

Revised 06 January 2026

Accepted 29 January 2026

Available online 01 January 2027

Keywords:

FRP confinement

Compressive strength

Predictive model

Design-oriented model

Confined concrete

A B S T R A C T

This study presents a new design-oriented, regression-based model for predicting the ultimate compressive strength of circular concrete columns confined with fiber-reinforced polymer (FRP) jackets. The model is grounded in fundamental confinement mechanics and accounts for key parameters, including FRP elastic modulus, ultimate tensile strain, confinement stiffness, unconfined concrete strength, and column diameter. A comprehensive and rigorously filtered experimental database comprising 1,376 FRP-confined circular concrete specimens was assembled, covering concrete strengths from 6.6 to 204 MPa and FRP types including CFRP, GFRP, BFRP, and AFRP. A carefully curated experimental database of 1,376 circular FRP-confined specimens was assembled, covering a broad spectrum of concrete strengths and FRP types. Regression analysis was used to calibrate the model, and a dimension-based correction factor was incorporated to capture the influence of cross-sectional geometry. The resulting formulation demonstrates robust predictive capability and general applicability across diverse concrete strengths and column geometries, providing a reliable tool for practical engineering design. Parametric studies further illustrate how confinement efficiency varies with concrete strength and FRP properties, offering guidance for optimizing FRP confinement in practice.

How to cite this article: Shayanfar, S., Ghasemi Naghibdehi, M., Shayanfar, J. Data-Driven Predictive Formulation for FRP-Confined Circular Concrete Columns. Civil Engineering and Applied Solutions. 2027; 3(1): 25–36. doi:10.22080/ceas.2026.30751.1060.

1. Introduction

In recent years, fiber-reinforced polymer (FRP) composites have emerged as a highly effective and widely adopted method for the seismic retrofitting and performance enhancement of reinforced concrete (RC) columns originally designed without seismic considerations [1-7]. The application of externally bonded FRP jackets provides significant improvements in both axial load-carrying capacity and lateral dilation resistance of concrete columns under compressive loading by constraining the transverse expansion of the concrete core. This confinement mechanism not only increases the ultimate compressive strength but also enhances ductility and energy dissipation under seismic actions [8-11]. Despite the extensive practical implementation of FRP confinement, the development of accurate constitutive models that predict the combined effects of FRP-induced confinement on the axial and lateral responses of concrete remains an active area of research. These models aim to capture the nonlinear interaction between concrete core behavior, FRP stiffness and thickness, number of layers, and the influence of concrete strength, providing reliable tools for both design and assessment of confined columns [12-16].

Under axial compressive loading, FRP-confined concrete columns with circular cross-sections may exhibit strain-softening behavior, which is influenced primarily by (i) the stiffness of the FRP confinement and (ii) the concrete strength class [17-21]. In general, low-strength concrete (LSC) and normal-strength concrete (NSC) columns that are adequately confined by an FRP jacket tend to demonstrate a full hardening stress-strain response accompanied by distributed micro-cracking. However, as the imposed confinement stiffness decreases, LSC and NSC columns begin to display post-peak strain-softening behavior after the transition

* Corresponding author.
E-mail addresses: arch3d.ir@gmail.com (J. Shayanfar).

https://doi.org/10.22080/ceas.2026.30751.1060
ISSN: 3092-7749/© 2027 The Author(s). Published by University of Mazandaran.

zone, similar to unconfined concrete (UC) columns when the confinement stiffness is very low. Experimental investigations into high-strength concrete (HSC) and ultra-high-strength concrete (UHSC) columns confined with FRP jackets reveal behaviors that differ notably from NSC columns, highlighting several key phenomena. Ozbakkaloglu and Akin [17] demonstrated that the confinement-induced enhancements in compressive strength and strain ductility decrease significantly as the concrete strength increases. This results in a delayed development of axial strain and stress relative to the confining FRP strain and stress. While increasing FRP confinement stiffness generally improves the response of confined concrete, the degree of improvement is strongly dependent on the concrete strength: NSC columns benefit more from increased stiffness than HSC or UHSC columns [22-26]. Unlike NSC columns, FRP-confined HSC and UHSC columns tend to exhibit post-peak strain-softening behavior following the transition zone due to this confinement lag, which often manifests as localized macro-cracks [27]. By increasing the FRP confinement stiffness, the lateral restraint can sufficiently counteract the expansive tendencies of the concrete, mitigating post-peak strength degradation. In such cases, the column may exhibit either a strain post-peak softening-hardening response or a fully hardening stress-strain behavior [19, 28-33].

For simulating the mechanical behavior of FRP-confined concrete under concentric compressive loading, numerous constitutive models have been developed [8, 24, 25, 34-40] , which can generally be classified into two categories: analysis-oriented and design-oriented models. Analysis-oriented models predict the stress–strain behavior of FRP-confined concrete using incremental dilation-based approaches (e.g., [41-48]). Axial strain is first computed from a given FRP hoop strain (i.e., confinement pressure) using a dilation model, and the corresponding axial stress is then determined via a stress–strain relation developed for actively confined concrete. Although these models assume that passively and actively confined concrete behave similarly at a given hoop strain, differences are accounted for through the failure surface function, known as the confinement path effect. Design-oriented models, in contrast, provide simplified closed-form expressions for the stress–strain response of FRP-confined concrete columns, with model parameters calibrated against experimental data [8, 49-51]. For instance, Lam and Teng [8] proposed a parabolic–linear stress–strain relationship for FRP-confined NSC columns, predicting ultimate axial stress and strain based on the actual FRP hoop strain at rupture. However, this model does not account for a descending branch in the stress–strain curve. Subsequent guidelines, such as ACI [52] and fib [53], adopted Lam and Teng's recommendations with modifications, including confinement pressure thresholds below which strength enhancement is neglected and updated formulations for calculating FRP hoop strain. Teng et al. [49] refined Lam and Teng's model by updating the ultimate strength and strain expressions using numerical results from Jiang and Teng [41] and an extended experimental database. By introducing a confinement stiffness threshold, this refined model can capture either hardening or softening behavior in the stress–strain curve. Lim and Ozbakkaloglu [54] formulated predictive expressions for ultimate axial strength and strain of FRP-confined NSC and HSC columns based on a comprehensive test dataset, though a full stress–strain model was not provided. Fallah Pour et al. [51] proposed a simplified design-oriented model using a large database of NSC and HSC columns, providing closed-form expressions for stress and strain at ultimate and transition stages. Despite the significant progress in developing stress–strain models for FRP-confined concrete, most existing models are constrained to specific concrete strength classes (e.g., NSC or HSC), limiting their general applicability across the full spectrum of concrete strengths.

Most existing models were calibrated using relatively limited experimental databases, often encompassing a narrow range of parameters such as confinement stiffness, concrete strength, and specimen geometry, and featuring low data density [55]. Consequently, their predictive reliability becomes questionable when applied to broader datasets that cover a wider spectrum of concrete strengths, FRP properties, and column geometries. The accuracy and reliability of regression-based predictive formulations for FRP-confined concrete are fundamentally dependent on the quality, diversity, and comprehensiveness of the experimental database used for model calibration [56]. A high-quality database must encompass a wide range of key parameters, including concrete compressive strength, FRP mechanical properties, column geometry, and confinement configurations, to fully capture their individual and interactive effects on structural behavior. Inadequate, sparse, or biased datasets can lead to models that are valid only within limited parameter ranges, thereby reducing their generalizability and predictive robustness. Moreover, a comprehensive and statistically representative database enables rigorous regression analysis, allowing the derivation of model coefficients that accurately reflect both the mean response and variability in experimental outcomes. This ensures that the resulting predictive formulation can reliably estimate ultimate axial strength, strain capacity, and stress–strain behavior under various confinement conditions, while also providing a sound basis for uncertainty quantification in practical design applications.

In this study, a new design-oriented constitutive model is developed to predict the ultimate compressive strength of circular concrete columns confined with FRP jackets. The model is grounded in the fundamental mechanics of confinement, explicitly incorporating the effects of FRP material properties (elastic modulus and ultimate tensile strain), confinement stiffness, unconfined concrete strength, and, critically, the cross-sectional size through a dimension-based correction factor. Leveraging a large, high-quality experimental database of 1,376 specimens that spans low- to ultra-high-strength concrete and a wide array of FRP types and configurations, the model is calibrated using robust regression techniques. Unlike many existing formulations that are limited to specific concrete strength ranges or neglect geometric scale effects, the proposed model offers a unified, accurate, and broadly applicable prediction framework. Its development addresses a critical gap in current practice by reconciling mechanistic principles with empirical evidence across the full spectrum of practical FRP confinement scenarios, thereby enhancing the reliability of strength assessments in both retrofit and new-design applications. It should be emphasized that the contribution of this study extends beyond empirical recalibration using an expanded dataset. A key innovation lies in the explicit recognition and quantification of geometric scale effects, specifically, the reduction in confinement effectiveness with increasing column diameter, which has been historically overlooked or implicitly absorbed into empirical coefficients in existing models. This work introduces a mechanistically informed, dimension-based correction factor that directly accounts for this phenomenon. Furthermore, the proposed formulation achieves true unification across an unprecedented concrete strength range (6.6–204 MPa) through a single, continuous expression governed by confinement stiffness, rather than relying on piecewise functions or strength-class-specific calibrations. These features represent a conceptual advance in transitioning from purely empirical correlations toward physics-informed, data-driven modeling of FRP-confined concrete.

2. Compressive behavior of concrete confined with FRP jackets

The fundamental principle governing the confinement mechanism of FRP-jacketed concrete is as follows: when a certain level of axial strain (ε_c) is applied to the concrete, a corresponding radial (lateral) strain $\varepsilon_l = \nu \times \varepsilon_c$ develops according to Poisson's ratio (ν) [57]. Since the radial strain is equal to the hoop strain ($\varepsilon_h = \varepsilon_l$) [34], the radial expansion of the concrete transforms into hoop strain around the concrete core. Assuming full compatibility between the concrete and the FRP sheets, this hoop strain is subsequently transferred to the FRP jacket as tensile strain ($\varepsilon_{h,f} = \varepsilon_h = \varepsilon_l = \nu \times \varepsilon_c$). Therefore, to produce a given level of axial strain in the concrete, an equivalent level of tensile strain (and consequently tensile stress (f_f)) must be induced in the FRP sheets. In other words, under axial loading, confined concrete requires a higher axial compressive stress (f_c) than unconfined concrete to reach the same axial and lateral strain levels that mobilize the desired tensile response in the FRP. The tensile stress developed in the FRP is then transferred back to the concrete in the form of a confining pressure ($f_{l,f}$), which restrains the lateral expansion of the concrete column. Therefore, by using FRP sheets, it is possible to restrain the axial and lateral deformation of concrete, which would otherwise lead to cracking and stiffness degradation. This restraining action is referred to as the confinement mechanism of concrete. The force equilibrium in a concrete column section with width b and height L, between the tensile force developed in the FRP and the confining pressure applied to the concrete, can be expressed as:

$$f_{l,f} \times Lb = 2f_f \times Ln_f t_f \tag{1}$$

where n_f and t_f denote the number of FRP layers and the thickness of each FRP layer, respectively. By simplifying the above relation, the confining pressure $f_{l,f}$ can be computed as follows:

$$f_{l,f} = 2\frac{n_f t_f f_f}{b} \tag{2}$$

By considering that the tensile stress developed in the FRP sheets (f_f) is equal to the product of the elastic modulus (E_f) and the tensile strain in the FRP jacket ($\varepsilon_{h,f}$), the above expression can be rewritten as follows:

$$f_{l,f} = 2\frac{n_f t_f E_f \varepsilon_{h,f}}{b} \tag{3}$$

Based on experimental studies conducted on concrete columns confined with FRP, it has been shown that at the ultimate state corresponding to the maximum compressive strength (f_{cc}), the hoop rupture strain in the FRP ($\varepsilon_{h,rup}$) is smaller than the ultimate tensile strain of the FRP (ε_{fu}) obtained from direct tensile testing. For example, ACI [52] recommends a ratio of 0.55 between $\varepsilon_{h,rup}$, and ε_{fu}. Therefore, by assuming a constant ratio η between these two parameters, $\varepsilon_{h,rup}$ can be expressed as:

$$\varepsilon_{h,rup} = \eta \varepsilon_{fu} \tag{4}$$

By substituting Eq. 4 into Eq. 3, the ultimate stress developed in the FRP corresponding to the maximum confining pressure can be written as:

$$f_{l,f,u} = 2\frac{n_f t_f E_f \varepsilon_{h,rup}}{b} = 2\eta\frac{n_f t_f E_f \varepsilon_{fu}}{b} \tag{5}$$

The lateral confinement stiffness provided by the FRP is defined as the ratio of the confining pressure ($f_{l,f}$) to the hoop strain developed in the FRP ($\varepsilon_{h,f}$), and can be expressed as:

$$K_L = \frac{f_{l,f}}{\varepsilon_{h,f}} = \frac{f_{l,f,u}}{\varepsilon_{h,rup}} = 2\frac{n_f t_f E_f}{b} \tag{6}$$

Therefore, Eq. 5 can be simplified as follows:

$$f_{l,f,u} = \eta K_L \varepsilon_{fu} \tag{7}$$

On the other hand, the ultimate compressive strength of FRP-confined concrete columns is generally expressed as:

$$f_{cc} = f_{c0} + \beta_1 \left(f_{l,f,u}\right)^{\beta_2} \tag{8}$$

where β_1 and β_2 are constant coefficients obtained through regression analysis. By normalizing the above equation with respect to the compressive strength of unconfined concrete (f_{c0}), the following relation is obtained:

$$\frac{f_{cc}}{f_{c0}} = 1 + \beta_1 \left(\frac{f_{l,f,u}}{f_{c0}}\right)^{\beta_3} \tag{9}$$

where β_3 is another constant determined from regression analysis. Therefore, by substituting Eq. 7 into Eq. 9, we obtain:

$$\frac{f_{cc}}{f_{c0}} = 1 + \beta_1 \left(\frac{\eta K_L \varepsilon_{fu}}{f_{c0}}\right)^{\beta_3} = 1 + \beta_1 \eta^{\beta_3} {K_L}^{\beta_3} {\varepsilon_{fu}}^{\beta_3} {f_{c0}}^{-\beta_3} \tag{10}$$

Considering that the expression $\beta_1 \eta^{\beta_3}$ is a constant value, it may be replaced by a new constant coefficient β_4. Therefore, Eq. 10

can be rewritten as:

$$\frac{f_{cc}}{f_{c0}} = 1 + \beta_4 {K_L}^{\beta_3} {\varepsilon_{fu}}^{\beta_3} {f_{c0}}^{-\beta_3} \tag{11}$$

As can be observed, the above relation is a function of K_L, ε_{fu}, and f_{c0}. To obtain a suitable form for regression analysis, the structure of the equation is modified as follows:

$$\frac{f_{cc}}{f_{c0}} = \beta_5 {K_L}^{\beta_6} {\varepsilon_{fu}}^{\beta_7} {f_{c0}}^{\beta_8} \geq 1 \tag{12}$$

where β_5 to β_8 are constant coefficients obtained from regression analysis, which will be presented later. It is important to note that although the structure of Eq. 11 is modified, the key parameters (K_L, ε_{fu}, and f_{c0}) are still included in Eq. 12. Furthermore, for the case where the confinement stiffness (K_L) approaches zero (representing unconfined concrete), the result of both equations becomes equal to unity ($\frac{f_{cc}}{f_{c0}} = 1$).

3. Test database of FRP-confined concrete columns

To calibrate the proposed formula in Eq. 12 through regression analysis, a comprehensive database of experimental results from FRP-confined concrete columns is required. This database also enables the evaluation of the reliability of the proposed formula as well as existing models in the literature.

In this paper, an extensive database has been compiled from experimental specimens tested under axial compressive loading. To ensure a consistent and unified database of experimental results, the following criteria were applied:

1. Specimens containing conventional steel longitudinal or transverse reinforcement were excluded.
2. Specimens with partial confinement configurations were excluded.
3. Specimens confined using spiral wrapping were excluded.
4. Specimens exhibiting FRP debonding as the failure mode were excluded.
5. Specimens confined simultaneously with different types of FRP materials (hybrid confinement) were excluded.
6. Specimens subjected to eccentric axial loading were excluded.
7. Experimental results in which the ultimate compressive strength of the confined specimen (f_{cc}) was lower than that of the unconfined concrete (f_{c0}) were excluded (i.e., $f_{cc} < f_{c0}$).
8. Only specimens confined with CFRP, BFRP, AFRP, and GFRP (materials with linear tensile stress–strain behavior) were included.
9. Specimens confined with PEN- or PET-based fibers, which exhibit nonlinear tensile stress–strain behavior, were excluded.

Table 1 summarizes the statistical characteristics of 1,376 FRP-confined circular concrete column specimens compiled from various experimental studies. This database captures a wide range of parameters, reflecting differences in material properties, geometry, and FRP confinement characteristics, which is crucial for developing and calibrating predictive models. Concrete Strengths (f_{c0} and f_{cc}): The compressive strength of unconfined concrete (f_{c0}) spans from 6.6 MPa to 204 MPa, with a mean value of 48.5 MPa and a coefficient of variation (CoV) of 0.71. This indicates that the database includes low- to high-strength concrete. The compressive strength of FRP-confined concrete (f_{cc}) ranges from 17.8 MPa to 381 MPa, with a mean of 87.4 MPa and a CoV of 0.58, reflecting the strength enhancement due to FRP confinement. The confinement effect, measured as the ratio f_{cc} / f_{c0}, varies between 1.05 and 6.9, with a mean of 2.03 and a CoV of 0.41, showing substantial variability in the confinement efficiency across specimens. Specimen Geometry (L and b): The column heights (L) range from 100 mm to 915 mm, with a mean of 301 mm (CoV = 0.37). The diameters of circular sections (b) vary from 50 mm to 305 mm, with a mean of 144 mm (CoV = 0.31). These variations capture both small-scale laboratory specimens and larger-scale columns, ensuring that the database can support models applicable to a wide range of practical scenarios. FRP Material Properties (E_f, $n_f \times t_f$, ε_{fu}): The FRP elastic modulus (E_f) ranges from 13.6 GPa to 657 GPa, with a mean of 190 GPa (CoV = 0.52), representing different FRP types including glass, carbon, basalt, and aramid fibers. The total thickness of the FRP layers ($n_f \times t_f$) spans 0.057 mm to 5.1 mm, with a mean of 0.581 mm (CoV = 1.19), showing a wide range of confinement intensities. The ultimate tensile strain of the FRP (ε_{fu}) varies from 0.004 to 0.037, with a mean of 0.018 (CoV = 0.32), reflecting the diverse ductility characteristics of the FRP materials used. Overall, this database is comprehensive, covering a broad spectrum of concrete strengths, column geometries, and FRP confinement properties. The statistical distributions of the key parameters (strength, geometry, and FRP characteristics) demonstrate significant variability, which is essential for developing reliable regression models and for evaluating the performance of FRP-confined concrete under axial loading. The large sample size (1,376 specimens) ensures robust statistical analysis and model calibration.

The dataset was screened for outliers using standardized residuals and leverage diagnostics. Observations with standardized residuals greater than ±3 were identified as extreme. Leverage statistics were used to evaluate the influence of predictor values: observations with leverage below 0.2 were considered non-influential, those between 0.2 and 0.5 were monitored but generally retained unless accompanied by near-extreme residuals, and values exceeding 0.5 were subjected to detailed scrutiny for possible measurement errors or undue influence on the model.

Table 1. Details of the database of FRP-confined concrete columns.

Section shape	Number of data	Statistical index	f_{c0} (MPa)	f_{cc} (MPa)	f_{cc}/f_{c0}	L (mm)	b (mm)	E_f (GPa)	$n_f\ t_f$ (mm)	ε_{fu}
Circle	1376	Minimum	6.6	17.8	1.05	100	50	13.6	0.057	0.004
		Maximum	204	381	6.9	915	305	657	5.1	0.037
		Mean	48.5	87.4	2.03	301	144	190	0.581	0.018
		CoV	0.71	0.58	0.41	0.37	0.31	0.52	1.19	0.32

Data points identified by either diagnostic were excluded only when they were determined to meaningfully distort the regression results, thereby supporting the robustness and reliability of the analysis.

4. Proposed formula for circular FRP-confined concrete columns

In the present study, the experimental data from the database were used to determine the coefficients of Eq. 12. Based on 1376 experimental specimens of circular concrete columns, a relationship between the ratio of the maximum compressive strength of confined concrete (f_{cc}/f_{c0}) and the key parameters ε_{fu}, K_L, and f_{c0} is proposed as follows:

$$\frac{f_{cc}}{f_{c0}} = 3.1{K_L}^{0.36}{\varepsilon_{fu}}^{0.23}{f_{c0}}^{-0.55} \geq 1 \tag{13}$$

The predictive capability of the proposed formula is illustrated in Fig. 1. As can be observed, based on statistical indices such as the mean, coefficient of variation (CoV), mean absolute percentage error (MAPE), and the coefficient of determination (R^2), Eq. 13 provides satisfactory accuracy for predicting the ultimate compressive strength of circular FRP-confined concrete columns.

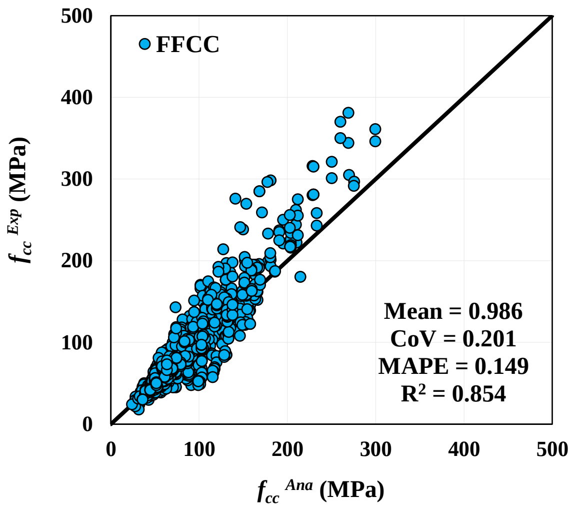

Fig. 1. Comparison of the predicted ultimate compressive strength from the proposed model based on 1376 experimental circular FRP-confined concrete column specimens.

It should be noted that in Eq. 13, the effects of section dimensions were not considered in the regression analysis. Experimental studies [11–13] have shown that, as the column cross-sectional dimensions increase, the effectiveness of the FRP confinement decreases. Therefore, to account for the influence of this parameter, an error analysis of the proposed model must be conducted. Fig. 2a shows the relationship between the analytical-to-experimental ratio ($Y_1 = f_{cc}^{Ana} / f_{cc}^{Exp}$) and the section aspect factor ($R_b = b / 150$). As observed, there is a clear dependency between the error (Y_1) and R_b, indicating the necessity of considering the effects of section dimensions. For specimens with low RbR_bRb, the proposed model tends to provide slightly conservative predictions, whereas for specimens with high R_b, the model also produces conservative estimates. Using regression analysis, the relationship between the prediction error (Y_1) and the section aspect factor (R_b) was obtained as follows:

$$Y_1 = \frac{{f_{cc}}^{Ana}}{{f_{cc}}^{Exp}} = {R_b}^{0.14} \tag{14}$$

By substituting Eq. 14 into Eq. 13, the ultimate compressive strength of the confined concrete (f_{cc}) can be determined.

$$\frac{f_{cc}}{f_{c0}} = \frac{3.1{K_L}^{0.36}{\varepsilon_{fu}}^{0.23}{f_{c0}}^{-0.55}}{{R_b}^{0.14}} \geq 1 \tag{15}$$

The above equation can also be expressed in the following form:

$$\frac{f_{cc}}{f_{c0}} = 3.1{K_L}^{0.36}{\varepsilon_{fu}}^{0.23}{f_{c0}}^{-0.55}{R_b}^{-0.14} \geq 1 \tag{16}$$

Based on the statistical indicators presented in Fig. 2b, Eq. 16 demonstrates high accuracy in predicting the ultimate compressive strength of circular concrete columns confined with FRP jackets. The statistical evaluation includes metrics such as the mean ratio, coefficient of variation (CoV), mean absolute percentage error (MAPE), and the coefficient of determination (R^2), all of which indicate that the proposed model closely matches the experimental results. Furthermore, by comparing the statistical indices obtained for Eq. 13 and Eq. 16, it can be concluded that incorporating the effects of cross-sectional dimensions significantly improves the predictive performance of the model. Specifically, while Eq. 13 tends to exhibit systematic deviations for specimens with high or low aspect ratios (R_b), Eq. 16 accounts for these geometric effects, resulting in reduced bias and error variability. Fig. 2c illustrates the relationship between the prediction error of Eq. 16 and the section aspect factor (R_b). As observed, after applying the correction factor $R_b^{-0.14}$ in the proposed equation, the prediction error, defined as $Y_2 = f_{cc}^{Ana} / f_{cc}^{Exp} - 1$, exhibits no significant correlation with R_b. This indicates that the proposed formula successfully captures the influence of cross-sectional dimensions on the confinement effectiveness, leading to a more robust and dimension-independent predictive model for circular FRP-confined concrete columns.

The proposed formulation is developed specifically for circular FRP-confined concrete columns under axial compressive loading using linear-elastic FRP materials (CFRP, BFRP, AFRP, GFRP) with full and uniform confinement. Specimens with conventional steel reinforcement, partial confinement, spiral wrapping, hybrid FRP types, eccentric loading, nonlinear FRP materials (e.g., PEN or PET-based fibers), or cases where $f_{cc}<f_{c0}$ were excluded from the database. Therefore, the model is not directly applicable to columns outside these conditions. Users should exercise caution when applying the formulation to partially confined columns, internally reinforced columns, eccentrically loaded specimens, columns with nonlinear FRP, or large-scale structural columns, as the predictive accuracy under these conditions has not been validated.

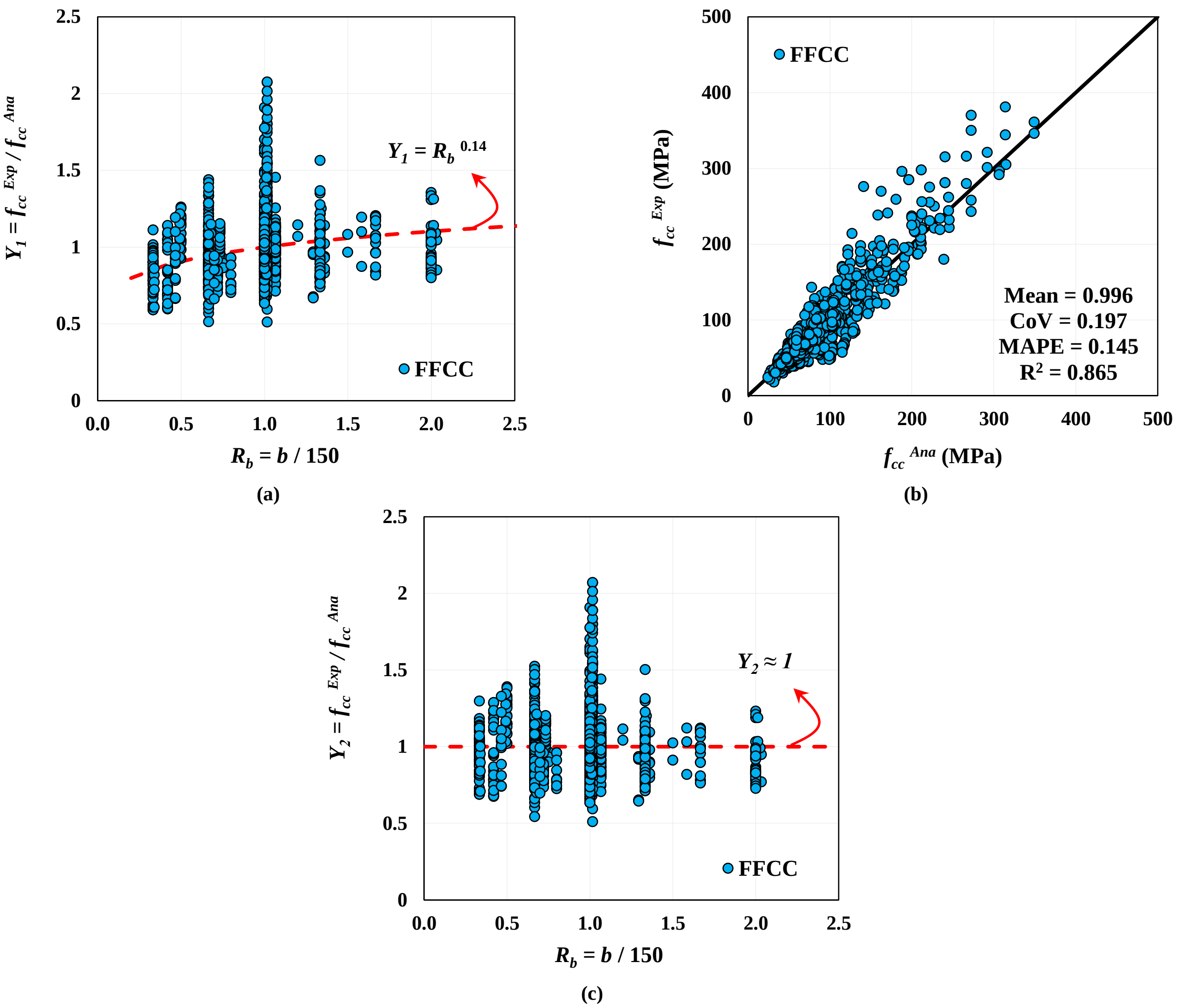

Fig. 2. Evaluation of the predicted ultimate compressive strength of FRP-confined circular columns using the proposed model, based on 1376 experimental specimens.

In this section, a parametric study was conducted to investigate the influence of key parameters on the ultimate compressive strength of FRP-confined concrete columns. For this purpose, a circular concrete column with a smaller dimension of b = 250 mm was considered. The mechanical properties of the FRP were assumed as follows: elastic modulus E_f = 240GPa, nominal thickness t_f = 0.17mm, and ultimate tensile strain ε_{fu}=0.017. Fig. 3 illustrates the effects of FRP confinement stiffness (K_L) and the compressive strength of unconfined concrete (f_{c0}) on the confinement effectiveness for circular concrete columns. In this figure, the relationship between the compressive strength of the FRP-confined column (f_{cc}) and the unconfined concrete strength (f_{c0}) is plotted for different levels of lateral confinement stiffness (K_L). As shown, increasing the unconfined concrete strength (f_{c0}) has a negative effect on the compressive strength of the confined column (f_{cc}), indicating that higher-strength concrete benefits less from FRP confinement. For instance, when K_L = 321MPa, no significant increase in the column strength is observed for unconfined concrete strengths exceeding 50 MPa. However, as the lateral confinement stiffness (K_L) increases, the negative influence of f_{c0} is substantially reduced, and a pronounced enhancement in the ultimate compressive strength of the column is achieved. This underscores the pivotal role of K_L in controlling the lateral restraint and hoop stress development in FRP-confined concrete columns. Higher K_L values lead to more effective engagement of the confinement mechanism, mitigating the reduction in lateral dilation observed in high-strength concrete, which inherently exhibits lower volumetric strain under axial loading. Consequently, the stiffness of the FRP jacket not only enhances the ultimate compressive strength (f_{cc}) but also improves ductility and delays premature failure modes such as concrete crushing or FRP rupture. These effects highlight that accurate specification of FRP material properties, layer thickness, and number of layers is essential for optimizing the performance of confined columns, particularly when designing for high-strength concrete applications where confinement efficiency is otherwise reduced.

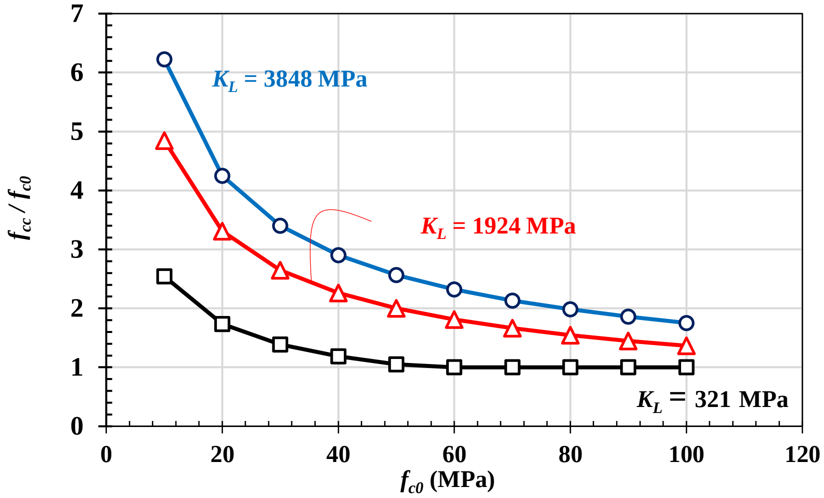

Fig. 3. Investigation of the effects of FRP confinement stiffness and unconfined concrete compressive strength on the ultimate strength of circular concrete columns.

5. Comparison of the proposed model with existing models

Fig. 4 and Table 2 compare the experimental results with the predictions obtained from existing analytical models and the proposed model. In both the figure and the table, the statistical indices presented include the mean absolute percentage error (MAPE), mean squared error (MSE), coefficient of variation (CoV), mean value (MV), and coefficient of determination (R^2).

$$MV = \frac{1}{n}\sum_{1}^{n}\frac{T_i}{E_i} \tag{17}$$

$$CoV = \frac{SD}{MV} \tag{18}$$

$$MSE = \frac{1}{n}\sum_{1}^{n}(T_i - E_i)^2 \tag{19}$$

$$MAPE = \frac{1}{n}\sum_{1}^{n}\left|1 - \frac{T_i}{E_i}\right| \tag{20}$$

$$R^2 = \left(\frac{\sum_{1}^{n}[(T_i - \bar{T}_i)(E_i - \bar{E}_i)]}{\sqrt{\sum_{1}^{n}[(T_i - \bar{T}_i)^2(E_i - \bar{E}_i)^2]}}\right)^2 \tag{21}$$

where T_i and E_i are $\frac{f_{cc}}{f_{c0}}$ obtained analytically and experimentally, respectively. *SD* is standard deviation; n is the number of data; $\bar{T}$and $\bar{E}_i$represents the mean values of the analytical and experimental predictions, respectively.

These indices provide a comprehensive evaluation of the predictive accuracy of each model relative to the experimental data. As can be observed, based on MV and CoV, the model proposed by Fib [17] exhibits the best performance among the existing models, with MV = 0.892 and CoV = 0.226. However, this model still tends to slightly underestimate the experimental values, producing somewhat conservative predictions. In terms of MSE and MAPE, the fib [17] model also achieves the lowest values among the existing models, confirming its superior predictive performance. The coefficient of determination (R^2) for both the fib [17] model and Guo et al. [51] is 0.820, indicating a strong correlation with the experimental data. Overall, the fib [17] model performs best among the existing models for predicting the ultimate compressive strength of circular FRP-confined concrete columns. On the other hand, the model proposed by Cao et al. [50] shows the weakest performance among the existing models, providing non-conservative predictions with high scatter. When comparing the proposed model with the fib [17] model, it is evident that the proposed model outperforms all existing models across all statistical indices. This enhanced performance is attributed to the inclusion of critical parameters such as FRP tensile strain, confinement stiffness, unconfined concrete strength, and geometric effects, which are grounded in the mechanical behavior of FRP-confined concrete. The results confirm that the proposed model provides a robust, statistically significant improvement over existing formulations and captures the underlying confinement mechanics more accurately.

Table 2. Comparison of existing analytical models' predictions of ultimate strength for circular FRP-confined concrete columns.

Analytical Model	R2	MAPE	MSE	CoV	MV
ACI [52]	0.812	0.189	0.375	0.279	0.938
fib [53]	0.82	0.185	0.343	0.226	0.892
Cao et al. [47]	0.782	0.257	1.03	0.313	1.219
Wei and Wu [50]	0.812	0.189	0.426	0.282	1.078
Guo et al. [46]	0.82	0.266	0.628	0.252	0.77
Proposed Model	0.865	0.145	0.202	0.197	0.996

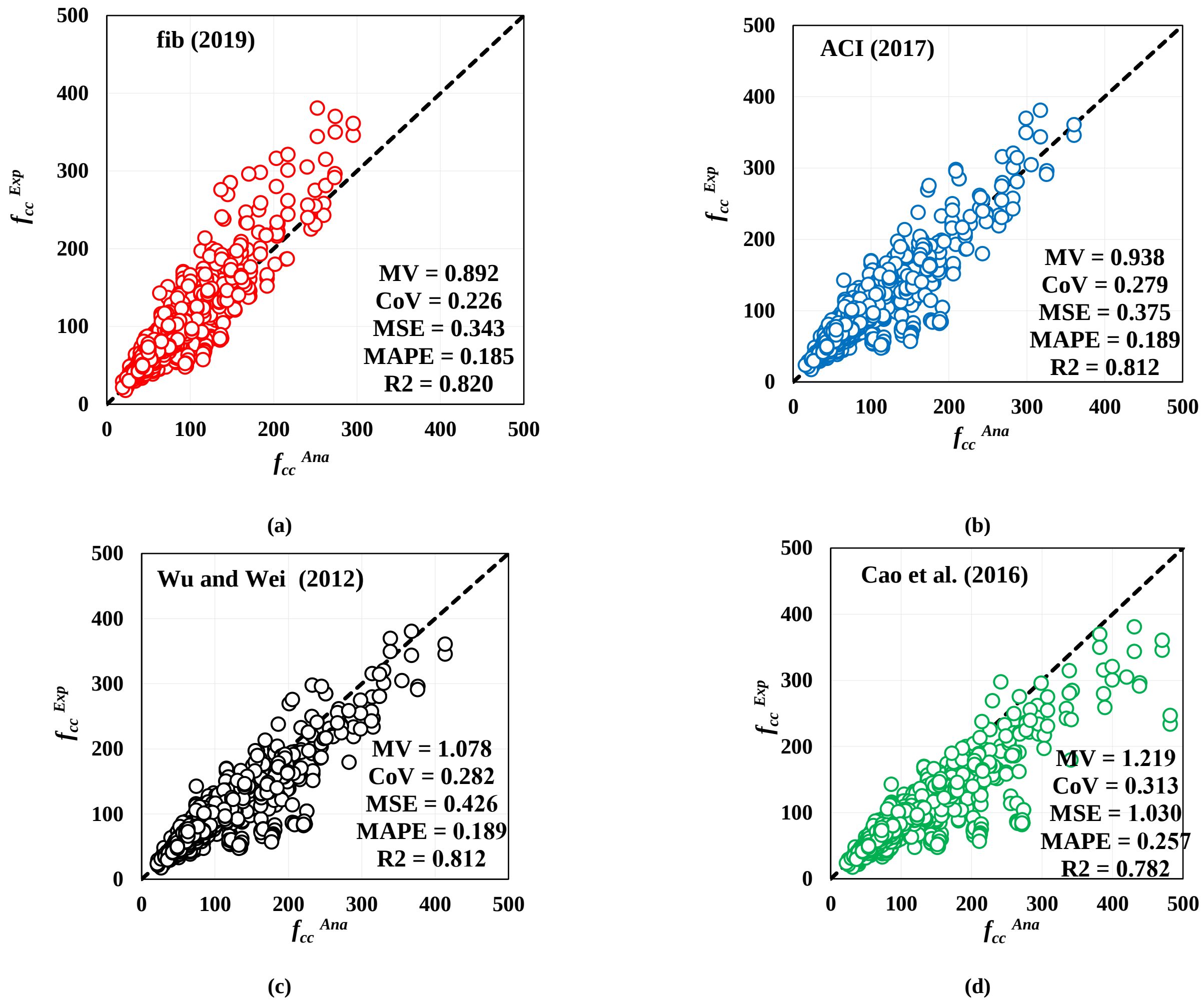

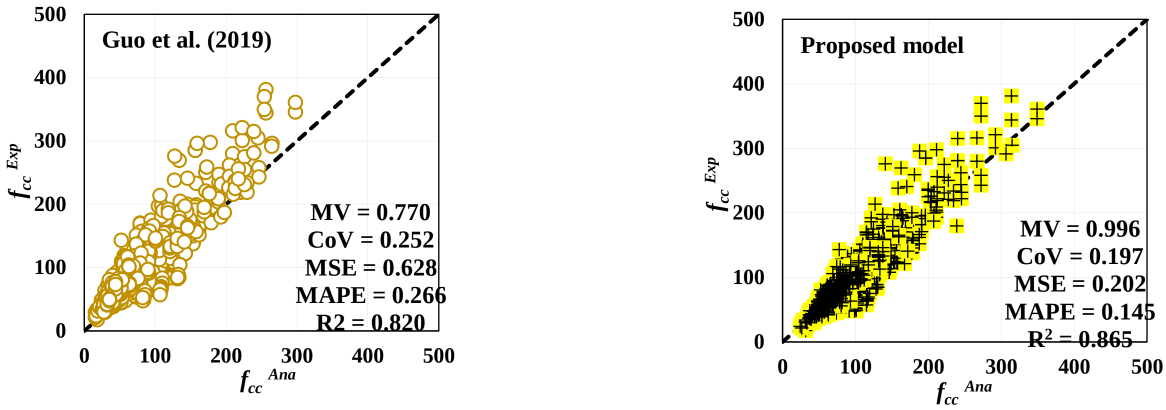

(e) (f)

Fig. 4. Comparison of experimental results and predictions from analytical models based on 1376 circular concrete column specimens.

6. Numerical example

In this section, numerical examples are presented to demonstrate the application of the proposed formula for predicting the ultimate compressive strength of FRP-confined concrete columns under different confinement scenarios. Consider a circular concrete column with a diameter of b = 250 mm, confined with three layers of CFRP (n_f = 3). The mechanical properties of the CFRP are assumed as follows: E_f = 240 GPa, t_f = 0.17 mm, and ε_{fu} = 0.017. The unconfined concrete compressive strength is assumed to be f_{c0} = 25 MPa. The goal is to calculate the compressive strength of the FRP-confined column (f_{cc}).

Step 1: Calculation of confinement stiffness (K_L)

$$K_L = 2\frac{n_f t_f E_f}{b} = 2\frac{3 \times 0.17 \times 240000}{250} = 979.2 \text{ MPa}$$

Step 2: Calculation of ultimate compressive strength (f_{cc})

$$\frac{f_{cc}}{f_{c0}} = 3.1 {K_L}^{0.36} {\varepsilon_{fu}}^{0.23} {f_{c0}}^{-0.55} {R_b}^{-0.14} \geq 1$$

$$\frac{f_{cc}}{f_{c0}} = 3.1(979.2)^{0.36}(0.017)^{0.23}(25)^{-0.55}\left(\frac{250}{150}\right)^{-0.14} = 2.30 \geq 1$$

$$\rightarrow f_{cc} = 2.30 \times f_{c0} = 2.30 \times 25 = 57.4 \text{ MPa}$$

Thus, the predicted compressive strength of the CFRP-confined circular column is 57.4 MPa.

7. Conclusion

This study presents a comprehensive analytical and empirical investigation into the compressive behavior of concrete confined with fiber-reinforced polymer (FRP) jackets, with a focus on circular columns. Based on a mechanistic understanding of the confinement mechanism, where lateral expansion of concrete under axial loading induces hoop tensile stresses in the FRP jacket, which in turn generate confining pressure, the study derives a physically consistent formulation for predicting the ultimate compressive strength of FRP-confined concrete. A large and rigorously filtered experimental database comprising 1,376 circular FRP-confined concrete specimens was compiled to support model development and validation. The database spans a wide range of concrete strengths (6.6–204 MPa), column geometries (diameter: 50–305 mm; height: 100–915 mm), and FRP material properties (E_f: 13.6–657 GPa; ε_{fu}: 0.004–0.037), ensuring broad representativeness and enhancing the generalizability of the derived model. Through regression analysis, a new predictive formula (Eq. 13) was initially proposed, capturing the influence of FRP ultimate tensile strain, confinement stiffness, and unconfined concrete strength on the strength enhancement ratio (f_{cc}/f_{c0}). Subsequent error analysis revealed a systematic dependency of prediction accuracy on column diameter, consistent with known size effects in FRP confinement. To address this, a dimension-based correction factor tied to the section aspect ratio (R_b = b/150) was introduced, yielding a refined model (Eq. 16) that effectively eliminates geometric bias. The final proposed model demonstrates superior predictive performance compared to existing analytical approaches. Statistical evaluation shows a mean prediction ratio of 0.996, a low coefficient of variation (CoV = 0.197), a high coefficient of determination (R^2 = 0.865), and the lowest mean absolute percentage error (MAPE = 14.5%) among all considered models, including the widely used fib Model Code formulation. Importantly, the proposed predictive model is not merely a re-calibrated version of existing formulations but embodies two fundamental advances: (i) the explicit incorporation of a geometric scale effect via a dimension-based correction factor derived from systematic error analysis, and (ii) a unified, continuous functional form that consistently captures the interaction between FRP properties and concrete strength, from conventional to ultra-high-strength concrete, using confinement stiffness as a governing parameter. This approach moves beyond traditional empirical fitting by embedding physical insight into a data-driven framework, thereby offering both improved accuracy and broader generalizability. Parametric analysis further underscores two critical insights: (1) the effectiveness of FRP confinement diminishes as unconfined concrete strength increases, and (2) this adverse effect can be mitigated by increasing the lateral confinement stiffness through higher FRP modulus, greater thickness, or additional layers. This highlights the importance of tailoring FRP jacket design to the concrete strength class to achieve optimal performance. In summary, the proposed model offers a robust, physically grounded, and empirically validated tool for predicting the ultimate compressive strength of circular FRP-confined concrete columns. Explicitly accounting for material properties, confinement mechanics, and geometric scale effects, it provides a significant advancement over existing formulations, supporting more accurate and reliable design of FRP-strengthened structural elements in practice. This enables engineers to optimize FRP jacket configurations for different concrete strength classes and reliably assess confinement effectiveness across a broad range of column geometries and FRP types. Additionally, the study advances existing knowledge by integrating mechanistic understanding with data-driven regression, introducing a unified functional form that captures the interaction between confinement stiffness and concrete strength, and explicitly addressing size effects through a dimension-based correction factor. These contributions collectively enhance both the scientific understanding of FRP confinement and the practical applicability of predictive models in structural engineering design.

Statements & Declarations

Author contributions

Sajjad Shayanfar: Investigation, Formal analysis, Data curation, Software, Writing - Original Draft.

Meysam Ghasemi Naghibdehi: Project administration, Resources, Writing - Review & Editing.

Javad Shayanfar: Conceptualization, Methodology, Software, Writing - Review & Editing.

Funding

The authors received no financial support for the research, authorship, and/or publication of this article.

Data availability

The data presented in this study will be available on request from the corresponding author.

Declarations

The authors declare no conflict of interest.

References

[1] Isleem Haytham, F., Wang, Z., Wang, D., Smith Scott, T. Monotonic and Cyclic Axial Compressive Behavior of CFRP-Confined Rectangular RC Columns. Journal of Composites for Construction, 2018; 22: 04018023. doi:10.1061/(ASCE)CC.1943-5614.0000860.

[2] Shayanfar, J., Bengar, H. A. A practical model for simulating nonlinear behaviour of FRP strengthened RC beam-column joints. Steel and Composite Structures, 2018; 27: 49–74. doi:10.12989/scs.2018.27.1.049.

[3] Nematzadeh, M., Mousavimehr, M., Shayanfar, J., Omidalizadeh, M. Eccentric compressive behavior of steel fiber-reinforced RC columns strengthened with CFRP wraps: Experimental investigation and analytical modeling. Engineering Structures, 2021; 226: 111389. doi:10.1016/j.engstruct.2020.111389.

[4] Shayanfar, J., Barros Joaquim, A. O., Abedi, M., Rezazadeh, M. Unified Compressive Strength and Strain Ductility Models for Fully and Partially FRP-Confined Circular, Square, and Rectangular Concrete Columns. Journal of Composites for Construction, 2023; 27: 04023053. doi:10.1061/JCCOF2.CCENG-4336.

[5] Shayanfar, J., Barros, J. A. O., Pereira, J. P. C. A versatile model with a design framework for axially-loaded FRP-confined concrete with/without a stress reduction-recovery behavior. Construction and Building Materials, 2024; 448: 138097. doi:10.1016/j.conbuildmat.2024.138097.

[6] Shayanfar, J., Pereira, J. P. C., Barros, J. A. O. Passive confinement scenarios for strengthening fire-damaged concrete columns: Experimental and analytical research. Structures, 2025; 73: 108375. doi:10.1016/j.istruc.2025.108375.

[7] Liu, P., Wang, X., He, W., Lu, D., Wu, Z., Zhang, X., Shao, Y. Axial compressive behavior of concrete columns strengthened with BFRP grids. Construction and Building Materials, 2025; 477: 141305. doi:10.1016/j.conbuildmat.2025.141305.

[8] Lam, L., Teng, J. G. Design-oriented stress–strain model for FRP-confined concrete. Construction and Building Materials, 2003; 17: 471–489. doi:10.1016/S0950-0618(03)00045-X.

[9] Fallah Pour, A., Nguyen, G. D., Vincent, T., Ozbakkaloglu, T. Investigation of the compressive behavior and failure modes of unconfined and FRP-confined concrete using digital image correlation. Composite Structures, 2020; 252: 112642. doi:10.1016/j.compstruct.2020.112642.

[10] Shayanfar, J., Barros, J. A. O., Rezazadeh, M. Cross-sectional and confining system unification on peak compressive strength of FRP confined concrete. Structural Concrete, 2023; 24: 1531–1545. doi:10.1002/suco.202200105.

[11] Shayanfar, J., Barros, J. A. O., Rezazadeh, M. Analytical model to predict axial stress-strain behavior of heat-damaged unreinforced concrete columns wrapped by FRP jacket. Engineering Structures, 2023; 289: 116244. doi:10.1016/j.engstruct.2023.116244.

[12] Liao, J., Zeng, J.-J., Zhuge, Y., Zheng, Y., Ma, G., Zhang, L. FRP-confined concrete columns with a stress reduction-recovery behavior: A state-of-the-art review, design recommendations and model assessments. Composite Structures, 2023; 321: 117313. doi:10.1016/j.compstruct.2023.117313.

[13] Shayanfar, J., Barros, J. A. O., Rezazadeh, M. Analysis-oriented model for partially FRP-and-steel-confined circular RC columns under compression. Engineering Structures, 2023; 276: 115330. doi:10.1016/j.engstruct.2022.115330.

[14] Shayanfar, J., Barros Joaquim, A. O., Rezazadeh, M. Stress–Strain Model for FRP-Confined Circular Concrete Columns Developing Structural Softening Behavior. Journal of Composites for Construction, 2024; 28: 04023065. doi:10.1061/JCCOF2.CCENG-4364.

[15] Shayanfar, J., Barros, J. A. O., Rezazadeh, M., Kafshgarkolaei, H. J. Enhancing the performance of heat-damaged rectangular RC columns using prestressed FRP confinement. Construction and Building Materials, 2025; 501: 144346. doi:10.1016/j.conbuildmat.2025.144346.

[16] Zeng, J.-J., Chen, J.-D., Liao, J., Chen, W.-J., Zhuge, Y., Liu, Y. Behavior of ultra-high performance concrete under true tri-axial compression. Construction and Building Materials, 2024; 411: 134450. doi:10.1016/j.conbuildmat.2023.134450.

[17] Ozbakkaloglu, T., Akin, E. Behavior of FRP-Confined Normal- and High-Strength Concrete under Cyclic Axial Compression. Journal of Composites for Construction, 2012; 16: 451–463. doi:10.1061/(ASCE)CC.1943-5614.0000273.

[18] Wei, Y., Wu, Y.-F. Experimental Study of Concrete Columns with Localized Failure. Journal of Composites for Construction, 2016; 20: 04016032. doi:10.1061/(ASCE)CC.1943-5614.0000686.

[19] Shan, B., Gui, F. C., Monti, G., Xiao, Y. Effectiveness of CFRP Confinement and Compressive Strength of Square Concrete Columns. Journal of Composites for Construction, 2019; 23: 04019043. doi:10.1061/(ASCE)CC.1943-5614.0000967.

[20] Shayanfar, J., Barros Joaquim, A. O. Design-Oriented Model of Unified Character to Determine Softening–Hardening Stress–Strain Behavior of FRP-Confined Concrete Columns of General Cross Section. Journal of Composites for Construction, 2024; 28: 04024059. doi:10.1061/JCCOF2.CCENG-4772.

[21] Wang, J., Xiao, H., Lu, L., Yang, J., Lu, S., Shayanfar, J. Axial stress-strain model for concrete in partially FRP wrapped reinforced concrete columns. Construction and Building Materials, 2024; 416: 135028. doi:10.1016/j.conbuildmat.2024.135028.

[22] Demir, U., Ispir, M., Sahinkaya, Y., Arslan, G., Ilki, A. Axial Behavior of Noncircular High-Performance Fiber-Reinforced Cementitious Composite Members Externally Jacketed by CFRP Sheets. Journal of Composites for Construction, 2019; 23: 04019022. doi:10.1061/(ASCE)CC.1943-5614.0000940.

[23] de Oliveira Diôgo, S., Raiz, V., Carrazedo, R. Experimental Study on Normal-Strength, High-Strength and Ultrahigh-Strength Concrete Confined by Carbon and Glass FRP Laminates. Journal of Composites for Construction, 2019; 23: 04018072. doi:10.1061/(ASCE)CC.1943-5614.0000912.

[24] Shayanfar, J., Barros, J. A. O., Rezazadeh, M. Generalized Analysis-oriented model of FRP confined concrete circular columns. Composite Structures, 2021; 270: 114026. doi:10.1016/j.compstruct.2021.114026.

[25] Shayanfar, J., Barros, J. A., Rezazadeh, M. Unified model for fully and partially FRP confined circular and square concrete columns subjected to axial compression. Engineering Structures, 2022; 251: 113355. doi:10.1016/j.engstruct.2021.113355.

[26] Shayanfar, J., Barros, J. A. O., Rezazadeh, M. Design-oriented stress–strain model for RC columns with dual FRP- steel confinement mechanism. Composite Structures, 2024; 330: 117821. doi:10.1016/j.compstruct.2023.117821.

[27] Vincent, T., Ozbakkaloglu, T. Influence of concrete strength and confinement method on axial compressive behavior of FRP confined high- and ultra high-strength concrete. Composites Part B: Engineering, 2013; 50: 413–428. doi:10.1016/j.compositesb.2013.02.017.

[28] Xiao, Q. G., Teng, J. G., Yu, T. Behavior and Modeling of Confined High-Strength Concrete. Journal of Composites for Construction, 2010; 14: 249–259. doi:10.1061/(ASCE)CC.1943-5614.0000070.

[29] Ozbakkaloglu, T. Axial Compressive Behavior of Square and Rectangular High-Strength Concrete-Filled FRP Tubes. Journal of Composites for Construction, 2013; 17: 151–161. doi:10.1061/(ASCE)CC.1943-5614.0000321.

[30] Wang, D. Y., Wang, Z. Y., Smith, S. T., Yu, T. Size effect on axial stress-strain behavior of CFRP-confined square concrete columns. Construction and Building Materials, 2016; 118: 116–126. doi:10.1016/j.conbuildmat.2016.04.158.

[31] Bengar, H. A., Kiadehi, M. A., Shayanfar, J., Nazari, M. Effective flexural rigidities for RC beams and columns with steel fiber. Steel and Composite Structures, 2020; 34: 453–465. doi:10.12989/scs.2020.34.3.453.

[32] Shayanfar, J., Rezazadeh, M., Barros Joaquim, A. Analytical Model to Predict Dilation Behavior of FRP Confined Circular Concrete Columns Subjected to Axial Compressive Loading. Journal of Composites for Construction, 2020; 24: 04020071. doi:10.1061/(ASCE)CC.1943-5614.0001087.

[33] Shayanfar, J., Barros, J. A. O., Rezazadeh, M. Stress–strain model for FRP confined heat-damaged concrete columns. Fire Safety Journal, 2023; 136: 103748. doi:10.1016/j.firesaf.2023.103748.

[34] Shayanfar, J., Akbarzadeh Bengar, H. Nonlinear analysis of RC frames considering shear behaviour of members under varying axial load. Bulletin of Earthquake Engineering, 2017; 15: 2055–2078. doi:10.1007/s10518-016-0060-z.

[35] Shayanfar, J., Bengar, H. A. Numerical model to simulate shear behaviour of RC joints and columns. Computers and Concrete, An International Journal, 2016; 18: 877–901. doi:10.12989/cac.2016.18.4.877.

[36] Han, Q., Yuan, W., Bai, Y., Du, X. Compressive behavior of large rupture strain (LRS) FRP-confined square concrete columns: experimental study and model evaluation. Materials and Structures, 2020; 53: 99. doi:10.1617/s11527-020-01534-4.

[37] Tariq, M., Khan, A., Shayanfar, J., Hanif, M. U., Ullah, A. A regression model for predicting the shear strength of RC knee joint subjected to opening and closing moment. Journal of Building Engineering, 2021; 41: 102727. doi:10.1016/j.jobe.2021.102727.

[38] Tariq, M., Khan, A., Ullah, A., Shayanfar, J., Niaz, M. Improved Shear Strength Prediction Model of Steel Fiber Reinforced Concrete Beams by Adopting Gene Expression Programming. Materials, 2022; 15: 3758. doi:10.3390/ma15113758.

[39] Shayanfar, J., Kafshgarkolaei, H. J., Barros, J. A. O., Rezazadeh, M. Unified strength model for FRP confined heat-damaged circular and square concrete columns. Composite Structures, 2023; 307: 116647. doi:10.1016/j.compstruct.2022.116647.

[40] Li, P.-D., Zeng, Q., Jiang, J.-F. Stiffness-based stress–strain model of FRP-confined high-strength and ultra-high strength concrete column with various corner radii. Construction and Building Materials, 2023; 409: 133873. doi:10.1016/j.conbuildmat.2023.133873.

[41] Jiang, T., Teng, J. G. Analysis-oriented stress–strain models for FRP–confined concrete. Engineering Structures, 2007; 29: 2968–2986. doi:10.1016/j.engstruct.2007.01.010.

[42] Lim, J. C., Ozbakkaloglu, T. Hoop strains in FRP-confined concrete columns: experimental observations. Materials and Structures, 2015; 48: 2839–2854. doi:10.1617/s11527-014-0358-8.

[43] Shayanfar, J., Akbarzadeh Bengar, H., Niroomandi, A. A proposed model for predicting nonlinear behavior of RC joints under seismic loads. Materials & Design, 2016; 95: 563–579. doi:10.1016/j.matdes.2016.01.098.

[44] Shayanfar, J., Bengar, H. A., Parvin, A. Analytical prediction of seismic behavior of RC joints and columns under varying axial load. Engineering Structures, 2018; 174: 792–813. doi:10.1016/j.engstruct.2018.07.103.

[45] Shayanfar, J., Hemmati, A., Bengar, H. A. A simplified numerical model to simulate RC beam–column joints collapse. Bulletin of Earthquake Engineering, 2019; 17: 803–844. doi:10.1007/s10518-018-0472-z.

[46] Guo, Y.-C., Xiao, S.-H., Luo, J.-W., Ye, Y.-Y., Zeng, J.-J. Confined Concrete in Fiber-Reinforced Polymer Partially Wrapped Square Columns: Axial Compressive Behavior and Strain Distributions by a Particle Image Velocimetry Sensing Technique. Sensors, 2018; 18: 4118. doi:10.3390/s18124118.

[47] Cao, Y.-G., Jiang, C., Wu, Y.-F. Cross-Sectional Unification on the Stress-Strain Model of Concrete Subjected to High Passive Confinement by Fiber-Reinforced Polymer. Polymers, 2016; 8: 186. doi:10.3390/polym8050186.

[48] Cao, Y., Liu, Y., Li, X., Wu, Y. Axial stress strain behavior of FRP-confined rectangular rubber concrete columns with different aspect ratio. Engineering Structures, 2023; 297: 116987. doi:10.1016/j.engstruct.2023.116987.

[49] Teng, J. G., Jiang, T., Lam, L., Luo, Y. Z. Refinement of a Design-Oriented Stress–Strain Model for FRP-Confined Concrete. Journal of Composites for Construction, 2009; 13: 269–278. doi:10.1061/(ASCE)CC.1943-5614.0000012.

[50] Wei, Y.-Y., Wu, Y.-F. Unified stress–strain model of concrete for FRP-confined columns. Construction and Building Materials, 2012; 26: 381–392. doi:10.1016/j.conbuildmat.2011.06.037.

[51] Fallah Pour, A., Ozbakkaloglu, T., Vincent, T. Simplified design-oriented axial stress-strain model for FRP-confined normal- and high-strength concrete. Engineering Structures, 2018; 175: 501–516. doi:10.1016/j.engstruct.2018.07.099.

[52] American Concrete Institute (ACI). ACI 440.2R-17: Guide for the design and construction of externally bonded FRP systems for strengthening concrete structures. Farmington Hills (MI): ACI; 2017.

[53] International Federation for Structural Concrete. CEB-FIP: Externally applied FRP reinforcement for concrete structures. Lausanne (CH): FIB BULLETIN NO. 90; 2019.

[54] Lim, J. C., Ozbakkaloglu, T. Stress–strain model for normal- and light-weight concretes under uniaxial and triaxial compression. Construction and Building Materials, 2014; 71: 492–509. doi:10.1016/j.conbuildmat.2014.08.050.

[55] Shayanfar, J. Integrated modelling strategy for FRP-based confinement imposed to RC columns: From undamaged to post-fire damage (PhD Thesis). Braga (PT): University of Minho; 2024.

[56] Akbarzadeh Bengar, H., Abdollahtabar, M., Shayanfar, J. Predicting the Ductility of RC Beams Using Nonlinear Regression and ANN. Iranian Journal of Science and Technology, Transactions of Civil Engineering, 2016; 40: 297–310. doi:10.1007/s40996-016-0033-0.

[57] Shayanfar, J., Omidalizadeh, M., Nematzadeh, M. Analysis-oriented model for seismic assessment of RC jacket retrofitted columns. Steel and Composite Structures, 2020; 37: 371–390. doi:10.12989/scs.2020.37.3.371.

Civil Engineering and Applied Solutions

Research Article

journal homepage: ceas.journals.umz.ac.ir

CEAS Civil Engineering and Applied Solutions

Influence of Geometric Configuration on the Seismic Response of T-Shaped Reinforced Concrete Shear Walls in Steel High-Rise Buildings

Mehran Rahimi [a], Khosrow Bargi [a*]

[a] *School of Civil Engineering, College of Engineering, University of Tehran, Tehran, Iran*

ARTICLE INFO

Article history:

Received 28 January 2026

Revised 23 February 2026

Accepted 12 May 2026

Available online 01 January 2027

Keywords:

Geometric configuration

Response spectrum analysis

High-rise building

T-shaped shear wall

ABSTRACT

T-shaped shear walls, due to their three-dimensional behavior, effectively enhance seismic resistance in both principal directions of high-rise buildings. Their performance is strongly influenced by geometric parameters, particularly the flange length-to-thickness ratio and web position. In this study, the seismic behavior of steel high-rise buildings equipped with reinforced concrete T-shaped shear walls was investigated for various flange length-to-thickness ratios, and a comparative assessment with +-shaped shear walls was conducted. Linear dynamic response spectrum analysis was performed on 10-, 20-, and 30-story buildings. Maximum story displacements and inter-story drifts were evaluated. The results indicate that with an increase in the flange length-to-thickness ratio, maximum story displacement decreases by 7–22%, and with a further increase in the ratio, the reduction reaches 20–44% compared to the baseline model across different building heights. Furthermore, T-shaped shear walls consistently outperform +-shaped configurations, reducing maximum story displacement by 30, 33, and 43% for 10-, 20-, and 30-story buildings, respectively. These findings highlight the significant influence of geometric parameters on seismic performance and provide practical guidance for preliminary design and optimization of shear walls in high-rise steel structures.

How to cite this article: Rahimi, M., Bargi, K. Influence of Geometric Configuration on the Seismic Response of T-Shaped Reinforced Concrete Shear Walls in Steel high-rise Buildings. Civil Engineering and Applied Solutions. 2027; 3(1): 37–50. doi:10.22080/ceas.2026.31135.1074.

1. Introduction

The rapid growth of urban populations and the increasing demand for urban services have made high-rise buildings indispensable elements of modern cities [1-4]. Ensuring both the safety and economic efficiency of these structures requires careful evaluation of various structural systems [4-7]. Steel frames are commonly adopted in high-rise buildings due to their lightweight nature, ease of construction, and high strength-to-weight ratio. However, providing adequate lateral stiffness and resistance against wind and seismic forces remains a critical challenge. Reinforced concrete shear walls are among the most effective systems for resisting lateral loads, significantly reducing story drifts and mitigating non-structural damage [8-10]. Their high shear stiffness compared to other lateral load-resisting systems makes them particularly attractive for both new construction and retrofitting of existing steel buildings [6, 11, 12].

T-shaped reinforced concrete shear walls have gained considerable attention due to their three-dimensional behavior [13-15]. This configuration enables resistance to lateral loads in both principal directions [16, 17]. The geometric characteristics of these walls, such as flange length-to-thickness ratio, web dimensions, and relative positioning of components, directly influence lateral stiffness, energy dissipation capacity, and seismic performance [13, 18-20]. Adjusting these parameters provides opportunities to optimize the seismic response and material efficiency of high-rise buildings [18, 21-23].

* Corresponding author.

E-mail addresses: kbargi@ut.ac.ir (K. Bargi).

https://doi.org/10.22080/ceas.2026.31135.1074

ISSN: 3092-7749/© 2027 The Author(s). Published by University of Mazandaran.

Experimental and numerical studies have extensively examined T-shaped shear walls under various loading conditions. Lefas et al. [24, 25] investigated thirty full-scale walls under combined axial and lateral loads, highlighting the influence of height-to-width ratio, axial force, concrete strength, and horizontal reinforcement on wall performance. Their results indicated that wall strength largely depends on concrete in compression zones, while these zones enhance load-carrying capacity. Thomsen and Wallace [9] observed higher ductility in compression flanges compared to tensioned flanges. Brueggen et al. [21] and Brueggen [26] reported that T-shaped composite walls exhibit lower displacement capacity than rectangular or symmetrically flanged walls, emphasizing careful free-edge design. Rahimi et al. [27, 28] conducted two investigations on T-shaped shear walls in steel high-rise buildings. In the first study [27], they compared rectangular and T-shaped reinforced concrete shear walls within dual systems. Their results showed that T-shaped walls consistently outperform rectangular walls in terms of lateral displacement, inter-story drift, and overall stiffness distribution. The study further demonstrated that optimal performance is achieved when T-shaped walls are placed in intermediate frames, minimizing displacements in both principal directions. In a second study, Rahimi et al. [28] performed an economic assessment, revealing that T-shaped walls require less material while achieving smaller deformations, making them more cost-effective than rectangular walls. Despite the clear advantages highlighted in these studies, the influence of key geometric parameters, particularly the flange length-to-thickness ratio, on seismic performance has not been fully explored. Moreover, comparative assessments with alternative configurations, such as ┼-shaped walls, remain limited.

The present study addresses these research gaps by evaluating the seismic behavior of steel high-rise buildings equipped with T-shaped reinforced concrete shear walls for varying flange length-to-thickness ratios using linear dynamic response spectrum analysis. In addition, a comparative assessment with ┼-shaped walls is performed to examine the impact of geometric modifications on lateral stiffness, story displacement, and inter-story drift. Buildings of 10, 20, and 30 stories are considered to represent typical high-rise structures. The findings provide practical guidance for optimizing shear wall geometry, enhancing seismic performance, and achieving cost-effective design in high-rise building construction.

2. Methodology

2.1. Three-dimensional modeling

The structural modeling of the 10-, 20-, and 30-story buildings was performed using ETABS v15.2.2, which was also employed for the response spectrum dynamic analysis. Three-dimensional models were developed to capture the complete spatial behavior of the structures under both gravity and seismic loads. Fig. 1 illustrates the 3D views and floor plans of the studied buildings, showing a five-bay configuration in both longitudinal and transverse directions, with each bay measuring 6 meters. The typical story height for all buildings was set to 3.5 meters.

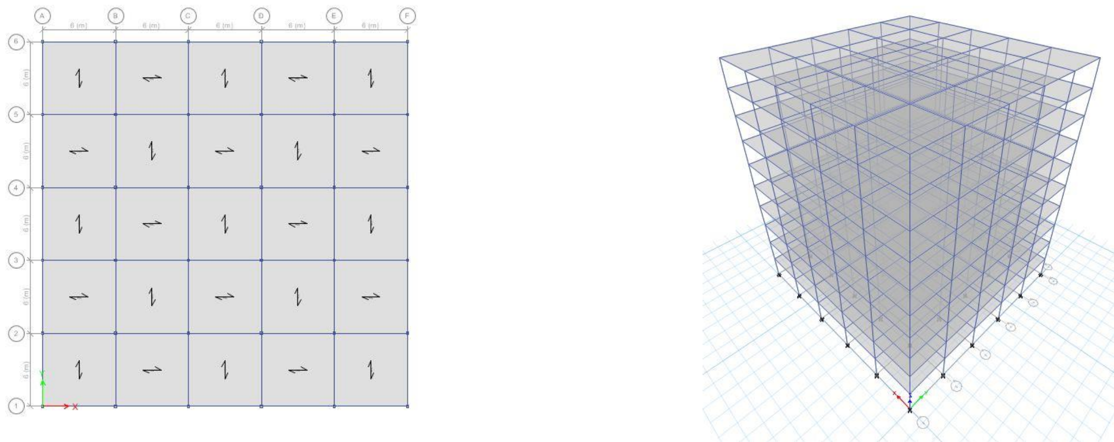

(a)

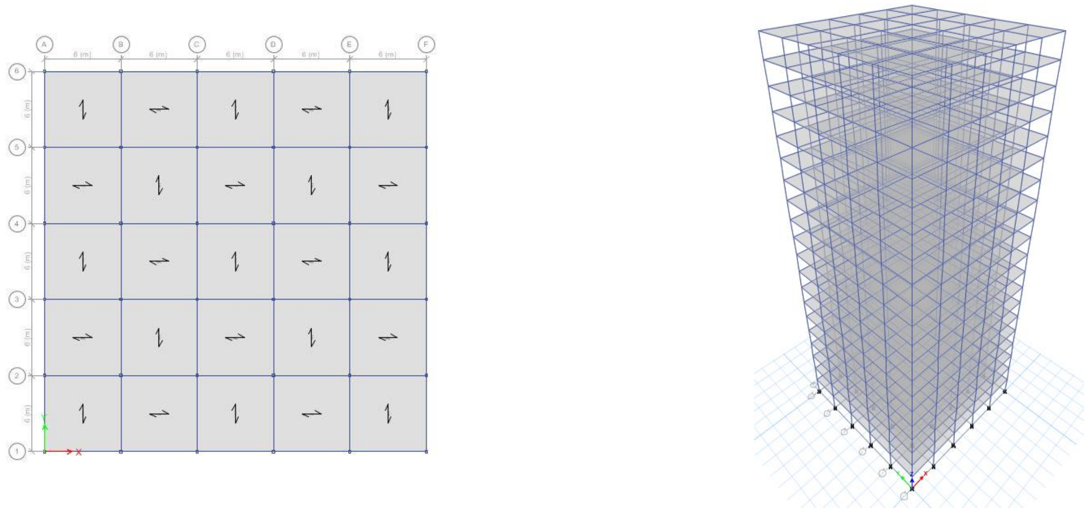

(b)

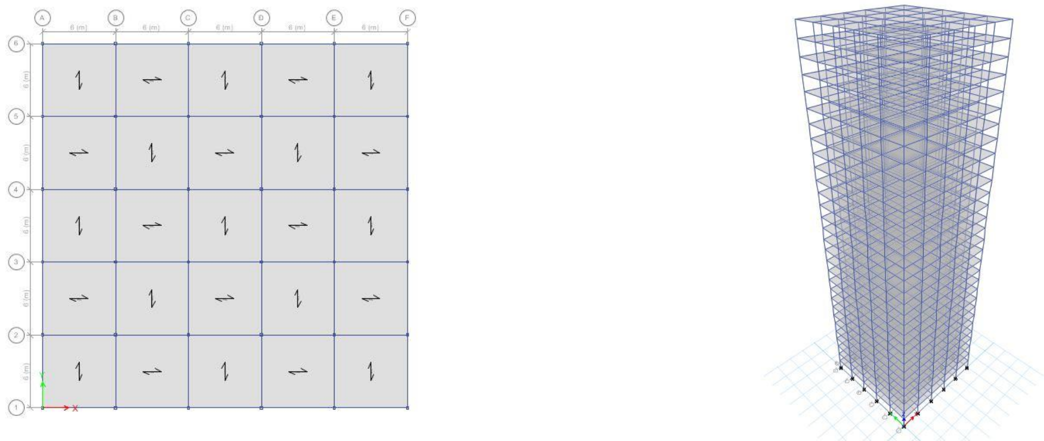

(c)

Fig. 1. Three-dimensional views and floor plans of the studied high-rise buildings: (a) 10-story, (b) 20-story, and (c) 30-story structures.

This detailed 3D modeling approach allows for accurate representation of the interaction between steel frames and reinforced concrete shear walls, ensuring realistic prediction of lateral displacements, inter-story drifts, and base shear demands. By using ETABS, both structural response and performance indicators can be precisely evaluated for different geometric configurations of the shear walls.

2.2. Structural configuration and loading

The buildings were designed as dual systems, integrating steel moment-resisting frames with reinforced concrete shear walls. For the 10- and 20-story buildings, intermediate steel moment-resisting frames (IMRFs) were combined with special reinforced concrete shear walls (S-RCWs), while the 30-story building employed special steel moment-resisting frames (SMRFs) along with S-RCWs. For the 10-story building, the thickness of the shear wall on all floors is 30 cm. In the 20-story building, the thickness of the shear wall is 40 cm for the lower 10 floors and 30 cm for the upper 10 floors. In the 30-story building, the thickness of the shear wall is 50 cm for the lower 10 floors, 40 cm for the middle 10 floors, and 30 cm for the upper 10 floors.

Gravity loads were applied as follows: typical floors were assigned a dead load of 500 kg/m², partition load of 100 kg/m², live load of 200 kg/m², and a perimeter wall load of 600 kg/m. For roof floors, dead load was 500 kg/m², live load 150 kg/m², and perimeter wall load 300 kg/m. Seismic analysis was conducted according to the Iranian Seismic Code (Standard 2800, 4th edition) using the response spectrum method. The response spectrum is defined according to the Iranian Seismic Code (Standard 2800, 4th edition), with a damping ratio of 5% for all structural modes. The modal combination was performed using the Square Root of the Sum of the Squares (SRSS) method. For each building, the number of modes considered was sufficient to achieve at least 90% of the total mass participation in both X and Y directions. These additions ensure that the dynamic analysis procedure is fully transparent, reproducible, and consistent with standard engineering practice. Structural steel was modeled as ST37 with a yield strength of 2400 kg/cm² and ultimate strength of 3700 kg/cm², while concrete compressive strength was 25 MPa, reinforced with AIII steel bars. The frames were modeled as I-shaped beams and box-section columns, and P–Delta effects were considered to account for second-order geometric nonlinearities.

This approach provides a robust framework for assessing the influence of geometric parameters, such as flange length-to-thickness ratio, on the seismic performance of T-shaped shear walls and allows for comparative evaluation with ┼-shaped configurations. Key performance indicators, including lateral stiffness, story displacement, inter-story drift, and material consumption, were extracted for detailed analysis.

It should be noted that the present study is based on linear dynamic response spectrum analysis, which evaluates the structural response within the elastic range. Nonlinear material behavior, stiffness degradation, and damage progression under severe earthquakes are not explicitly captured and would require nonlinear time-history analysis.

3. Results and discussion

The results of the present study are presented in two main sections. The first section (Section 3.1) focuses on the effects of varying the flange length-to-thickness ratio on the seismic performance of T-shaped reinforced concrete shear walls in steel high-rise buildings. The second section (Section 3.2) provides a comparative assessment between T-shaped and ┼-shaped (cross-shaped) shear walls, in which the web position relative to the flange is altered, while all other parameters remain constant. Sections 3.1 and 3.2 are complementary but examine different aspects of the study: Section 3.1 explores how geometric variations of the T-shaped shear walls influence the building's seismic response, while Section 3.2 investigates how the overall configuration affects lateral displacement, inter-story drift, and structural behavior.

3.1. Placement of T-shaped shear walls with different flange length-to-thickness ratios

In this section, the seismic behavior of 10-, 20-, and 30-story steel high-rise buildings equipped with T-shaped reinforced concrete shear walls was evaluated for varying flange length-to-thickness ratios using response spectrum analysis. The flange area was kept constant while only the length-to-thickness ratio was varied, and the web dimensions of the shear walls were assumed unchanged. For consistency, the steel frame configuration was maintained identical across all models. As previously mentioned, the plans of the 10-, 20-, and 30-story buildings consist of five bays in both longitudinal and transverse directions, with each bay measuring 6 meters. For the 10-story building, the thickness of the shear wall on all floors is 30 cm. In the 20-story building, the thickness of the shear wall is 40 cm for the lower 10 floors and 30 cm for the upper 10 floors. In the 30-story building, the thickness of the shear wall is 50 cm for the lower 10 floors, 40 cm for the middle 10 floors, and 30 cm for the upper 10 floors.

It is noted that for all models, the cross-sectional area of the shear wall in plan is kept constant to maintain a consistent amount of material. The web dimensions are also fixed across all models. The flange area of the T-shaped shear wall is maintained constant, and the only parameter varied is the flange length-to-thickness ratio. The specific values of these ratios for the different building heights and models are provided in Table 1. This table presents the selected flange length-to-thickness ratios for the T-shaped shear walls in the 10-, 20-, and 30-story buildings. Figs. 2 to 4 illustrate the layout of T-shaped shear walls with different length-to-thickness ratios in the floor plans of the respective buildings.

The results are depicted in Figs. 5 to 7, showing the variations in story displacement and inter-story drift. These analyses allow a detailed assessment of how the flange geometry influences the lateral stiffness and overall seismic response of high-rise buildings.

Table 1. Flange length-to-thickness ratios of T-shaped shear walls in 10-, 20-, and 30-story buildings.

	10 Story	20 Story	30 Story
Model 1	5	6	6
Model 2	20	16	11
Model 3	80	25	24

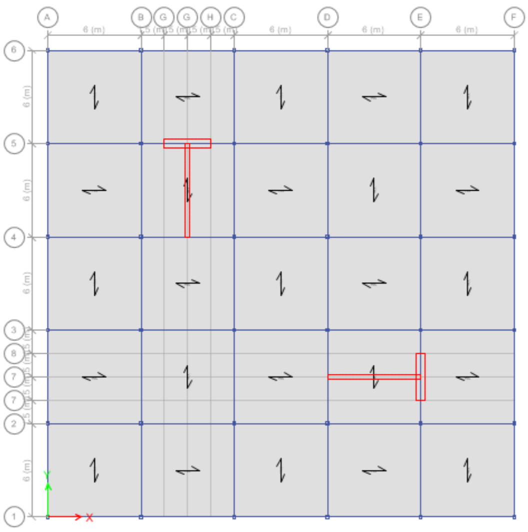

Model 1

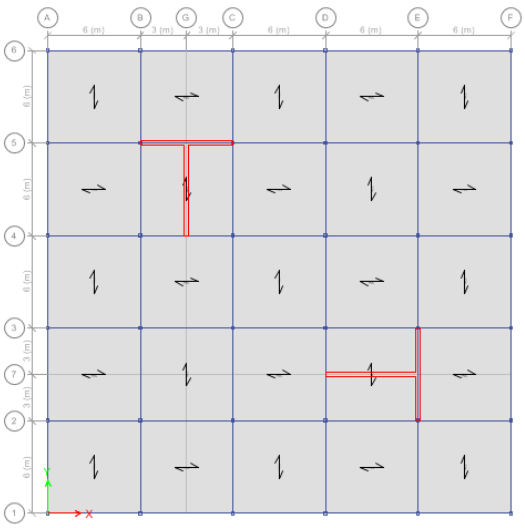

Model 2

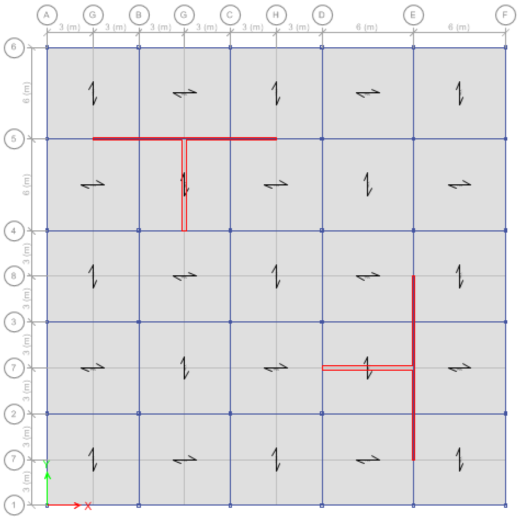

Model 3

Fig. 2. Layout of T-shaped shear walls with different flange length-to-thickness ratios in the floor plan of the 10-story building.

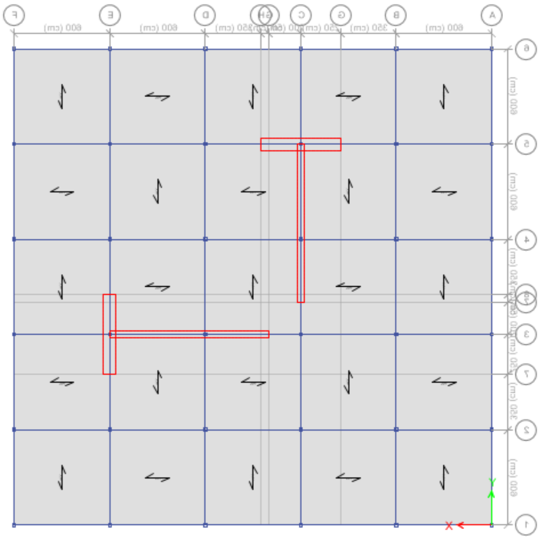

Model 1

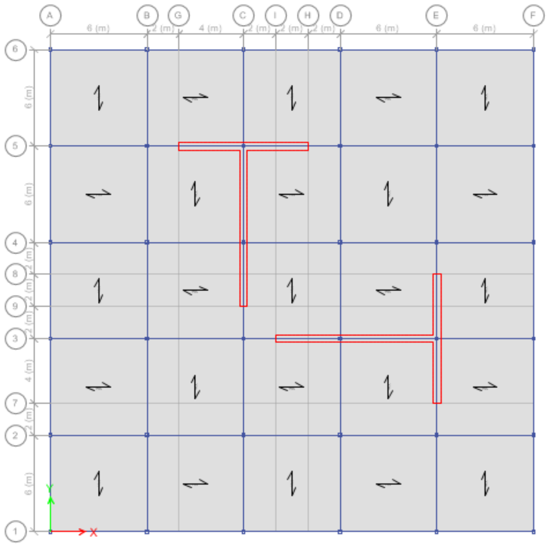

Model 2

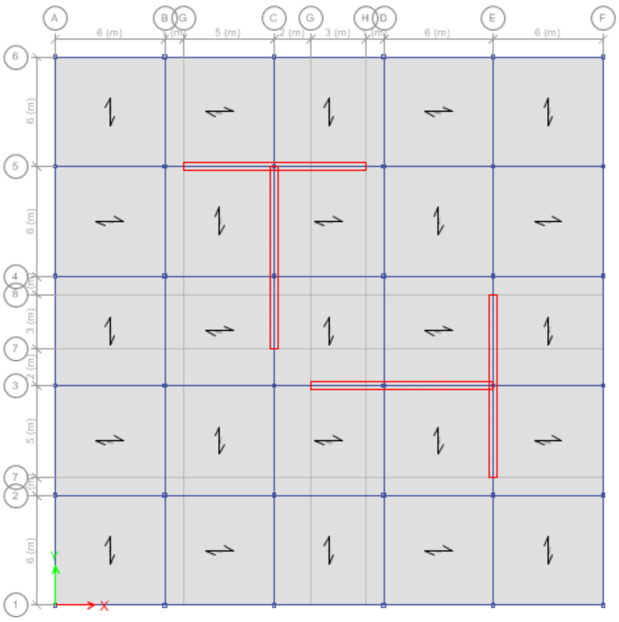

Model 3

Fig. 3. Layout of T-shaped shear walls with different flange length-to-thickness ratios in the floor plan of the 20-story building.

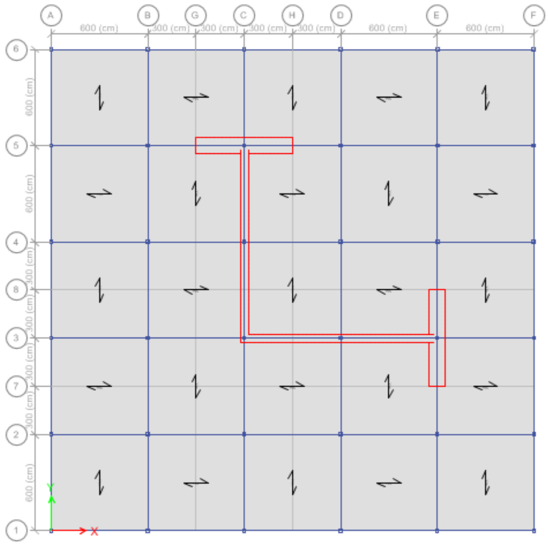

Model 1

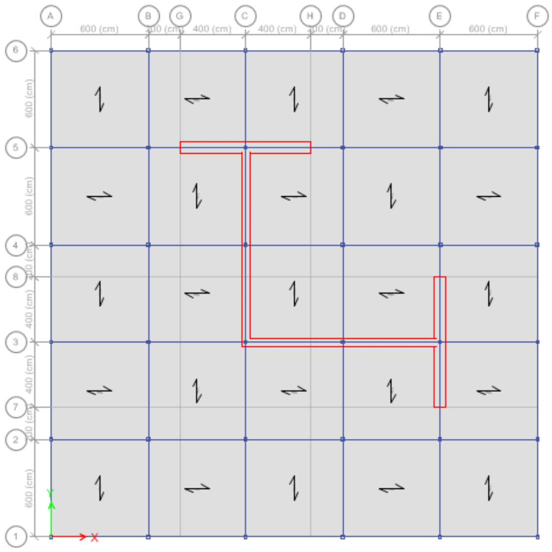

Model 2

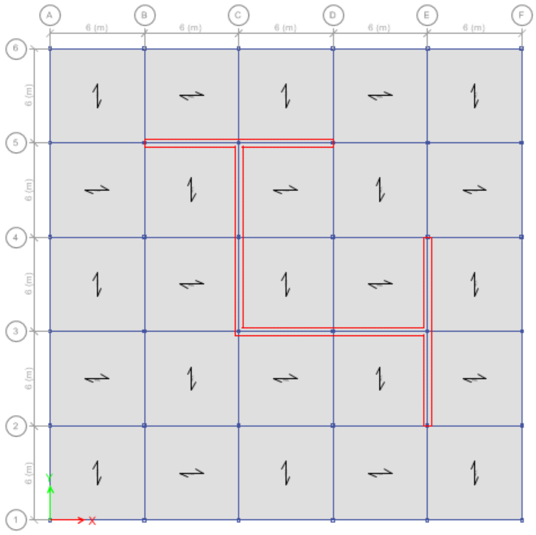

Model 3

Fig. 4. Layout of T-shaped shear walls with different flange length-to-thickness ratios in the floor plan of the 30-story building.

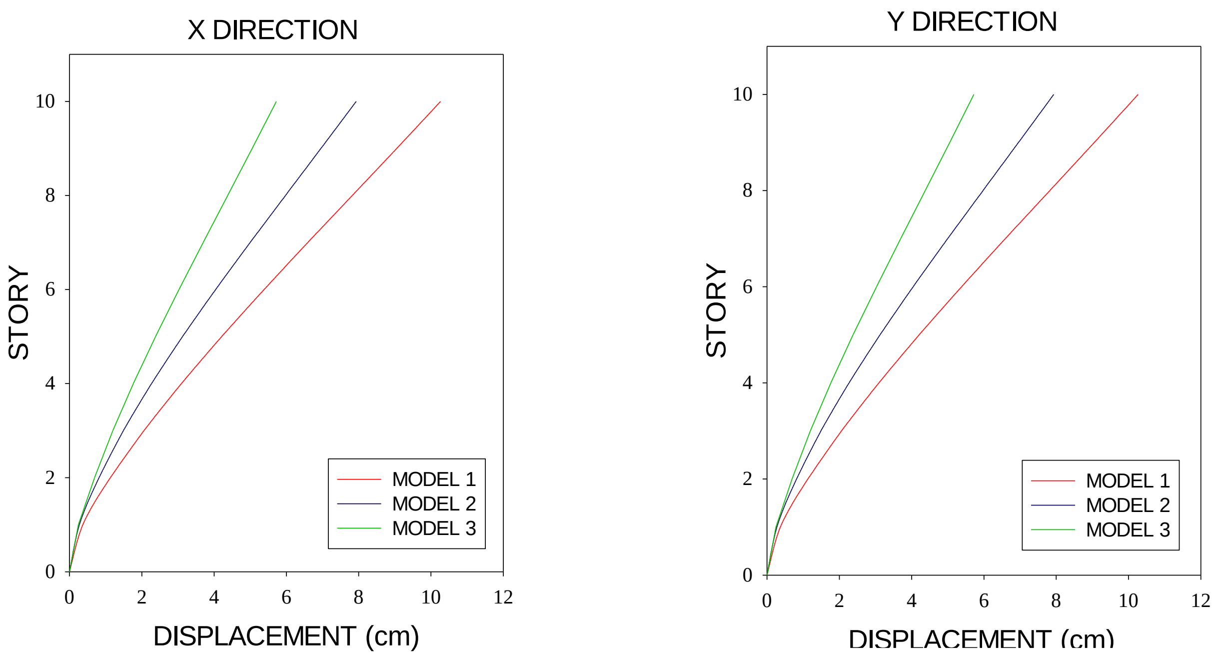

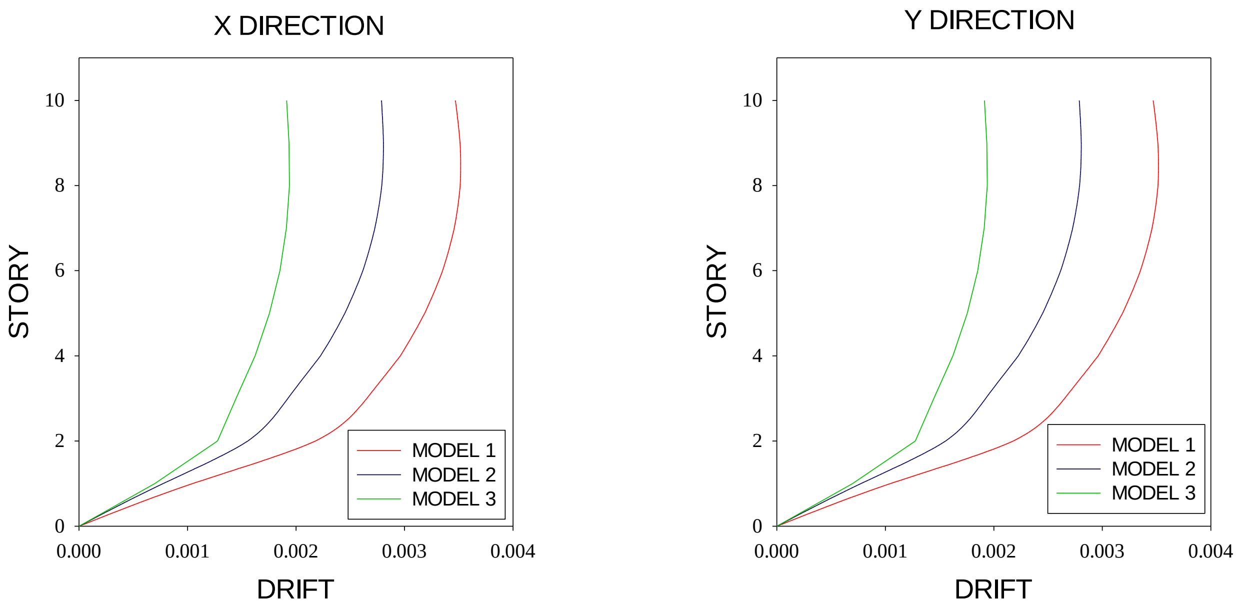

Fig. 5. Story displacement and inter-story drift of the 10-story building with T-shaped shear walls for different flange length-to-thickness ratios in the X and Y directions.

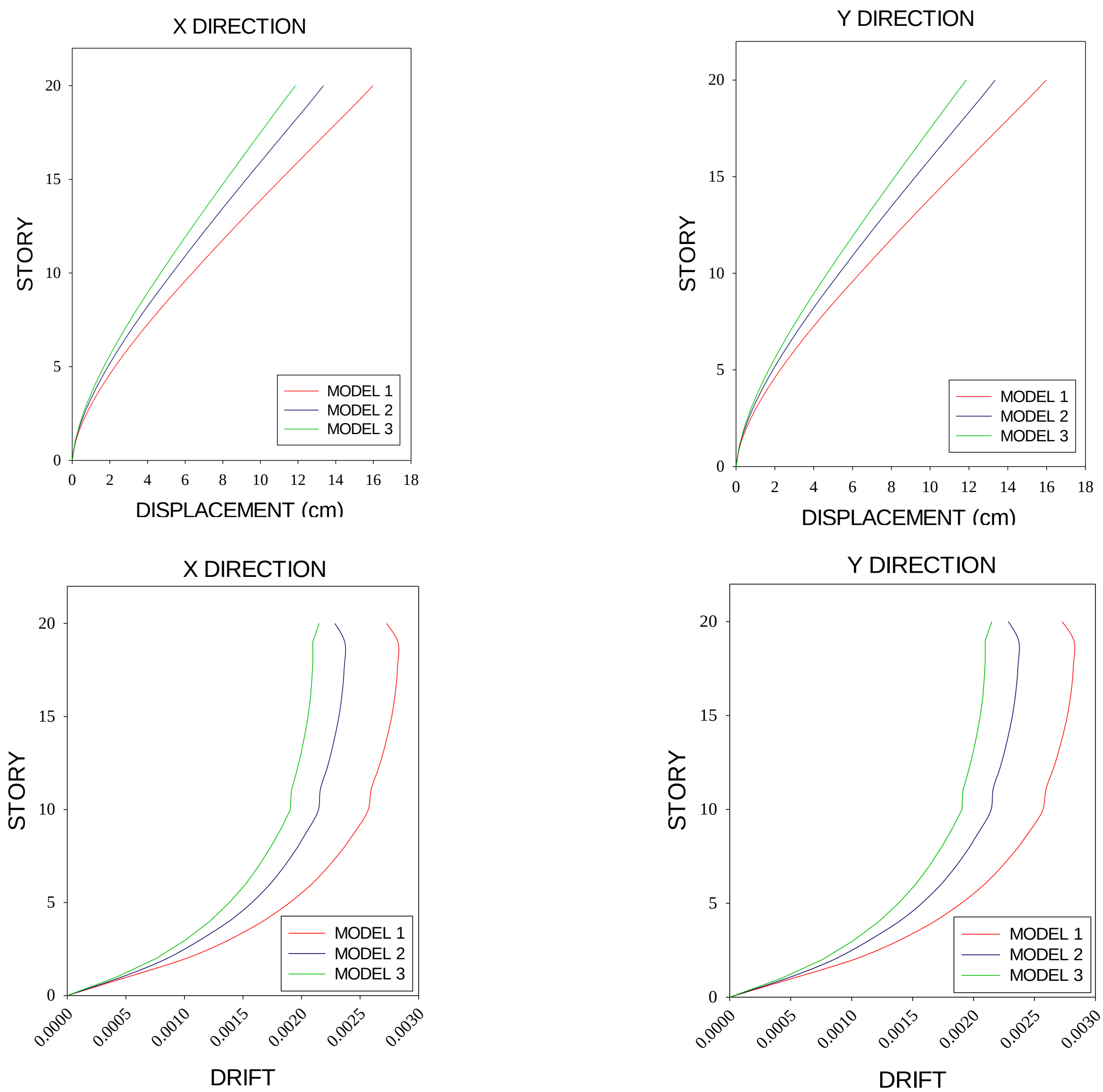

Fig. 6. Story displacement and inter-story drift of the 20-story building with T-shaped shear walls for different flange length-to-thickness ratios in the X and Y directions.

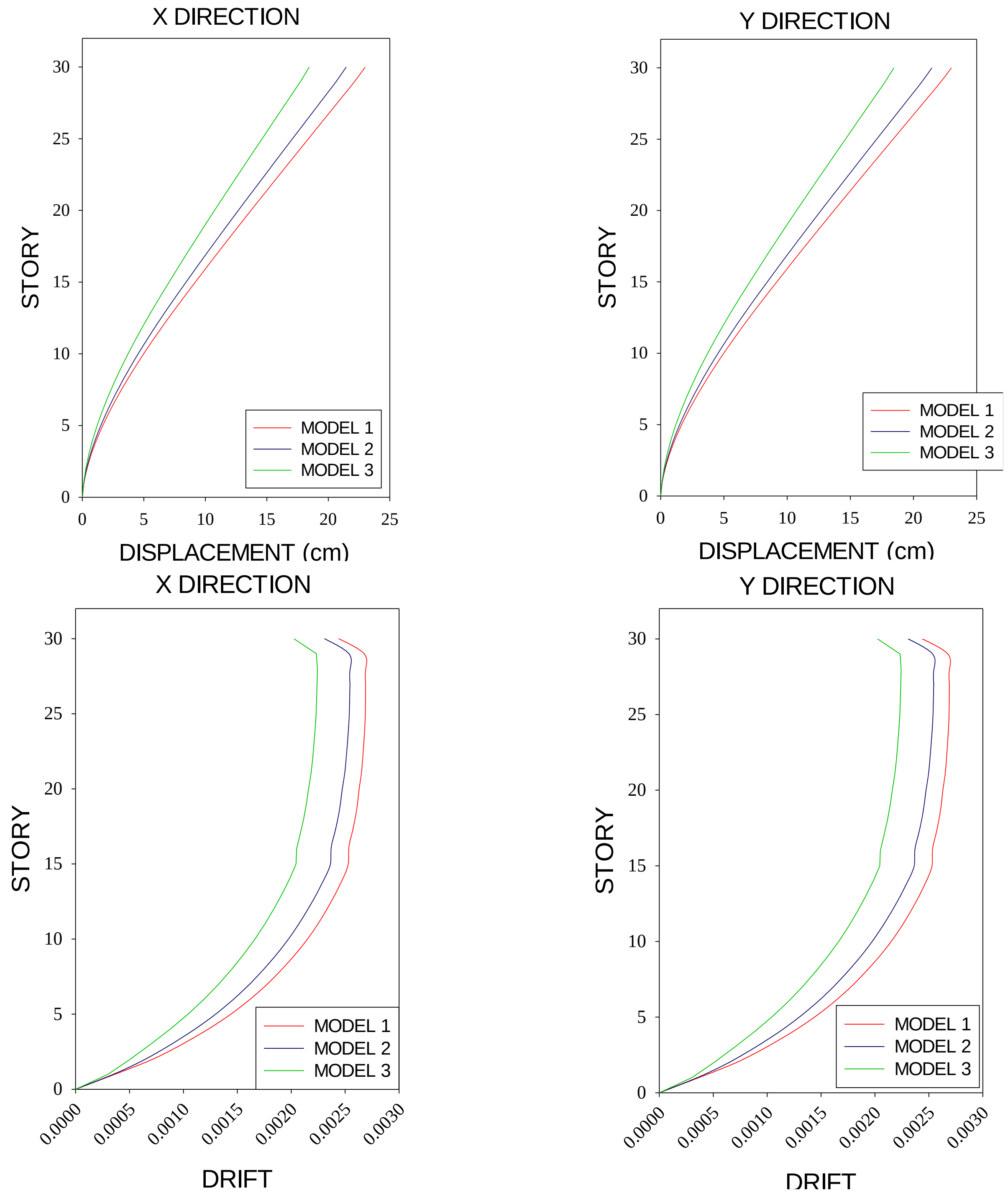

Fig. 7. Story displacement and inter-story drift of the 30-story building with T-shaped shear walls for different flange length-to-thickness ratios in the X and Y directions.

As observed, for the 10-, 20-, and 30-story high-rise buildings, when the web dimensions are kept constant and the flange area of the T-shaped shear wall remains unchanged, increasing the flange length-to-thickness ratio leads to a noticeable reduction in both story displacements and inter-story drifts. This behavior can be attributed to the increase in the moment of inertia of the shear wall section as the flange becomes longer and thinner. With a constant web, a higher flange length-to-thickness ratio enhances the in-plane flexural rigidity of the T-shaped wall, resulting in greater lateral stiffness of the structural system. Consequently, the increased stiffness effectively limits lateral deformations, leading to improved seismic performance of the building.

To provide a quantitative comparison of the maximum story displacements under different configurations, the peak story displacement values for Models 1, 2, and 3 in the 10-, 20-, and 30-story buildings are presented in Table 2. Due to the structural symmetry in the X and Y directions, the reported values are representative of both directions. In addition, the percentage reduction in maximum story displacement relative to Model 1 is reported alongside the numerical values for clarity. As observed, increasing the flange length-to-thickness ratio in Model 2 compared to Model 1 results in a reduction of the maximum story displacement in the range of approximately 7% to 22%, depending on the building height. With a further increase in the flange length-to-thickness ratio in Model 3, the reduction becomes more pronounced, reaching approximately 20% to 44% relative to Model 1.

Table 2. Maximum story displacement values for models 1, 2, and 3 in 10-, 20-, and 30-story buildings.

	Model 1	Model 2	Model 3
10 Story	10.2	7.9 (22%)	5.7 (44%)
20 Story	16	13.2 (17%)	11.9 (26%)
30 Story	23.1	21.5 (7%)	18.4 (20%)

3.2. Comparison of seismic performance of T-shaped and ┼-shaped shear walls

Fig. 8 illustrates the layout of T-shaped and ┼-shaped shear walls in the floor plans of the 10-, 20-, and 30-story buildings. For the 10-story building, the thickness of the shear wall in all floors is 30 cm. In the 20-story building, the thickness of the shear wall is 40 cm for the lower 10 floors and 30 cm for the upper 10 floors. In the 30-story building, the thickness of the shear wall is 50 cm for the lower 10 floors, 40 cm for the middle 10 floors, and 30 cm for the upper 10 floors.

The comparison results of T-shaped and ┼-shaped shear walls in the 10-, 20-, and 30-story buildings are presented in the form of story displacement and inter-story drift diagrams in the X and Y directions, as shown in Figs. 9 to 11.

It is noted that the comparison between the T-shaped and ┼-shaped shear walls was conducted based on equivalent geometric and material assumptions. The cross-sectional area of the shear walls in plan was kept constant to ensure a similar quantity of material in both configurations. In addition, the material properties and overall modeling assumptions were identical for all models. Therefore, the comparison is based solely on the effect of configuration and geometric arrangement on seismic performance.

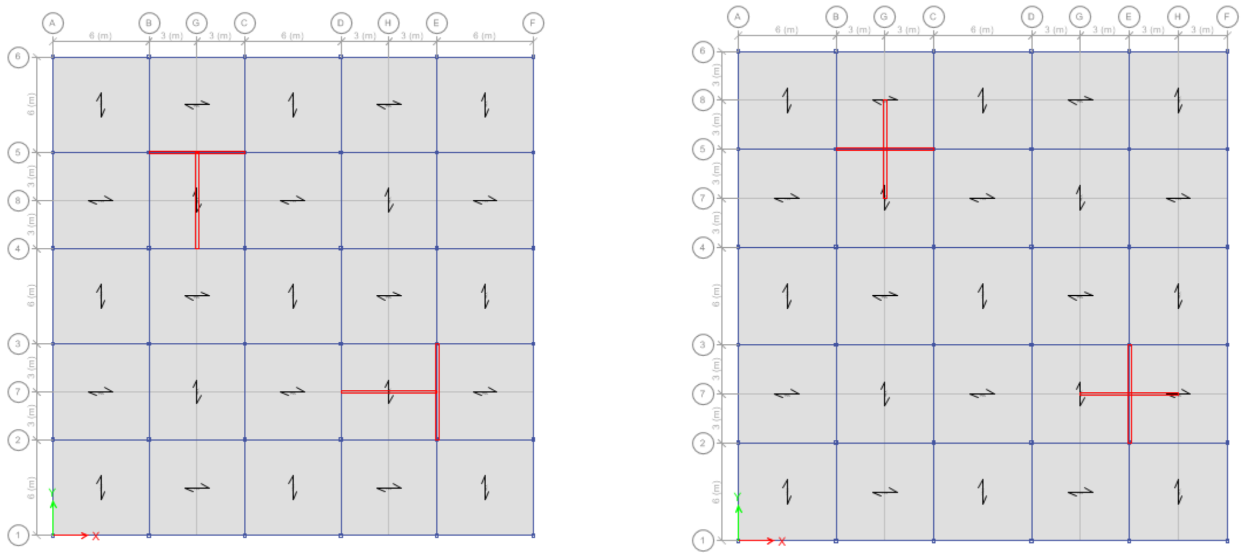

(a)

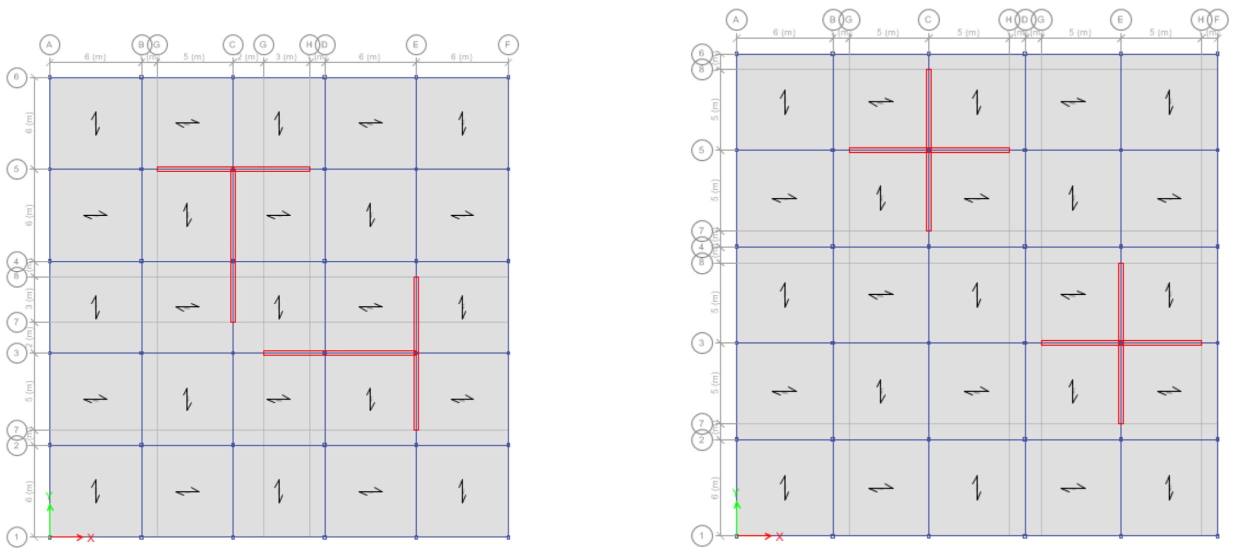

(b)

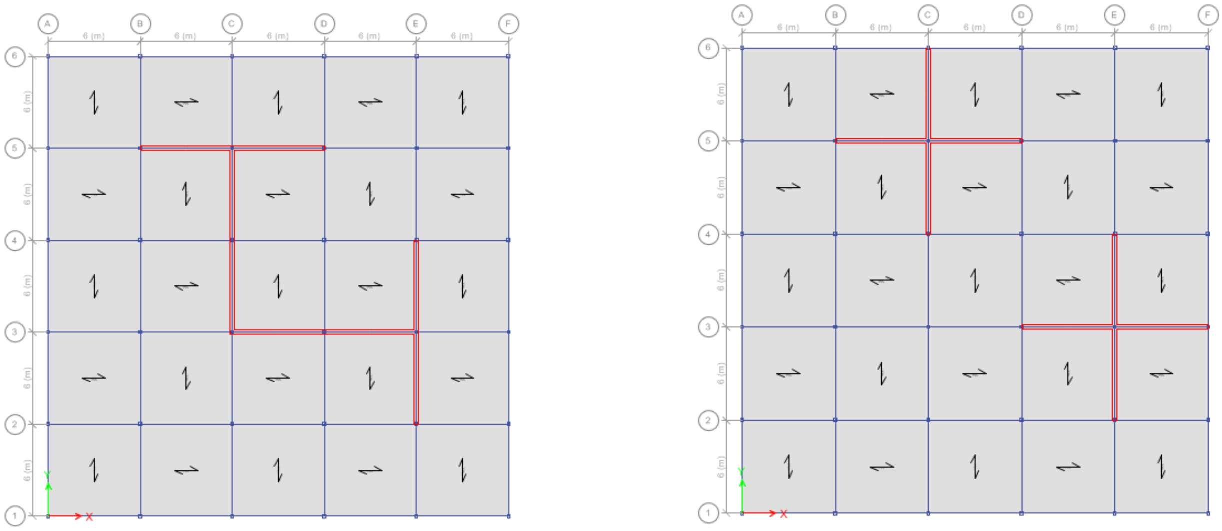

(c)

Fig. 8. Layout of T-shaped and ┼-shaped shear walls in the floor plans of high-rise buildings: (a) 10-story, (b) 20-story, and (c) 30-story buildings.

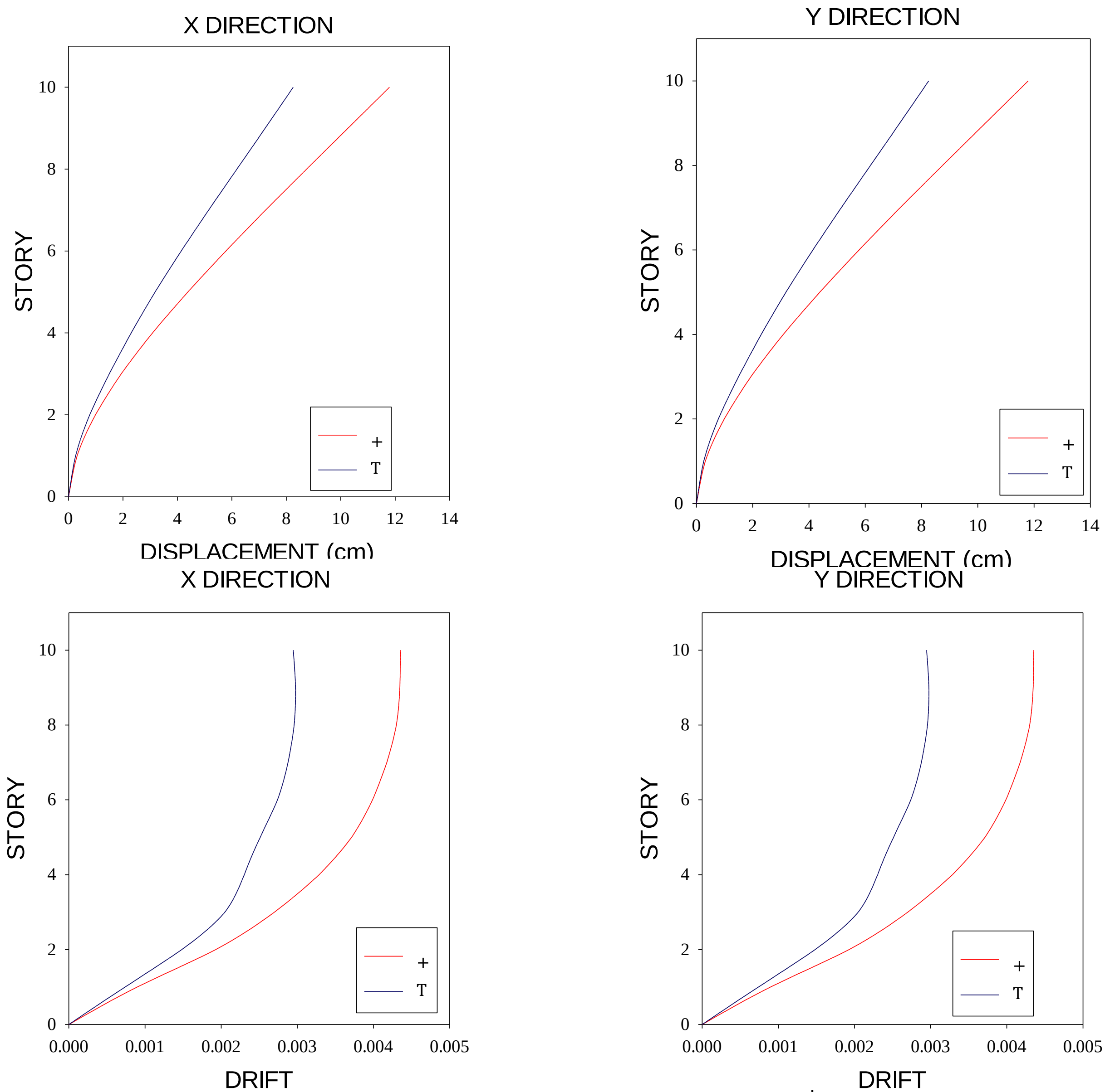

Fig. 9. Story displacement and inter-story drift of the 10-story building with T-shaped and ┼-shaped shear walls in the X and Y directions.

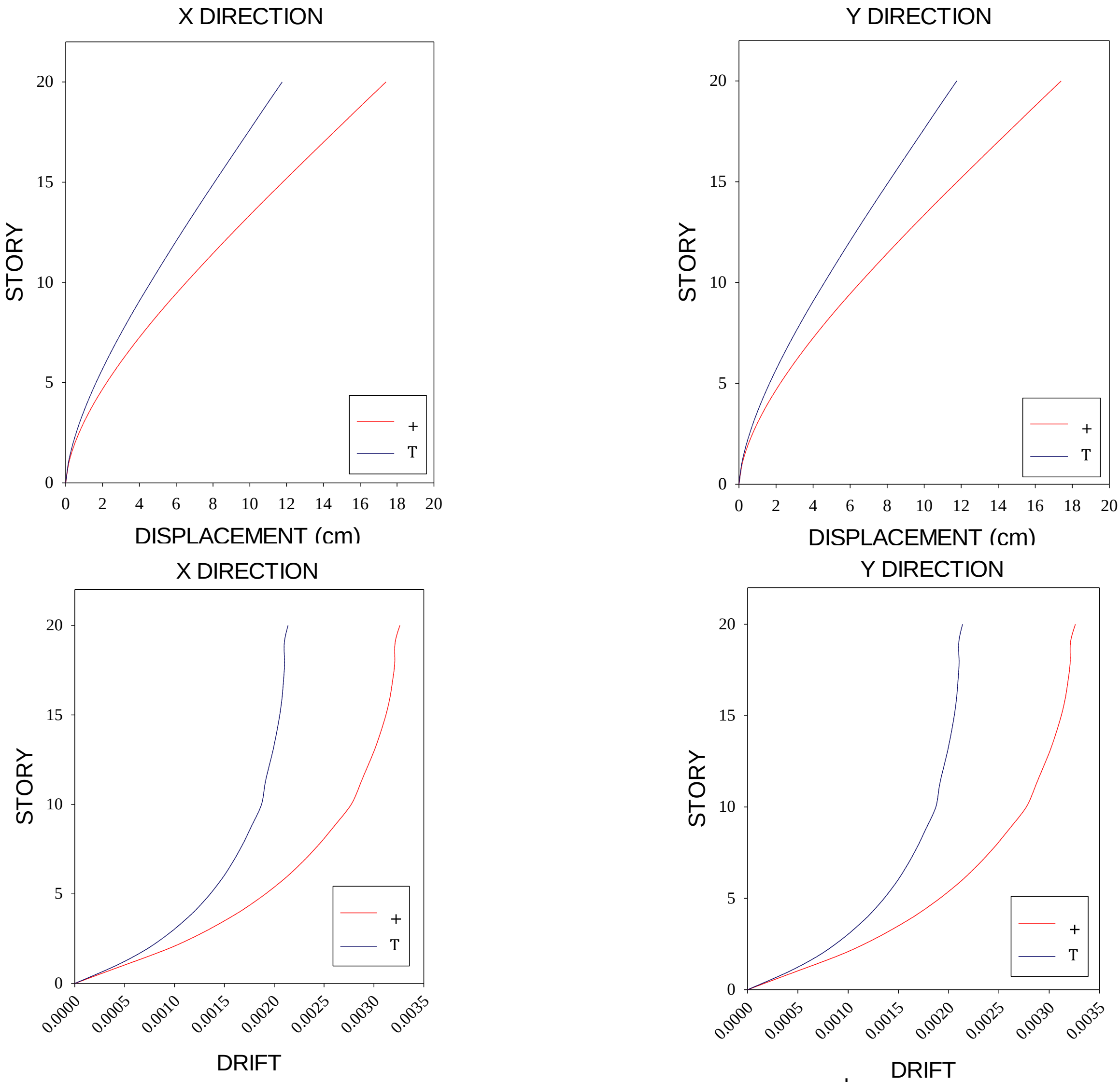

Fig. 10. Story displacement and inter-story drift of the 20-story building with T-shaped and ┼-shaped shear walls in the X and Y directions.

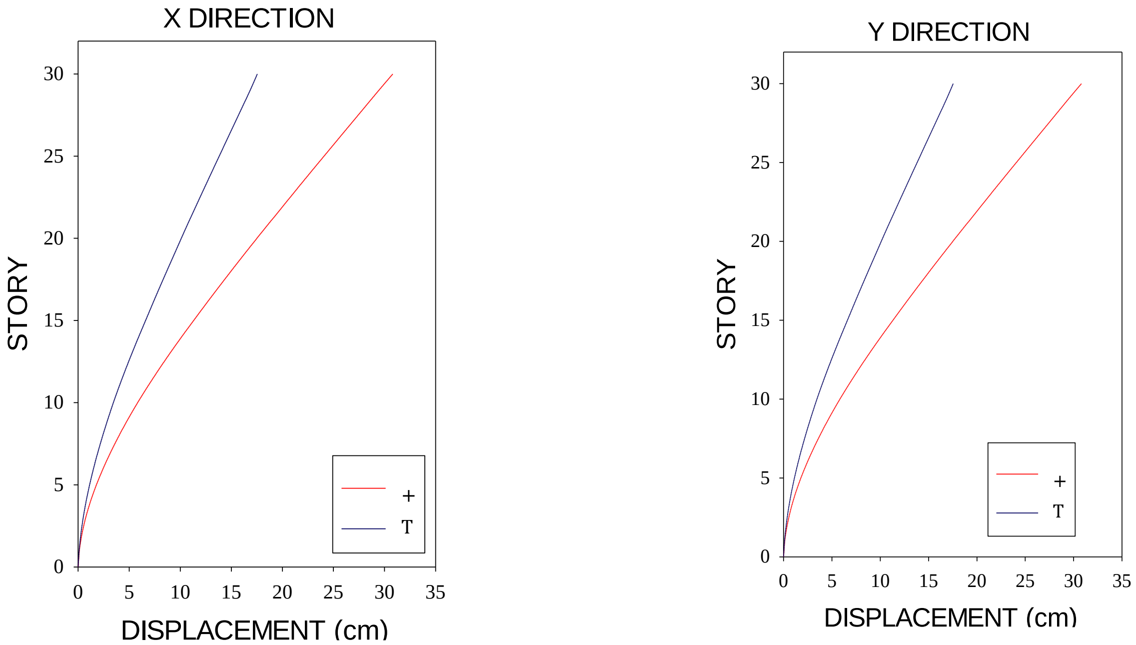

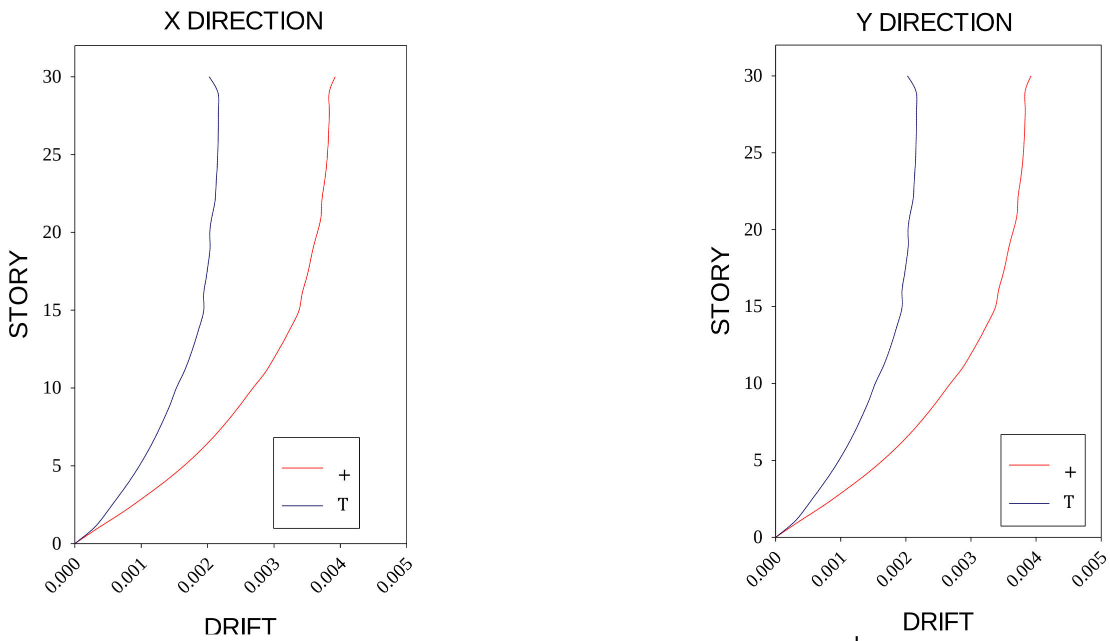

Fig. 11. Story displacement and inter-story drift of the 30-story building with T-shaped and ┼-shaped shear walls in the X and Y directions.

As observed, in the 10-, 20-, and 30-story buildings, structures equipped with T-shaped shear walls exhibit superior seismic performance compared to those with ┼-shaped shear walls in terms of both story displacement and inter-story drift. This improvement is primarily attributed to the higher lateral stiffness of the T-shaped configuration. The stiffness of a shear wall is directly related to its in-plane moment of inertia, and the moment of inertia of a T-shaped wall is greater than that of a ┼-shaped wall due to the more effective distribution of material farther from the centroidal axis of the section. Consequently, the increased moment of inertia enhances the lateral stiffness of the structural system, leading to reduced lateral displacements and inter-story drifts.

To provide a quantitative comparison between the T-shaped and ┼-shaped shear wall configurations, the maximum story displacement values for both systems in the 10-, 20-, and 30-story buildings are presented in Table 3. Due to structural symmetry in the X and Y directions, the reported displacement values are representative of both directions. In addition, the percentage reduction in maximum story displacement relative to the ┼-shaped configuration is provided alongside the numerical values for clarity. As observed, the T-shaped shear wall configuration leads to a significant reduction in maximum story displacement compared to the ┼-shaped system. Specifically, the reductions are approximately 30%, 33%, and 43% in the 10-, 20-, and 30-story buildings, respectively. These results indicate that the T-shaped configuration provides improved lateral stiffness efficiency, particularly as building height increases.

Table 3. Maximum story displacement for T-shaped and ┼-shaped shear walls in 10-, 20-, and 30-story buildings.

	┼-shaped	**T-shaped**
10 Story	11.8	8.2 (30%)
20 Story	17.5	11.7 (33%)
30 Story	30.8	17.6 (43%)

4. Conclusion

This study investigated the seismic behavior of steel high-rise buildings equipped with T-shaped reinforced concrete shear walls, focusing on the influence of flange length-to-thickness ratio and comparing T-shaped walls with ┼-shaped walls. Buildings with 10, 20, and 30 stories were analyzed using three-dimensional modeling and linear response spectrum dynamic analysis. The main conclusions drawn from this research are as follows:

1. Increasing the flange length-to-thickness ratio of T-shaped shear walls, while keeping the flange area and web dimensions constant, significantly enhances the lateral stiffness of the walls. This increase in stiffness leads to reduced story displacements and inter-story drifts in all examined buildings. The improvement is attributed to the higher moment of inertia associated with larger flange ratios, which effectively resists lateral forces.
2. T-shaped shear walls consistently outperform ┼-shaped walls in terms of lateral displacement and inter-story drift. The higher moment of inertia of T-shaped walls, due to the greater distance of the flange from the wall center, results in enhanced plan stiffness and better overall seismic performance.
3. The results indicate that careful adjustment of geometric parameters, particularly the flange length-to-thickness ratio, can be an effective strategy for optimizing seismic performance without increasing material usage. T-shaped walls offer a cost-effective and efficient lateral load-resisting system, suitable for both new constructions and retrofitting of existing high-

rise steel buildings.

4. For high-rise buildings in seismic-prone regions, placing T-shaped shear walls in intermediate frames is recommended to achieve balanced stiffness distribution and minimize displacements in both principal directions. Additionally, adopting T-shaped walls over ┼-shaped configurations can lead to more resilient and economical structural designs.

In conclusion, T-shaped reinforced concrete shear walls provide a superior solution for lateral load resistance in steel high-rise buildings, and optimizing their geometric properties can significantly enhance both structural performance and cost efficiency. Future studies may explore nonlinear dynamic analyses, multi-hazard effects, and hybrid shear wall configurations to further refine design guidelines for high-rise structures.

5. Application of research results

The findings of this study have practical implications for the design and optimization of lateral load-resisting systems in steel high-rise buildings. By adjusting the flange length-to-thickness ratio of T-shaped shear walls, engineers can significantly enhance lateral stiffness, reduce story displacements, and minimize inter-story drifts, improving the overall seismic performance of high-rise buildings. Furthermore, the demonstrated superiority of T-shaped walls over ┼-shaped configurations provides guidance for selecting optimal shear wall geometries, enabling more efficient use of materials, cost-effective design, and improved structural resilience. These results can be directly applied in the planning and retrofitting of high-rise structures in seismic-prone regions.

Statements & Declarations

Author contributions

Mehran Rahimi: Conceptualization, Investigation, Formal analysis, Resources, Writing - Original Draft, Writing - Review & Editing.

Khosrow Bargi: Conceptualization, Formal analysis, Resources, Supervision, Project administration, Writing - Review & Editing.

Funding

The authors received no financial support for the research, authorship, and/or publication of this article.

Data availability

The data presented in this study will be available on request from the corresponding author.

Declarations

The authors declare no conflict of interest.

References

[1] Rahimi, M., Davoodi, M.-R., Nematzadeh, M., Yousefpour, H. Bond performance of GFRP bars with mechanical steel anchors using RILEM beam bond tests: Experimental and theoretical study. Engineering Structures, 2024; 304: 117615. doi:10.1016/j.engstruct.2024.117615.

[2] Rahimi, M., Davoodi, M.-R., Nematzadeh, M., Yousefpour, H. The effect of type of mechanical anchors on bond behavior of ribbed-surface GFRP bars embedded in concrete. Journal of Building Engineering, 2024; 82: 108307. doi:10.1016/j.jobe.2023.108307.

[3] Razavi, M., Rahimi, M., Hasanpoor Tichi, A., Nematzadeh, M. Synergistic effects of recycled nylon granules and bacterial nano-cellulose in lightweight concrete: Experiments and predictions. Construction and Building Materials, 2025; 493: 143124. doi:10.1016/j.conbuildmat.2025.143124.

[4] Tiwari, N. D., Sarkar, P. P. Prediction of dynamic loads and responses of a tall building in tornado wind: Numerical analysis and experimental validation. Engineering Structures, 2025; 326: 119510. doi:10.1016/j.engstruct.2024.119510.

[5] Das, A., Konar, T. Asymmetric nonlinear compliant deep tank dampers-inerter for mitigating response of tall buildings under near-fault ground motions. Structures, 2025; 76: 108970. doi:10.1016/j.istruc.2025.108970.

[6] Rahimi, M., Davoodi, M.-R., Nematzadeh, M., Yousefpour, H., Azarbera, M., Fattahi, Z. A comparative study between beam and pull-out tests on bond behavior of ribbed GFRP bar in concrete conforming to RILEM standards. Archives of Civil and Mechanical Engineering, 2024; 25: 37. doi:10.1007/s43452-024-01095-1.

[7] Wang, J., Cao, S., Tse, T. K. T., Li, S., Fung, J. C. H., Li, Y. A novel life-cycle analysis framework to assess the performances of tall buildings considering the climate change. Engineering Structures, 2025; 323: 119258. doi:10.1016/j.engstruct.2024.119258.

[8] Sun, P., Nie, P., Liang, K., Wang, D. The performance analysis of shear walls with opening based on quantitative identification method of vibration modes. Alexandria Engineering Journal, 2025; 120: 637–647. doi:10.1016/j.aej.2025.02.074.

[9] Thomsen, J. H., Wallace, J. W. Displacement-Based Design of Slender Reinforced Concrete Structural Walls—Experimental Verification. Journal of Structural Engineering, 2004; 130: 618–630. doi:10.1061/(ASCE)0733-9445(2004)130:4(618).

[10] Zhou, Y., Lu, X., Dong, Y. Seismic behaviour of composite shear walls with multi-embedded steel sections. Part I: experiment. The Structural Design of Tall and Special Buildings, 2010; 19: 618–636. doi:10.1002/tal.597.

[11] Rezapour, M., Ghassemieh, M. Macroscopic modelling of coupled concrete shear wall. Engineering Structures, 2018; 169: 37–54. doi:10.1016/j.engstruct.2018.04.088.

[12] Rezapour, M., Ghassemieh, M. Macroscopic Modelling of the Concrete Shearwall with Asymmetrical Openings. Modares Civil Engineering journal, 2023; 23: 35–49. doi:10.22034/23.5.4.

[13] Mo, X., Yuan, Z., Jia, Y., Lu, L., Wei, X., Ke, N. An Experimental and Numerical Parametric Study on a Novel T-Shaped Steel–Concrete Composite Shear Wall. Buildings, 2024; 14: 2148. doi:10.3390/buildings14072148.

[14] Pin-Le, Z., Qing-ning, L. Cyclic loading test of T-shaped mid-rise shear wall. The Structural Design of Tall and Special Buildings, 2013; 22: 759–769. doi:10.1002/tal.723.

[15] Shen, S.-D., Pan, P., He, Z.-Z., Xiao, G.-Q., Ren, J.-Y. Experimental study and finite element analysis of T-shaped precast shear walls with H-shaped shear keys. Earthquake Engineering & Structural Dynamics, 2022; 51: 1158–1179. doi:10.1002/eqe.3609.

[16] Wang, B., Wu, M.-Z., Shi, Q.-X., Cai, W.-Z. Effects of biaxial loading path on seismic behavior of T-shaped RC walls. Engineering Structures, 2022; 273: 115080. doi:10.1016/j.engstruct.2022.115080.

[17] Yang, L., Zheng, S.-S., Zheng, Y., Dong, L.-G., Wu, H.-L. Experimental investigation and numerical modelling of the seismic performance of corroded T-shaped reinforced concrete shear walls. Engineering Structures, 2023; 283: 115930. doi:10.1016/j.engstruct.2023.115930.

[18] Ji, X., Liu, D., Qian, J. Improved design of special boundary elements for T-shaped reinforced concrete walls. Earthquake Engineering and Engineering Vibration, 2017; 16: 83–95. doi:10.1007/s11803-017-0370-4.

[19] Ji, X., Sun, L., Wang, S., Kolozvari, K. Seismic behavior and modeling of T-shaped reinforced concrete walls under high axial force ratios. Earthquake Engineering & Structural Dynamics, 2024; 53: 1085–1106. doi:10.1002/eqe.4060.

[20] Lu, X., Yang, J. Seismic behavior of T-shaped steel reinforced concrete shear walls in tall buildings under cyclic loading. The Structural Design of Tall and Special Buildings, 2015; 24: 141–157. doi:10.1002/tal.1158.

[21] Brueggen Beth, L., French Catherine, E., Sritharan, S. T-Shaped RC Structural Walls Subjected to Multidirectional Loading: Test Results and Design Recommendations. Journal of Structural Engineering, 2017; 143: 04017040. doi:10.1061/(ASCE)ST.1943-541X.0001719.

[22] Dan, D., Fabian, A., Stoian, V. Nonlinear behavior of composite shear walls with vertical steel encased profiles. Engineering Structures, 2011; 33: 2794–2804. doi:10.1016/j.engstruct.2011.06.004.

[23] Gu, Q., Zhao, D., Li, J., Peng, B., Deng, Q., Tian, S. Seismic performance of T-shaped precast concrete superposed shear walls with cast-in-place boundary columns and special boundary elements. Journal of Building Engineering, 2022; 45: 103503. doi:10.1016/j.jobe.2021.103503.

[24] Lefas, I., Kotsovos, M. Behavior of reinforced concrete structural walls. Strength, deformation characteristics, and failure mechanism. ACI Structural Journal, 1990; 87: 23–31. doi:10.14359/2911.

[25] Lefas, I. D., Kotsovos, M. D. NLFE Analysis of RC Structural Walls and Design Implications. Journal of Structural Engineering, 1990; 116: 146–164. doi:10.1061/(ASCE)0733-9445(1990)116:1(146).

[26] Brueggen, B. L. Performance of T-shaped reinforced concrete structural walls under multi-directional loading [PhD Thesis]. Minneapolis–Saint Paul (MN): University of Minnesota; 2009.

[27] Rahimi, M., Bargi, K. Comparative Evaluation of Seismic Behavior of T-Shaped versus Rectangular Concrete Shear Walls in High-Rise Buildings. Civil Engineering and Applied Solutions, 2025; 1: 16–26. doi:10.22080/ceas.2025.29715.1029.

[28] Rahimi, M., Bargi, K., Rezapour, M. Balancing Cost and Seismic Performance: Rectangular vs. T-shaped Shear Walls in Steel Frame Tall Buildings. Civil Engineering and Applied Solutions, 2026; 2: 12–21. doi:10.22080/ceas.2025.30091.1043.

Civil Engineering and Applied Solutions

Research Article

journal homepage: ceas.journals.umz.ac.ir

CEAS Civil Engineering and Applied Solutions

A Field-Based Polynomial Model for Estimating the 28-Day Compressive Strength of Concrete from Slump, Temperature, and Density

Aliakbar Yahyaabadi [a*], Seyyed Ghasem Rostami [a], Masood Mohammadi [a]

[a] *Faculty of Engineering, University of Bojnord, Bojnord, Iran*

ARTICLE INFO

Article history:

Received 22 February 2026

Revised 31 March 2026

Accepted 12 May 2026

Available online 01 January 2027

Keywords:

Ready-mixed concrete

Slump

Temperature

Density

Compressive strength

Prediction model

ABSTRACT

Concrete is one of the most widely used materials in the construction industry. Quality control of ready-mixed concrete is important due to the many factors that influence its quality from the production phase to placement and curing. Slump, temperature, density, and compressive strength are commonly used tests for evaluating the quality of concrete. Since the compressive strength test requires 28 days, predicting it using site-specific in situ tests can help engineers assess on-site conditions. To develop a prediction model for compressive strength, 92 samples of ready-mixed concrete were collected in collaboration with the National Standard Organization of Iran in accordance with the relevant national standards. The samples were divided into two groups of training and testing datasets, including 83 and nine randomly selected samples, respectively. According to the proposed model, compressive strength can be predicted from a twelve-term polynomial function in terms of powers of density, slump, and temperature, and their products. The performance of the model was assessed by calculating statistical indicators for the training samples as well as external validation with testing samples not used during model development. The model predicted the 28-day compressive strength with a mean absolute error (MAE) of 0.849 MPa and a coefficient of determination (R^2) of 0.744 for new samples.

How to cite this article: Yahyaabadi, A., Rostami, S. G., Mohammadi, M. A Field-Based Polynomial Model for Estimating the 28-Day Compressive Strength of Concrete from Slump, Temperature, and Density. Civil Engineering and Applied Solutions. 2027; 3(1): 51–60. doi:10.22080/ceas.2026.31362.1081.

1. Introduction

Ready-mixed concrete is produced in a plastic, fresh, and workable state by the manufacturer under standard conditions, then delivered to the consumer by truck mixers. Evaluating the quality of ready-mixed concrete is challenging, as numerous factors, such as transportation conditions, ambient temperature, and curing methods, can influence its properties from production to placement. Compressive strength is a key factor in determining the quality of ready-mixed concrete that strongly affects the durability and load-bearing capacity of structures. This strength is determined through standard compressive strength tests on concrete specimens. These tests require waiting until the conventional 28-day testing age to obtain the strength. Current standard criteria have some limitations, making the development of alternative evaluation methods necessary [1]. Various parameters can be used to estimate this strength at the time of concrete placement. Some studies focus on pre-production factors to optimize the mix design of concrete. However, studying in situ parameters, such as slump, temperature, and density of fresh concrete, is necessary to control the quality of concrete.

Slump is a widely used test for evaluating the workability of concrete [2]. Recent studies have used machine learning methods to predict concrete properties, including slump [3]. Both the temperature of fresh concrete and the curing temperature significantly influence compressive strength. Since higher temperatures accelerate the hydration process, early strength develops faster, but long-

* Corresponding author.
E-mail addresses: a.yahyaabadi@ub.ac.ir (A. Yahyaabadi).

https://doi.org/10.22080/ceas.2026.31362.1081
ISSN: 3092-7749/

term strength is reduced [4-6]. Density is another important parameter that affects compressive strength. In general, denser concretes have higher compressive strength, although the type and gradation of aggregates may alter this relationship [7-9].

However, many existing models predict compressive strength using production-phase characteristics such as the cement-to-water ratio or aggregate type. Based on these characteristics, Nguyen and Phan generated a hybrid adaptive boosting-particle swarm optimization (AB-PSO) model to predict high-performance concrete strength [10]. According to Mahajan and Sharma, aggregate type and cement content can be used in random forest and reduced error pruning tree (REPTree) models to predict compressive strength [11]. Brahmeswari and Rao also utilized machine learning models such as gradient boosting and XGBoost to predict compressive strength using production-stage parameters [12]. Some recent research has utilized fresh concrete test results, particularly slump, in machine learning-based models to improve the accuracy of compressive strength estimation [13]. Reviews of empirical prediction models for high-strength concrete indicate that the majority of these models are based on mix design variables and laboratory testing, rather than on in situ parameter measurements [14]. While some of these methods are effective, developing models that use real-time, in situ parameters of fresh concrete is necessary to support practical decision-making during construction. Predicting concrete strength before 28 days allows an early decision on the need for corrective or remedial actions. While this skill is crucial, only a few research models utilize in situ characteristics for real-time decision-making during construction.

In contrast, the aim of the present study is to fill this gap by developing a comprehensive predictive model using slump, temperature, and density as key parameters measured directly on-site. This model is based on field data from multiple projects across North Khorasan province, Iran. In the development of the model, real-world data from various construction sites were used to make rapid and evidence-based decisions about concrete management. This approach, unlike laboratory-based models, includes the variety of conditions and variability found in the field, making predictions accurate and actionable in real time.

2. Sampling and testing methods

A sampling and testing program was conducted to develop a prediction model for the compressive strength of ready-mixed concrete. For this purpose, 92 samples were collected and tested with the support of the Provincial Standard Offices of North Khorasan. All sampling and testing, including slump, fresh concrete temperature, density, and compressive strength, were conducted following the relevant Iranian National Standards [15-19], which are aligned with the corresponding internationally recognized standards, including ISO, ASTM, EN, and BS EN standards [20-24]. Results from 83 samples were used to develop the rapid prediction model for compressive strength based on slump, temperature, and density. The remaining 9 samples, randomly selected from 92 samples, were used for the final evaluation of the developed model.

Tables 1 and 2 provide the specifications of the 83 samples used for modeling and the 9 samples used for evaluation, respectively. The complete experimental dataset is provided in Table A1 (Appendix A). Tables 1 and 2 display the mean, standard deviation, minimum, maximum, and units for slump, temperature, density, and compressive strength. In the data used for modeling (Table 1), slump ranged from 45 to 140 mm, temperature from 7 to 32°C, density from 2037 to 2430 kg/m³, and compressive strength from 19.6 to 31.5 MPa. These tables show that the samples cover a wide range of different conditions well, which helps to investigate the effect of different variables on the compressive strength of concrete more comprehensively and accurately. Fig. 1 presents the histograms of the variables used in the model. Data normality was examined using the Jarque–Bera, Lilliefors, and Kolmogorov–Smirnov tests at $\alpha = 0.05$ [25]. Based on these tests, compressive strength values approximately followed a normal distribution, slump and density showed non-normal behavior, and temperature showed mixed results across the tests. Slump and density are operational field variables, and temperature is affected by local environmental conditions. Therefore, some departure from normality in the raw input variables of slump and density is practically understandable in field-based concrete data. A key strength of this dataset is that it comes from various construction projects in the North Khorasan province using standardized sampling and testing procedures. The model can accurately represent field conditions because it was developed based on field data rather than laboratory or simulated data.

Table 1. Data specifications of 83 samples used for developing the prediction model.

Parameters	Abbreviation	Type	Mean	Standard Deviation	Minimum	Maximum	Unit
Slump	S	Input	83	21	45	140	mm
Temperature	T	Input	24	7	7	32	℃
Density	D	Input	2296	79	2037	2430	Kg/m^3
Compressive strength	P	Output	26.4	2.7	19.6	31.5	MPa

Table 2 .Data specifications of 9 samples used for evaluating the prediction model.

Parameters	Abbreviation	Type	Mean	Standard Deviation	Minimum	Maximum	Unit
Slump	S	Input	79	11	65	90	mm
Temperature	T	Input	22	8	10	32	℃
Density	D	Input	2341	52	2233	2390	Kg/m^3
Compressive strength	P	Output	27.4	2.7	23.3	30.4	MPa

3. Development of the prediction model

Slump, temperature, and density are the input variables for the compressive strength prediction model. To identify an appropriate form of the prediction model, the correlation between concrete compressive strength (as the output) and different functional forms of the input variables was examined, including exponential, logarithmic, radical, trigonometric, and power functions.

An initial analysis of the results indicates that the highest correlation coefficient with compressive strength exists for first-, second-, and third-order power terms, as well as selected products and ratios of input variables, as summarized in Table 3. The corresponding p-values are also reported in Table 3, and most of the correlations are statistically significant at $p < 0.05$. However, a few combinations, such as $D/(S·T)$ and $1/T$, are not statistically significant and were therefore not considered in the final model. Based on these results, all effective parameters were included in developing a polynomial regression model for predicting the compressive strength of concrete. The influence of each term was examined during the regression process, and terms with negligible effects on prediction accuracy were removed. The final model, obtained by the least squares method, is shown in Eq. 1. In this equation, the compressive strength is expressed as a polynomial function of slump (S), temperature (T), and density (D):

$$F_c' = a_1 + a_2 S + a_3 S^2 + a_4 S^3 + a_5 T + a_6 T^2 + a_7 T^3 + a_8 D + a_9 S.D + a_{10} T.D + a_{11} S.T + a_{12} S.T.D \qquad (1)$$

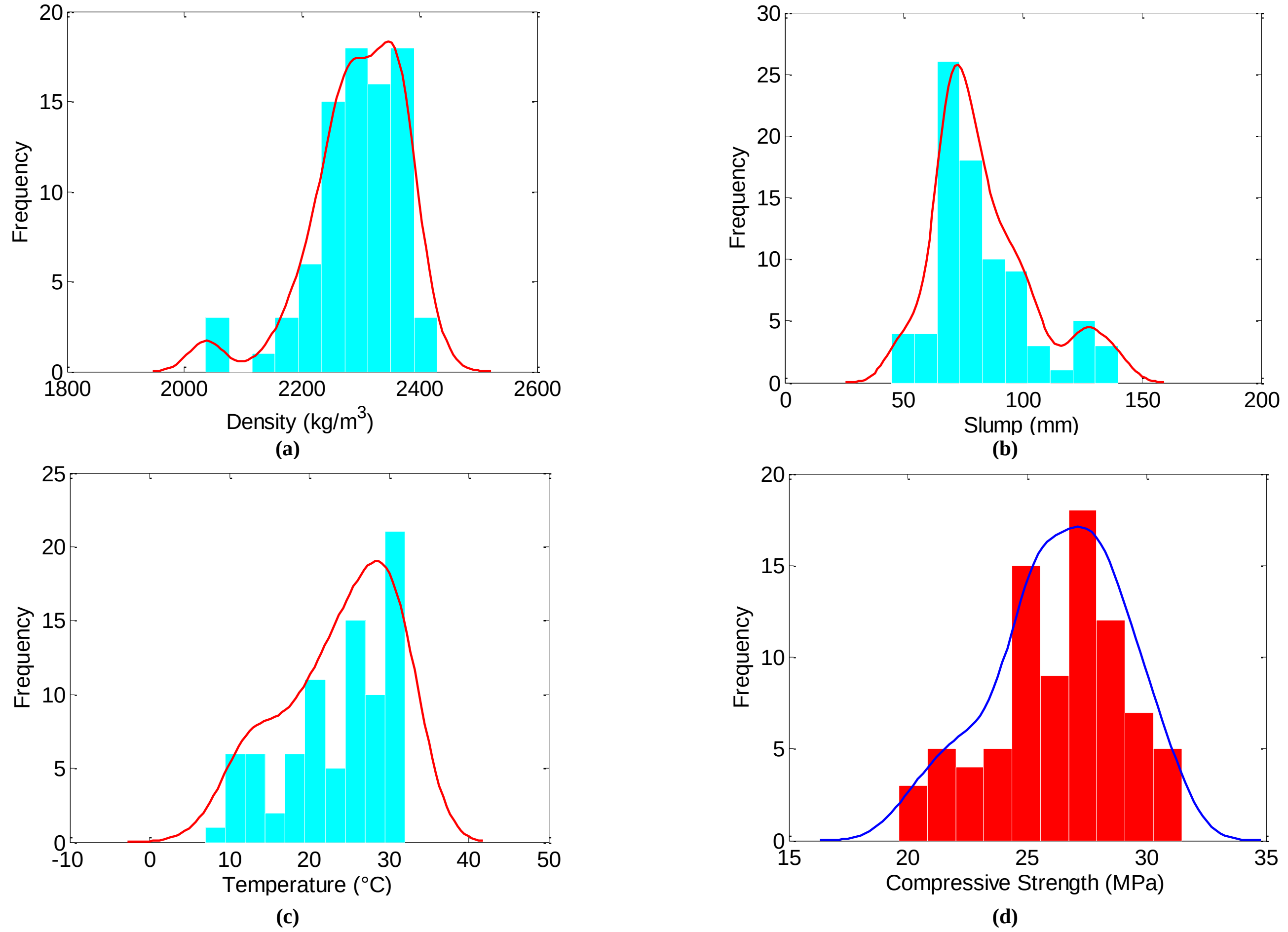

Fig. 1. Normal distribution of the data: (a) Density (kg/m³), (b) Slump (mm), (c) Temperature (°C), (d) Compressive strength (MPa).

Table 3. Correlation coefficients between different forms of input variables and concrete compressive strength.

Parameters	**S**	**T**	**D**	**S²**	**T²**	**D²**	**S³**	**T³**	**D³**
Correlation coefficient	-0.357	-0.303	0.227	-0.419	-0.354	0.223	-0.468	-0.391	0.219
P-value	0.004	0.003	0.028	0.003	0.004	0.031	0.002	0.009	0.034
Parameters	**S.T**	**S.D**	**T.D**	**S.D.T**	**1/S**	**1/T**	**1/D**	**S/(T.D)**	**D/(S.T)**
Correlation coefficient	-0.468	-0.334	-0.274	-0.455	0.217	0.157	-0.230	-0.481	-0.029
P-value	0.002	0.001	0.008	0.004	0.036	0.131	0.023	0.009	0.784

Fig. 2 shows a diagram of the overall modeling procedure. This includes preparing the database, selecting the input and output parameters, dividing the data into training and testing sets, conducting the regression process, and evaluating the model. This diagram provides a visual summary of the main steps from the raw data to the final prediction model.

In Eq. 1, F_c' is the compressive strength in MPa, and the coefficients a_1 to a_{12} are the unknown coefficients of the model. All parameters for the data samples are set in the form of a matrix according to Eq. 2:

$$[F_c'] = [1 \quad S \quad S^2 \quad S^3 \quad T \quad T^2 \quad T^3 \quad D \quad S.D \quad T.D \quad S.T \quad S.D.T\,] \begin{bmatrix} a_1 \\ \vdots \\ a_{12} \end{bmatrix} \tag{2}$$

According to the least squares method, the vector of unknown coefficients (*X*) can be calculated from Eq. 3:

$$y_{n\times 1} = A_{n\times 12}X_{12\times 1} \Rightarrow X = (A^TA)^{-1}A^Ty \tag{3}$$

Then the residual vector can be obtained from Eq. 4:

$$e = y - AX \tag{4}$$

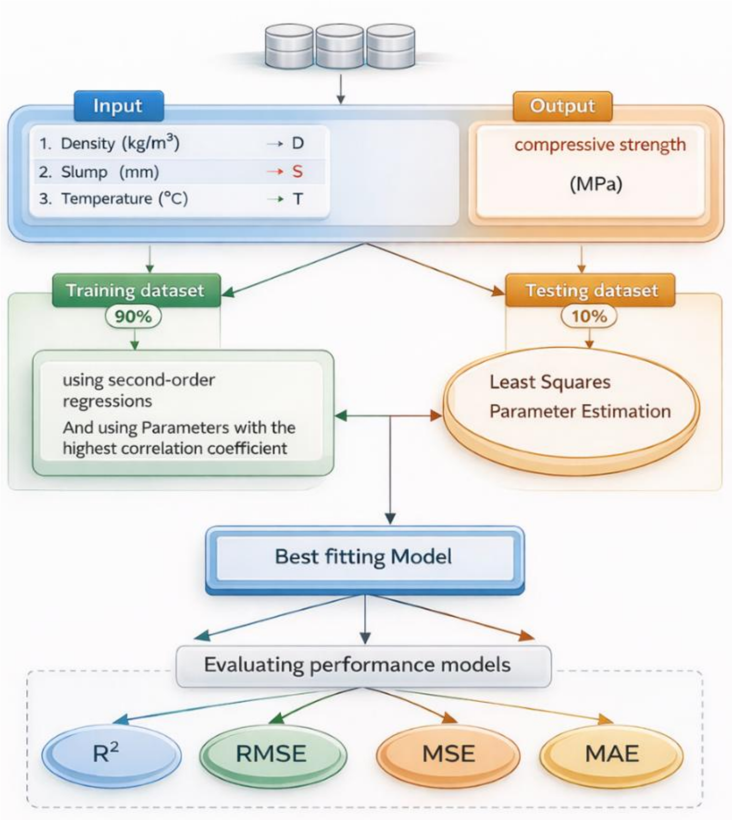

Fig. 2. Schematic overview of the modeling process, from data preparation and input and output parameter selection to regression analysis and model evaluation.

If a singularity occurred in the inverse matrix of Eq. 3, Tikhonov's method of regularization was used to solve it. A secondary factor variance test was used to ensure error adjustment and correct estimation of coefficients. The test is based on the chi-square distribution at a 95% confidence level [26] and was applied in this study as Eq. 5:

$$\frac{\sigma_0^2\chi^2_{df,\frac{\alpha}{2}}}{df} < \hat{\sigma}_0^2 < \frac{\sigma_0^2\chi^2_{df,1-\frac{\alpha}{2}}}{df} \tag{5}$$

In this equation, σ_0^2 is the estimated variance factor, *df* is the degree of freedom (equal to the number of observations minus 12 unknown coefficients), and α *is* the significance level (Type I error). This inequality gives the confidence interval for the variance. Also, to evaluate the stability of the coefficients of each model, the intentional error method was applied to each coefficient to test the residuals on the estimated observations through error simulation [27].

Table 4 presents the coefficients, their standard deviations, and corresponding p-values of the twelve-term prediction model. Most coefficients are statistically significant, and their small standard deviations indicate precise estimation. Although the ninth coefficient (slump × density) is not individually statistically significant, it was retained for structural and predictive reasons. Because of the limited sample size and the resulting ill-conditioning (near-singularity) of the design matrix associated with the model structure, the coefficient estimates may become unstable. Therefore, the p-value of this term was not used as the sole criterion for exclusion. Since the model includes the three-way interaction term (slump × temperature × density), retaining the slump × density term preserves the hierarchical structure of the polynomial model. In addition, this term showed a non-negligible negative correlation with compressive strength relative to the other transformed input variables (Table 3), and its removal increased the overall mean squared error by 0.469%, indicating a slight reduction in predictive accuracy.

Table 4. Coefficients and standard deviations of the compressive strength prediction model.

Coefficients	Values	Standard deviation	P-Value
a_1	-0.01223751	0.005117	0.0194
a_2	-0.58810606	0.246722	0.0198
a_3	0.00852123	0.002610	0.0016
a_4	-0.00003820	0.000009	0.0000
a_5	-0.11111143	0.046205	0.0187
a_6	-0.08002689	0.029171	0.0076
a_7	0.00093905	0.000456	0.0433
a_8	0.01114784	0.003672	0.0033
a_9	0.00000556	0.000089	0.9505
a_{10}	0.00090258	0.000255	0.0007
a_{11}	0.02373212	0.010056	0.0210
a_{12}	-0.00001050	0.000004	0.0171

4. Evaluating the efficiency of the proposed model

The efficiency of the proposed model and its prediction accuracy were evaluated in two stages. First, the internal performance of the model was assessed by calculating statistical indicators. Second, external validation was carried out using data not employed during model development.

To evaluate the error via statistical indicators, the residuals of the model are provided in Fig. 3. In this figure, the residual values are presented to display both the general trend and the variations corresponding to each of the samples. The residuals are small and mostly distributed symmetrically around zero, showing that the model's predictions are generally reliable and free from systematic bias. In addition, other indicators were calculated to better assess the accuracy of the predictions. The considered indicators include mean absolute error (MAE), mean squared error (MSE), root mean squared error (RMSE), the coefficient of determination (R^2), and the minimum and maximum prediction errors (differences between the predicted and observed values). Table 5 presents the evaluation results for both training and test datasets. The p-values of the coefficients are reported in Section 3, where they are shown to be statistically significant and within acceptable ranges. Therefore, they are not discussed further in this section.

The mean absolute error (MAE) for the training dataset was 1.237 MPa, roughly 4.7% of the average compressive strength, reflecting the average size of the prediction errors. The mean squared error (MSE) reached 2.155 MPa², while the residual variance, adjusted for degrees of freedom, was 1.578 MPa². Both values are low compared with the variability in compressive strength, indicating that the average prediction errors are relatively small. The coefficient of determination (R^2) was 0.699, showing that 69.9% of the variation in the observed data is captured by the model, while 30.1% remains unexplained. This conclusion is also supported by the comparison graph (Fig. 4), where the fitted line is close to the ideal y = x line, and most points lie near it.

To evaluate the external performance of the model, nine data points that were randomly set aside at the beginning and not used during model training were employed. The MAE and RMSE for the nine testing samples are 0.849 MPa and 1.285 MPa, respectively. These values are slightly lower than the corresponding values for the training dataset. This observation indicates that the model can effectively predict the unseen data. The coefficient of determination, $R^2 = 0.744$, confirms that the model can capture a substantial proportion of the variance. Furthermore, the minimum and maximum prediction errors are -3.48 MPa and 0.89 MPa, respectively. These values show limited variation and are smaller than those observed for the training data. A closer look at the residuals indicates that the model can predict samples with compressive strengths below 25 MPa more accurately. Since such low early-age strengths are undesirable, the model's ability to estimate the 28-day compressive strength from initial measurements (slump, density, and temperature) can help guide decisions on-site.

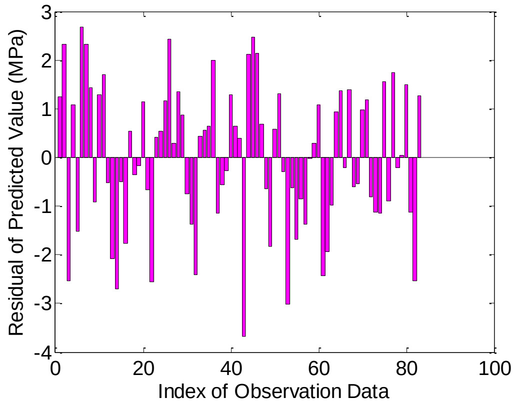

Fig. 3. Residuals of model predictions for all samples.

The main objective of this model is to offer a fast and simple method for estimating compressive strength based on basic slump, temperature, and density tests. Thus, the observed errors mainly reflect natural variations in concrete quality and uncertainties in production, transportation, and placement. Considering these, the proposed model can be used as a useful and efficient tool for rapid and practical prediction of the compressive strength of ready-mixed concrete in real conditions and on-site projects. It should be mentioned that this model is applicable to the range of input parameters considered in this study. According to Table 1 and considering the accuracy of the prediction model, the recommended ranges for input parameters are 50 to 140 mm, 7°C to 32°C, and 2040 to 2430 kg/m^3 for slump, temperature, and density, respectively. At the same time, one limitation of this study is the relatively small number of training and testing samples. This was mainly due to the need to use only sufficiently reliable and well-documented data for modeling and validation. Therefore, a smaller but more reliable dataset was preferred. Future work should validate the model using larger independent datasets when such reliable data become available.

Table 5. Model performance metrics for the training and testing datasets (MAE, MSE, RMSE in MPa; R^2 unitless).

Dataset	MAE	MSE	RMSE	R^2	Min Error	Max Error
Training dataset	1.237	2.155	1.468	0.699	-3.68	2.67
Testing dataset	0.849	1.651	1.285	0.744	-3.48	0.89

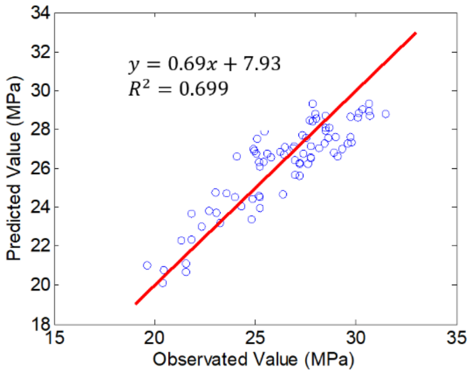

Fig. 4. Comparison of observed and predicted compressive strength values.

5. Effects of temperature, density, and slump on the compressive strength of ready-mixed concrete

After developing the prediction model, the influence of key input parameters on compressive strength is considered. In this section, the effects of temperature, density, and slump on the compressive strength of ready-mixed concrete are analyzed using the proposed model. Fig. 5 provides a clearer analysis of how variations in temperature, density, and slump affect compressive strength. To illustrate parameter interactions, graphs were created by varying two parameters along the axes while holding the third constant. Based on the adopted approach, the following parameter values were chosen for constructing the interaction graphs: Density: 2000, and 2400 kg/m³, Slump: 40 and 120 mm, and Temperature: 15 and 35°C.

5.1. Effect of temperature and slump on compressive strength

The contour plots in Figs. 5a and 5b show an approximately circular region in the temperature–slump space where the predicted compressive strength reaches its highest values. For both densities of 2000 and 2400 kg/m³, the peak region is observed around slump values near 91–103 mm and temperatures approximately 14–21°C. Moving away from this region in either direction, whether by increasing or decreasing the slump or by changing the temperature, is associated with a gradual reduction in predicted strength. For example, at a density of 2000 kg/m³, increasing slump to 140 mm at 15°C corresponds to a decrease in predicted strength from 26.6 MPa down to 20.7 MPa. A similar trend is seen at 2400 kg/m³, where predicted strength decreases from near 30.4 MPa to 21.4 MPa under comparable conditions. Likewise, fixing slumps and increasing temperatures tend to reduce predicted strength. After observing the patterns in Figs. 5a and 5b, the optimal ranges for slump and temperature were calculated using the prediction model across the studied density interval (2000-2450 kg/m³). The optimal ranges for slump and temperature that lead to maximum compressive strength are found to be 89–105 mm and 17–18°C, respectively. The optimum temperature range is close to the standard curing temperature of 20 ± 2 °C used in the Iranian and European standards and is also consistent with ASTM practice and previous studies [5, 19, 23, 28].

It is recognized that workability (as indicated by slump) and temperature affect hydration and compaction, and as a result, influence compressive strength. While earlier studies such as Neville emphasize the influence of mixture proportions and curing on strength, they do not prescribe a single optimum for slump and temperature under all conditions [6]. Our results similarly show a peak region in the parameter space where predicted compressive strength is highest.

5.2. Effect of density and temperature on compressive strength

Figs. 5c and 5d show the effects of density and temperature on compressive strength at two fixed slump levels, 40 mm and 120 mm, respectively. As can be seen in these figures, increasing density leads to higher compressive strength. For example, at a slump of 40 mm and within the temperature range of 14–21°C, raising density from 2000 to 2400 kg/m³ increases the predicted strength from about 22.5 MPa to roughly 30.3 MPa, a 35% increase. At the higher slump of 120 mm, the same amount of change in density results in a smaller increase of about 8%, from around 25.7 MPa to 27.8 MPa. This indicates that the influence of density on compressive strength is more evident at lower slump levels.

As observed in Figs. 5a and 5b, the effect of temperature follows a similar trend, with an optimal range identified between 14 and 21°C. Moving outside this range reduces the predicted strength. Unlike the slump–temperature plots, there is no distinct optimal density, and higher density consistently improves strength. This conclusion is consistent with the finding of other research, such as that of Mehta and Monteiro, that concrete density significantly affects compressive strength [7]. These observations highlight that both density and temperature are important parameters, while the magnitude of density effects depends on the slump level.

The effect of temperature on strength reduction is investigated at a representative density of 2400 kg/m³. At this density, the maximum compressive strength of 30.37 MPa occurs at a slump of 92 mm and a temperature of 17°C, according to Eq. 1. Keeping slump and density constant, increasing the temperature to 32°C reduces the predicted strength by 11.2% to 26.98 MPa. Decreasing the temperature to 7°C reduces the strength by 17.8%, resulting in a new value of 24.96 MPa. These results show how deviations from the optimal temperature range can reduce the compressive strength.

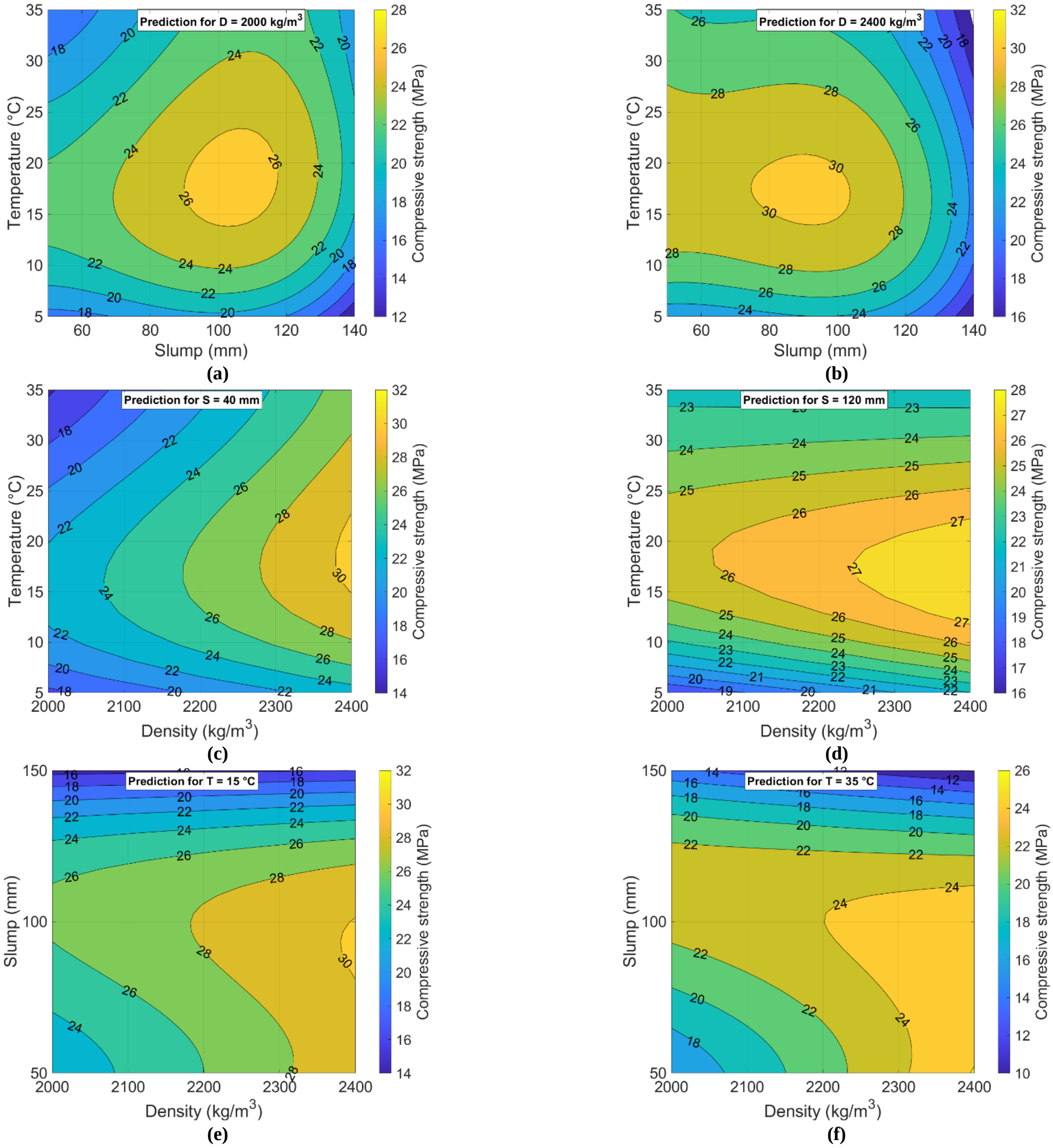

Fig. 5. Effect of key parameters on the 28-day compressive strength of ready-mixed concrete: (a and b) density fixed at 2000 and 2400 kg/m³, (c and d) slump fixed at 40 and 120 mm, and (e and f) temperature fixed at 15 and 35 °C.

5.3. Effect of density and slump on compressive strength

Figs. 5e and 5f show the combined effect of density and slump on compressive strength at fixed temperatures of 15°C and 35°C, respectively. The general shape of these plots is similar to that observed in Figs. 5c and 5d. In contrast to Figs. 5a and 5b, no distinct optimum region is observed for slump and density. Instead, compressive strength consistently increases with an increase in density in both figures. For example, at a slump of about 100 mm, increasing density from 2000 to 2400 kg/m³ raises the compressive strength from approximately 26.3 MPa to about 30 MPa at 15°C and from around 22.7 MPa to nearly 25.3 MPa at 35°C. At the same time, the influence of slump follows a pattern similar to that of Figs. 5a and 5b. Slump values in the range of approximately

90–100 mm lead to higher compressive strength, and deviations from this range reduce the strength. These results confirm that an intermediate slump range remains favorable across different temperature conditions.

Similar to section 5.2, the effect of slump is investigated at a representative density of 2400 kg/m³. Increasing slump to 140 mm from the optimum value of 92 mm at a constant density and temperature of 2400 kg/m^3 and 17 °C reduces the compressive strength by 30.3% to 21.4 MPa. Conversely, decreasing slump to 50 mm reduces the compressive strength by 3.2%. These results show that increasing slump is more effective in reducing the compressive strength, and the effect of reducing the slump is negligible. The asymmetry in the predicted effect of slump is seen across the studied slump range in Fig. 5(a) and Fig. 5(b), not only at the extreme values. Therefore, it is not interpreted as a boundary effect of the model and may be explained as follows. At high slump, strength decreases due to an increase in the water-cement ratio. In contrast, at low slump, the mix becomes less workable and harder to compact, but the lower water-cement ratio partly balances this effect.

6. Conclusion

In this study, a prediction model was developed for the 28-day compressive strength of concrete based on density, slump, and temperature of fresh concrete. Non-time-consuming tests can be used to predict the results of time-dependent compressive strength tests, enabling engineers to make quick decisions about concrete quality control. For this purpose, 92 ready-mixed concrete samples were tested from real projects in North Khorasan province. Using real samples instead of laboratory ones increases the validity and reliability of the model for use in the construction industry. Results from 83 samples were used to develop the rapid prediction model for compressive strength, while the remaining randomly selected 9 samples were used for the final evaluation of the developed model.

- A prediction model consisting of twelve terms was developed to estimate the compressive strength of concrete based on slump, temperature, and density. For this purpose, different combinations and functional forms of these variables were examined. The model includes a constant term, polynomial terms up to the third order for slump and temperature, a linear density term, and product terms of slump–density, temperature–density, slump–temperature, and the product of these three variables. The prediction model is applicable to the considered range of input parameters, 50 to 140 mm, 7°C to 32°C, and 2040 to 2430 kg/m^3 for slump, density, and temperature, respectively.
- The performance of the proposed model was evaluated for both training and testing datasets. Statistical indicators included p-values of the coefficients, mean absolute error (MAE), mean squared error (MSE), root mean squared error (RMSE), coefficient of determination (R^2), and maximum and minimum prediction errors. In all cases, the model predicted the results with good accuracy. It is notable that the performance of the model on the testing data was close to and slightly better than the training data. This evidence shows that this model can estimate the compressive strength in terms of density, slump, and temperature for new samples.
- It was found that the optimal ranges for slump and temperature across all studied densities leading to maximum compressive strength are 89–105 mm and 17–18°C, respectively.
- In contrast to slump and temperature, density does not have a specific optimum range, and increasing density increases the compressive strength.
- The prediction model demonstrates that the optimum values for slump and temperature at a density of 2400 kg/m³ are 92 mm and 17°C. At these conditions, the compressive strength reaches 30.37 MPa. Keeping density and slump constant and increasing the temperature to 32°C reduces the strength by 11.2%, while decreasing it to 7°C causes a 17.8% reduction. These findings indicate that the impact of temperature deviations on compressive strength is significant.
- In a similar manner, keeping density and temperature constant and increasing the slump to 140 mm reduces the strength by 30.3%, whereas decreasing slump to 50 mm reduces it by only 3.2%. These results show that the effect of increasing slump on compressive strength is considerable, while the effect of reducing the slump is negligible.

Statements & Declarations

Author contributions

Aliakbar Yahyaabadi: Conceptualization, Supervision, Methodology, Validation, Formal analysis, Writing – Original Draft, Writing – Review & Editing.

Seyyed Ghasem Rostami: Methodology, Formal analysis, Modelling.

Masood Mohammadi: Data collection, Performing experimental tests.

Funding

The authors received no specific funding for this study.

Declarations

The authors declare no conflict of interest.

Data availability

The data presented in this study are available in the article.

Appendix — Supplementary Experimental Data

Table A1. Experimental results of 92 concrete samples used for model development (slump, temperature, density, and 28-day compressive strength).

No.	Slump (mm)	Temperature (℃)	Density (kg/m^3)	Compressive strength (MPa)	No.	Slump (mm)	Temperature (℃)	Density (kg/m^3)	Compressive strength (MPa)
1	70	22	2212	27.8	47	95	12	2390	25.4
2	80	26	2283	29.3	48	90	28	2292	28.9
3	75	27	2297	24.1	49	95	29	2300	29.1
4	70	25	2402	29.8	50	100	26	2308	29.8
5	100	18	2303	27.8	51	90	7	2265	25.2
6	100	18	2243	31.5	52	70	10	2360	26.5
7	90	26	2272	29.6	53	70	32	2233	21.8
8	120	32	2192	24.8	54	45	13	2137	25.2
9	110	27	2244	25.4	55	85	22	2338	30.3
10	70	30	2314	27.0	56	90	17	2390	30.2
11	80	21	2330	30.7	57	130	32	2365	20.5
12	80	18	2273	28.1	58	70	25	2380	25.5
13	100	25	2188	24.9	59	75	25	2039	23.1
14	100	18	2196	25.7	60	70	30	2380	25.1
15	125	32	2310	21.8	61	50	22	2370	28.0
16	90	24	2233	26.9	62	60	25	2380	26.8
17	70	27	2197	23.0	63	70	28	2390	27.5
18	70	15	2282	28.5	64	135	29	2360	20.4
19	100	12	2238	27.3	65	70	27	2370	28.6
20	70	13	2252	26.9	66	70	29	2350	25.9
21	70	12	2276	28.2	67	90	29	2430	25.5
22	125	30	2350	22.3	68	90	30	2350	25.0
23	80	18	2266	25.9	69	125	32	2350	21.3
24	80	13	2288	28.5	70	100	31	2360	27.2
25	70	30	2360	27.0	71	80	31	2350	27.6
26	80	32	2280	24.2	72	80	25	2268	26.9
27	110	25	2303	28.5	73	90	13	2207	29.0
28	65	22	2281	29.8	74	90	27	2263	26.3
29	75	32	2236	24.3	75	70	23	2350	27.9
30	75	20	2360	30.7	76	70	31	2350	26.4
31	140	22	2360	21.5	77	80	31	2350	27.2
32	80	12	2350	27.7	78	70	30	2370	27.8
33	130	32	2280	19.6	79	70	29	2350	25.8
34	60	23	2314	25.1	80	70	32	2390	25.2
35	140	14	2370	21.5	81	70	29	2360	25.6
36	65	10	2350	23.3	82	70	32	2350	27.2
37	80	18	2236	28.7	83	80	29	2290	25.2
38	105	26	2266	27.8	84	50	32	2310	26.4
39	90	22	2300	30.7	85	80	22	2325	28.5
40	80	32	2263	23.6	86	90	18	2380	30.4
41	50	32	2304	24.0	87	55	14	2037	23.2
42	85	23	2164	26.4	88	70	12	2410	30.1
43	70	32	2250	25.2	89	65	20	2037	22.7
44	70	27	2320	27.4	90	80	20	2264	25.7
45	60	28	2233	24.9	91	65	16	2350	30.1
46	90	13	2390	30.0	92	65	22	2350	29.4

References

[1] Skrzypczak, I., Kokoszka, W., Zięba, J., Leśniak, A., Bajno, D., Bednarz, L. A Proposal of a Method for Ready-Mixed Concrete Quality Assessment Based on Statistical-Fuzzy Approach. Materials, 2020; 13: 5674. doi:10.3390/ma13245674.

[2] Tattersall, G. H., Banfill, P. The rheology of fresh concrete. 1st ed. London (UK): Pitman Publishing 1983.

[3] Wang, Z., Sun, T., Sun, Y., Liu, N. Evaluating the strength properties of high-performance concrete in the form of ensemble and hybrid models using deep learning techniques. Scientific Reports, 2025; 15: 25453. doi:10.1038/s41598-025-10860-y.

[4] Mahboub, K. C., Cutshaw, Q. A. Effects of Fresh Concrete Temperature and Mixing Time on Compressive Strength of Concrete. ACI Materials Journal, 98: doi:10.14359/10161.

[5] Kaleta-Jurowska, A., Jurowski, K. The Influence of Ambient Temperature on High Performance Concrete Properties. Materials, 2020; 13: 4646. doi:10.3390/ma13204646.

[6] Neville, A. M. Properties of concrete. 4th ed. Longman; 1995.

[7] P.K. Mehta, P. J. M. Concrete: Microstructure, properties, and materials. 3rd ed. Columbus (OH): McGraw-Hill; 2006.

[8] Iffat, S. Relation Between Density and Compressive Strength of Hardened Concrete. Challenge Journal of Concrete Research Letters; Vol 6, No 4 (2015), 2017; doi:10.20528/cjcrl.

[9] Sánchez-Mendieta, C., Galán-Díaz, J. J., Martinez-Lage, I. Relationships between density, porosity, compressive strength and permeability in porous concretes: Optimization of properties through control of the water-cement ratio and aggregate type. Journal of Building Engineering, 2024; 97: 110858. doi:10.1016/j.jobe.2024.110858.

[10] Nguyen, D.-L., Phan, T.-D. Enhanced prediction of compressive strength in high-strength concrete using a hybrid adaptive boosting - particle swarm optimization. Asian Journal of Civil Engineering, 2025; 26: 1059–1076. doi:10.1007/s42107-024-01233-3.

[11] Mahajan, A., Sharma, P. K. Machine learning-based prediction of high-strength concrete compressive strength incorporating limestone aggregates using ensemble and pruned tree models. Asian Journal of Civil Engineering, 2025; 26: 4595–4613. doi:10.1007/s42107-025-01445-1.

[12] Brahmeswari, L. C., Rao, B. D. V. C. M. Ultra-high performance concrete compressive strength prediction using machine learning boosting algorithms. Asian Journal of Civil Engineering, 2025; 26: 5139–5154. doi:10.1007/s42107-025-01476-8.

[13] Zviazhynski, B., White, C., Lees, J. M., Conduit, G. J. Predicting concrete strength using machine learning and fresh-state measurements. Data-Centric Engineering, 2025; 6: e37. doi:10.1017/dce.2025.10018.

[14] Mostofinejad, D., Bahmani, H., Eshaghi-Milasi, S., Nozhati, M. Empirical Relationships for Prediction of Mechanical Properties of High-Strength Concrete. Iranian Journal of Science and Technology, Transactions of Civil Engineering, 2023; 47: 315–332. doi:10.1007/s40996-022-01023-4.

[15] Iranian National Standardization Organization (INSO). 11268: Concrete – Measuring of temperature of freshly mixed hydraulic-cement concrete – Test method (2nd rev.). Tehran (IR): INSO; 2021.

[16] Iranian National Standardization Organization (INSO). 3201-1: Fresh concrete – Part 1: Sampling. Tehran (IR): INSO; 2010.

[17] Iranian National Standardization Organization (INSO). 3203-2: Fresh concrete – Part 2: Determining the consistency by slump – Test method (3rd rev.). Tehran (IR): INSO; 2023.

[18] Iranian National Standardization Organization (INSO). 3203-6: Fresh concrete – Part 6: Density – Test method (2nd rev.). Tehran (IR): INSO; 2025.

[19] Iranian National Standardization Organization (INSO). 1608-2: Hardened concrete – Part 2: Making and curing specimens for strength tests. Tehran (IR): INSO; 2023.

[20] ASTM International. C1064/C1064M-17: Standard test method for temperature of freshly mixed hydraulic-cement concrete. West Conshohocken (PA): ASTM; 2017. doi:10.1520/C1064_C1064M-17.

[21] European Committee for Standardization (CEN). EN 12350-2: Testing fresh concrete – Part 2: Slump test. Brussels (BE): EN; 2019.

[22] European Committee for Standardization (CEN). EN 12350-6: Testing fresh concrete – Part 6: Density. London (UK): EN; 2019.

[23] European Committee for Standardization (CEN). EN 12390-2: Testing hardened concrete – Part 2: Making and curing specimens for strength tests. Brussels (BE): EN; 2019.

[24] International Organization for Standardization (ISO). 1920-1: Testing of concrete – Part 1: Sampling of fresh concrete. Geneva (SW): ISO; 2004.

[25] Shapiro, S. S., Wilk, M. B. An analysis of variance test for normality (complete samples). Biometrika, 1965; 52: 591–611. doi:10.2307/2333709.

[26] Montgomery, D. C., Runger, G. C. Applied statistics and probability for engineers. 6th ed. Hoboken (NJ): John wiley and sons; 2014.

[27] Garbade, K. D. The initialization problem in variable parameter regression [PhD Thesis]. New York (NY): New York University, Graduate School of Business Administration; 1975.

[28] ASTM International. C192/C192M-24: Standard practice for making and curing concrete test specimens in the laboratory. West Conshohocken (PA): ASTM; 2024. doi:10.1520/C0192_C0192M-26.

Civil Engineering and Applied Solutions

Research Article

journal homepage: ceas.journals.umz.ac.ir

CEAS Civil Engineering and Applied Solutions

Comparative Numerical Assessment of Blast Resistance of Steel, Steel–Concrete Composite, and Fiber Metal Laminate Roofs

Hadi Zakeri Khatir [a], Mohammad Javad Shabani [a], Muhamed Shaaebanlu [b*], Mojtaba Araghizadeh [a]

[a] *Faculty of Passive Defense, Malek Ashtar University of Technology, Tehran, Iran*
[b] *Department of Civil Engineering, Shahid Beheshti University, Tehran, Iran*

ARTICLE INFO

Article history:

Received 28 January 2026

Revised 18 February 2026

Accepted 12 May 2026

Available online 01 January 2027

Keywords:

Blast loading

Roof systems

Steel plate deck

Steel–concrete composite

Fiber metal laminate

CFRP

ABSTRACT

Blast loading poses a serious threat to building roof systems due to their relatively low mass and stiffness compared to vertical structural components. This study presents a comprehensive numerical investigation of the blast response of three different roof systems: steel plate deck (SPD), steel–concrete composite deck (SCD), and fiber metal laminate (FML) composed of two steel sheets with intermediate CFRP layers oriented at 0° and 90°. Finite element models were developed in Abaqus to simulate both near-field and far-field blast scenarios using equivalent TNT charges with various stand-off distances and charge weights. A detailed parametric study was conducted to evaluate the influence of key design parameters, including material thickness, explosive weight, and stand-off distance, on the maximum von Mises stress. The results demonstrate that the stand-off distance is the governing parameter controlling the structural response under blast loading. The steel–concrete composite system exhibited the most stable performance due to the combined effects of increased mass, energy absorption, and composite action, while the steel plate deck showed significant plastic deformation under close-in explosions. The FML system provided excellent performance at moderate and large stand-off distances; however, it was highly sensitive to near-field blasts due to the brittle failure characteristics of CFRP layers. Furthermore, blast design charts based on scaled distance were developed and power-law relationships were proposed to enable rapid estimation of maximum stress for preliminary design purposes. The findings provide practical insights for selecting and designing roof systems with improved blast resistance.

How to cite this article: Zakeri, H., Shabani, M., Shaaebanlu, M., Araghizadeh, M. Comparative Numerical Assessment of Blast Resistance of Steel, Steel–Concrete Composite, and Fiber Metal Laminate Roofs. Civil Engineering and Applied Solutions. 2027; 3(1): 61–77. doi:10.22080/ceas.2026.31139.1075.

1. Introduction

Blast loading represents one of the most severe and unpredictable extreme actions that civil engineering structures may experience during their service life [1]. Accidental explosions in industrial facilities, gas detonations, transportation-related incidents, and intentional attacks have demonstrated the catastrophic consequences that blast-induced damage can impose on buildings and infrastructure. Unlike conventional static or quasi-static loads, blast loads are characterized by extremely high peak pressures, very short duration, and complex wave–structure interaction mechanisms [2]. These characteristics may induce intense stress wave propagation, localized failure, progressive collapse, and significant loss of structural integrity [3].

Among structural components, slab and roof systems are particularly vulnerable to blast loading due to their large exposed surface area and relatively limited thickness compared to vertical load-bearing members. Damage to roof structures not only compromises local structural capacity but may also trigger internal pressurization effects and cascading failure of supporting

* Corresponding author.
E-mail addresses: shabanlou@mail.ir (M. Shaaebanlu).

https://doi.org/10.22080/ceas.2026.31139.1075
ISSN: 3092-7749/© 2027 The Author(s). Published by University of Mazandaran.

elements. Consequently, enhancing the blast resistance of slab and roof systems has become an important research topic in protective structural engineering [4-6].

Extensive experimental and numerical investigations have been conducted on the blast behavior of reinforced concrete (RC) slabs. Previous studies have examined the influence of reinforcement ratio, slab thickness, concrete strength, boundary conditions, and scaled distance on dynamic response and failure modes. It has been shown that slab response may transition from global flexural deformation to localized punching shear as the stand-off distance decreases. In addition, quantitative performance indices such as support rotation angle, residual deflection, and damage level classifications have been proposed to evaluate blast resistance [7]. In parallel, steel plates and steel structural components have been widely studied under impulsive loading. Numerical and experimental investigations have highlighted the significant role of plate thickness, boundary restraint, and strain-rate effects in controlling deformation and failure patterns. Compared with reinforced concrete slabs, steel plates exhibit different energy absorption mechanisms governed primarily by membrane action and plastic yielding [8, 9].

To combine the advantages of steel and concrete, steel–concrete composite (SC) systems have increasingly attracted attention in protective engineering. Composite action between steel plates and concrete cores can enhance stiffness, increase mass participation, and improve energy dissipation capacity. Previous research has demonstrated that SC composite slabs generally exhibit improved blast resistance compared to conventional RC or steel-only systems, although their failure modes depend strongly on charge weight and stand-off distance [10].

More recently, lightweight advanced materials such as fiber-reinforced polymers (FRP) and fiber metal laminates (FML) have been explored for protective applications [11, 12]. These hybrid systems offer high strength-to-weight ratio, corrosion resistance, and favorable fatigue performance. However, despite growing interest in FRP-strengthened and hybrid composite members, systematic investigations of FML roof systems subjected to external blast loading remain limited. In particular, the interaction between metallic layers and brittle composite plies under high-intensity impulsive loading is not yet fully understood.

Although the existing body of literature provides valuable insights into individual structural systems, several limitations remain. First, most studies focus on a single structural configuration, making direct performance comparison among steel plate decks, steel–concrete composite roofs, and fiber metal laminate systems difficult. Second, the majority of numerical investigations report peak stresses or displacements without establishing generalized design-oriented relationships that can assist engineers in rapid preliminary assessment. Third, the mechanical interpretation of blast response in terms of material yielding, damage initiation, and failure mechanisms, especially for hybrid systems involving CFRP layers, has received comparatively limited attention.

In light of these gaps, this study presents a comprehensive comparative numerical assessment of three roof systems: a steel plate deck (SPD), a steel–concrete composite deck (SCD), and a fiber metal laminate (FML) roof configuration subjected to external blast loading. Explicit dynamic finite element simulations [13] are conducted to evaluate stress demand, deformation characteristics, and damage development under varying stand-off distances. Advanced constitutive models are employed to capture material nonlinearity and damage mechanisms. Furthermore, blast design charts based on the scaled distance concept are developed by correlating peak stress demand with scaled distance through regression-based power-law relationships. These charts provide a practical tool for rapid estimation of blast response without requiring detailed numerical analysis.

By systematically comparing three distinct roof systems under identical blast scenarios, this study aims to (i) quantify their relative blast resistance, (ii) interpret the governing material-level failure mechanisms, and (iii) provide generalized performance relationships that may support preliminary protective design and decision-making. The outcomes of this study aim to provide both scientific insight and engineering guidance for the selection and optimization of roof systems in structures exposed to explosive hazards.

2. Methodology

2.1 Research framework

Three roof systems were investigated in this study: steel plate deck (SPD), steel–concrete composite deck (SCD), and fiber metal laminate (FML). All numerical models were developed with identical supporting frames to ensure a consistent basis for comparison.

The study adopts a comparative numerical framework in which three roof configurations are evaluated under identical boundary and loading conditions to ensure a consistent performance basis.

2.2. Parametric study design

A systematic one-variable-at-a-time parametric framework was adopted to quantify the influence of key design variables on the blast response while avoiding confounding effects. For each roof system, the investigated parameters included:

- SPD: steel plate thickness, explosive charge weight, and stand-off distance.
- SCD: concrete thickness, concrete compressive strength f_c', explosive charge weight, and stand-off distance (with steel thickness and reinforcement parameters varied in selected cases).
- FML: steel sheet thickness, CFRP layer thickness, explosive charge weight, and stand-off distance (with the CFRP layup maintained at 0°/90°).

For each parameter set, all other variables were held constant to isolate the primary trend. This structured approach provides a consistent basis for (i) cross-system performance comparison and (ii) development of generalized blast design relationships based on scaled distance. The selected parameters were chosen based on their direct influence on structural stiffness, mass distribution, and energy absorption capacity under blast loading.

2.3. Performance evaluation criteria

The primary response parameter used for performance comparison was the maximum von Mises stress within the roof panel. The von Mises equivalent stress represents a scalar measure of the combined multiaxial stress state at a material point and is widely accepted as a reliable yielding criterion for ductile materials such as structural steel. By integrating the effects of normal and shear stress components into a single parameter, it provides a rational indicator of the onset of plastic deformation and overall stress demand in structural elements subjected to complex loading conditions.

Under blast loading, structural components experience highly transient and non-uniform stress distributions involving bending, membrane action, and shear interaction. Therefore, the maximum von Mises stress was adopted as a consistent and physically meaningful metric for comparing the structural response and damage potential of the investigated roof systems. This approach enables objective cross-system performance evaluation while maintaining a unified comparison basis across different material configurations.

2.4. Scaled distance formulation

To generalize the blast loading scenarios and enable comparison across different explosive weights and stand-off distances, the concept of scaled distance was adopted. The scaled distance Z is defined as $Z = {}^{R}/_{W^{1/3}}$ where R is the stand-off distance, and W is the equivalent TNT charge weight. This formulation, derived from Hopkinson–Cranz scaling law [14, 15], normalizes blast parameters by accounting for the cube-root relationship between explosive energy and distance. As a result, blast scenarios with different combinations of charge weight and stand-off distance but identical scaled distance produce similar pressure–time characteristics.

The use of scaled distance allows the structural response to be interpreted in a dimensionless and generalized manner, thereby facilitating comparison between different blast cases and supporting the development of broader design-oriented relationships beyond the specific numerical values considered in this study.

The overall sequence of steps followed in the present investigation is summarized in Fig. 1. The study begins with the selection of the investigated roof systems (SPD, SCD, and FML) and the definition of key design and loading parameters. Subsequently, detailed finite element models are developed for each configuration. Blast loading scenarios are then applied; Dynamic explicit analyses are performed to capture the transient structural response. Finally, key response parameters, particularly the maximum von Mises stress, are extracted and used for comparative performance assessment and trend evaluation. This structured framework ensures methodological clarity, reproducibility of the analysis procedure, and consistency in cross-system comparison.

Fig. 1. Schematic flowchart of the research methodology showing the sequential procedure followed in the numerical investigation.

3. Numerical modeling

3.1. Geometry and boundary conditions

The roof panel had a square plan with dimensions of 5 m × 5 m and was connected to the surrounding frame members.

The roof system was modeled as simply supported along its edges, allowing rotation while restraining vertical displacement. This boundary condition was selected to represent typical roof–frame connections in practical structures and to isolate the influence of material configuration and blast parameters on structural response. Beam and column members were modeled using frame elements, while the roof panels (steel plates, concrete slabs, and composite laminates) were modeled using shell elements to accurately capture bending, membrane action, and in-plane stress distribution.

A mesh sensitivity study was conducted to ensure that the numerical results are independent of element size. Several mesh densities were evaluated, and key response parameters including maximum mid-span displacement, peak von Mises stress, and damage initiation indices were monitored. It was observed that refinement beyond an element size of 50 × 50 mm resulted in negligible changes in the primary response quantities, with variations remaining within acceptable numerical tolerance. Given the global dimensions of the slab systems and the focus on comparative structural performance, the 50 × 50 mm mesh was selected as it provides a suitable balance between computational efficiency and solution accuracy. The convergence assessment confirms that the reported results are mesh-independent.

3.2. Material properties and constitutive models

This section thoroughly explains the material properties and constitutive models, including the modeling assumptions.

3.2.1. Steel

Steel components were modeled using elastic–plastic constitutive laws. Two different steel grades were considered to accurately represent the mechanical behavior of structural plates/frames and reinforcing bars in the composite roof system.

For all steel plates and structural frame members (SPD, SCD steel sheets, and FML steel layers), the elastic modulus and Poisson's ratio were taken as E = 206 GPa and ν = 0.30, respectively. Plastic behavior was defined by a yield stress of F_y = 240 MPa and an ultimate tensile stress of F_u = 514 MPa. These properties were used to assess yielding onset, plastic deformation, and potential severe damage in the steel roof components under blast loading. For the reinforcing bars embedded in the concrete layer of the SCD system, a higher-strength steel grade was adopted. The reinforcing steel was modeled with a yield stress of F_y = 400 MPa and an ultimate tensile stress of F_u = 600 MPa, while the elastic modulus and Poisson's ratio were assumed identical to those of structural steel (E = 206 GPa, ν = 0.30). This distinction allows realistic simulation of stress redistribution between the concrete matrix and the steel reinforcement and enables accurate interpretation of reinforcement yielding and post-yield behavior under extreme blast-induced loading.

3.2.2. Concrete

The concrete layer in the steel–concrete composite deck was modeled using the Concrete Damaged Plasticity (CDP) model available in Abaqus to capture nonlinear behavior, cracking in tension, and crushing in compression under dynamic loading [16, 17]. The key CDP parameters adopted in the simulations are tabulated in Table 1.

The concrete compressive strength f_c' and slab thickness were varied as part of the parametric study, while the above CDP parameters were kept constant. This modeling approach enables realistic representation of stiffness degradation and energy dissipation mechanisms that are essential for evaluating blast resistance in composite roof systems.

Table 1. Plastic parameters of concrete in the CDP model.

Dilation Angle	Eccentricity	f_{b0}/f_{c0}	K	Viscosity Parameter
30°	0.1	1.16	0.667	0.001

3.2.3. CFRP layers

In the fiber metal laminate (FML) configuration, carbon fiber reinforced polymer (CFRP) sheets were placed between two steel layers. The CFRP plies were arranged in two orthogonal directions (0°/90°) to enhance in-plane stiffness and improve stress redistribution. CFRP was modeled as an orthotropic elastic material with an elastic modulus of E = 42.7 GPa and Poisson's ratio ν = 0.05. The ultimate tensile strength of CFRP was taken as σ_u = 634 MPa.

To realistically capture progressive damage and failure mechanisms in the composite layers under blast loading, the Hashin damage criterion was employed to predict damage initiation in different failure modes, including fiber tension and compression. Following damage initiation, stiffness degradation was governed by an energy-based damage evolution law, in which the post-failure softening behavior was defined using fracture energy (Table 2 and Table 3). This approach allows gradual stiffness reduction after damage onset and enables accurate simulation of brittle failure and energy dissipation in CFRP layers subjected to high-rate dynamic loading [18, 19].

Table 2. Hashin elastic damage parameters.

E_1 (GPa)	E_2 (GPa)	ν_{12}	G_{12} (GPa)	G_{13} (GPa)	G_{23} (GPa)
42.7	42.7	0.05	4.4	4.4	2.3

Table 3. Hashin elastic damage parameters.

Longitudinal tensile strength (MPa)	Longitudinal compressive strength (MPa)	Transverse tensile strength (MPa)	Transverse compressive strength (MPa)	Longitudinal shear strength (MPa)
643	267	643	267	37

The thickness of each CFRP layer was treated as a parametric variable, while the stacking sequence (0°/90°) and damage model parameters were kept constant in the baseline configuration. This modeling strategy ensures that both elastic response and post-damage softening behavior of the composite layers are appropriately represented in the numerical simulations.

3.3. Blast loading and analysis procedure

Blast loads were applied using the CONWEP (Conventional Weapons Effects Program) formulation implemented in Abaqus [20, 21]. Equivalent TNT charges with different explosive weights W and stand-off distances R were considered to simulate both far-field and near-field blast scenarios [22, 23]. The pressure–time history generated by the CONWEP model was applied normal to the roof surface, accounting for incident and reflected pressure effects as described in the reference blast model.

Dynamic explicit analyses were performed to capture the highly transient response induced by short-duration, high-intensity blast loading. For each simulation case, the primary response parameter extracted was the maximum von Mises stress in the roof system, which was used as the main metric for evaluating stress demand and comparing the performance of different roof configurations under blast loading. As illustrated in Fig. 2, a 4 kg C4 explosive charge, which is equivalent to 8.22 kg TNT, considering the conversion and safety factors, was placed at 3 m standoff distance.

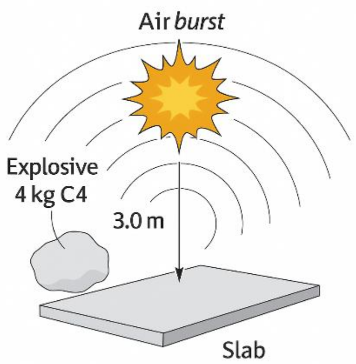

Fig. 2. Schematic view of explosive charge and standoff distance.

3.4. Model validation and verification

The numerical modelling framework adopted in this study is based on previously validated approaches reported in the literature [8, 10, 24, 25]. The Concrete Damage Plasticity (CDP) model has been widely employed in blast and impact simulations of reinforced concrete slabs, demonstrating good agreement with experimental deflection histories, crack patterns, and failure modes. The CDP parameters used herein were selected according to published calibration studies conducted under dynamic loading conditions [16].

Similarly, the Hashin failure criteria and progressive damage modelling for fiber-reinforced laminates have been extensively validated in impact and blast analyses of composite structures. The material properties and failure parameters adopted in the present study are directly taken from experimentally characterized composite systems reported in the literature [11].

The blast loading was defined using the CONWEP formulation, which is based on the empirical Kingery–Bulmash data and has been widely accepted for engineering-level blast simulations [26, 27].

Although a direct specimen-specific experimental validation was not performed for the investigated configurations, the modelling strategy, constitutive parameters, and loading formulation are consistent with previously validated numerical–experimental studies. Moreover, the predicted deformation patterns and failure mechanisms are qualitatively consistent with experimentally reported flexural-dominated behavior in slab-type structures under blast loading.

3.5. Consideration of strain-rate effects

Explosive loading typically generates extremely high strain rates in structural components, commonly in the range of 10^2–10^4 s^{-1}, whereas static loading conditions generally produce strain rates on the order of 10^{-6}–10^{-5} s^{-1} [28-30]. Under such rapid loading, material behavior may deviate significantly from its quasi-static response, potentially altering both strength characteristics and failure modes.

It is well established that increasing strain rate generally enhances the yield strength and ultimate tensile strength of steel. Experimental investigations reported by Chen et al. (2017), McDonald et al. [31], and Norris et al. [32] demonstrate that plastic flow stress increases markedly under impulsive loading conditions. In blast-resistant design practice, this enhancement is commonly accounted for using Strength Increase Factors (SIF) and Dynamic Increase Factors (DIF), whereby static material strengths are amplified to reflect dynamic conditions [23].

Similarly, concrete exhibits rate-dependent enhancement in both compressive and tensile strengths under high strain rates. Although the dynamic modulus of elasticity of steel remains essentially unchanged, concrete may experience a slight increase. These variations influence stiffness and cracking response under blast loads.

In the present study, strain-rate enhancement factors were not explicitly incorporated into the constitutive models of steel, concrete, or CFRP materials. Static material properties were adopted for all simulations. This modelling choice was made to ensure consistent and directly comparable baseline behavior across the roof systems under identical loading scenarios. It is acknowledged that neglecting strain-rate effects may lead to conservative predictions of strength for steel and concrete components under near-field blast conditions, as their actual dynamic strength would be higher than the static values used herein.

For CFRP layers, available literature [33-35] indicates that although some rate sensitivity exists, the magnitude of dynamic enhancement is generally lower than that observed in metals and concrete. Therefore, omission of strain-rate effects is not expected to alter the relative ranking of the investigated roof systems but may influence the absolute magnitude of reported stresses.

Accordingly, the results presented herein should be interpreted as conservative estimates of structural resistance, particularly for near-field scenarios. Incorporation of fully rate-dependent constitutive models represents an important direction for future work.

4. Results

4.1. Overall numerical trends

The numerical results indicate that the blast response of the roof systems is primarily governed by the stand-off distance, while the explosive charge weight plays a secondary role. For all configurations, decreasing the stand-off distance leads to a highly nonlinear increase in the maximum von Mises stress. Moreover, the overall response is strongly influenced by the structural configuration and energy dissipation mechanisms rather than by material strength alone.

For very small stand-off distances (0.5 m and 0.1 m), all roof systems exhibit severe nonlinear behavior, including extensive plasticity in steel components and progressive damage in composite layers. These findings confirm that system-level characteristics such as mass distribution, stiffness, and composite action are critical in mitigating blast-induced damage.

4.2. Steel plate deck (SPD)

The effects of steel plate thickness, standoff distance, and explosive charge weight on the behavior of the steel plate deck are investigated in the following sections.

4.2.1. Effect of steel plate thickness

Fig. 3 illustrates the effect of steel plate thickness on the maximum von Mises stress for the SPD system at a stand-off distance of 3 m and an explosive weight of 8.22 kg. Increasing the plate thickness leads to a substantial reduction in stress demand. Specifically, reducing the thickness from 20 mm to 3 mm results in an increase in peak stress from approximately 68 MPa to nearly 280 MPa, corresponding to an increase of more than 300%.

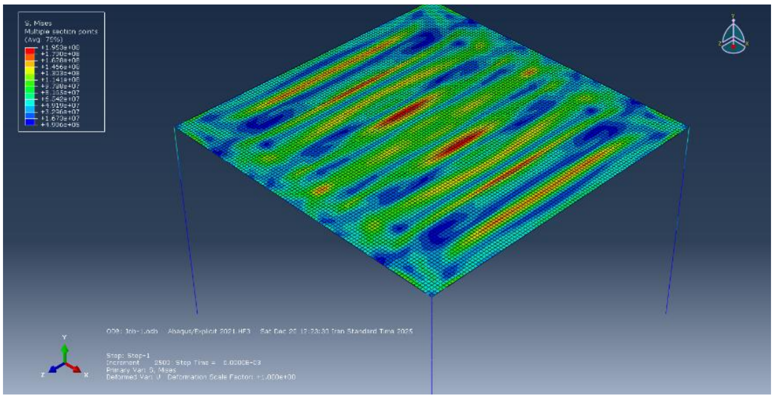

Fig. 3. Von Mises stress of the steel plate deck (SPD) at ultimate state by a stand-off distance of 3 m and an explosive charge of 8.22 kg TNT equivalent.

Thin plates (3–5 mm) clearly exceed the yield stress of structural steel (240 MPa), indicating the onset of widespread plastic deformation. In contrast, thicker plates exhibit significantly lower stress levels, remaining largely within the elastic or near-yield regime (Fig. 4). This behavior is attributed to the increase in flexural stiffness and membrane capacity with thickness.

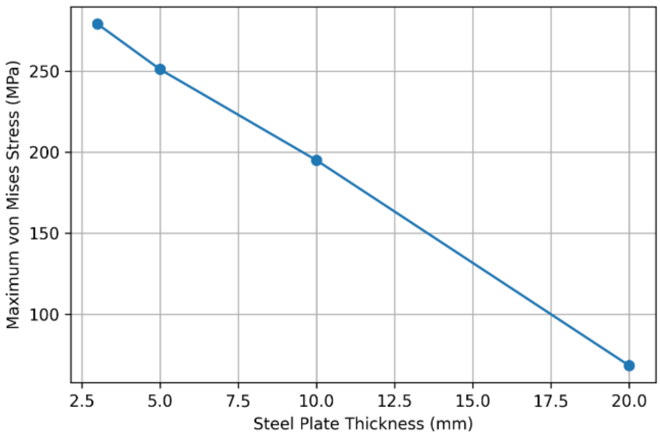

Fig. 4. Effect of steel plate thickness on the maximum von Mises stress of the steel plate deck (SPD) at a stand-off distance of 3 m and an explosive charge of 8.22 kg TNT equivalent.

4.2.2. Effect of stand-off distance

The sensitivity of the SPD system to stand-off distance is shown in Fig. 5, where the maximum stress is normalized by the steel yield stress. At distances of 4–5 m, the normalized stress remains well below unity, indicating elastic behavior. However, when the distance decreases below 2 m, the stress rapidly exceeds the yield limit. At 0.1 m, the normalized stress reaches nearly 2.0, corresponding to a von Mises stress of approximately 470 MPa.

These results demonstrate that the SPD system is extremely vulnerable to near-field explosions, with stress levels approaching the ultimate tensile strength of steel (514 MPa), suggesting a high risk of rupture and severe permanent deformation.

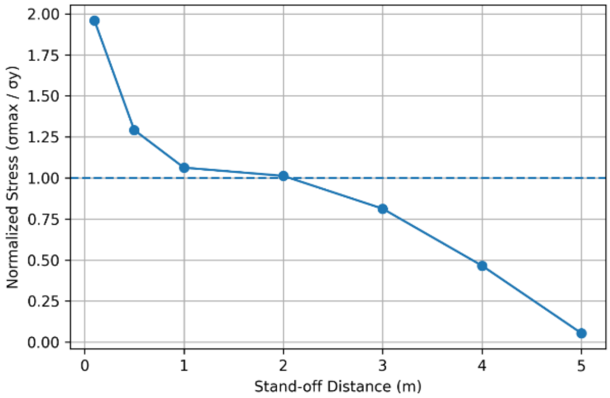

Fig. 5. Normalized maximum von Mises stress (σ_{max}/σ_y) versus stand-off distance for the SPD system with a steel plate thickness of 10 mm under an 8.22 kg TNT equivalent blast.

4.2.3. Effect of explosive charge weight

Fig. 6 presents the influence of TNT equivalent weight at a fixed stand-off distance of 3 m and plate thickness of 10 mm. Increasing the charge weight from 4.11 kg to 24.66 kg increases the maximum stress from approximately 117 MPa to 247 MPa. Although the effect of charge weight is evident, it is less pronounced than that of stand-off distance, confirming that proximity to the blast source is the dominant parameter.

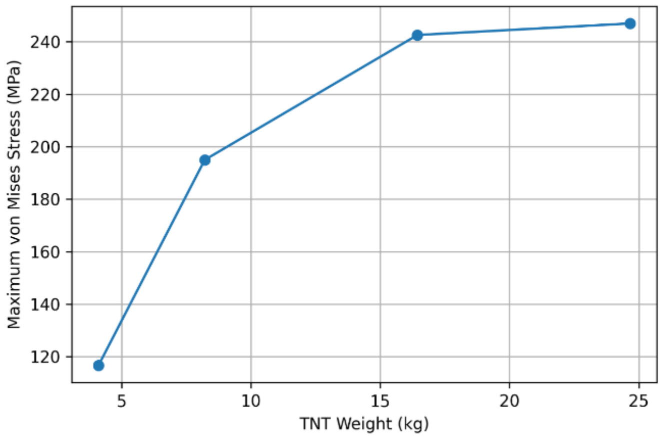

Fig. 6. Influence of TNT equivalent charge weight on the maximum von Mises stress of the SPD system at a stand-off distance of 3 m and a steel plate thickness of 10 mm.

4.3. Steel–concrete composite deck (SCD)

The effects of concrete thickness, concrete compressive strength, standoff distance, and explosive charge weight in the behavior of the steel plate deck are investigated in the following sections.

4.3.1. Concrete damage evaluation using DAMAGET

To further evaluate the capability of the adopted constitutive model in capturing tensile damage under blast loading, the tensile damage variable (DAMAGET) obtained from the Concrete Damage Plasticity (CDP) model is presented. DAMAGET ranges from 0 (undamaged material) to 1 (fully cracked tensile failure), allowing a clear visualization of crack initiation and propagation within the slab.

For the near-field blast scenario, as shown in Fig. 7, the contour distribution of DAMAGET indicates that the tensile damage parameter approaches a value close to 1.00 over a large portion of the slab surface. The highest damage concentration is observed at the mid-span region, where flexural demand and reflected blast pressure are maximum. The widespread distribution of serious damage indices confirms the severe tensile cracking induced by the impulsive loading.

The results demonstrate that the adopted CDP formulation effectively captures the spatial extent and intensity of tensile cracking.

The near-unity damage values across the slab are consistent with the expected flexural failure mechanism under near-field blast conditions, indicating that the model realistically reproduces the progressive degradation of concrete stiffness and strength.

While material-specific damage parameters were used to characterize local failure mechanisms, a unified comparison among all investigated specimens was performed using the von Mises stress distribution. Although von Mises stress does not directly represent a failure criterion for brittle materials, it reflects the intensity of the multiaxial stress state and serves as a consistent indicator of global structural demand under blast loading. This approach enables a rational comparison of overall performance across different structural systems subjected to identical loading conditions.

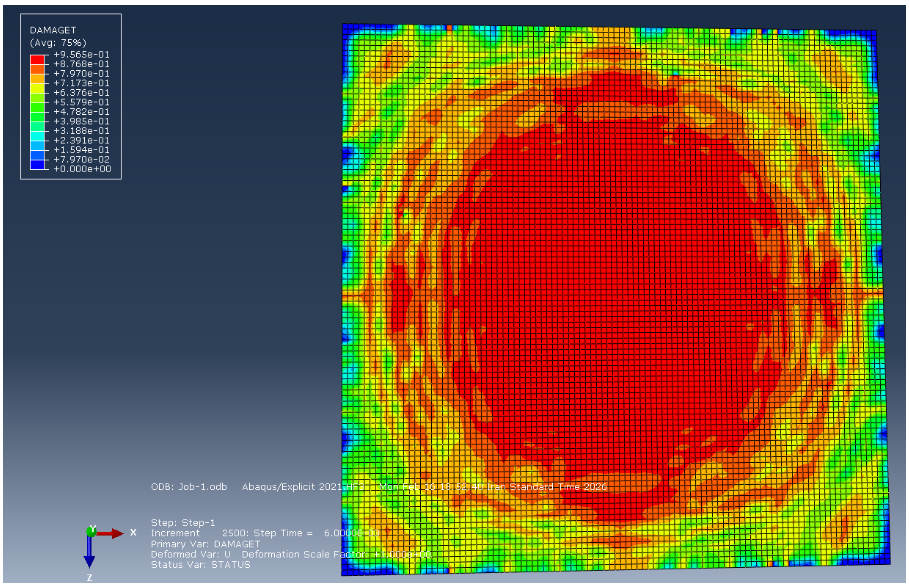

Fig. 7. Contour distribution of tensile damage variable (DAMAGET) for the steel–concrete composite slab under near-field blast loading.

4.3.2. Effect of concrete thickness

Increasing the concrete thickness from 50 mm to 200 mm leads to a marked reduction in the maximum von Mises stress, from approximately 96 MPa to about 43 MPa (Fig. 8). The influence of concrete slab thickness on the blast response is illustrated in Fig. 9. This demonstrates that increasing the effective mass and flexural stiffness of the composite section significantly improves blast resistance.

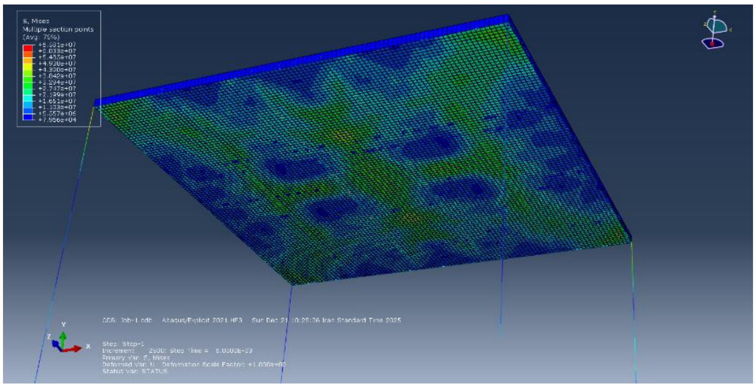

Fig. 8. Von Mises stress of the steel–concrete composite deck (SCD) at a stand-off distance of 3 m under an 8.22 kg TNT equivalent blast.

4.3.3. Effect of concrete compressive strength

Fig. 10 shows the effect of concrete compressive strength f_c' under identical geometric and loading conditions. Variations in f_c' from 15 MPa to 35 MPa result in only minor changes in stress levels. This indicates that, unlike thickness, material strength has a limited influence on the global blast response, which is primarily governed by inertia and stiffness rather than compressive capacity.

4.3.4. Effect of stand-off distance

The variation of maximum stress with stand-off distance for the baseline SCD configuration is shown in Fig. 11. At distances greater than 3–5 m, the stress remains below 25 MPa, indicating a predominantly elastic response. As the stand-off distance decreases below 1 m, the stress increases sharply, exceeding 240 MPa and reaching approximately 242 MPa at 0.1 m.

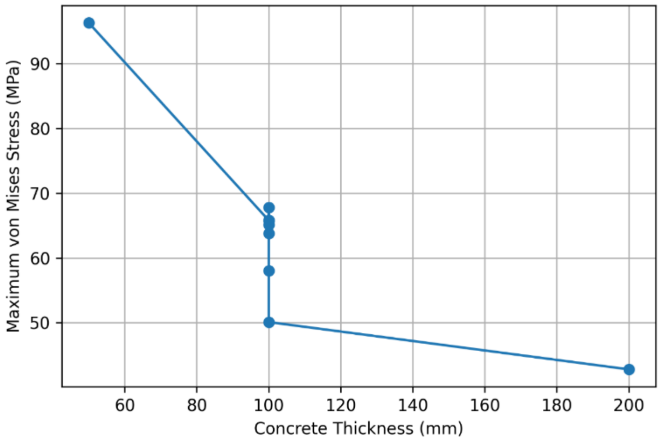

Fig. 9. Effect of concrete slab thickness on the maximum von Mises stress of the steel–concrete composite deck (SCD) at a stand-off distance of 3 m under an 8.22 kg TNT equivalent blast.

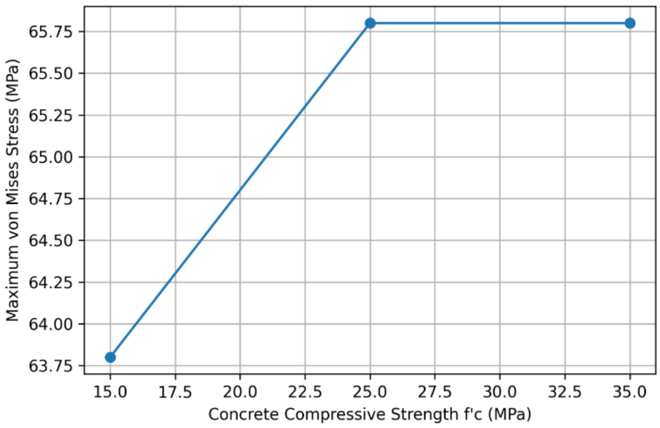

Fig. 10. Effect of concrete compressive strength f'c on the maximum von Mises stress of the SCD system for identical geometric and loading conditions (R = 3 m, W = 8.22 kg).

Although these stress levels indicate yielding of the structural steel components, the reinforcing bars, modeled with a higher yield stress of 400 MPa, remain largely elastic until more severe loading is applied. This promotes stress redistribution and delays localized failure.

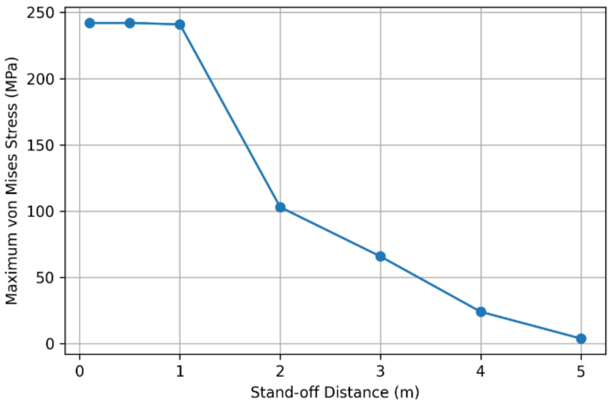

Fig. 11. Variation of maximum von Mises stress with stand-off distance for the baseline SCD configuration (3 mm steel plate + 100 mm concrete slab, fc′=25 MPa, reinforcement diameter = 12 mm) under an 8.22 kg TNT blast.

4.4. Fiber metal laminate (FML)

4.4.1. Failure criterion assessment using HSNFTCRT

To complement the damage evaluation, the Hashin fiber tensile failure criterion (HSNFTCRT) is examined for the composite slab configuration. The HSNFTCRT parameter represents the fiber tensile damage index, where values approaching 1.0 indicate initiation of fiber rupture.

For the near-field blast case, as can be seen in Fig. 12, the HSNFTCRT contour plot shows that the damage index reaches values close to 1.0 at the central region of the slab. This region corresponds to the maximum bending moment and tensile stresses generated by the high-intensity impulsive load. The localization of near-unity values at mid-span confirms the critical role of flexural tensile stresses in governing the failure response.

The concentration of HSNFTCRT values near 1.0 under severe loading demonstrates that the implemented composite material model successfully captures fiber-dominated tensile failure. The predicted failure pattern aligns with the expected structural behavior of fiber-reinforced systems subjected to high-rate dynamic loading.

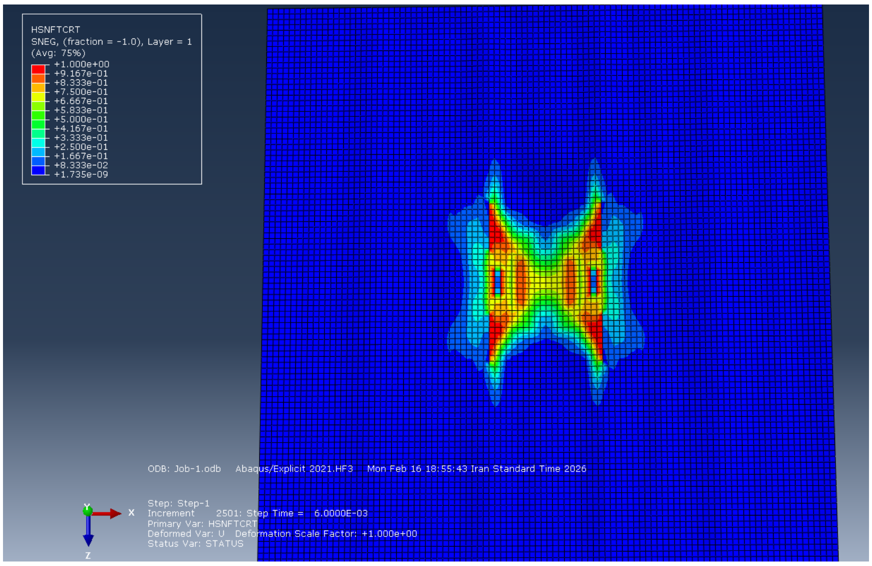

Fig. 12. Contour distribution of Hashin fiber tensile failure index (HSNFTCRT) for the composite laminate system under near-field blast loading.

4.4.2. Effect of steel layer thickness

Fig. 13 illustrates the influence of steel layer thickness on the FML system at a stand-off distance of 3 m. Increasing the steel thickness from 1 mm to 10 mm reduces the maximum stress from approximately 250 MPa to about 55 MPa, demonstrating that the metallic layers play the dominant role in resisting blast-induced bending and membrane forces (Fig. 14).

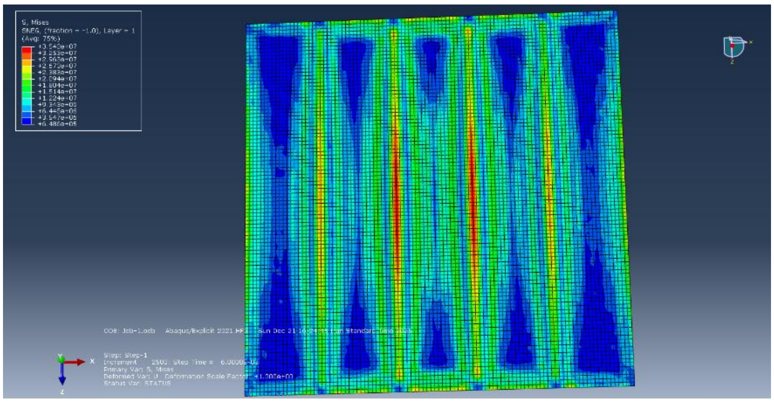

Fig. 13. Von Mises stress of the fiber metal laminate (FML) roof system at a stand-off distance of 3 m and an explosive charge of 8.22 kg TNT equivalent.

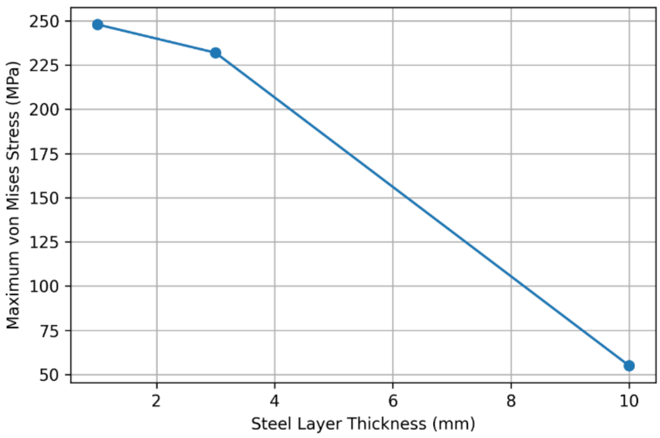

Fig. 14. Effect of steel layer thickness on the maximum von Mises stress of the fiber metal laminate (FML) roof system at a stand-off distance of 3 m and an explosive charge of 8.22 kg TNT equivalent.

4.4.3. Effect of CFRP layer thickness

The effect of CFRP layer thickness is shown in Fig. 15. Increasing the thickness from 0.5 mm to 2 mm results in a moderate reduction in stress. Although CFRP contributes to in-plane stiffness and stress redistribution, its influence is clearly secondary compared to that of the steel layers.

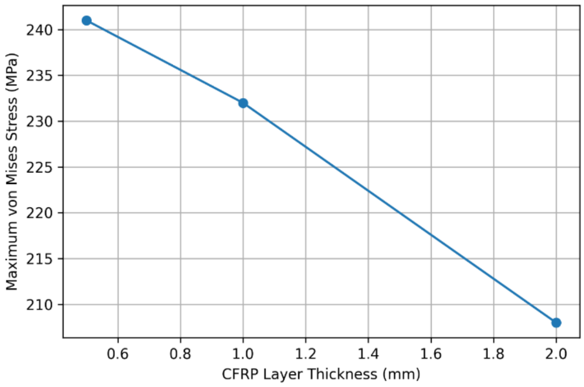

Fig. 15. Effect of CFRP layer thickness on the maximum von Mises stress of the FML system at a stand-off distance of 3 m with a steel layer thickness of 3 mm and an 8.22 kg TNT equivalent blast.

4.4.4. Effect of stand-off distance

Fig. 16 presents the variation of maximum stress with stand-off distance for the baseline FML configuration. At a distance of 5 m, the stress drops to approximately 5 MPa, indicating excellent far-field performance. However, as the distance decreases, the stress rises sharply, reaching about 439 MPa at 0.5 m and approximately 625 MPa at 0.1 m.

These values approach or exceed the ultimate tensile strength of CFRP (634 MPa), indicating the initiation of fiber tensile failure, matrix cracking, and progressive stiffness degradation according to the Hashin damage criterion with energy-based evolution.

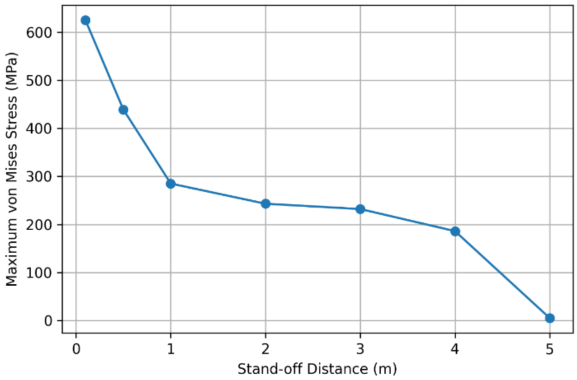

Fig. 16. Variation of maximum von Mises stress with stand-off distance for the baseline FML configuration (3 mm steel + 2 × 1 mm CFRP layers) under an 8.22 kg TNT equivalent blast.

4.5. Comparative performance of roof systems

Fig. 17 compares the three roof systems under identical loading conditions. The SCD system consistently exhibits the lowest stress levels across the entire range of stand-off distances. The SPD system shows rapid stress escalation as the distance decreases, while the FML system, despite its excellent far-field behavior, experiences the highest peak stresses in near-field conditions. This comparison highlights the beneficial role of concrete in increasing effective mass, reducing structural acceleration, and enhancing energy dissipation through cracking, plasticity, and composite interaction.

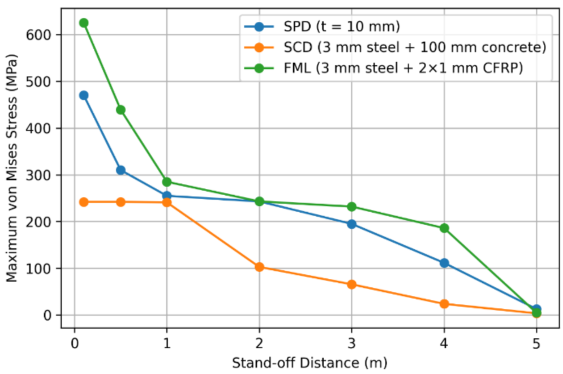

Fig. 17. Comparison of maximum von Mises stress versus stand-off distance for SPD, SCD, and FML roof systems under identical blast loading conditions (W = 8.22 kg TNT equivalent).

4.6. Scaled distance and blast design charts

To assess the universality of the power-law relationship $\sigma_{max} = aZ^{-b}$, two additional simulations with identical scaled distance Z = 1 m/kg^1/3 were performed: (i) R = 2 m, W = 8 kg, and (ii) R = 4 m, W = 64 kg. The von Mises stress contours in Fig. 18 demonstrate that while the overall shape of stress distribution and damage patterns is similar, the far-field scenario with the larger explosive weight exhibits higher peak stresses. To generalize the results, the scaled distance was defined as $Z = R/W^{1/3}$. Fig. 19 shows the variation of maximum von Mises stress with scaled distance for the three systems. As Z decreases, stress increases in a strongly nonlinear manner, particularly in the near-field regime. The SCD system maintains the lowest stress levels over the entire range of Z, while the SPD and FML systems exhibit steeper increases at small Z.

Based on regression analysis, power-law relationships of the form $\sigma_{max} = aZ^{-b}$, were obtained for each system, as illustrated in Fig. 20. These fitted curves provide practical blast design charts that allow rapid estimation of stress levels for different combinations of charge weight and stand-off distance.

Although Hopkinson–Cranz scaling ensures similarity in general blast wave characteristics, the nonlinear structural response is additionally influenced by dynamic interaction effects and strain-rate sensitivity. These results confirm that scaled distance captures general trends in structural behavior, but absolute stress magnitudes depend on the actual explosive charge. Therefore, the derived design charts represent empirical correlations within the investigated parameter domain and are most accurately applied for the specific TNT weight considered, rather than being universally unique scaling laws.

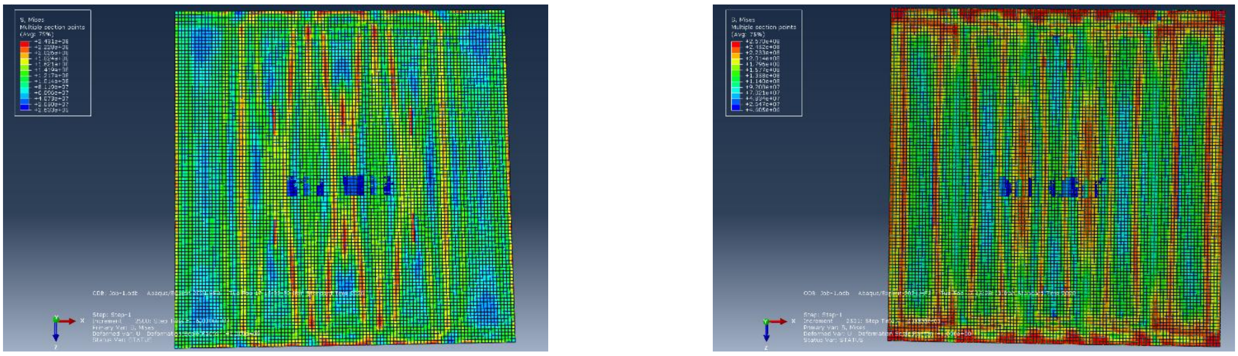

(a) (b)

Fig. 18. Comparison of the predicted ultimate compressive strength from the proposed model based on 1376 experimental circular FRP-confined concrete column specimens.

The SCD system exhibits the lowest baseline stress levels, while the FML system shows the steepest increase in stress at small Z, confirming its vulnerability to near-field explosions.

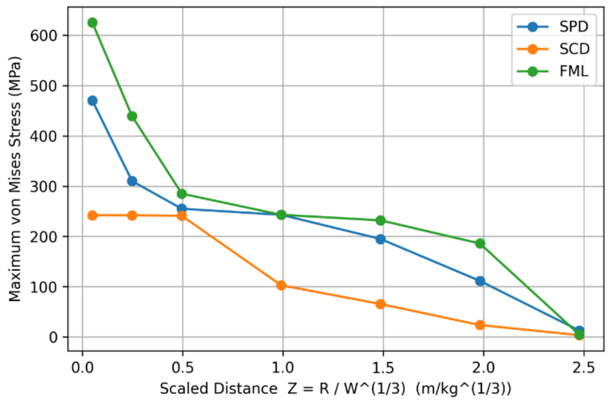

Fig. 19. Maximum von Mises stress as a function of scaled distance Z for SPD, SCD, and FML roof systems based on baseline configurations and an 8.22 kg TNT equivalent blast.

To provide a single, quantitative measure for comparing the blast performance of different roof systems, an integrated performance index was introduced based on the area under the curve (AUC) of maximum von Mises stress versus scaled distance (Z). For each roof system, the von Mises stress at multiple scaled distances was plotted, and the AUC was calculated using numerical integration. This parameter represents the cumulative stress exposure of a system across the range of blast scenarios considered.

In this formulation, lower values of the AUC indicate better blast performance, as the structure experiences lower stress levels over the range of scaled distances, reflecting enhanced resistance to impulsive loading. Conversely, higher AUC values indicate higher cumulative stress and greater vulnerability. Using this approach, as can be seen in Fig. 21, the three investigated systems exhibit the following relative performance: the steel–concrete composite deck (SCD) has the lowest AUC, demonstrating the best overall performance; the steel plate deck (SPD) shows intermediate performance; and the fiber metal laminate (FML) exhibits the highest AUC, indicating the highest susceptibility to near-field and far-field blast effects.

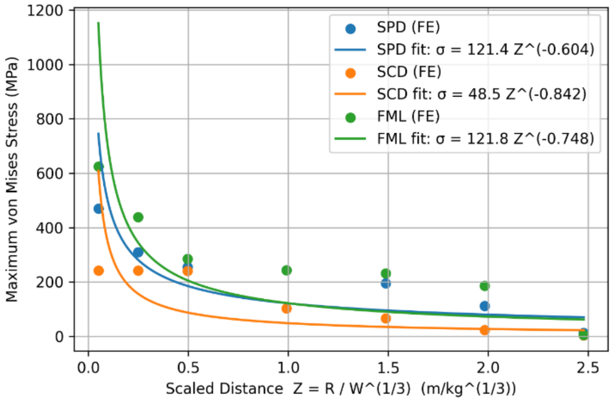

Fig. 20. Blast design chart showing the relationship between maximum von Mises stress and scaled distance for SPD, SCD, and FML roof systems, including power-law fitted curves derived from finite element results.

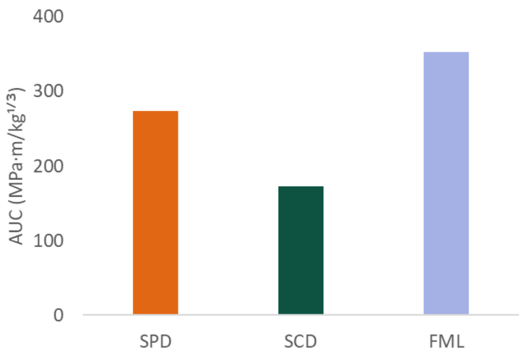

Fig. 21. Integrated performance index (area under σ_{max} –Z curve) for the three roof systems (SPD, SCD, FML). Lower values indicate better blast resistance.

This metric provides a rational and comparative engineering tool, enabling a clear visual and numerical assessment of structural performance under varying blast scenarios, which complements traditional peak stress or damage-based evaluations.

5. Discussion

5.1. Governing parameters in blast response

The numerical results indicate that the stand-off distance is the most critical parameter controlling blast response, while the explosive charge weight plays a secondary role. As the stand-off distance decreases, all roof systems exhibit a highly nonlinear increase in von Mises stress, particularly in near-field conditions. This is consistent with classical blast mechanics, where the incident pressure scales inversely with distance and dominates structural demand.

The structural configuration and energy dissipation mechanisms strongly influence the response. For the SPD system, the blast energy is resisted mainly by plate bending and in-plane tension due to the absence of additional damping mechanisms. In contrast, SCD and FML systems benefit from distributed energy absorption mechanisms (composite action and CFRP layers, respectively), which moderate stress escalation. Therefore, the system-level characteristics, mass distribution, stiffness, and energy dissipation pathways govern performance more than material strength alone.

It should be noted that the CONWEP approach is based on empirical Kingery–Bulmash blast functions developed for spherical or hemispherical TNT charges in air and does not explicitly model detonation-product expansion or gas–structure interaction. In very close-in detonations, particularly within or near the fireball region, the pressure field may be highly non-uniform and influenced by explosive geometry and confinement effects. Nevertheless, CONWEP remains widely used for engineering-level blast analysis due to its computational efficiency and reasonable prediction of free-field and reflected pressures. In this study, since all structural configurations were subjected to identical loading assumptions, the comparative evaluation among specimens remains consistent. However, the absolute magnitudes of stress concentration and localized damage predicted for the smallest stand-off distances should be interpreted considering the inherent limitations of the CONWEP formulation.

5.2. Role of material properties and structural stiffness

For the steel plate deck (SPD), thin plates with thicknesses of 3–5 mm exceed the yield stress of structural steel even under moderate blast loads, while thicker plates tend to remain largely within the elastic range. The increase in plate thickness improves flexural stiffness and activates membrane action, which delays the onset of plastic deformation. However, even substantial increases in thickness do not provide effective resistance against near-field blasts because the SPD system lacks additional energy dissipation mechanisms. As a result, large plastic deformations and potential rupture occur, making the SPD roof the weakest system under close-in explosive scenarios despite its structural simplicity.

The steel–concrete composite deck (SCD) exhibits a more gradual and controlled stress development compared to SPD. Increasing the concrete slab thickness significantly reduces the peak von Mises stress, while variations in compressive strength have only a minor effect on the global response. The concrete layer absorbs blast energy through progressive cracking and crushing, and the reinforcing bars provide post-cracking load-carrying capacity. The composite action between steel, concrete, and reinforcement ensures that stresses are distributed across multiple components, mitigating localized failure. This behavior results in predictable and progressive damage under extreme loads, emphasizing that composite action and overall system mass are more influential for blast mitigation than material strength alone.

In the fiber metal laminate (FML) system, the metallic layers dominate the initial resistance to blast-induced bending and membrane forces, while the CFRP layers contribute to in-plane stress redistribution. Under far-field blast conditions, the FML system exhibits high stiffness and low stress levels, demonstrating excellent performance. However, in near-field scenarios, damage initiation in the CFRP layers leads to rapid stiffness degradation, resulting in a relatively brittle response. Although the FML system offers superior strength-to-weight efficiency and excels in far-field applications, its sensitivity to near-field blasts requires careful design of the CFRP stacking sequence and thickness to prevent abrupt failure.

5.3. Comparative performance of roof systems

The comparative analysis of the three roof systems reveals important design insights. The steel plate deck (SPD) exhibits rapid stress escalation under near-field blasts, leading to large plastic deformations and limited energy dissipation. In contrast, the steel–concrete composite deck (SCD) demonstrates a gradual and predictable response, effectively dissipating energy through concrete cracking and reinforcement action, which results in the most stable overall behavior among the investigated systems. The fiber metal laminate (FML) roof performs exceptionally well under far-field conditions, maintaining low stress levels, but exhibits a relatively brittle response under near-field loading due to the initiation of damage in the CFRP layers.

5.4. Near-field vs far-field behavior

The observations highlight the trade-off between strength, stiffness, and energy absorption. In particular, the distribution of mass and the presence of composite mechanisms often have a more significant impact on blast resistance than simply increasing the material strength. In near-field scenarios, where the scaled distance is small, the SPD and FML systems reach stresses that approach or exceed the yield or ultimate limits, with abrupt failure observed in the FML system once the CFRP layers start to degrade. Conversely, in far-field scenarios with larger scaled distances, all systems remain predominantly elastic, with the FML roof showing the lowest stress levels and demonstrating high efficiency in low-demand conditions. These findings suggest that near-field blast protection favors composite solutions like the SCD, whereas far-field lightweight solutions may benefit from high-strength, efficient systems such as the FML.

5.5. Engineering implications and design recommendations

The results of this study provide several important implications for the blast-resistant design of roof systems in critical and protective structures. Beyond comparing the structural performance of different configurations, the numerical findings offer practical guidance for preliminary design and system selection.

First, the dominant role of stand-off distance highlights the importance of architectural and site-planning strategies in blast mitigation. Increasing the separation between potential explosive sources and structural components is significantly more effective than increasing material strength alone. Even lightweight systems such as FML can perform satisfactorily when adequate stand-off distance is available, whereas all systems become highly vulnerable under near-field conditions.

Second, increasing effective mass and flexural stiffness is shown to be the most efficient structural strategy for improving blast resistance. The steel–concrete composite deck benefits from the inertia of the concrete layer and the composite interaction between steel, concrete, and reinforcement, resulting in reduced acceleration, more uniform stress distribution, and progressive, non-brittle damage mechanisms. From a design perspective, increasing concrete slab thickness is more beneficial than increasing concrete compressive strength, which has only a minor effect on global response.

Third, for lightweight protective systems such as fiber metal laminates, steel layer thickness plays a more critical role than CFRP thickness in controlling peak stress. While CFRP layers enhance in-plane stiffness and strength-to-weight efficiency, near-field blast loading can induce stress levels close to the ultimate tensile capacity of the fibers, leading to rapid damage accumulation and stiffness degradation. Therefore, FML systems should be employed only in applications where blast proximity can be controlled or where weight reduction is the primary design constraint.

Finally, the scaled-distance-based design charts developed in this study provide a practical tool for preliminary assessment of roof performance under explosive loading. The power-law relationships between maximum stress and scaled distance enable rapid estimation of expected stress levels for different charge weights and stand-off distances without the need for time-consuming finite element analyses. These charts can assist engineers in selecting appropriate roof systems, identifying critical loading scenarios, and optimizing geometric parameters in the early stages of blast-resistant design.

6. Conclusions

This study presented a comprehensive numerical investigation of the blast response of three roof systems: steel plate deck (SPD), steel–concrete composite deck (SCD), and fiber metal laminate (FML). Finite element simulations incorporating realistic material models, including elastic–plastic steel behavior, concrete damaged plasticity, and progressive composite damage using the Hashin criterion with energy-based softening, were used to evaluate structural performance under various blast scenarios. Based on the results, the following conclusions can be drawn:

- Stand-off distance is the governing parameter.
- For all roof systems, the maximum von Mises stress increased in a highly nonlinear manner as the stand-off distance decreased. The influence of explosive charge weight was noticeable but consistently secondary compared to the effect of distance, particularly in near-field blast conditions.
- The steel–concrete composite deck (SCD) exhibited the most stable and reliable performance.
- The presence of the concrete layer significantly increased the effective mass and flexural stiffness of the system, leading to reduced structural acceleration and enhanced energy dissipation through cracking, plasticity, and composite action. Even under severe loading, damage developed gradually, and the reinforcement, modeled with a higher yield stress, contributed to stress redistribution and delayed failure.
- The steel plate deck (SPD) showed the weakest blast resistance in near-field conditions. Although increasing plate thickness reduced stress levels, thin plates rapidly exceeded the steel yield stress and developed extensive plastic deformation. The lack of secondary energy dissipation mechanisms makes this system highly vulnerable to close-in explosions, limiting its suitability for blast-resistant design.
- The fiber metal laminate (FML) system demonstrated excellent far-field efficiency but poor near-field robustness. At moderate and large stand-off distances, FML provided very low stress levels and high strength-to-weight efficiency. However, under near-field loading, stresses approached or exceeded the ultimate tensile strength of CFRP, triggering progressive damage, stiffness degradation, and a relatively brittle global response. Increasing steel layer thickness proved more effective than increasing CFRP thickness in improving blast resistance.
- Increasing effective mass and stiffness is more effective than increasing material strength alone.
- Geometric parameters such as concrete thickness and steel layer thickness had a far greater impact on blast performance than material strength parameters such as concrete compressive strength. This highlights the dominant role of inertia and structural configuration in blast-resistant design.
- The use of the scaled distance parameter enabled generalization of the numerical results for different charge weights and stand-off distances. The derived power-law relationships between maximum stress and scaled distance allow rapid preliminary assessment of roof performance without the need for detailed finite element analyses.
- Overall, the steel–concrete composite roof system is recommended for applications where blast resistance and structural robustness are critical. The fiber metal laminate system is suitable for lightweight structures where sufficient stand-off distance can be ensured, while the steel plate deck is not recommended for near-field blast scenarios.

Statements & Declarations

Author contributions

Hadi Zakeri Khatir: Investigation, Visualization, Validation, Formal analysis, Resources, Writing - Original Draft, Writing - Review & Editing.

Mohammad Javad Shabani: Investigation, Visualization, Validation, Formal analysis, Resources, Writing - Original Draft, Writing - Review & Editing.

Muhamed Shaaebanlu: Conceptualization, Methodology, Formal analysis, Project administration, Supervision, Writing - Review & Editing.

Mojtaba Araghizadeh: Investigation, Resources, Visualization, Writing - Review & Editing.

Funding

The authors received no financial support for the research, authorship, and/or publication of this article.

Data availability

The data presented in this study will be available on request from the corresponding author.

Declarations

The authors declare no conflict of interest.

References

[1] Federal Emergency Management Agency (FEMA). FEMA 427: Risk Management Series: Primer for Design Professionals – Communicating with Owners and Managers of New Buildings on Earthquake Risk. Washington (D.C): FEMA; 2003.

[2] Engineers, U. S. Structures to Resist the Effects of Accidental Explosions. Washington (D.C): U.S. Army Corps of Engineers; 2008. Report No.: UFC 3-340-02.

[3] Luccioni, B. M., Ambrosini, R. D., Danesi, R. F. Analysis of building collapse under blast loads. Engineering Structures, 2004; 26: 63–71. doi:10.1016/j.engstruct.2003.08.011.

[4] Zhao, C., He, K., Zhi, L., Lu, X., Pan, R., Gautam, A., Wang, J., Li, X. Blast behavior of steel-concrete-steel sandwich panel: Experiment and numerical simulation. Engineering Structures, 2021; 246: 112998. doi:10.1016/j.engstruct.2021.112998.

[5] Yao, S., Zhang, D., Chen, X., Lu, F., Wang, W. Experimental and numerical study on the dynamic response of RC slabs under blast loading. Engineering Failure Analysis, 2016; 66: 120–129. doi:10.1016/j.engfailanal.2016.04.027.

[6] Zolghadr Jahromi, H., Izzuddin, B. A., Nethercot, D. A., Donahue, S., Hadjioannou, M., Williamson, E. B., Engelhardt, M., Stevens, D., Marchand, K., Waggoner, M. Robustness Assessment of Building Structures under Explosion. Buildings, 2012; 2: 497–518. doi:10.3390/buildings2040497.

[7] Chen, G. Q., Wu, H., Cheng, Y. H., Lu, J. X. Comparative studies on blast resistance of precast concrete composite and cast-in-place slabs. Journal of Building Engineering, 2025; 110: 113077. doi:10.1016/j.jobe.2025.113077.

[8] Tian, S., Yan, Q., Du, X., Chen, F., Zhang, B. Experimental and numerical studies on the dynamic response of precast concrete slabs under blast load. Journal of Building Engineering, 2023; 70: 106425. doi:10.1016/j.jobe.2023.106425.

[9] Lin, Y., Wang, Y., Wan, S., Yang, C., Zong, Z., Qian, H., Xu, X., Elchalakani, M., Cai, J. Experimental studies on behavior of one-part geopolymer composite slabs subjected to blast loading. Structures, 2024; 66: 106825. doi:10.1016/j.istruc.2024.106825.

[10] Zhu, W., Xiao, Y., Yu, J., Jia, J., Li, Z. Damage modes and mechanism of steel-concrete composite bridge slabs under contact explosion. Journal of Constructional Steel Research, 2024; 212: 108223. doi:10.1016/j.jcsr.2023.108223.

[11] Rao, N. N. Static and Dynamic Analysis of Fiber Metal Laminates-A Review. Journal of Failure Analysis and Prevention, 2025; 25: 1576–1591. doi:10.1007/s11668-025-02258-9.

[12] Costa, R. D. F. S., Sales-Contini, R. C. M., Silva, F. J. G., Sebbe, N., Jesus, A. M. P. A Critical Review on Fiber Metal Laminates (FML): From Manufacturing to Sustainable Processing. Metals, 2023; 13: 638. doi:10.3390/met13040638.

[13] Zhuang, Z. Extended Finite Element Formulation. 1st ed. Hoboken (NJ): John Wiley & Sons, Inc.; 2014. doi:10.1002/9781118869673.ch2.

[14] Almustafa, M. K., Nehdi, M. L. Trajectory solution to the reflected blast wave problem. Physics of Fluids, 2025; 37: 116119. doi:10.1063/5.0295470.

[15] Needham, C. E. Blast Waves (Shock Wave and High Pressure Phenomena). 1st ed. Berlin (DE): Springer 2010. doi:10.1007/978-3-642-05288-0.

[16] Le Minh, H., Khatir, S., Abdel Wahab, M., Cuong-Le, T. A concrete damage plasticity model for predicting the effects of compressive high-strength concrete under static and dynamic loads. Journal of Building Engineering, 2021; 44: 103239. doi:10.1016/j.jobe.2021.103239.

[17] SIMULIA Abaqus/CAE User's Manual. 1st ed. Providence (RI): 2012.

[18] Tajmir-Riahi, A., Moshiri, N., Mostofinejad, D. Inquiry into bond behavior of CFRP sheets to concrete exposed to elevated temperatures – Experimental & analytical evaluation. Composites Part B: Engineering, 2019; 173: 106897. doi:10.1016/j.compositesb.2019.05.108.

[19] Xu, Q., Chen, L., Han, C., Harries, K. A., Xu, Z. Experimental research on fire-damaged RC continuous T-beams subsequently strengthened with CFRP sheets. Engineering Structures, 2019; 183: 135–149. doi:10.1016/j.engstruct.2019.01.025.

[20] Li, B., Pan, T.-C., Nair, A. A case study of the structural responses of a tall building in Singapore subjected to close-in detonations. The Structural Design of Tall and Special Buildings, 2011; 20: 223–246. doi:10.1002/tal.531.

[21] Abbas, A., Ahmad, M., Khan, A. H., Alam, J., Ghani, A. Numerical Study on the Behavior of Reinforced Concrete Sandwich Panels (RCSPs) under Blast Load. Iranian Journal of Science and Technology, Transactions of Civil Engineering, 2024; 48: 3049–3068. doi:10.1007/s40996-024-01446-1.

[22] Khalifa, Y. A., Lotfy, M. N., Fathallah, E. Effectiveness of Sacrificial Shielding for Blast Mitigation of Steel Floating Pontoons. Journal of Marine Science and Engineering, 2023; 11: 96. doi:10.3390/jmse11010096.

[23] Building and Housing Research Center (BHRC). Iranian National Building Code, Part 21. Tehran (IR): BHRC; 2016.

[24] Moghimi, H., Driver, R. G. Performance assessment of steel plate shear walls under accidental blast loads. Journal of Constructional Steel Research, 2015; 106: 44–56. doi:10.1016/j.jcsr.2014.11.010.

[25] Abd-El-Nabi, E., El-Helloty, A., Summra, A. Numerical analysis of reinforced concrete buildings subjected to blast load. Structural Concrete, 2023; 24: 3727–3743. doi:10.1002/suco.202200726.

[26] Hussein, A., Heyliger, P. On the accuracy of CEL blast simulations: validation and application. Asian Journal of Civil Engineering, 2025; 26: 843–866. doi:10.1007/s42107-024-01226-2.

[27] Chen, S., Li, Z., Zhang, C., Wen, B., Tang, D. Large deflection analysis of the fully clamped square plates under explosive loading. International Journal of Impact Engineering, 2026; 207: 105514. doi:10.1016/j.ijimpeng.2025.105514.

[28] Syed, Z. I., Raman, S. N., Ngo, T., Mendis, P., Pham, T. The Failure Behaviour of Reinforced Concrete Panels Under Far-field and Near-field Blast Effects. Structures, 2018; 14: 220–229. doi:10.1016/j.istruc.2018.03.009.

[29] Shabanlou, M., Moghaddam, H., Saedi Daryan, A. The Effect of Geometry on Structural Behavior of Buildings with Steel Plate Shear Wall System Subjected to Blast Loading. International Journal of Steel Structures, 2021; 21: 650–665. doi:10.1007/s13296-021-00463-4.

[30] Ngo, T., Mendis, P., Gupta, A., Ramsay, J. Blast Loading and Blast Effects on Structures - An Overview. Electronic Journal of Structural Engineering, 2007; doi:10.56748›ejse.671.

[31] McDonald, B., Bornstein, H., Langdon, G. S., Curry, R., Daliri, A., Orifici, A. C. Experimental response of high strength steels to localised blast loading. International Journal of Impact Engineering, 2018; 115: 106–119. doi:10.1016/j.ijimpeng.2018.01.012.

[32] Norris, G. H., Hansen, R. J., Holly, M. J., Biggs, J. M., S., J. K., Minami Structural Design for Dynamic Loads. 1st ed. Ann Arbor (MI): McGraw-Hill; 1959.

[33] Perry, J. I., Walley, S. M. Measuring the Effect of Strain Rate on Deformation and Damage in Fibre-Reinforced Composites: A Review. Journal of Dynamic Behavior of Materials, 2022; 8: 178–213. doi:10.1007/s40870-022-00331-0.

[34] Liu, Q., Guo, B., Chen, P., Zhai, H., Guo, Y., Tang, S. Experimental investigation blast resistance of CFRP/polyurea composite plates under blast loading. Thin-Walled Structures, 2022; 181: 110149. doi:10.1016/j.tws.2022.110149.

[35] Xu, S., Zhou, S., Zhao, C., Huang, H., Kuang, N., Chen, J., Chen, X., Zhang, W. Strain Rate Effects on the Compressive Behavior of Unidirectional CFRP. Polymer Composites, 2026; 47: 5013–5030. doi:10.1002/pc.70469.

Civil Engineering and Applied Solutions

Research Article

journal homepage: ceas.journals.umz.ac.ir

CEAS Civil Engineering and Applied Solutions

Evaluating Building Information Modeling (BIM) for Residential Project Management: A Case Study of the Panorama Twin Towers

Masoud Ahmadvand [a], Hossein Eghbali [b*]

[a] *Department of Civil Engineering, University of Eyvanekey, Eyvanekey, Iran*
[b] *Department of Industrial Engineering, University of Eyvanekey, Eyvanekey, Iran*

ARTICLE INFO

Article history:

Received 31 December 2025

Revised 11 February 2026

Accepted 12 May 2026

Available online 01 January 2027

Keywords:

Building information modeling (BIM)

Project management

Linear regression

Data analysis

Cost and time optimization

ABSTRACT

In recent years, Building Information Modeling (BIM) has emerged as an innovative technology in the construction industry, playing a crucial role in enhancing project management processes. This study aims to evaluate and assess the impact of BIM on improving residential project management, with a case study of the Panorama Twin Towers in Pasdaran. The research examines the extent to which BIM influences key project management indicators, including cost reduction, schedule control, resource optimization, improved coordination among project stakeholders, and delay mitigation. To analyze the data, linear regression analysis has been employed. Linear regression is a widely used statistical method for examining the relationships between independent and dependent variables, which in this study is utilized to assess the impact of BIM on project management indicators. Data related to project execution were collected, preprocessed, and analyzed using a regression model. The coefficients of this statistical model determined the magnitude and direction of the influence of various variables, revealing with high precision the relationship between BIM implementation and project management enhancement. The modeling results indicate that the adoption of BIM has a significant and positive impact on improving project management processes. According to regression analysis, BIM contributes to project delay reduction, optimization of execution costs, increased scheduling accuracy, minimization of rework, improved coordination among project teams, and overall productivity enhancement. Furthermore, statistical analysis of the regression model suggests that BIM can accurately predict management trends and enhance strategic decision-making. These findings can assist project managers, consulting engineers, and other stakeholders in the construction industry in making more efficient and effective decisions, fostering the broader adoption of BIM in future projects.

How to cite this article: Ahmadvand, M., Eghbali, H. Evaluating Building Information Modeling (BIM) for Residential Project Management: A Case Study of the Panorama Twin Towers. Civil Engineering and Applied Solutions. 2027; 3(1): 78–97. doi:10.22080/ceas.2026.30968.1070.

1. Introduction

The construction industry has long been confronted with numerous challenges, including inefficiencies arising from fragmented workflows, reliance on traditional tools such as 2D drawings and manual reporting, and communication gaps among stakeholders. These issues frequently result in project delays, cost overruns, and inconsistent reports. For instance, project managers often organize multi-disciplinary meetings to assess progress, yet these gatherings produce conflicting outcomes due to isolated information sources [1]. Historically, the roots of these problems can be traced back to the pre-digital era, where paper-based documentation dominated, leading to errors in interpretation and coordination. The evolution of digital tools in the late 20th century began to address some of

* Corresponding author.
E-mail addresses: h.eghbali@eyc.ac.ir (H. Eghbali).

https://doi.org/10.22080/ceas.2026.30968.1070
ISSN: 3092-7749/

these, but it was the advent of Building Information Modeling (BIM) in the early 2000s that marked a paradigm shift. BIM serves as an integrated digital platform that centralizes data for all stakeholders throughout the project lifecycle, enabling real-time collaboration, error reduction, and resource optimization [2]. This technology not only digitizes building elements but also embeds parametric information, transforming static designs into dynamic, intelligent models that adapt to changes seamlessly [3].

Recent advancements in BIM technology have significantly enhanced its role in addressing these challenges, particularly in residential projects where budget and timeline constraints are more stringent. BIM goes beyond mere 3D visualization by incorporating intelligent attributes, such as metadata for materials, costs, and maintenance schedules, into model elements. This rich dataset persists from initial feasibility studies through design, procurement, construction, commissioning, operation, and even demolition phases [4]. Studies conducted between 2023 and 2025 demonstrate that BIM, through virtual clash detection in the design stage, can substantially reduce costly on-site rework and improve interdisciplinary coordination [5]. In high-rise residential developments, BIM has been shown to decrease delays by 20–30% and enhance scheduling accuracy via advanced simulation tools [6]. Moreover, the integration of BIM with virtual reality (VR) technologies, such as smartphone-based VR systems, has opened new avenues for client engagement in residential architecture, allowing immersive walkthroughs that refine designs before physical construction begins [7]. This has proven particularly beneficial in customizing residential spaces to user preferences, reducing post-construction modifications by up to 15% in case studies [8]. In the context of residential project management, the term stakeholder conflict refers to misalignments, disagreements, or incompatibilities in objectives, responsibilities, or decision-making processes among key project participants, including owners, designers, contractors, and consultants. Such conflicts often arise due to fragmented information flows, lack of transparency, and inconsistent interpretations of project requirements. Similarly, stakeholder gaps denote structural or informational discontinuities between stakeholders, manifested as communication breakdowns, delayed information exchange, or insufficient coordination across different project phases. These gaps can negatively affect cost control, schedule adherence, and overall project performance. The implementation of Building Information Modeling (BIM) aims to reduce both stakeholder conflicts and gaps by providing an integrated, data-driven platform that facilitates real-time collaboration, information sharing, and coordinated decision-making throughout the project lifecycle.

Furthermore, the adoption of BIM aligns with global trends toward sustainability and digitalization. By simulating energy performance and material lifecycles early in the process, BIM minimizes environmental impact and lifecycle costs; recent research indicates potential operational savings of 15–30% in residential buildings [9]. Integration of BIM with off-site construction and prefabrication reduces on-site waste and assembly time, as evidenced in systematic reviews of modular residential projects [10]. Analyses from 2024–2025 emphasize that BIM-enabled projects can be completed up to 30% faster, primarily due to proactive conflict resolution and data-driven decision-making [11]. In the context of sustainable civil engineering, BIM facilitates the incorporation of green materials and energy-efficient systems, contributing to lower carbon emissions in residential complexes [12]. For example, strategic frameworks like ADAPTE (Adaptation Process for Existing Buildings) leverage BIM to retrofit older residential structures, aligning them with modern sustainability standards and extending their usability [13]. Additionally, BIM's role in integrating Environmental, Social, and Governance (ESG) factors and Sustainable Development Goals (SDGs) has been highlighted as a key driver for long-term project viability, with studies identifying critical implementation factors such as stakeholder training and policy support [14]. The integration of BIM with emerging technologies such as artificial intelligence (AI) and the Internet of Things (IoT) enables risk prediction, resource optimization, and stricter adherence to scope, cost, time, and quality constraints [15]. AI-enhanced BIM models can automate routine tasks like quantity takeoffs and predictive maintenance, further streamlining residential project workflows [16]. However, barriers such as training requirements, interoperability issues, and initial costs, particularly in developing countries like Iran, have slowed widespread adoption [17]. In high-rise residential projects, BIM reinforces green principles and reduces carbon footprints [18]. Early adoption of BIM in high-rise planning has improved design coordination, time efficiency, and cost control, highlighting its strategic value [19]. Beyond these, the use of digital twins, virtual replicas of physical assets, integrated with BIM, promotes human-centric approaches in supply chains, enhancing collaboration and sustainability in residential construction [20]. Bibliometric analyses of AI in urban planning reveal that BIM serves as a foundational layer for smart city initiatives, where residential management benefits from data analytics for optimized resource allocation [21]. In smart buildings, AI-BIM synergies enable real-time monitoring of energy usage, with recent reviews underscoring their potential in residential IoT ecosystems [22]. Despite these advantages, challenges persist in fully realizing BIM's potential. For instance, in regions with limited digital infrastructure, adoption rates lag due to skill gaps and regulatory hurdles [23]. Global case studies, however, demonstrate that targeted policies and education programs can accelerate uptake, leading to measurable improvements in project outcomes [24]. Looking ahead, the future of BIM in residential construction lies in its convergence with technologies like blockchain for secure data sharing and augmented reality for on-site guidance, promising even greater efficiencies [3].

Despite the increasing adoption of BIM worldwide, its practical role in addressing the managerial challenges of residential construction projects remains insufficiently explored, particularly in developing countries. Residential projects are characterized by tight budgets, strict schedules, high stakeholder involvement, and direct impacts on occupants' quality of life. Traditional management approaches often fail to effectively handle these complexities, resulting in cost overruns, delays, and coordination conflicts. Therefore, evaluating BIM as an integrated project management approach, rather than solely as a design or visualization tool, constitutes the main problem addressed in this study. The Panorama Twin Towers project was selected as a case study due to its scale, functional complexity, and the involvement of multiple stakeholders, making it a suitable and representative context for examining the effectiveness of BIM in improving residential project management processes. This study builds upon these insights to evaluate the impact of BIM on residential project management through a case study of the Panorama Twin Towers in Pasdaran. The research methodology involves data collection via questionnaires, statistical analysis using SPSS software, normality tests, and linear regression modeling to quantify BIM's effects on key indicators such as cost reduction and delay mitigation. Although the advantages of Building Information Modeling, such as cost reduction, time optimization, and improved coordination, have been widely discussed in previous studies, this research offers several distinct contributions. First, it provides an empirical assessment of BIM implementation in a real high-rise residential project within a developing-country context, where institutional, technological, and organizational conditions differ significantly from those typically examined in prior studies. Second, the study proposes a comprehensive conceptual framework that links BIM adoption not only to traditional project management indicators, but also to organizational and socio-environmental dimensions, including fair payment, safe work environment, organizational integration, and capability development. Third, by applying linear regression analysis, this research quantitatively measures the relative influence of BIM-related factors on residential project management performance, moving beyond descriptive evaluations commonly found in the literature. The structure of this paper is as follows: following this introduction, the data analysis section presents demographic profiles, reliability tests, and descriptive statistics; subsequent sections discuss regression models and result interpretations; finally, the conclusion and recommendations outline practical implications and directions for future research.

2. Methodology

This study adopts a quantitative and applied research methodology to evaluate the impact of Building Information Modeling (BIM) on residential project management processes. A case study strategy is employed to enable an in-depth examination of BIM implementation within a real-world residential high-rise project. Data are collected using a structured, closed-ended questionnaire based on a five-point Likert scale and analyzed using statistical techniques. The methodological framework of the study is designed to ensure reliability, analytical rigor, and alignment between the research objectives, data collection process, and empirical analysis. The conceptual research model is presented in Fig. 1.

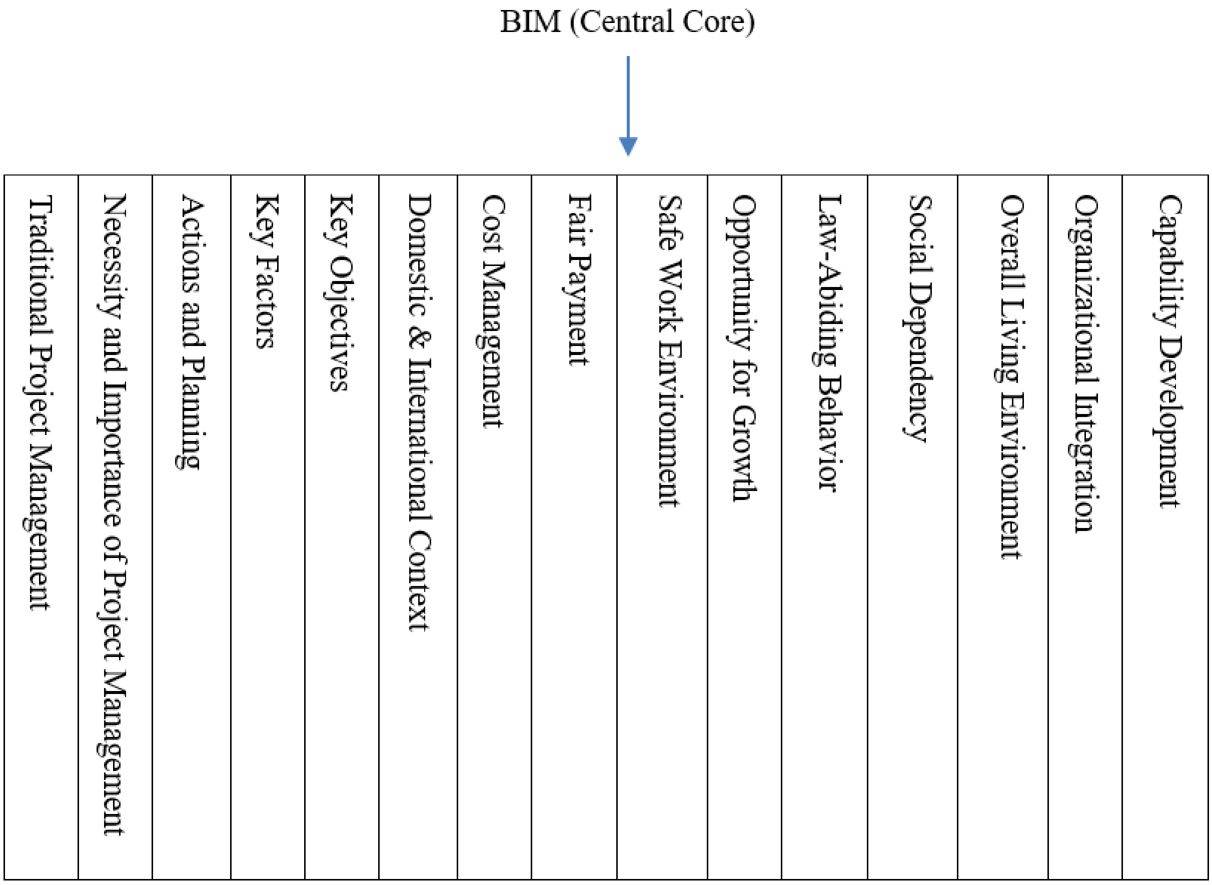

Fig. 1. Conceptual research model.

2.1. Research work

The research workflow of this study is designed to provide a clear and systematic roadmap for evaluating the impact of Building Information Modeling (BIM) on residential project management processes. The workflow begins with the identification of key challenges associated with traditional residential project management practices, followed by a comprehensive review of the relevant literature to establish the theoretical foundation of the study. Based on this review, a BIM-based conceptual framework encompassing factors F1–F15 is developed to guide the empirical analysis. Subsequently, a case study approach is adopted, focusing on the Panorama Twin Towers residential high-rise project. A structured questionnaire comprising 43 Likert-scale items is then designed and administered through face-to-face surveys with managers and engineers during the project execution phase. The collected data are prepared and coded for statistical analysis using SPSS software. Reliability and validity are assessed using Cronbach's alpha, after which descriptive statistics and linear regression analysis are employed to examine the relationships between BIM adoption and residential project management indicators. Finally, the results are interpreted and discussed in light of existing literature, leading to conclusions and practical recommendations for future BIM implementation. The research methodology is summarized in Fig. 2.

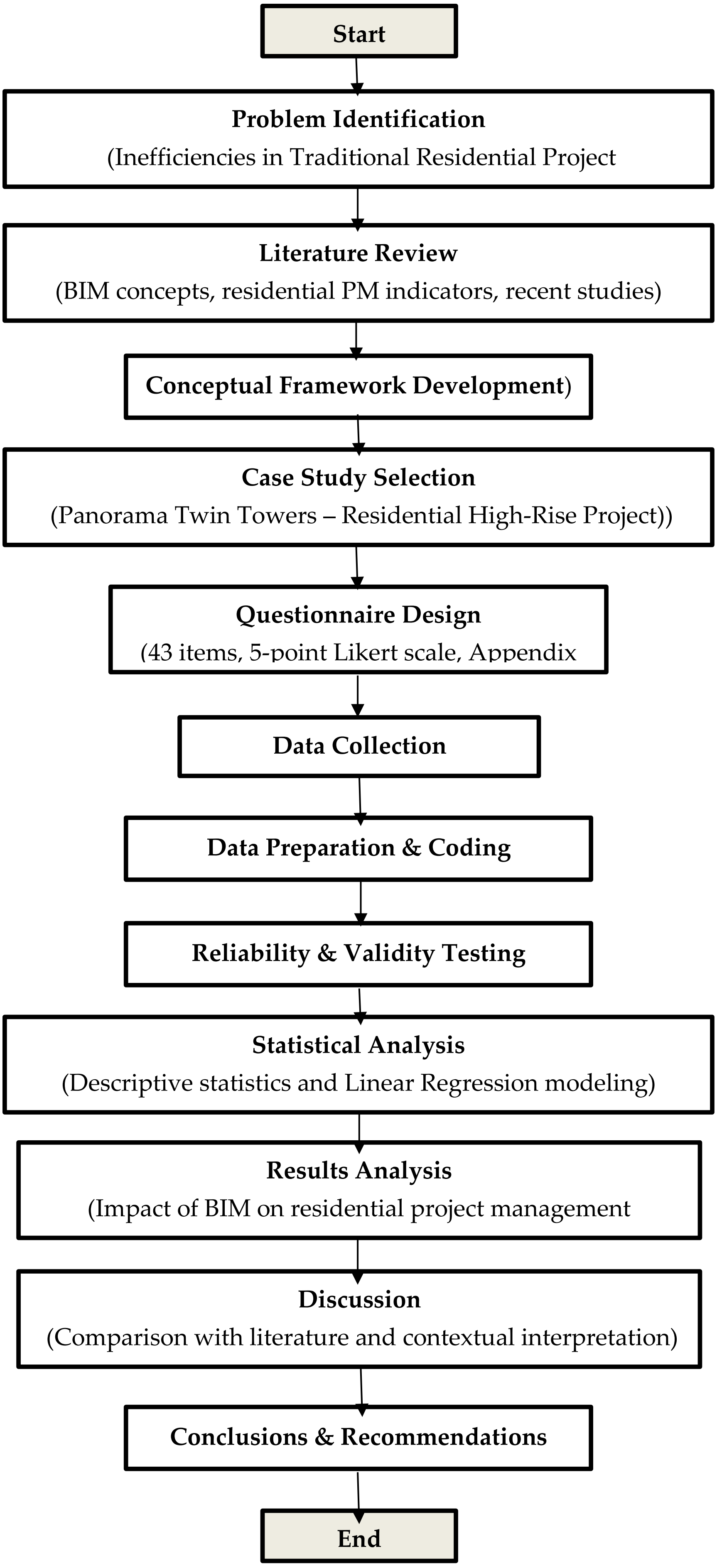

Fig. 2. Research methodology flowchart.

2.2. Research design

This study adopts a quantitative research design using a case study approach to evaluate the impact of Building Information Modeling (BIM) on residential project management processes. The research focuses on the Panorama Twin Towers project located in Pasdaran, Iran, as a representative high-rise residential development. A structured questionnaire was employed as the primary data collection instrument to capture the perceptions and experiences of professionals involved in the project.

2.3. Case study description

The Panorama Twin Towers is a large-scale residential construction project characterized by complex coordination requirements, multiple stakeholders, and stringent cost and time constraints. Due to these characteristics, the project provides a suitable context for assessing the effectiveness of BIM in improving residential project management practices. The case study approach enables an in-depth evaluation of BIM implementation within a real-world project environment. The case study implementation is shown in Figs. 3 and 4.

Fig. 3. Implementation of the pasdaran twin towers.

Fig. 4. The twin towers of the Pasdaran.

2.4. Data collection method

Data were collected through a structured, closed-ended questionnaire administered via face-to-face distribution. The target population consisted of engineers, project managers, supervisors, and technical experts directly involved in the Panorama Twin Towers project. This method of administration ensured accurate understanding of the questionnaire items and enhanced the reliability of the collected responses. A total of 120 valid questionnaires were collected and used for statistical analysis.

2.5. Questionnaire design

The questionnaire was designed based on the proposed conceptual model of BIM impacts on residential project management. It consisted of 43 declarative statements grouped into 15 dimensions, including traditional project management practices, cost management, scheduling, safety, fair payment, capability development, and organizational cohesion. All items were measured using a five-point Likert scale ranging from Very Low (1) to Very High (5). No open-ended questions were included.

2.6. Reliability and validity

The reliability of the questionnaire was assessed using Cronbach's alpha coefficient. The results indicate alpha values exceeding the acceptable threshold of 0.70, confirming the internal consistency and reliability of the measurement instrument. These findings support the suitability of the questionnaire for evaluating BIM-related impacts in residential project management studies.

2.7. Data analysis techniques

The collected data were analyzed using SPSS statistical software. Descriptive statistics, including frequencies, percentages, means, and standard deviations, were used to summarize respondent characteristics and questionnaire responses. Inferential statistical analyses were conducted using normality tests and linear regression models to examine the relationships between BIM implementation and key residential project management indicators such as cost reduction, delay mitigation, coordination improvement, and productivity enhancement.

The overall research approach follows a structured sequence beginning with the identification of challenges in traditional residential project management, followed by the development of a BIM-based conceptual framework. Subsequently, relevant management dimensions were defined and translated into questionnaire statements. Data were collected through structured questionnaires, and reliability was assessed using Cronbach's Alpha. Normality tests and linear regression analysis were then conducted to evaluate the impact of BIM on residential project management processes, followed by interpretation and discussion of results. Linear regression analysis was employed in this study to examine the relationship between BIM-related factors and residential project management indicators. This method was selected due to its suitability for exploratory studies with moderate sample sizes and its ability to provide clear and interpretable estimates of the magnitude and direction of variable relationships. Unlike Structural Equation Modeling (SEM), which requires strong theoretical assumptions regarding causal pathways and larger sample sizes, linear regression allows for the assessment of individual factor contributions without imposing complex structural constraints. It should be noted that the objective of this research is not to establish definitive causal relationships, but to identify statistically significant associations between BIM implementation and project management performance indicators. The results therefore reflect perceived and experienced impacts of BIM adoption within the case study context, rather than direct cause–effect proof.

3. Data analysis

Data analysis encompasses multiple stages, beginning with the preparation and organization of data required for hypothesis testing, followed by the examination of relationships between variables, and ultimately the comparison of observed results. In this study, the collected sample data were categorized and integrated using statistical methods and software, then analyzed and interpreted. To achieve this, both descriptive and inferential statistics were employed with the assistance of SPSS statistical analysis software. In the descriptive statistics section, key frequency indices including frequency, percentage frequency, central tendency measures, dispersion measures, and bar charts were utilized. In the inferential statistics section, after quantification, statistical tests were applied to evaluate the research hypotheses. The necessary data were collected through a structured questionnaire, and subsequently converted into quantitative variables using statistical methods. This transformation enabled the application of advanced statistical tests, ensuring the practical usability of the research findings. The data for this study were collected through a structured questionnaire administered to professionals directly involved in the Panorama Twin Towers residential project in Pasdaran. The respondents included project managers, site engineers, supervisors, and technical experts who had direct experience with residential project management processes and exposure to BIM-related practices. Questionnaires were distributed during the active execution and management phases of the project to ensure that participants' responses reflected real-time project conditions rather than retrospective judgments. Prior to data collection, the purpose of the study was explained to all participants, and confidentiality of responses was assured. Participation was voluntary, and respondents completed the questionnaires based on their professional experience within the project environment. To enhance data reliability, only completed questionnaires with consistent and valid responses were included in the final analysis. This project-based data collection approach ensured that the findings accurately represent the practical impacts of BIM on residential project management under real operational conditions.

Before conducting the analysis of the collected questionnaires and performing computations using the Analytic Network Process (ANP), this section presents demographic information related to the research sample. The demographic data include gender, age, work experience, level of education, and field of study. These variables are presented in the form of frequency distribution tables and graphical charts to provide a clearer understanding of the sample's characteristics. The selection of sample characteristics in this study was guided by established research in the fields of Building Information Modeling (BIM) adoption and construction project management. Demographic and professional variables such as age, level of education, work experience, and employment-related attributes were selected because previous studies have shown that these factors significantly influence technology adoption, decision-making behavior, and the effectiveness of BIM implementation in construction projects. In particular, professional experience and educational background affect stakeholders' ability to interpret digital models, coordinate project information, and engage in BIM-based workflows. Accordingly, the selected sample characteristics are consistent with prior empirical studies on BIM adoption and project management performance in residential and infrastructure projects, ensuring the comparability and methodological validity of the research findings.

To enhance transparency and reproducibility, the raw format of the questionnaire used for data collection is provided in Appendix A. The questionnaire items were designed based on the proposed conceptual model and measured respondents' perceptions of BIM impacts using a five-point Likert scale ranging from Very Low (1) to Very High (5). The demographic characteristics of the questionnaire respondents are summarized in Tables 1 to 5.

Table 1. Age distribution of questionnaire respondents.

Age group	Frequency	Percentage frequency	Sample percentage	Cumulative percentage frequency
25-35	60	50%	50%	50%
35-45	42	42.9%	42.9%	92.9%
55+	18	7.1%	7.1%	100%
Total	120	100%	100%	100%

Table 2. Frequency distribution of respondents' educational level.

Education level	Frequency	Percentage frequency	Sample percentage	Cumulative percentage frequency
Bachelor's Degree	20	14.3%	14.3%	14.3%
Master's Degree	89	78.6%	78.6%	92.9%
Ph.D.	11	7.1%	7.1%	100%
Total	120	100%	100%	100%

Table 3. Frequency distribution of respondents' work experience.

Years of experience	Frequency	Percentage frequency	Sample percentage	Cumulative percentage frequency
Less than 10 years	60	50%	50%	50%
10-20 years	45	35.7%	35.7%	85.7%
More than 20 years	15	14.3%	14.3%	100%
Total	120	100	100%	100%

Table 4. Frequency distribution of respondents' marital status.

Marital status	Frequency	Percentage frequency	Sample percentage	Cumulative percentage frequency
Single	33	28.6%	28.6%	28.6%
Married	87	71.4%	71.4%	100%
Total	120	100%	100%	100%

Table 5. Frequency distribution of respondents' insurance coverage.

Insurance type	Frequency	Percentage frequency	Sample percentage	Cumulative percentage frequency
Social Security (Tamin Ejtemaei)	98	85.7%	85.7%	85.7%
Health Services Insurance	22	14.3%	14.3%	100%
Total	120	100%	100%	100%

The data collection instrument was a structured, closed-ended questionnaire designed using Likert-scale statements. The questionnaire did not include open-ended questions. Data were collected through face-to-face distribution of the questionnaires among engineers, project managers, and technical staff involved in the Panorama Twin Towers residential project in Pasdaran. This approach ensured clarity of responses and increased the reliability of the collected data.

4. Cronbach’s alpha test

Cronbach was the individual who developed the Cronbach's alpha coefficient. This coefficient is now widely recognized as one of the most commonly used methods for measuring reliability in scientific questionnaires. This measurement method calculates the correlation between two questions that are posed to achieve a specific goal. It is primarily used to assess the reliability, or in other words, the consistency, of questionnaires. In addition to this measurement method, other methods also exist for examining the reliability of questionnaires. In questionnaires, we typically examine several traits. If we evaluate the same traits under the same conditions but at different times, and obtain consistent results, we can conclude that the questionnaire is reliable and valid. Using Cronbach’s alpha, we can gain insights into the opinions and attitudes of respondents. This coefficient helps determine how respondents interpret the questions in the questionnaire. In essence, a group of respondents may have a similar understanding of the questions, and Cronbach's alpha clearly indicates how many individuals share similar attitudes. This coefficient is based on scales, which are sets of numbers that represent quality in measurable terms. The Likert scale is one of the most common scales used in social research. Cronbach’s alpha is a coefficient calculated using established statistical relationships. Cronbach defined a formula for this coefficient, which can be manually applied to assess the correlation between questions. In this relationship, k represents the number of questions. For conducting scientific research, it is advisable not to rely solely on this formula. Using advanced software is a more appropriate option for obtaining accurate results, as it reduces the time needed for analysis. Cronbach’s alpha coefficient was used to evaluate the internal consistency and reliability of the questionnaire. In addition to the descriptive explanation, the mathematical formulation of Cronbach's alpha is presented as follows. The reliability and validity of the questionnaire are presented in Table 6 based on Eq. 1.

$$\alpha = (k / (k - 1)) \times [1 - (\Sigma\sigma^2{}_i / \sigma^2{}_t)] \quad (1)$$

where α represents Cronbach's alpha coefficient, k is the number of questionnaire items, σ^2_i denotes the variance of each individual item, and σ^2_t represents the total variance of the summed scale. Values of α greater than 0.70 indicate acceptable reliability.

Table 6. Cronbach's alpha test for questionnaire reliability and validity.

Cronbach's alpha	Number of items
0.728	9
0.733	43

Based on the Cronbach's alpha test, we observe that the alpha value for both questionnaires is greater than 70%, indicating that the Job Performance and Quality of Work Life questionnaires have high reliability and validity. In this section, we will present the frequency and percentage of responses to the questionnaire's questions, along with the mean and standard deviation for each variable. Regarding the coding of the questionnaire questions, it is important to note that since the Likert scale was used to design the questions, with scores assigned as follows:

Very High = 5, High = 4, Average = 3, Low = 2, Very Low = 1

A higher average score for a question or variable, especially approaching 5, indicates that the question or variable is perceived more positively. Descriptions of the sample distributions are given in Tables 7 to 20.

Table 7. Sample breakdown based on building information modeling (BIM) in improving residential project management processes using traditional methods.

F1 statements	Very low	Low	Somewhat	High	Very high	Standard deviation	Mean
A1	12%	20%	22.7%	29.3%	16%	1.673	3.173
A2	4%	18.7%	18.7%	30.7%	28%	1.684	1.432
Total		4.605					

In this section, the mean, standard deviation, and percentage of responses to the BIM-related statements for improving residential project management processes using traditional methods are presented. The overall mean of the residential project management variable in traditional methods was calculated to be 4.605. The lowest mean corresponds to statement A2, and the highest mean corresponds to statement A1.

Table 8. Sample breakdown based on building information modeling (BIM) in improving the necessity and importance of residential project management.

F2 statements	Very low	Low	Somewhat	High	Very high	Standard deviation	Mean
B1	1.3%	13.3%	17.3%	32%	36%	1.090	3.880
B2	2.7%	14.7%	21.3%	30.7%	37%	1.376	3.720
Total							7.6

In this section, the mean, standard deviation, and percentage of responses to the statements regarding the necessity and importance of BIM in improving residential project management are presented. The overall mean for the necessity and importance of BIM in residential project management was calculated as 7.6. The lowest mean corresponds to statement B2, while the highest mean corresponds to statement B1.

Table 9. Sample breakdown based on building information modeling (BIM) in improving the actions and planning of residential project management.

F3 Statements	Very low	Low	Somewhat	High	Very high	Standard deviation	Mean
C1	1.3%	14.7%	18.7%	22.7%	42%	1.528	3.906
C2	0%	5.3%	24%	17.3%	53%	0.982	4.876
C3	0%	2.7%	37.3%	24%	36%	0.920	3.933
Total							12.267

In this section, the mean, standard deviation, and percentage of responses to the statements regarding the BIM-related actions and planning for improving residential project management are presented. The overall mean for the actions and planning of residential project management was calculated to be 12.267. The lowest mean corresponds to statements C1 and C3, while the highest mean corresponds to statement C2.

Table 10. Sample breakdown based on building information modeling (BIM) in improving key factors of residential project management.

F4 statements	Very low	Low	Somewhat	High	Very high	Standard deviation	Mean
D1	1.3%	5.3%	30.3%	30.7%	32%	0.977	3.867
D2	29.3%	26.7%	17.3%	17.3%	9.3%	1.239	2.507
Total							6.373

In this section, the mean, standard deviation, and percentage of responses to the statements regarding key factors in residential project management using BIM are presented. The overall mean for key factors in residential project management was calculated to be 6.373. The lowest mean corresponds to statement D2, while the highest mean corresponds to statement D1.

Table 11. Sample breakdown based on building information modeling (BIM) in improving key Objectives of residential project management.

F5 statements	Very low	Low	Somewhat	High	Very high	Standard deviation	Mean
E1	6.7%	8%	30.7%	25.3%	29.3%	1.182	3.627
E2	1.3%	8%	24%	22.7%	44%	1.065	4.000
Total							7.627

In this section, the mean, standard deviation, and percentage of responses to the statements regarding improving key objectives in residential project management using BIM are presented. The overall mean for key objectives in residential project management was calculated to be 7.627. The lowest mean corresponds to statement E1, while the highest mean corresponds to statement E2.

Table 12. Sample breakdown based on building information modeling (BIM) and residential project management in domestic and international contexts.

F6 statements	Very low	Low	Somewhat	High	Very high	Standard deviation	Mean
H1	0%	17.3%	32%	21.3%	29.3%	1.087	3.627
H2	1.3%	14.7%	32%	18.7%	33.3%	1.289	3.680
H3	0%	16%	32%	21.3%	30.7%	1.082	3.667
Total							10.973

In this section, the mean, standard deviation, and percentage of responses to the statements regarding residential project management in domestic and international contexts using BIM are presented. The overall mean for key factors in residential project management in both domestic and international contexts was calculated to be 10.973. The lowest mean corresponds to statements H1 and H3, while the highest mean corresponds to statement H2.

Table 13. Sample breakdown based on building information modeling (BIM) and improvement of residential project management costs.

F7 statements	Very low	Low	Somewhat	High	Very high	Standard deviation	Mean
K1	13.3%	21.3%	28%	21.3%	21.3%	1.331	3.107
K2	14.7%	14.7%	28%	22.7%	20%	1.322	3.187
Total							6.293

In this section, the mean, standard deviation, and percentage of responses to the statements regarding improving residential project management costs using BIM are presented. The overall mean for residential project management costs was calculated to be 6.293. The lowest mean corresponds to statement K1, while the highest mean corresponds to statement K2.

Table 14. Sample breakdown based on building information modeling (BIM) and improvement of fair payment.

F8 statements	Very low	Low	Somewhat	High	Very high	Standard deviation	Mean
L1	8%	26.7%	29.3%	18.7%	17.3%	1.214	1.107
L2	4%	24%	24%	16%	32%	1.277	3.480
L3	0%	22.7%	37%	16%	30%	1.152	3.547
Total							8.133

In this section, the mean, standard deviation, and percentage of responses to the statements regarding fair payment improvement using BIM are presented. The overall mean for fair payment was calculated to be 8.133. The lowest means correspond to statements L1 and L2, while the highest mean corresponds to statement L3.

Table 15. Sample breakdown based on building information modeling (BIM) and improvement of a safe work environment.

F9 statements	Very low	Low	Somewhat	High	Very high	Standard deviation	Mean
Q1	0%	22.7%	32%	16%	29%	1.143	3.520
Q2	1.3%	12%	32%	29.3%	25.3%	1.033	3.653
Q3	0%	16%	30.7%	25.3%	28%	1.058	3.653
Total							10.827

In this section, the mean, standard deviation, and percentage of responses to the statements regarding a safe work environment improvement using BIM are presented. The overall mean for a safe work environment was calculated to be 10.827. The lowest mean corresponds to statement Q1, while the highest means correspond to statements Q2 and Q3.

Table 16. Sample breakdown based on building information modeling (BIM) and improvement of growth opportunities.

F10 statements	Very low	Low	Somewhat	High	Very high	Standard deviation	Mean
W1	4%	12%	30.7%	33.3%	20%	1.069	3.533
W2	2.7%	14.7%	32%	33.3%	17.3%	1.031	3.480
W3	4%	14.7%	22.7%	34.7%	24%	1.127	3.600
Total							10.613

In this section, the mean, standard deviation, and percentage of responses to the statements regarding growth opportunities improvement using BIM are presented. The overall mean for growth opportunities was calculated to be 10.613. The lowest mean corresponds to statement W2, while the highest mean corresponds to statement W3.

Table 17. Sample breakdown based on building information modeling (BIM) and improvement of law-abiding behavior.

F11 statements	Very low	Low	Somewhat	High	Very high	Standard deviation	Mean
R1	9.3%	13.3%	25.3%	25.3%	26.7%	1.276	3.467
R2	1.3%	21.3%	26.7%	13.3%	37.3%	1.226	3.640
R3	0%	20%	46.7%	18.7%	14.7%	0.922	3.280
R4	1.3%	14%	40%	17.3%	25.3%	1.082	3.493
Total							13.580

In this section, the mean, standard deviation, and percentage of responses to the statements regarding law-abiding behavior improvement using BIM are presented. The overall mean for law-abiding behavior was calculated to be 13.580. The lowest mean corresponds to statement R3, while the highest mean corresponds to statement R2.

Table 18. Sample breakdown based on building information modeling (BIM) and improvement of social dependency.

F12 statements	Very low	Low	Somewhat	High	Very high	Standard deviation	Mean
Y1	0%	18.7%	49.3%	22.7%	9.3%	0.863	3.227
Y2	14.7%	20%	30.7%	14.7%	20%	1.324	3.053
Y3	10.7%	20%	28%	25.3%	16%	1.230	3.160
Total							9.440

In this section, the mean, standard deviation, and percentage of responses to the statements regarding social dependency improvement using BIM are presented. The overall mean for social dependency was calculated to be 9.440. The lowest mean corresponds to statement Y2, while the highest mean corresponds to statement Y1.

Table 19. Sample breakdown based on building information modeling (BIM) and improvement of the overall living environment.

F13 statements	Very low	Low	Somewhat	High	Very high	Standard deviation	Mean
U1	13.3%	18.7%	25.3%	17.3%	25.3%	1.371	3.227
U2	6.7%	17.3%	22.7%	21.3%	32%	1.287	3.547
U3	1.3%	20%	33.3%	13.3%	32%	1.177	3.547
Total							10.320

In this section, the mean, standard deviation, and percentage of responses to the statements regarding improvement of the overall living environment using BIM are presented. The overall mean for the overall living environment was calculated to be 10.320. The lowest means correspond to statements U1 and U2, while the highest mean corresponds to statement U3.

Table 20. Sample breakdown based on building information modeling (BIM) and improvement of capability development.

F15 statements	Very low	Low	Somewhat	High	Very high	Standard deviation	Mean
M1	1.3%	17.3%	22.7%	40%	18.7%	1.028	3.573
M2	1.3%	20%	14.7%	40%	24%	1.096	3.653
M3	6.7%	20%	14.7%	29.3%	29.3%	1.287	3.547
M4	2.7%	18.7%	24%	13.3%	41.3%	1.258	3.720
Total							14.493

In this section, the mean, standard deviation, and percentage of responses to the statements regarding capability development using BIM are presented. The overall mean for capability development was calculated to be 14.493. The lowest mean corresponds to statement M3, while the highest mean corresponds to statement M4. The analysis of mean values across different dimensions demonstrates that BIM has a particularly strong influence on capability development, law-abiding behavior, and safe work environments. These results indicate that BIM adoption enhances not only technical performance but also organizational and regulatory compliance in residential projects.

5. Assessment of data normality

As previously discussed, when selecting a statistical test, it is essential to determine whether parametric or non-parametric tests should be used. This decision relies on evaluating the normality of the data. One of the primary methods for this assessment is the Kolmogorov-Smirnov (K-S) test. Hypotheses of the Kolmogorov-Smirnov Test: Null Hypothesis (H_0): The distribution of the research variables is normal. Alternative Hypothesis (H_1): The distribution of the research variables is not normal. By conducting the K-S test, we can determine whether the data follows a normal distribution, which directly influences the selection of statistical analysis methods. If the data is normally distributed (H_0 is accepted), parametric tests can be used. However, if the data is not normally distributed (H_1 is accepted), non-parametric tests should be applied. The K-S test for normality of the variables is shown in Table 21.

Table 21. Kolmogorov-Smirnov test for normality of variables.

Variable	Z-statistic	Significance level (Sig)	Result
Residential project management in traditional methods	1.325	0.06	Normal
Necessity and importance of residential project management	1.491	0.023	Normal
Actions and planning in residential project management	1.725	0.005	Non-Normal
Key factors in residential project management	1.956	0.001	Non-Normal
Key objectives in residential project management	1.62	0.011	Non-Normal
Residential project management in domestic and international contexts	1.113	0.154	Normal
Residential project management costs	1.095	0.182	Normal
Fair payment	0.878	0.724	Normal
Safe work environment	1.055	0.216	Normal
Growth opportunities	0.919	0.367	Normal
Law-abiding behavior	1.386	0.043	Non-Normal
Social dependency	1.265	0.082	Normal
Overall living environment	1.144	0.146	Normal
Organizational integrity and cohesion	1.022	0.247	Normal
Capability development	1.112	0.169	Normal

5.1. Implications of data normality results

The Kolmogorov–Smirnov test results indicate that while some variables do not follow a normal distribution, the majority of the constructs meet the normality assumption. This supports the robustness of the regression models applied in this study and justifies the use of both parametric and non-parametric statistical techniques.

6. Analysis of the Kolmogorov-Smirnov test for normality

1. Based on the Kolmogorov-Smirnov normality test, the following observations can be made:

For the variables related to actions and planning, key objectives, key factors, and law-abiding behavior, the significance level is below 5%, indicating that the data do not follow a normal distribution. Therefore, the null hypothesis (H_0) is rejected, and we can accept the alternative hypothesis (H_1: The data are not normally distributed) with 95% confidence.

2. For the remaining variables, the significance level is equal to or greater than 5%, indicating that the data follow a normal distribution.

3. Since the significance level for most variables is greater than 0.05, we do not reject the null hypothesis (H_0) and accept that the distribution of these variables is normal.

7. Linear regression analysis

As previously observed, the 15 dimensions contributing to the impact of Building Information Modeling (BIM) on improving residential project management (case study: Panorama Twin Towers, Pasdaran) were identified through Pearson correlation analysis. Now, we will conduct a linear regression test to develop a predictive linear equation that models the relationship between the dependent variable (residential project management) and the independent variable (BIM implementation). This analysis will help us construct an appropriate structural equation for forecasting the influence of BIM on project management. For this purpose, linear regression analysis is employed to formulate the residential project management process and its 15 dimensions, which include:

- Residential project management in traditional methods
- Necessity and importance of residential project management
- Actions and planning in residential project management
- Key factors in residential project management
- Key objectives in residential project management
- Residential project management in domestic and international contexts
- Residential project management costs
- Fair payment
- Safe work environment
- Growth opportunities
- Law-abiding behavior
- Social dependency
- Overall living environment
- Organizational integrity and cohesion
- Capability development
- Through linear regression modeling, we aim to establish a predictive equation that explains how BIM contributes to improving these key aspects of residential project management.

To examine the relationship between BIM implementation and residential project management performance, a linear regression model was employed. The general form of the regression equation used in this study is expressed as follows:

$$Y = \beta_0 + \beta_1 X_1 + \beta_2 X_2 + \dots + \beta_n X_n + \varepsilon \tag{2}$$

where in Eq. 2, Y represents the dependent variable (overall residential project management performance), X_1 to X_n denote independent variables related to BIM implementation factors, β_0 is the intercept, β_1 to β_n are regression coefficients indicating the magnitude of influence of each variable, and ε represents the error term. Prior to interpreting the regression results, key diagnostic tests were conducted to validate the underlying assumptions of the linear regression models. Multicollinearity among independent variables was assessed using the Variance Inflation Factor (VIF), with all values remaining below the commonly accepted threshold, indicating no severe multicollinearity issues. Model goodness-of-fit was evaluated using the coefficient of determination (R^2 and adjusted R^2), which reflects the proportion of variance in the dependent variables explained by BIM-related factors. In addition, residual diagnostics were examined to assess normality, linearity, and homoscedasticity, confirming the suitability of the regression models for inferential analysis. The linear regression for BIM is shown in Table 22.

Table 22. Linear regression for BIM in improving residential project management process in domestic and international contexts.

Test	Unstandardized coefficients (B)	Standardized coefficients (Beta)	t	sig
Constant	133.620	-	34.165	0.000
Management in domestic and international contexts	1.606	0.749	4.650	0.000

Linear Regression Test: Building Information Modeling (BIM) in Improving Residential Project Management Process in Domestic and International Contexts and Overall Living Environment Given that the sig value is below 0.05, the corresponding B coefficient can be included in the structural equation. Based on the linear regression results, the predictive model for forecasting the residential project management process both domestically and internationally (Y) using BIM modeling (X) is formulated as Eq. 3.

$$Y = 133.620 + 1.606x_1 \tag{3}$$

This equation represents how BIM (X) influences the management process (Y) in both domestic and international residential projects. Now, for the overall living environment in conjunction with BIM, you would perform a similar regression test to establish the relationship between BIM and the overall living environment (Z) in the project management process. The process would involve analyzing the relationship between BIM and this additional dimension (living environment), using the same statistical framework. If you would like to extend this model to the living environment, you could proceed with the regression analysis as follows:

$$Z = [\text{Constant}] + [\text{Beta coefficient for BIM impact on the living environment}] \times X \quad (4)$$

Table 23. Linear regression test: building information modeling (BIM) in improving residential project management process in domestic and international contexts and overall living environment.

Test	Unstandardized coefficients (B)	Standardized coefficients (Beta)	t	sig
Constant	117.310	-	26.509	0.000
Residential project management in domestic and international contexts (x_1)	1.615	0.291	0.481	5.543
Overall living environment (x_2)	1.571	0.248	0.480	5.305

Interpretation of the Results:

Both Residential Project Management in Domestic and International Contexts (x_1) and Overall Living Environment (x_2) have significant positive impacts on the project management process with sig values less than 0.05, indicating that their B coefficients can be included in the structural equation. Linear regression based on Eq. 4 and Table 23 shows the results mentioned in Eq. 5. The regression equation for predicting the residential project management process (Y) in terms of BIM, domestic/international project management (x_1), and overall living environment (x_2) is formulated as follows:

$$Y = 117.310 + 1.615x_1 + 1.571x_2 \quad (5)$$

This equation shows that BIM (through x_1 and x_2) significantly influences the management process both in domestic/international contexts and in the overall living environment of residential projects. The coefficients (1.615 and 1.571) reflect the strength of this influence.

Table 24. Linear regression test: building information modeling (BIM) in improving residential project management process in domestic and international contexts, overall living environment, and fair payment.

Test	Unstandardized coefficients (B)	Standardized coefficients (Beta)	t	sig
Constant	107.484	-	21.761	0.000
Residential project management in domestic and international contexts (x_1)	1.555	0.271	0.463	5.746
Overall living environment (x_2)	1.595	0.263	0.487	6.055
Fair payment (x_3)	1.010	0.283	0.283	3.573

Interpretation of the Results:

All the variables in Table 24 (Residential Project Management in Domestic and International Contexts (x_1), Overall Living Environment (x_2), and Fair Payment (x_3)) have significant impacts on project management with sig values below 0.05, meaning their B coefficients can be included in the structural equation. The regression equation for predicting the residential project management process (Y) with respect to BIM is formulated as Eq. 6.

$$Y = 107.484 + 1.555x_1 + 1.595x_2 + 1.010x_3 \quad (6)$$

This equation indicates that BIM significantly influences the project management process through domestic/international project management (x_1), overall living environment (x_2), and fair payment (x_3). The coefficients (1.555, 1.595, and 1.010) represent the respective strength of influence of each variable on the overall management process.

Table 25. Building information modeling (BIM) in improving residential project management process in domestic and international contexts, overall living environment, fair payment, and growth opportunities.

Test	Unstandardized coefficients (B)	Standardized coefficients (Beta)	t	sig
Constant	87.030	-	14.123	0.000
Residential project management in domestic and international contexts (x_1)	1.645	0.239	0.490	6.894
Overall living environment (x_2)	1.847	0.238	0.564	7.769
Fair payment (x_3)	1.387	0.261	0.395	5.310
Growth opportunities (x_4)	1.228	0.263	0.357	4.678

Interpretation of the Results based on Table 25:

All the variables (Residential Project Management in Domestic and International Contexts (x_1), Overall Living Environment (x_2), Fair Payment (x_3), and Growth Opportunities (x_4)) have significant impacts on project management, as indicated by the sig values below 0.05, meaning their B coefficients can be included in the structural equation. The regression equation for predicting the residential project management process (Y) with respect to BIM is formulated as Eq. 7.

$$Y = 87.030 + 1.645x_1 + 1.847x_2 + 1.387x_3 + 1.228x_4 \quad (7)$$

This equation shows that BIM significantly influences the project management process through domestic/international project management (x_1), overall living environment (x_2), fair payment (x_3), and growth opportunities (x_4). The coefficients (1.645, 1.847, 1.387, and 1.228) represent the strength of influence of each variable on the overall management process.

Table 26. Linear regression test: building information modeling (BIM) in improving residential project Management Process in Domestic and International Contexts, Overall Living Environment, Fair Payment, Growth Opportunities, and Capability Development.

Test	Unstandardized coefficients (B)	Standardized coefficients (Beta)	t	sig
Constant	75.832	-	12.292	0.000
Residential project management in domestic and international contexts (x_1)	1.597	0.215	0.475	7.420
Overall living environment (x_2)	1.840	0.214	0.562	8.590
Fair payment (x_3)	1.344	0.236	0.383	5.706
Growth opportunities (x_4)	1.212	0.237	0.352	5.123
Capability development (x_5)	0.857	0.206	0.265	4.158

Interpretation of the Results based on Table 26:

All the variables (Residential Project Management in Domestic and International Contexts (x_1), Overall Living Environment (x_2), Fair Payment (x_3), Growth Opportunities (x_4), and Capability Development (x_5)) have significant impacts on project management, as indicated by the sig values below 0.05, meaning their B coefficients can be included in the structural equation.

The regression equation for predicting the residential project management process (Y) with respect to BIM is formulated as Eq. 8.

$$Y = 75.832 + 1.597x_1 + 1.840x_2 + 1.344x_3 + 1.212x_4 + 0.857x_5 \quad (8)$$

This equation shows that BIM significantly influences the project management process through domestic/international project management (x_1), overall living environment (x_2), fair payment (x_3), growth opportunities (x_4), and capability development (x_5). The coefficients (1.597, 1.840, 1.344, 1.212, and 0.857) represent the strength of influence of each variable on the overall management process.

8. Purpose and importance of regression analysis

The main objective of the regression method is to predict one or more dependent (criterion) onstructs based on one or more independent (predictor) constructs. This method evaluates the simultaneous impact of multiple predictor variables on a dependent variable. Unlike correlation analysis, which only considers pairwise relationships, regression analysis takes into account all variables collectively, allowing for a comprehensive examination of their combined effects.

9. Key applications of regression analysis

Predicting dependent variables using independent variables. Assessing the combined effect of multiple independent variables on a single dependent variable. Utilizing in Path Analysis, which helps in identifying direct and indirect relationships between variables. With the advancement of statistical methods and the emergence of Partial Least Squares (PLS) and Structural Equation Modeling (SEM), the use of traditional regression analysis has declined in some cases. However, regression analysis remains an essential tool in statistical research, particularly when the objective is to develop predictive models and assess the strength of relationships between variables in various scientific and applied fields. The linear regression model for all the variables considered is shown in Fig. 26 and Eq. 9.

Table 27. Linear regression model for all dependent variables related to building information modeling (BIM) in improving residential project management processes.

Regression Test	Unstandardized coefficients (B)	Standard error	Standardized coefficients (Beta)	t	Sig
Constant	3.847	3.000	-	1.282	0.205
X1 - Management Status	1.100	0.074	0.328	14.773	0.000
X2 - Overall Living Environment	1.038	0.073	0.317	14.286	0.000

X3 - Fair Payment	1.210	0.083	0.345	14.612	0.000
X4 - Growth Opportunities	1.032	0.068	0.300	15.122	0.000
X5 - Capability Development	1.055	0.063	0.327	16.821	0.000
X6 - Necessity and Importance	0.928	0.105	0.181	8.857	0.000
X7 - Organizational Integrity and Cohesion	0.943	0.073	0.249	12.856	0.000
X8 - Law-Abiding Behavior	1.025	0.078	0.258	13.221	0.000
X9 - Key Factors	1.239	0.118	0.194	10.465	0.000
X10 - Actions and Planning	1.118	0.092	0.267	12.098	0.000
X11 - Social Dependency	1.036	0.085	0.262	12.225	0.000
X12 - Cost Management	1.018	0.088	0.236	11.576	0.000
X13 - Maintenance Management	0.897	0.081	0.215	11.007	0.000
X14 - Safe Work Environment	0.752	0.095	0.181	7.948	0.000

$$Y=3.847+1.100x1+1.038x2+1.210x3+1.032x4+1.055x5+0.928x6+0.943x7+1.025x8+1.239x9+1.118x10+1.036x11+1.018x12+0.897x13+0.752x14 \tag{9}$$

9.1. Discussion of regression results

The dependent variables examined in this study are grounded in a multi-layered conceptual framework of BIM-enabled project management. These variables are not treated as isolated or redundant outcomes, but as complementary dimensions reflecting different levels of BIM influence. Technical and operational variables capture BIM's direct effects on project execution processes, such as coordination, cost management, scheduling accuracy, and rework reduction. In contrast, organizational and socio-environmental variables, including organizational cohesion, social dependency, law-abiding behavior, fair payment, and overall living environment, represent indirect outcomes arising from improved transparency, information integration, and collaborative decision-making enabled by BIM. The findings of this study extend existing BIM literature by demonstrating that the impact of BIM in residential project management is not limited to technical and operational improvements. In contrast to many previous studies that focus primarily on cost and schedule performance, this research highlights the multidimensional influence of BIM on managerial, organizational, and human-centered factors. The results indicate that BIM functions not only as a digital modeling tool, but also as an integrative management mechanism that enhances coordination, transparency, and organizational capability in residential construction projects. The regression analyses confirm that BIM has a significant and positive impact on residential project management across multiple dimensions. The increasing explanatory power of the models, as additional variables are introduced, indicates that BIM functions as a multidimensional management framework rather than a single technological solution. Variables such as overall living environment, fair payment, and capability development show strong coefficients, highlighting BIM's influence on social, financial, and human-capital-related outcomes in residential projects.

9.2. Main findings and practical implications of BIM adoption

The main findings of this study indicate that Building Information Modeling (BIM) plays a critical role in enhancing residential project management beyond mere technological improvement. While the descriptive statistics and regression analyses quantify BIM's effects, the underlying results reveal several strategic insights relevant to both theory and practice. First, the consistently high mean values across key factors, including planning and execution (F3), management objectives (F5), and coordination in domestic and international contexts (F6), demonstrate that BIM is not limited to design-stage benefits. Instead, it functions as an integrative management platform that improves decision-making accuracy throughout the project lifecycle. This finding highlights BIM's capacity to reduce fragmentation in traditional residential project management, where isolated information sources often lead to delays and inefficiencies. Second, the results related to cost management (F7) and delay mitigation confirm that BIM adoption contributes to more effective resource allocation and schedule control. Although cost-related indicators show moderate mean values compared to planning and coordination factors, this suggests that BIM's financial benefits are primarily realized indirectly through reduced rework, improved clash detection, and enhanced coordination among stakeholders rather than immediate cost reduction alone. Third, the findings associated with fair payment, safe working environments, and organizational integration (F8 and subsequent factors) indicate that BIM adoption also has important socio-organizational implications. By increasing transparency in information flow and task responsibilities, BIM supports fairer payment structures, safer work environments, and stronger organizational cohesion. These outcomes extend the contribution of BIM beyond technical efficiency, positioning it as a tool that enhances the overall quality of project governance in residential developments. Finally, the regression analysis confirms a statistically significant and positive relationship between BIM implementation and overall residential project management performance. This relationship suggests that BIM can serve as a predictive and strategic decision-support tool for project managers, particularly in complex high-rise residential projects such as the Panorama Twin Towers. Collectively, these findings demonstrate that BIM adoption leads to multidimensional improvements- technical, managerial, and organizational—thereby validating its strategic importance for modern residential project management. The main findings of this study reveal that the impact of Building Information Modeling (BIM) on residential project management extends beyond numerical improvements in cost and time indicators and encompasses broader managerial and organizational dimensions. While the statistical analyses quantify these effects, the results collectively indicate BIM's role as an integrative management framework in residential projects. Based on the descriptive statistics (Tables 7–11), BIM demonstrates its strongest influence on planning and execution processes, management actions, and key project objectives. High mean values observed in factors related to actions and planning (F3) and management objectives (F5) confirm that BIM significantly enhances decision-making accuracy, coordination of activities, and alignment of project goals. This finding suggests that BIM is most effective when applied as a proactive planning and control tool rather than being limited to design visualization. The findings related to coordination in domestic and international project management contexts (F6) further emphasize BIM's capability to reduce fragmentation among stakeholders. The relatively consistent mean values across statements H1–H3 indicate that BIM improves information transparency and communication flow, which are critical challenges in high-rise residential projects. This reinforces the argument that BIM functions as a shared information environment that supports integrated project delivery. In terms of cost management (F7), the results show moderate mean values compared to planning-related factors. This suggests that BIM's financial benefits are primarily realized indirectly through reduced rework, improved coordination, and better planning accuracy rather than immediate cost reductions alone. Consequently, cost optimization should be interpreted as an outcome of improved managerial processes enabled by BIM. Importantly, the findings associated with fair payment, safe working environment, organizational integration, and capability development (F8 and subsequent factors) highlight BIM's socio-managerial implications. As reflected in Tables 14 and 15, BIM contributes to increased transparency, clearer role definitions, and improved information accessibility, which in turn support fairer payment mechanisms, safer work environments, and stronger organizational cohesion. These results align with the conceptual BIM evaluation framework presented in the study, demonstrating that BIM adoption positively affects both technical performance and the quality of organizational and working conditions in residential projects. Overall, the regression analysis confirms a significant and positive relationship between BIM implementation and residential project management performance. The main findings indicate that BIM adoption leads to multidimensional improvements—technical, managerial, and organizational, thereby validating its strategic importance for complex residential developments such as the Panorama Twin Towers.

9.3. Generalizability and case study limitations

This research is based on a single high-rise residential project, which inherently limits the statistical generalizability of the findings. The Panorama Twin Towers project is located in an urban context and is characterized by a relatively large scale, complex coordination requirements, and a structured management system. These project-specific characteristics may influence the observed impact of BIM on project management outcomes. However, the objective of this study is not statistical generalization, but analytical generalization. The identified relationships between BIM implementation and improvements in cost control, scheduling accuracy, coordination, and organizational integration are likely to be transferable to residential projects with similar characteristics, particularly in developing-country contexts where traditional management practices and digital transformation challenges are comparable. Factors such as project location, organizational structure, level of BIM maturity, and stakeholder experience can affect the extent to which BIM delivers performance improvements. For instance, large-scale residential developments with multiple stakeholders and complex interfaces are more likely to benefit from BIM-based coordination and information integration than smaller projects. Therefore, while the quantitative results are specific to the studied case, the underlying mechanisms through which BIM enhances project management remain relevant for a broader range of residential projects.

10. Limitation

The study relies on self-reported questionnaire data, which may be subject to perceptual and response bias. However, this approach is commonly used in construction management research due to the limited accessibility of objective performance records. To mitigate this limitation, the questionnaire was distributed among experienced professionals, including project managers, site engineers, and technical staff directly involved in the execution of the Panorama Twin Towers project. Future studies may enhance robustness by integrating objective performance metrics or adopting mixed-method approaches combining quantitative and qualitative data.

11. Conclusion

The findings of this research indicate that Building Information Modeling (BIM), as an innovative technology in the construction industry, has a significant impact on improving the management of residential projects. Using the Analytic Network Process (ANP), the key factors influencing the successful implementation of BIM were identified and weighted. The results suggest that BIM contributes to reducing execution costs, optimizing project scheduling, enhancing construction quality, improving coordination among project stakeholders, and minimizing execution conflicts. Additionally, this technology increases information transparency, enhances workforce productivity, and improves decision-making processes in construction projects. Statistical analyses and ANP computations revealed that the most critical factors for successful BIM implementation include: Optimization of execution costs; improved coordination and communication among stakeholders; reduction of errors and rework; enhanced accuracy in design and execution; improved project planning and control processes. Furthermore, case study analyses demonstrated that construction projects utilizing BIM have superior performance in resource management, waste reduction, and final quality compared to traditional projects. Recommendations: Based on these findings, it is recommended that BIM be adopted as a standard approach in residential projects, with necessary measures taken to promote awareness, provide training, and develop both software and hardware infrastructure. The following practical recommendations can help accelerate BIM adoption:

- Developing specialized training programs for project managers and engineers

- Establishing supportive regulations and policies to facilitate BIM integration
- Integrating BIM with other project management systems to enhance efficiency
- Future research directions
- Future studies can focus on:
- Operational challenges of BIM implementation
- Acceptance and adoption rates of BIM across various projects
- Its impact on overall construction industry productivity
- Comparisons between BIM and other project management methodologies
- Additionally, research on BIM applications in infrastructure projects, public buildings, and commercial constructions could further expand its practical use cases.
- Final thoughts

These conclusions are strongly supported by the descriptive and regression analyses presented in this study, which demonstrate BIM's multidimensional impact on residential project management performance. This study emphasizes that BIM should not be regarded merely as a technological tool but as a transformative shift in the construction industry. The adoption of BIM in residential projects can lead to:

- Optimized resource management
- Cost reduction
- Increased productivity
- Overall project performance enhancement
- Ultimately, BIM plays a crucial role in modernizing and advancing the construction industry, paving the way for a more efficient, cost-effective, and sustainable future in project management.

Statements & Declarations

Author contributions

Masoud Ahmadvand: Investigation, Formal analysis, Data curation, Software, Writing - Original Draft.

Hossein Eghbali: Project administration, Resources, Writing - Review & Editing.

Funding

The authors received no financial support for the research, authorship, and/or publication of this article.

Data availability

The data presented in this study will be available on request from the corresponding author.

Declarations

The authors declare no conflict of interest.

Appendix A – Raw questionnaire format

Please indicate the extent to which you believe Building Information Modeling (BIM) contributes to each of the following aspects of residential project management.

Scale:

1 = Very Low 2 = Low 3 = Moderate 4 = High 5 = Very High

F1. BIM in Traditional Project Management

- A1. BIM reduces errors compared to traditional project management methods.
- A2. BIM improves coordination among project stakeholders compared to traditional approaches.

F2. Necessity and Importance of BIM

- B1. BIM is essential for improving residential project management efficiency.

- B2. BIM plays a key role in modern residential construction projects.

F3. Actions and Planning

- C1. BIM improves planning accuracy in residential projects.
- C2. BIM enhances scheduling and sequencing of construction activities.
- C3. BIM supports better decision-making during project execution.

F4. Key Factors

- D1. BIM improves cost control in residential project management.
- D2. BIM reduces rework and construction conflicts.

F5. Key Objectives

- E1. BIM contributes to achieving project objectives within the planned timeframe.
- E2. BIM improves quality management in residential projects.

F6. Domestic and International Contexts

- H1. BIM facilitates alignment with international project management standards.
- H2. BIM improves coordination in complex residential projects.
- H3. BIM supports benchmarking against global best practices.

F7. Project Management Costs

- K1. BIM reduces overall residential construction costs.
- K2. BIM improves financial control during project execution.

F8. Fair Payment

- L1. BIM improves transparency in payment processes.
- L2. BIM supports timely payments to contractors and suppliers.
- L3. BIM reduces disputes related to financial claims.

F9. Safe Work Environment

- Q1. BIM enhances safety planning in construction sites.
- Q2. BIM reduces workplace accidents.
- Q3. BIM improves hazard identification and risk management.

F10. Growth Opportunities

- W1. BIM enhances professional skill development.
- W2. BIM creates new career opportunities in project management.
- W3. BIM supports organizational learning.

F11. Law-Abiding Behavior

- R1. BIM improves compliance with construction regulations.
- R2. BIM supports adherence to legal and contractual requirements.
- R3. BIM reduces violations during project execution.

F12. Social Dependency

- Y1. BIM enhances collaboration among project stakeholders.
- Y2. BIM strengthens trust and interdependence within project teams.

F13. Overall Living Environment

- U1. BIM improves environmental quality in residential projects.
- U2. BIM enhances sustainability performance of residential buildings.
- U3. BIM contributes to better living conditions for occupants.

F14. Organizational Integrity and Cohesion

- O1. BIM improves organizational coordination.
- O2. BIM enhances communication across project teams.

F15. Capability Development

- M1. BIM improves technical capabilities of project teams.
- M2. BIM enhances problem-solving skills.
- M3. BIM supports innovation in residential project management.
- M4. BIM strengthens long-term organizational competencies.

References

[1] Bakhtiari, A., Naghash Toosi, H., Sebt, M. H. A practical implementation method for risk management process and its application in construction project management – Case study: 1000-unit residential complex. In: The First National Conference on Engineering and Management of Infrastructures; 2009 Oct 23–24; Tehran, Iran. p. 10–19.

[2] Gharaibeh, L., Matarneh, S., Lantz, B., Eriksson, K. Quantifying the influence of BIM adoption: An in-depth methodology and practical case studies in construction. Results in Engineering, 2024; 23: 102555. doi:10.1016/j.rineng.2024.102555.

[3] Succar, B. Building information modelling framework: A research and delivery foundation for industry stakeholders. Automation in Construction, 2009; 18: 357–375. doi:10.1016/j.autcon.2008.10.003.

[4] Wang, T., Chen, H.-M. Integration of building information modeling and project management in construction project life cycle. Automation in Construction, 2023; 150: 104832. doi:10.1016/j.autcon.2023.104832.

[5] Parsamehr, M., Perera, U. S., Dodanwala, T. C., Perera, P., Ruparathna, R. A review of construction management challenges and BIM-based solutions: perspectives from the schedule, cost, quality, and safety management. Asian Journal of Civil Engineering, 2023; 24: 353–389. doi:10.1007/s42107-022-00501-4.

[6] Das, K., Khursheed, S., Paul, V. K. The impact of BIM on project time and cost: insights from case studies. Discover Materials, 2025; 5: 25. doi:10.1007/s43939-025-00200-2.

[7] Stabryła, R., Grudzińska, M. Smartphone-Based Virtual Reality in Residential Architecture: Enhancing Spatial Understanding Through Immersive BIM+ VR Visualization. Sustainability, 2025; 17: 9959. doi:10.3390/su17229959.

[8] Jang, Y., Park, J., Kim, Y., Yu, K.-H. Energy Savings, Carbon-Equivalent Abatement Cost, and Payback of Residential Window Retrofits: Evidence from a Heating-Dominated Mid-Latitude City—Gyeonggi Province, South Korea. Buildings, 2026; 16: 71. doi:10.3390/buildings16010071.

[9] Kaur, R., Mwambegele, B. J., Abraham, A. G., Basheer, S. A., Garia, S. A comprehensive review on building information modelling (BIM), its implementations and applications. Discover Civil Engineering, 2025; 2: 177. doi:10.1007/s44290-025-00342-5.

[10] Torres, K., Sánchez, O., Castañeda, K., Noguera, M., Carrasco-Beltrán, D., Vidal-Méndez, S., Lozano-Ramírez, N. E. Exploring the knowledge structure of building information modeling (BIM) adoption in construction scheduling: A bibliometric analysis from 2008 to 2024. Ain Shams Engineering Journal, 2025; 16: 103446. doi:10.1016/j.asej.2025.103446.

[11] Pérez, Y., Ávila, J., Sánchez, O. Influence of BIM and Lean on mitigating delay factors in building projects. Results in Engineering, 2024; 22: 102236. doi:10.1016/j.rineng.2024.102236.

[12] Ligarda-Samanez, C. A., Huamán-Carrión, M. L., Cabel-Moscoso, D. J., Marlene Muñoz Sáenz, D., Antonio Martinez Hernandez, J., Garcia-Espinoza, A. J., Fermín Calderón Huamaní, D., Carrasco-Badajoz, C., Pino Cordero, D., Sucari-León, R., Aroquipa-Durán, Y. Technological Innovations in Sustainable Civil Engineering: Advanced Materials, Resilient Design, and Digital Tools. Sustainability, 2025; 17: 8741. doi:10.3390/su17198741.

[13] Erdene, K., Kim, B.-G., Lee, S.-H. ADAPTE Process-Based Strategic Framework Development for National BIM Adoption: The Case for Sustainable Advancement in Mongolia. Sustainability, 2026; 18: 71. doi:10.3390/su18010071.

[14] Jing, W., Alias, A. H. Key Factors for Building Information Modelling Implementation in the Context of Environmental, Social, and Governance and Sustainable Development Goals Integration: A Systematic Literature Review. Sustainability, 2024; 16: 9504. doi:10.3390/su16219504.

[15] Attia, A. R. The impact of integrating artificial intelligence and Building information modeling (BIM) systems on the development of construction methodologies. Journal of Umm Al-Qura University for Engineering and Architecture, 2025; 16: 1537–1554. doi:10.1007/s43995-025-00193-2.

[16] Si, S., Yao, Y., Wu, J. Artificial Intelligence in Urban Planning: A Bibliometric Analysis and Hotspot Prediction. Land, 2025; 14: 2100. doi:10.3390/land14112100.

[17] Ghorbanalipour, R., Ahmadvand, A., Ahmadvand, M., Eghbali, H. Designing human health risk management model for dam construction projects. Civil Engineering Journal, 2018; 4: 2173–2185. doi:10.28991/cej-03091148.

[18] Raza, M. S., Tayeh, B. A., Abu Aisheh, Y. I., Maglad, A. M. Potential features of building information modeling (BIM) for application of project management knowledge areas in the construction industry. Heliyon, 2023; 9: doi:10.1016/j.heliyon.2023.e19697.

[19] Omrany, H., Ghaffarianhoseini, A., Chang, R., Ghaffarianhoseini, A., Pour Rahimian, F. Applications of Building information modelling in the early design stage of high-rise buildings. Automation in Construction, 2023; 152: 104934. doi:10.1016/j.autcon.2023.104934.

[20] Okimi, T. O. Human centric digital twins for sustainable supply chain in construction. Smart Construction and Sustainable Cities, 2025; 3: 31. doi:10.1007/s44268-025-00078-2.

[21] Luan, B., Feng, X. Artificial intelligence in Smart Buildings: a bibliometrics-based visualization analysis. Journal of Asian Architecture and Building Engineering, 2025; 1–25. doi:10.1080/13467581.2025.2552448.

[22] Sacoto-Cabrera, E. J., Perez-Torres, A., Tello-Oquendo, L., Cerrada, M. IoT, AI, and Digital Twins in Smart Cities: A Systematic Review for a Thematic Mapping and Research Agenda. Smart Cities, 2025; 8: 175. doi:10.3390/smartcities8050175.

[23] Chen, Y., Baddeley, M. Collaborative Building Information Modelling (BIM): Insights from Behavioural Economics and Incentive Theory. London (UK): Royal Institution of Chartered Surveyors (RICS); 2015. Report No.: 20200.

[24] Smith, P. BIM Implementation – Global Strategies. Procedia Engineering, 2014; 85: 482–492. doi:10.1016/j.proeng.2014.10.575.

Civil Engineering and Applied Solutions

Research Article

journal homepage: ceas.journals.umz.ac.ir

CEAS Civil Engineering and Applied Solutions

Flood Hazard Assessment and Mitigation in the Tigris River: An HEC-RAS Approach (Al-Kut Dam to Al-Musandawq)

Mahmoud Mohammad Rezapour Tabari [a*], Milad Rahshabdiz [a], Mustafa Khudhair Tuama [a]

[a] *Department of Civil Engineering, Faculty of Engineering and Technology, University of Mazandaran, Mazandaran, Iran*

ARTICLE INFO

Article history:

Received 13 March 2026

Revised 31 March 2026

Accepted 01 June 2026

Available online 01 January 2027

Keywords:

Flood hazard management

HEC-RAS

Tigris river

Floods control

Flood wave routing

Hydraulic modeling

ABSTRACT

This study addresses the critical issue of flood hazard management in the Maysan region of Iraq, a city highly susceptible to recurrent and devastating floods, as tragically demonstrated by the 2019 flood event. Focusing on a 169 km reach of the Tigris River downstream of the Al-Kut barrage, including the Al-Musandawq channel, this research investigates the impact of riverine obstacles on flood dynamics. The primary objective is to assess and mitigate flood hazards through advanced hydrological modeling. The study employed the HEC-RAS model, utilizing 169 cross-sections surveyed in 2017 and incorporating digital elevation model (DEM) data. Model calibration, using hydrological and topographical inputs, yielded a Manning's roughness coefficient of 0.031 for the Tigris River and 0.028 for the Al-Musandawi channel. High accuracy was confirmed by Nash-Sutcliffe Efficiency (NSE) indices of 0.979 and 0.986, respectively, alongside other error metrics (RMSE, MAE). Model simulations revealed that flood waves were primarily delayed, reaching Maysan city with minimal dispersion, leading to inundation. To mitigate these risks, two management approaches were considered: (1) removal of islands and sidebars within the river reach, and (2) construction of a weir. Due to the high cost and limited effectiveness of removing natural obstacles, the focus shifted to structural solutions. Scenarios were developed to design a weir with an optimal crest elevation. The goal was to prevent downstream flow to Maysan city from exceeding 700 m³s during flood seasons, while ensuring a minimum flow of 250 m³s during dry seasons. Simulations of peak flow rates (4000, 2500, 1050, 533, and 250 m³s) established an optimal weir crest elevation of 9.4 meters. This study provides crucial insights into flood mitigation strategies for the Tigris River, offering a data-driven approach to protect vulnerable downstream areas.

How to cite this article: Rezapour Tabari, M-M., Rahshabdiz, M., Khudhair Tuama, M. Flood Hazard Assessment and Mitigation in the Tigris River: An HEC-RAS Approach (Al-Kut dam to Al-Musandawq). Civil Engineering and Applied Solutions. 2027; 3(1): 98–116. doi:10.22080/ceas.2026.31452.1085.

1. Introduction

Floods affect more people than any other natural disaster, killing more people each year, and climate change will exacerbate the problem of floods. Floods have an impact on the environment, social, and economic affairs [1]. Recurrent and high-magnitude flooding in agricultural areas poses a serious threat to crop productivity and food security, often resulting in substantial economic losses. This reality underscores the necessity of systematic flood analysis, not only to enhance our understanding of flood behavior but also to inform the development of effective and context-specific flood mitigation strategies. Although direct, in situ flood observations provide invaluable insights, their acquisition is frequently constrained by logistical, temporal, and safety limitations, highlighting the need for complementary analytical and modeling approaches.

* Corresponding author.

E-mail addresses: mrtabari@umz.ac.ir (M. Mohammad Rezapour Tabari).

https://doi.org/10.22080/ceas.2026.31452.1085

ISSN: 3092-7749/© 2027 The Author(s). Published by University of Mazandaran.

2. Literature review

In the Middle East, the continued and widespread use of the HEC-RAS model is largely driven by the limited availability and reliability of high-resolution elevation data. Studies conducted along the Tigris River clearly illustrate this constraint. For instance, Mohammed Ali and Khairallah, despite having access to only four years of discharge records, successfully identified flood-prone streets in the city of Tikrit with notable spatial accuracy [2]. Similarly, the study by Sabeeh and Alabdraba demonstrated that minor adjustments to the Manning roughness coefficient were sufficient to achieve a close agreement between simulated water levels and observed gauge data [3]. These outcomes highlight not only the robustness of HEC-RAS under data-scarce conditions, but also its practical value in regions where field measurements and detailed topographic datasets are difficult to obtain.

At the global scale, however, a contrasting pattern emerges. By systematically analyzing three decades of Landsat imagery, Pekel and colleagues documented a net loss of approximately 90,000 square miles of permanent lakes and river surfaces worldwide, while simultaneously noting the expansion of artificial water bodies, largely driven by dam construction across Asia [4, 5]. Complementing this physical perspective, Sullivan et al. employed nighttime light data as a proxy for human settlement and revealed a marked demographic shift toward areas classified as low flood risk, where the proportion of residents increased from 8 to 11% within a 15-year period [6]. Importantly, this change reflects patterns of human relocation and land-use decisions rather than any abrupt intensification of rainfall regimes, underscoring the growing role of socio-economic dynamics in reshaping global flood exposure.

Some researchers now combine conventional hydrological models with machine learning to provide very good predictions of extreme flooding in ungauged areas [7]. In the Kerala floods of 2018, Suresh and his team monitored the dams from satellites and proved that if the dam operators had opened the gates two days earlier, half of the disaster would not have occurred [8].

Coastal municipalities face a particularly precarious trajectory. A comprehensive systematic review by Aziz et al. [9] underscores a global systemic lag: the rate of urban expansion in nearly all major coastal hubs is currently outstripping the deployment of flood-defense infrastructure. While robust decision-support frameworks are theoretically available [10, 11], their practical integration into urban governance remains alarmingly deficient. This misalignment is starkly evident in the United States; Hino et al. [12] demonstrated that in regions like North Carolina, the continued authorization of floodplain construction has caused the inherent risk profile to escalate at a pace far exceeding eustatic sea-level rise. A parallel socio-spatial inequity is documented in the Canadian context, where Chakraborty et al. [13] identified a troubling correlation between socio-economic vulnerability and proximity to high-risk riparian zones.

Within the African context, the adoption of Nature-Based Solutions (NBS) has gained significant empirical support. Research conducted by Jemberie and Melesse [14] in Addis Ababa, complemented by the modeling efforts of Long'or Lokidor et al. [15] in East Africa, demonstrates that decentralized interventions, specifically retention ponds, permeable sewerage systems, and vegetative roofing, can substantially attenuate peak runoff. However, these studies converge on a critical socio-political caveat: the hydrological efficacy of such green infrastructure is fundamentally contingent upon robust municipal oversight and the stringent enforcement of building codes by local authorities.

While satellite imagery is a popular tool for flood mapping, its utility is frequently hampered during actual flood events by persistent cloud cover, rendering the acquired data unusable [16]. Consequently, observation-based maps, though valuable for documenting specific occurrences, are insufficient for predictive purposes, such as forecasting extreme events or evaluating the efficacy of engineered flood defenses like levees. This underscores the indispensable role of numerical hydrological models. These models enable scenario analyses by allowing for the simulation of various hydrological conditions, including altered precipitation regimes, land-use changes, and dam operational strategies, to predict their respective impacts. Widely adopted tools, such as HEC-RAS developed by the U.S. Army Corps of Engineers, have become de facto industry standards due to their robust computational capabilities, user-friendly interfaces, and, critically, their open-source accessibility [17]. Researchers leverage these platforms for diverse applications: generating flood risk maps for urban planning, reconstructing past flood events to identify causal factors and system failures, and pre-emptively assessing mitigation strategies before substantial capital investment in physical infrastructure [18, 19]. The ongoing development and updates by the Corps ensure the continued relevance and accuracy of HEC-RAS, maintaining its utility for predictive flood management over extended periods.

In summary, while the technical repertoire for flood mitigation, ranging from advanced numerical modeling and satellite-based monitoring to cost-effective green infrastructure, is already well-established, the primary impediment to effective flood management is no longer a deficit in technological expertise, but rather a crisis of political agency and the prioritization of short-term economic gains over the protection of socio-economically vulnerable populations. Flood hazards pose a significant and growing threat to populations and infrastructure worldwide, exacerbated by climate change and increasing urbanization. The Tigris River basin, a vital water resource for Iraq, is particularly susceptible to severe flood events. While historical flood management efforts have been undertaken, the dynamic interplay between river discharge, channel morphology, and the capacity of escape routes, especially in densely populated areas like the region surrounding Amarah, remains inadequately understood. Previous studies in the Tigris basin have often relied on simplified one-dimensional (1D) hydraulic models, limited spatial data resolution, or did not comprehensively evaluate integrated flood mitigation strategies, hindering the accurate prediction of flood inundation extent and the effective assessment of management interventions. This study aims to bridge this knowledge gap by employing a state-of-the-art integrated 1D–2D HEC-RAS model. We focus on a critical 169-km reach of the Tigris River between the Kut and Al-Musandawq dams, a stretch characterized by increasing alluvial formations and dikes that have significantly compromised the flow gradient. Utilizing HEC-RAS for one- and two-dimensional hydraulic modeling, we assess this critical reach. Historical data underscores a dramatic hydrological shift: peak discharge at the Kut Dam has plummeted from 3,000 m³/s in 1988 to a mere 200 m³/s by 2010. Despite this reduction in baseflow, the region remains susceptible to catastrophic flooding, as evidenced by major events in 1950, 1957, and 1988, as well as more recent inundations in 2013 and 2019. Our research addresses the following: (1) developing and calibrating a high-resolution coupled 1D–2D model for this complex reach; (2) quantitatively assessing the effectiveness of two distinct flood mitigation scenarios, natural modification (island removal) and structural control (submerged weir); and (3) determining the optimal design parameters for the most promising mitigation measure. By providing a detailed, data-driven analysis, this work offers crucial insights for enhancing flood resilience and informing sustainable water management practices in the Tigris River basin.

3. Methodology

3.1. Study area

The study reach encompasses approximately 87 kilometers along the Tigris River, situated within the Wasit Governorate of central Iraq (Fig. 1). This segment extends from the immediate upstream vicinity of the Kut Dam (32°30'N, 45°50'E) to its terminus at the Al-Musandawq spillway (32°15'N, 46°15'E). Geomorphologically, the area is positioned within the heart of the historic Mesopotamian floodplain, a region defined by the convergence of the Tigris and Euphrates hydrological systems. The study area is bounded by latitudes 32.10–32.40°N and longitudes 45.40–46.30°E. The regional climate is characterized as semi-arid, experiencing extreme thermal peaks during the summer months and temperate winters. Precipitation is notably limited, with average annual rainfall ranging between 150 and 200 mm.

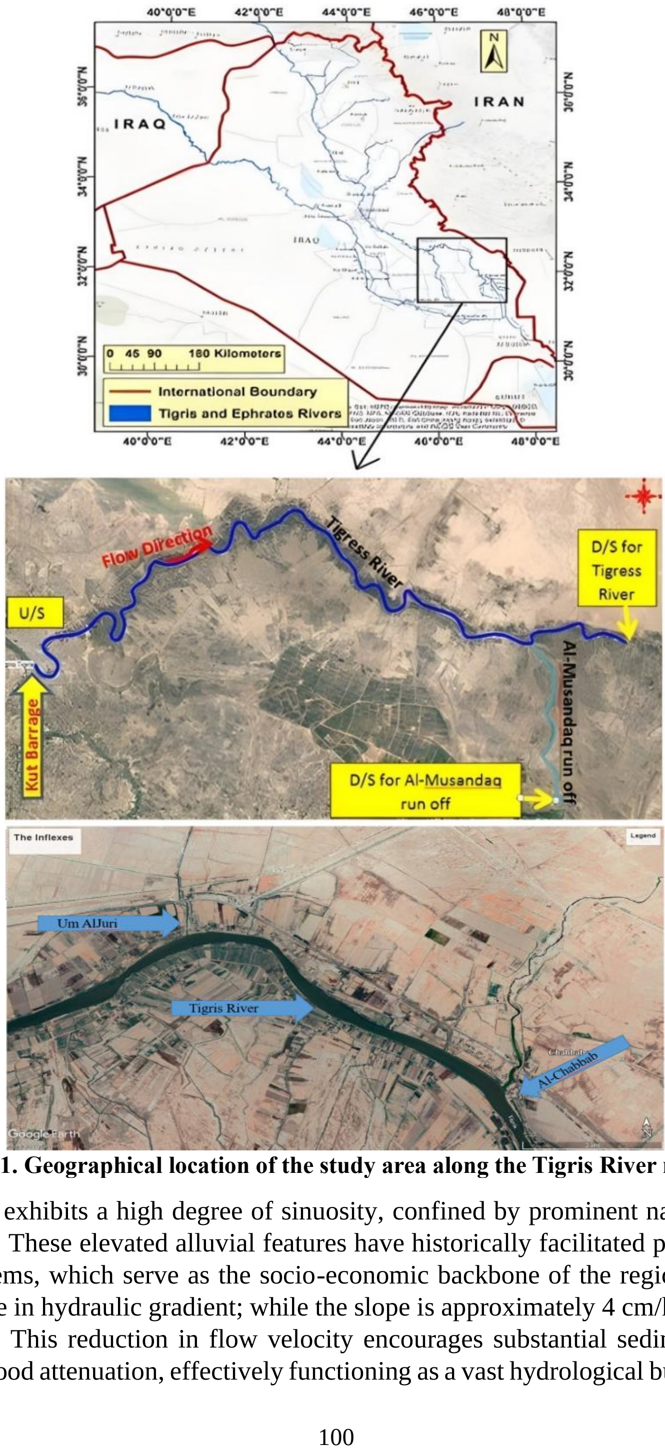

Fig. 1. Geographical location of the study area along the Tigris River reach.

In this reach, the Tigris River exhibits a high degree of sinuosity, confined by prominent natural levees that rise to 20 meters above the surrounding floodplain. These elevated alluvial features have historically facilitated productive irrigated agriculture and supported dense riparian ecosystems, which serve as the socio-economic backbone of the region. The longitudinal profile of the river shows a progressive decrease in hydraulic gradient; while the slope is approximately 4 cm/km near the Kut Dam, it attenuates significantly further downstream. This reduction in flow velocity encourages substantial sediment deposition and enhances the floodplain's natural capacity for flood attenuation, effectively functioning as a vast hydrological buffer during high-discharge events.

A central feature of the regional flood-control infrastructure is the Al-Musandawq escape channel (Fig. 2), a major regulated spillway situated on the right bank of the Tigris. Spanning approximately 400 m at its confluence with the main river, this strategic diversion was engineered to mitigate catastrophic flood risks by rerouting surplus discharge into adjacent topographic depressions. The facility's hydraulic significance was most notably demonstrated during the historic flood of 1974, when it successfully diverted a peak flow of 1,800 cubic feet per second, thereby safeguarding downstream agricultural lands and primary irrigation canals. To this day, the spillway remains under the operational jurisdiction of the Ministry of Water Resources, serving as a critical safeguard for the basin's hydraulic stability.

Fig. 2. Flood-control infrastructure in the Al-Musandawq channel.

3.2. Study approach

At the initial stage, the hydraulic model is calibrated using the 2019 flood event to reproduce the observed flood dynamics and to quantify its impacts along the selected reach of the Tigris River, extending from downstream of Kut Barrage to the outlet of the Al-Musandawq channel. To support this calibration and ensure hydraulic realism, the study begins with a systematic identification and characterization of flood-prone reaches through field visits along the river corridor, where historically inundated and high-risk areas were documented. In parallel, long-term hydrological records and flood event statistics were compiled to obtain the flood discharge time series required for modeling.

Alongside the hydrological dataset, the hydraulic geometry of the river in the selected cross-sections was extracted using available topographic information, with DEM maps playing a key role in determining the channel-bed characteristics and the overall topography of the flow path. Based on a detailed review of the river's cross-sections, the geometric dataset was refined by identifying locations with noticeable changes in hydraulic behavior (e.g., significant variations in flow velocity and cross-sectional form). Accordingly, additional cross-sections were introduced in reaches exhibiting hydraulic complexity to improve the representativeness of the model geometry.

Using the compiled and refined hydrological and topographic inputs, the HEC-RAS model was developed under both steady and unsteady flow conditions. Key model parameters, particularly Manning's roughness coefficient, were calibrated using the 2019 flood discharge time series. Model calibration aimed to reproduce observed flood behavior with acceptable accuracy, and performance was evaluated using standard hydraulic modeling metrics and comparisons between simulated water levels and observed flood characteristics along the study reach.

Following calibration, two alternative flood management strategies were systematically examined to identify the most efficient approach for mitigating flood risk in the study area. The first strategy investigates the hydraulic implications of removing riverine islands from the Tigris River channel. This scenario evaluates whether the flood wave can be conveyed safely at lower water levels than those currently experienced. To implement this intervention, cross-sections containing islands were modified accordingly, and the model was rerun using the 2019 flood hydrograph. The resulting water levels and flow characteristics were then compared with observed flood data to assess the effectiveness of island removal.

The second strategy considers the implementation of a hydraulic control structure in the form of a submerged weir installed upstream of the Al-Musandawq channel bifurcation. The crest elevation of the weir was optimized at 9.406 m to enable controlled diversion of surplus floodwater toward the Al-Musandawq channel. During flood conditions, the structure limits the discharge directed toward Amarah City to a maximum of 700 m^3/s, while efficiently routing excess flows away from the urban reach. Conversely, during low-flow periods when the Tigris River discharge falls below 250 m^3/s, the flow configuration preferentially directs the available discharge toward Amarah City, with negligible or no diversion to the Al-Musandawq channel. The overall methodological framework adopted in this study is summarized in the flowchart presented in Fig. 3.

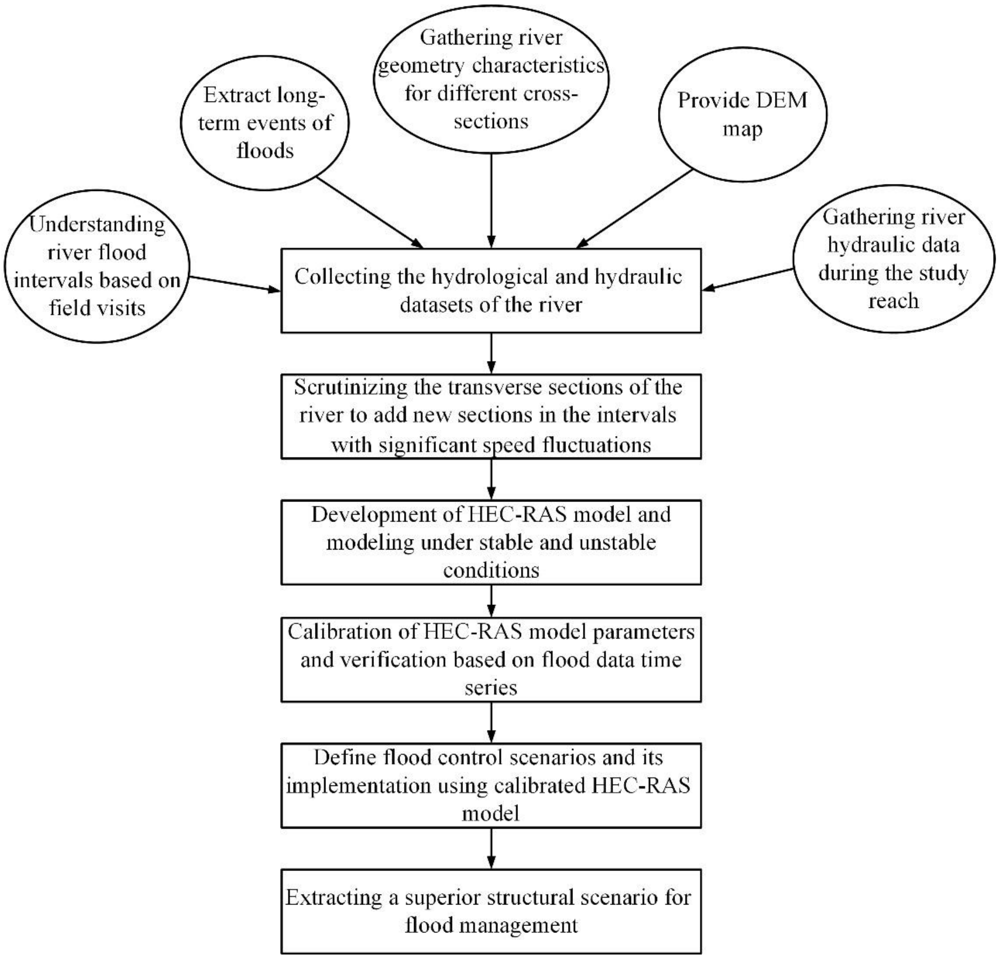

Fig. 3. Structure of the proposed approach to flood management.

3.2.1. Mathematical modeling of unsteady open-channel flow

The fundamental governing equations for one-dimensional (1D) and two-dimensional (2D) unsteady flow are first introduced. Alongside the full formulations, simplified forms of these equations are presented, accompanied by a concise explanation of their mathematical solution procedures. To enhance understanding, the discussion is supplemented with illustrative examples that demonstrate practical applications of the governing principles. In turbulent open-channel flows, both spatial and temporal variations play a significant role in defining the flow behavior. Under such conditions, the mass conservation and momentum provide the most reliable framework for describing flow dynamics. The Shallow Water Equations, commonly referred to as the Saint-Venant equations, offer an accurate representation of flow processes when these conservation laws are satisfied.

The solutions to these governing equations are presented for both one-dimensional and two-dimensional cases. The following section focuses on unsteady one-dimensional flow, beginning with the formulation of the one-dimensional continuity equation.

3.2.2. The two-dimensional unsteady flow

The one-dimensional continuity equation (Eq. 1):

$$\frac{\delta A}{\delta T}+\frac{\delta Q}{\delta x}=q \quad (1)$$

where, A indicates the cross-section (m^2), Q represents the flow in cross-section (m^3/s), x shows the distance along the channel (m) and q is the lateral inflow (m^2/s).

The one-dimensional momentum equation (Eq. 2):

$$\frac{\delta Q}{\delta t}+\frac{\delta VQ}{\delta X}+gA\left(\frac{\delta z}{\delta x}+S_o+S_f\right)=0 \quad (2)$$

where, V denotes the flow velocity ($\mathrm{m/s}$), g represents the gravitational acceleration ($\mathrm{m/s^2}$), z is the water depth (m), S_0 is the channel bed slope, S_f denotes the friction slope, and t represents time (s).

3.2.3. The two-dimensional unsteady flow

The two-dimensional continuity equation (Eq. 3):

$$\frac{\partial H}{\partial t}+\frac{\partial (hu)}{\partial x}+\frac{\partial (hv)}{\partial y}+q=0 \tag{3}$$

where, g is the gravitational acceleration, u denotes the flow velocity in the x-direction, and R is the hydraulic radius. In addition, H represents the water surface elevation, h is the water depth, u and v are the depth-averaged velocity components in the x- and y-directions, respectively, and q is the source term accounting for external inflows, such as precipitation and lateral contributions from surrounding areas [20].

The two-dimensional momentum equation (Eqs. 4 and 5):

$$\frac{\partial u}{\partial t}+u\frac{\partial u}{\partial x}+v\frac{\partial u}{\partial y}=-g\frac{\partial H}{\partial x}+v_t\left(\frac{\partial^2 u}{\partial_y^2}\right)-c_f u+f_v \tag{4}$$

$$\frac{\partial v}{\partial t}+u\frac{\partial v}{\partial x}+v\frac{\partial v}{\partial y}=-g\frac{\partial H}{\partial y}+v_t\left(\frac{\partial^2 v}{\partial x^2}+\frac{\partial^2 v}{\partial y^2}\right)-c_f v+f_u \tag{5}$$

where, v_t is the eddy viscosity coefficient, c_f represents the bed friction coefficient, f is the Coriolis parameter [21]. The first term corresponds to convective acceleration, while the subsequent terms account for the forces induced by gravity, turbulent diffusion, bed friction, and the Coriolis effect. By applying Manning's formulation, the friction coefficient c_f in the x-direction can be expressed as follows (Eq. 6):

$$c_f=\frac{n^2 g|u|}{R^{4/3}} \tag{6}$$

Where, n denotes Manning's roughness coefficient.

3.2.4. Modeling simplifications

To improve computational efficiency and minimize the risk of numerical instability, the full Shallow Water Equations are commonly simplified by neglecting selected terms in the momentum equations. Such simplifications are most frequently adopted in two-dimensional modeling frameworks, where reducing computational complexity is essential for achieving stable and practical simulations.

3.2.5. Diffusive wave approximation

When gravity and friction are assumed to be the dominant forces acting on the control volume, the momentum equation can be simplified to the diffusive wave approximation. This assumption is based on the premise that these forces exert the greatest influence on the flow dynamics under the conditions considered.

$$g\nabla H=-c_f V \tag{7}$$

where, V denotes the flow velocity vector, expressed as $V=(u,v)$ and ∇ denotes the differential operator. When bottom friction is evaluated using Manning's formulation, Eq. 7 can be rewritten as:

$$V=\frac{-(R(H))^{\frac{2}{3}}}{n} \tag{8}$$

where, $R(H)$ represents the hydraulic radius corresponding to the water surface elevation H, Substituting Eq. 8 into the continuity equation (Eq. 3) and expressing the result in vector form yields the following expression (Eqs. 9 and 10):

$$\frac{\partial H}{\partial t}+\nabla\beta\nabla H+q=0 \tag{9}$$

where,

$$\beta=\frac{-(R(H))^{\frac{2}{3}}}{n} \tag{10}$$

By applying the diffusive wave approximation to the Shallow Water Equations, the governing equations for two-dimensional flow (Eqs. 3, 4, and 5) can be simplified to the form presented in Eq. 9. This approximation reduces computational time and can improve numerical stability. It is particularly suitable for representing flow variations in moderately steep to steep channel reaches. However, it does not capture flow separation, eddies, or momentum transfer effects [22].

3.2.6. Solving techniques

The Shallow Water Equations constitute a set of partial differential equations that cannot be solved analytically. To obtain numerical solutions for the flow variables, these equations must be integrated using appropriate numerical methods. Both the water surface elevation and the flow velocity vary continuously in space and time, and at each computational time step, the model must determine the values of these variables across the entire domain. Numerical schemes typically impose constraints on the Courant number to ensure solution accuracy and stability. The Courant number can be calculated using Eq. 11:

$$C = \frac{V\Delta t}{\Delta x} \tag{11}$$

where, Δt is the computational time step, and Δx represents the spatial discretization- corresponding to cross-section spacing in one-dimensional models and cell size in two-dimensional models.

The unsteady flow component of the model incorporates a variety of advanced features, including automatic calibration, user-defined rules, hybrid one-dimensional and two-dimensional unsteady flow modeling, dam-break analysis, levee overtopping and failure, pumping station operation, navigation dam management, and pressurized pipe systems, among others. These functionalities are accessible under the "unsteady flow" module and collectively enhance the model's ability to represent complex hydraulic and hydrologic processes while preserving the real-world characteristics of the study area.

In this study, Manning's roughness coefficient (n) was assigned based on standard references, including Chow, Maidment and Mays [23] This coefficient quantifies the resistance to flow and is critical for accurately simulating channel hydraulics. The computational grid consists of cells, with flow interactions occurring across cell faces, which act as the interfaces between adjacent elements. A 100 m × 100 m square cell grid was employed, with the cells oriented at various angles to accommodate the river geometry.

The governing equations were solved using a stepwise finite-volume approach, which estimates mean flow quantities by integrating over each reference volume. This methodology allows for flexible handling of unstructured grids and complex channel geometries. Subsequently, elevation–volume relationships were computed for each cell, followed by derivation of hydraulic properties such as wetted perimeter and cross-sectional area, using procedures analogous to those applied in one-dimensional preprocessing.

River calibration was performed by adjusting Manning's roughness coefficient along the reach to match observed flow rates and water levels. HEC-RAS was used to simulate these hydraulic variables. Conceptually, calibration can be viewed as an inverse problem, in which initial and local parameters of the system are estimated by comparing model outputs to observed data. During this process, the objective function (error index) is minimized by iteratively updating parameter values within defined ranges, ensuring that the model accurately reproduces the observed flow behavior along the study reach. In this section, the mathematical formulations of the error indicators employed during the model calibration process are presented in the form of Eqs. 12-14.

- **Root Mean Square Error (RMSE)**

The Root Mean Square Error (RMSE) provides a measure of the average magnitude of errors between observed and simulated values, giving higher weight to larger deviations. It is defined as:

$$RMSE = \sqrt{\frac{\sum_{i=1}^{N}(o_i - o_f)^2}{N}} \tag{12}$$

where, N is the total number of observations, o_i is the observed value, and o_f is the simulated value.

RMSE values range from 0 to infinity, with lower values indicating better model performance and a value of zero representing a perfect match between observations and simulations.

- **Nash–Sutcliffe Efficiency (NSE)**

The Nash–Sutcliffe Efficiency (NSE) evaluates the predictive skill of the model relative to the variance of the observed data. It is expressed as:

$$NSE = 1 - \frac{\sum_{i=1}^{N}\left(o_i - o_f\right)^2}{\sum_{i=1}^{N}(o_i - \bar{o})^2} = 1 - (\frac{RMSE}{SD}) \tag{13}$$

where, $\bar{O}$ is the mean of observed values, SD is the standard deviation of the observations. NSE values range from $-\infty$ to 1. A value of 1 indicates a perfect agreement between observed and simulated values, while values below zero suggest that the model performs worse than using the mean of observations as a predictor. An NSE value above 0.75 is considered acceptable, and above 0.90 is deemed excellent for hydrodynamic models.

- **Mean Absolute Error (MAE)**

The Mean Absolute Error (MAE) provides the average magnitude of errors in absolute terms, without considering their direction. It is calculated as:

$$MAE = \frac{1}{n}\sum_{i}^{n} =_1 |o_i - \bar{o}| \tag{14}$$

MAE is a non-negative metric with no theoretical upper limit. A value of zero corresponds to a perfect simulation, with increasing values indicating larger deviations between observed and predicted data.

3.3. Hydraulic modeling using HEC-RAS

3.3.1. Input data

The geometric framework of the investigated reach was constructed by integrating high-resolution spatial data into the HEC-RAS environment. This setup involved the parameterization of a Digital Elevation Model (DEM), the definition of representative cross-sections along the 87-km segment, and the establishment of hydraulic boundary conditions. The core components of the model geometry are synthesized below:

a) Digital elevation model (DEM)

The topographic foundation of the hydraulic model was established using a Digital Elevation Model (DEM), which provides a high-fidelity three-dimensional representation of the terrain. For the Tigris River basin, where topographical accuracy is paramount for flood routing, SRTM (Shuttle Radar Topography Mission) data was utilized. Over the last decade, SRTM has become a benchmark in global hydrological studies due to its consistent homogeneity and proven accuracy relative to other open-source datasets. In this study, the SRTM-derived DEM was instrumental in delineating the floodplain's geomorphological features and extracting the precise elevation profiles required for the 1D and 2D hydraulic simulations.

b) Cross-section

Bathymetric data for the Tigris River were obtained from the Department of Irrigation in Kut. This dataset, comprising detailed cross-sectional profiles from the downstream of the Kut Dam to the Al-Musandawq escape channel, was provided in tabular format. These profiles were subsequently integrated into the HEC-RAS modeling environment, where the river's geometry was meticulously reconstructed within the geometric editor to ensure a high-fidelity representation of the channel morphology.

c) Interpolation of the Cross-section

To enhance the numerical stability of the hydraulic simulation and ensure a refined representation of the river's profile, additional cross-sections were generated via interpolation between the field-surveyed stations (Table 1). This procedure is essential in reaches where significant fluctuations in velocity head occur, as abrupt changes can impede the accurate calculation of the energy gradient. By establishing uniform computational intervals through interpolation, the model more effectively captures the transition of flow energy and reduces potential convergence errors.

Table 1. Comparative analysis of cross-sectional profiles between the geometric data editor and ras mapper for a 21-km segment of the Al-Musandawq reach (starting at sta. 0+000).

Cross-section station (From Downstream to Upstream)	Elevation in Geometry Edit	Elevation in the RasMapper	Difference
21+000	4.7	7	-2.3
20+000	10.53	8	2.53
19+000	10.48	8	2.48
18+000	10.24	6.534	3.706
17+000	10.3	7	3.3
16+000	9.86	7	2.86
15+000	9.82	7	2.82
14+000	9.58	8	1.58
13+000	9.54	7.832	1.708
12+000	7.3	8	-0.7
11+000	8	7.83	0.17
10+000	8	8	0
9+000	9	7.241	1.759
8+000	9	8	1
7+000	9	8.438	1.438
6+000	9.62	8	1.62
5+000	10	7.98	2.02
4+000	9.98	7.563	2.417
3+000	9.66	7	2.66
2+000	9.5	8	1.5
1+000	10	8.85	1.15
0+000	10	9	1

d) Boundary conditions(unsteady flow data)

Boundary conditions are critical parameters for linking one- and two-dimensional flow areas within the HEC-RAS environment.

In this study, the hydraulic regime was driven by three specific flow hydrographs, derived from hydrological data provided by the Al-Kut Water Resources Division for the high-flow period of April 2019. The primary upstream boundary condition was defined by the main Tigris flow hydrograph. To ensure a comprehensive water balance within the reach, two additional lateral inflow hydrographs were integrated to account for the contributions of the Um Aljury and Al-Chabab tributaries. This configuration allows the model to accurately simulate the interaction between the main channel and its secondary inflows during peak discharge events.

e) Development of the Integrated 1D-2D Hydrodynamic Model

Within the HEC-RAS modeling framework, the unsteady flow module provides a flexible environment for representing flow dynamics across complex river systems. This component allows one-dimensional, two-dimensional, and coupled one–two-dimensional simulations within interconnected networks of open channels, floodplains, and alluvial fans. It is designed to accommodate a wide range of flow conditions, enabling the analysis of subcritical, supercritical, and transitional regimes, including hydraulic jumps and drawdown processes, as they evolve over time. A key strength of this module lies in its seamless integration of hydraulic computations previously developed for steady-flow conditions. Calculations associated with cross-sections, bridges, culverts, and other hydraulic structures are directly embedded in the unsteady-flow framework, ensuring consistency in the representation of channel geometry and structural controls. In addition, the module offers advanced functionalities such as dam-break and levee-breach simulations, overtopping analysis, pumping station operations, navigation dam controls, and pressurized pipe systems. The inclusion of automated calibration options, user-defined operational rules, and the ability to combine one- and two-dimensional domains further enhances its applicability for realistic and site-specific flood modeling studies.

f) One-Dimensional Hydraulic Modeling Using HEC-RAS

Hydraulic modeling in the HEC-RAS environment begins with a structured data preparation stage, in which real-world terrain and river features are translated into a computational framework through GIS-based processing. During this stage, spatial registration and georeferencing are applied to ensure that all geometric elements accurately reflect their physical location and scale. This workflow facilitates efficient data organization and calibration, while maintaining the essential spatial characteristics of the study area. In the present study, all spatial analyses and data integration tasks were carried out using the RAS Mapper module in HEC-RAS version 5.0.7.

Following data preparation, the model was populated with the required geometric and hydraulic inputs. These included a digital elevation model (DEM) representing watershed topography, detailed river cross-section geometries, and Manning’s roughness coefficients assigned separately to the main channel and adjacent floodplains. Cross-sections derived from the DEM, supplemented by available field survey data, formed the core geometric basis of the hydraulic model. Within the Geometry Editor, the river system was defined by sequentially connecting 126 cross-sections from upstream to downstream, thereby establishing a continuous representation of flow conveyance along the modeled reach.

g) Calibration of the HEC-RAS model

In river hydraulic simulations, Manning’s roughness coefficient is widely recognized as the most sensitive parameter influencing flow resistance and water-level predictions. Model calibration is therefore performed by systematically comparing simulated outputs with field observations collected at corresponding locations and iteratively adjusting the roughness coefficient (n) to achieve the closest possible agreement. In this study, calibration was undertaken along the entire modeled reach by simulating observed discharges and flow depths using the HEC-RAS framework and refining the overall resistance represented by Manning’s n.

From a methodological perspective, calibration constitutes an inverse problem, as it seeks to infer representative initial and spatially distributed parameters of the river system based on a limited set of observed hydraulic variables. Traditionally, hydrodynamic models have relied on manual calibration, in which parameter values are progressively modified to reduce discrepancies between modeled and measured data. This process effectively minimizes an objective function by adjusting parameter sets within physically reasonable ranges, thereby ensuring that the calibrated model remains consistent with the hydraulic behavior of the river under the prevailing flow conditions, as described below.

h) Output of HEC-RAS

The graphical and reporting modules provide a comprehensive set of visualization tools for interpreting model outputs. These tools generate x–y plots representing the river schematic, cross-sectional geometry, longitudinal water-surface profiles, rating curves, hydrographs, and a range of additional hydraulic variables. Such visual outputs play a key role in diagnosing model behavior, evaluating simulation performance, and effectively communicating hydraulic responses under different flow conditions.

3.3.2. Flood control methods

Flood control strategies are implemented to reduce or eliminate the damaging consequences of floodwaters on human settlements and infrastructure. Such strategies range from long-established practices, such as the use of vegetation to enhance water retention, hillside terracing to slow surface runoff, and the construction of diversion channels to redirect excess flows, to engineered interventions including embankments, artificial lakes, dams, reservoirs, and retention basins designed to temporarily store floodwater during extreme events. In the context of the present study, expert consultations with engineers responsible for the Kut Dam and the Al-Architecture Dam, combined with field observations and measurements obtained during the 2019 flood event, were used to estimate the maximum discharge that can be safely conveyed through the modeled river reach. This threshold was determined to be approximately 700 m^3/s. Building on this constraint, the objective of this research is to identify an optimal flood management approach capable of protecting downstream urban areas along the Tigris River, particularly in the vicinity of the Al-Musandawq channel branching, from future flood hazards.

4. Results and discussion

4.1. HEC-RAS Model calibration and verification

Along a river reach, Manning's roughness coefficient can vary downstream due to changes in channel and floodplain characteristics. Factors influencing n include bed and bank surface texture, vegetation, water stage, discharge, and channel irregularities. In general, n may be relatively high during high-stage flows in rocky or vegetated sections, whereas in most cases, the coefficient tends to decrease as discharge increases. In this study, calibration of the global Manning's n values formed a key part of the model validation strategy. The calibration process was carried out using observed data from April 2019. Based on iterative model runs, Manning's n values were systematically adjusted within physically plausible ranges: 0.021 to 0.037 for the Tigris river and 0.020 to 0.028 for the Al-Musandawq channel. These ranges are based on established literature values for similar riverine and engineered channel conditions (e.g., Chow [24]) and preliminary field observations. These calibrated values are summarized in Table 2. The verification of the unsteady flow model was performed by comparing simulated discharges against measured values. This comparison, illustrated in Fig. 4, demonstrates the model's ability to reproduce the observed variability in flow along the study reach and provides confidence in its predictive capability for flood routing and hydraulic analysis.

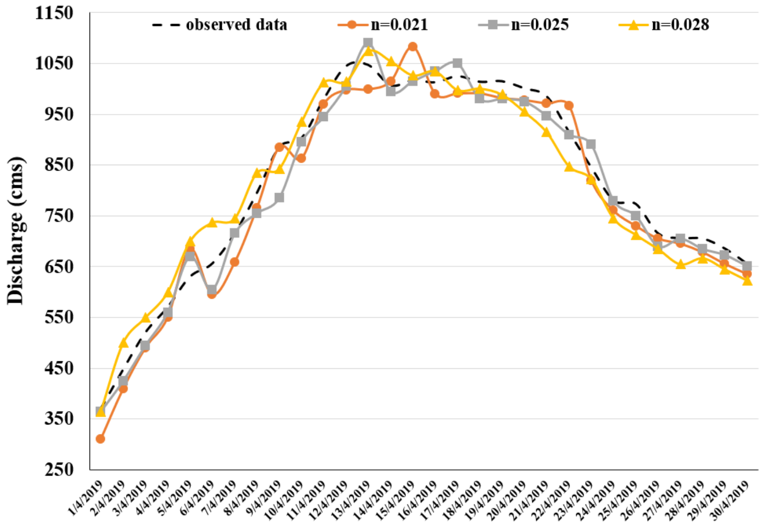

Fig. 4. Comparison of simulated and observed discharge hydrographs for the Tigris River.

4.2. Simulation of stages and discharges for different Manning's values

The HEC-RAS model simulations underscore a critical point: the model's output, specifically river flow and water levels, demonstrates significant sensitivity to adjustments in Manning's roughness coefficient. This parameter, which accounts for the frictional resistance of the channel surface, was varied within a plausible range. For the Tigris River, the 'n' values explored were between 0.021 and 0.037, while for the Al-Musandawq channel, the range was from 0.020 to 0.030. These ranges were selected based on typical values for riverine environments and were adjusted during the calibration process. It is also acknowledged that the simulations are inherently influenced by the uncertainties present in the historical hydrographic data, a common challenge in hydrological modeling.

To rigorously evaluate the model's performance and the reliability of the calibration, several key statistical indicators were employed. These metrics allow for a quantitative comparison between the simulated flow data generated by the model and the actual observed flows. The RMSE and NSE were the primary indicators selected for this performance assessment, with calculations performed assuming a daily time step (t=1 day).

4.2.1. For the Tigris river cross-section

The calibration process yielded a range of statistical results across different Manning's 'n' values. When 'n' was set to 0.021, the MAE was 33.038, the NSE was 0.964, and the RMSE was 37.358. As the 'n' value increased, the performance generally improved. The optimal 'n' value of 0.031 for the Tigris River resulted in the most favorable statistical outcomes: an MAE of 24.350, an outstanding NSE of 0.979, and an RMSE of 28.474. This high NSE value (closer to 1) signifies a very strong agreement between the simulated and observed flows, indicating that the model, with this roughness coefficient, accurately captures the river's dynamic behavior. Even with slightly higher 'n' values (0.034 and 0.037), the NSE remained strong (0.978 and 0.976, respectively), with comparable RMSE values (29.078 and 30.105), suggesting a robust performance over a narrow range of roughness coefficients. The chosen value of n = 0.031 represents the best fit, balancing accuracy with realistic parameterization (Table 2).

4.2.2. For the Al-Musandawq channel

The calibration for the Al-Musandawq channel also demonstrated excellent model performance. With an 'n' value of 0.020, the

MAE was 12.833, the NSE was 0.972, and the RMSE was 14.090. The performance metrics consistently improved as the ‘n’ value increased. The highest NSE value of 0.986 was achieved when Manning’s ‘n’ was set to 0.028, accompanied by an MAE of 9.033 and an RMSE of 10.571. This exceptionally high NSE value indicates a near-perfect match between the simulated and observed flows in the Al-Musandawq channel, reflecting the model’s high fidelity in representing the flow dynamics within this specific channel. The subsequent increase in ‘n’ to 0.030 still yielded strong results (NSE: 0.983, RMSE: 11.422), but the value of n=0.028 provided the most accurate representation (Table 3).

The comprehensive statistical evaluation unequivocally shows that setting Manning’s roughness coefficient to 0.031 for the Tigris River and 0.028 for the Al-Musandawq channel yielded hydrographs that most closely align with the observed data. The reported statistical indicators, particularly the high NSE values (0.979 for the Tigris and 0.986 for the Al-Musandawq) and relatively low RMSE values, provide strong quantitative evidence of the model’s accuracy and robustness. These values signify that the calibrated model is highly capable of reproducing the historical flow patterns.

Fig. 4 visually corroborates these findings by presenting the flow hydrographs for the Tigris River cross-section. The plots clearly illustrate the superior agreement between the simulated discharges (using the optimized ‘n’ values) and the measured discharges, providing a compelling qualitative complement to the statistical results. The visual concordance reinforces confidence in the model’s calibration and its suitability for subsequent simulation tasks, such as evaluating flood management strategies.

Table 2. Statistical evaluation of calibration results for the Tigris River cross-section.

n	RMSE	NSE	MAE
0.021	37.358	0.964	33.038
0.025	34.103	0.971	27.564
0.028	32.667	0.952	30.549
0.031	28.474	0.979	24.35
0.034	29.078	0.978	25.884
0.037	30.105	0.976	24.796

Table 3. Statistical evaluation of calibration results for the Al-Musandawq channel.

n	RMSE	NSE	MAE
0.02	14.09	0.972	12.833
0.024	12.205	0.981	10.033
0.028	**10.571**	**0.986**	**9.033**
0.03	11.422	0.983	9.833

4.3. Results of one- and two-dimensional mathematical models

a) Water depth, velocity, and water surface profile

Figs. 5 to 7 illustrate the simulated hydraulic parameters along the study reach, including water depth, flow velocity, and water surface profile, as generated by the HEC-RAS model. Analysis of the model outputs indicates that flow velocities range from 0 to 2.3 m/s, with the maximum value of 2.3 m/s occurring at station 23+596. Simulated water depths vary between 0 and 7.2 m across the study reach. Accordingly, the water surface elevations at the upstream and downstream boundaries are 17.11 meters above sea level (masl). and 6.55 masl, respectively, reflecting the overall bed gradient and hydraulic conditions along the river reach.

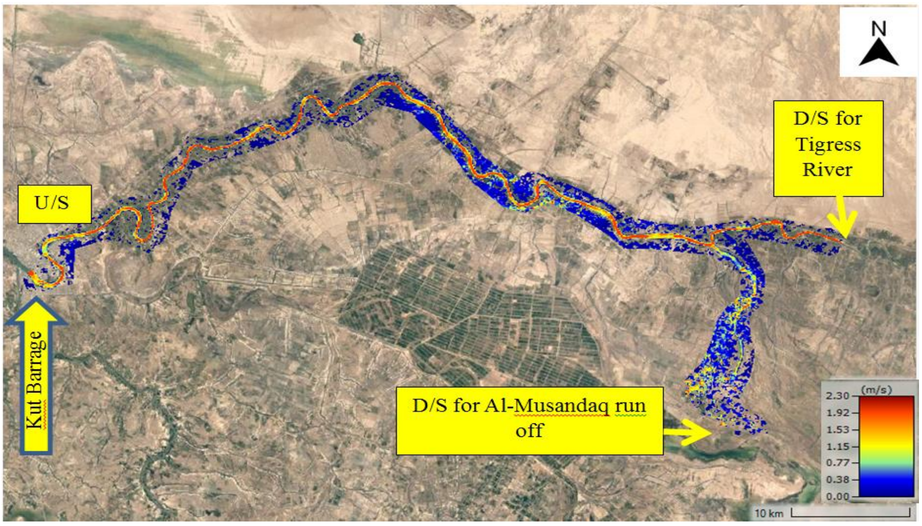

Fig. 5. Spatial distribution of water depth corresponding to the peak flow condition.

Fig. 6. Flow velocity field corresponding to the peak flow condition.

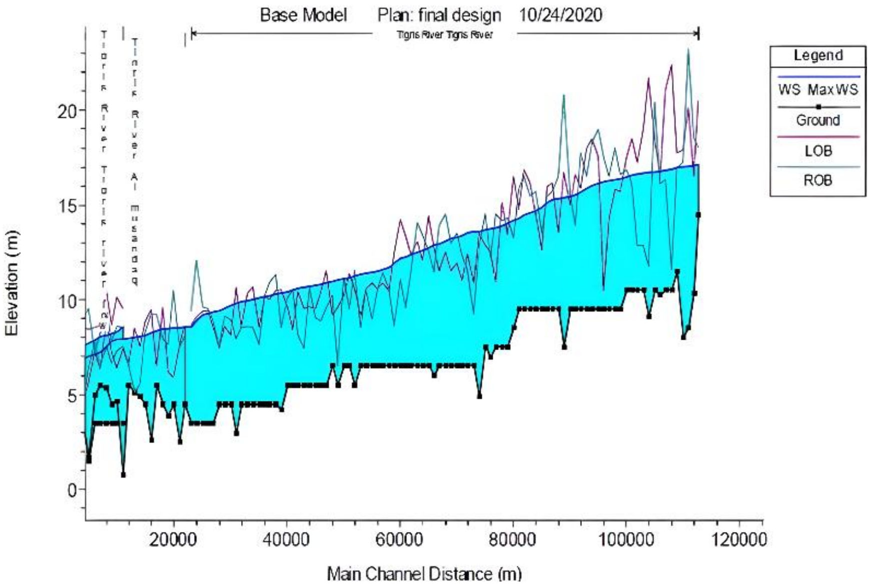

Fig. 7. Simulated water surface profile of the study reach at peak flow conditions.

4.4. Removal of islands and sidebars from the Tigris River in the study area

As noted earlier, the flood wave originating downstream of the Kut Dam propagated rapidly, reaching Maysan City within three days and causing flooding. To mitigate this risk and restore the river's capacity to convey expected flood discharges, a scenario was developed in which islands and sidebars within the river reach, from downstream of the Kut Dam to the Al-Musandawq channel, were removed. This was achieved by modifying the river cross-sections in the HEC-RAS model to reflect the absence of these features. Fig. 8 presents a satellite image of the five islands and one sidebar along the study reach of the Tigris River, highlighting their positions. The sequence and locations of these features are summarized in Table 4, providing a reference for their removal in the hydraulic simulations.

Table 4. Spatial coordinates of islands and sidebars along the study reach.

Sample	Station	Type
1	112+596	Island
2	107+596	Sidebar
3	99+596	Island
4	63+596	Island
5	34+596	Island
6	25+596	Island

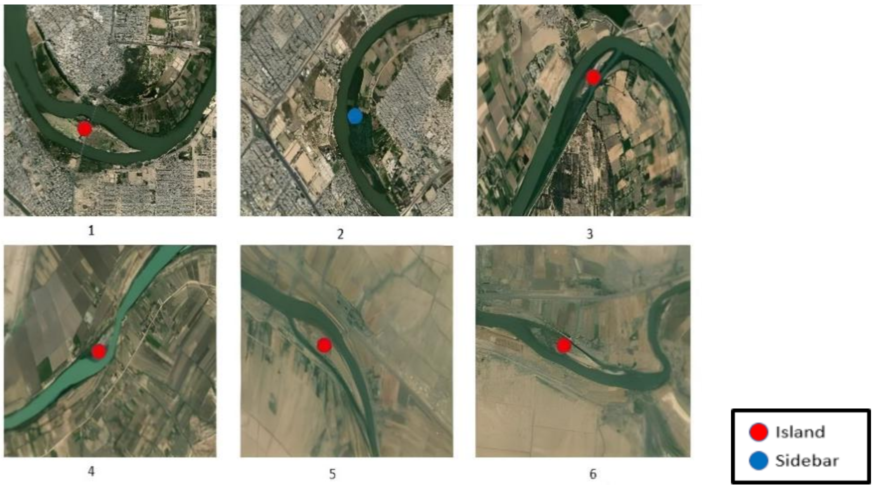

Fig. 8. Satellite imagery showing the locations of islands and a sidebar along the Tigris River study reach.

The cross-sections of the Tigris River at the identified islands and sidebars were modified by reshaping them to represent unobstructed flow paths. The resulting adjusted cross-sections are presented in Figs. 9 to 14, illustrating the hydraulic configuration after the removal of these features.

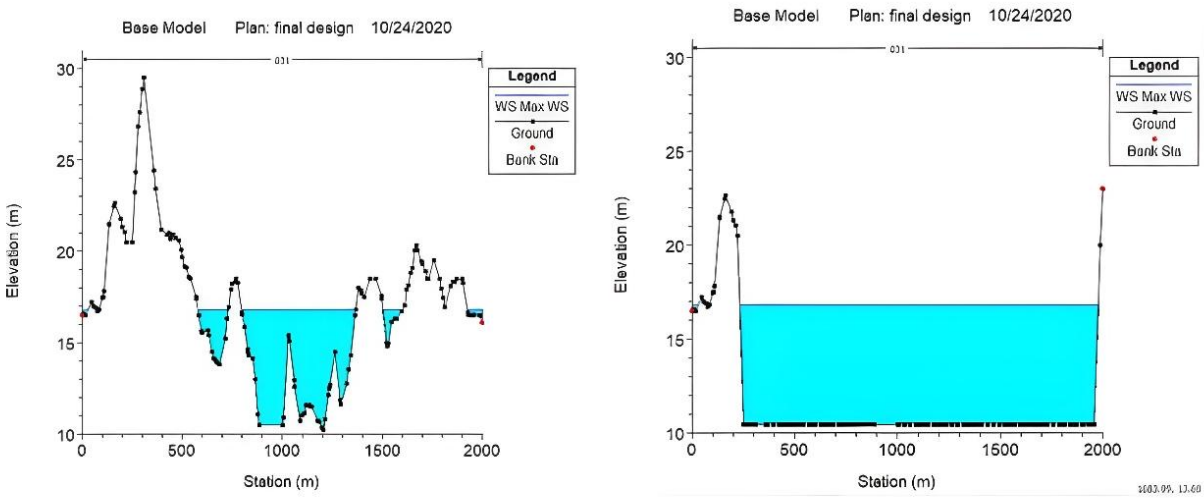

Original cross-section Modified cross-section

Fig. 9. Modified river cross-section at station 112+596 after removal of islands and sidebars.

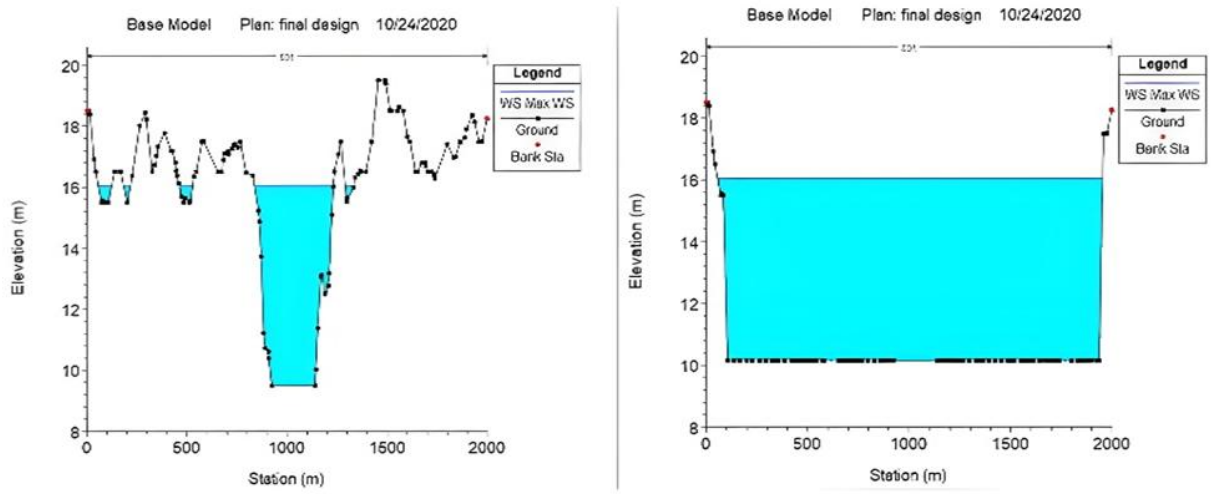

Original cross-section Modified cross-section

Fig. 10. Modified river cross-section at station 107+596 following the removal of islands and sidebars.

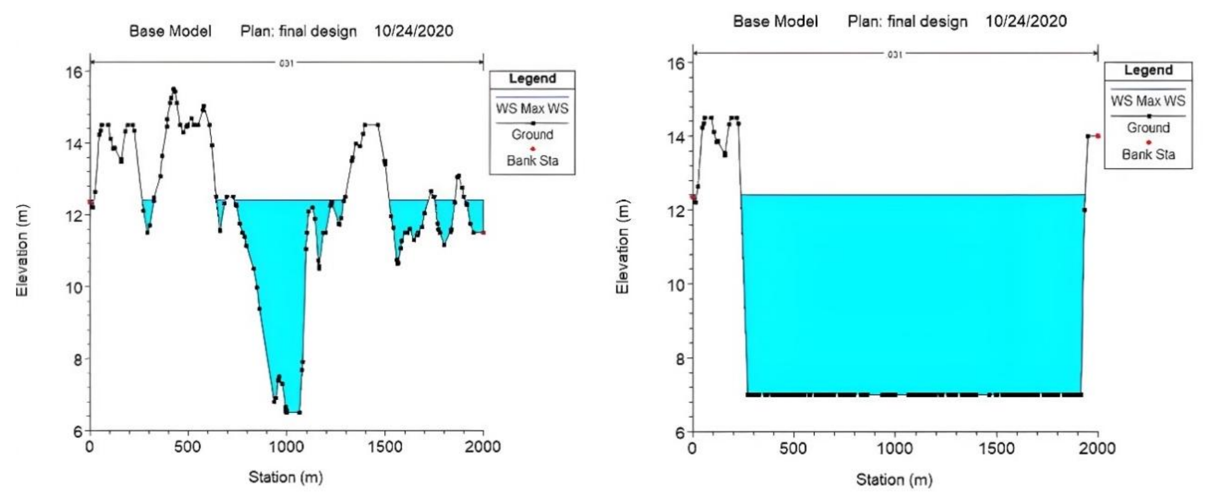

Original cross-section Modified cross-section

Fig. 11. Modified river cross-section at station 99+596 following the removal of islands and sidebars.

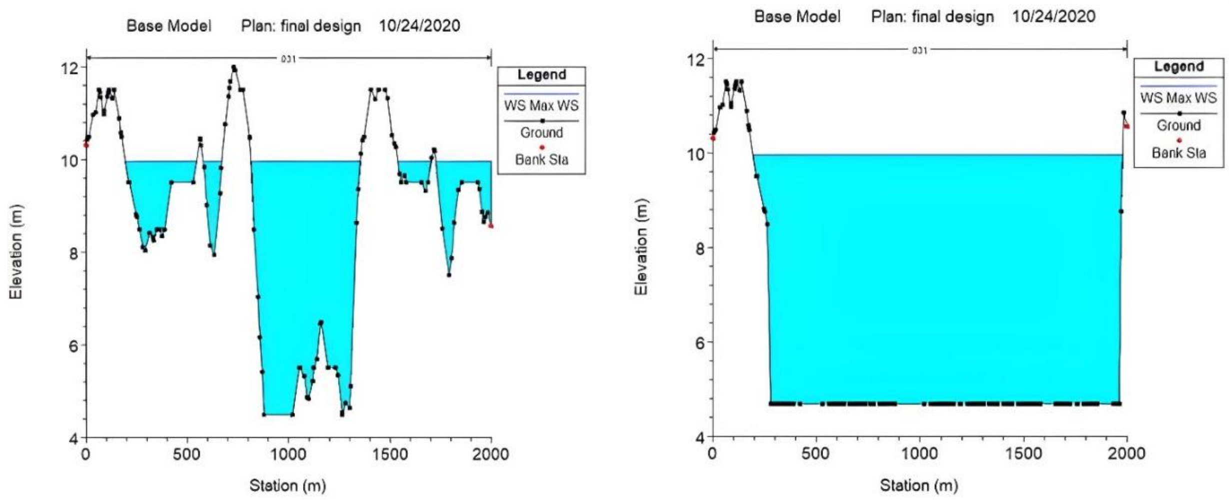

Original cross-section Modified cross-section

Fig. 12. Modified river cross-section at station 63+596 following the removal of islands and sidebars.

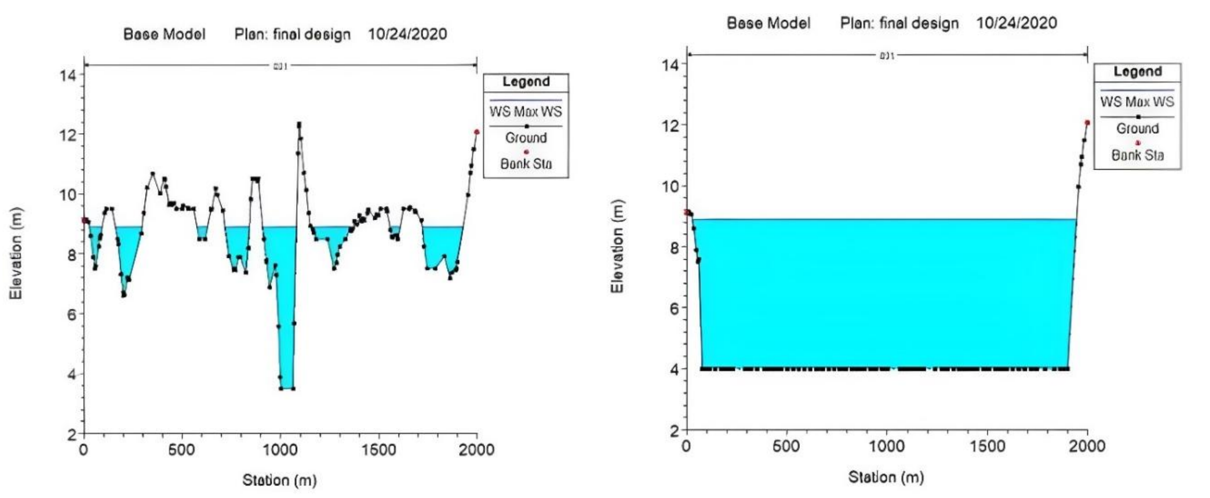

Original cross-section Modified cross-section

Fig. 13. Modified river cross-section at station 34+596 following the removal of islands and sidebars.

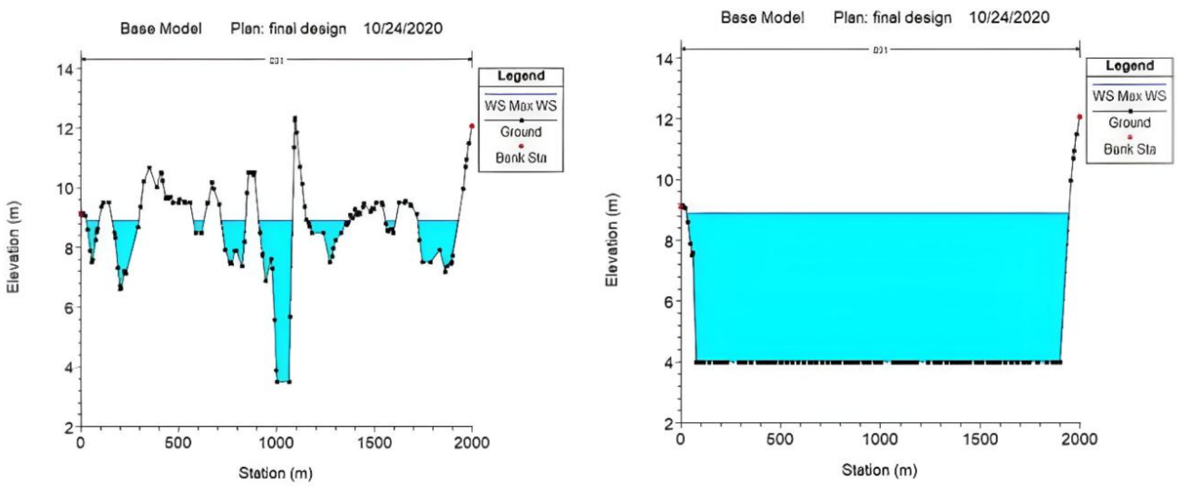

Original cross-section Modified cross-section

Fig. 14. Modified river cross-section at station 25+596 following the removal of islands and sidebars.

The simulation results obtained using the modified cross-sections, in which the islands and sidebars were removed (Fig. 15 and 16), indicated that the flood wave neither attenuated nor experienced a significant delay in reaching stations 114+307 and 24+596. Consequently, the strategy of physically removing islands and sidebars, or undertaking extensive river pruning and channel modifications, was deemed impractical due to its technical complexity and prohibitive cost.

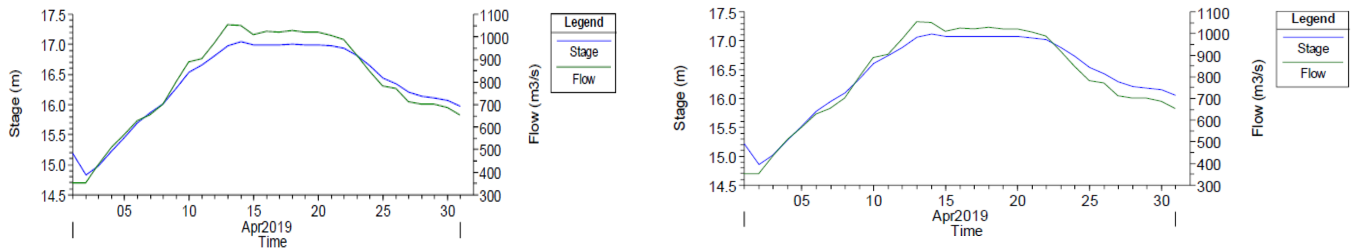

(a) **(b)**

Fig. 15. Stage and flow hydrographs at Kut Barrage with (a) original cross-section and (b) modified cross-section (station 114+307).

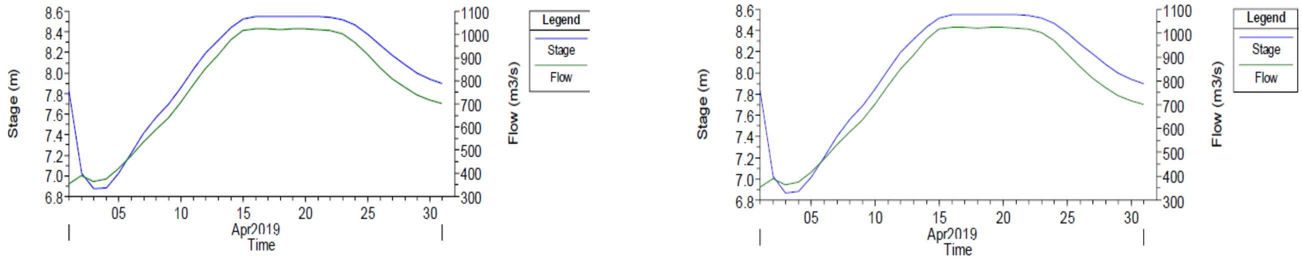

(a) **(b)**

Fig. 16. Stage and flow hydrographs at the Al-Musandawq diversion point from the Tigris River with (a) original cross-section and (b) modified cross-section (station 24+596).

4.5. Design of a weir with optimal crest elevation

HEC-RAS provides multiple approaches to simulate hydraulic control structures, which include bridges, culverts, inline and lateral structures, and connections between 1D and 2D flow zones. These hydraulic controls modify the standard conservation equations applied over 1D cross-sections or 2D cells using empirically derived and typically stable formulations.

Among these, weir structures are widely used to represent flow regulation over barriers. HEC-RAS allows weir flow to be modeled in several ways, depending on the type of structure: inline weirs without gates, lateral weirs without gates, and gated weirs. Although all approaches are based on the same fundamental equations, each scenario requires specific considerations in applying the weir formulation. The discharge over a weir is calculated using Eq. 15:

$$Q = CLH^{2/3} \tag{15}$$

where, Q is the flow rate (m³/s), C is the weir coefficient, L is the crest length of the weir, and H is the energy head above the crest.

This investigation employs ungated inline weirs as a strategic approach for flood control. Specifically, a weir was implemented upstream of the Al-Musandawq channel at station 23+410, configured with a 10 m crest width and a weir coefficient of 3.1, situated 20 m from the upstream cross-section. To thoroughly assess the efficacy of this submerged weir in moderating Tigris River floods across the study reach, five distinct scenarios were devised. The overarching design objective is to regulate the flow reaching Amarah city, restricting it to 700 m³/s during peak flood seasons while ensuring a minimum passage of below 250 m³/s during drier periods.

As an illustrative example, the outcomes derived from one scenario are detailed in this section. A comprehensive presentation of the results across all five scenarios is subsequently provided in Table 7.

4.6. Scenario with peak flow of 1025 m³/s

This scenario was designed based on the maximum observed discharge of 1025 m³/s released from the Kut Dam, as recorded in the flood events of 1995 and 2019. Two sub-cases were considered for the simulation:

- **Case 1:** Lateral inflow equal to 0 m³/s
- **Case 2:** Lateral inflow equal to 525 m³/s

The corresponding hydraulic data for these scenarios are summarized in Tables 5 and 6. These simulations were used to evaluate the optimal crest elevation of the weir to ensure effective flood diversion while maintaining safe flow conditions downstream.

Table 5. Assumed lateral inflow parameters along the study reach for a total discharge of 1025 m³/s (Case 1).

Discharge in Tigris River (m^3/s)	Name of lateral inflows	Discharge (m^3/s)	Weir elevation (m)
1025	-	-	9.406
1025	Um Aljury	0	9.406
1025	Al-Chabbab	0	9.406

Based on this scenario (Case 1), the peak flow entering Maysan City is 346.29 m^3/s, while the maximum discharge directed toward the Al-Musandawq channel reaches 675.73 m³/s. The maximum water surface elevation is 8.65 m at station 23+610, located upstream of the Al-Musandawq channel, and 8.32 m at station 23+596, situated downstream of the Al-Musandawq channel.

Table 6. Assumed lateral inflow parameters along the study reach for a total discharge of 1025 m³/s (Case 2).

Discharge in Tigris River (m^3/s)	Name of lateral inflows	Discharge (m^3/s)	Weir elevation (m)
1025	-	-	9.406
1050	Um Aljury	25	9.406
1550	Al-Chabbab	500	9.406

In Case 2, the hydraulic analysis indicated that the maximum inflow rate into the Maysan city area is 389.18 m^3/s, while the maximum flow entering the Al-Musandawq channel is 1159.73 m^3/s. Specifically, the maximum water surface elevation reaches 8.71 m at station $23 + 610$ (upstream of the Al-Musandawq channel structure) and 8.41 m at station $23 + 596$ (downstream).

The simulation results, generated using historical flood data spanning from 1995 to 2019, were instrumental in pinpointing the optimal design parameters for the proposed weir. The simulations revealed that a crest elevation of 9.406 meters for the weir is the most effective in managing river discharge. This specific elevation ensures that the flow directed towards Maysan city is capped at a maximum of 700 m^3/s, thereby preventing catastrophic inundation. Simultaneously, it guarantees a minimum flow of 250 m^3/s, crucial for maintaining ecological balance and water supply during drier periods. This optimized elevation underpins the decision to implement the final flood control structure as a submerged weir precisely at 9.406 m.

The proposed structure is not merely defined by its elevation but also by its physical characteristics and strategic placement. With a crest width of 5 meters and an approximate total length of 130 meters, the weir is designed for robust performance. Its location upstream of the Al-Musandawq channel is a key design feature, allowing for the strategic diversion of excess floodwaters.

Table 7 provides a quantitative summary of the simulation outcomes across various scenarios, focusing on different discharge rates. For a peak inflow of 4000 m^3/s in the Tigris River, the weir at 9.406 m elevation successfully diverts 3322.51 m^3/s through the Al Musandawi channel while allowing only 675.62 m^3/s to pass towards Maysan. Similar effective flow management is observed for other simulated peak flows, such as 2500 m^3/s (with 1907.09 m^3/s diverted and 582.27 m^3/s to Maysan) and 1025 m^3/s (with 675.73 m^3/s diverted and 346.29 m^3/s to Maysan). The simulations demonstrate a consistent pattern: as the total discharge in the Tigris River increases, a proportionally larger volume of water is successfully managed and diverted through the Al Musandawi channel, significantly reducing the burden on the Maysan reach.

Fig. 17. visually complements these findings by presenting flood hazard maps for different river reaches under the proposed flood control strategy. The generated water depth zoning maps surrounding the Tigris River offer a compelling qualitative depiction of the results. They clearly illustrate a substantial reduction in flood risk across the studied areas. The maps effectively demonstrate how the submerged weir, by controlling and diverting flood flows, ensures the safe passage of excess water away from vulnerable zones, thereby confirming the structural approach's efficacy in managing flood events. This visual evidence strongly supports the quantitative data, highlighting the practical impact of the designed intervention in mitigating flood hazards.

Table 7. Summary of simulation outcomes across different scenarios of weir discharge rates.

Discharge in Tigris River (m^3/s)	Flow pass through Maysan (m^3/s)	Flow pass through the Al Musandaq (m^3/s)	Weir elevation (m)
4000	675.62	3322.51	9.406
2500	582.27	1907.09	9.406
1025	346.29	675.73	9.406
533	330.18	203.1	9.406
1058	371.18	686.13	9.406

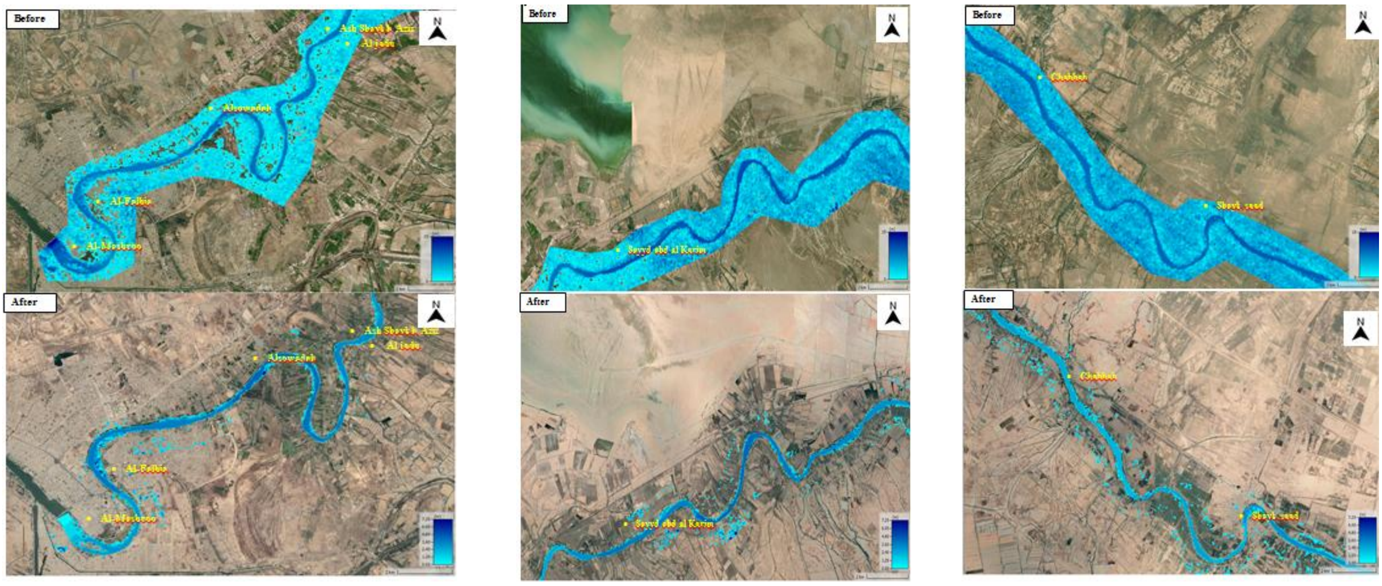

(a) (b) (c)

Fig. 17. Flood depth zoning map for before and after application of the proposed structural approach in: a) Al-Mashroo to Aziz Al-Jadu b) Sayyd Abd Al Karim c) Al-Chbbab to Shayk Saad.

4.7. Strategic policy implications and decision-making guidance

The insights derived from this research provide a foundational basis for refining water resource management and strengthening flood mitigation strategies within the Tigris River basin, with a specific focus on the vulnerability of Amarah. By successfully deploying an integrated 1D–2D HEC-RAS framework, this study underscores the model's capacity as a dependable diagnostic tool for deciphering intricate flood dynamics, even in regions characterized by data scarcity. Such an analytical approach facilitates evidence-based governance by delivering precise inundation projections and enabling a rigorous, quantitative appraisal of diverse flood control interventions. A primary takeaway for infrastructure planning is the validated efficacy of the proposed submerged weir at the Al-Musandawq channel. Specifically, maintaining an optimized crest elevation of 9.41 meters presents a technically viable structural intervention to shield Amarah from projected high-magnitude flood events. It is recommended that the Ministry of Water Resources and associated regulatory bodies integrate these technical parameters into forthcoming flood defense systems and regional developmental agendas. Moreover, the computational architecture developed herein offers a scalable blueprint for real-time early warning systems, which are essential for orchestrating timely evacuations and risk-reduction protocols. Beyond structural recommendations, this inquiry highlights the necessity of accounting for spatial heterogeneity in hydraulic variables, most notably Manning’s roughness, and the complex interplay between primary riverine conduits and diversionary escape routes. Future policy frameworks should prioritize the incorporation of high-fidelity topographic datasets and sophisticated hydraulic modeling into standard management practices. Finally, while isolated natural mitigation measures showed limited success in this particular context, their evaluation points toward the imperative for a hybrid mitigation paradigm. This entails a synergistic combination of engineered structures and non-structural tactics, such as strategic land-use zoning and community-driven awareness initiatives, to achieve a holistic and resilient flood risk management posture.

5. Conclusion

This study successfully addressed the critical challenge of managing flood hazards in the Tigris River downstream of the Kut Dam, with a specific focus on protecting the city of Amarah by modeling the Al-Musandawq channel. The primary objective was to investigate flood behavior and explore effective flood management strategies within this reach. Through the development and calibration of an integrated 1D–2D HEC-RAS hydraulic model, we achieved a robust simulation of flood wave propagation for the 2019 event, applying both one-dimensional and more advanced two-dimensional modeling approaches to assess flood behavior and control. The findings confirm the critical role of advanced hydraulic modeling, particularly coupled 1D–2D approaches, in understanding complex flood dynamics and assessing mitigation alternatives in regions with limited data. This research provides valuable insights and practical recommendations for water resource managers and policymakers in Iraq, offering a scientifically validated strategy for enhancing flood resilience in vulnerable areas. The key findings of this research are summarized as follows:

- **Calibration of Manning's Roughness Coefficient:** The optimal Manning's n values, 0.031 for the Tigris River and 0.028 for the Al-Musandawq channel, demonstrated an excellent agreement between simulated and observed flow data. The model performance metrics were robust, with MAE values of 9.033 m³/s, RMSE values of 10.57 m³/s, and NSE values of 0.986, all within acceptable ranges.
- **Effect of Island and Sidebar Removal:** Simulations indicated that the removal of all islands and sidebars along the river did not significantly dissipate the flood wave. Additionally, this approach is often considered impractical due to the technical difficulty and high cost associated with large-scale river modification.
- **Optimal Weir Design for Flood Control:** The study identified that the most effective method for managing floodwaters is the implementation of a weir with an optimal crest elevation. A barrier set at 9.4 m effectively limits peak flows to less than 700 m³/s entering Maysan City, ensures minimal flows (below 250 m³/s) during dry seasons, and allows controlled flows between 250 and 700 m³/s to pass downstream.

Based on the findings of this study, the following avenues are suggested for future work:

- **Construction of the Al-Musandawq Diversion System:** Development of an engineered system to divert water from the Tigris River into the Al-Musandawq pond in Maysan City could further enhance flood mitigation.
- **Irrigation Potential During Low Flows:** Investigate the feasibility of using the Al-Musandawq channel to supply water for agricultural or roadside irrigation during the winter months, providing a secondary benefit of managed water storage.
- Integrating the proposed model into a real-time forecasting system and exploring the long-term morphological impacts of the proposed weir.

Statements & Declarations

Author Contributions

Mahmoud Mohammad Rezapour Tabari: Conceptualization, Supervision, Methodology, investigation, editing, Formal analysis, Resources, Original Draft

Milad Rahshabdiz: Visualization, Editing

Mustafa Khudhair Tuama: Software, Visualization, writing-original draft preparation

Funding

The authors received no financial support for the research, authorship, and/or publication of this article.

Data availability

The data presented in this study will be available on request from the corresponding author.

Declarations

The authors declare no conflict of interest.

References

[1] Aerts, J. C., Botzen, W. W. Climate change impacts on pricing long-term flood insurance: A comprehensive study for the Netherlands. Global environmental change, 2011; 21: 1045–1060. doi:10.1016/j.gloenvcha.2011.04.005.

[2] Mohammed-Ali, W. S., Khairallah, R. S. Flood Risk Analysis: The Case of Tigris River (Tikrit/Iraq). Tikrit Journal of Engineering Sciences, 2023; 30: 112–118. doi:10.25130/tjes.30.1.11.

[3] Sabeeh, N. N., Alabdraba, W. M. S. The Hydrodynamic Model using HEC-RAS: The case of Tigris River Downstream of Samarra Barrage (Iraq). In: InIOP Conference Series: Earth and Environmental Science; 2022; p. 012017.

[4] Pekel, J. F., Cottam, A., Gorelick, N., Belward, A. S. High-resolution mapping of global surface water and its long-term changes. Nature, 2016; 540: 418–422. doi:10.1038/nature20584.

[5] Yarahmadi, M., Eskandari Damaneh, H., Khalighi Sigaroodi, S. Assessment of the Impact of Land Use/Land Cover Changes in the Hamoun Wetland on Land Surface Temperature Using Satellite Imagery. Civil Engineering and Applied Solutions, 2025; 1: 31–42. doi:10.22080/ceas.2025.29153.1009.

[6] Tellman, B., Sullivan, J. A., Kuhn, C., Kettner, A. J., Doyle, C. S., Brakenridge, G. R., Erickson, T. A., Slayback, D. A. Satellite imaging reveals increased proportion of population exposed to floods. Nature, 2021; 596: 80–86. doi:10.1038/s41586-021-03695-w.

[7] Nearing, G., Cohen, D., Dube, V., Gauch, M., Gilon, O., Harrigan, S., Hassidim, A., Klotz, D., Kratzert, F., Metzger, A., Nevo, S. Global prediction of extreme floods in ungauged watersheds. Nature, 2024; 627: 559–563. doi:10.1038/s41586-024-07145-1.

[8] Suresh, S., Hossain, F., Minocha, S., Das, P., Khan, S., Lee, H., Andreadis, K., Oddo, P. Satellite-based tracking of reservoir operations for flood management during the 2018 extreme weather event in Kerala, India. Remote Sensing of Environment, 2024; 307: 114149. doi:10.1016/j.rse.2024.114149.

[9] Aziz, F., Wang, X., Mahmood, M. Q., Awais, M., Trenouth, B. Coastal urban flood risk management: Challenges and opportunities− A systematic review. Journal of Hydrology, 2024; 645: 132271. doi:10.1016/j.jhydrol.2024.132271.

[10] Hansson, K., Danielson, M., Ekenberg, L. A framework for evaluation of flood management strategies. Journal of environmental management, 2008; 86: 465–480. doi:10.1016/j.jenvman.2006.12.037.

[11] Menoni, S., Molinari, D., Ballio, F., Minucci, G., Mejri, O., Atun, F., Berni, N., Pandolfo, C. Flood damage: a model for consistent, complete and multipurpose scenarios. Natural Hazards and Earth System Sciences, 2016; 16: 2783–2797. doi:10.5194/nhess-16-2783-2016.

[12] Hino, M., BenDor, T. K., Branham, J., Kaza, N., Sebastian, A., Sweeney, S. Growing safely or building risk? Journal of the American Planning Association, 2024; 90: 50–62. doi:10.1080/01944363.2022.2141821.

[13] Chakraborty, L., Thistlethwaite, J., Scott, D., Henstra, D., Minano, A., Rus, H. Assessing social vulnerability and identifying spatial hotspots of flood risk to inform socially just flood management policy. Risk Analysis, 2023; 43: 1058–1078. doi:10.1111/risa.13978.

[14] Jemberie, M. A., Melesse, A. M. Urban flood management through urban land use optimization using LID techniques, city of Addis Ababa, Ethiopia. Water, 2021; 13: 1721. doi:10.3390/w13131721.

[15] Long'or Lokidor, P., Taka, M., Lashford, C., Charlesworth, S. Nature-based solutions for sustainable flood management in East Africa. Journal of Flood Risk Management, 2024; 17: e12954. doi:10.1111/jfr3.12954.

[16] Erena, S. H., Worku, H., De Paola, F. Flood hazard mapping using FLO-2D and local management strategies of Dire Dawa city, Ethiopia. Journal of Hydrology: Regional Studies, 2018; 19: 224–239. doi:10.1016/j.ejrh.2018.09.005.

[17] Nigusse, A. G., Adhanom, O. G. Flood hazard and flood risk vulnerability mapping using geo-spatial and MCDA around Adigrat, Tigray region, Northern Ethiopia. Momona Ethiopian Journal of Science, 2019; 11: 90–107. doi:10.4314/mejs.v11i1.6.

[18] Ban, H. J., Kwon, Y. J., Shin, H., Ryu, H. S., Hong, S. Flood monitoring using satellite-based RGB composite imagery and refractive index retrieval in visible and near-infrared bands. Remote Sensing, 2017; 9: 313. doi:10.3390/rs9040313.

[19] Ruiz-Bellet, J. L., Balasch, J. C., Tuset, J., Barriendos, M., Mazon, J., Pino, D. Historical, hydraulic, hydrological and meteorological reconstruction of Santa Tecla flash floods in Catalonia (NE Iberian Peninsula). Journal of Hydrology, 2015; 524: 279–295. doi:10.1016/j.jhydrol.2015.02.023.

[20] Chaudhry, M. H. Applied hydraulic transients. 3 ed. New York (US): Springer; 2014. doi:10.1007/978-1-4614-8538-4.

[21] Brunner, G. W. HEC-RAS river analysis system 2D modeling user’s manual. US Army Corps of Engineers—Hydrologic Engineering Center. 2016. Report No.:

[22] Babister, M., Barton, C. Australian Rainfall and Runoff Revision Project 15: Two Dimensional Modelling in Urban and Rural Floodplains. Canberra (AUS): Geoscience; 2012. Report No.: P15/S1/009.

[23] Maidment, D. R., Mays, L. W. Applied hydrology, Water Resources Handbook. Applied hydrology, Water Resources Handbook. New York, NY, USA: McGraw-Hill. ed. 1988.

[24] Chow, V. T. Open Channel Hydraulics. Il ed. Mc Graw Hill, New York; 1950.

Civil Engineering and Applied Solutions

Research Article

journal homepage: ceas.journals.umz.ac.ir

CEAS Civil Engineering and Applied Solutions

A Hybrid CFD–Machine Learning Framework for Modeling Discharge Hysteresis in Twin Circular Culverts

Ehsan Behnamtalab [a*], Mohsen Behnamtalab [b]

[a] *Department of Engineering, Civil Engineering Group, Hakim Sabzevari University, Sabzevar, Iran*
[b] *Civil Engineering Department, Sharif University of Technology, Tehran, Iran*

ARTICLE INFO

Article history:

Received 18 February 2026

Revised 26 March 2026

Accepted 03 June 2026

Available online 01 January 2027

Keywords:

Twin culvert

Head-Discharge

Numerical simulation

Machine learning

RANS

ABSTRACT

This study investigates the hydraulic behavior of twin circular culverts under unsteady flow, considering rising and receding inlet flows and varying upstream water levels. Three-dimensional numerical simulations were conducted using RANS equations with the RNG k–ε turbulence model and validated against laboratory data, showing excellent agreement. Results indicate that through-flow discharge remains nearly constant across rising and receding phases, while overtopping flow exhibits significant differences (~22%). Outflow during recession is approximately 1.5 times higher than during the rising stage. Complementary data-driven modeling using eight machine learning algorithms, including Gradient Boosting, AdaBoost, Random Forest, and Neural Networks, demonstrated high accuracy in predicting nonlinear discharge–head relationships, with R^2 up to 0.992 for numerical and 0.985 for experimental data. Models performed better during receding phases due to more stable flow conditions. The integration of CFD simulations and machine learning provides detailed flow insights and rapid, accurate discharge estimation, offering a reliable framework for culvert design, flow assessment, and hydraulic optimization under complex unsteady conditions.

How to cite this article: Behnamtalab, E., Behnamtalab, M. A Hybrid CFD–Machine Learning Framework for Modeling Discharge Hysteresis in Twin Circular Culverts. Civil Engineering and Applied Solutions. 2027; 3(1): 117–130. doi:10.22080/ceas.2026.31318.1079.

1. Introduction

Drainage systems along highways and railways are designed to convey surface water and prevent upstream flooding, with culverts being a primary component. Compared to bridges, culverts are more cost-effective initially, require precise hydraulic design, and depend on backfill quality for structural strength, though their maintenance costs can be higher [1]. Culverts are typically designed based on historical rainfall records to estimate discharge rates. However, with the substantial changes in precipitation patterns driven by global warming, there is an increased likelihood of future flood disasters due to undersized and poorly designed culverts [2-5]. Recent flood events have emphasized the vital role of culverts in safely conveying surface water beneath roads, railways, and dams. Proper design, construction, and maintenance are crucial, as culverts protect channels and embankments and ensure long-term structural performance.

In recent years, many researchers have investigated different aspects and behaviors of culvers. In a study, researchers analyzed vertical earth pressure on Hinged Prefabricated Box Culverts (HPBC) using field tests and FLAC3D simulations, comparing them

* Corresponding author.
E-mail addresses: e.behnamtalab@hsu.ac.ir (E. Behnamtalab).

https://doi.org/10.22080/ceas.2026.31318.1079
ISSN: 3092-7749/

with Monolithic Box Culverts (MBC). They proposed a modified calculation method that improved the accuracy of vertical pressure estimation beyond existing AASHTO and Chinese design codes [6]. A Decision Tree–SMOTE framework was developed to predict culvert conditions and prioritize inspections. Applied to 12,400 culverts, it achieved high accuracy and reduced inspections by 44% [7]. In a study, a comprehensive review of local scour downstream of culverts emphasized the influence of flow regime, sediment properties, and geometric factors. The study highlighted that incorporating these parameters into culvert design is crucial for enhancing structural safety and long-term durability [8]. In another study, a physical modeling study compared scour development at box and circular culvert outlets under varying blockage ratios and flow conditions. Results showed that circular culverts caused greater scour, and scour depth increased with discharge, providing useful insights for optimizing culvert outlet design. [9].

Culverts are available in various geometric shapes, with rectangular and circular types being the most common. The most suitable culvert design is the culvert that can pass the design flow well with the lowest cost. Many researches have been done regarding the design method and different flow conditions in culverts, among which it can refer to the studies of Dasika [10], Montes and Dasika [11], Hager and Giudice [12], Johnson and Brown [13] and Ansar et al. [14]. Most of these studies demonstrated significant differences in discharge behavior between the rising and falling limbs of the hydrograph, attributable to varying flow conditions during culvert filling and draining phases. Lee and Jin [15] created a computer program for designing rectangular culverts, which requires multiple iterations to reach a final solution. Ku and Jun [16] developed a computational tool that integrates non-uniform flow characteristics in culverts by comprehensively incorporating updated data from the FHWA. Richmond et al. [17] investigated the impact of velocity distributions across cross sections within a corrugated culvert barrel on juvenile fish migration, emphasizing ecological considerations in culvert design.

Although culverts are straightforward to construct, their hydraulic design is inherently complex and influenced by multiple factors. The flow cannot always be classified strictly as pressurized or free flow; in some cases, it represents a combination of both regimes [18]. Chow [19] classified the flow inside the culvert into six hydraulic types. The upstream water depth, the height of the culvert, the water depth inside the culvert, the length and slope of the culvert are the factors that determine the type of flow inside the culvert. Yoo and Lee [20] stated that the classification of flow in a culvert is expressed according to three characteristics. The first characteristic is whether the culvert inlet flow is submerged or not, which is determined by the upstream water level. The second characteristic includes the characteristics of the flow regime inside the channel, and the third characteristic is the flow condition downstream of the culvert. Culvert design is generally based on the flood discharge corresponding to a specified return period, which varies according to regional and climatic conditions. Kang et al. [21] suggested that the concept of critical storm duration is appropriate for estimating design flood discharge in culvert design. The preliminary and optimal design involves a submerged inlet operating with near-full flow conditions, ensuring supercritical flow and maximizing channel capacity [22].

Hydraulically optimized designs have had limited impact on culvert practice, as guidelines focus on pipe sizing but offer little advice on materials, wing wall angles, or slopes. Consequently, inefficient designs like square inlets or high-friction barrels remain common, with HDS-5 from the FHWA being one of the most comprehensive references [23]. The equations presented in HDS-5 are based on the Bernoulli equation, modified in accordance with experimental findings from studies conducted during the 1950s and 1960s [24-29]. Culvert flow is classified into inlet control (IC) and outlet control (OC) based on hydraulic theory. Experimental studies using HEC-RAS and HY-8 showed that culvert length and roughness significantly affect performance, with HY-8 performing better under rough-bed conditions and no clear advantage for bridge hydraulics. [30].

Under inlet control, the flow is solely limited by the size, shape, and configuration of the inlet. The sudden reduction in cross-sectional flow area at the inlet, where an open channel enters the culvert, causes head loss [31]. The culvert barrel may still convey higher flow rates and therefore does not limit the flow. In these situations, culvert flows are treated as weir (unsubmerged) or orifice (submerged) flows. The flow rate, cross-sectional area, shape, and inlet configuration of the culvert determine the headwater height under inlet control. Under outlet-control conditions, head loss is influenced not only by inlet parameters but also by culvert length, material, and tailwater depth, making the barrel a key factor in determining overall flow capacity [23]. Under submerged-inlet conditions, culverts behave like orifices with air recirculation limiting the effective flow area. Full submergence at the outlet displaces all air, fills the cross-section, and causes a transition from open-channel to pressurized flow conditions [10].

In parallel to traditional methods, Machine Learning (ML) has emerged as a transformative tool in water resources engineering, demonstrated by its use in developing efficient surrogate models for complex flow simulations [32], predicting scour depth at coastal structures with over 80% accuracy using ensemble methods [33]and deriving compact design equations for spillways via gene expression programming [34]. In addition, hybrid and soft computing approaches have been widely applied in civil engineering problems; for example, [35] developed a hybrid ANFIS-based framework for predicting pipe failure rates, showing that combining multiple models can significantly improve predictive accuracy. Similarly, Tabari and Sanayei [36] employed artificial neural networks and support vector regression for predicting dam crest displacement, highlighting the effectiveness of data-driven models in capturing complex structural responses. Subsequently, deep learning architectures like CNNs and LSTMs have enhanced the modeling of spatiotemporal hydrologic systems [37] and improved urban drainage management through real-time flood prediction and pipe defect detection [38], with notable success in culvert blockage detection achieving 94% accuracy [39]. More recently, reinforcement learning techniques have also been introduced for adaptive water resources management; for instance, Masoumi et al. [40] demonstrated the effectiveness of Q-learning in optimizing reservoir operations under dynamic and uncertain conditions. The most significant advancement is the integration of physical principles into physics-informed ML models, which has substantially improved the reliability and speed of CFD simulations [41] and coastal hazard forecasting Židek et al. [42], marking a shift towards more robust, physics-conscious predictive tools.

Despite the significant progress in both numerical modeling and machine learning applications in hydraulic engineering, most studies have treated these approaches separately. The proposed hybrid framework leverages the strengths of both approaches: CFD provides a detailed physical representation of flow behavior, while machine learning enables rapid prediction with significantly reduced computational cost. This combination offers improved accuracy and practical utility compared to traditional empirical or purely numerical methods.

Considering the above-mentioned factors and previous research gaps, this study employs numerical simulations to investigate the turbulent flow characteristics of twin circular culverts. Also, the receding and rising inlet flow to culverts and the upstream water level change rate are parameters that have been investigated in this research. Moreover, this research evaluates numerically the discharge passing through the culverts and the overtopping flow.

2. Governing equations

This study employs the Reynolds-Averaged Navier-Stokes (RANS) equations to simulate turbulent flow. The RANS equations represent the time-averaged conservation of momentum and mass for turbulent, incompressible Newtonian fluids [43-45]. The continuity and momentum equations are:

$$\frac{\partial u_i}{\partial x_i} = 0 \tag{1}$$

$$\frac{\partial u_i}{\partial t} + u_i \frac{\partial u_j}{\partial x_i} = -\frac{1}{\rho}\frac{\partial p}{\partial x_j} - \frac{\partial(\overline{u_i u_j})}{\partial x_i} \tag{2}$$

where ρ denotes the density of the fluid, u_i represents the time-averaged velocities, and p is the time-averaged pressure. Also, in this study, the results of numerical simulation for the culvert were compared against RNG k-ε turbulence model, standard k-ε and k-ω models. Results indicated that the RNG k-ε turbulence model predicts turbulent flow in the culvert with higher accuracy. Its results will be presented below.

3. Numerical simulation

In this study, Flow-3D software [46] was used to simulate the twin circular culvert. The Finite Volume Method (FVM) was employed to solve the three-dimensional governing equations. Fractional Area–Volume Obstacle Representation (FAVOR) method [47] was applied to detect the geometry of the structure. The FAVOR method uses the value of cell porosity and determines its value with a number between 0 and 1 separating solid boundaries from the fluid domain. The solver utilizes FVM and the VOF method to discretize and solve the governing equations and track the free surface of water. In the VOF method [45], a quantity is defined in each cell that indicates the ratio of water occupancy. A value of one indicates that the cell is completely filled with water and a value of zero indicates that the cell is empty. By knowing this quantity, the location of the water surface and its interfacial angle between the cells of the solution field is determined by the model. In addition, in simulating the twin circular culvert, no-slip conditions were applied at the contact surface of the fluid flow with the wall [48].

The Generalized Minimal Residual (GMRES) method has been used as an implicit pressure-velocity solver to establish pressure-velocity coupling. This method is very accurate and efficient for a wide range of problems and has excellent convergence, symmetry, and speed properties. However, it uses more memory than other methods. When the velocity, Reynolds stress, and continuity equation residuals reach values less than 10^{-6}, the convergent numerical solution is considered. Also, in all numerical models in this research, water density and dynamic viscosity and its temperature were set to 1000 kg/m^3, 0.001 N.s/m2 and 20°C, respectively.

The numerical simulation of the twin culvert is made according to the experimental model developed by Meselhe and Hebert [49]. The desired structure has the specifications presented in Fig.1. According to this figure, the length and diameter (D_o) of the culvert are 380 mm and 76 mm, respectively.

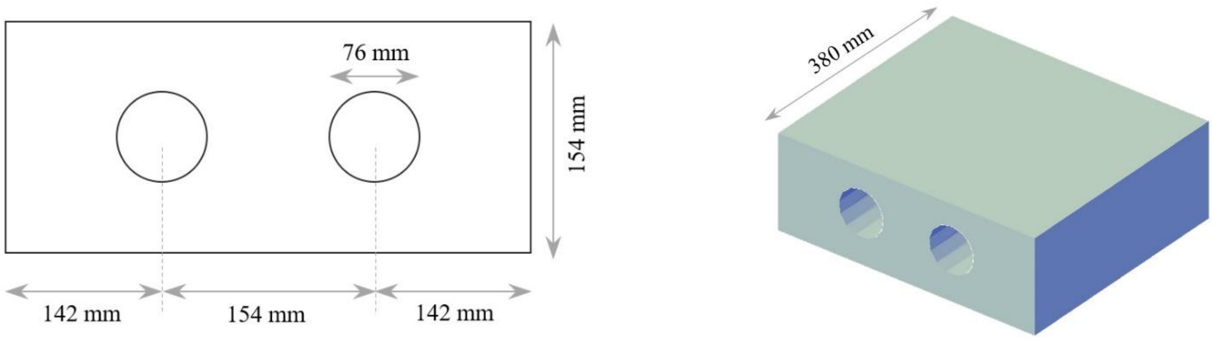

a) Section view **b) 3D view**

Fig. 1. Geometry of the twin circular culvert [29].

The laboratory experiments of Meselhe and Hebert [49] were performed at the University of Louisiana at Lafayette Hydraulic Engineering Laboratory. They were conducted in a flume consisting of a glass bed and walls supported by a stainless-steel frame. The flume is 0.438 m wide, 0.305 m deep, and 3.2 m long. In the laboratory tests, various conditions, including two parts, were examined. The first part includes a) flow passing through the culvert without allowing the flow to overtop (Culvert-only) b) closing the culvert and passing the flow only over the culvert (Overtopping-only) c) flowing through the culvert and over the culvert with the gradual increase of the upstream water level (Combined-Rising) d) Flow passing through the culvert and on the culvert with the gradual decrease of the upstream water level (Combined-Receding). The second part includes a) unsteady hydrograph with rising and receding of upstream water level.

In the present numerical study, in the first part, only Combined-Receding and combined-Rising tests were simulated. Subsequently, the unsteady hydrograph of the inlet flow to the culvert was investigated. In the Combined-Receding simulation, the H/D_o increases from 1.3 to 3.3 (this means that the upstream water level changes from 0.1 m to 0.25 m), and in the Combined-Rising simulation, the H/D_o decreases from 3.3 to 1.3. These characteristics are presented in Fig. 2.

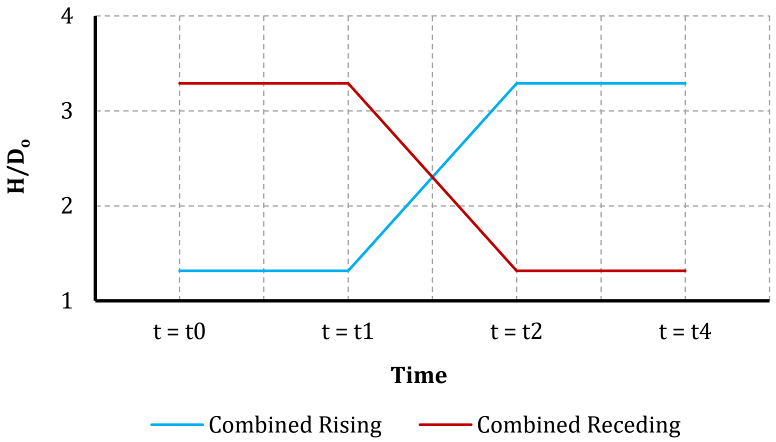

Fig. 2. Upstream water level change of the first part simulations.

The computational domain in the longitudinal direction is 100 cm from the upstream edge of the culvert and 40 cm from the downstream edge, with a width of 43.8 cm and a water depth of about 30 cm from the channel floor. For discretizing the computational domain, one mesh block was used (Fig. 3). The flow characteristic upstream of the culvert (x_{min}) was set to a certain depth and pressure. At the end of the domain, the flow will exit the computational domain (x_{max}) using the outlet boundary condition. The downstream boundary was defined as an outflow condition. This choice was justified by the fact that the flow at the outlet remained predominantly free-surface in all simulated scenarios, and no full submergence occurred. To prevent numerical instability and possible backflow effects, the computational domain was extended sufficiently downstream, and the velocity field near the outlet was monitored to ensure stable flow conditions. To simulate the water surface in contact with air (z_{max}), a symmetry condition was applied to simulate relative zero-pressure. All boundary conditions are presented in Table (1).

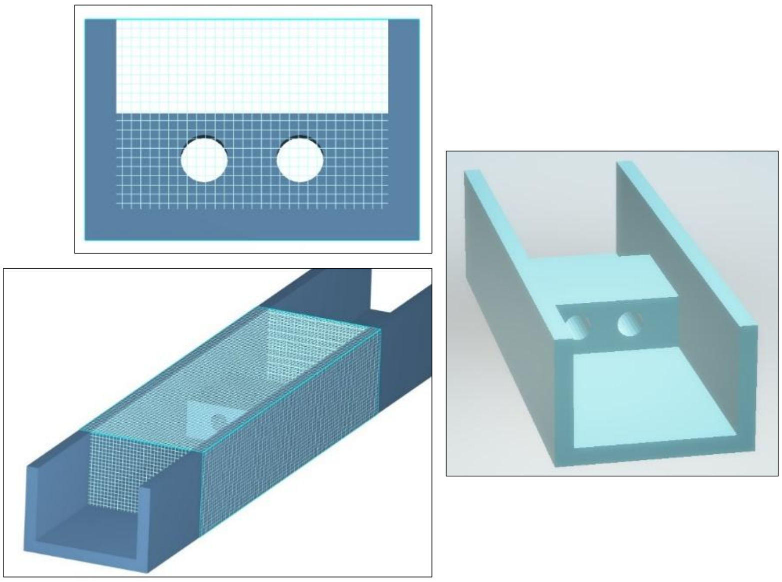

Fig. 3. Computational Grid.

Table 1. Boundary conditions in mesh blocks.

	Xmin	Xmax	Ymin	Ymax	Zmin	Zmax
Mesh Block	Specified Pressure	Outflow	Wall	Wall	Wall	Symmetry

The results are presented as dimensionless values according to standard design parameters [42]. The upstream water level (H) is normalized as H/D_o where D_o is the culvert diameter (0.076 m) and the dimensionless discharge Q^* is defined by $Q^* =$

$Q/\sqrt{g \times {D_o}^5}$.

3.1. Upstream water level rate sensitivity

As mentioned in the previous section and as shown in Fig. 2, to determine the hydraulic behavior of the culvert and how water drains downstream against variation in the upstream water level rate, H/D_o was increased from 1.3 to 3.3 (Rising-Models) and decreased from 3.3 to 1.3 (Receding-Models). The change in the upstream water level was implemented in the numerical model with different rates. For this purpose, to check the effect of this rate, H/D_o was changed from 3.3 to 1.3 and vice versa according to Table (2), and the effect of each of these conditions on the head-discharge curve was evaluated.

Table 2. Model characteristics to investigate the effect of upstream water level variation rate.

Receding Models					Rising Models				
Name	**t (s)**	**H (m)**	**H/Do**	**Rate (head (m)/s)**	**Name**	**t (s)**	**H (m)**	**H/Do**	**Rate (head (m)/s)**
	0	0.25	3.3			0	0.1	1.3	
CRE-1	30	0.25	3.3	-0.0100	**CRI-1**	30	0.1	1.3	0.0100
	45	0.1	1.3			45	0.25	3.3	
	0	0.25	3.3			0	0.1	1.3	
CRE-2	30	0.25	3.3	-0.0050	**CRI-2**	30	0.1	1.3	0.0050
	60	0.1	1.3			60	0.25	3.3	
	0	0.25	3.3			0	0.1	1.3	
CRE-3	30	0.25	3.3	-0.0033	**CRI-3**	30	0.1	1.3	0.0033
	75	0.1	1.3			75	0.25	3.3	
	0	0.25	3.3			0	0.1	1.3	
CRE-4	30	0.25	3.3	-0.0025	**CRI-4**	30	0.1	1.3	0.0025
	90	0.1	1.3			90	0.25	3.3	
	0	0.25	3.3			0	0.1	1.3	
CRE-5	30	0.25	3.3	-0.0020	**CRI-5**	30	0.1	1.3	0.0020
	105	0.1	1.3			105	0.25	3.3	

Fig. 4 shows the curves head-discharge changes for the receding and rising models. As seen in Fig. 4. a, CRE-2 to CRE-5 models exhibit consistency, but CRE-1 deviates from the others. Thus, receding models with rates slower than -0.0050 m/s (CRE-2 onward) show negligible rate dependency. Similarly, in Fig. 4. b, models CRI-2 to CRI-5 match each other, while CRI-1 diverges from the others. Therefore, rising models with rates below 0.0050 m/s (CRI-2 onward) are appropriate.

The deviation observed in the fastest rate cases (CRE-1 and CRI-1) can be attributed to physical flow behavior rather than numerical instability. At high rates of upstream water level variation, the flow does not have sufficient time to fully develop and adjust to changing boundary conditions. This results in a transient lag between head and discharge, reflecting the hysteretic nature of unsteady flow. Therefore, these deviations represent a real hydraulic phenomenon associated with flow inertia and turbulence effects.

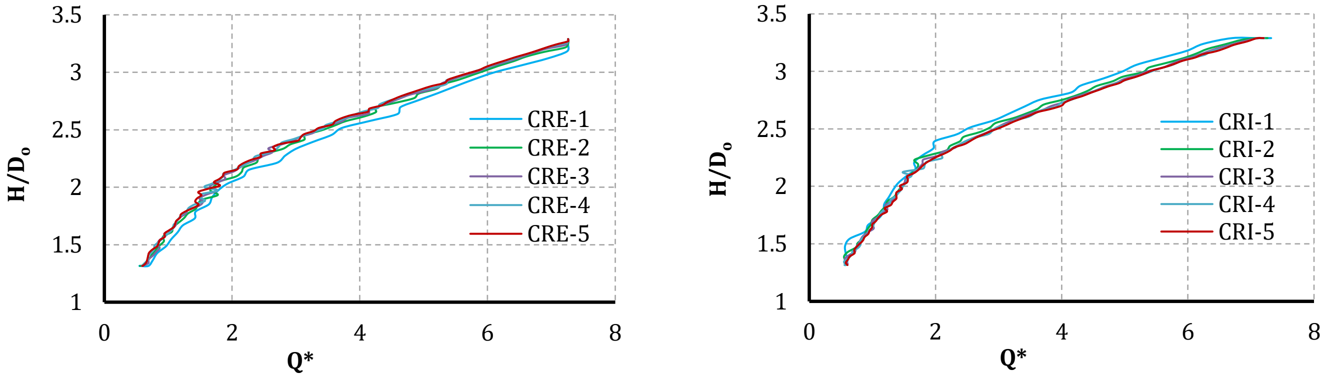

a) Receding models **b) Rising models**

Fig. 4. Head-discharge curves for different water level variation rate.

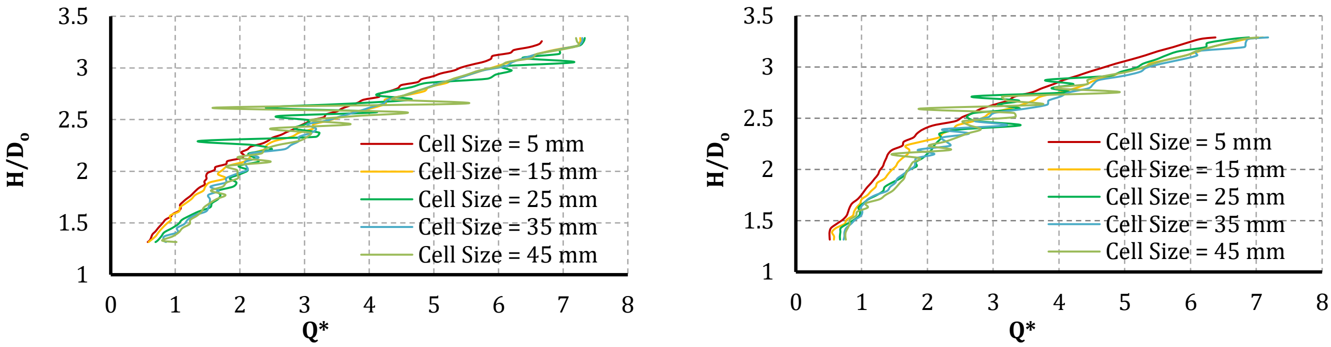

a) Receding models CRE-2 **b) Rising models CRI-2**

Fig. 5. Head-discharge curves for different cell sizes.

3.2. Mesh cell size sensitivity

To study the independence of the research results from the mesh cell size, both receding and rising models, including CRE-2 and CRI-2 models, with five different cell sizes in the range of 5 to 45 mm were simulated. In all cases, the head-discharge curve was considered as a criterion for selecting the optimal cell size. The effect of cell size on these curves' accuracy is shown in Fig. 5. The results show that the head-discharge curve for cell sizes of 25, 35, and 45 mm differs from the other two meshes in both receding and rising models, but there is a slight difference between the predicted head-discharge curve of cell sizes of 5 and 15 mm. Therefore, to reduce the simulation time, a 15 mm cell size is selected as the optimal mesh cell size.

3.3. Turbulence model study

To use a suitable turbulence model for predicting the turbulent flow in the culvert, the effect of applying different turbulence models, including RNG, *k-ε* and *k-ω* on the head-discharge curve was evaluated. For this purpose, the CRE-2 receding model and CRI-2 rising model with a cell size of 15 mm were simulated with three different turbulence models. In Fig. 6, the head-discharge curve for different turbulence models for receding and rising models is compared with the experimental results of Meselhe and Hebert [49]. The results show that all three turbulence models can predict the turbulent flow inside the culvert with high accuracy. Therefore, the RNG model was selected for the following models.

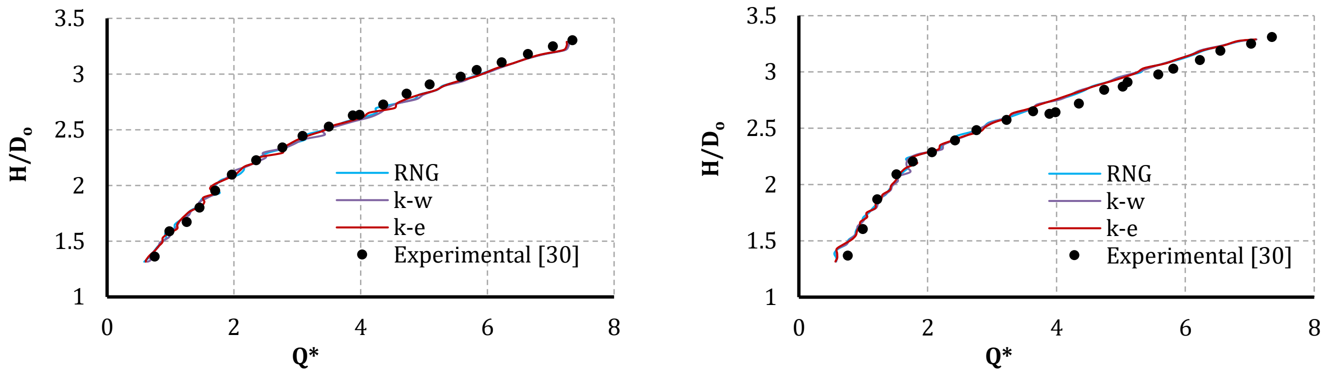

a) Receding model of CRE-2 **b) Rising model of CRI-2**

Fig. 6. Head-discharge curves for different turbulence models.

3.4. Numerical model validation

To validate the numerical model, the results of the present study are compared with the results of Meselhe and Hebert [49] experimental results. Fig. 6 compares the head-discharge curve in the present numerical model (RNG turbulence model) and Meselhe and Hebert [49] laboratory results, for receding and rising models, respectively. The results of these two figures show that the numerical model accurately predicts the head-discharge curve compared to the laboratory curve with excellent agreement. The percent error is 1.3% for the receding model and 2.3% for the rising model.

4. Results and discussion

In this section, the details of the head-discharge characteristics in the twin circular culvert will be investigated.

4.1. Combined receding and rising

Fig. 7 illustrates the flow field for the rising condition with $H/D_o = 3.3$. Qualitative analysis of the flow reveals that the maximum velocity occurs at the point where the flow impacts the downstream bed. Additionally, the flow passing over the culvert exhibits higher velocity at its intersection with the flow passing through the culvert, likely due to the greater free fall of the overtopping flow. Furthermore, the flow field observation indicates three rotational flow regions with negligible velocity, trapped in place. These three regions are located along the lateral sides, in the middle of the channel, and adjacent to the downstream side of the culvert.

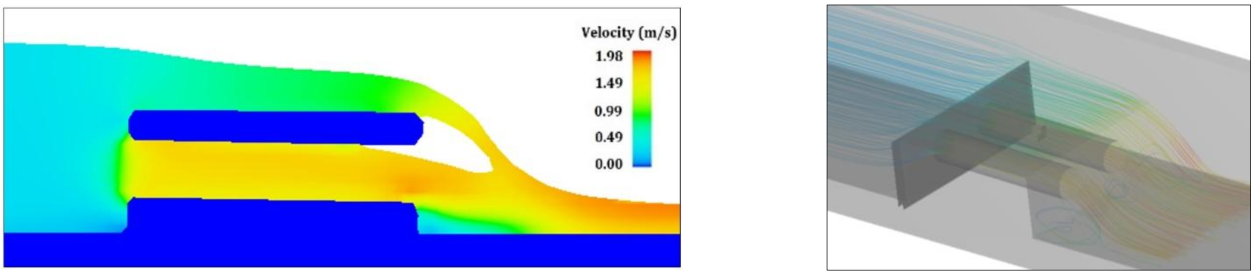

a) Longitudinal cross-section through the center of the culvert **b) Three-dimensional streamlines**

Fig. 7. Velocity field of the flow simultaneously passing through and over the culvert ($H/D_o = 3.3$).

Fig. 8. a shows the discharge passing through the culvert and over the culvert (culvert overtopping) during the rising of H/D_o from 1.3 to 3.3. As can be seen, when H/D_obetween 1.3 to about 2.3 ranges, the overtopping discharge is zero. The parameter of discharge per head ($Q^*/\left(\frac{H}{D_o}\right)$) passing through the culvert during the rising of H/D_o from 1.3 to 3.3 remains nearly constant at 1.573. Also, this parameter ($Q^*/\left(\frac{H}{D_o}\right)$) for discharge passing over the culvert is much higher than the discharge passing through the culvert. When H/D_o is higher than 2.3, this parameter is almost equal to 3.877. This is due to the free flow passing over the culvert and the greater width of the flow than through the culvert. Also, Fig. 8. b shows the percentage of discharge passing through the culvert structure and the flow passing over the culvert for different H/D_o for rising models. It can only be seen that near the $H/D_o =$ 2.3, the Q^* shows a slight fluctuation.

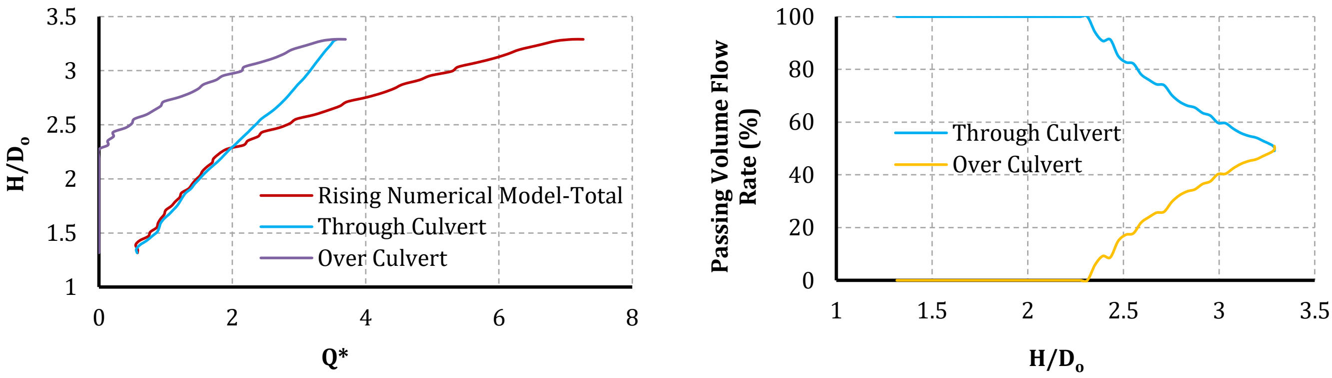

a) Head-Discharge **b) Discharge Percent**

Fig. 8. Discharge passing through and over the culvert in rising model.

Fig shows discharge passing through the culvert and over the culvert during the receding of H/D_o from 3.3 to 1.3. As can be seen, when H/D_o ranges from 1.3 to ~2, the discharge over the culvert is zero. The parameter of discharge per head ($Q^*/\left(\frac{H}{D_o}\right)$) passing through the culvert during the receding of H/D_o from 3.3 to 1.3 is almost constant and equals 1.639. Also, this parameter ($Q^*/\left(\frac{H}{D_o}\right)$) for discharge passing over the culvert is much higher than the discharge passing through the culvert. when H/D_o is higher than 2, this parameter is almost equal to 3.175. This is due to the free flow passing over the culvert and the greater width of the flow than through the culvert.

The results show that the discharge rate ($Q^*/\left(\frac{H}{D_o}\right)$) from inside the culvert in receding models (1.639) is higher than in rising models (1.639), while the discharge rate over the culvert in rising models (3.877) is higher than in receding models (3.175).

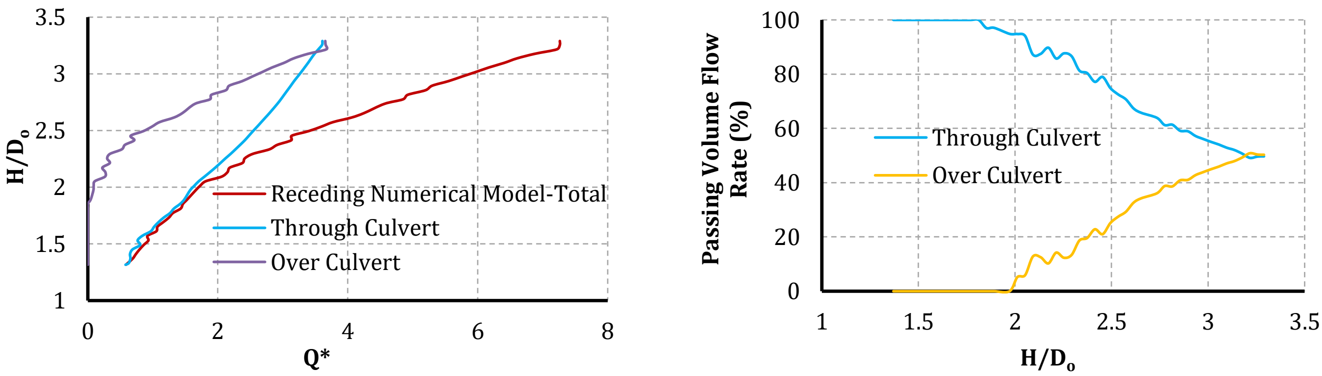

a) Head-Discharge **b) Discharge Percents**

Fig. 9. Discharge passing through and over the culvert in receding model.

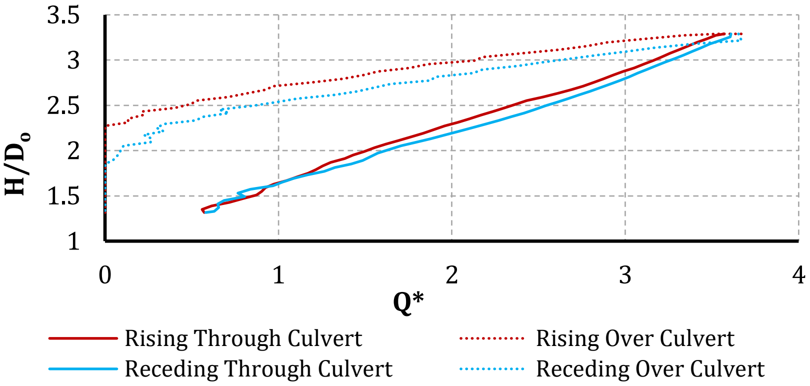

Fig. 10. Discharge passing through and over the culvert in receding and rising models.

In Fig. 10, the discharge changes over the culvert and through the culvert are shown simultaneously for the rising and receding models. It can be seen that the discharge passing through the culvert for the two models of rising and receding shows no significant difference, but the discharge passing over the culvert in the two mentioned models is completely different, and for the same heads, the receding model has a higher discharge.

4.2. Unsteady hydrograph

In this section, the effect of the unsteady flow on the hydraulic performance of the twin culvert was investigated. The upstream water level has both rising and receding limbs as shown in Fig. 10 (Upstream Head-Time curve). In the numerical model, the upstream water level was used to investigate discharge downstream of the culvert, as well as over and through the culvert.

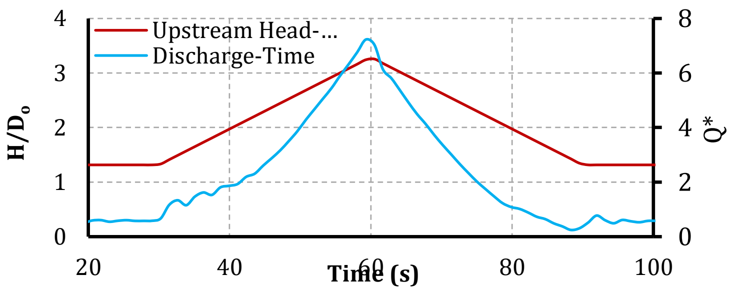

Fig. 11. Head-discharge curves for unsteady hydrograph including rising and receding limbs.

Fig. 11 shows the head-discharge curve versus time for the hydrograph. According to the figure, the rising limb of the discharge curve has a lower slope than the receding limb, and the discharge has reached the minimum in a shorter period of time. In the rising limb, it can be seen that from about time equal to 35 s, non-dimensional volume flow rate Q^* has reached 1.47 to 7 in about time equal to 60 s, showing the Q^* increasing in the rising limb is equal to 0.22, while, in the receding limb, it can be seen that from about time equal to 60 s, the Q^* has reached 7 to 1.48 in about time equal to 77 s, that show the approximate rate of outlet flow decreasing in the receding limb is equal to 0.32. The results indicate that, under the specific conditions of the present study, the discharge during the receding limb is approximately 1.5 times higher than during the rising limb. It should be noted that this ratio is dependent on the culvert geometry and hydrograph characteristics and may vary under different conditions. However, the general trend of higher discharge during the receding phase reflects the hysteretic behavior of unsteady flow in culverts.

In Fig. 12, the discharge passing percentage over the culvert and through the culvert is given for the unsteady hydrograph. For this purpose, this curve is presented in two separate sections for the rising limb and the receding limb. According to the figure, it can be seen that in the rising limb at depths close to the surface of the culvert, the passing percentages fluctuate greatly, while in the receding limb at $H/D_o < 2.4$, the discharge completely passes through the culvert.

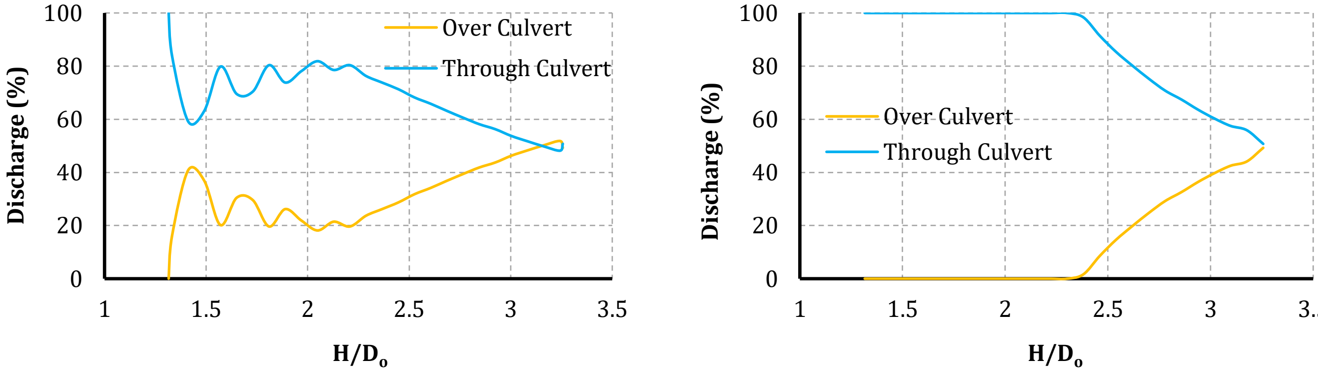

a) Rising limb **b) Receding limb**

Fig. 12. Passing discharge percent for unsteady hydrograph.

4.3. Data-driven modeling and machine learning analysis

In addition to the numerical simulations, a series of data-driven modeling techniques were applied to predict the discharge behavior of the twin circular culvert under various hydraulic conditions. The purpose of this complementary analysis was to evaluate the ability of machine learning algorithms to reproduce the complex, nonlinear relationship between the upstream water depth and the corresponding discharge, as presented in both numerical and laboratory data. The use of multiple machine learning algorithms was intended not only to evaluate predictive performance but also to compare different modeling approaches in capturing nonlinear hydraulic behavior. This comparative analysis helps identify the most reliable and robust model for practical applications. The dataset used for training and validation included upstream head values as input features and the measured or simulated discharge values as output targets. The models were trained and evaluated separately for rising and receding water levels to account for the hysteretic behavior of culvert flow. A total of eight algorithms with distinct learning paradigms were implemented using the Orange data mining platform, including Random Forest (RF), K-Nearest Neighbors (KNN), Decision Tree (Tree), Gradient Boosting (GB), Support Vector Machine (SVM), Linear Regression (LR), AdaBoost (AB), and Neural Network (NN). The choice of these algorithms was motivated by their ability to represent both linear and nonlinear mappings. Ensemble methods such as Random Forest, Gradient Boosting, and AdaBoost were included because of their high accuracy and robustness in regression problems, while the Neural Network model was incorporated to evaluate the potential of deep learning for capturing higher-order nonlinearities in the flow regime. Model performance was assessed using standard statistical indicators—mean squared error (MSE), root mean square error (RMSE), mean absolute error (MAE), mean absolute percentage error (MAPE), and coefficient of determination (R^2), to ensure consistent comparison.

The dataset consisted of 51 data points obtained from numerical simulations and 22 data points obtained from experimental measurements. The input parameter included the normalized upstream head (H/D_o), while the output variable was the dimensionless discharge. The data were divided into training and testing sets using an 80-20 split. In addition, k-fold cross-validation was applied to ensure robustness and avoid overfitting.

The results of the numerical dataset showed a clear dominance of ensemble-based algorithms. For the rising head condition, Gradient Boosting and AdaBoost achieved the best performance, with R^2 values of approximately 0.992 and RMSE around 0.176, indicating excellent agreement with the simulated discharges. KNN and Random Forest also exhibited strong performance ($R^2 > 0.988$), confirming their ability to generalize the underlying nonlinear trends. In contrast, Linear Regression yielded the lowest accuracy ($R^2 = 0.914$), reflecting the inadequacy of a linear model in representing the hydraulic relationship between head and discharge. During the receding phase, KNN, Gradient Boosting, and AdaBoost maintained superior predictive capability ($R^2 \approx 0.992$, RMSE ≈ 0.18), while the Random Forest model remained competitive with slightly higher error values. The overall numerical results confirmed that ensemble learning and local-instance-based methods can effectively capture the nonlinearities inherent in the CFD-based head–discharge relationship.

The results obtained from the experimental dataset followed a similar trend but with slightly larger errors due to unavoidable measurement uncertainties and physical variability. For the rising condition, the Neural Network achieved the best performance ($R^2 = 0.980$, RMSE = 0.284), demonstrating its capability to adapt to experimental noise while maintaining high predictive accuracy. Gradient Boosting and AdaBoost ranked second and third ($R^2 \approx 0.948$), proving again the reliability of boosting-based ensembles in hydraulic prediction. The weakest model was the single Decision Tree ($R^2 = 0.848$), which tends to overfit limited data. For the receding experimental dataset, the Neural Network once more outperformed all other algorithms ($R^2 = 0.985$, RMSE = 0.249), followed closely by Gradient Boosting and AdaBoost ($R^2 \approx 0.969$). These outcomes highlight that data-driven approaches, particularly those with adaptive or ensemble learning mechanisms, can successfully approximate the nonlinear discharge behavior even in laboratory environments.

Comparing the performance between rising and receding conditions reveals that the models generally achieved higher accuracy in the receding phase. This can be attributed to the more stable hydraulic regime during flow recession, where turbulence intensity and free-surface fluctuations are less pronounced. Consequently, the receding limb provides smoother relationships between head and discharge, allowing machine learning models to fit the data more consistently. This behavior mirrors the hysteretic characteristics identified in the CFD simulations, where discharge during the receding limb was higher for the same head values compared to the rising limb. The close agreement between these two modeling approaches demonstrates that machine learning can not only complement but also validate numerical simulation outcomes. The difference in model performance between numerical and experimental datasets can be explained by the intrinsic characteristics of the data and the learning mechanisms of the algorithms. The experimental dataset contains measurement uncertainties and noise, which makes flexible models such as Neural Networks more suitable due to their ability to capture complex nonlinear patterns and generalize under noisy conditions. In contrast, the numerical dataset is smoother and more structured, allowing ensemble methods such as Gradient Boosting to achieve higher accuracy by effectively learning precise relationships without being affected by noise. This highlights the importance of selecting machine learning models based on data characteristics. This behavior also suggests that Neural Networks can implicitly act as noise-tolerant models, effectively reducing the influence of experimental uncertainties during the learning process.

The quantitative comparison of models' performance for each condition is presented in Tables 3 and 4. The statistical performance metrics presented in Tables 3 and 4 correspond to the testing dataset.

Table 3. Statistical evaluation metrics for the numerical simulations.

	Rising					Receding				
Model	**MSE**	**RMSE**	**MAE**	**MAPE**	**R^2**	**MSE**	**RMSE**	**MAE**	**MAPE**	**R^2**
Random Forest	0.044	0.210	0.144	6.061	0.988	0.105	0.324	0.262	9.540	0.976
kNN	0.043	0.208	0.128	5.410	0.989	0.059	0.243	0.136	7.048	0.987
Tree	0.100	0.316	0.236	9.305	0.974	0.048	0.218	0.162	6.860	0.989
Gradient Boosting	0.031	0.176	0.134	4.877	0.992	0.075	0.274	0.209	7.738	0.983
SVM	0.069	0.262	0.134	6.598	0.982	0.224	0.474	0.400	23.794	0.949
Linear Regression	0.329	0.573	0.483	31.233	0.914	0.033	0.182	0.125	5.070	0.992
AdaBoost	0.031	0.176	0.132	4.724	0.992	0.034	0.185	0.157	6.003	0.992
Neural Network	0.121	0.348	0.265	11.370	0.968	0.034	0.183	0.154	5.832	0.992

Table 4. Statistical evaluation metrics for the experimental simulations.

	Rising					Receding				
Model	**MSE**	**RMSE**	**MAE**	**MAPE**	**R^2**	**MSE**	**RMSE**	**MAE**	**MAPE**	**R^2**
Random Forest	0.379	0.615	0.538	22.518	0.904	0.268	0.518	0.356	16.477	0.936
kNN	0.370	0.609	0.438	19.439	0.907	0.229	0.479	0.318	12.732	0.945
Tree	0.603	0.777	0.687	24.221	0.848	0.417	0.646	0.516	16.087	0.900
Gradient Boosting	0.204	0.451	0.407	13.870	0.949	0.128	0.358	0.334	11.970	0.969
SVM	0.439	0.662	0.384	18.957	0.889	0.325	0.570	0.307	14.185	0.922
Linear Regression	0.509	0.714	0.537	30.052	0.872	0.248	0.498	0.412	19.420	0.941
AdaBoost	0.207	0.455	0.411	13.931	0.948	0.128	0.358	0.334	11.969	0.969
Neural Network	0.081	0.284	0.242	8.484	0.980	0.062	0.249	0.173	4.851	0.985

Table 3 lists the statistical evaluation metrics for the rising and receding datasets obtained from the numerical simulations, while Table 4 provides the corresponding results derived from the laboratory experiments. In both tables, the ensemble-based and neural network models consistently outperform traditional algorithms, confirming their ability to represent the strongly nonlinear hydraulic processes involved in culvert flow.

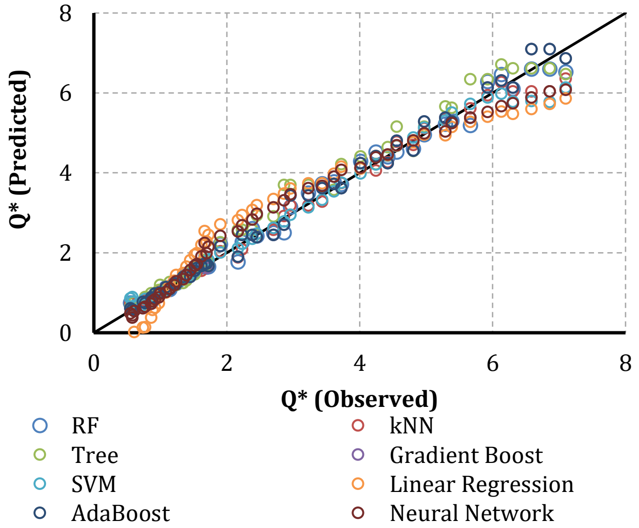

a) Rising model

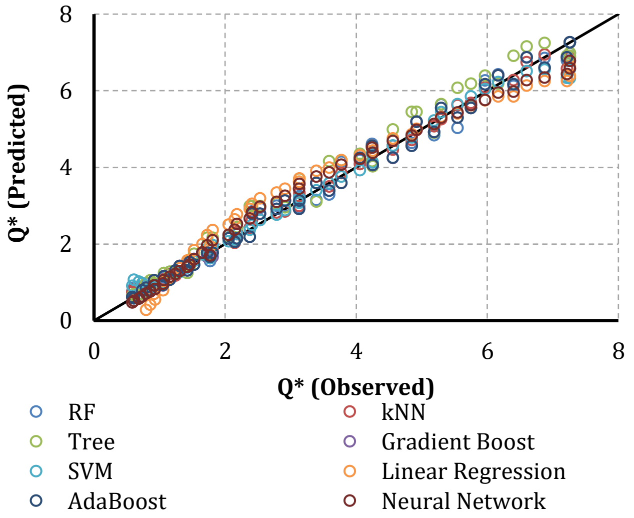

b) Receding model

Fig. 13. Comparison between observed and predicted discharge values for numerical datasets using different machine learning models.

Fig. 13 presents a comparison between the observed laboratory discharges and those predicted by various machine learning models. The Neural Network and ensemble models (Gradient Boosting and AdaBoost) show the best alignment with the 1:1 line, confirming their capability to generalize experimental flow behavior under both rising and receding conditions.

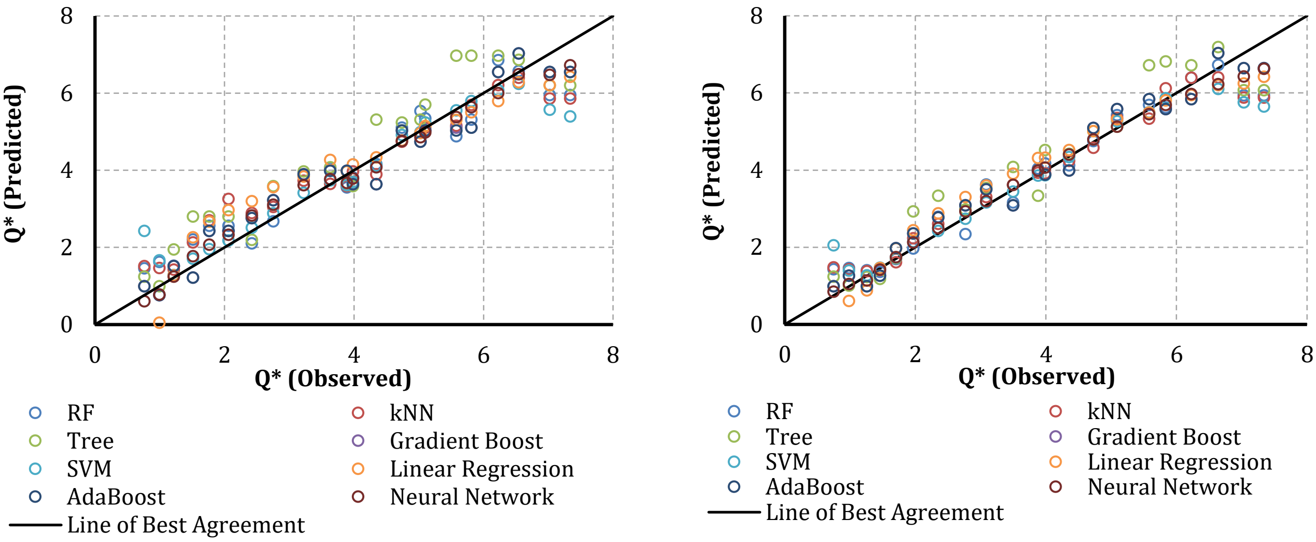

a) Rising model **b) Receding model**

Fig. 14. Comparison between observed and predicted discharge values for experimental datasets using different machine learning models.

Fig. 14 illustrates the relationship between the observed (Flow-3D simulated) and predicted discharge values for both rising and receding conditions. The close clustering of points around the 1:1 reference line indicates that ensemble and neighborhood-based models (particularly Gradient Boosting, AdaBoost, and KNN) provide the highest accuracy in reproducing the numerical discharge behavior of twin circular culverts.

Overall, the data-driven modeling results demonstrate that machine-learning approaches can effectively complement physics-based CFD simulations. The strong consistency between the numerical, experimental, and ML-based predictions supports the feasibility of hybrid modeling frameworks in hydraulic engineering. Such frameworks can significantly reduce computational time while maintaining high accuracy, offering a reliable tool for discharge estimation and culvert design optimization under varying flow conditions. The performance of the machine learning models in this study is consistent with previous research in hydraulic engineering, where ensemble methods and neural networks have shown superior capability in capturing nonlinear flow behavior. Compared to earlier studies, the achieved accuracy (R^2 up to 0.99) indicates a high level of reliability in predicting culvert discharge under unsteady flow conditions.

5. Summary and conclusion

This research comprehensively analyzed the hydraulic behavior of twin circular culverts under unsteady flow conditions using numerical simulations complemented by data-driven modeling. The study examined the effects of rising and receding inlet flows, upstream water level variations, and unsteady hydrographs on culvert discharge and flow distribution. Numerical modeling was performed by solving the Reynolds-Averaged Navier–Stokes (RANS) equations for incompressible flow with the RNG k–ε turbulence model, providing reliable predictions of turbulent flow fields and discharge characteristics. Validation against laboratory data confirmed excellent agreement, ensuring that the chosen turbulence model and computational setup accurately captured the observed physical flow features. Sensitivity analyses on mesh resolution, turbulence modeling, and upstream water level variation rates further ensured the robustness and convergence of the numerical results.

The numerical simulations revealed that through-flow discharge during the rising phase (H/Do = 1.3–3.3) remained nearly constant at approximately 1.573 $m^3/s/m$, while overtopping discharge increased substantially after the upstream head exceeded 2.3, reaching nearly 3.877 $m^3/s/m$. In the receding phase, through-flow discharge stayed roughly constant at 1.639 $m^3/s/m$, whereas overtopping discharge reached around 3.175 $m^3/s/m$ before the head ratio fell below 2. Overall, through-flow discharge differed only slightly between rising and receding stages (≈4%), but overtopping discharge showed a significant difference of ≈22%. The rising limb of the unsteady hydrograph exhibited a lower slope than the receding limb, indicating that outflow during recession was about 1.5 times higher. At shallow depths near the culvert crown, flow distribution fluctuated considerably during the rising limb, while for H/Do < 2.4 in the receding limb, nearly all discharge passed through the culvert.

To complement the numerical results, a data-driven modeling framework using machine learning algorithms was developed to evaluate whether AI methods could replicate the nonlinear hydraulic behavior observed in CFD and laboratory data. Eight algorithms were tested using the Orange data mining platform, including Random Forest (RF), K-Nearest Neighbors (KNN), Decision Tree, Gradient Boosting (GB), Support Vector Machine (SVM), Linear Regression (LR), AdaBoost (AB), and Neural Network (NN). Model performance was evaluated separately for rising and receding phases using R^2, RMSE, MAE, and MAPE metrics. The results indicated that ensemble-based models and neural networks effectively captured the complex discharge–head relationships. For numerical data, Gradient Boosting and AdaBoost achieved the highest accuracy ($R^2 \approx 0.992$, RMSE ≈ 0.176), followed by KNN and Random Forest, while Linear Regression performed weakest, confirming the strong nonlinearity of the system. For experimental data, the Neural Network achieved the best accuracy ($R^2 = 0.980$ for rising, $R^2 = 0.985$ for receding), closely followed by Gradient Boosting and AdaBoost. In both datasets, models performed better during the receding phase, likely due to more stable flow conditions.

The integration of numerical and data-driven approaches provides complementary insights into culvert hydraulics: CFD models offer detailed flow visualization and physical interpretation, while machine learning enables rapid discharge prediction with low computational cost once trained. The strong agreement among experimental, numerical, and AI-based results confirms that hybrid modeling can enhance predictive accuracy, improve design efficiency, and serve as a reliable tool for assessing flow transitions, discharge hysteresis, and unsteady hydraulic responses in culverts and similar drainage structures.

Statements & Declarations

Author contributions

Ehsan Behnamtalab: Conceptualization, Investigation, Methodology, Writing - Review & Editing.

Mohsen Behnamtalab: Formal analysis, Validation, Writing - Original Draft, Writing - Review & Editing.

Funding

The authors received no financial support for the research, authorship, and/or publication of this article.

Data availability

The data presented in this study will be available on request from the corresponding author.

Declarations

The authors declare no conflict of interest.

References

[1] Norman, J. M., Houghtalen, R.J. and Johnston, W.J Hydraulic design of highway culverts. Second ed. Washington, DC (US): FHWA; 2001.

[2] Chang, H.-K., Tan, Y.-C., Lai, J.-S., Pan, T.-Y., Liu, T.-M., Tung, C.-P. Improvement of a drainage system for flood management with assessment of the potential effects of climate change. Hydrological Sciences Journal, 2013; 58: 1581–1597. doi:10.1080/02626667.2013.836276.

[3] Mamo, T. G. Evaluation of the Potential Impact of Rainfall Intensity Variation due to Climate Change on Existing Drainage Infrastructure. Journal of Irrigation and Drainage Engineering, 2015; 141: 05015002. doi:10.1061/(ASCE)IR.1943-4774.0000887.

[4] Pereira, M., Fernandes, L., Macário, E., Gaspar, S., Pinto, J. Climate Change Impacts in the Design of Drainage Systems: Case Study of Portugal. Journal of Irrigation and Drainage Engineering, 2015; 141: 05014009. doi:10.1061/(ASCE)IR.1943-4774.0000788.

[5] Todeschini, S. Trends in long daily rainfall series of Lombardia (northern Italy) affecting urban stormwater control. International Journal of Climatology, 2012; 32: 900–919. doi:10.1002/joc.2313.

[6] Wang, S., Feng, Z., Guo, C., Wei, J., Zhao, R. Research on the method of identifying vertical earth pressure of hinged prefabricated culvert box culvert on the top slab. Scientific Reports, 2024; 14: 18844. doi:10.1038/s41598-024-69893-4.

[7] Gao, C., Elzarka, H. The use of decision tree based predictive models for improving the culvert inspection process. Advanced Engineering Informatics, 2021; 47: 101203. doi:10.1016/j.aei.2020.101203.

[8] Othman, K., Kavianpour, M., Amini, A., Aminpour, Y. A state-of-the-art review of physical modeling of scouring at the culvert outlet. ISH Journal of Hydraulic Engineering, 2024; 30: 1–8. doi:10.1080/09715010.2024.2340626.

[9] Ahmed, K. O., Kavianpour, M. R., Amini, A., Aminpour, Y. Physical modeling of the effect of shape, blockage, and flow variability on scour in culvert outlets. PLoS One, 2024; 19: e0306252. doi:10.1371/journal.pone.0306252.

[10] Dasika, B. New Approach to Design of Culverts. Journal of Irrigation and Drainage Engineering, 1995; 121: 261–264. doi:10.1061/(ASCE)0733-9437(1995)121:3(261).

[11] Montes, J. S., Dasika, B. Discussion and Closure: New Approach to Design of Culverts. Journal of Irrigation and Drainage Engineering, 1997; 123: 71–72. doi:10.1061/(ASCE)0733-9437(1997)123:1(71).

[12] Hager, W. H., Giudice, G. D. Generalized Culvert Design Diagram. Journal of Irrigation and Drainage Engineering, 1998; 124: 271–274. doi:10.1061/(ASCE)0733-9437(1998)124:5(271).

[13] Johnson, P., Brown, E. Stream Assessment for Multicell Culvert Use. Journal of Hydraulic Engineering-asce - J HYDRAUL ENG-ASCE, 2000; 126: 381–386. doi:10.1061/(ASCE)0733-9429(2000)126:5(381).

[14] Ansar, M., Alexis, A., Damisse, E. Flow computations at Kissimmee River gated structures: A comparative study. South Florida (FL): Hydrology and Hydraulics Dept; 2002. Report No.:

[15] Lee, K. S., Jin, R. S. Development of program for box culverts design. In: Proceedings of the 35th Conference; 2003; South Korea. p. 2686–2689.

[16] Ku, H. J., Jun, K. S. Development of culvert design model. In: Proceedings of Korea Water Resources Association Conference; 2008; South Korea. p. 645–649.

[17] Richmond, M. C., Deng, Z., Guensch, G. R., Tritico, H., Pearson, W. H. Mean flow and turbulence characteristics of a full-scale spiral corrugated culvert with implications for fish passage. Ecological Engineering, 2007; 30: 333–340. doi:10.1016/j.ecoleng.2007.04.011.

[18] Chanson, H. Hydraulics of open channel flow. Second ed. London (UK): Elsevier; 2004. doi:10.1016/B978-0-7506-5978-9.X5000-4.

[19] Chow, V. T. Open-Channel Hydraulic. First ed. Columbus (OH): McGraw-Hill Education; 1959.

[20] Yoo, D.-H., Lee, S. Direct determination of the width or the height for a box culvert applying dimensionless equations. KSCE Journal of Civil Engineering, 2012; 16: 1302–1307. doi:10.1007/s12205-012-1695-1.

[21] Kang, M. S., Koo, J. H., Chun, J. A., Her, Y. G., Park, S. W., Yoo, K. Design of drainage culverts considering critical storm duration. Biosystems Engineering, 2009; 104: 425–434. doi:10.1016/j.biosystemseng.2009.07.004.

[22] May, L. W. Hydraulic Design Handbook. First ed. Columbus (OH): McGraw-Hill Education; 1999.

[23] Schall, J. D., Thompson, P. L., Zerges, S. M., Kilgore, R. T., Morris, J. L. Hydraulic Design of Highway Culverts. Third ed. Washington, DC (US): FHWA; 2012.

[24] French, J. L. First Progress Report on Hydraulics of Short Pipes: Hydraulic Characteristics of Commonly Used Pipe Entrances. Washington, DC (US): U.S. Dept. of Commerce, National Bureau of Standards; 1955. Report No.: NBS Report no. 4444.

[25] French, J. L. Second Progress Report on Hydraulics of Culverts: Pressure and Resistance Characteristics of a Model Pipe Culvert. Washington, DC (US): U.S. Dept. of Commerce, National Bureau of Standards; 1956. Report No.: NBS Report no. 4911.

[26] French, J. L. Third Progress Report on Hydraulics of Culverts: Effect of Approach Channel Characteristics on Model Pipe Culvert Operation. Washington, DC (US): U.S. Dept. of Commerce, National Bureau of Standards; 1957. Report No.:

[27] French, J. L. Fourth Progress Report on Hydraulics of Culverts: Hydraulics of improved Inlet Structures for Pipe Culverts. Washington, DC (US): U.S. Dept. of Commerce, National Bureau of Standards; 1961. Report No.: NBS Report no. 7178.

[28] French, J. L. Sixth progress report on hydraulics of culverts: Tapered box culvert inlets. Washington, DC (US): U.S. Dept. of Commerce, National Bureau of Standards; 1966. Report No.: NBS Report no. 9355.

[29] French, J. L., Bossy, H. G. Seventh progress report on hydraulics of culverts: Tapered box culvert inlets with fall concentration in the inlet structure. Washington, DC (US): U.S. Dept. of Commerce, National Bureau of Standards; 1967. Report No.: NBS Report no. 9528.

[30] Lyn, D., Dey, S., Saksena, S., Merwade, V. Culvert versus Bridge Hydraulics for Larger-Span or Short Culverts. Journal of Hydraulic Engineering, 2024; 150: 04024002. doi:10.1061/JHEND8.HYENG-13650.

[31] Bodhaine, G. L. Measurement of peak discharge at culverts by indirect methods. Washington, DC (US): US Government Printing Office; 1968. Report No.: 03-A3.

[32] Aly, A. M. Machine Learning Reshaping Computational Fluid Dynamics: A Paradigm Shift in Accuracy and Speed. Fluids, 2025; 10: 275. doi:10.3390/fluids10100275.

[33] Mao, R., Lan, Y., Liang, L., Yu, T., Mu, M., Leng, W., Long, Z. Rapid CFD Prediction Based on Machine Learning Surrogate Model in Built Environment: A Review. Fluids, 2025; 10: 193. doi:10.3390/fluids10080193.

[34] Nie, Y., Yu, K. H., Wang, Y., Liu, P. Applications of machine learning and deep learning in hydrology from a bibliometric perspective: a comprehensive review. Discover Artificial Intelligence, 2025; 5: 242. doi:10.1007/s44163-025-00471-x.

[35] Jafari, S. M., Zahiri, A. R., Bozorg Hadad, O., Mohammad Rezapour Tabari, M. A hybrid of six soft models based on ANFIS for pipe failure rate forecasting and uncertainty analysis: a case study of Gorgan city water distribution network. Soft Computing, 2021; 25: 7459–7478. doi:10.1007/s00500-021-05706-4.

[36] Tabari, M. M. R., Sanayei, H. R. Z. Prediction of the intermediate block displacement of the dam crest using artificial neural network and support vector regression models. Soft Computing, 2019; 23: 9629–9645. doi:10.1007/s00500-018-3528-8.

[37] Qin, Y., Su, C., Chu, D., Zhang, J., Song, J. A Review of Application of Machine Learning in Storm Surge Problems. Journal of Marine Science and Engineering, 2023; 11: 1729. doi:10.3390/jmse11091729.

[38] Habib, M. A., Abolfathi, S., O'Sullivan, J. J., Salauddin, M. Efficient data-driven machine learning models for scour depth predictions at sloping sea defences. Frontiers in Built Environment, 2024; Volume 10 - 2024: doi:10.3389/fbuil.2024.1343398.

[39] Shah, S. A., Jehanzaib, M., Yoo, J., Hong, S., Kim, T.-W. Investigation of the Effects of Climate Variability, Anthropogenic Activities, and Climate Change on Streamflow Using Multi-Model Ensembles. Water, 2022; 14: 512. doi:10.3390/w14040512.

[40] Masoumi, F., Jorabloo, M., Shobeyri, G. Optimizing Reservoir Operations with Reinforcement Learning: A Data-Driven Framework. Civil Engineering and Applied Solutions, 2025; 1: 56–67. doi:10.22080/ceas.2025.29738.1032.

[41] Rodrigues, D. T., Santos e Silva, C. M., dos Reis, J. S., Palharini, R. S. A., Cabral Júnior, J. B., da Silva, H. J. F., Mutti, P. R., Bezerra, B. G., Gonçalves, W. A. Evaluation of the Integrated Multi-SatellitE Retrievals for the Global Precipitation Measurement (IMERG) Product in the São Francisco Basin (Brazil). Water, 2021; 13: 2714. doi:10.3390/w13192714.

[42] Židek, K., Piteľ, J., Balog, M., Hošovský, A., Hladký, V., Lazorík, P., Iakovets, A., Demčák, J. CNN Training Using 3D Virtual Models for Assisted Assembly with Mixed Reality and Collaborative Robots. Applied Sciences, 2021; 11: 4269. doi:10.3390/app11094269.

[43] Anderson, J. D., & Wendt, J. Computational fluid dynamics. ed. New York (NY): McGraw-hill; 1995.

[44] Hirt, C. W., Nichols, B. D. Volume of fluid (VOF) method for the dynamics of free boundaries. Journal of Computational Physics, 1981; 39: 201–225. doi:10.1016/0021-9991(81)90145-5.

[45] White, F. M., Majdalani, J. Viscous fluid flow. Fourth ed. New York (NY): McGraw-Hill; 2006.

[46] Santa Fe. Incorporated: FLOW-3D User's Manual Version 9.3. New Mexico (NM): 2008.

[47] Hirt, C. W., Sicilian, J. M. A porosity technique for the definition of obstacles in rectangular cell meshes. In: International Conference on Numerical Ship Hydrodynamics, 4th; 1985; Washington, DC (US). p. 19.

[48] Hirt, C. W. T. CFD-101: The Basics of Computational Fluid Dynamics Modeling, FLOW-3D Manual, Flow Science Press, Flow Science, Inc. 2011. https://www.flow3d.com/resources/cfd-101/.

[49] Meselhe, E., Hebert, K. Laboratory Measurements of Flow through Culverts. Journal of Hydraulic Engineering-asce - J HYDRAUL ENG-ASCE, 2007; 133: 973–976. doi:10.1061/(ASCE)0733-9429(2007)133:8(973).

Civil Engineering and Applied Solutions

Research Article

journal homepage: ceas.journals.umz.ac.ir

CEAS Civil Engineering and Applied Solutions

Finite Element Investigation of Stiffened Beam-Only Connected Steel Plate Shear Walls under Cyclic Loading

Zeinab Meghdadi [a*], Mohammad Shabanlou [a], Massood Mofid [a]

[a] *Department of Civil Engineering, Sharif University of Technology, Tehran, Iran*

A R T I C L E I N F O

Article history:

Received 07 February 2026

Revised 29 April 2026

Accepted 06 June 2026

Available online 01 January 2027

Keywords:

Steel plate shear wall

Stiffener

Nonlinear analysis

Finite element method

Cyclic behavior

Dissipated energy

A B S T R A C T

This study investigates a novel type of steel plate shear wall (SPSW) system in which the infill plate is detached from the boundary columns and reinforced using side, horizontal, or cross stiffeners. Although conventional SPSW systems offer several advantages, their main drawback is the requirement for large column sections due to the significant tension field forces developed in the infill plate after buckling. According to the capacity design concept, boundary columns must resist these forces to prevent the formation of plastic hinges along the column height. In recent years, the concept of separating the steel plate from the boundary columns has been proposed to mitigate these demands. In this study, the behavior of stiffened beam-only connected steel plate shear walls (BO SPSWs) is investigated using finite element analysis. The effects of stiffener arrangement, stiffener cross section, stiffener dimensions, and web plate thickness are examined. The numerical results demonstrate stable cyclic responses with no sudden strength degradation, indicating the ductile and reliable behavior of the proposed system. For configurations with side, horizontal, and cross stiffeners, tension fields develop within the steel plate, forming between the stiffeners and boundary beams and within the resulting subpanels. Among the investigated stiffener sections, T-shaped stiffeners provide superior structural performance. Furthermore, increasing the stiffener dimensions and the web plate thickness leads to higher ultimate strength and improved energy dissipation capacity.

How to cite this article: Meghdadi, Z., Shabanlou, M. Mofid, M. Finite Element Investigation of Stiffened Beam-Only Connected Steel Plate Shear Walls under Cyclic Loading. Civil Engineering and Applied Solutions. 2027; 3(1): 131–145. doi:10.22080/ceas.2026.31223.1077.

1. Introduction

In recent decades, the Steel Plate Shear Wall (SPSW) system has become one of the main lateral load-resisting systems in modern construction projects due to its inherent high stiffness, ductility, and redundancy, as well as stable cyclic behavior. While unstiffened SPSWs are more prevalent in the United States, stiffened SPSWs are mainly preferred in Japan, located in a high seismic area [1, 2]. Compared to concrete shear walls, this system is more easily erected and occupies less space, which makes it suitable for architectural purposes. Despite the mentioned advantages, the main drawback of this system is the large column sections needed for resisting the lateral forces imposed on the boundary columns resulting from the tension field formed in the steel plate. In addition, the section of the column depends on the thickness of the web plate, making it hard to satisfy the drift demands [3, 4].

Elgaaly et al. [5] performed cyclic tests on six unstiffened SPSW systems. The results showed that the behavior of an unstiffened SPSW system with thin and thick web plates is mainly governed by the yielding of the plates and columns, respectively. Ghosh et al. [6]proposed a performance-based design framework for unstiffened SPSW systems based on inelastic drift demands by performing a test on a four-story building. The cyclic tests of four two-story narrow SPSWs performed by Li et al. [7], Li et al. [8]

* Corresponding author.
E-mail addresses: zeinab.meghdadi@sharif.edu (Z. Meghdadi).

https://doi.org/10.22080/ceas.2026.31223.1077

showed that the capacity design method could guarantee the formation of plastic hinges at the bottom of the first-story column.

Numerous solutions have been proposed to decrease or eliminate the tension field forces imposed on boundary columns. For instance, Roberts and Sabouri-Ghomi [9] were the first to investigate the behavior of perforated steel shear panels by performing a series of quasi-static experiments on steel shear panels with circular openings in the center of the panel. The results showed good s-shape hysteretic behavior with satisfying ductility. Purba and Bruneau [10] conducted finite element monotonic pushover analyses to study the behavior of perforated SPSWs with multiple circular openings in a regular pattern. As a result, they suggested a formulation for estimating the shear strength of this system as a function of perforation diameter, the distance between perforations, and the shear strength of the solid panel. Chan et al. [11] recommended using perforated steel web plates to reduce the forces imposed on the boundary elements. Valizadeh et al. [12]studied the behavior of perforated SPSWs by performing experiments on eight one-story, one-bay specimens. Bahrebar et al. [13]investigated the behavior of curved-corrugated SPSWs with perforations by conducting nonlinear finite element analysis on 128 models. Ahmad Khan and Srivastava [14] have comprehensively studied the effect of different shapes, sizes, and locations of openings in unstiffened SPSWs by performing finite element analyses on 98 models.

Another alternative for reducing tension field forces found in the steel plate is to use Low Yield Steel (LYS) for web plates. Vian et al. [15] conducted four experiments on LYS SPSW specimens in which two of the panels were solid, and the other two were perforated. The results showed that the LYS web plate could be used to efficiently design boundary elements. Chen and Jhang [16] proposed a design method for LYS SPSWs by performing cyclic tests on five specimens considering the beam-to-column connections detailing and the width-to-thickness ratio of steel plates.

For the main purpose of postponing the buckling of the infill plate, the installation of concrete panels has been proposed. Astaneh-Asl [17] presented a report on seismic behavior and design of steel plate shear walls covered by reinforced concrete panels. Zhao and Astaneh-Asl [18] performed cyclic tests on three-story specimens of composite SPSW systems. The concrete panels were bolted to the steel web plates with a gap between the concrete panels and boundary elements, which reacted adequately ductile and exhibited stable cyclic behavior. Arabzadeh et al. [19] experimentally studied one-story and three-story specimens. They found that the bolt spacing to plate thickness ratio is positively correlated with system ductility, while the plate yield point is negatively correlated with this ratio.

Also, using corrugated steel plates not only postpones the buckling of the infill plate but also provides more energy dissipation capacity. Emami and Mofid [20], Emami et al. [21] conducted a series of experimental studies on unstiffened and trapezoidally corrugated SPSWs. They showed that although the ultimate strength of the unstiffened SPSW is higher than that of corrugated SPSWs, the energy dissipation capacity of corrugated SPSWs is much greater. Farzampour et al. [22] studied the behavior of corrugated SPSWs with and without openings by performing finite element analysis on 540 numerical models that resulted in proposing an ultimate strength prediction procedure. Hosseinzadeh et al. [23] studied the effect of the trapezoidal plate angle on the performance of corrugated SPSW. The results showed that the stiffness and energy dissipation of the corrugated SPSW are adverse to the trapezoidal plate angle.

Another solution for preventing the web plates from premature elastic buckling is installing stiffeners on either one face or both faces of the web plate. Using more stiffeners results in higher energy dissipation capacity. In addition, stiffeners reduce out-of-plane deformation of web plates and prevent global buckling, leading to extensive yielding in the web plate. Alinia [24] investigated the behavior of stiffened steel plates by conducting 1200 finite element analyses. The results showed that the optimum arrangement of stiffeners in fully connected SPSWs is determined such that the critical stress of subpanels does not exceed the yield stress. Besides, the stiffeners are most effective when they change the global buckling mode of SPSW to local buckling mode in subpanels. Alinia and Dastfan [25] numerically investigated the cyclic behavior of stiffened SPSWs and figured out that while unstiffened SPSWs have high ductility, the stiffened SPSWs have high energy dissipation capacity and suggested an optimized stiffening ratio. Alinia and Sarraf Shirazi [26] also proposed procedures for designing stiffeners with optimum dimensions. Sabouri-Ghomi and Sajjadi [27] experimentally studied the behavior of SPSWs and verified the plate-frame interaction theory.

Guo et al. [28] investigated the effects of joint properties classified as hinged, rigid, and semi-rigid connections on the behavior of unstiffened and stiffened SPSWs. It is concluded that the semi-rigid connections perform very well within the frame of SPSW systems. Also, Guo et al. [29] experimentally investigated the behavior of cross-stiffened SPSWs with semi-rigid frame connections, which benefit from a much easier type of construction. The specimens showed highly ductile behavior and great energy dissipation capacity. Ma et al. [30] presented a novel buckling-restrained multi-stiffened low-yield-point SPSW. The experimental results indicated that the suggested system complies with the limitations of available design codes.

Several studies have been carried out to eliminate the tension field forces imposed on boundary columns by separating the web plate from the vertical boundary elements. The survey of Beam-Only connected Steel Plate Shear Walls (BO-SPSW) began in the early 1990s by Xue and Lu [31]. Choi and Park determined the inclination angle of the partial tension field by conducting experiments on three-story BO-SPSWs. Furthermore, the results showed that while the deformation capacity of BO-SPSW is equal to that of a fully-connected SPSW, its load-bearing capacity is lower [32]. Guo et al. [33] tested BO-SPSWs with and without secondary columns. The experiments illustrated that using secondary columns doesn't significantly affect the ultimate strength but increases the energy dissipation capacity.

Clayton et al. [34], Ozcelik and Clayton [35] proposed to connect the web plates only to horizontal boundary elements to diminish the web plate damage. The experimental results showed that this detailing could effectively reduce and postpone the initiation of the tear in the web plate. Yet, it is essential to use larger plate thicknesses to provide enough load-bearing capacity equal to that of a fully-connected SPSW [34, 36]. Rong et al. [37] investigated the use of concrete panels on the face of BO-SPSW, which prevents the infill plate from out-of-plane buckling and increases the ductility capacity as well as the energy absorption of the composite SPSW. Ozcelik and Clayton [38] proposed a new strip model used in the macro-modeling of BO-SPSWs based on the partial tension field formed in web plates.

Shekastehband et al. [39] experimentally studied the behavior of beam-only connected perforated and solid SPSWs with secondary columns. Shekastehband et al. [40] also investigated the behavior of Low Yield Strength (LYS) and High Yield Strength (LYS) BO-SPSWs. The experimental results revealed that, as the HYS specimen was more vulnerable to web plate failure in connections when compared to the LYS specimen, it showed higher strength degradation. However, HYS steel can be used to compensate for the reduced strength of BO-SPSWs. Ozcelik and Clayton [41] studied the behavior of columns in BO-SPSW systems. As separating the SPSW from the columns can result in unequal drifts of columns, the instability of columns in BO-SPSWs is expected. As a result, an equation is proposed for a reduction factor of column buckling strength. Other experimental and numerical studies have investigated the behavior of BO-SPSWs with different construction details and materials that are not discussed herein for the sake of brevity [42-44].

The stiffness, strength, and energy absorption capacity of BO-SPSWs were investigated in previous research. As the literature lacks the investigation of stiffened BO-SPSWs, this study aims to capture the structural performance of stiffened BO-SPSWs with different web plate thicknesses and various arrangements along with the sections of stiffeners included. To this end, the unstiffened BO-SPSW of Guo et al. [33] was selected, and numerical studies were conducted by varying the arrangement and sections of stiffeners in different web plate thicknesses.

2. Characteristics of the BO-SPSW specimens

This study investigates the structural performance of stiffened BO-SPSWs with different construction details using the finite element method by analyzing fifteen specimens in three main categories, as illustrated in Fig. 1 The varying parameters in this study are the web plate thickness, arrangement, and sections of stiffeners, as tabulated in Table 1 Furthermore, the dimensions and slenderness ratio of subpanels and their critical stress are controlled according to previous research and design codes [3, 45]. Also, the dimensions of stiffeners are controlled to meet the weldability requirements based on AASHTO specifications [46].

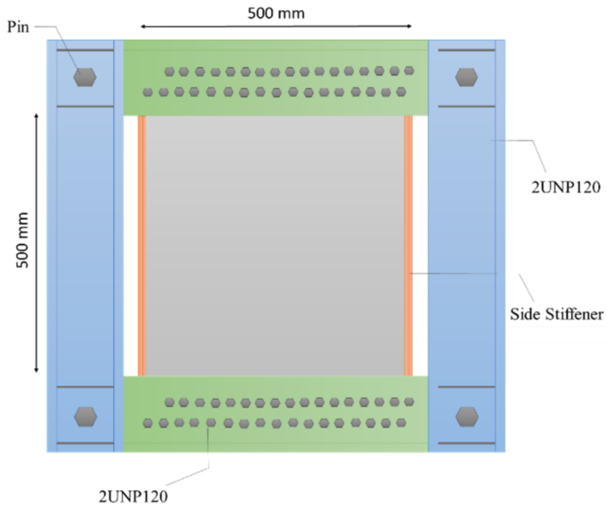

(a)

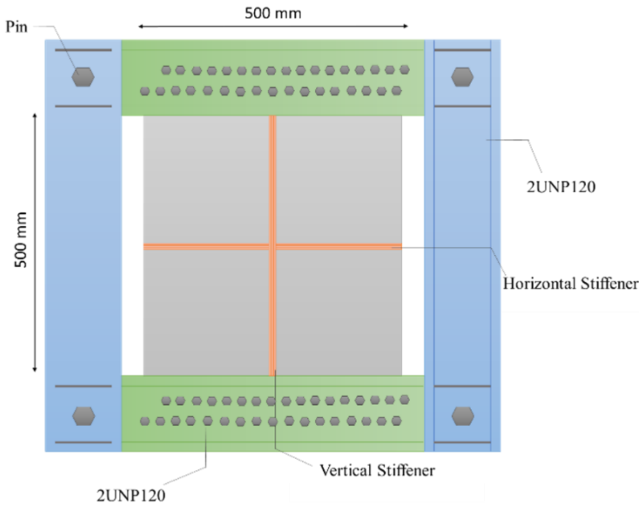

(b)

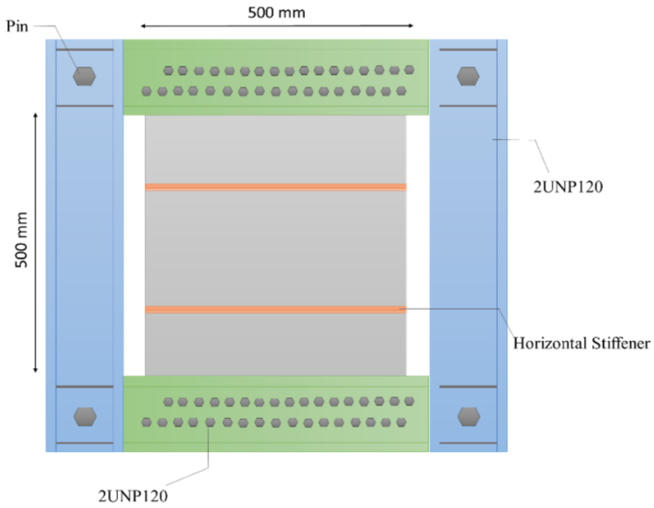

(c)

Fig. 1. Details of the BO-SPSW modeled specimens in three main categories: (a) Side-stiffened (b) Cross-stiffened and (c) Double-horizontally stiffened.

Table 1. Details of the stiffened BO-SPSW models.

Specimen Name	Stiffener Section	Web Plate Thickness
SSt1T20	T20x20x2	0.4 mm
SSt2T20	T20x20x2	0.8 mm
SSt3T20	T20x20x2	2 mm
SSt2T30	T30x30x3	0.8 mm
SSt2B20	B20x20x1	0.8 mm
CSt1T20	T20x20x2	0.4 mm
CSt2T20	T20x20x2	0.8 mm
CSt3T20	T20x20x2	2 mm
CSt2T30	T30x30x3	0.8 mm
CSt2B20	B20x20x1	0.8 mm
DHSt1T20	T20x20x2	0.4 mm
DHSt2T20	T20x20x2	0.8 mm
DHSt3T20	T20x20x2	2 mm
DHSt2T30	T30x30x3	0.8 mm
DHSt2B20	B20x20x1	0.8 mm

The details of the specimens are tabulated in Table 1. Each name tag provides information about the details of a specimen; for example, SS, CS, and DHS stand for side, cross, and double-horizontal arrangement of stiffeners, respectively. In addition, t1, t2, and t3 represent the different thicknesses of web plates equal to 0.4 mm, 0.8 mm, and 2 mm, respectively. Also, Taxbxc and Baxbxc stand for T-shape and box-section stiffeners in which a, b and c represent the width, height, and thickness of the stiffener, respectively.

3. Finite element modeling and verification

A finite element model is developed using a continuum web plate model to clearly represent the tension field that emerged in the single-bay single-story stiffened beam-only connected steel plate shear wall. In cases where extremely high ductility and redundancy are not needed, SPSWs with simple beam-to-column connections are a proper ideal system. Also, the tension field formed in the infill plate of SPSWs in simple frames is presumed to be uniform [47].

In many practical lateral load–resisting systems, such as frames with braces or steel plate shear walls, the beam–column connections in the bays containing these systems are typically detailed as pinned connections. Under such configurations, the gravity frame in the SPSW bay contributes minimally to the overall lateral stiffness, and the primary resistance to lateral loads is provided by the wall or bracing system. In this study, the boundary frame in the SPSW bay is therefore modeled as a pinned frame, consistent with these common design practices. Moreover, this modeling approach allows a focused assessment of the behavior of web plates in stiffened BO-SPSWs, where the frame action does not take part in lateral load resistance [38, 41, 48]. Besides, the boundary frame bases are pinned, and the frame is restrained against out-of-plane displacement.

The stiffened BO-SPSWs are modeled using a finite element software developed at Sharif University of Technology by Khoei et al. [49] [50, 51]. There are various methods for modeling the infill plate of SPSW systems, including a tension-only strip model [3], tension-compression strip model [52], and shell element. Although shell element modeling has the highest computational cost among the other methods, it provides high accuracy, especially when there are strain concentration and localized stress in the web plate [53]. The elements used for modeling the web plates and stiffeners are four-noded shell elements with reduced integration. Moreover, the beams and columns are modeled as very stiff line elements using three-dimensional beam elements. To ensure the adequacy of the finite element discretization, a mesh sensitivity analysis was conducted for the web plate elements. Four different mesh sizes (40 × 40 mm, 30 × 30 mm, 25 × 25 mm, and 20 × 20 mm) were examined, and their influence on key response parameters was evaluated. The comparison focused on initial stiffness, ultimate strength, and overall hysteretic response characteristics. The results showed that reducing the mesh size from 40 mm to 30 mm led to noticeable changes in the predicted ultimate strength (approximately 6%) and initial stiffness (about 5%). However, further refinement from 30 mm to 25 mm resulted in differences of less than 2% in ultimate strength and less than 2.5% in initial stiffness. Refinement from 25 mm to 20 mm produced negligible changes (below 1%) in global response parameters, while significantly increasing computational time. In addition to global response quantities, the 25 × 25 mm mesh was verified to adequately capture localized buckling modes and strain concentration patterns in the stiffened web panels, with no meaningful change in buckling shape observed upon further refinement. Therefore, a mesh size of 25 × 25 mm was adopted as an optimal compromise between numerical accuracy and computational efficiency for web plate elements. Also, the sections of beams and columns are chosen as double UNP120. The bolted connection between the web plate and boundary beams is modeled using a tie constraint.

The bilinear hardening steel material based on the true stress-strain curve data is used for modeling the web plate and the materials of stiffeners [54, 55]. This material model incorporates isotropic strain hardening and is capable of reproducing the primary yielding and post-yield stiffness characteristics of structural steel under cyclic loading. The von Mises yield criterion was adopted to simulate the onset of yielding. In contrast, the boundary beams and columns were modeled using linear elastic steel material, as their behavior remained essentially within the elastic range in the present study. It should be noted that an explicit combined hardening model including calibrated kinematic and isotropic hardening parameters was not employed. The adopted bilinear model was considered adequate for capturing the global cyclic response, overall hysteretic behavior, and energy dissipation capacity of the system, which constitute the primary objectives of this study. However, potential cyclic degradation effects such as low-cycle fatigue and detailed cyclic hardening/softening phenomena are not explicitly modeled and may influence the response under very large inelastic deformations. Here, the yield stress of the steel material is considered 300 MPa. The Young's modulus of elasticity and Poisson's ratio are presumed to be E = 200 GPa and 0.3, respectively. Besides, the von Mises yield criterion is utilized as the failure criterion.

The web plates are not perfectly flat due to fabrication tolerances and construction-related geometric irregularities. Therefore, in order to capture the shear buckling behavior of the web plates, an initial geometric imperfection was introduced into the numerical models. The imperfection shape was defined as a linear combination of the first five buckling modes obtained from an eigenvalue buckling analysis, with a maximum amplitude equal to H/1000, where H represents the plate height. This imperfection magnitude has been widely adopted in numerical simulations of steel plate shear walls and thin steel plates, as it provides a realistic representation of typical fabrication tolerances while preventing unrealistically large geometric deviations [56]. In addition, employing a combination of several buckling modes allows a more representative initial imperfection pattern compared with a single-mode imperfection and improves the ability of the model to capture the interaction of local buckling shapes and the subsequent tension field development in the web plate during cyclic loading. Both material and geometrical nonlinearities of stiffened BO-SPSWs are considered in the analyses, and the models are cyclically loaded at the top corner of the frame according to the SAC loading protocol, which is depicted in Fig. 2 [57].

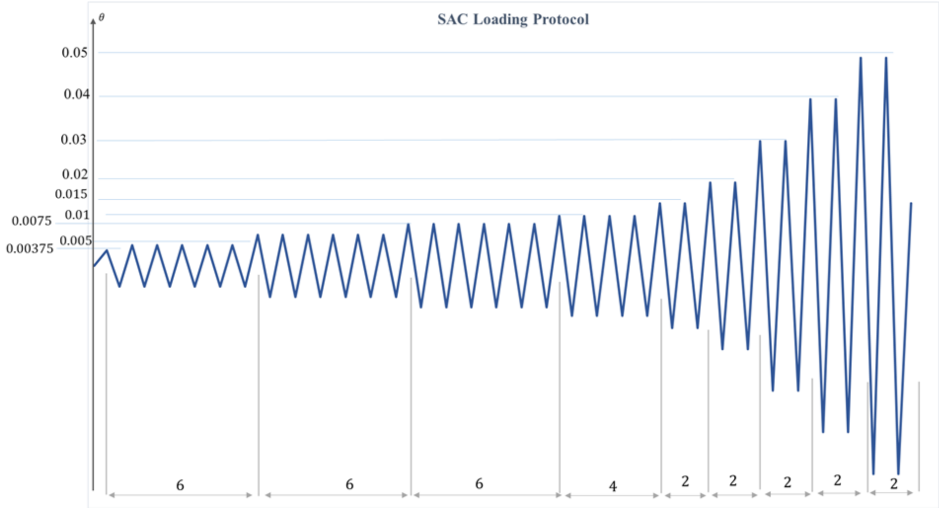

Fig. 2. SAC loading protocol.

It should be noted that, to the best of the authors' knowledge, experimental research on beam-only connected steel plate shear walls is very limited, and no experimental data are currently available for stiffened BO-SPSW specimens. Therefore, in order to validate the accuracy of the finite element modeling, a verification analysis is conducted based on the 1/3 scale one-story one-bay experimental specimen tested by Guo et al. [33]. The analysis results indicated good agreement with experimental results as depicted in Fig. 3 and Fig . 4 The envelope curves indicate that the maximum lateral strength obtained experimentally is approximately 210 kN in the positive loading direction and about 220 kN in the negative direction. The corresponding numerical predictions are approximately 200 kN (positive) and 203 kN (negative). Accordingly, the discrepancy in peak strength is about 4–5% in the positive direction and 7–9% in the negative direction, demonstrating good agreement. The initial elastic stiffness, estimated from the slope of the load–displacement response within the first loading cycle, is also closely captured. The numerical model slightly overestimates the initial stiffness by approximately 5–7%, which may be attributed to unavoidable experimental factors such as minor slip, connection flexibility, and residual imperfections not fully represented in the model. The yield point, identified from the deviation of linearity in the backbone curve, occurs at approximately 150–160 kN experimentally and 145–155 kN numerically, resulting in a difference of less than 5%. Furthermore, the numerical model successfully reproduces the stable hysteresis loop shape observed experimentally, including absence of significant pinching, gradual stiffness degradation with increasing drift, and stable strength development up to ±40 mm displacement. The cumulative energy dissipation capacity, inferred from the relative area enclosed by the hysteresis loops at large displacement amplitudes, shows comparable magnitude between the two responses, with only minor underestimation in the numerical model due to slightly lower peak loads. Overall, the small discrepancies observed in peak strength, yield load, and stiffness (all within approximately 10%) confirm that the developed finite element model provides an accurate and reliable representation of the cyclic behavior of the tested BO-SPSW specimen.

The infill plates of SPSW systems exhibit complex behavior in cyclic loading because of tension fields that form in different orientations; hence, implicit analysis is usually hard to converge. Therefore, the explicit analysis is chosen from the available alternatives for analyzing these continuum finite element models. It is worth mentioning that, as the analysis itself is performed using an explicit solver, some noise is expected in the results [58, 59].

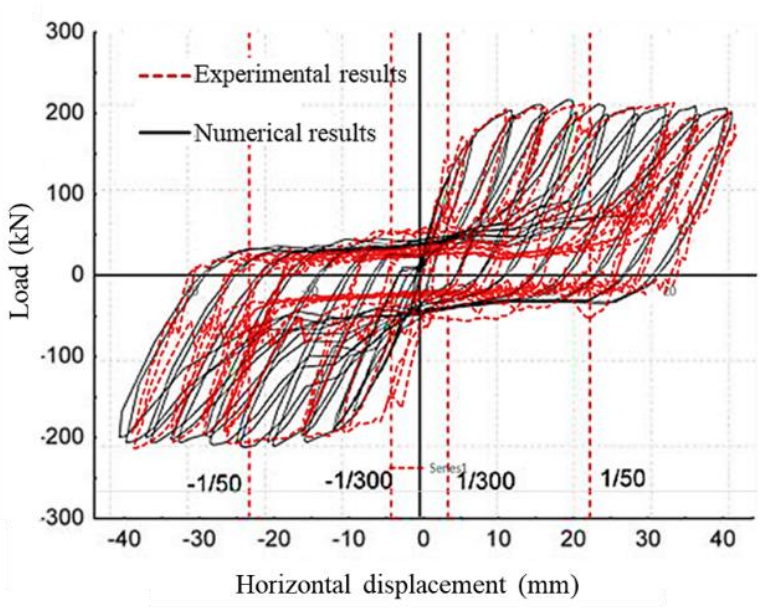

Fig. 3. Comparison of experimental and numerical results.

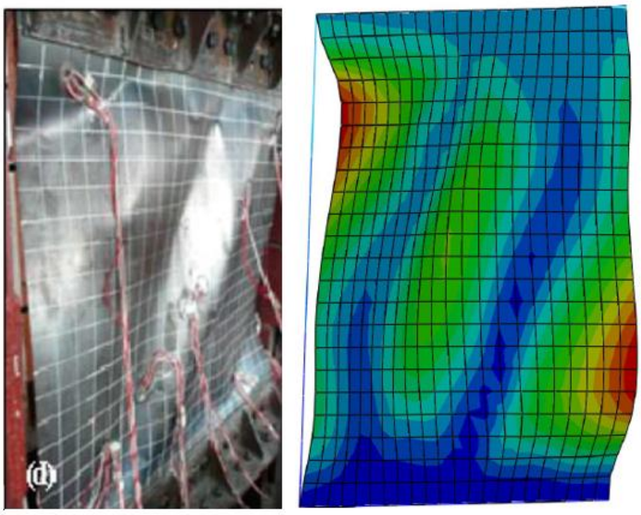

Fig. 4. Comparison of deformations in experimental [33] and numerical model of BO-SPSW specimen.

4. Numerical results and discussions

4.1. Effect of stiffener arrangement on tension field formation

A BO-SPSW subjected to lateral load is analogous to a plate-girder in shear in which the vertical boundary elements, horizontal boundary elements, and the infill plate are similar to flanges, stiffeners, and web of the plate girder, respectively. The ultimate shear strength of plate girders results from the shear buckling strength of the plate girder's web and the tension field formed within it [60]. However, the shear buckling strength is ignored in thin web plates, as they are assumed to buckle right after being subjected to loading [61]. The flanges of plate girders are sufficiently stiff to make it possible for the plate girder's web to form a complete tension field. Hence, as the vertical boundary elements are separated in BO-SPSW, the Partial Tension Field (PTF) is assumed to be similar to the one found in plate girders. Fig. 5 illustrates the PTF in side-stiffened BO-SPSW specimens.

Evidently, it can be seen that the PTF is formed along the web plate height, meaning that the plate still buckles globally. In addition, Fig. 6 indicates that the local tension fields emerge in each subpanel individually in cross-stiffened specimens, and the stiffeners efficiently change the buckling mode of the steel plate from global to local buckling modes in subpanels. Also, according to Fig. 7, the PTF appears between the beams and the adjacent horizontal stiffeners, improving the performance of BO-SPSW. Also, the middle subpanel does not play a considerable role in the PTF formation.

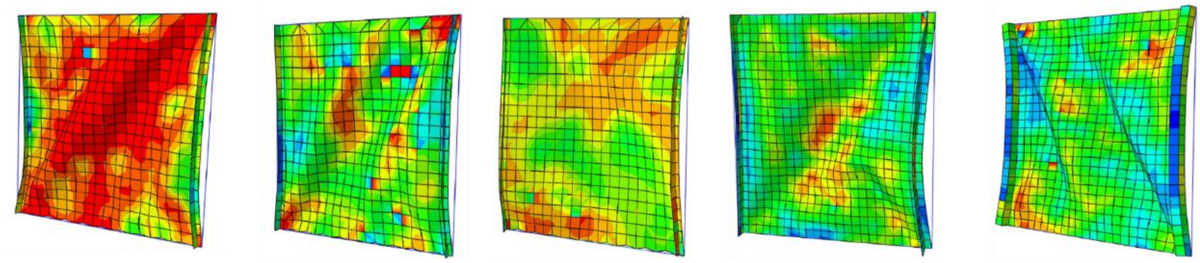

Fig. 5. Partial tension field in side-stiffened specimens.

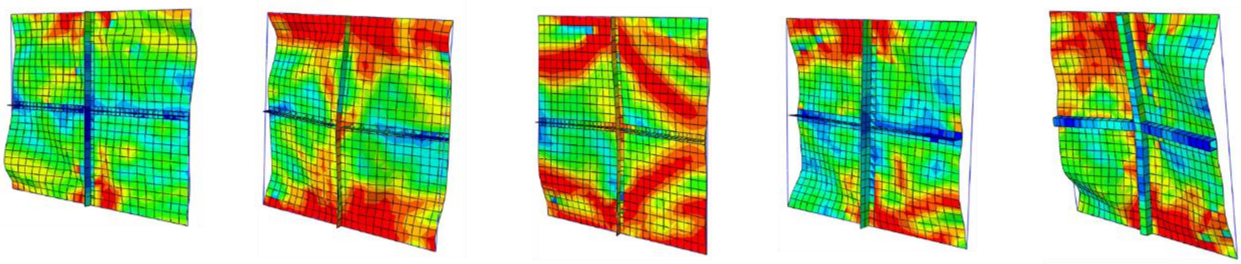

Fig. 6. Partial tension field in cross-stiffened specimens.

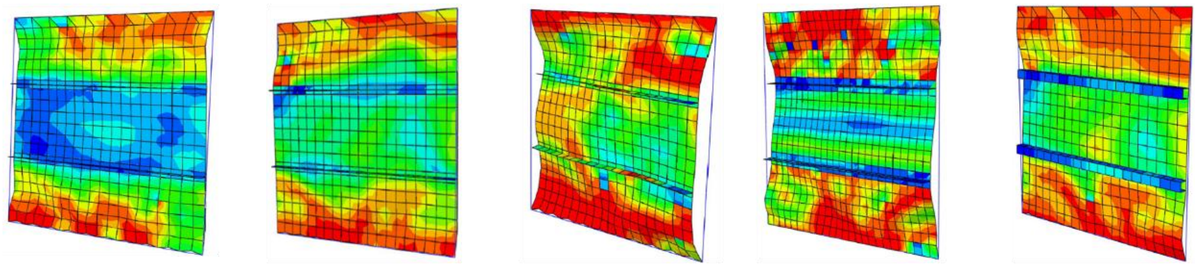

Fig. 7. Partial tension field in double-horizontally stiffened specimens.

4.2. Effect of web plate thickness

In common fully-connected SPSWs, by increasing the thickness of the infill plate, the overall structural performance of the system, such as the ultimate strength, stiffness, and energy absorption capacity, improves. Nevertheless, it may also result in designs that are not economically cost-effective due to the increase in the demand for boundary elements [3]. On the other hand, in BO-SPSWs, there is no contact between the infill plate and the boundary columns, making it possible to increase the thickness of the web plates freely. As evidently illustrated in Fig. 8, the ultimate strength, stiffness, and energy absorption capacity of the stiffened BO-SPSWs are increased in and throughout all arrangements of stiffeners by utilizing a thicker web plate. However, it is noticeable that the ductility ratio (μ) of the system, which is defined as the ratio of the ultimate displacement (Δ_u) to yielding displacement (Δ_y), is independent of plate thickness and is based on the geometry of the specimen rather than the infill plate thickness. Since yielding in SPSW systems develops gradually and does not exhibit a sharply defined transition, the yield point was determined from the equivalent monotonic backbone curve using a bilinear idealization of the response. Moreover, there is no sudden strength degradation in the hysteresis curves of the studied specimens, meaning that this system can be used as a reliable structural system.

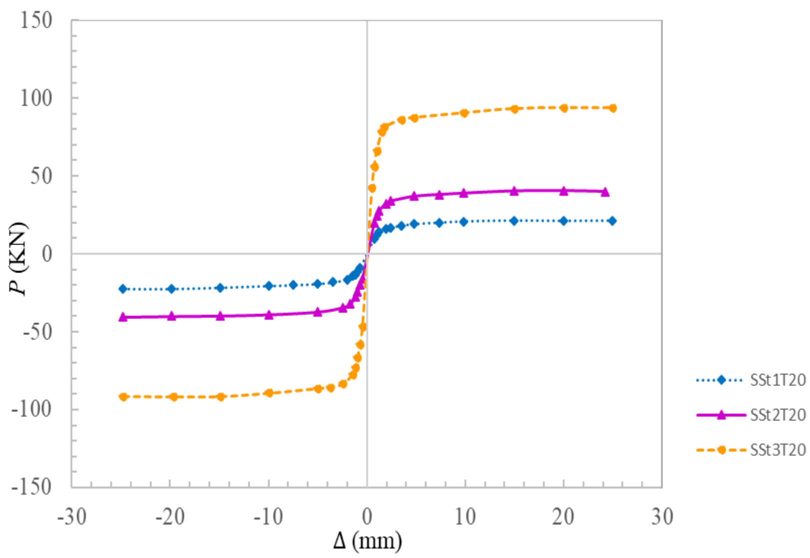

(a)

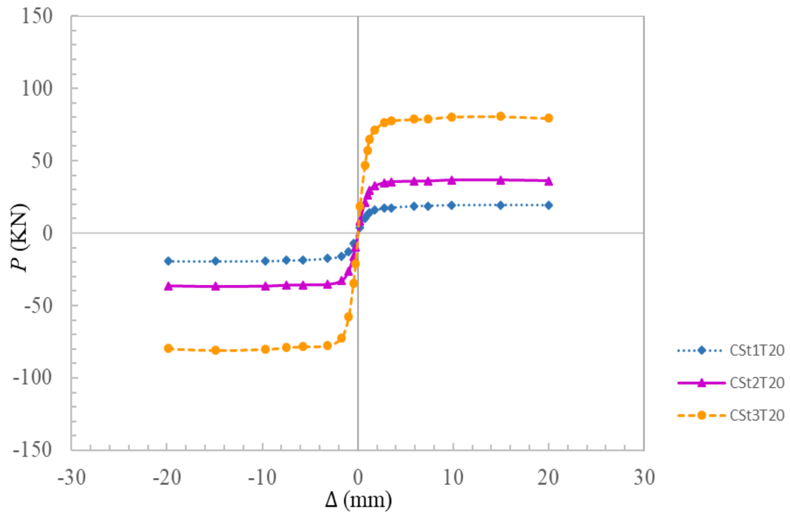

(b)

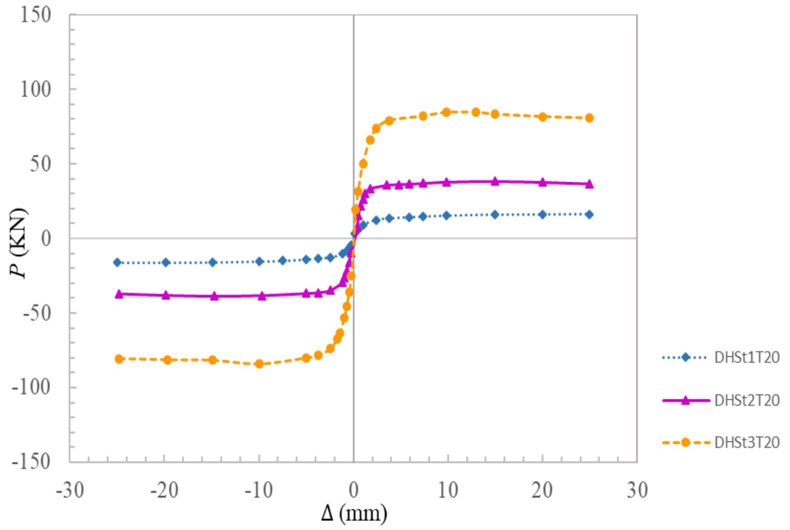

(c)

Fig. 8. Effect of web plate thickness on (a) side-stiffened, (b) cross-stiffened, and (c) double-horizontally stiffened.

4.3. Effect of stiffener section

The tension field in fully-connected SPSWs emerges in the whole infill plate. In contrast, the tension field in BO-SPSWs is partial and appears in different patterns, as discussed in previous sections. In this part, the BO-SPSWs with a consistent plate thickness categorized in three different stiffener arrangements are investigated with attention to the section of stiffeners. As evidently presented in Fig. 9, in all arrangements of stiffeners, using T-shape stiffeners results in higher yielding and ultimate strength compared to box stiffeners, which are more significant in double-horizontally stiffened BO-SPSW specimens (Fig. 9 (c)). Also, increasing the stiffener section from T20x20x2 to T30x30x3 considerably increases the ultimate strength and stiffness of the BO-SPSW systems in all arrangements of stiffeners.

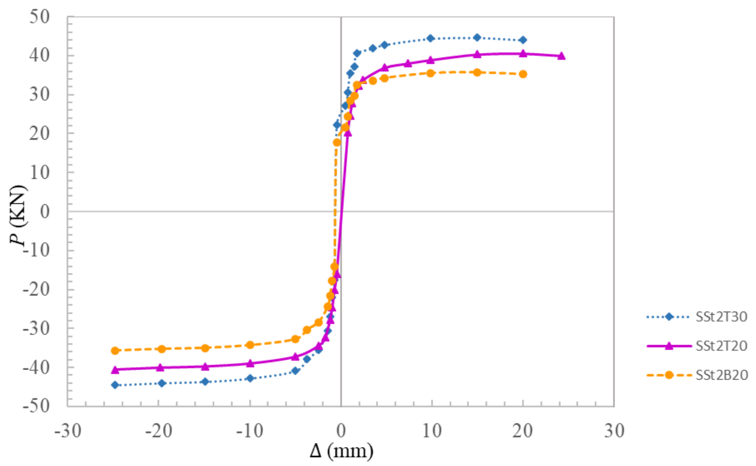

(a)

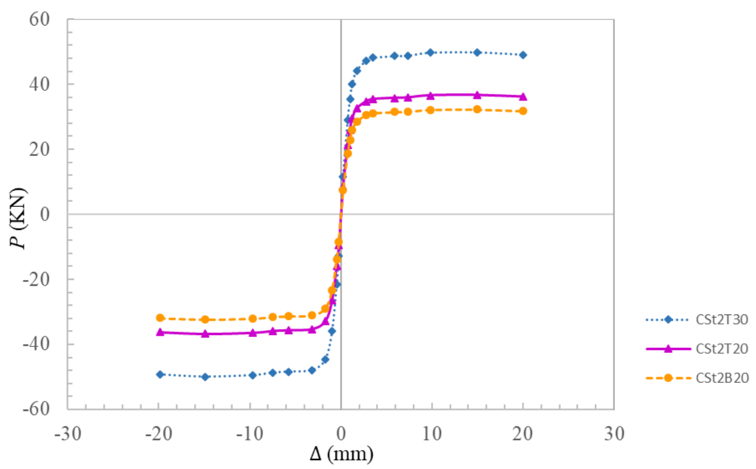

(b)

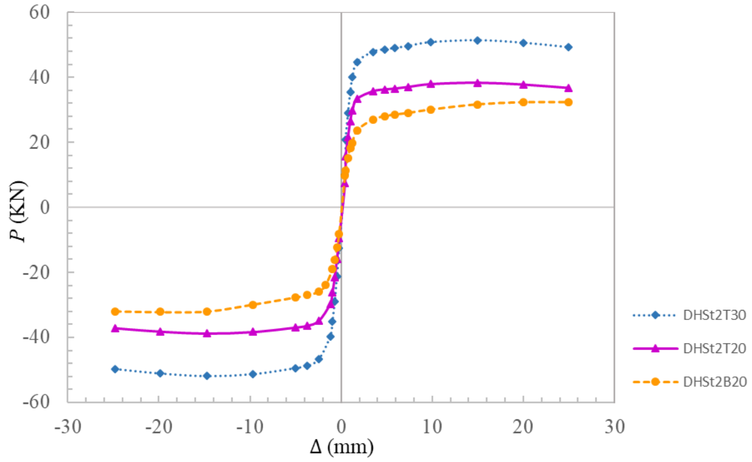

(c)

Fig. 9. Effect of stiffener section on (a) side-stiffened, (b) cross-stiffened and (c) double-horizontally stiffened.

4.4. Effect of stiffener arrangement

One of the most critical parameters in the design of stiffened BO-SPSWs is the section and arrangement of the stiffeners. Thus, in order to capture the effect of stiffener arrangement, two types of stiffeners with equal cross sections, namely T20x20x2 and B20x20x1, are selected and shown in Fig. 10 (a) and (b), respectively. Fig. 10 (a) illustrates that the stiffness, yielding strength, and ductility ratio do not change in different stiffener arrangements when using T-shape stiffeners. However, the ultimate strength of the side-stiffened specimen is a bit more than that of the cross-stiffened specimen, which both are higher than that of the double-horizontal specimen. In addition, Fig. 10 (b) shows that the stiffness and yielding strength of the side-stiffened specimen are more than those of the cross-stiffened specimen, which both are more than that of the double-horizontal specimens when utilizing box stiffeners.

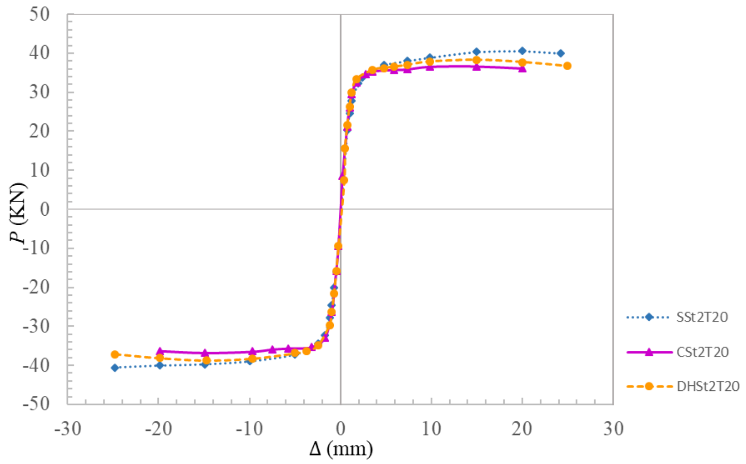

(a)

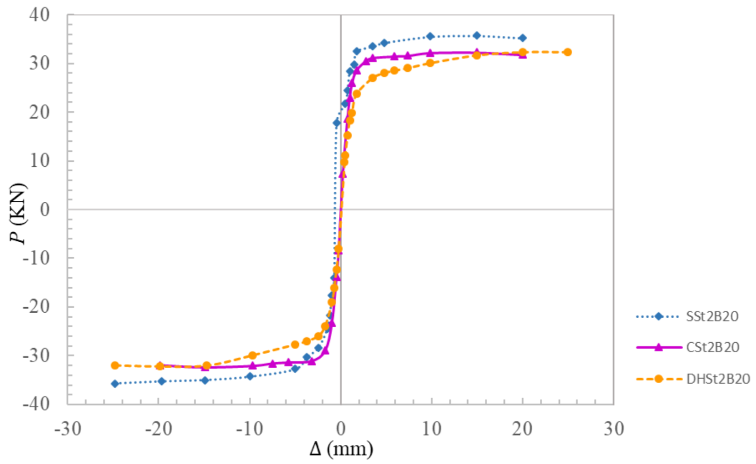

(b)

Fig. 10. Effect of stiffener arrangement using (a) T-shape stiffener and (b) box stiffener.

4.5. Comparison of energy absorption

The energy absorption capacity is determined as the area under the force-displacement curve of each specimen. Fig. 11 (a) compares energy absorption in different infill plate thicknesses with T20x20x2 used as stiffener section in various arrangements of stiffeners. Evidently, it can be seen that by increasing the web plate thickness, the energy absorption capacity of the BO-SPSW system increases significantly. Besides, it is found that the energy absorption capacity of side-stiffened specimens is remarkably more than double that of horizontally and cross-stiffened specimens. Fig. 11 (b) illustrates the comparison of energy absorption capacity in different stiffener sections. As seen in Fig. 11 (b), using T-shape stiffeners provides more energy absorption capacity than box stiffeners with the same cross-sectional area. Moreover, by increasing the dimensions of the stiffeners, the energy absorption capacity increases. Also, the side-stiffened specimens exhibit the best energy absorption performance among all other arrangements of stiffeners.

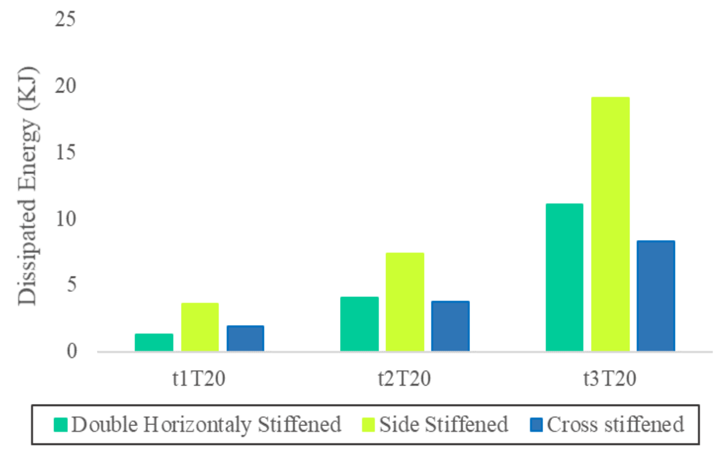

(a)

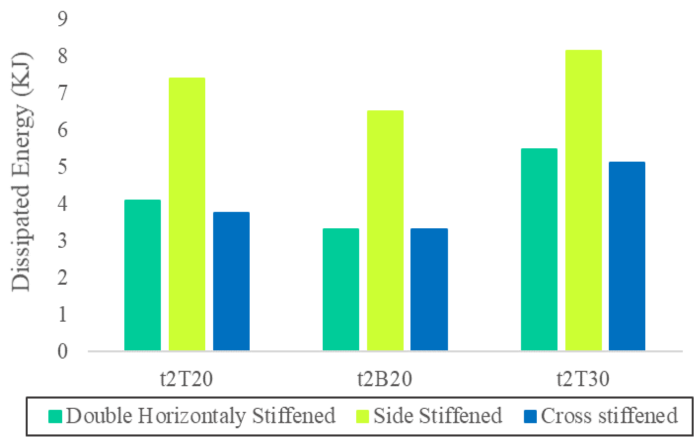

(b)

Fig. 11. Comparison of energy absorption capacity in (a) different infill plate thickness and (b) different stiffener sections.

5. Practical implications and future research

From a practical perspective, the numerical results highlight several trends that may assist engineers in the design of stiffened BO-SPSWs. Increasing the web plate thickness was found to significantly enhance the lateral stiffness, ultimate shear capacity, and energy dissipation capability of the system, while also delaying excessive out-of-plane deformations. In addition, the inclusion of stiffeners improved the stability of the hysteretic response by promoting a more uniform stress distribution in the web plate and delaying local buckling effects. Appropriate stiffener arrangements therefore contribute to more stable cyclic behavior and improved structural performance under seismic loading. Although the present study focuses on behavioral trends rather than formal design provisions, the findings suggest that the combined use of adequately thick web plates and properly arranged stiffeners can be an effective strategy for improving the seismic performance of BO-SPSWs. Further studies involving broader parametric ranges and design-oriented calibration are recommended to establish detailed design guidelines.

In addition to structural performance, practical considerations such as fabrication complexity and construction cost are important in selecting an appropriate stiffener arrangement. Side-stiffened configurations generally require fewer stiffening elements and provide easier welding access, which may simplify fabrication and installation. In contrast, cross-stiffened and double-horizontally stiffened configurations involve additional stiffeners and welding operations that may increase fabrication time and cost. Therefore, from a practical standpoint, side-stiffened arrangements may offer advantages in terms of constructability while still providing favorable structural performance.

The findings of this study provide insight into the cyclic behavior and performance trends of stiffened beam-only connected steel plate shear walls with different stiffener configurations. Although the present investigation is based on detailed finite element simulations at the component level, further research may expand upon these results through additional parametric studies considering a wider range of geometric properties, material characteristics, and stiffener layouts. Experimental investigations would also be valuable to further validate the numerical observations and to better capture potential local effects that may arise in practical applications. Moreover, future studies may evaluate the seismic performance of BO-SPSW systems within complete structural frames subjected to earthquake ground motions in order to assess their global response characteristics. Such investigations could also contribute to the estimation of seismic performance factors, including the response modification factor (R-factor), thereby facilitating the development of design-oriented recommendations for the practical implementation of stiffened BO-SPSW systems in seismic-resistant structures.

6. Conclusion

This study investigates the structural performance of stiffened beam-only connected steel plate shear walls (BO-SPSWs) using detailed finite element analysis. BO-SPSW systems provide a more economical alternative to conventional SPSWs because the infill plate is detached from the vertical boundary elements, reducing the demand on columns. The parameters considered in this study include the web plate thickness, the dimensions and cross-sections of stiffeners, and the arrangement of stiffeners. Based on the numerical results, the following conclusions can be drawn:

- The stiffened BO-SPSW system exhibits stable cyclic behavior under repeated loading, with no significant or sudden strength degradation observed in the hysteretic response.
- In BO-SPSWs with side, cross, and double-horizontal stiffeners, partial tension fields develop within the infill plate. These tension fields form in the subpanels created by the stiffeners and between the stiffeners and the adjacent beams.
- T-shaped stiffeners provide higher ultimate strength compared with box stiffeners having the same cross-sectional area. In addition, increasing the stiffener dimensions leads to an increase in the ultimate strength for all stiffener arrangements.
- Increasing the web plate thickness or the stiffener dimensions significantly enhances the energy absorption capacity of the system. Among the investigated configurations, side-stiffened specimens demonstrate the highest energy dissipation capacity.
- The ultimate strength of BO-SPSWs is influenced by the stiffener arrangement. Side-stiffened configurations generally exhibit higher strength compared with cross-stiffened and double-horizontal stiffened systems, while the overall stiffness and ductility remain relatively similar when T-shaped stiffeners are used.
- Increasing the number of stiffeners in the web plate improves resistance to local buckling, resulting in a more uniform tension field distribution and enhanced overall stability of the BO-SPSW system.
- The performance of BO-SPSWs shows relatively low sensitivity to boundary frame stiffness, indicating that the system can maintain reliable strength and ductility even when simple or semi-rigid beam-to-column connections are used.

Statements & Declarations

Author contributions

Zeinab Meghdadi: Conceptualization, Methodology, Validation, Formal analysis, Writing – Original Draft, Writing-Review & Editing.

Mohammad Shabanlou: Conceptualization, Methodology, Validation, Writing-Review & Editing.

Massood Mofid: Conceptualization, Supervision, Methodology, Validation, Writing-Review & Editing.

Funding

The authors received no financial support for the research, authorship, and/or publication of this article.

Data availability

The data presented in this study will be available on interested request from the corresponding author.

Declarations

The authors declare no conflict of interest.

References

[1] Sarcheshmehpour, M., Shabanlou, M., Meghdadi, Z., Estekanchi, H. E., Mofid, M. Seismic evaluation of steel plate shear wall systems considering soil-structure interaction. Soil Dynamics and Earthquake Engineering, 2021; 145: 106738. doi:10.1016/j.soildyn.2021.106738.

[2] Shabanlou, M., Moghaddam, H., Daryan, A. The Effect of Geometry on Structural Behavior of Buildings with Steel Plate Shear Wall System Subjected to Blast Loading. International Journal of Steel Structures, 2021; 21: 650–665. doi:10.1007/s13296-021-00463-4.

[3] American Institute of Steel Construction (AISC). Steel Design Guide 20: Steel Plate Shear Walls. Farmington Hills (MI): AISC; 2006.

[4] Sarcheshmehpour, M., Estekanchi, H. E. Life cycle cost optimization of earthquake-resistant steel framed tube tall buildings. Structures, 2021; 30: 585–601. doi:10.1016/j.istruc.2021.01.038.

[5] Elgaaly, M., Caccese, V., Du, C. Postbuckling Behavior of Steel-Plate Shear Walls under Cyclic Loads. Journal of Structural Engineering, 1993; 119: 588–605. doi:10.1061/(ASCE)0733-9445(1993)119:2(588).

[6] Ghosh, S., Adam, F., Das, A. Design of steel plate shear walls considering inelastic drift demand. Journal of Constructional Steel Research, 2009; 65: 1431–1437. doi:10.1016/j.jcsr.2009.02.008.

[7] Li, C.-H., Tsai, K.-C., Lin, C.-H., Chen, P.-C. Cyclic tests of four two-story narrow steel plate shear walls. Part 2: Experimental results and design implications. Earthquake Engineering & Structural Dynamics, 2009; 39: 801–826. doi:10.1002/eqe.964.

[8] Li, C. H., Tsai, K. C., Chang, J. T., Lin, C. H. Cyclic Test of a Coupled Steel Plate Shear Wall Substructure. Procedia Engineering, 2011; 14: 582–589. doi:10.1016/j.proeng.2011.07.073.

[9] Roberts, T. M., Sabouri-Ghomi, S. Hysteretic characteristics of unstiffened perforated steel plate shear panels. Thin-Walled Structures, 1992; 14: 139–151. doi:10.1016/0263-8231(92)90047-Z.

[10] Purba, R., Bruneau, M. Seismic Performance of Steel Plate Shear Walls Considering Two Different Design Philosophies of Infill Plates. I: Deterioration Model Development. Journal of Structural Engineering, 2015; 141: 04014160. doi:10.1061/(ASCE)ST.1943-541X.0001098.

[11] Chan, R., Albermani, F., Kitipornchai, S. Stiffness and Strength Of Perforated Steel Plate Shear Wall. Procedia Engineering, 2011; 14: 675–679. doi:10.1016/j.proeng.2011.07.086.

[12] Valizadeh, H., Sheidaii, M., Showkati, H. Experimental investigation on cyclic behavior of perforated steel plate shear walls. Journal of Constructional Steel Research, 2012; 70: 308–316. doi:10.1016/j.jcsr.2011.09.016.

[13] Bahrebar, M., Lim, J. B. P., Clifton, G. C., Zirakian, T., Shahmohammadi, A., Hajsadeghi, M. Perforated steel plate shear walls with curved corrugated webs under cyclic loading. Structures, 2020; 24: 600–609. doi:10.1016/j.istruc.2020.01.047.

[14] Ahmad Khan, N. A., Srivastava, G. Models for strength and stiffness of steel plate shear walls with openings. Structures, 2020; 27: 2096–2113. doi:10.1016/j.istruc.2020.07.037.

[15] Vian, D., Lin, Y.-C., Bruneau, M., Tsai, K.-C. Cyclic performance of low yield strength steel panel shear walls. In: Proceedings of The Sixteenth KKCNN Symposium on Civil Engineering; 2003; Kolon Hotel, Gyeongju, Korea. p. 379–384.

[16] Chen, S.-J., Jhang, C. Cyclic behavior of low yield point steel shear walls. Thin-Walled Structures, 2006; 44: 730–738. doi:10.1016/j.tws.2006.08.002.

[17] Astaneh-Asl, A. Seismic Behavior and Design of Composite Steel Plate Shear Walls. San Francisco (CA): Structural Steel Educational Council; 2002.

[18] Zhao, Q., Astaneh-Asl, A. Cyclic Behavior of Traditional and Innovative Composite Shear Walls. Journal of Structural Engineering, 2004; 130: 271–284. doi:10.1061/(ASCE)0733-9445(2004)130:2(271).

[19] Arabzadeh, A., Soltani, M., Ayazi, A. Experimental investigation of composite shear walls under shear loadings. Thin-walled Structures - THIN WALL STRUCT, 2011; 49: 842–854. doi:10.1016/j.tws.2011.02.009.

[20] Emami, F., Mofid, M. On the hysteretic behavior of trapezoidally corrugated steel shear walls. The Structural Design of Tall and Special Buildings, 2014; 23: 94–104. doi:10.1002/tal.1025.

[21] Emami, F., Mofid, M., Vafai, H. Experimental study on cyclic behavior of trapezoidally corrugated steel shear walls. Engineering Structures, 2013; 48: 750–762. doi:10.1016/j.engstruct.2012.11.028.

[22] Farzampour, A., Laman, J. A., Mofid, M. Behavior prediction of corrugated steel plate shear walls with openings. Journal of Constructional Steel Research, 2015; 114: 258–268. doi:10.1016/j.jcsr.2015.07.018.

[23] Hosseinzadeh, L., Emami, F., Mofid, M. Experimental investigation on the behavior of corrugated steel shear wall subjected to the different angle of trapezoidal plate. The Structural Design of Tall and Special Buildings, 2017; 26: e1390. doi:10.1002/tal.1390.

[24] Alinia, M. M. A study into optimization of stiffeners in plates subjected to shear loading. Thin-Walled Structures, 2005; 43: 845–860. doi:10.1016/j.tws.2004.10.008.

[25] Alinia, M. M., Dastfan, M. Cyclic behaviour, deformability and rigidity of stiffened steel shear panels. Journal of Constructional Steel Research, 2007; 63: 554–563. doi:10.1016/j.jcsr.2006.06.005.

[26] Alinia, M. M., Sarraf Shirazi, R. On the design of stiffeners in steel plate shear walls. Journal of Constructional Steel Research, 2009; 65: 2069–2077. doi:10.1016/j.jcsr.2009.06.009.

[27] Sabouri-Ghomi, S., Sajjadi, S. R. A. Experimental and theoretical studies of steel shear walls with and without stiffeners. Journal of Constructional Steel Research, 2012; 75: 152–159. doi:10.1016/j.jcsr.2012.03.018.

[28] Guo, H.-C., Hao, J.-P., Liu, Y.-H. Behavior of stiffened and unstiffened steel plate shear walls considering joint properties. Thin-Walled Structures, 2015; 97: 53–62. doi:10.1016/j.tws.2015.09.005.

[29] Guo, H., Li, Y., Liang, G., Liu, Y. Experimental study of cross stiffened steel plate shear wall with semi-rigid connected frame. Journal of Constructional Steel Research, 2017; 135: 69–82. doi:10.1016/j.jcsr.2017.04.009.

[30] Ma, Z.-y., Hao, J.-p., Yu, H.-s. Shaking-table test of a novel buckling-restrained multi-stiffened low-yield-point steel plate shear wall. Journal of Constructional Steel Research, 2018; 145: 128–136. doi:10.1016/j.jcsr.2018.02.009.

[31] Xue, M., Lu, L.-W. Influence of steel shear wall panels with surrounding frame members. Proc. SSRC annual technical session. 1994:339-354.

[32] Choi, I.-R., Park, H.-G. Steel Plate Shear Walls with Various Infill Plate Designs. Journal of Structural Engineering, 2009; 135: 785–796. doi:10.1061/(ASCE)0733-9445(2009)135:7(785).

[33] Guo, L., Rong, Q., Ma, X., Zhang, S. Behavior of steel plate shear wall connected to frame beams only. International Journal of Steel Structures, 2011; 11: 467–479. doi:10.1007/s13296-011-4006-7.

[34] Clayton, P., Berman, J., Lowes, L. Seismic performance of self-centering steel plate shear walls with beam-only-connected web plates. Journal of Constructional Steel Research, 2015; 106: 198–208. doi:10.1016/j.jcsr.2014.12.017.

[35] Ozcelik, Y., Clayton, P. M. Seismic design and performance of SPSWs with beam-connected web plates. Journal of Constructional Steel Research, 2018; 142: 55–67. doi:10.1016/j.jcsr.2017.12.004.

[36] Clayton, P. M., Berman, J. W., Lowes, L. N. Subassembly testing and modeling of self-centering steel plate shear walls. Engineering Structures, 2013; 56: 1848–1857. doi:10.1016/j.engstruct.2013.06.030.

[37] Rong, Q., Guo, L., Ma, X., Zhang, S. Analysis of composite steel plate shear walls connected with frame beams only. Proceedings of the ICE - Structures and Buildings, 2013; 166: 507–518. doi:10.1680/stbu.11.00089.

[38] Ozcelik, Y., Clayton, P. M. Strip model for steel plate shear walls with beam-connected web plates. Engineering Structures, 2017; 136: 369–379. doi:10.1016/j.engstruct.2017.01.051.

[39] Shekastehband, B., Azaraxsh, A. A., Showkati, H., Pavir, A. Behavior of semi-supported steel shear walls: Experimental and numerical simulations. Engineering Structures, 2017; 135: 161–176. doi:10.1016/j.engstruct.2017.01.004.

[40] Shekastehband, B., Azaraxsh, A., Showkati, H. Experimental and numerical study on seismic behavior of LYS and HYS steel plate shear walls connected to frame beams only. Archives of Civil and Mechanical Engineering, 2017; 17: 154–168. doi:10.1016/j.acme.2016.09.006.

[41] Ozcelik, Y., Clayton, P. M. Behavior of columns of steel plate shear walls with beam-connected web plates. Engineering Structures, 2018; 172: 820–832. doi:10.1016/j.engstruct.2018.06.087.

[42] Mu, Z., Yang, Y. Experimental and numerical study on seismic behavior of obliquely stiffened steel plate shear walls with openings. Thin-Walled Structures, 2020; 146: 106457. doi:10.1016/j.tws.2019.106457.

[43] Shekastehband, B., Azaraxsh, A. A., Showkati, H. Experimental seismic study on shear walls with fully-connected and beam-only-connected web plates. Journal of Constructional Steel Research, 2018; 141: 204–215. doi:10.1016/j.jcsr.2017.11.013.

[44] Özçelik, A. Y., Clayton, P. Tension field inclination angle in steel plate shear walls with beam- connected web plates. In: 2nd International Conference on Natural Hazards & Infrastructure; 2019; Athens (GR).

[45] American Institute of Steel Construction (AISC). ANSI/AISC 360-16: Specification for structural steel buildings. Farmington Hills (MI): AISC; 2016.

[46] American Association of State Highway and Transportation Officials (AASHTO). AASHTO LRFD Bridge Design Specifications. Washington, DC (US): AASHTO; 2005.

[47] Moghimi, H., Driver Robert, G. Beam Design Force Demands in Steel Plate Shear Walls with Simple Boundary Frame Connections. Journal of Structural Engineering, 2014; 140: 04014046. doi:10.1061/(ASCE)ST.1943-541X.0000993.

[48] Habashi, H. R., Alinia, M. M. Characteristics of the wall–frame interaction in steel plate shear walls. Journal of Constructional Steel Research, 2010; 66: 150–158. doi:10.1016/j.jcsr.2009.09.004.

[49] Khoei, A. R., Gharehbaghi, S. A., Azami, A. R., Tabarraie, A. R. SUT-DAM: An integrated software environment for multi-disciplinary geotechnical engineering. Advances in Engineering Software, 2006; 37: 728–753. doi:10.1016/j.advengsoft.2006.03.001.

[50] Shabanlou, M., Meghdadi, Z., Ghaffar, S. Experimental and Analytical Study of the Residual Performance of Reinforced Concrete Deep Beams with Circular Web Openings. Results in Engineering, 2025; 25: 104229. doi:10.1016/j.rineng.2025.104229.

[51] Shabanlou, M., Mofid, M., Tavakoli, A. Experimental and Numerical Study on the Behavior of Reinforced Concrete Deep Beams with Normal-Strength and High-Strength Concrete After Being Exposed to Fire. Arabian Journal for Science and Engineering, 2024; 49: 13457–13476. doi:10.1007/s13369-023-08676-x.

[52] Webster, D., Berman, J., Lowes, L. Experimental Investigation of SPSW Web Plate Stress Field Development and Vertical Boundary Element Demand. Journal of Structural Engineering, 2014; 140: 04014011. doi:10.1061/(ASCE)ST.1943-541X.0000989.

[53] Clayton, P., Tsai, C.-Y., Berman, J., Lowes, L. Comparison of web plate numerical models for self-centering steel plate shear walls. Earthquake Engineering & Structural Dynamics, 2015; 44: 2093–2110. doi:10.1002/eqe.2578.

[54] Meghdadi, Z., Khaloo, A. Experimental, theoretical and numerical study on flexural behavior of hybrid steel-GFRP reinforced concrete slabs. Structural Concrete, 2024; 26: 739–758. doi:10.1002/suco.202301085.

[55] Meghdadi, Z., Khaloo, A., Ashour, A. Residual structural performance of fire-exposed concrete slabs reinforced with hybrid GFRP-steel bars: Experimental and numerical studies. Structures, 2025; 80: 109757. doi:10.1016/j.istruc.2025.109757.

[56] Wang, M., Yang, W., Shi, Y., Xu, J. Seismic behaviors of steel plate shear wall structures with construction details and materials. Journal of Constructional Steel Research, 2015; 107: 194–210. doi:10.1016/j.jcsr.2015.01.007.

[57] Clark, P. W. F., Karl H.; Krawinkler, Helmut; Shaw, Robert E Protocol for fabrication, inspection, testing and documentation of beam-column connection tests and other experimental specimens. Berkeley (CA): The Earthquake Engineering Online Archive NISEE e-Library; 1997. Report No.: SAC/BD-97/02.

[58] Shabanlou, M., Mofid, M., Eslami, M., Kodur, V., Meghdadi, Z., Tavakoli, A. Experimental, analytical and numerical investigation on the effects of different shear reinforcement on residual post-fire behavior of reinforced concrete deep beams. Structure and Infrastructure Engineering, 2025; 1–18. doi:10.1080/15732479.2025.2456466.

[59] Shabanlou, M., Mofid, M., Tavakoli, A. Post-fire performance of GFRP reinforced concrete deep beams: experimental and numerical study. Structure and Infrastructure Engineering, 2024; 1–19. doi:10.1080/15732479.2024.2382131.

[60] Basler, K. Strength of plate girders in shear. Journal of the Structural Division, 1961; 87: 151–180. doi:10.1061/JSDEAG.0000697.

[61] Thorburn, L. J., Montgomery, C. J., Kulak, G. L. Analysis of steel plate shear walls. Alberta (CA): Department of Civil Engineering the University of Alberta; 1983. Report No.: SER107.

Civil Engineering and Applied Solutions

Research Article

journal homepage: ceas.journals.umz.ac.ir

CEAS Civil Engineering and Applied Solutions

A Comparison of Machine Learning Models in Predicting Competition Between High-Speed Rail (HSR) and Air Transport: The Tehran-Mashhad Case Study

Mohammad Feli [a], Ali Naderan [a*], Mahmoud Saffarzadeh [b]

[a] *Department of Civil Engineering, SR.C., Islamic Azad University, Tehran, Iran*
[b] *Department of Civil and Environmental Engineering, Tarbiat Modares University, Tehran, Iran*

ARTICLE INFO

Article history:

Received 26 March 2026

Revised 23 April 2026

Accepted 18 May 2026

Available online 01 January 2027

Keywords:

High-speed rail

Mode choice

Machine learning

Classification report

ABSTRACT

Mode choice modeling represents a fundamental domain within transportation engineering and urban-regional planning. The competition between high-speed rail (HSR) and air travel holds particular significance for demand forecasting, revenue optimization, environmental policy, and infrastructure development. Traditional discrete choice models have long served as the cornerstone of mode choice analysis. These models offer interpretability, compatibility with stated and revealed preference data, and the capacity to compute policy-relevant elasticities. However, they suffer from critical limitations, such as the independence of irrelevant alternatives (IIA) assumption and inability to accommodate large, noisy datasets. Conversely, Machine Learning (ML) methodologies have gained prominence for their capacity to handle complex, nonlinear, and high-dimensional data. By applying Artificial Neural Network (ANN), Random Forest (RF), Decision Tree (DT), and K-Nearest Neighbor (KNN), this study addresses two critical research gaps: (1) the scarcity of ML applications in developing countries with limited HSR infrastructure, and (2) the limited incorporation of psychological factors alongside socio-economic variables. Using stated preference data from 100 Iranian respondents across 18 travel scenarios, this research develops ML-based models, examining variables such as travel time, cost, income, service frequency, previous travel experiences, and psychological factors including fear of flying. The findings reveal that ANN emerged as the top performer with an overall accuracy of 84.67%. The RF model followed with 82.44% accuracy, showing robust predictive capability with relatively balanced class-wise performance, though slightly favoring the majority class. Also, class-specific analysis across all models consistently demonstrated higher precision for airplane predictions.

How to cite this article: Feli, M., Naderan, A. Saffarzadeh, M. A Comparison of Machine Learning Models in Predicting Competition Between High-Speed Rail (HSR) and Air Transport: The Tehran- Mashhad Case Study. Civil Engineering and Applied Solutions. 2027; 3(1): 146–160. doi:10.22080/ceas.2026.31482.1086.

1. Introduction

Mode choice modeling is considered one of the most important and fundamental fields of transportation engineering and urban-regional planning. This field specifically addresses the examination, analysis, and prediction of passengers' or transport users' choice behavior among various transport mode options, where individuals or groups decide which vehicle or combination of vehicles to use for a particular trip. Among the various options, the competition between high-speed rail (HSR) and airplane is one of the most practical topics, as these two modes often compete directly with each other over medium to long distances (typically 300 to 1200 kilometers), and the choice of one has a significant impact on the other, particularly in the areas of demand, operators' revenue,

* Corresponding author.
E-mail addresses: naderan@iau.ac.ir (A. Naderan).

https://doi.org/10.22080/ceas.2026.31482.1086
ISSN: 3092-7749/© 2027 The Author(s). Published by University of Mazandaran.

environmental policies, and infrastructure development [1, 2].

Mode choice models help predict future demand with greater accuracy, optimize infrastructure, and strengthen sustainable policies. Classic mode choice models, such as the Multinomial Logit (MNL) model, binary logit model, mixed logit models, or Bayesian logit models, have been among the most widely used approaches for decades. These models are built upon discrete choice theory and the assumption of random utility maximization, and they offer important advantages. High interpretability, compatibility with stated preference (SP, i.e., hypothetical scenarios) and revealed preference (RP, i.e., actual observed behavior) data, and the ability to calculate policy-relevant indicators such as demand elasticities are among the key strengths of this modeling approach [3, 4]. Despite the aforementioned positive aspects, this approach also has serious limitations, including the assumption of independence of irrelevant alternatives (IIA), which is often violated; linear or simplified relationships between variables; inability to handle unobserved heterogeneity; and weaker performance in accurate prediction when the data are large and noisy [5].

In recent years, this field has witnessed a remarkable surge in the use of machine learning methods, the main reason for this shift being the high capability of ML in handling large, complex, and nonlinear data; data that include numerous variables such as travel time, cost, income, trip purpose, accessibility, service frequency, demographic characteristics, and even ticket purchasing behavior, which often exhibit nonlinear, interactive, and heterogeneous relationships. The succeeding section will delve into the available literature review addressing mode choice in HSR-airplane competition.

The remainder of this paper is structured as follows. Section 2 reviews the relevant literature on HSR-airplane competition and the evolution of mode choice modeling approaches. Section 3 describes the materials and methods, including data collection, variable specification, and the four machine learning algorithms employed (ANN, RF, DT, and KNN). Section 4 presents the modeling results, including classification reports and confusion matrices for each model. Section 5 provides a comparative discussion of model performance. Finally, Section 6 concludes the paper with key findings, policy implications, and directions for future research.

2. Literature review

The modeling of travel mode choice has been extensively studied through two primary methodological streams: traditional discrete choice models grounded in random utility theory and, more recently, machine learning (ML) approaches. Comprehensive systematic reviews by Ali [6], Fale et al. [7] highlight that while the multinomial logit model remains the most widely used framework due to its interpretability and solid theoretical foundations, it suffers from critical limitations such as the Independence of Irrelevant Alternatives (IIA) assumption, reliance on linear or oversimplified variable relationships, and an inability to fully capture unobserved heterogeneity across decision-makers. The concept of unobserved heterogeneity, referring to variations in preferences or decision processes that are not captured by observed variables, has been a central concern in choice modeling. As noted by Forsythe et al. [8], traditional approaches to modeling heterogeneity, such as mixed logit models, rely on strong parametric assumptions about the distribution of random parameters. In contrast, their proposed Mixed Aggregate Preference Logit (MAPL) model leverages machine learning to relax these assumptions and capture unobserved heterogeneity more flexibly.

The overall trend in the literature review indicates a gradual transition from traditional logit models to advanced machine learning algorithms, which have increased prediction accuracy and enabled the discovery of nonlinear relationships and better interpretability. The evolutionary trend in the literature review has moved from simple comparisons of machine learning with logit to the use of real large-scale data, hybrid frameworks, and advanced models.

To identify the variables affecting this competition, numerous studies have been conducted. Variables such as cost [9, 10], fleet speed [11, 12], travel time and its components [13, 14], individuals' socio-economic characteristics such as age [15], income [16], gender [17], education [15], pollutant and pollution considerations [18, 19], service frequency [20, 21], and comfort and convenience [22, 23]. This research, relying on these variables, creates various functional forms of them, and variables such as previous travel experiences with the train or fear of flying are also considered in the modeling process.

From the perspective of modeling and the approach used, initial studies focused on comparing the performance of machine learning with logit models in intercity mode choice (including HSR, airplane, conventional train, and bus). For example, Li and colleagues compared Bayesian Mixed Multinomial Logit (BMNL), Multinomial Logit (MNL), Multi-Layer Perceptron (MLP), and Radial Basis Function (RBF) neural networks. The results showed that neural networks (especially with balanced data) have higher prediction accuracy, but Bayesian models were superior in handling unobserved heterogeneity. Key factors included travel time, cost, and demographic characteristics [3, 24].

Focus on the application of machine learning in predicting demand and mode choice behavior in specific contexts, such as the impact of the COVID-19 pandemic on HSR in the United States, represents another aspect of the conducted research. Pan's study, in the Los Angeles-San Francisco corridor, using stated preference data, identified factors such as total travel time, accessibility, comfort, travel frequency, gender, and mobility issues. Multinomial Logit Regression models showed accuracy of approximately 67-80 percent, but it was suggested that machine learning could improve accuracy [25].

In a study in Thailand (with a focus on HSR development), the Binary Logit model was compared with machine learning algorithms such as boosting XGBoost, LightGBM, and CatBoost. CatBoost showed the best performance (accuracy ≈0.885, AUC ≈0.958). Influential factors included travel time, cost, household income, service frequency, access time, and trip purpose. The results indicated that XGBoost and CatBoost interpret nonlinear relationships well, and machine learning is generally superior to logit [1].

In a study using real large-scale ticketing data and ticket sales integration, the MNL model was compared with eight algorithms including RF, SVM, and KNN, and the results showed that RF had the best prediction accuracy. This study proposed a new framework for mode choice analysis using real data [2].

Extending their previous work in Thailand, Banyong et al. (2025) used large-scale stated preference data (3,200 respondents) to compare the MNL model with XGBoost, LightGBM, CatBoost, Deep Neural Network (DNN), and Convolutional Neural Network (CNN). The results showed that CatBoost was the superior model (AUC ≈ 0.911, accuracy ≈ 0.756). Key factors included travel cost, service frequency, and waiting time. Tree-based models such as CatBoost were more stable and resistant to overfitting in large datasets compared to deep neural networks. This study emphasized the application of machine learning in developing countries for HSR policy-making [4].

While the reviewed studies demonstrate the superiority of machine learning over traditional logit models in capturing nonlinear relationships and improving prediction accuracy, there remains a paucity of applications in developing countries with limited high-speed rail infrastructure. Moreover, few investigations incorporate psychological factors such as fear of flying or prior travel experiences alongside socio-economic variables.

Although the competition between high-speed rail and air travel has been extensively studied in developed countries, its investigation in developing nations, and particularly in Iran, remains critically limited. The Tehran-Mashhad corridor, as one of the busiest domestic air routes in the Middle East, offers a unique yet underexplored context for mode choice modeling. With a distance of approximately 900 kilometers, high passenger demand, and ongoing discussions about HSR infrastructure development in Iran, understanding the behavioral and environmental factors influencing mode choice in this corridor has direct implications for transportation policy, investment prioritization, and emission reduction strategies. This study, therefore, focuses specifically on the Tehran-Mashhad scenario to provide the first machine learning-based mode choice analysis in Iran that incorporates psychological variables alongside socio-economic attributes.

2.1. Application of artificial neural networks (ANN) in mode choice

Artificial Neural Networks (ANNs) have gained considerable attention in travel mode choice modeling due to their ability to capture complex, nonlinear relationships without imposing predefined utility structures. Unlike traditional discrete choice models, ANNs learn patterns directly from data through interconnected layers of neurons, making them particularly suitable for high-dimensional and noisy datasets. In the context of intercity travel, Li et al. [3] compared Bayesian mixed multinomial logit, multinomial logit, MLP, and RBF neural networks. Their results showed that neural networks, especially when trained on balanced data, achieved higher prediction accuracy than logit models, although Bayesian models remained superior in handling unobserved heterogeneity. Similarly, in the competition between high-speed rail and air travel, ANNs have been employed to model passenger preferences using variables such as travel time, cost, income, and psychological factors [7, 26]. More recent studies have demonstrated that deep neural networks (DNNs) can achieve accuracy levels above 85% in binary mode choice tasks, outperforming traditional logit models in predictive performance [4, 27].

These findings suggest that ANNs are a viable alternative or complement to classical utility-based approaches, particularly when the underlying decision process involves strong nonlinearities and interaction effects. Also, in transportation regression problems, neural networks are employed to predict continuous values such as travel demand, travel time, traffic flow, or energy consumption. For instance, LSTM and DNN models, using inputs such as speed, density, weather, fuel price, and historical data, forecast hourly or daily demand with high accuracy (often above 85–90%) [27, 28]. These models are widely used in Intelligent Transportation Systems (ITS) and navigation applications, although they require large volumes of data and careful hyperparameter tuning [29, 30].

2.2. Application of random forest (RF) in mode choice

Random Forest (RF) is an ensemble learning method that builds multiple decision trees on bootstrapped samples and aggregates their predictions through majority voting (classification) or averaging (regression). In transportation mode choice research, RF has become increasingly popular because of its robustness against overfitting, ability to handle mixed data types (numerical and categorical), and built-in feature importance measures that enhance interpretability. Cao et al. [2] compared the Multinomial Logit model with eight machine learning algorithms, including Random Forest, Support Vector Machine, and K-Nearest Neighbors, using large-scale ticketing data. Their results indicated that Random Forest achieved the best prediction accuracy among all tested models. In the specific context of HSR-airplane competition, RF has been applied to stated preference data incorporating socio-economic variables, trip attributes, and environmental awareness, achieving accuracies of 82-85% [31, 32]. Furthermore, RF's resistance to noise and missing values makes it particularly suitable for developing-country contexts where survey data may contain irregularities [33]. Several studies have also used feature importance from RF to identify key determinants of mode choice, such as travel cost, service frequency, and waiting time [1, 4]. Some features of RFs have made them a practical tool to model regression and classification problems in transportation, such as handling mixed types of data, handling missing data, and outlier robustness [6, 32, 34].

2.3. Application of decision tree (DT) in mode choice

Decision Trees (DT) are among the most interpretable machine learning algorithms, partitioning the feature space recursively based on criteria such as Gini impurity or information gain. Each internal node represents a decision rule on a single feature, and leaf nodes provide the final class prediction. In mode choice modeling, decision trees have been used to generate simple, rule-based representations of traveler behavior, which are highly valuable for policy-making and transport planning [35, 36]. For instance, decision trees can reveal threshold effects, such as “if travel time by HSR exceeds 5 hours and ticket price is above 20 million IRR, then the probability of choosing air travel increases significantly.” While individual decision trees are prone to overfitting, they serve as building blocks for more robust ensemble methods like Random Forest and Gradient Boosting. In comparative studies, decision trees typically achieve accuracy levels between 70% and 85% in mode choice classification tasks, depending on tree depth and pruning strategies [37, 38]. Despite their lower predictive power compared to ensemble methods, decision trees remain widely used for exploratory analysis and for generating interpretable if-then rules that can directly inform transport policies [39].

2.4. Application of k-nearest neighbor (KNN) in mode choice

The K-Nearest Neighbors (KNN) algorithm is a non-parametric, instance-based learning method that classifies a new observation based on the majority class among its k closest neighbors in the feature space, using distance metrics such as Euclidean or Manhattan distance. KNN has been applied in mode choice modeling due to its simplicity, absence of a training phase, and ability to adapt to local data structures without assuming any functional form [40, 41]. In the context of intercity travel, KNN has been compared with logit models and other machine learning algorithms, showing competitive performance on moderate-sized datasets. For example, Cao et al. [2] included KNN in their benchmark of eight algorithms and found that KNN achieved reasonable accuracy, though it was outperformed by tree-based ensembles. KNN is particularly effective when the decision boundary between modes is irregular and when the dataset is not excessively large, as computational cost grows with the number of samples and features [34]. However, KNN is sensitive to feature scaling and the choice of k, requiring careful preprocessing. In HSR-airplane choice studies, KNN has achieved accuracy levels of approximately 78-80%, with higher precision typically observed for the more frequent mode (e.g., airplane) [40, 42]. Its transparency and ease of implementation make KNN a useful baseline model for evaluating more complex algorithms.

3. Material and methods

This section describes the data collection process, variable specification, preprocessing steps, model implementation details, and evaluation metrics used in this study.

3.1. Data collection and sample characteristics

An online questionnaire was designed to collect stated preference data from passengers traveling on the Tehran-Mashhad corridor, one of the busiest domestic routes in Iran. The survey was distributed to 100 respondents, each of whom was presented with 18 hypothetical travel scenarios. In each scenario, respondents were asked to choose between High-Speed Rail (HSR) and Airplane (APL) based on a set of trip attributes. The questionnaire also collected socio-economic and psychological characteristics of the respondents.

Stated preference (SP) refers to data collected from hypothetical scenarios where respondents are asked to choose among travel alternatives that are not yet available (e.g., high-speed rail). Revealed preference (RP) refers to data collected from actual past travel decisions, reflecting real-world behavior. This study uses SP data because HSR is not yet operational in the Tehran-Mashhad corridor, making RP data unavailable. SP surveys allow researchers to model choice behavior for new transport services

The socio-economic variables included age (AGE), gender (GENDER), education level (EDU), personal income (INCOME), household income (HHINCOME), previous experience with HSR (HSREXP), number of air trips in the past year (LYAPLTRV), cost of air travel in the past year (LYAPLCST), percentage of monthly income spent on intercity travel (PRCINCMINCTY), maximum acceptable ticket price for Tehran-Mashhad HSR (MAXHSRTCKTM), and affordability for purchasing airplane tickets (ATEFFRD).

Psychological and attitudinal variables included importance of environmental protection in daily decision-making (ENVDDCS), impact of environmental variables on mode choice (ENVEFFCTIMP), awareness of negative impacts of air transportation (ANGTIMPCT), awareness of lower emissions of HSR (LWHSRPLT), willingness to pay more for reduced pollution (MRCSTLWPLT), importance of weekly service frequency (WKFRQ), likelihood of choosing HSR if its frequency exceeds that of APL (HSRMRWFRQ), suitable number of weekly HSR services (HSRSFCWFRQ), fear of flying (APLFEAR), safety concerns during flight (SFTCN), and being forced to use another option due to fear of flying (APLFEALT).

Trip-related attributes varied across the 18 scenarios, including travel time (TIME_HSR, TIME_APL in hours), ticket cost (CST_HSR, CST_APL in Million IRR), availability of comfortable seats (CMSEAT_HSR, CMSEAT_APL), and availability of entertainment (ENTRTMNT_HSR, ENTRTMNT_APL).

3.2. Variable specification

For modeling in this research, the following variables were collected through an online questionnaire from 100 individuals. Passengers with various socio-economic characteristics were presented with 18 scenarios and asked to select their preferred travel mode. The collected variables include those listed in Table 1. In this table, APL stands for airplane, and HSR stands for high-speed rail. In addition to the variables in Table 1, Table 2 also examines the levels of variation in three fundamental variables, namely travel time, cost, and utility. It should be noted that the variables in this research are categorized according to the following description:

- ✓ AGE: age of respondent
- ✓ GENDER: gender of respondent

- ✓ EDU: education level of respondent
- ✓ INCOME: income level of respondent
- ✓ HHINCOME: household income level of respondent
- ✓ HSREXP: previous experience of traveling by HSR
- ✓ LYAPLTRV: the number of air trips in the past year
- ✓ LYAPLCST: the cost of air travel in the past year
- ✓ PRCINCMINCTY: the percentage of monthly income spent on intercity travel
- ✓ MAXHSRTCKTM: the maximum ticket price for the Tehran-Mashhad HSR
- ✓ ATEFFRD: respondents’ affordability for purchasing APL tickets
- ✓ ENVDDCS: importance of environmental protection in daily decision-making
- ✓ ENVEFFCTIMP: impact of environmental variables on travel mode choice
- ✓ ANGTIMPCT: awareness of the negative impacts of air transportation
- ✓ LWHSRPLT: awareness of the lower emissions of HSR
- ✓ MRCSTLWPLT: willingness to pay more for reduced pollution
- ✓ WKFRQ: importance of weekly service frequency in mode choice
- ✓ HSRMRWFRQ: likelihood of choosing HSR if its service frequency exceeds that of APL
- ✓ HSRSFCWFRQ: the suitable number of weekly high-speed rail services
- ✓ APLFEAR: fear of flying
- ✓ SFTCN: safety concerns during a flight
- ✓ APLFEALT: being forced to use another option due to fear of flying
- ✓ CST_HSR or CST_APL: Cost of ticket for HSR and APL respectively.
- ✓ TIME_HSR or TIME_APL: In-vehicle travel time in hour for HSR and APL respectively.
- ✓ CMSEAT_HSR or CMSEAT_APL: Availability of comfortable seat for HSR and APL respectively.
- ✓ ENTRTMNT_HSR or ENTRTMNT_APL: Availability of entertainment for HSR and APL respectively.

Table 1. Description of socio-economic feature collected for this study.

Variables					
AGE		**EDU**		**LYAPLTRV**	
Below 20	2%	Associate diploma and lower	3%	No trip	27%
20 to 30	9%	Bachelor	18%	1 to 4 trips	42%
30 to 40	34%	Masters	58%	5 to 8 trips	13%
40 to 50	32%	PhD and equivalent	21%	9 to 16 trips	11%
More than 50	23%	**INCOME (Million IRR)**		More than 16 trips	7%
GENDER		Below 65	2%	**HHINCOME (Million IRR)**	
Male	66%	65 to 115	4%	Less than 200	20%
Female	34%	115 to 150	6%	200 to 350	26%
HSREXP		150 to 175	7%	350 to 500	29%
Yes	29%	175 to 200	13%	500 to 650	19%
No	71%	200 to 230	9%	**ATEFFRD**	
LYAPLCST (Million IRR)		230 to 267	7%	Poor	20%
Below 50	36%	267 to 315	10%	Fairly poor	26%
50 to 100	15%	315 to 390	15%	Average	40%
100 to 150	23%	More than 390	27%	Fairly good	11%
150 to 300	17%	**PRCINCMINCTY**		Good	3%
More than 300	9%	Below 5%	40%	**ENVDDCS**	
MAXHSRTCKTM (Million IRR)		50 to 10 %	37%	Not important	2%

Below 15	43%	10 to 20%	18%	Low	10%
15 to 20	42%	More than 20%	5%	Medium	22%
20 to 30	15%	**ENVEFFCTIMP**		High	28%
More than 30	0%	Not important	2%	Very high	38%
LWHSRPLT		Low	10%	ANGTIMPCT	
Yes	78%	Medium	22%	Yes	60%
No	22%	High	28%	No	40%
MRCSTLWPLT		Very high	38%	**HSRMRWFRQ**	
Not paying	24%	**WKFRQ**		Not important	4%
To 5%	25%	Not important	5%	Low	3%
5 to 10%	26%	Low	8%	Medium	31%
10% to 20%	19%	Medium	42%	High	47%
More than 20%	6%	High	33%	Very high	15%
HSRSFCWFRQ		Very high	12%	**SFTCN**	
Below 5 trips	13%	**APLFEAR**		Not worried	14%
5 to 10 trips	23%	Yes	22%	Low	26%
10 to 15 trips	30%			Medium	24%
15 to 20 trips	16%	No	78%	High	21%
More than 20 trips	18%			Very high	15%

Table 2. Values of cost, time, and utility in scenarios.

Variable	Values
CST_HSR	10, 15, 20 (Million IRR)
TIME_HSR	4, 5, 6 (Hour)
CMSEAT_HSR	“Yes”, “No”
ENTRTMNT_HSR	“Yes”, “No”
CST_APL	20, 30, 40 (Million IRR)
TIME_APL	1, 1.5, 2 (Hour)
CMSEAT_ APL	“Yes”, “No”
ENTRTMNT_ APL	“Yes”, “No”

3.3. Model selection rationale

Four machine learning algorithms were selected to cover a diverse range of learning paradigms: ANN represents connectionist models capable of capturing highly nonlinear interactions through multiple layers [4]RF is an ensemble method that reduces overfitting via bagging and provides built-in feature importance [32]DT offers maximum interpretability and transparent decision rules [42]; and K-Nearest Neighbors (KNN) is a simple, non-parametric instance-based learner [31]. These models were chosen because they are widely used in transportation mode choice studies, they differ substantially in their underlying mechanisms (neural, tree-based, distance-based), and they allow a fair comparison between complex (ANN, RF) and simpler (DT, KNN) algorithms. Other powerful methods such as gradient boosting (XGBoost, LightGBM, CatBoost) or deep learning architectures (CNNs, RNNs) are certainly suitable, but they typically require larger datasets or are optimized for specific data structures (e.g., images, sequences). Given our moderate sample size (1,800 observations) and the tabular nature of our data, we focused on these four well-established and computationally efficient models.

3.4. Data preprocessing

Prior to model training, the following preprocessing steps were applied:

Handling missing values: No missing values were present in the collected dataset, as all questionnaire items were mandatory.

Train-test split: The dataset, consisting of 100 respondents × 18 scenarios = 1,800 observations, was randomly split into training (75%, i.e., 1,350 samples) and testing (25%, i.e., 450 samples) sets. The test set contained 200 HSR and 250 APL instances (slight imbalance), as reported in the classification reports. To ensure reproducibility, a fixed random seed (42) was used.

Due to the moderate dataset size, hyperparameters were selected based on default values and existing literature, and the final models were evaluated only on the held-out test set. Future work could incorporate cross-validation for more robust hyperparameter optimization. Also, in future research directions, applying metaheuristic algorithms, as described in [43, 44], is practical and can be considered.

3.5. Evaluation metrics

To evaluate the performance of the four machine learning models, this study uses standard classification metrics commonly employed in imbalanced binary prediction tasks. A brief introduction to these metrics is provided here for readers less familiar with machine learning terminology.

Accuracy: The proportion of all predictions that are correct. While intuitive, accuracy can be misleading when class sizes are unequal.

Precision (for a given class): Among all instances predicted as that class, how many were truly that class. High precision means few false alarms (Type-I errors).

Recall (also known as Sensitivity or True Positive Rate): Among all actual instances of that class, how many were correctly predicted. High recall means few missed detections (Type-II errors).

F1-score: The harmonic mean of precision and recall. It provides a single balanced measure when both false positives and false negatives are important.

Macro average: The unweighted average of a metric (e.g., precision) across classes. It treats both classes equally regardless of their sample size.

Weighted average: The average of a metric weighted by the number of instances in each class. It reflects the overall performance on the entire test set.

These metrics are computed on the test set (450 samples) for each model. The results are presented in classification reports and confusion matrices.

3.6. Feature importance analysis

To address the interpretability limitation commonly associated with machine learning models, we conducted a feature importance analysis. This method measures the decrease in model accuracy when the values of a single feature are randomly shuffled across the test set, thereby breaking the relationship between that feature and the target variable (CHOICE). A large drop in accuracy indicates that the model relies heavily on that feature. Permutation importance is model-agnostic, allowing fair comparison across ANN, RF, DT, and KNN. The numerical results are provided in sections 4-5.

4. Modeling results

This section presents the results of applying the aforesaid methods on the dataset of this research.

4.1. Classification report and confusion matrix of ANN

Table 3 shows the results of classification conducted by ANN. According to this table, the neural network model developed for binary classification of travel mode choice between High-Speed Rail (HSR) and airplane (APL) was evaluated on a test set of 450 samples, consisting of 200 instances labeled as HSR and 250 instances labeled as APL. The model achieved an overall accuracy of 84.67%, indicating strong overall discriminative performance across the two classes. This means that out of 450 instances, the model correctly predicted 381 cases (171+210 in the confusion matrix). This level of accuracy reflects the network's ability to capture the complex, nonlinear relationships among socio-economic, trip-related, and attitudinal features used as predictors.

Looking at class-specific metrics, the model showed balanced yet slightly asymmetric behavior. For the HSR class, precision reached 0.8104, recall was 0.8550, and the F1-score stood at 0.8321. This means the model correctly identified 85.50% of actual HSR choosers (high recall) while 81.04% of the instances predicted as HSR were truly HSR (solid precision). These values indicate that among all instances predicted as HSR, 81.04% were actually HSR (precision), and among all true HSR instances, 85.50% were correctly identified (recall). The remaining 18.96% of HSR predictions were false positives, and 14.50% of true HSR instances were missed (false negatives). The F1-score of 0.8321 balances these two aspects. For the airplane class, precision was higher at 0.8787, recall was 0.8400, and the F1-score reached 0.8589. The higher precision indicates fewer false positives when predicting airplane choice, while the recall shows that 84.00% of true airplane choosers were correctly identified.

The aggregate performance metrics show small differences between macro-averaged and weighted-averaged values. The macro-average precision = 0.8445, recall = 0.8475, and F1-score = 0.8455. The weighted average precision = 0.8483, recall = 0.8467, and F1-score = 0.8470. The difference between macro and weighted F1-score is 0.0015, and the difference between macro F1-score and overall accuracy (0.8467) is 0.0012. These negligible differences indicate that class imbalance (200 HSR vs. 250 APL) does not substantially affect the aggregated metrics.

In summary, the neural network classifier exhibits good generalization with balanced class-wise performance, better precision for airplane predictions and higher recall for high-speed rail predictions. A direct quantitative comparison with traditional discrete choice models is not provided here but is suggested for future research.

Table 3. The classification report of ANN.

	Precision	Recall	F1-score	Support
HSR	0.8104	0.8550	0.8321	200
APL	0.8787	0.8400	0.8589	250
Accuracy			0.8467	450
Macro avg	0.8445	0.8475	0.8455	450
Weighted avg	0.8483	0.8467	0.8470	450

Also, the confusion matrix shown in Fig. 1 reveals more facts about the performance of ANN. The confusion matrix for the neural network model reveals a strong and well-balanced classification performance in distinguishing between High-Speed Rail (HSR, class 0) and airplane (APL, class 1) choices on the test set of 450 samples.

Out of the 200 actual HSR choices, the model correctly classified 171 instances (true positives), achieving a recall of 85.50%, meaning it successfully captured the vast majority of passengers who preferred high-speed rail. Only 29 HSR choosers were misclassified as airplane users (false negatives), indicating relatively low omission error for this class. On the airplane side, out of 250 true airplane preferences, the model correctly identified 210 instances (true negatives), corresponding to a recall of 84.00%. The 40 false positives (actual HSR labeled as airplane) suggest the model is somewhat conservative when predicting airplane, but still maintains very good coverage.

Overall, the matrix shows 381 correct predictions (171 + 210) out of 450, yielding the reported 84.67% accuracy. The off-diagonal elements are relatively small and nearly symmetric (29 vs. 40), which confirms the absence of severe class bias despite the slight imbalance in the test set (200 vs. 250).

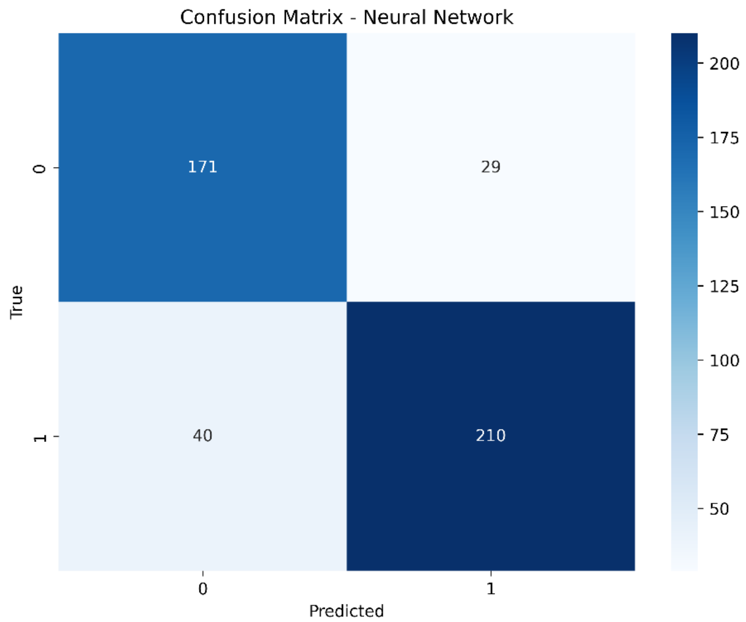

Fig. 1. The confusion matrix of ANN.

4.2. Classification report and confusion matrix of RF

The RF model attained an overall accuracy of 82.44%, reflecting predictive capability in separating the two transport modes using the input features encompassing socio-economic, trip attributes, and attitudinal variables.

Class-level performance metrics indicate reasonably balanced results with a slight edge toward the majority class (airplane), such that the precision difference between airplane (0.8490) and HSR (0.7951) is 0.0539, and the recall difference is 0.0170 (0.8320 vs. 0.8150). For the HSR class, precision was 0.7951, recall reached 0.8150, and the F1-score stood at 0.8049. This shows that the model recovered 81.50% of actual HSR preferences, while 79.51% of predictions labeled as HSR were correct; that indicates reliable performance on the minority class. For the airplane class, precision was higher at 0.8490, recall was 0.8320, and the F1-score reached 0.8404. The elevated precision demonstrates fewer false positives when predicting airplane choice, and the recall confirms that 83.20% of true airplane users were correctly identified.

The aggregate metrics reinforce the model's consistency across classes. The macro-average (unweighted) yielded precision of 0.8221, recall of 0.8235, and F1-score of 0.8227, confirming that performance is not heavily skewed toward the larger class despite the modest imbalance. The weighted average, which accounts for support, produced precision of 0.8250, recall of 0.8244, and F1-score of 0.8246, values that closely mirror the overall accuracy and attest to robust generalization. Overall, the classifier delivers discriminative power with an accuracy of 82.44% and class-wise F1-scores between 0.805 and 0.840. The precision difference (0.7951 vs. 0.8490) suggests a 5.4% higher false positive rate for HSR predictions. This pattern may reflect underlying behavioral biases, though further analysis with revealed preference data would be required to confirm. The results of RF classification are shown in Table 4.

Table 4. The classification report of RF.

	Precision	Recall	F1-score	Support
HSR	0.7951	0.8150	0.8049	200
APL	0.8490	0.8320	0.8404	250
Accuracy			0.8244	450
Macro avg	0.8221	0.8235	0.8227	450
Weighted avg	0.8250	0.8244	0.8246	450

As evident in Fig. 2, the matrix reveals that the model achieved a robust overall accuracy of approximately 82.4%, successfully predicting 371 out of 450 total samples. This performance is underpinned by 163 True Negatives for the HSR class and 208 True Positives for the airplane class. Regarding classification errors, the model exhibited a balanced error profile with 37 False Positives (Type I errors) and 42 False Negatives (Type II errors) (the slightly higher frequency of False Negatives suggests a marginal challenge in detecting the airplane class relative to HSR). The class imbalance ratio in the test set is 1.25. The false positive rate for HSR is 0.185, and for APL is 0.168, yielding a ratio of 1.10, close to the class imbalance ratio. In conclusion, the RF model demonstrates stable and reliable predictive capabilities within this context.

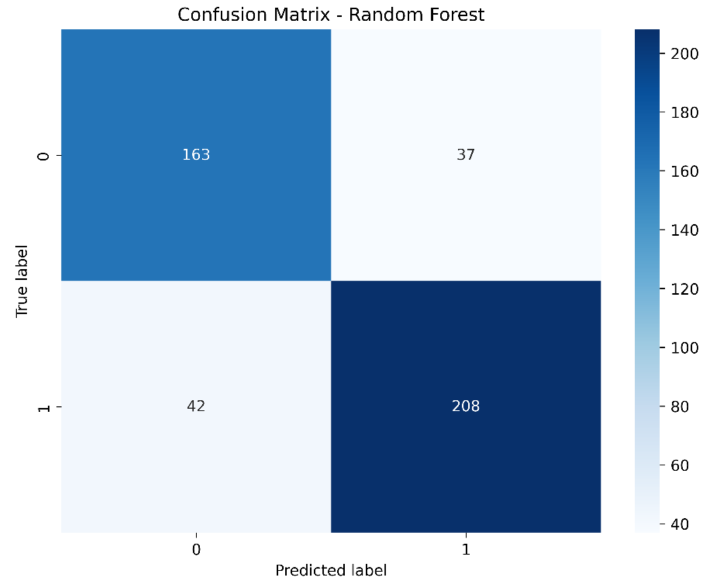

Fig. 2. The confusion matrix of RF.

4.3. Classification report and confusion matrix of DT

The DT model achieves an overall Accuracy of 75.56%. HSR class exhibits a higher Recall (0.7950) compared to its Precision (0.6974). The recall for HSR is 0.7950, while precision is 0.6974, indicating a false positive rate of 30.26% for HSR predictions. The resulting F1-score of 0.7430 represents a balance between these two metrics. Conversely, the airplane class demonstrates superior Precision (0.8153) but a relatively lower Recall (0.7240). This indicates that when the model predicts a sample as airplane, it is highly likely to be correct, although it misses approximately 27.6% of actual airplane cases. The F1-score for airplane (0.7669) is slightly higher than that of HSR. The macro-averaged F1-score (0.7550) treats both classes equally regardless of their support size. Since this value is close to the overall accuracy, it suggests that the model's performance is relatively stable and does not suffer significantly from the slight class imbalance (200 vs. 250). The weighted F1-score (0.7563) accounts for the sample distribution. The proximity between the macro and weighted averages further confirms a consistent performance across both categories. In conclusion, the model demonstrates a robust predictive capability with an F1-score exceeding 0.74 for both classes. There is a clear trade-off between the two classes. Precision for APL (0.8153) exceeds that for HSR (0.6974) by 0.1179, while recall for HSR (0.7950) exceeds that for APL (0.7240) by 0.0710. The results of DT classification are shown in Table 5.

Table 5. The classification report of DT.

	Precision	Recall	F1-score	Support
HSR	0.6974	0.7950	0.7430	200
APL	0.8153	0.7240	0.7669	250
Accuracy			0.7556	450
Macro avg	0.7563	0.7595	0.7550	450
Weighted avg	0.7629	0.7556	0.7563	450

Also, as Fig. 3 suggests, the matrix reveals 159 true negatives (correctly identified HSR instances), 181 true positives (correctly identified airplane instances), 41 false positives (HSR misclassified as airplane), and 69 false negatives (airplane misclassified as HSR), yielding an overall accuracy of 75.56%. For the HSR class (Class 0), the model achieves a recall of 79.5% and precision of 69.7%, indicating it successfully captures the majority of HSR instances but occasionally misidentifies them as airplane. Conversely, the airplane class (Class 1) demonstrates superior precision at 81.5% with a recall of 72.4%, suggesting the model is more conservative when predicting airplane(when it does, it is highly likely to be correct, though some actual airplane cases are missed). The confusion matrix reveals that Correct predictions (159 + 181 = 340) outnumber misclassifications (41 + 69 = 110) by a ratio of 3.09:1, which confirms the model's overall predictive reliability.

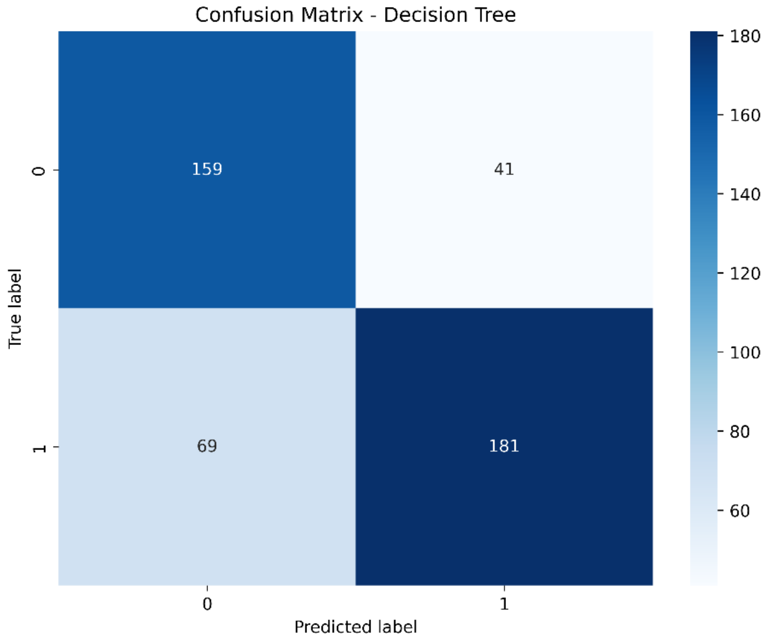

Fig. 3. The confusion matrix of DT.

4.4. Classification report and confusion matrix of KNN

The KNN model achieves an overall Accuracy of 78.44%, indicating good performance across the entire dataset. The HSR class exhibits balanced values for Precision and Recall (0.7225 and 0.7300, respectively). This convergence suggests that the model performs without significant bias in identifying HSR instances (the difference between precision and recall for HSR is 0.0075). In contrast, the airplane class demonstrates superior performance, with Precision of 0.7931, Recall of 0.8280, and F1-score of 0.8102. This indicates that the model possesses high proficiency in identifying airplane patterns. The macro-average (Macro avg), which assigns equal weight to each class, shows an F1-score of 0.7804, closely aligned with the overall Accuracy (78.44%). The macro F1-score (0.7804) and weighted F1-score (0.7837) differ by 0.0033, demonstrating that the model maintains good stability against the slight class imbalance in data distribution (200 vs. 250 samples). The weighted F1-score (Weighted avg) at 0.7837 also shows close alignment with the macro-average, further confirming the model's consistent performance across both categories. In conclusion, the model demonstrates reliable predictive capability, with F1-scores exceeding the 75% threshold for both classes. The classification report results for KNN are presented in Table 6.

Table 6. The classification report of KNN.

	Precision	Recall	F1-score	Support
HSR	0.7225	0.7300	0.7506	200
APL	0.7931	0.8280	0.8102	250
Accuracy			0.7844	450
Macro avg	0.7828	0.7790	0.7804	450
Weighted avg	0.7839	0.7844	0.7837	450

The KNN matrix in Fig 4 reveals146 true negatives (correctly identified HSR instances), 207 true positives (correctly identified airplane instances), 54 false positives (HSR misclassified as airplane), and 43 false negatives (airplane misclassified as HSR), yielding an overall accuracy of 78.44%. For the HSR class (Class 0), the model achieves a recall of 73.0% and precision of 77.2%, indicating it successfully captures the majority of HSR instances with relatively balanced performance between capturing true instances and avoiding false classifications. Conversely, the airplane class (Class 1) demonstrates strong performance with precision at 79.3% and recall at 82.8%, suggesting the model is particularly proficient at identifying airplane patterns, both catching most actual airplane cases and maintaining high confidence when it makes such predictions. The diagonal dominance in the confusion matrix, where correct predictions (146 and 207) significantly outnumber misclassifications (54 and 43), confirms the model's overall predictive reliability. The KNN model shows improved accuracy compared to the DT (78.44% vs. 75.56%), with notably lower misclassification rates for airplane (43 vs. 69 false negatives).

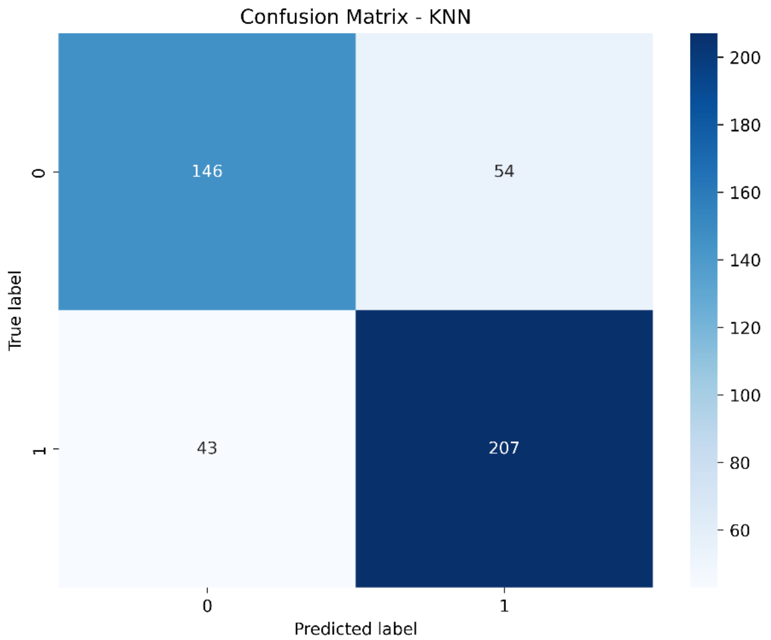

Fig. 4. The confusion matrix of KNN.

4.5. Feature importance analysis

Fig. 5 presents the permutation importance results for the top 15 features for the superior model, ANN. Based on this diagram, CST_APL (airplane ticket cost) was the most influential predictor, with a mean decrease in accuracy of 13.87% when shuffled. CST_HSR (HSR ticket cost) ranked second, with an importance of 11.71%. Travel time variables ranked third and fourth: TIME_APL (6.08%) and TIME_HSR (5.45%). The fifth most important feature was LYAPLCST (cost of air travel in the past year) at 3.76%. Household income (HHINCOME, 3.51%) and personal income (INCOME, 3.43%) showed moderate importance, followed by ATEFFRD (affordability for APL tickets, 3.18%), HSRMRWFRQ (likelihood of choosing HSR if frequency exceeds APL, 3.17%), and ENVEFFCTIMP (impact of environmental variables on mode choice, 3.16%). The remaining features, including HSRSFCWFRQ (3.16%), SFTCN (safety concerns, 3.08%), WKFRQ (weekly service frequency importance, 3.08%), ENVDDCS (environmental protection importance, 3.02%), and MRCSTLWPLT (willingness to pay more for reduced pollution, 2.90%), all showed importance values below 3.5%. Overall, the top four features (CST_APL, CST_HSR, TIME_APL, TIME_HSR) account for a total importance of 34.87%, indicating that travel cost and travel time dominate mode choice predictions in this dataset.

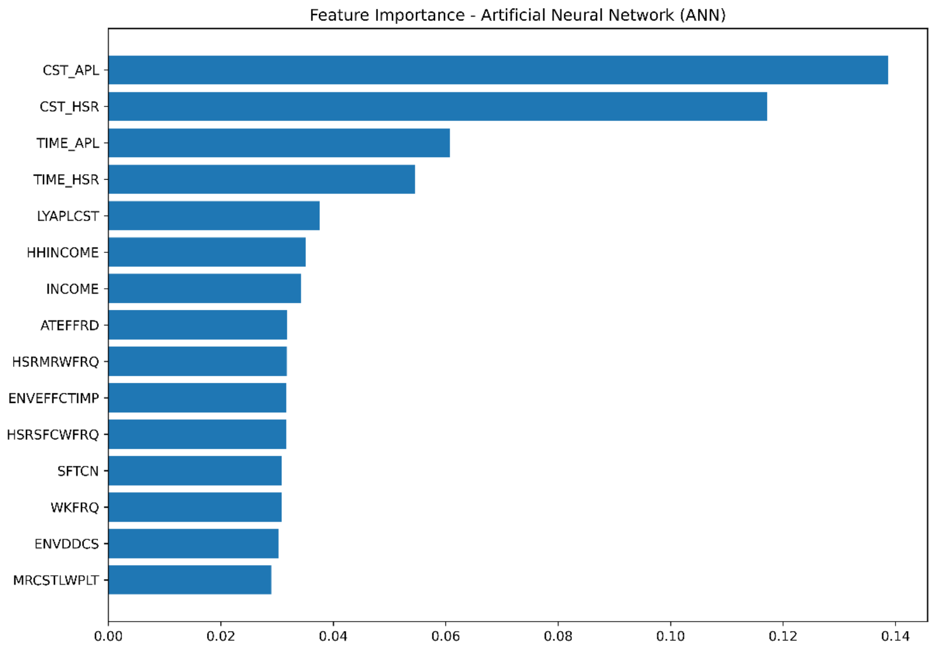

Fig. 5. The feature importance of ANN.

5. Discussion

In the previous section, numerical results of different models were provided by the classification report and confusion matrix. This section is an attempt to address a major question: “Which model could outperform others?” and provide numerical insights into answering it.

The comparative analysis of machine learning models for travel mode choice classification reveals distinct performance characteristics across the four algorithms evaluated. The ANN emerged as the top performer with an overall accuracy of 84.67%, demonstrating capability in capturing complex non-linear relationships between socio-economic, trip-related, and attitudinal predictors. The RF model followed with 82.44% accuracy, showing robust predictive capability with relatively balanced class-wise performance, though slightly favoring the majority class. The KNN model achieved 78.44% accuracy with good performance on the airplane class (F1-score of 0.8102), suggesting pattern recognition for air travel preferences. Meanwhile, the DT model recorded 75.56% accuracy, exhibiting a distinct trade-off pattern characterized by higher recall for HSR (0.7950) paired with lower precision (0.6974), indicating a classification approach for rail choice at the cost of increased false positives.

Class-specific analysis across all models consistently demonstrated higher precision for airplane predictions, reflecting fewer false positives when identifying air travel choices, while recall metrics were generally superior for HSR classifications. The proximity between macro-averaged and weighted F1-scores in all models confirmed consistent performance despite the slight class imbalance (200 HSR vs. 250 airplane samples).

Overall, the findings suggest that ensemble methods and neural network architectures offer advantages over simpler decision-based algorithms for modeling multimodal transport choices, with ANN particularly excelling in capturing the intricate interplay between attitudinal variables and mode selection behavior. These results demonstrate the predictive performance of machine learning models on this dataset. A quantitative comparison with traditional discrete choice models is not provided here but is recommended for future research.

Fig. 6a and 6b depict frameworks in which the numerical indicators of these methods are presented, hence a better numerical comparison and inference can be made.

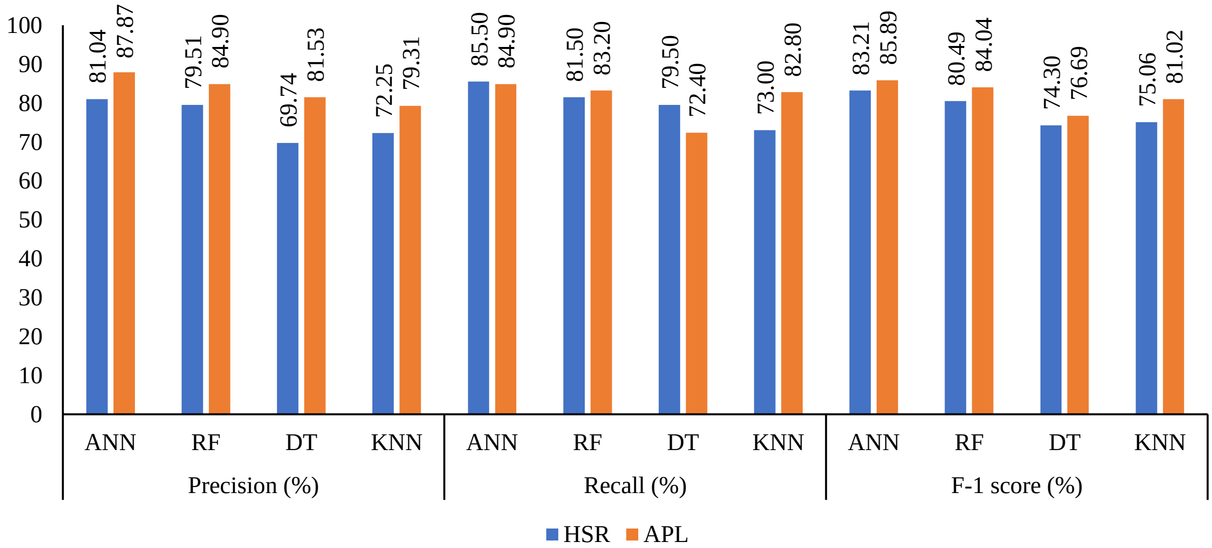

(a)

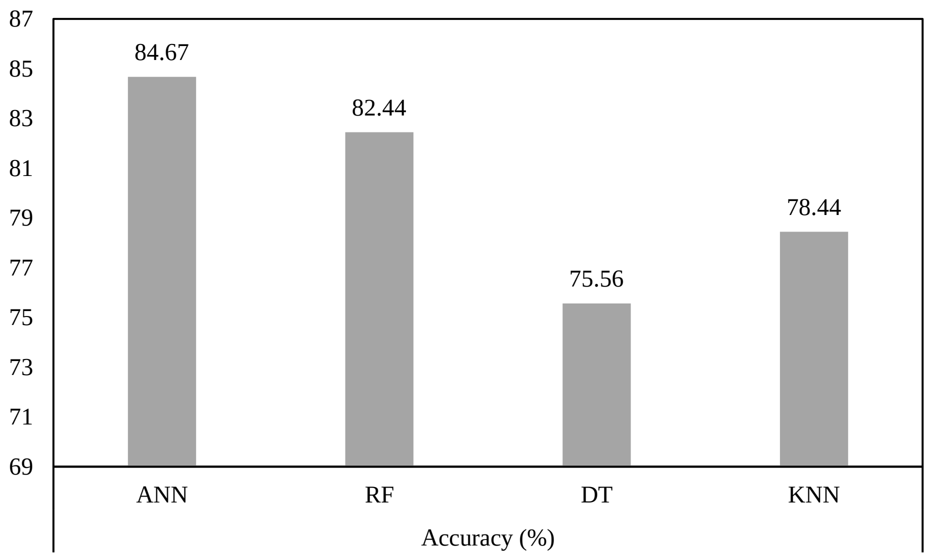

(b)

Fig. 6. Models evaluating mode choice: (a) Precision, Recall and F-1 Score for ML, and (b) Precision, Recall and Accuracy for ML.

6. Conclusion

This study investigated the application of machine learning algorithms for mode choice modeling between high-speed rail (HSR) and airplane in Iran's transportation network, using stated preference data collected from 100 respondents across 18 travel scenarios. The comparative analysis of four machine learning models, ANN, RF, KNN, and DT, revealed that ANN achieved the highest overall accuracy (84.67%), followed by RF (82.44%), KNN (78.44%), and DT (75.56%). This ranking indicates that ensemble methods and neural network architectures are more effective in capturing complex nonlinear relationships in this dataset. Class-specific analysis showed higher precision for airplane predictions across all models, while recall metrics were generally superior for HSR classifications, suggesting that distinct psychological and attitudinal factors influence rail preferences.

- This research addresses three critical gaps in mode choice literature by being among the first Iranian studies to apply machine learning for HSR-airplane competition, successfully incorporating psychological variables (fear of flying, environmental awareness, willingness to pay) alongside socio-economic predictors, and providing algorithm evaluation using standardized metrics.
- While this study demonstrates ML's potential, limitations such as reliance on stated preference data, focus on a single corridor (Tehran-Mashhad), and limited sample size warrant future research integrating revealed preference data, multi-corridor analysis, and larger diverse datasets. Also, since the study has focused exclusively on a single corridor (Tehran-Mashhad), results may not be transferable to other routes with different distance, demographic, or competitive characteristics. Finally, psychological variables were measured using single questions rather than validated multi-item scales, which may not capture the full complexity of attitudes such as fear of flying or environmental concern.
- Regarding generalizability, the findings of this study are derived from stated preference data collected along a single corridor (Tehran-Mashhad, approximately 900 km) in Iran, a country where high-speed rail is not yet operational. While this setting provides a valuable developing-country perspective, caution should be exercised when extrapolating the results to other contexts. Several factors may limit generalizability, such as the distance and travel time values that are specific to this corridor, different income levels, price sensitivity, and modal availability across countries, psychological factors, and the absence of actual HSR service means respondents' stated preferences may differ from revealed behavior once HSR is implemented. Nevertheless, the relative ranking of model performance (ANN > RF > KNN > DT) and the dominance of cost and time as predictors suggest that certain patterns may transfer. Future research should apply the same modeling framework to multiple corridors and different developing or developed nations to test the robustness of our conclusions.
- A point that could be considered as a potential future direction is using metaheuristic algorithms, such as Water Cycle Algorithm (WCA), Wild Horse Optimization (WHO), Particle Swarm Optimization (PSO), genetic algorithm (GA), and other known algorithms for tuning hyperparameters [43-45]. Also, exploring hybrid models that embed logit-based interpretability into machine learning frameworks could be considered. In these approaches, such as utility-consistent neural networks or two-stage approaches, ML identifies nonlinear patterns and logit provides behavioral coefficients.

Statements & Declarations

Author contributions

Mohammad Feli: Conceptualization, Methodology, Validation, Formal analysis, Writing – Original Draft, Writing-Review & Editing.

Ali Naderan: Conceptualization, Methodology, Formal analysis, Project administration, Supervision, Writing - Review & Editing.

Mahmoud Saffarzadeh: Conceptualization, Methodology, Project administration, Supervision, Writing - Review & Editing.

References

[1] Banyong, C., Hantanong, N., Wisutwattanasak, P., Champahom, T., Theerathitichaipa, K., Seefong, M., Ratanavaraha, V., Jomnonkwao, S. A machine learning comparison of transportation mode changes from high-speed railway promotion in Thailand. Results in Engineering, 2024; 24: 103110. doi:10.1016/j.rineng.2024.103110.

[2] Cao, W., Chen, Z., Shi, F., Xu, J. Analysis of travel mode choice behavior between high-speed rail and air transport utilizing large-scale ticketing data. Transportation Research Record: Journal of the Transportation Research Board, 2024; 2679: 1344–1358. doi:10.1177/03611981241270169.

[3] Li, X., Wang, Y., Wu, Y., Chen, J., Zhou, J. Modeling Intercity Travel Mode Choice with Data Balance Changes: A Comparative Analysis of Bayesian Logit Model and Artificial Neural Networks. Journal of Advanced Transportation, 2021; 2021: 9219176. doi:10.1155/2021/9219176.

[4] Banyong, C., Hantanong, N., Nanthawong, S., Se, C., Wisutwattanasak, P., Champahom, T., Ratanavaraha, V., Jomnonkwao, S. Machine learning-based analysis of travel mode preferences: Neural and boosting model comparison using stated preference data from Thailand's emerging high-speed rail network. Big Data and Cognitive Computing, 2025; 9: 155. doi:10.3390/bdcc9060155.

[5] Zhao, X., Yan, X., Yu, A., Van Hentenryck, P. Prediction and behavioral analysis of travel mode choice: A comparison of machine learning and logit models. Travel Behaviour and Society, 2020; 20: 22–35. doi:10.1016/j.tbs.2020.02.003.

[6] Ali, M. Discrete Choice Models and Artificial Intelligence Techniques for Predicting the Determinants of Transport Mode Choice—A Systematic Review. Computers, Materials and Continua, 2024; 81: 2161–2194. doi:10.32604/cmc.2024.058888.

[7] Fale, M., Wang, Y., Rupnik, B., Kramberger, T., Vizinger, T. Systematic review of transportation choice modeling. Applied Sciences, 2025; 15: 9235. doi:10.3390/app15179235.

[8] Forsythe, C. R., Arteaga, C., Helveston, J. P. The Mixed Aggregate Preference Logit Model: A Machine Learning Approach to Modeling Unobserved Heterogeneity in Discrete Choice Analysis. arXiv preprint arXiv:2402.00184, 2024; doi:10.48550/arXiv.2402.00184.

[9] Givoni, M., Dobruszkes, F. A review of ex-post evidence for mode substitution and induced demand following the introduction of high-speed rail. Transport Reviews, 2013; 33: 720–742. doi:10.1080/01441647.2013.853707.

[10] Fu, X., Oum, T. H., Yan, J. An analysis of travel demand in Japan's intercity market empirical estimation and policy simulation. Journal of Transport Economics and Policy (JTEP), 2014; 48: 97–113. doi:10.3828/jtep.2014.48.1.97.

[11] Raturi, V., Verma, A. A game-theoretic approach to analyse inter-modal competition between high-speed rail and airlines in the Indian context. Transportation Planning and Technology, 2020; 43: 20–47. doi:10.1080/03081060.2020.1701666.

[12] Xia, W., Wang, K., Zhang, A. Air transport and high-speed rail interactions in China: review on impacts of low-cost carriers, rail speed, and modal integration. Advances in Airline Economics, 2018; 7: 103–122. doi:10.1108/S2212-160920180000007007.

[13] Xia, W., Zhang, A. Air and high-speed rail transport integration on profits and welfare: Effects of air-rail connecting time. Journal of Air Transport Management, 2017; 65: 181–190. doi:10.1016/j.jairtraman.2017.06.008.

[14] Park, Y., Ha, H.-K. Analysis of the impact of high-speed railroad service on air transport demand. Transportation Research Part E: Logistics and Transportation Review, 2006; 42: 95–104. doi:10.1016/j.tre.2005.09.003.

[15] Román, C., Martín, J. Potential demand for new high speed rail services in high dense air transport corridors. International Journal of Sustainable Development and Planning, 2010; 5: 114–129. doi:10.2495/SDP-V5-N2-114-129.

[16] Raturi, V., Verma, A. Analyzing competition between High Speed Rail and Bus mode using market entry game analysis. Transportation Research Procedia, 2017; 25: 2373–2384. doi:10.1016/j.trpro.2017.05.264.

[17] Raturi, V., Verma, A. Competition between High Speed Rail and Conventional Transport Modes: Market Entry Game Analysis on Indian Corridors. Networks and Spatial Economics, 2019; 19: 763–790. doi:10.1007/s11067-018-9421-2.

[18] D'Alfonso, T., Jiang, C., Bracaglia, V. Would competition between air transport and high-speed rail benefit environment and social welfare? Transportation Research Part B: Methodological, 2015; 74: 118–137. doi:10.1016/j.trb.2015.01.007.

[19] D'Alfonso, T., Jiang, C., Bracaglia, V. Air transport and high-speed rail competition: Environmental implications and mitigation strategies. Transportation Research Part A: Policy and Practice, 2016; 92: 261–276. doi:10.1016/j.tra.2016.06.009.

[20] Wang, J., Jiao, J., Du, C., Hu, H. Competition of spatial service hinterlands between high-speed rail and air transport in China: Present and future trends. Journal of Geographical Sciences, 2015; 25: 1137–1152. doi:10.1007/s11442-015-1224-5.

[21] Edrissi, A., Javanbakht, N., Ganjipour, H. Modeling the behavior of disordered taxi drivers of Tehran for choosing passenger and destination. International Journal of Human Capital in Urban Management, 2019; 4: 69–76. doi:10.22034/IJHCUM.2019.01.08.

[22] Pagliara, F., Vassallo, J. M., Román, C. High-speed rail versus air transportation: Case study of Madrid–Barcelona, Spain. Transportation Research Record: Journal of the Transportation Research Board, 2012; 2289: 10–17. doi:10.3141/2289-02.

[23] Javanbakht, N., Mirbaha, B. Evaluating Drivers' Response to Road Hazard: A Simulation Study. Advances in Civil Engineering, 2024; 2024: 6788857. doi:10.1155/2024/6788857.

[24] Javanbakht, N., Mirbaha, B. From Traits to Speed Control: Engineering Insights from a Driving-Simulator Hazard Scenario. Contributions of Science and Technology for Engineering, 2026; 3: 10–19. doi:10.22080/cste.2025.29839.1075.

[25] Pan, J. High-Speed Rail in the US—Mode Choice Decision and Impact of COVID-19. Sustainability, 2024; 16: 4041. doi:10.3390/su16104041.

[26] Hillel, T., Bierlaire, M., Elshafie, M. Z. E. B., Jin, Y. A systematic review of machine learning classification methodologies for modelling passenger mode choice. Journal of Choice Modelling, 2021; 38: 100221. doi:10.1016/j.jocm.2020.100221.

[27] Chmielewski, J., Wójcik, M. The Use of Deep Neural Networks (DNN) in Travel Demand Modelling. Applied Sciences, 2025; 15: 11290. doi:10.3390/app152011290.

[28] Buijs, R., Koch, T., Dugundji, E. Using neural nets to predict transportation mode choice: Amsterdam network change analysis. Journal of Ambient Intelligence and Humanized Computing, 2021; 12: 121–135. doi:10.1007/s12652-020-02855-6.

[29] Tang, L., Tang, C., Fu, Q., Ma, C. Predicting travel mode choice with a robust neural network and Shapley additive explanations analysis. IET Intelligent Transport Systems, 2024; 18: 1339–1354. doi:10.1049/itr2.12514.

[30] Amoei Khorshidi, N., Zargari, S., Mirzahossein, H., Heidari, H., Waller, S. Predicting travel-time reliability in road networks: a Fitrnet-based approach–a case study of England. Scientific Journal of Silesian University of Technology. Series Transport, 2025; 126: 79–95. doi:10.20858/sjsutst.2025.126.5.

[31] Bhosle, N., Jagtap, J., Svitek, M. Machine Learning-Based Travel Mode Prediction: A Comparative Methodological Approach. In: 2025 Smart City Symposium Prague (SCSP); 2025; Prague. p. 1–5. doi:10.1109/SCSP65598.2025.11037720.

[32] Zhang, W., Luo, Z. Research on intercity travel mode recognition and network structure characteristics based on complex network and random forest classification. Scientific Reports, 2025; 15: 35339. doi:10.1038/s41598-025-19392-x.

[33] Naseri, H., Waygood, E. O. D., Patterson, Z., Alousi-Jones, M., Wang, B. Travel mode choice prediction: developing new techniques to prioritize variables and interpret black-box machine learning techniques. Transportation Planning and Technology, 2025; 48: 582–605. doi:10.1080/03081060.2024.2411611.

[34] Afandizadeh Zargari, S., Amoei Khorshidi, N., Mirzahossein, H., Heidari, H. Analyzing the effects of congestion on planning time index–Grey models vs. random forest regression. International Journal of Transportation Science and Technology, 2023; 12: 578–593. doi:10.1016/j.ijtst.2022.05.008.

[35] Kalantari, H., Sabouri, S., Brewer, S., Ewing, R., Tian, G. Machine learning in mode choice prediction as part of mpos' regional travel demand models: Is it time for change? Sustainability, 2025; 17: 3580. doi:10.3390/su17083580.

[36] Uddin, M., Anowar, S., Eluru, N. Modeling freight mode choice using machine learning classifiers: a comparative study using Commodity Flow Survey (CFS) data. Transportation Planning and Technology, 2021; 44: 543–559. doi:10.1080/03081060.2021.1927306.

[37] Ghosh, T., Nagaraj, N. Evaluating the determinants of mode choice using statistical and machine learning techniques in the Indian megacity of Bengaluru. arXiv preprint arXiv:2401.13977, 2024; doi:10.48550/arXiv.2401.13977.

[38] Dahmen, V., Weikl, S., Bogenberger, K. Interpretable machine learning for mode choice modeling on tracking-based revealed preference data. Transportation Research Record: Journal of the Transportation Research Board, 2024; 2678: 2075–2091. doi:10.1177/03611981241246973.

[39] Afandizadeh, S., Amoei Khorshidi, N., Mirzahossein, H., Shakoori, S. Predicting the fluctuation of travel time reliability as a result of congestion variations by bagging-based regressors. Civil Engineering Infrastructures Journal, 2024; 57: 85–101. doi:10.22059/ceij.2023.349853.1878.

[40] Jang, J. Travel-time prediction using K-nearest neighbor method with distance metric of correlation coefficient. The Open Transportation Journal, 2019; 13: 141–150. doi:10.2174/1874447801913010141.

[41] Lagos, F., Moreno, S., Yushimito, W. F., Brstilo, T. Urban Origin–Destination Travel Time Estimation Using K-Nearest-Neighbor-Based Methods. Mathematics, 2024; 12: 1255. doi:10.3390/math12081255.

[42] Afandizadeh Zargari, S., Amoei Khorshidi, N., Mirzahossein, H., Kalantari, N. Comparative approach for predicting travel time reliability (a case study of Virginia interstate). Innovative Infrastructure Solutions, 2021; 6: 229. doi:10.1007/s41062-021-00597-8.

[43] Khorshidi, N., Rezashoar, S., Amini, P., Zargari, S. A., Mirzahossein, H. Metaheuristic-optimized neural networks for travel time index prediction: a comparative study of wild horse and coot optimization algorithms. Transportation Engineering, 2025; 22: 100395. doi:10.1016/j.treng.2025.100395.

[44] Khorshidi, N., Zargari, S. A., Rezashoar, S., Mirzahossein, H. Optimizing Travel Time Reliability with XAI: A Virginia Interstate Network Case Using Machine Learning and Meta-Heuristics. Machine Learning with Applications, 2025; 21: 100709. doi:10.1016/j.mlwa.2025.100709.

[45] Zargari, S. A., Khorshidi, N. A., Mirzahossein, H., Shakoori, S., Jin, X. Travel time reliability prediction by genetic algorithm and machine learning models. Proceedings of the Institution of Civil Engineers - Transport, 2022; 177: 214–223. doi:10.1680/jtran.22.00065.

Civil Engineering and Applied Solutions

Research Article

journal homepage: ceas.journals.umz.ac.ir

CEAS Civil Engineering and Applied Solutions

Experimental Assessment for Restoring the Flexural Strength of Severely Damaged RC Beams Using NSM Steel Bars and External Confinement

Rasha A. Aljazaari [a], Javad Vaseghi Amiri [b*], Hayder Alghazali [a]

[a] *Department of Civil Engineering, Engineering College/ Kufa University, Najaf, Iraq*
[b] *Department of Civil Engineering, Babol Noshirvani University of Technology, Babol, Iran*

ARTICLE INFO

Article history:

Received 15 April 2026

Revised 03 May 2026

Accepted 10 June 2026

Available online 01 January 2027

Keywords:

Repairing

Near-surface mounting (NSM)

Hooked bar configuration

Epoxy

Cementitious material

External bonding

ABSTRACT

Reinforced concrete beams may require repair to regain lost capacity due to unforeseen events, such as accidents or loading exceeding the limits that weren't predicted in the design. The purpose of this research is to restore the load capacity of RC beams after severe mid-span damage. Eight reinforced concrete beams were utilized in this study. A near-surface mounting (NSM) technique was examined, with various variables including the configuration of repair bars, adhesive materials, diameter of repair bars, as well as externally bonded repair with a steel plate in the damaged zone. The result revealed that straight bars restored up to 94.5% of ultimate strength, while hooked bars slightly exceeded the control by 5%. Epoxy bonds achieved up to 105.6% recovery, surpassing cementitious systems that ranged from 66.8% to 110.6%. Larger repairing bars of 16 mm restored capacities up to 115.6%, significantly higher than the recovery range from 66.8% to 82.4% for 12 mm bars. Confinement raised the ultimate load marginally above control, of 5.4%, while unconfined beams recovered only 82.4%. Cementitious adhesives offered an economical repair option for moderate-demand applications; however, both bonding systems reduced ductility by up to 55.6% and energy absorption by up to 89.3%. Straight bars improved stiffness and ductility compared with hooked bars, while larger bar diameters of 16 mm reduced performance losses and enhanced stiffness. Confinement improved service stiffness and partially limited energy-absorption losses, although ductility remained below that of the control beam.

How to cite this article: Aljazaari, R.A. Vaseghi Amiri, J. Alghazali, H. Experimental Assessment for Restoring the Flexural Strength of Severely Damaged RC Beams Using NSM Steel Bars and External Confinement .Civil Engineering and Applied Solutions. 2027; 3(1): 161–178. doi:10.22080/ceas.2026.31548.1090.

1. Introduction

The structural components experience higher service loads or deformations than their design capacity due to overloads or changes in function, leading to cracks induced through insufficient ultimate strength [1]. Bridges are a common example of a bridge girder failing locally due to excessive use, overloading, failure to follow height specifications for each bridge, and various other reasons [2]. During the initial design, these considerations were not taken into account, which contributed to stress exceeding their capacity [3].

In general, repairing damaged concrete structures is essential not only to ensure they function as intended during their expected service trajectory but also to guarantee the safety and functionality of related components so that they meet the precise requirements of modern and future structures [4]. A good repair boosts the function and performance of structures, restoring and increasing their strength and stiffness. In fact, repairing techniques, rather than replacing structures, have become both efficient and more economically beneficial. Maintaining structural elements tends to be cheaper and faster than reconstructing them [5, 6]. Generally,

* Corresponding author.
E-mail addresses: vaseghi@nit.ac.ir (J. Vaseghi Amiri).

https://doi.org/10.22080/ceas.2026.31548.1090
ISSN: 3092-7749/© 2027 The Author(s). Published by University of Mazandaran.

repair is seen as a process where the behavior of the concrete element after repair does not deviate much from its original behavior. Its main goal is to restore the architectural shape and function of the concrete structure without significantly enhancing its performance [7]. In the current economic environment, repairing concrete structures that were damaged to comply with the stricter restrictions regarding the maximum strength and serviceability of the latest codes, as well as repairing preexisting concrete constructions to support more allowable loads, appear to be more viable options compared to demolition and building from scratch [8].

A variety of new and complex repair materials and procedures have been successfully developed to improve the functionality and performance of damaged reinforced concrete structures. The two traditional methods are the NSM method and bonding by steel plate [9, 10]. The NSM was the more effective approach and was also easier and faster to use, ensuring fewer fragile failure modes. Rods or strips can be used to perform this technique [11]. In Near-surface-mounted (NSM) systems, the embedded bars or plates are installed into premade grooves on the concrete surface; bonding between the bar and the grooves can be achieved using a suitable adhesive cured in place. In NSM systems, the groove dimensions should be a minimum of 1.5 times the diameter of the embedded bar. The clear groove spacing, which is at least twice the groove depth of the NSM system, should be used to prevent overlapping tensile stresses around the embedded bars. Additionally, a clear edge space of four times the groove depth of the NSM must be provided to reduce the influence of debonding-type failures at the edge [12].

NSM offers many privileges over the (EB) approach, such as protection, enhanced bonding, good appearance, and surface prepping. The bond quality has improved significantly over the EB method; it remains the key consideration for designing elements strengthened or repaired in the NSM method [13]. NSM is also superior to EBR because it has a more even distribution of strain, which maximizes strain utilization and provides greater resistance to environmental influences, as it is plumbed beneath the surface of the concrete. Sometimes, the embedded rods are placed under grout, which means the visual effect of the NSM technique is almost imperceptible. For parking lot slabs experiencing low negative moment levels, embedded bars in the NSM approach are used to enhance the structure's capacity, as the surface cuts shield the embedded bars from the effects of vehicular traffic. According to the NSM approach, bar installation requires less work since treating pre-existing concrete surfaces is unnecessary. Surface non-regularity or weakened cover of concrete no longer presents an issue, given that the drilled cuts for embedded bars for the NSM method have been profound and narrow [14].

Some researchers evaluated the NSM using steel rods. Rahman et al. [15] examined the flexural behavior of RC beams strengthened using NSM steel bars and confirmed that this technique is a cost-effective solution for enhancing flexural performance. In addition, cement mortar was verified to perform nearly as well as using 100% epoxy adhesive when partially replaced by 50% epoxy glue in the NSM groove. The NSM technique outperformed the plate bonding method, requiring only one-third of the steel, thereby highlighting its efficiency and economic potential for retrofitting applications. Mobin and Haque [16] evaluated the performance of the NSM with steel bars, demonstrating that doubling the amount of NSM steel reinforcement raised the maximum load by 102.4%, offered a high level of ductility, and resulted in a ductile failure mechanism. The employment of cement paste instead of epoxy adhesive exhibits adequate strength and ductility, significantly reducing costs with only a minor decrease in performance. Sabah and Hamza [17] evaluated the effectiveness of the NSM technique using steel rebars. The outcomes revealed that NSM steel bars increased the ultimate load by 28.5% and ductility by 24.6%. Kholil et al. [18] employed finite element analysis to examine the flexural repair of RC beams using the NSM-steel bars technique, demonstrating that providing 80% NSM reinforcement to the tensile zone improved the ultimate load by approximately 1.64 times and enhanced stiffness by 2.24 times.

Other papers have studied the use of a steel plate as an external strengthening or repair method. Olajumoke and Dundu [19] reviewed various techniques for strengthening RC elements in bending. They highlighted the effectiveness of steel plates in enhancing flexural strength through both Externally Bonded Reinforcement (EBR) and NSM methods. While both methods are effective, the study found that EBR offers better practical applicability than NSM in real-world scenarios. Abuodeh et al. [20] experimentally evaluated the performance of RC beams strengthened using externally bonded and bolted Aluminum Alloy (AA) plates. Beams with bonded AA plates increased capacity by 32% and deflection by 45%, whereas those with both bolting and bonding increased capacity by 24% and deflection by 84%. In conclusion, combining bolting and bonding significantly enhances ductility and reduces debonding, resulting in an effective anchorage solution with minimal loss of strength. Zhang et al. [21] introduced a new steel plate strengthening technique for damaged RC beams. The strengthened beams exhibited an increase in cracking moments from 214.5% to 271.5%, and a bearing capacity boost of 53.1% to 73.7%. The primary failure mode was interface peeling. Moreover, the flexural stiffness nearly doubled on average, and further increasing the steel plate thickness improved both stiffness and strain performance.

While prior research has examined NSM strengthening approaches, limited attention has been devoted to the repair of severely damaged lap-spliced reinforced concrete (RC) beams using NSM steel bars. Additionally, the comprehensive assessment of hook-bar configuration, epoxy versus cementitious adhesives, and external confinement remains insufficiently explored. Consequently, this study aims to address these research gaps through a systematic experimental program.

2. Research significant

The research highlights practical, evidence-based solutions for repairing damaged RC beams, showing how repair combinations restore performance and improve serviceability. It emphasizes the importance of bar configuration and steel plate confinement in stress distribution and ductility. Advocating for repair over replacement, the study supports sustainable, cost-effective practices that extend the lifespan of structures and deepen the understanding of material-structure interactions, guiding more effective restoration techniques.

3. Research obejectives

Accordingly, the objectives of the present study are summarized as follows:

1. To investigate the effect of repair bar configuration (straight versus hooked bars) on the behavior of severely damaged RC beams repaired using the NSM technique.
2. To evaluate the influence of bonding material type (epoxy versus cementitious adhesive) on repair effectiveness.
3. To examine the effect of repair bar diameter on the flexural response of repaired beams.
4. To assess the contribution of external steel plate confinement to the performance of the proposed repair system.
5. To evaluate the effectiveness of the previous parameters based on the recorded and calculated response metrics, namely ultimate load capacity (Pu), ductility index (μ), stiffness, and energy absorption, in order to identify the most efficient and practical repair strategy.

4. Experimental work

4.1. Specimens details

Eight reinforced concrete beam specimens with rectangular cross-sections, measuring 200 mm in width and 300 mm in depth, with a total length equal to 2000 mm and a clear span of 1800 mm, were utilized in this study. Lap splicing was employed in the tested beams to establish a controlled weak region, thereby simulating a localized incident. Consequently, using a splice length shorter than the recommended ACI value prevents reinforcement from yielding in flexure, failing by debonding or bond-slip at the splice. The reference beam specimen had no mid-span splice, so the reinforcement was continuous. The other reinforced concrete beams were lap-spliced at their centers. Three 12 mm deformed steel bars served as the primary longitudinal reinforcement. The beam splice specimen design utilized 70% of the predicted development length, based on earlier work by [22]. The adopted splice length was 200 mm, and lap splicing was used, which is below the recommended value in the ACI Code; as a result, the specimens are likely to experience debonding of the lap-spliced bars. Stirrup spacing was reduced to ensure that a shear failure would not occur before a bond failure. The stirrups were not placed within the lap spliced area to avoid being confined inside the splice zone. Within the stirrups, two bars, each 10 mm in diameter, located in the top part of the section, served as the primary reinforcement in the compression zone to align and stabilize the reinforcement cage. According to the ACI Code, the concrete cover was specified to be 25 mm, which is the recommended minimum concrete cover to ensure a complete bond between the steel bars and the concrete. Fig. 1 illustrates the details of the reinforcement used in the tested specimens. The severe damage was intentionally inflicted by exerting a load equivalent to approximately 70% of the control beam's ultimate load, which is about 126 kN. The preloading procedure, as previously stated, may significantly diminish the load-bearing capacity of the tested specimens, given that it surpasses the service limit of the reference specimen when considering the lap-splice effect. The concrete cover has been scraped away, which is 300 mm wide and reaches the height of the concrete cover, leaving the steel bars uncovered to simulate damage in the lower area of the concrete beams, as illustrated in Fig. 2.

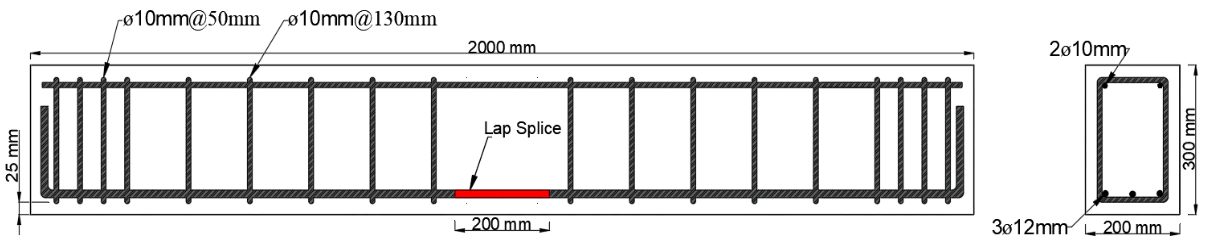

Fig. 1. Details of reinforcement: (a) front view, (b) cross-section.

Fig. 2. Damage at the bottom of the specimens (Inverted Specimens).

The matrix of the work followed a methodology that involved studying four parameters. The first parameter examined the effect of the shape of repairing bars, comparing the performance of bars with hooked ends to that of straight ones. The second parameter evaluated the bond material, comparing the cementitious material used as a bond agent to the epoxy one. The third parameter involved in assessing the role of confinement by external repair through a steel plate attached with a bonding agent and fixed in the middle of the span by nails. The fourth and final parameter investigated the impact of the diameter of repairening bars, comparing the performance of a larger diameter of 16 mm with a smaller one of 12 mm. Table. 1 outlines the details of the tested specimens, including the coding procedure.

Table 1. Specimen details.

Number	Specimen	Configuration of Strengthening Bars	Confinement by Steel Plate	Diameter of Strengthening Bars (mm)	Bonding Material
1	BC*	N.A.**	N.A.	N.A.	N.A.
2	HCE12	Hook	with	12	Epoxy
3	SCE12	Straight	with	12	Epoxy
4	HCM12	Hook	without	12	CM***
5	HE12	Hook	without	12	Epoxy
6	HCM16	Hook	without	16	CM
7	HE16	Hook	without	16	Epoxy
8	HCCM12	Hook	with	12	CM

*BC= Control Beam, **N.A. = Not Applied, **CM = Cementitious material.

4.2. Repairing procedure

The beams were installed upside down, with the soffit at the top, to facilitate more straightforward repairs in the lab. Under and around the reinforcements, damaged and broken concrete was scraped away utilizing a pneumatic hammer. The rebar was cleaned with a wire brush, allowing a better bond with the new repair materials.

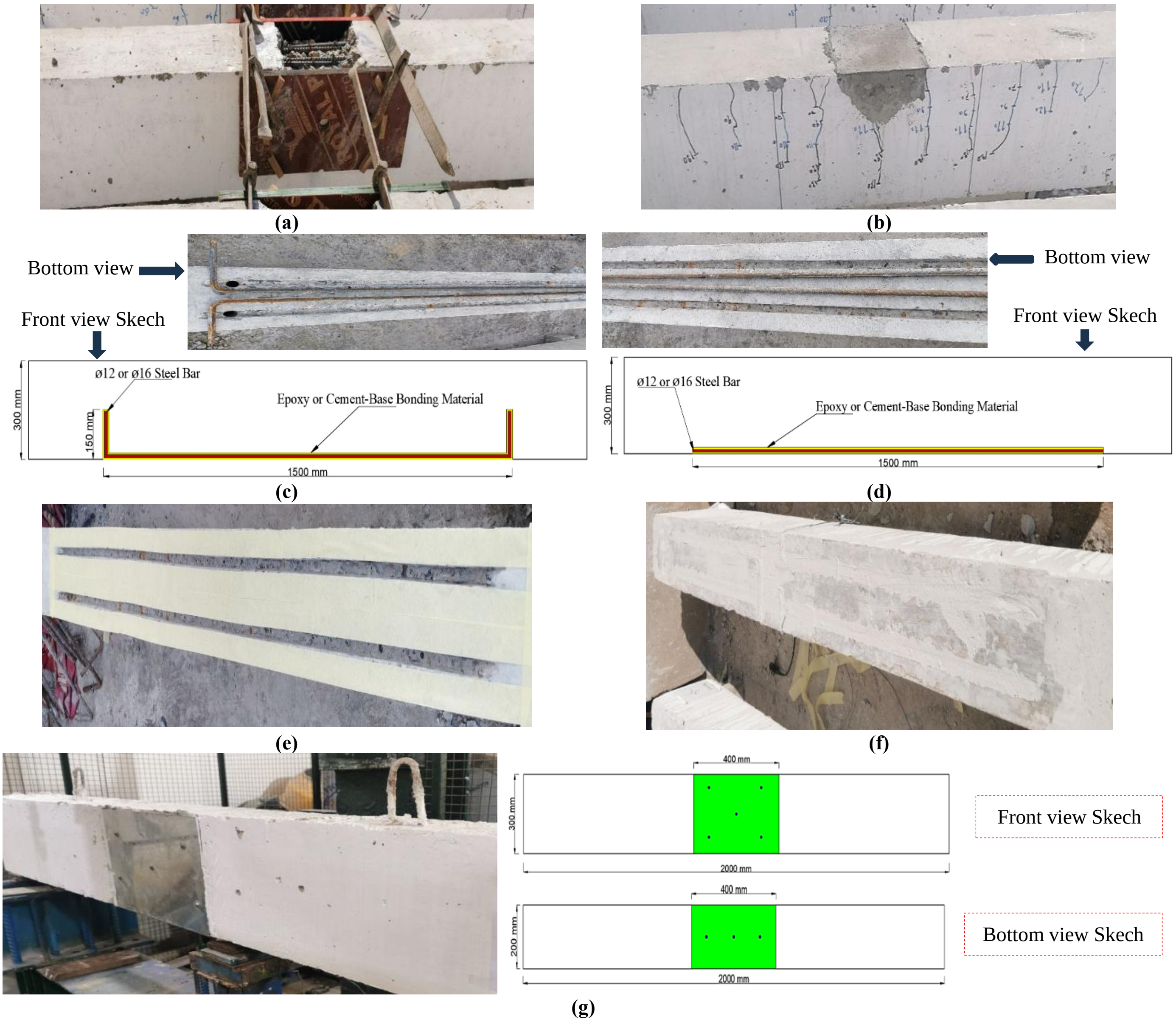

Fig. 3. Repairing procedure; (a) preparing to pour SCC layer, (b) after pouring and leveling the surfaces of SCC layer, (c) hooked ends repairing bars, (d) straight state repairing bars, (e) drilling grooves, (f) filling grooves with bonding agent, (g) repairing with an externally bonded steel plate.

Additionally, employing a high-pressure air jet, dust and loose particles were expelled from the surface. The surface was moistened with water before the mending concrete was put in. The damaged concrete was repaired through self-compacting concrete (SCC), which is characterized by high deformability and the ability to flow through spaces between steel reinforcing bars without segregation or blocking, as demonstrated in Fig. 3, a and b.

All repaired specimens were repaired with two steel bars, each 1500 mm long and 10 mm in diameter. The specimens with hooked repair bars were bent at both ends so that the free vertical ends extended 150 mm. This hook was designed in accordance with ACI 318-19 [23], which requires a 90-degree bend with a minimum bend diameter of 75 mm, as illustrated in Fig. 3, c and d.

The repair process using the NSM approach was started by carving grooves into the concrete cover at the bottom of all specimens, except the control. These grooves were drilled approximately 1.5 to 2 times the diameter of the steel bar-NSM, depending on the bonding material. Grooves were made with a concrete cutter, and any leftover concrete lumps were removed. The bottom surface of the grooves was roughened with a hammer and a hand chisel. Based on the paper methodology, two adhesive materials were used: epoxy and cementitious material, depending on the specimen type tested. These materials functioned as the bonding agents for attaching the steel rebar to the concrete. Fig. 3, e and f, reveals the NSM technique procedures.

In specimens with a steel plate, the plate covered both sides and the bottom part of the beam section, extending horizontally for 400 mm, centered at the middle portion of the beam, as shown in Fig. 3, g. The steel plate was fixed in place with epoxy and nets.

4.3. Mix properties

All of the concrete components in the test program were cast using either regular or self-compacting concrete. The NCM utilized 440 kg/m³ of cement and a water-to-cement (W/C) ratio of 0.4. The aggregate proportions included 690 kg/m³ of fine aggregate and 1000 kg/m³ of coarse aggregate. In the SCC mixture, 368 kg/m³ of cement was incorporated, and the W/C ratio was 0.45. The aggregate composition consisted of 754 kg/m³ of fine aggregate and 858 kg/m³ of coarse aggregate. Additionally, 10% silica fume (by weight of cement) was included to enhance its filling ability. The mix designs were based on mixes tested at 28 days, as specified in ACI 211-91 [24].

4.4. Materials properties

Ordinary Portland cement was used in casting all the specimens with sompressive strethegth of 29 MPa. The fine aggregate was sieved to 4.75 mm to remove particles larger than this size. Sand was used in a saturated state with a dry surface. The local gravel also had a maximum size of 19 mm. In this study, three deformable bars with diameters of 10mm, 12mm, and 16mm were used. The steel bars' mechanical test data show: the Ø10 mm bar had a yield stress of 526 MPa, ultimate stress of 730 MPa, and 10.2% elongation; the Ø12 mm bar had a yield stress of 550 MPa, ultimate stress of 751 MPa, and 12% elongation; the Ø16 mm bar had a yield stress of 540 MPa, ultimate stress of 710 MPa, and 12.3% elongation. These results are in accordance with ASTM A615M-24 [25] standards. The 2 mm steel plate was used for confinement. The ASTM A370-17 [26] guidelines were followed to create coupon samples. The steel plate had a yield stress of 274 MPa, an ultimate stress of 454 MPa, and 20.8% elongation, which is below the 22% limit specified in ASTM A36/A36M-19 [27].

Two different adhesive materials were used: epoxy and cement-based adhesive. The epoxy adhesive employed in this study (Sikadur®-31 CF Normal) demonstrated superior mechanical strength and bonding efficacy, with a tensile strength of 21 MPa and tensile adhesion to concrete surpassing 4 MPa. Conversely, the cementitious adhesive (Keraflex Extra S1) exhibited an initial tensile adhesion strength of 2.3 MPa. It was classified as an S1 deformable adhesive characterized by an extended open time and excellent substrate compatibility. The mechanical characteristics of concrete were assessed, including compressive, tensile, and flexural strengths. The compressive strength of the concrete was measured on the 28th day of testing in accordance with ASTM C39/C39M-24 [28]. The tensile strength of concrete was evaluated using ASTM C496/C496M-17 [29] by analyzing the split tensile strength of three cylinders, each measuring 200 mm in length and 100 mm in diameter, during the beam testing period. The flexural strength test was performed on three prisms measuring 100 mm × 100 mm × 400 mm, in accordance with ASTM C78/C78M-22 [30]. Normal concrete exhibited a compressive strength of 28.2 MPa, a tensile strength of 3.02 MPa, and a flexural strength of 4.4 MPa. Conversely, SCC demonstrated strengths of 28.2 MPa, 2.35 MPa, and 3.88 MPa, respectively.

Regarding SCC, a slump flow test on fresh specimens to determine the workability of SCC was conducted. The slump flow test for fresh SCC resulted in a value of 677 mm, which complies with the EFNARC recommended limit of 650 to 800 mm [31].

4.5. Test setup

All beams were tested, as shown in Fig. 4. The specimens were cured for 28 days and then painted with white pigment to facilitate crack detection during loading. The tested beams were simply supported, with steel plates and rollers positioned over the supports and beneath the loading points to prevent local concrete crushing. The supports were placed 100 mm from each beam end, resulting in a clear span of 1800 mm. All specimens were tested under four-point bending. The load was applied vertically in incremental steps, and the corresponding deflection was recorded at each 5 kN load step. A linear variable displacement transducer (LVDT) was installed at the beam mid-span beneath the soffit to measure vertical deflection throughout the test. Crack initiation and propagation were visually monitored on painted beam surfaces, marked with a pencil/marker. Fine crack widths up to 0.5 mm were measured using a crack meter, while larger crack widths were measured using a digital vernier caliper. After repairing and during loading until failure, the cracks were highlighted with a marker pen. During testing, the maximum load capacity, deflection, and failure mode were documented.

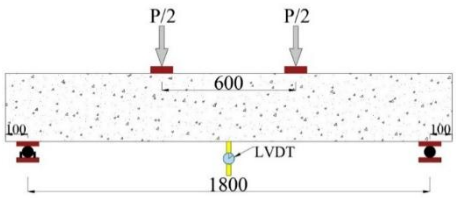

Fig. 4. Schematic details for application load and supports.

5. Experimental results

The load and corresponding deflection were recorded during all loading steps, and the load was incrementally increased up to failure. The first flexural crack was visually observed, and the corresponding load was identified. Table. 2 illustrates the test data regarding load and deflection for every tested beam specimen.

Table 2. Results of the test specimens for recorded data.

Specimens	Pcr (kN)	Δcr (mm)	Pu (kN)	Difference	Δu (mm)	Pu/Puc*
BC	25.2	0.59	180	---	19.35	1
HCE12	50	0.86	189	5.4%	6.11	1.1
SCE12	54	0.55	170	5.4%	8.12	0.9
HCM12	30	0.53	120	33.2%	4	0.7
HE12	35	0.63	148	17.6%	5.29	0.8
HCM16	30	0.36	163	9.3%	6.04	0.9
HE16	35	0.39	208	15.6%	8.1	1.2
HCCM12	40	0.74	199	10.6%	7.2	1.1

*Puc: Ultimate load of refernce specimen.

Ductility refers to the capacity of a structural element to maintain its load-bearing ability even after undergoing significant deformation or deflection. The ductility ratio (μ) is commonly defined as the ratio of the ultimate displacement to the displacement at yield, typically based on an idealized elastic–plastic response. The present study adopted an approach to calculate the yield displacement using the deflection corresponding to 75% of the ultimate load ($\Delta_{0.75}$Pu) proposed by Park [32]. For the tested repaired concrete beam specimens, the experimental ductility ratio (μ) was calculated by dividing the ultimate deflection (Δu) by the deflection at 75% of the peak load ($\Delta_{0.75}$Pu). Tab.3 presents the calculated ductility values for all tested specimens.

Two types of stiffness values were adopted in this study: initial stiffness and service stiffness. The initial stiffness was defined as the slope of the load–deflection response in the pre-cracking stage, i.e., before the appearance of the first visible crack [33]. It is common to estimate initial stiffness using the cracking load or a value below it. The analysis revealed that the lowest recorded cracking load corresponded to approximately 14% of the ultimate load. To ensure consistency and to remain safely within the elastic range, 10% of the ultimate load (Pu) was selected as the standard reference point for evaluating the initial stiffness. The service stiffness was determined based on the structural response under service-level loading, typically where deflection limits and cracking control are of primary concern. In this context, the service stiffness was calculated using a serviceability-based approach, corresponding to 65% of the ultimate load (0.65 Pu) [34, 35]. The computed values of both initial and service stiffness for all tested specimens are outlined in Table.3.

Table 3. Results of the test specimens for calculated data.

Specimen	Initial stiffness (kN/mm)	Service Stiffness (kN/mm)	Ductility Index (μ)	μ/μ_c*	Energy Absorption (kN.m) (EA)	EA/EA_c**
BC	44.2	27.1	3.84	1	4.451	1
HCE12	57.1	47.8	1.93	0.503	1.355	0.304
SCE12	100.0	89.1	5.62	1.464	1.519	0.341
HCM12	54.5	41.9	1.72	0.448	0.478	0.107
HE12	64.4	39.1	1.71	0.445	0.936	0.210
HCM16	79.7	25.5	3.2	0.833	1.009	0.227
HE16	109.3	20.8	3	0.781	1.819	0.409
HCCM12	85.1	39.7	1.75	0.456	1.488	0.334

*μc: Ductility of refernce specimen, *EAc: Energy absorption of refernce specimen.

The energy absorption capacity of reinforced concrete beam specimens is determined by calculating the area under the load-deflection curve, which represents the total energy absorbed by the specimen from the initiation of loading up to the point of failure. This area encompasses the entire deformation process of the beam, capturing both elastic and inelastic behavior, and provides insight into the beam's ability to undergo considerable displacements while maintaining structural integrity [36]. The present study calculated the energy absorption capacities of all tested specimens. This enables a consistent and comparative assessment of how different repairing configurations affect the energy dissipation behavior of the beams. Tab.3 reports the resulting values for each specimen.

6. Parameters

6.1. Effect of hooked bar

Two configurations for repairing steel bars, straight and hooked steel bars, were used to evaluate the impact of the hooked bar pattern on the effectiveness of the repair. One group of specimens was employed for this purpose: SCE12 and HCE12. Fig.5 illustrates the load mid-span deflection curves for specimens related to the current investigated parameter.

At the first cracking stage, the load values were 54 and 50 kN, respectively, resulting in increases of 113.9% and 98.8% for SCE12 and HCE12, respectively, compared to the reference specimen BC. The deflection at the cracking stage demonstrated two behaviors. For specimens with a hooked repairening bar, deflection increased by up to 45.9% corresponding to the HCE12 specimen, more than in the reference specimen BC. In contrast, the specimens with straight repairening bars, SCE12, exhibited a slight drop in deflection of 6.6%.

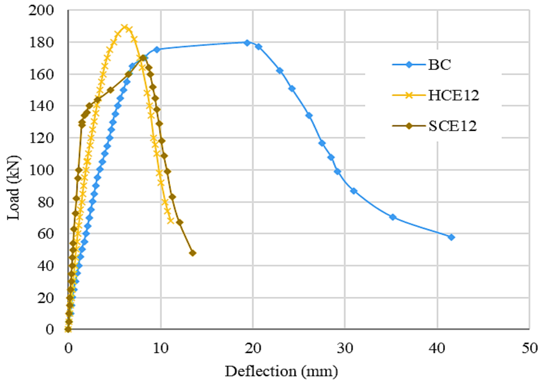

Fig. 5. Load to mid-span curves for specimens with hooked and straight ends.

At the ultimate loading stage, the hooked repairening pattern in the HCE12 specimen demonstrated an improved load-carrying capacity of 189, exceeding that found in the reference specimen BC by approximately 5%. Additionally, the load capacity in the straight repairening bars of the SCE12 specimen reached 170, representing a recovered capacity of roughly 94.5%, compared to the reference specimen BC. The ultimate deflection at failure significantly drops for all specimens tested and is correlated to the current study parameter. The recorded ultimate deflections were 8.12 and 6.11 mm, reflecting decreases of approximately 58% and 68.4% corresponding to specimens with straight and hooked ends, respectively, relative to the reference specimen BC.

Regarding the stiffness values, all repaired specimens exhibited a considerable increase in stiffness, either at the initial or service state, with the most notable improvement occurring at the service stiffness and for specimens with a straight repair bar. The specimen with hooked repairing steel bars exhibited a 29.2% enhancement in initial stiffness. Regarding service stiffness, it was 76.2%, which is higher than that of the reference specimen BC. The initial stiffness of the SCE12 specimen using straight repairening steel bars was enhanced by 126.4%, while the service stiffness of this specimen improved by 228.4% over the BC specimen. Fig. 6 demonstrates the effect of repairing the steel bar configuration on both initial and service stiffness.

The ductility values were positively affected in a specimen repaired by straight steel bars, where specimen SCE12 exhibited an increase in ductility by about 46.4%, relative to the reference specimen BC. In contrast, the HCE12 specimen with a hook-repairing steel bar suffered from a reduction in ductility by approximately 49.7% relative to the reference specimen BC. The energy absorption for the entire set of tested specimens, regarding the examined parameter, decreased by approximately 65.9% and 69.6% for SCE12 and HCE12 specimens, respectively, in the same beam order, compared to the reference specimen BC. Fig. 7 demonstrates the effect of repairing the steel bar configuration on ductility and energy absorption for each specimen tested under the current study parameters.

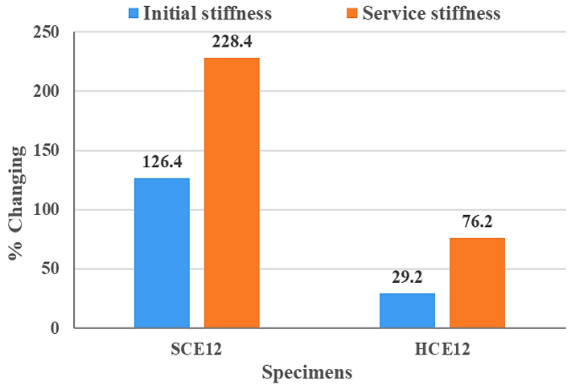

Fig. 6. The effect of repairing steel bar configuration on initial and service stiffnesses.

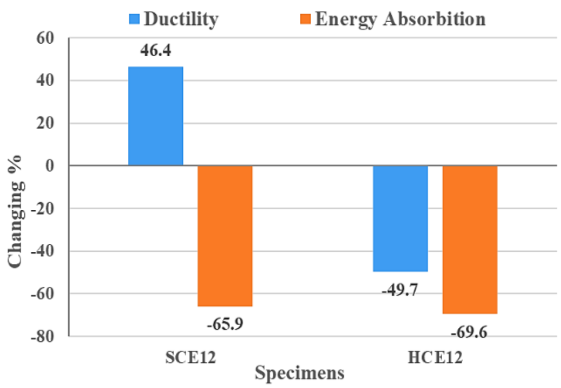

Fig.7. The effect of repairening steel bar configuration on ductility and energy absorption.

NSM steel bar repair systems were implemented on all repair specimens, resulting in a delayed onset of cracking compared to the unrepaired control beam. Hook-end-bar reinforcement demonstrated a more ductile response during cracking, which can be attributed to the enhanced mechanical anchorage and bond between the reinforcement and the concrete. However, this configuration also introduced localized stress concentrations near the hook areas, resulting in earlier crack formation under higher loads and a subsequent decrease in overall ductility. Straight steel bars, on the other hand, exhibited a stiffer response at the start of cracking but maintained better ductility and service stiffness because of uniform stress distribution and continuous alignment, which allowed for efficient load transfer. Although hooked bar specimens exhibited an increased ultimate load-carrying capacity, both repairing strategies reduced deflection at failure and decreased energy absorption, illustrating the typical trade-off between increased strength and reduced deformation after yield. While hooked bars provided better anchorage and peak strength, straight bars provided better stiffness characteristics during service loading conditions.The straight-bar setup likely ensured a more uniform bond stress and direct load transfer along the NSM groove, increasing stiffness and reducing early deformation. Conversely, the hooked-end anchorage of specimen HCE12 may have caused localized stress, microcracking, and uneven strain near the bends, thereby lowering stiffness.

6.2. Effect of adhesive material

This part of the study evaluated the effect of the bond material. Two groups of specimens were used: the first involved specimens HE12 and HCM12, and the second involved HCCM12 and HCE12 specimens. Fig. 8 demonstrates the curves of load-mid span deflection for specimens relevant to the present study's parameters. All repairing approaches using epoxy or cementitious material as a bonding substance showed a higher load at first cracking than the reference BC specimen. The specimens that used epoxy as an adhesive material had the most prominent enhancement. The HE12 and HCE12 (used epoxy) recorded the first crack at a load of 35 and 50 kN, with an increase of 39.4% and 98.8%, respectively, over the reference beam specimen BC. The HCM12 and HCCM12 specimens with cementitious material as an adhesive developed an initial crack at a load of 30 and 40 kN, with a gain of 18.8% and 59.3%, respectively, which is greater than that of the reference beam specimen BC. The specimen that used epoxy revealed an increase in cracking deflection of approximately 7.6% and 45.9%, while the specimens utilizing cementitious material showed a 10.7% drop in HCM12 or an increase in HCCM12 by 26.1%.

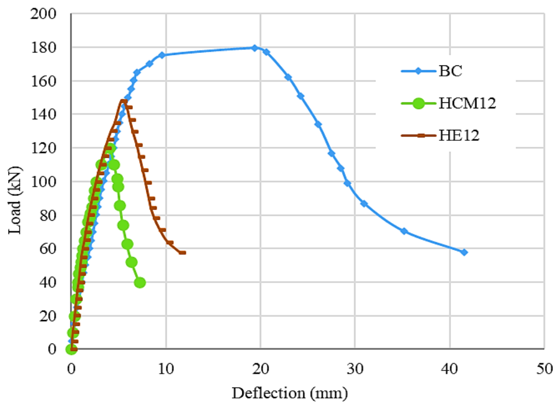

(a)

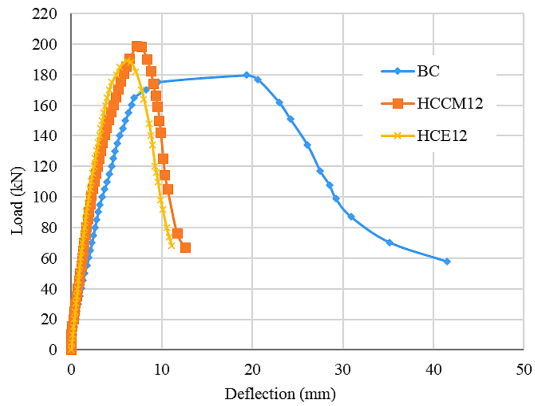

(b)

Fig. 8. Load to mid-span curves for specimens with epoxy and cementitious bond agents; (a) group 1 specimens, (b) group 2 specimens.

The repair with epoxy (in the HE12 specimen), in group 1, restored 83.4% of the bearing capacity of the BC reference specimen, outperforming the repair with cementitious material (in the HCM12 specimen), which restored 66.8%. In group 2, the repair using epoxy in the HCE12 exceeded the load capacity of the BC by only 5.6%, and in the HCCM12, the repair using cementitious material exceeded it by 10.6%. There was a clear trend toward reduced ultimate deflection in all specimens repaired with any bonding material. Specimens repaired with epoxy and a cementitious material experienced reductions in ultimate deflection of 72.7% and 79.3%, respectively. A noticeable contrast in stiffness performance was noted between specimens bonded with epoxy and those bonded with cementitious material. Epoxy-repaired specimens generally demonstrated more uniform improvement in initial and service stiffness values, with moderate improvements observed in HE12 by 45.8% and 44.2%, respectively. In contrast, HCM12 exhibited uneven behavior, indicating that it had improved service in stiffness, reaching 54.5% compared to the initial value of only 23.5%. Moderate improvements were observed in HCE12, with 29.2% for initial stiffness and 76.2% for service stiffness, reflecting the positive effect of epoxy reining. In contrast, HCCM12 has inconsistent behavior, showing a reverse pattern with an initial stiffness increase of 92.6% and a service stiffness of only 46.4%. Fig. 9 illustrates the effect of the adhesive material on initial and service stiffnesses.

In general, all repaired specimens exhibited reductions in ductility and energy absorption compared to the control specimen. For ductility, the epoxy-bonded specimens showed a reduction between 49.7% and 55.6%, while the cementitious-bonded specimens decreased between 55.1% and 54.3%, relative to the reference specimen BC. The findings indicate that ductility was affected to a similar extent by using both adhesive materials, resulting in a decrease in ductility. For energy absorption, the specimen bonded with epoxy experienced reductions ranging from 69.6% to 79%, whereas that bonded with cementitious material experienced reductions from 66.6% to 89.3%, relative to the reference specimen BC. According to the findings, both approaches utilizing adhesive materials showed only a slight difference in the decline in maximum energy absorption levels. Fig. 10 demonstrates the influence of bond material on ductility and energy absorption for each tested specimen under the current study's parameters.

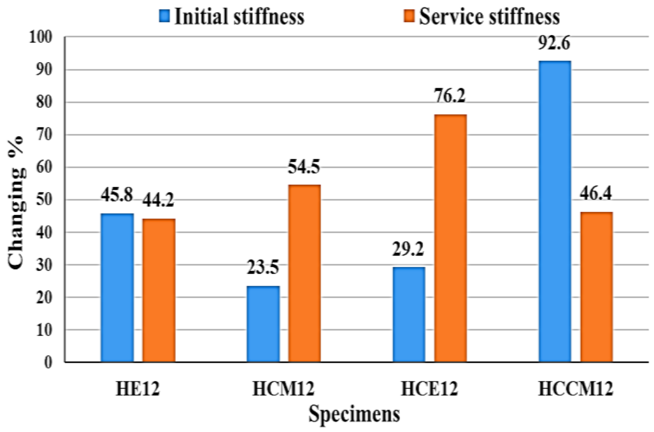

Fig. 9. The effect of bond material on initial and service stiffnesses.

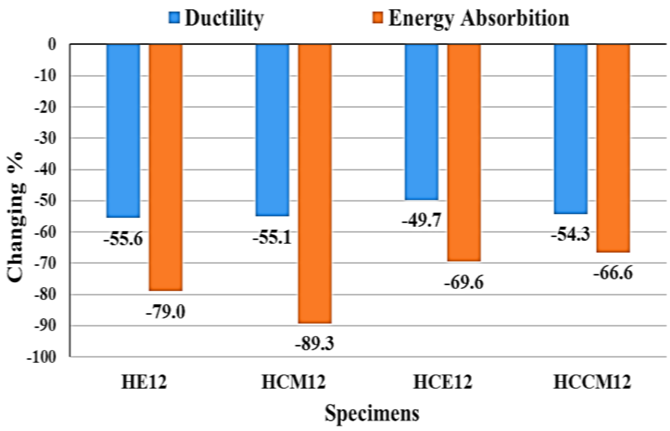

Fig. 10. The effect of bond material on ductility and energy absorption.

The improved cracking resistance seen in the repaired specimen is mainly due to the adhesive bonding layer, which helped effectively transfer stress between the concrete substrate and the embedded steel reinforcement. In comparison to the cementitious-bonded counterpart, the epoxy-bonded specimens consistently achieved higher cracking loads and greater initial stiffness, owing to their superior mechanical properties and bond efficiency at the adhesive interface. At the ultimate load stage, the epoxy-bonded beam demonstrated higher load-carrying capacity and improved anchorage performance, while the cementitious material showed lesser strength gains. Regarding deformation behavior, the cementitious-bonded beam exhibited a more significant reduction in ductility and ultimate deflection compared to the control specimen. Specimens bonded with epoxy also showed more consistent improvements in both initial and service-stage stiffness, and also maintained more post-peak energy capacity.

6.3. Effect of confinement

The confinement effect using a steel plate was evaluated with two specimens, HE12 and HCE12. Fig.11 shows the curves of load-mid span deflection for specimens associated with the current investigated parameter. Generally, all repairing methods, whether with or without confinement, noticeably delayed the initial flexural crack; however, confinement had a significant impact compared to a reference specimen. The specimen with confinement HCE12 recorded a first cracking load equal to 50 kN with an increase of approximately 98.8% over the control specimens BC. The specimens free of confinement HE12 had a cracking load of as much as

35 kN, with an improvement relative to the reference specimen BC of up to 38.6%. The deflection in a confined specimen rose to 45.9% against the reference specimen BC. In contrast, the unconfined specimens either revealed a modest increase in cracking deflection by 7.6%.

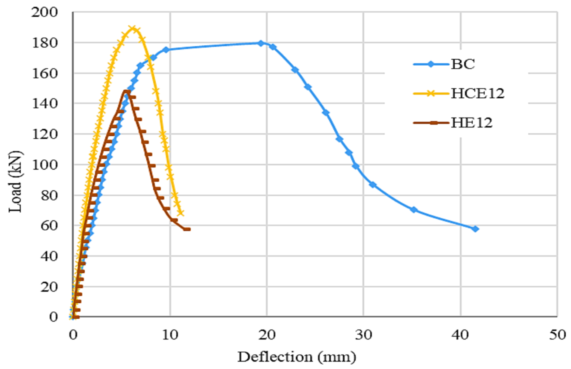

Fig. 11. Load to mid-span curves for specimens with and without confinements.

The confinement was also effective in a more pronounced manner at the ultimate stage. In the ultimate stage of loading, the load capacity was greater than that of the reference specimen BC, with 5.4% in the confined specimen. In contrast, the corresponding unconfined specimen HE12 restored only 82.4% of the original capacity of the reference specimen. The effect of steel plate confinement on ultimate deflection was assessed, where the non-confined specimen HE12 showed a 72.7% reduction in ultimate deflection. Conversely, the confined specimen HCE12 experienced a slightly lower reduction of 68.4%.

Confinement led to a gain in initial and service stiffnesses. The outcomes revealed that the improvement in initial and service stiffnesses was nearly the same in specimens lacking confinement. Conversely, the presence of confinement increased service stiffness more than the initial stiffness. The specimen with confinement HCE12 improved initial stiffness by around 29.2%. In contrast, the specimen free of confinement HE12 enhanced initial stiffness by around 45.8%, for the same specimen order, compared to the reference BC specimen. For stiffness values at the service stage, the unconfined specimen HE12 experiences a boost of 44.2% versus the BC reference specimen, with a semi-identical grade to the initial stiffness. The specimen with confinement exhibited substantial gains in service stiffness, as much as 76.2% against the BC reference specimen BC, and larger than the initial stiffness values. Fig.12 demonstrates the influence of confinement on initial and service stiffnesses.

The specimens that were repaired, either with or without confinement, generally experienced a reduction in ductility compared to the reference BC specimen. The specimens HE12 and HCE12 (unconfined and confined, respectively) exhibited ductility decreases of approximately 55.6% and 49.7% respectively. All tested specimens, regardless of confinement, also suffered from a reduction in energy absorption. The HE12 and HCE12 showed significant decreases of 79% and 69.6%, respectively. Fig.13 reveals the influence of confinement on ductility and energy absorption for every tested specimen under the present investigated parameters.

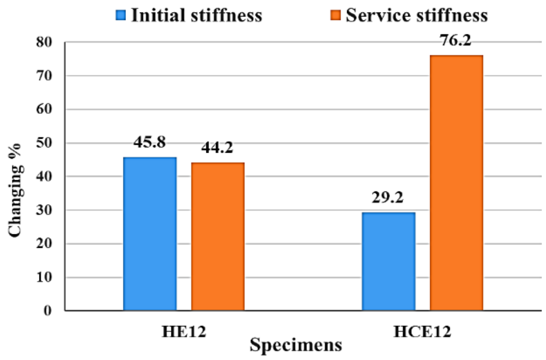

Fig. 12. The effect of confinement on initial and service stiffnesses.

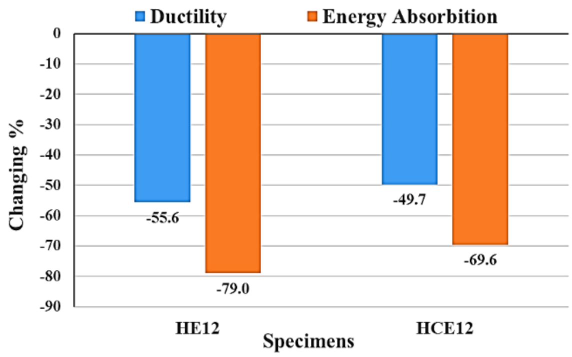

Fig. 13. The effect of confinement on ductility and energy absorption.

The improved structural behavior seen in confined reinforced concrete beams mainly results from the lateral restraint offered by externally attached steel plates, which effectively reduces transverse deformation in the tension zone and delays the start and spread of both splitting and flexural cracks. This confinement not only enhances the tensile strength of the concrete section but also permits greater deflection before cracking. Additionally, during final loading stages, the confinement significantly boosts the ultimate load capacity by improving the mechanical anchorage of repairing bars, preventing bar-concrete separation, and delaying crack propagation. Comparative experimental results show that confined specimens experienced smaller decreases in deflection compared to their unconfined counterparts, emphasizing the importance of confinement in enhancing deformation capacity and load resistance.

Although unconfined beams initially display higher stiffness because of stronger early NSM bonding, confined specimens exhibit greater service stiffness after cracking due to better crack control. However, a general decrease in ductility is observed across all repaired systems, mainly because increased stiffness and early crack suppression restrict plastic deformation and curvature capacity. While confinement does not directly improve ductility, it reduces its decline. The efficiency of the steel plate confinement system is further enhanced by mechanical nets, which keep the plate and concrete in strong contact, prevent early debonding, and ensure force transfer across the interface.

6.4. Effect of repair bar diameter

In this part of the results discussion, the influence of the diameter of the repairening bar was assessed. The specimens were organized into pairs, with one specimen having 12mm repair bars and the other measuring 16mm in diameter. The specimen groups were: Group 1 (HE12 and HE16) and Group 2 (HCE12 and HCE16). Fig.14 illustrates the curves of load-mid span deflection for specimens related to the currently studied parameter. For the HE specimens (group 1), the cracking load increased notably compared with BC. Both HE12 and HE16 carried 35 kN, corresponding to a 40% improvement over the control. However, cracking deflection showed different behavior: HE12 exhibited a slight increase of 7.6%, while HE16 experienced a reduction of 33.8% compared with BC. This indicates that the bar diameter did not affect the initial cracking load, but it reduced the deflection considerably. For the HCM specimens (group 2), the cracking load improved by 20% compared with BC, with both HCM12 and HCM16 reaching 30 kN. However, cracking deflection decreased in both cases: HCM12 was 10.7% lower, and HCM16 experienced a more severe reduction of 38.9% compared with BC. This reflects the almost identical trend of behavior as in group 1.

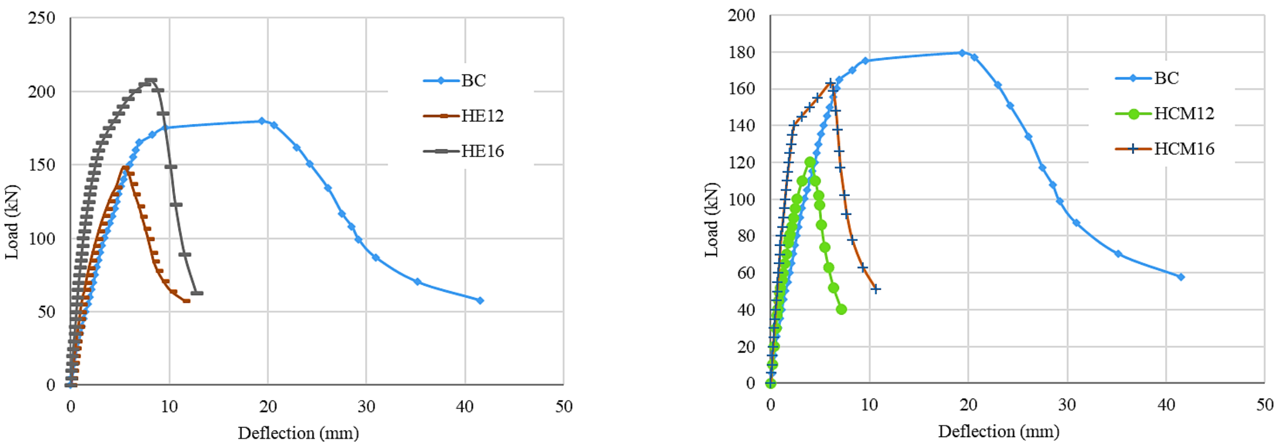

Fig. 14. Load to deflection curves for specimens with repairing bars of 12 mm and 16 mm; (a) group 1 specimens, (b) group 2 specimens.

The influence of steel bar diameter on the ultimate load capacity demonstrated apparent variation across the tested specimen groups relative to the value in the reference BC specimen. In the first group, the repair using steel bars of 12 mm diameter (HE12 specimen) restored 82.4% of the original capacity. In contrast, the specimen (HE16) with 16 mm diameter repairing bars exceeded the original capacity by 15.6% more than the BC reference specimen. The outcomes of the second group of specimens referred to recovering 66.8% in a specimen (HCM12) with a 12mm repairening bar diameter and an even higher ratio in the specimen (HCM16) containing a 16 mm repairening steel bar, reaching 90.7%, compared to the BC reference specimen.

The influence of steel bar diameter on the ultimate deflection exhibited notable variation across the tested specimen groups relative to the reference BC specimen. In the first group, the specimen repaired with 12 mm bars (HE12) showed a 72.7% reduction in deflection, while the specimen with 16 mm bars (HE16) exhibited a smaller decrease of 58.1%. The second group reflected a similar trend, with the HCM12 specimen (12 mm diameter) showing the highest reduction of 79.3%, compared to 68.8% for the HCM16 specimen (16 mm diameter).

Initial and service stiffness, using repairing bars with a diameter of 12 mm or 16 mm, led to a considerable improvement in these stiffnesses. The distinct context for the stiffness values was evident in more substantial increases in service stiffness, higher than the initial one, in most beam specimens. These increases were greater in specimens with a 16mm diameter of the repairing steel bar than in those with a 12 mm bar. For specimens repaired with 12 mm steel bars, the initial stiffness increased from 23.5% to 45.8%, while service stiffness improvements ranged from 44.2% to 54.5%. In comparison, specimens repaired with 16 mm steel bars exhibited greater enhancement, with initial stiffness increasing between 84.5% and 147.5% and service stiffness ranging from 145.1% to 151.9%. These results confirm that all repaired specimens outperformed the control in stiffness performance and that using 16 mm bars generally resulted in higher gains, particularly in service stiffness. Fig.15 shows the impact of the diameter of the repairing steel bar on initial and service stiffnesses.

All specimens exhibited reductions in ductility relative to the control specimen. The drop in ductility in the specimens with a 12 mm repairing bar ranged between 55.1% to 55.6%, while those with 16 mm bars were between 16.8% to 21.8%. These results verify the positive effect on ductility from larger bar diameters. Although the increase in bar diameter did not enhance ductility, it contributed to reducing the extent of ductility loss in most specimens. The energy absorption performance showed less improvement compared to ductility across all specimens as the repairing bar increased from 12 mm to 16 mm. All specimens experienced reductions relative to the reference specimen, with 12 mm bar specimens exhibiting reductions ranging from 79% to 89.3%. Specimens repaired with 16 mm bars displayed a decrease of 59.1% to 77.3%, indicating a less severe energy absorption loss than their 12 mm counterparts. This trend suggests that increasing the bar diameter may help mitigate the extent of energy dissipation loss. However, the overall performance remained below that of the original control specimen in all cases. Fig.16 illustrates the effect of the diameter of the repairening bar on ductility and energy absorption.

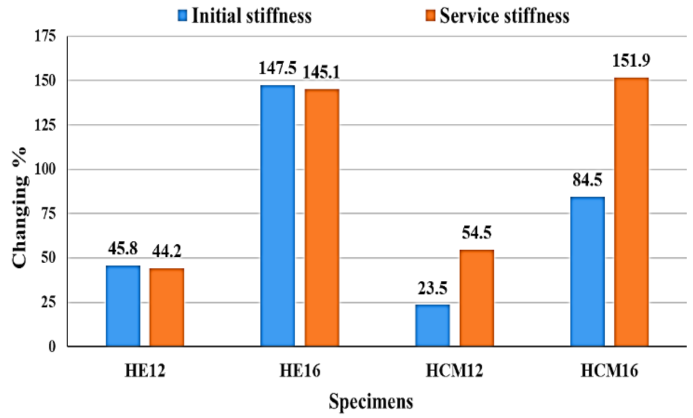

Fig. 15. The effect of repairing bar diameter on initial and service stiffnesses.

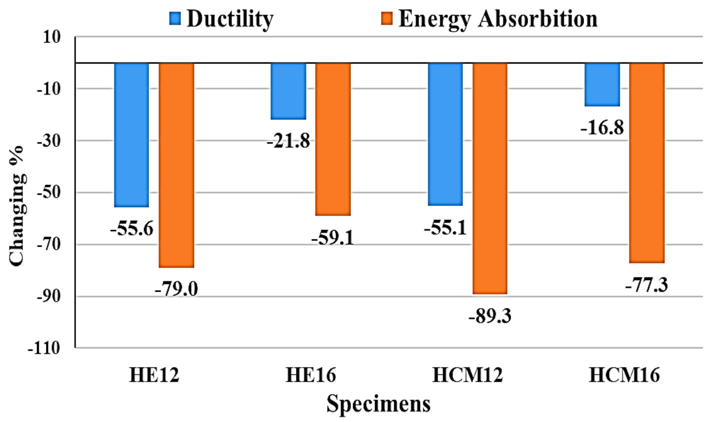

Fig. 16. The effect of repairing bar diameter on ductility and energy absorption.

Although stronger reinforcement bars theoretically provide better tensile resistance and control crack growth, experimental results show that these benefits do not always appear during early loading, when concrete's tensile strength mainly causes cracking, and reinforcement engagement is still limited. Since 16 mm bars have higher stiffness and less deformation capacity, they activate later and contribute minimally before cracking. Their structural effectiveness mainly appears in the post-cracking stage, when tensile stresses transfer from concrete to steel, enhancing stiffness, load capacity, and crack control during service. Compared to 16mm repairening bar diameter, 12 mm bars consistently result in greater reductions in first-cracking deflection. While 16mm bars maintain the stiffness in service, retain energy, and resist ultimate loads more effectively, they suffer from a loss of ductility. Unlike a control specimen, all repaired specimens showed reduced ductility and energy absorption, with 16 mm bars significantly mitigating these losses compared to 12 mm bars.

7. Response of load-deflection curves for repairing

A comparison of the load-deflection curves across all specimens reveals notable behavioral differences, influenced by the repairing materials, bar configuration, bonding material, and confinement. These can be summarized as follows:

7.1. Cracking behavior

All specimens exhibited an initial linear elastic response, with the slope of the initial segment reflecting initial stiffness. The control specimen BC demonstrated relatively high initial stiffness up to approximately 5 mm of deflection, with first cracking observed at approximately 25 kN. Conversely, epoxy-repaired specimens (HCE12, SCE12, HE12, HE16) exhibited delayed cracking, indicative of enhanced tensile resistance attributable to improved bond performance. Notably, SCE12 cracked at 54 kN, the highest among all specimens, primarily due to confinement effects and the robust adhesion provided by the epoxy resin. Cementitious-repaired specimens (HCM12, HCM16), on the other hand, cracked early, approximately 30 kN, despite having large-diameter bars in the HCM16 configuration. Confinement improves tensile cracking resistance even with a weaker bonding agent in HCCM12, as cracking began at about 40 kN. At first, the curve showed a steep slope, indicating good stiffness. Therefore, cementitious bonding alone does not provide adequate crack resistance, especially without confinement. The curve in HCCM12 begins with a linear ascending phase, indicating elastic behavior with effective initial stiffness. The first visible crack appeared at a load of about 40 kN, marking the onset of tensile cracking in the concrete. However, unlike the BC specimen, the transition from elastic to post-cracking behavior is gradual and not characterized by a sudden drop in stiffness.

7.2. Post-cracking and yielding behavior

The specimens entered a nonlinear phase after cracking. The control specimen sustained a near-linear response slightly beyond the cracking point. Epoxy-bonded specimens consistently exhibited higher yield loads and demonstrated a more stable post-cracking response. HCE12 and HE12 yielded at 142 kN and 111 kN, respectively, while HE16 yielded at the highest load of 156 kN, accompanied by a smooth curve and extended plastic deformation. These findings underscore the superior bond strength and energy dissipation capabilities inherent to epoxy-reinforced systems. SCE12 has a yield of 128 kN; however, what characterizes its behavior is the smooth curvature and the progressively reduced stiffness, which signify improved confinement effectiveness, even beyond the yield point. In contrast, cementitious systems (HCM12, HCM16) demonstrated lower yield loads of 90 kN and 122 kN, respectively, and experienced more abrupt transitions to failure. The HCCM12 specimen produced a relatively high load of approximately 149 kN, exceeding the performance of some epoxy-based configurations. However, in opposition to the epoxy-confined specimens, the post-yield curve of HCCM12 exhibited no curvature, indicating that although confinement postponed yielding, it was unable to eliminate stiffness control. In the HCM12 system, the interval between yield and failure was notably short, signifying limited ductility and a sudden decline in load-bearing capacity. In HCCM12As the load increased, the curve continued to rise in a steady, nonlinear manner. The yield load, defined according to Park's criterion, was approximately 149 kN. This yield point marks the end of the elastic regime and the beginning of significant inelastic deformation.

7.3. Post-yield performance and failure load

The BC specimen, despite its ductility, demonstrated a lower peak load of 175 kN and functioned as a benchmark for performance. The load plateau observed beyond yielding in BC underscores typical ductile behavior characterized by sustained energy absorption until failure. In contrast, HCM12 exhibited a flattened load-displacement curve beyond 100 kN and failed at approximately 120 kN, indicating limited energy absorption capacity and a brittle failure mode. Although HCM16 attained a peak load of 163 kN, its failure was characterized by the absence of a ductile plateau, thus reaffirming the somewhat limited post-yield behavior of cementitious materials. The specimen HCCM12subsequently reached its peak load of 199 kN, indicating a high load-bearing capacity but limited deformability. The absence of a distinct plateau or softening phase suggests a relatively brittle failure. Overall, specimen HCCM12 exhibited enhanced strength but compromised ductility and toughness, indicating a stiffness-governed failure mechanism. With an ultimate load of 199 kN, HCCM12 stands among the strongest specimens in terms of strength. Nevertheless, despite its robustness, the curve displayed no evident softening or ductile plateau before the peak load, indicating a failure characterized by stiffness-driven brittleness.

8. Failure mode

The first series of failures due to flexure cracking with compression crushing was observed in both control BC and epoxy-bonded HE12 specimens. HE12 exhibits a flexural mode similar to the control beam, manifesting a bond transfer effect due to epoxy and retaining part of its load capacity. A second series of failures involved a bond-related mechanism primarily characterized by cover separation and debonding of repairing bars, as demonstrated by SCE12 and HCM12. For SCE12, using straight bars, even when confined with epoxy-bonded steel plates, resulted in limited anchorage efficiency, causing premature cover separation and subsequent plate debonding. Similarly, HCM12, which utilized hooked bars adhered with a cementitious material, failed due to inadequate bond strength, resulting in the premature detachment of the concrete cover. In a third series, flexural-shear failures occurred in HCE12, HCCM12, and HCM16. In the confined specimen HCE12, hook bars and epoxy were used as bonding agents; however, shear cracking developed and caused debonding of the steel plate. Contrary to HCM16, which included larger-diameter bars without confinement, it failed in a similar flexural-shear manner due to elevated shear stresses, compounded by limited bonding capacity. In HCCM12 with hooked NSM bars and a confined steel plate, both repair methods caused the beam to develop additional stresses until shear cracks appeared, along with flexural failure; however, the steel plate debonded because the cementitious material can withstand less stress than epoxy under the same conditions. HE16 also demonstrated complex mixed-mode failures. With 16mm hooked bars bonded with epoxy, the specimen exhibited flexural cracking, concrete splitting, and compression crushing. Due to the larger bar diameter, bond-induced splitting stresses were effectively transferred to the surrounding concrete, eventually triggering splitting cracks. Overall, epoxy-bonded specimens suffered flexural or flexural-splitting failures. A cementitious-bonded specimen, on the other hand, was prone to premature cover separation. The effectiveness of steel plate confinement in delaying debonding-related failures is highly dependent on anchorage configuration. Larger diameter bars altered the governing failure mechanism by introducing additional splitting stresses, while hooked bars maintained bond integrity better than straight bars. Fig. 17 illustrates all failure patterns observed in the tested specimens.

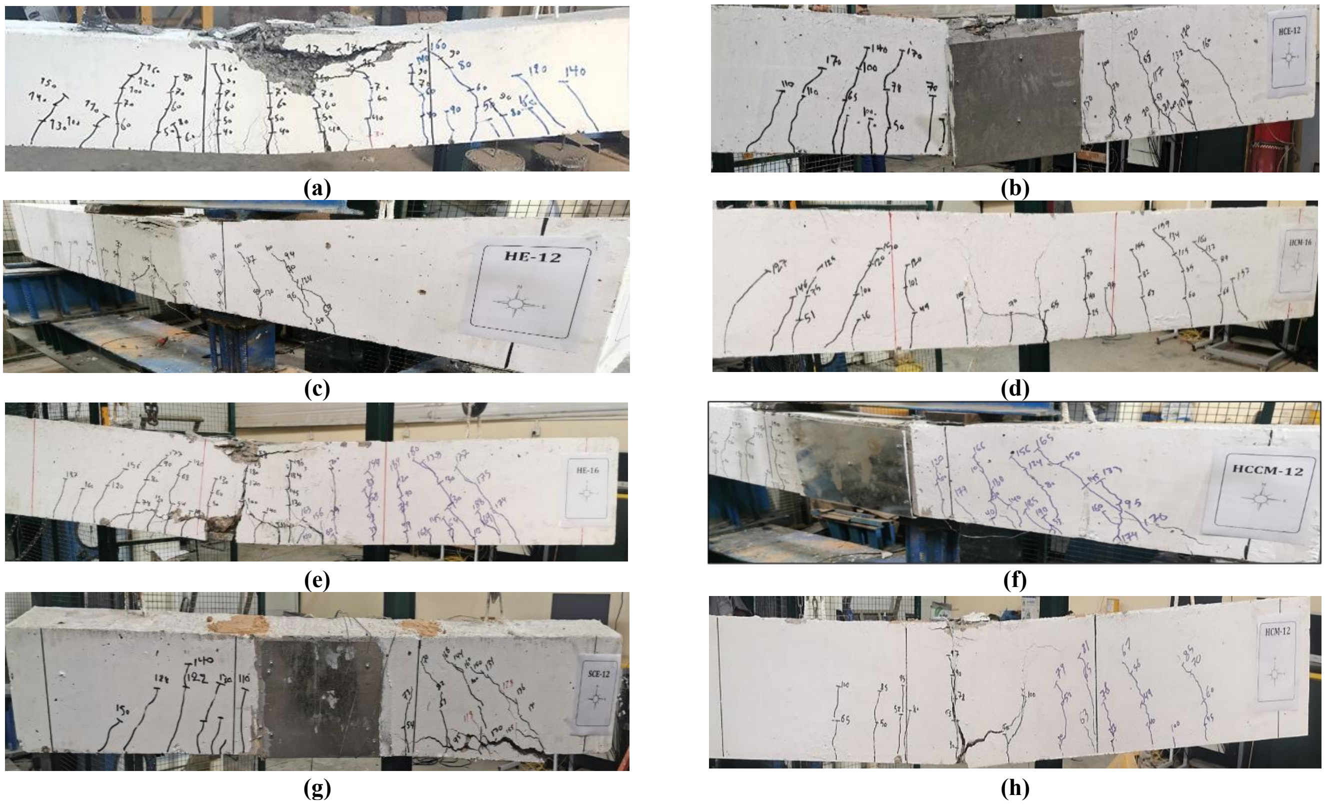

Fig. 17. Failure modes in specimens; (a) BC, (b) HCE12, (c) SCE12, (d) HCM12, (e) HE12, (f) HCM16, (g) HE16, (h) HCCM12.

9. Dimensionless comparison

The relative performance indicators presented in the Fig.18 provide a comprehensive assessment of the influence of the four investigated parameters on the flexural behavior of the repaired beams. Regarding bar-end configuration, the use of hooked-end bars increased the strength retention ratio from 0.945 for straight bars to 1.05, confirming the beneficial role of enhanced anchorage and improved bond mobilization. However, this increase in strength was accompanied by a substantial reduction in the ductility ratio, from 1.46 to 0.50, and a decrease in the energy dissipation ratio, from 0.342 to 0.304, indicating a stiffer response and a more brittle failure mechanism. Accordingly, straight bars provided a more even combination of strength, deformability, and toughness. The bonding material also exerted a pronounced influence on repair efficiency. For unconfined specimens, replacing cementitious adhesive with epoxy adhesive increased the strength retention ratio from 0.667 to 0.823, while the energy dissipation ratio improved from 0.108 to 0.210. These results reflect the superior bond characteristics, stress transfer efficiency, and composite interaction associated with epoxy systems. Under confined conditions, however, the differences between adhesive types became less significant, as the external confinement mechanism partially compensated for the weaker bond characteristics of the cementitious adhesive. The addition of external steel plate confinement consistently enhanced all principal response indices. The strength retention ratio increased from 0.823 to 1.05, the ductility ratio rose from 0.446 to 0.503, and the energy dissipation ratio improved from 0.210 to 0.304. This confirms that confinement effectively restrained crack propagation, stabilized the damaged mid-span region, delayed local deterioration, and improved post-yield response. Increasing the repair bar diameter from 12 mm to 16 mm produced one of the most favorable overall trends. For epoxy-bonded specimens, the strength retention ratio increased from 0.823 to 1.156, while the energy dissipation ratio rose from 0.210 to 0.409. For cementitious-bonded specimens, the corresponding values increased from 0.667 to 0.907 and from 0.108 to 0.227, respectively, with a concurrent improvement in ductility. Collectively, these findings indicate that increasing bar diameter and applying external confinement provided the most balanced enhancement in strength, ductility, and energy dissipation, whereas epoxy adhesive primarily improved bond-dependent behavior, and hooked-end bars mainly favored strength recovery at the expense of deformation capacity.

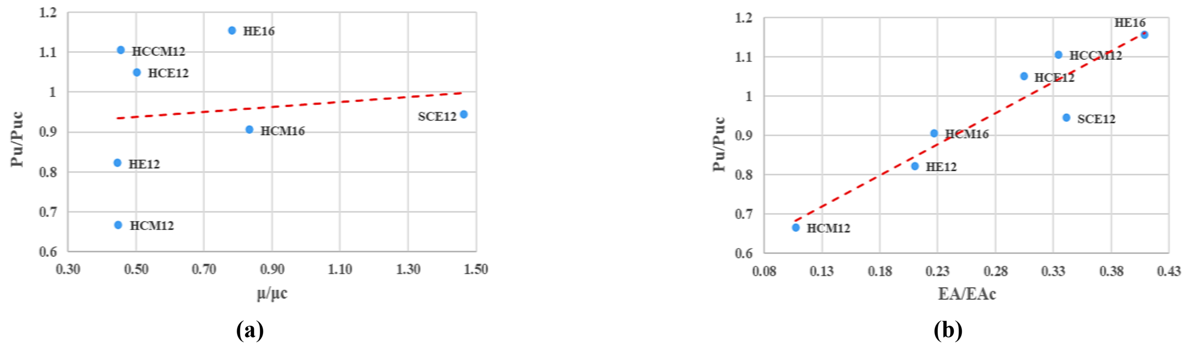

Fig. 18. Dimensionless comparison between load ratio (Pu/Puc) and: (a) ductility ratio (μ/μc), (b) energy dissipation ratio (EA/EAc).

10. Conclusions

The present study gives rise to several discernible conclusions, encapsulated succinctly in the following points:

1. The configuration of the repairing bars directly affected performance. At first, cracking, straight bars increased by 113.9%, while hooked bars grew by 98.1%. At ultimate load, hooked bars surpassed control by 5%, and straight bars recovered 94.5%. In stiffness, straight bars rose 126.4% in initial and 228.4% in service stiffness; hooked bars increased by 29.2% and 76.2%. Hooked bars may enhance anchorage at higher loads, but straight bars offer more efficient stiffness in elastic and serviceability ranges. Ductility improved by 46.4% with straight bars but decreased by 49.7% with hooked bars. Energy absorption declined 65.9% and 69.6%.
2. Hooked repair bars are a must, especially when anchorage deficiency, limited development length, or high debonding risk are present in conventional repair, particularly near damaged lap-splice zones or bar termination regions. However, they should be avoided for repairing beams found in seismic regions or areas exposed to cyclic loading, where high ductility, substantial post-yield deformation, and significant energy dissipation are essential. It is possible that straight-bar configurations will provide more balanced structural performance in these instances, or that hooked strengthening bars can be used in combination with another strengthening approach, such as confinement.
3. The bonding material also influenced repair outcomes. Epoxy increased the cracking load between 39.4% and 98.8%, whereas cementitious materials yielded smaller improvements from 18.8% to 59.3%. At the ultimate load, epoxy repairs restored between 83.4% and 105.6% of the control, while cementitious repairs ranged between 66.8% and 110.6%, depending on the confinement conditions. Stiffness values exhibited more consistent improvements with epoxy, showing increases of 29.2% to 45.8% in initial stiffness and 44.2% to 76.2% in service stiffness. Cementitious materials demonstrated less uniform results, with some cases achieving a 92.6% enhancement in initial stiffness but only 46.4% in service stiffness. Both adhesives significantly reduced ductility, with reductions from 49.7% to 55.6% for epoxy and from 54.3% to 55.1% for cementitious bonds. Additionally, energy absorption diminished from 66.6% to 89.3% across both bonding systems. Moreover, the utilization of hook-shaped strengthening bars, rather than conventional straight bars, effectively prevented debonding failure, a predominant and detrimental failure mode associated with the NSM strengthening technique.
4. Cement-based adhesives exhibit higher load-bearing capacity than undamaged reference specimens; however, they are less effective than epoxy-bonded systems. Their compatibility with concrete improves homogeneity and diminishes the likelihood of debonding or thermal stresses. Unlike epoxy, cementitious adhesive may be considered suitable for moderate-load or serviceability-governed structures, where economy, material availability, and ease of application are primary considerations. In contrast, epoxy adhesives are preferred for critical structural members and seismic-demanding applications, where considerable bond performance, higher energy dissipation, and more stable post-yield behavior are essential.
5. Beams repaired with 12 mm bars restored from 66.8% to 82.4% of their control ultimate capacity, while those repaired with 16 mm bars were restored to a range between 90.7% and 115.6%. Regarding ultimate deflection, a reduction between 72.7% and 79.3% was observed for beams repaired with 12 mm bars, whereas a decrease from 58.1% to 68.8% was noted for beams repaired with 16 mm bars. In the case of 12 mm bars, initial stiffness increased by 23.5 to 45.8%, whereas in the case of 16 mm bars, it increased by 84.5 to 147.5%. Service stiffness rose from 54.5% and 151.9% for 12- and 16-mm repairing bars, respectively, corresponding to the maximum gains. Ductility decreased by about 55% with 12 mm bars, but only in the range of 16.8 to 21.8% with 16 mm bars. Energy absorption losses were higher with smaller bars, ranging from 79% to 89.3%, compared to larger bars, which had losses from 59.1% to 77.3%.
6. The confined specimen demonstrated a remarkable increase in cracking load, which rose by 98.8% compared to a less dramatic increase of 38.6% observed in the unconfined case. At the ultimate load stage, the confinement resulted in a marginal yet significant enhancement of 5.4% over the control specimen. In contrast, the unconfined specimen managed to regain only 82.4% of its initial load capacity. In terms of initial stiffness, it was found that confinement contributed to a significant improvement of 29.2%. Meanwhile, the unconfined beams saw an even higher increase in stiffness, rising by 45.8%. However, in terms of service stiffness gains, confined beams outperformed their unconfined counterparts, achieving an impressive rise of 76.2% compared to just 44.2% for the unconfined beams. Ductility decreased in both confinement states in closer ratios. Furthermore, energy absorption capabilities were adversely affected, exhibiting a drop of 69.6% for confined specimens and an even more substantial 79% decline in non-confined specimens.
7. Epoxy-repaired beams showed flexural or flexural-splitting failures similar to the control. Cementitious specimens often failed by premature cover separation. Confinement produced flexural-shear failure with debonding of the steel plate, while larger bars tended to introduce splitting stresses in the concrete.
8. All specimens showed an initial linear-elastic response before cracking. Their later behavior depended on the repair medium and confinement. Epoxy systems performed better, delaying cracks, offering gradual post-cracking transitions, and improving ductility with stable energy dissipation, especially with confinement. Cementitious repairs often cracked early, had abrupt post-yield responses, and failed brittlely. Confinement helped, boosting strength and delaying cracks, but still resulted in stiffness-driven, brittle failure with higher ultimate strength.

9. The suggested NSM steel-bar repair system can restore load capacity, often exceeding the original strength. It reduces damage risk compared to external systems and allows localized repairs without demolition. It also enables the use of cheaper, locally available cementitious materials. However, for severely damaged RC beams requiring rapid restoration of flexural strength, stiffness, and serviceability under gravity and moderate loading conditions, the proposed repair method is not intended to be a seismic strengthening technique.

Based on the above results, it can be concluded that a suitable strengthening system, such as NSM, the use of hook-shaped steel repairing bars, can provide significant strength restoration even for severely damaged reinforced concrete beams, while also reducing or preventing debonding failure, which represents the common failure pattern of the NSM reinforcement system. Furthermore, the application of a bar binder, a component of the cementitious family, which is compatible in properties, is inexpensive and readily available, and yielded good results.

Statements & Declarations

Author contributions

Rasha A. Aljazaari: Investigation, Formal analysis, Resources, Writing - Original Draft, software, validation, and funding providing.

Javad Vaseghi Amiri: Conceptualization, Methodology, Project administration, Writing of Review and Editing, supervision.

Hayder Alghazali: Project administration, Writing of Review and Editing, and supervision.

All authors have read and agreed to the published version of the manuscript.

Acknowledgements

The author appreciates the Department of Civil Engineering, Noshirvani University of Technology, Babol, Iran, and the Engineering Consulting Bureau Laboratory, University of Kufa, for providing the necessary facilities for this research.

Funding

The authors received no financial support for the research, authorship, and/or publication of this article.

Declarations

The authors declare no conflict of interest.

Data availability

The data presented in this study are available on request from the corresponding author.

References

[1] Ivanova, I., Assih, J., Dontche, D. Repairing of short reinforced concrete corbel by bonding composite material under continuous load. In: 10th International Conference on Fracture Mechanics of Concrete and Concrete Structures; 2019; Porto (PT). p. 1–6. doi:10.21012/FC10.235590.

[2] Cerullo, D., Sennah, K., Azimi, H., Lam, C., Fam, A., Tharmabala, B. Experimental Study on Full-Scale Pretensioned Bridge Girder Damaged by Vehicle Impact and Repaired with Fiber-Reinforced Polymer Technology. Journal of Composites for Construction, 2013; 17: 662–672. doi:10.1061/(ASCE)CC.1943-5614.0000383.

[3] Al-Rifaie, W. N., Ismaeel, N. N., Riyad, H. Rehabilitation of Damaged Reinforced Concrete Beams. IOSR Journal of Mechanical and Civil Engineering 2017; 14: 58–70. doi:10.9790/1684-1403065870

[4] Nounu, G., Chaudhary, Z.-U. L. H. Reinforced concrete repairs in beams. Construction and Building Materials, 1999; 13: 195–212. doi:10.1016/S0950-0618(99)00014-8.

[5] Fayyadh, M. M., Abdul Razak, H. Assessment of effectiveness of CFRP repaired RC beams under different damage levels based on flexural stiffness. Construction and Building Materials, 2012; 37: 125–134. doi:10.1016/j.conbuildmat.2012.07.021.

[6] Haddad, R. H., Al-Mekhlafy, N., Ashteyat, A. M. Repair of heat-damaged reinforced concrete slabs using fibrous composite materials. Construction and Building Materials, 2011; 25: 1213–1221. doi:10.1016/j.conbuildmat.2010.09.033.

[7] Elkhatib, L., Khatib, J., Fırat, S., El Hassan, H., Elkordi, A. Rehabilitation of Concrete Structures - A Review. Gazi University Journal of Science, 2025; 38: 665–685. doi:10.35378/gujs.1503207.

[8] Alaee, F. J., Karihaloo, B. L. Retrofitting of Reinforced Concrete Beams with CARDIFRC. Journal of Composites for Construction, 2003; 7: 174–186. doi:10.1061/(ASCE)1090-0268(2003)7:3(174).

[9] Sevil Yaman, T. Behaviour of precast concrete beams prestressed with CFRP strands. Građevinar, 2016; 68: 775–786. doi:10.14256/JCE.1624.2016.

[10] Mashreia, M. A., Makkia, J. S., Sultana, A. A. Flexural Strengthening of Reinforced Concrete Beams Using Carbon Fiber Reinforced Polymer (CFRP) Sheets with Grooves. Latin American Journal of Solids and Structures, 2019; 16: e176. doi:10.1590/1679-78255514.

[11] Wu, H. C., Eamon, C. D. Strengthening of concrete structures using fiber reinforced polymers (FRP): design, construction and practical applications. 1st ed. Cambridge (UK): Woodhead Publishing; 2017.

[12] American Concrete Institute (ACI). ACI 440.2R-02: Guide for the design and construction of externally bonded FRP systems for strengthening concrete structures. Farmington Hills (MI): ACI; 2005. doi:10.1061/40753(171)159.

[13] Mostofinejad, D., Esfahani, M. R., Shomali, A. Experimental and numerical study of the RC beams shear-strengthened with NSM technique. Journal of Composite Materials, 2019; 53: 2377–2389. doi:10.1177/0021998319830777.

[14] Mirabi Banadaki, H., Eslami, A., Ronagh, H. Near-surface-mounted retrofitting of damaged/undamaged adobe walls using steel bars: Analytical evaluation of experimental results. Structures, 2020; 28: 2111–2121. doi:10.1016/j.istruc.2020.10.020.

[15] Rahman, M., Jumat, M., Hosen, M. A., Islam, A. B. M. Effect of adhesive replacement with cement mortar on NSM strengthened RC Beam. Revista de la construcción, 2016; 15: 61–72. doi:10.4067/S0718-915X2016000100006.

[16] Mobin, M. N., Haque, M. F. Re-strengthening of reinforced concrete (RC) beam using near surface mounted (NSM) steel re-bars. In: 4th International Conference on Civil Engineering for Sustainable Development; 2018; Khulna (BD). p.

[17] Sabah, S., Hamza, D. Flexural behavior of reinforced concrete beams strengthened with hybrid Steel-FRP reinforcements by using near surface mounted technique. Journal of Applied Engineering Science, 2023; 21: 1–9. doi:10.5937/jaes0-39645.

[18] Kholil, M., Shakib, S., Rakib, M., Morshed, A. Finite element modeling of RC beams retrofitted with near surface mounted steel bars. 2023; 21: 1–9. doi:10.1063/5.0130156.

[19] Olajumoke, A. M., Dundu, M. Methods for flexural strengthening of reinforced concrete elements using steel plates. In: International Conference on Construction Materials and Structures; 2014; Johannesburg, (ZA). p. 1080–1085.

[20] Abuodeh, O. R., Abdalla, J. A., Hawileh, R. A. The flexural behavior of bolting and bonding Aluminum Alloy plates to RC beams. Procedia Structural Integrity, 2019; 17: 395–402. doi:10.1016/j.prostr.2019.08.052.

[21] Zhang, Y., Wang, H., Qin, Y., Huang, S., Fan, W. Experimental and analytical studies on the flexural behavior of steel plate-UHPC composite strengthened RC beams. Engineering Structures, 2023; 283: 115834. doi:10.1016/j.engstruct.2023.115834.

[22] Looney, T. J. Bond behavior of high-volume fly ash and self-consolidating concrete [Master Thesis]. Rolla (MO): Missouri University of Science and Technology; 2012.

[23] American Concrete Institute (ACI). ACI 318-19: Building code requirements for structural concrete and commentary. Framington Hills (MI): ACI 318-19; 2019.

[24] American Concrete Institute (ACI). ACI 211-91: Standard Practice for Selecting Proportions for Normal, Heavyweight and Mass Concrete. Framington Hills (MI): ACI; 1991.

[25] ASTM International. ASTM A615/A615M-24: Standard Specification for Deformed and Plain Carbon-Steel Bars for Concrete Reinforcement. West Conshohocken (PA): ASTM International; 2024. doi:10.1520/A0615_A0615M-24

[26] ASTM International. ASTM A370-17: Standard test methods and definitions for mechanical testing of steel products. West Conshohocken (PA): ASTM International; 2017. doi:10.1520/A0370-17

[27] ASTM International. ASTM A36/A36M-19: Standard Specification for Carbon Structural Steel. West Conshohocken (PA): ASTM International; 2019. doi:10.1520/A0036_A0036M-19

[28] ASTM International. ASTM C39/C39M-24: Standard test method for compressive strength of cylindrical concrete specimens. West Conshohocken (PA): ASTM International; 2024. doi:10.1520/C0039_C0039M-24

[29] ASTM International. ASTM C496/C496M-17: Standard test method for splitting tensile strength of cylindrical concrete specimens. West Conshohocken (PA): ASTM International; 2017. doi:10.1520/C0496_C0496M-17

[30] ASTM International. ASTM C78/C78M-22: Standard test method for flexural strength of concrete. West Conshohocken (PA): ASTM International; 2022. doi:10.1520/C0078_C0078M-22.

[31] EFNARC. Specifications and Guidelines for Self-Compacting Concrete. Flums, (CH): EFNARC; 2002.

[32] Park, R. Evaluation of ductility of structures and structural assemblages from laboratory testing. Bulletin of the New Zealand Society for Earthquake Engineering, 1989; 22: 155–166. doi:10.5459/bnzsee.22.3.155-166.

[33] Kristiawan, S., Supriyadi, A., Sangadji, S., Santosa, D. Cracking behaviour and its effect on the deflection of patched-reinforced concrete beam under flexural loading. In: MATEC web of conferences; 2017; p. 02021. doi:10.1051/matecconf/201713802021.

[34] Porter, N. M., Stallings, J. M. Flexural strengthening of reinforced concrete beams with externally bonded CFRP plates with lap splices. Highway Research Center Auburn University; 2001. Report No.:1.

[35] Hamed, T., Said, A. Shear Strength and Serviceability of GFRP-Reinforced Concrete Beams: A Study on Varying Reinforcement Ratios. Civil Engineering Journal, 2025; 11: 857–883. doi:10.28991/CEJ-2025-011-03-04.

[36] Jomaah, M. M., Ghaidan, D. J. Energy Absorption Capacity Of Layered Lightweight Reinforced Concrete Beams With Openings In Web. Civil Engineering Journal, 2019; 5: 690–701. doi:10.28991/cej-2019-03091279.

Civil Engineering and Applied Solutions

Research Article

journal homepage: ceas.journals.umz.ac.ir

Upcycling PET Waste as Hybrid Aggregates in Self-Compacting Concrete: Synergistic Effects on Rheology and Strength

Baitollah Badarloo [a*], Mahdi Moradi [b], Hamid Reza Koohestani [c], Ali Attarzadeh [a]

[a] *Department of Civil Engineering, Qom University of Technology (QUT), Qom 37181-46645, Iran*
[b] *Department of Civil Engineering, Qo.C., Islamic Azad University, Qom, Iran*
[c] *Department of Civil Engineering, Shahab-Danesh University, Qom, Iran*

A R T I C L E I N F O

Article history:

Received 29 March 2026

Revised 24 April 2026

Accepted 12 June 2026

Available online 01 January 2027

Keywords:

Polyethylene terephthalate

Self-compacting concrete

Aggregate

Fresh and hardened properties

A B S T R A C T

The escalating demand for construction aggregates, combined with the growing environmental concerns associated with plastic waste, highlights the need for innovative and sustainable concrete technologies. This study evaluates the feasibility of upcycling Polyethylene Terephthalate (PET) waste as a partial replacement for natural aggregates in Self-Compacting Concrete (SCC). Unlike previous studies that relied on single replacement strategies, this work introduces a novel approach by examining the synergistic interaction between granulated PET (fine aggregate) and flake PET (coarse aggregate). A comprehensive experimental program was conducted using 20 mix design configurations, comprising 120 cubic and 80 cylindrical specimens. Key variables included PET morphology, replacement ratios, and targeted strength classes. The results showed that hybrid incorporation of PET types produced overall superior performance compared to single-mode substitutions. Mixes containing up to 180 kg/m³ of PET maintained acceptable rheological properties required for SCC. Although replacing 10% of both fine and coarse aggregates resulted in moderate reductions in compressive and tensile strengths (25% and 22%, respectively), the mixtures still demonstrated adequate performance for non-critical structural applications. Overall, the findings provide meaningful insights into high-volume plastic waste utilization in SCC, supporting more sustainable construction practices while reducing reliance on natural aggregates.

How to cite this article: Badarloo, B. Moradi, M. Koohestani, H.R. Attarzadeh, A. Upcycling PET Waste as Hybrid Aggregates in Self-Compacting Concrete: Synergistic Effects on Rheology and Strength. Civil Engineering and Applied Solutions. 2027; 3(1): 179–191. doi:10.22080/ceas.2026.31491.1087.

1. Introduction

The escalating global consumption of plastics has led to a severe environmental crisis, as plastic waste production reached approximately 400 million tons in 2020 and is projected to reach 1,100 million tons 1,100 million tons by 2050 [1]. Currently, plastic waste accounts for roughly 12% of global solid waste [2]. Despite various recycling efforts, global statistics indicate that only 32.5% of plastic waste is mechanically recycled and 42.6% is recovered for energy, while a substantial 24.9% accumulates in landfills or pollutes natural ecosystems [3]. Among various plastics, Polyethylene Terephthalate (PET) is widely used in packaging for beverages and pharmaceuticals. The non-biodegradability and long-term persistence of PET pose critical threats, including groundwater contamination, soil degradation, and chemical leaching [4]. Consequently, developing sustainable strategies to upcycle PET waste into value-added materials has become a priority for the circular economy.

The construction industry offers substantial potential capacity for recycling waste materials, especially considering the estimated concrete demand of 18 billion tons by 2050 [5]. Incorporating PET waste into concrete not only mitigates environmental pollution

* Corresponding author.
E-mail addresses: badarloo@qut.ac.ir (B. Badarloo).

https://doi.org/10.22080/ceas.2026.31491.1087
ISSN: 3092-7749/© 2027 The Author(s). Published by University of Mazandaran.

but also addresses the depletion of natural aggregate resources [6]. Previous investigations have explored the utility of PET as both fiber reinforcement and aggregate replacement in conventional concrete. While PET incorporation can enhance specific properties such as energy absorption and impact resistance [7, 8], it often compromises mechanical strength. For instance, replacing aggregates with PET often leads to density reduction and strength loss proportional to the replacement level [7]. Additionally, the inclusion of 1.5% PET fibers has been shown to reduce compressive strength by up to 10% while slightly improving tensile and flexural behaviors [8, 9].

In recent years, Self-Compacting Concrete (SCC) has gained prominence due to its superior flowability, homogeneity, and ability to consolidate under its own weight without mechanical vibration [10, 11]. Given the stringent rheological requirements of SCC, incorporating waste plastics presents unique challenges compared to conventional concrete. Extensive research has focused on using PET fibers in SCC, which are typically capped at 2% by volume to avoid blocking and segregation issues [12-17]. These studies show that although PET fibers can enhance tensile performance, they significantly reduce flowability and often cause rheological instability when used above 1% [12-17]. It is important to note that the primary objective of utilizing PET in this context extends beyond merely enhancing concrete properties to include the effective diversion of waste from the environment. Therefore, using PET as a volumetric aggregate replacement enables higher recycling rates and better supports this environmental objective.

PET has been used as fine aggregates in numerous studies, constituting up to 20% of SCC [7, 14, 18-20]. An increase in PET content generally leads to reduced slump-flow diameter and increased V-funnel time [14, 18-20]. However, some studies have reported contradictory trends [7]. It has also been reported that PET replacement levels above 10% can reduce slump flow to approximately 400 mm [14, 18-20]. Additionally, higher PET contents have been associated with longer V-funnel times and, in some cases, complete blockage [7, 14, 18-20]. However, there are reports with contrary results [18]. For instance, the compressive strength of SCC decreases with the increased PET content in conventional concrete, with the reduction percentage of strength corresponding to the percentage of PET used [7, 14, 18-20]. The study by Sadrmomtazi et al. [20] indicates that adding 15% PET aggregates results in an approximately 48.3% reduction in compressive strength while replacing 2.5% PET aggregates results in an 8% reduction in compressive strength [20]. Some researchers have suggested that PET replacement levels up to 15% may be feasible in SCC. However, replacements beyond this limit lead to unacceptable results in the rheological properties of SCC [7, 14, 18-20]. There are a limited number of studies on the use of PET as coarse aggregates. Odeyemi et al. [21] used PET and rubber crumbs at 10, 20, and 30 percent as replacements for coarse aggregates in SCC. Their results showed that the addition of PET leads to a reduction in compressive strength, with the least reduction observed in samples containing 10% PET, showing an 18.5% decrease in compressive strength. In their study, Odeyemi et al. [21] used PET as a coarse aggregate replacement and designed mixtures for a 20-MPa strength class. Beyond PET, other polymer-based waste materials and supplementary cementitious components have also been investigated in SCC. Abedi Mavaramkolaei et al. [22] studied SCC with recycled nylon granules replacing fine aggregates at 0–15% and, using three-point bending and the Boundary Effect Method (BEM), reported reductions of about 20–24% in fracture energy and toughness but a roughly 23% increase in a ductility-related crack length parameter at 15% replacement, illustrating the trade-off between strength and ductility in polymer-modified SCC. In another related study, Farrokh Ghatte and Nazari [23] employed gene expression programming (GEP) to model the compressive strength of SCC containing rice husk ash, achieving a correlation coefficient of about 0.97 with low prediction errors and providing an explicit predictive equation, which highlights the potential of advanced data-driven tools for designing sustainable SCC mixtures with waste-derived ingredients.

A critical gap remains in the existing literature as most studies have isolated the effects of PET either as fibers or as a single type of aggregate replacement. To the best of the authors’ knowledge, no comprehensive study has systematically investigated the synergistic effects of simultaneously replacing both fine and coarse natural aggregates with granulated and flake PET in SCC. Furthermore, the existing contradictory findings regarding rheological performance necessitate a more rigorous examination of mixture variables. This study aims to bridge this gap by conducting a multi-variable experimental program to evaluate the influence of PET morphology, replacement ratios, and their combined interaction on the fresh and hardened properties of SCC across different strength classes. The primary objective is to identify an optimal mix design that maximizes PET waste utilization while meeting the essential mechanical and rheological requirements for structural SCC.

2. Materials and experimental methods

2.1. Constituent materials of PET-SCC

2.1.1. Sand and gravel specifications

Semi-crushed gravel with a nominal maximum aggregate size of 9.5 mm was used to produce concrete, with river sand with standard grading being utilized. Table 1 presents the specifications of the sand and gravel used. Additionally, Fig. 1 provides a comparison of grading curves based on ASTM C33 [24].

Table 1. Properties of aggregates.

Properties	Coarse aggregate	Fine aggregate	Granule PET	Flake PET
Coefficient of Curvature (CC)	1	0.53	0.92	2.4
Coefficient of Uniformity (CU)	1.83	7.5	2	4.3
Los Angeles abrasion (%)	17.5	-	-	-
Fractured particles	47%	0%	-	-

Material finer than 75μm	1%	3.50%	-	-
Fineness Modulus	5.94	2.72	-	-

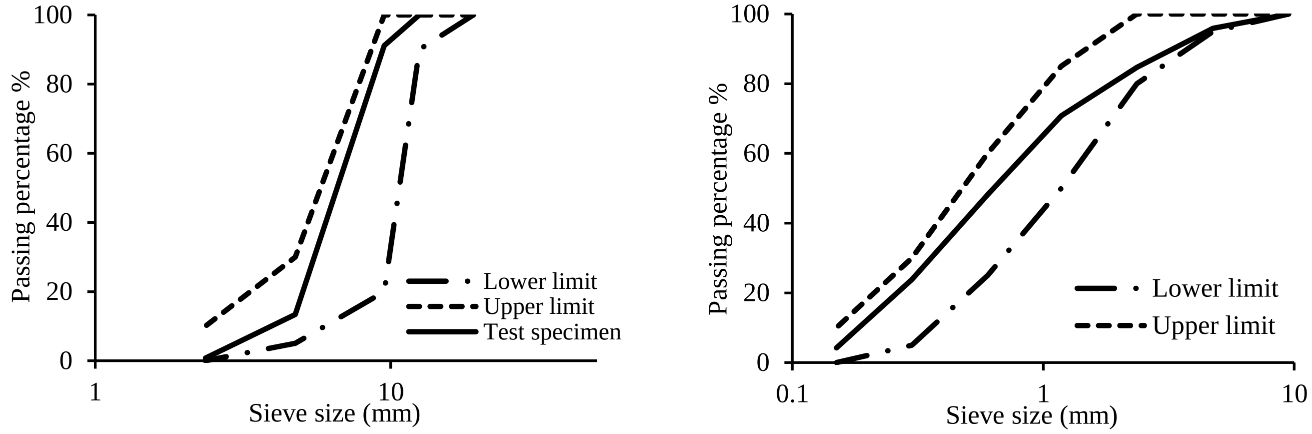

(a) **(b)**

Fig. 1. Grain size distribution chart control of aggregates according to ASTM C33 [24] (a) Results of gravel (b) Results of sand.

2.1.2. PET specifications

This study employed two different types of recycled PET materials to replace fine and coarse aggregates. Recycled PET granules were sourced from Rata Shomal Recycling Industries, Rata Shomal Recycling Industries in Amol, Iran, and recycled PET flakes were obtained from Qom, Iran. Fig. 2 shows the PET materials used in this study. The specifications of the PET granules and PET flakes used are listed in Table 2. As there is no standard grading system for PET aggregates, the grading curves were prepared similarly to conventional aggregates based on ASTM C33 [24]. Fig. 3 compares these grading curves with conventional aggregate criteria.

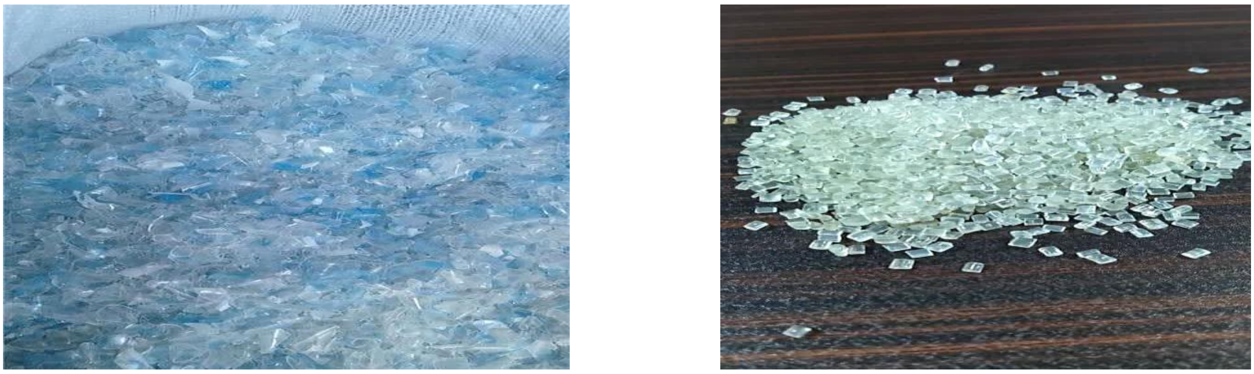

(a) **(b)**

Fig. 2. Recycled PET (a) PET flakes (b) PET granules.

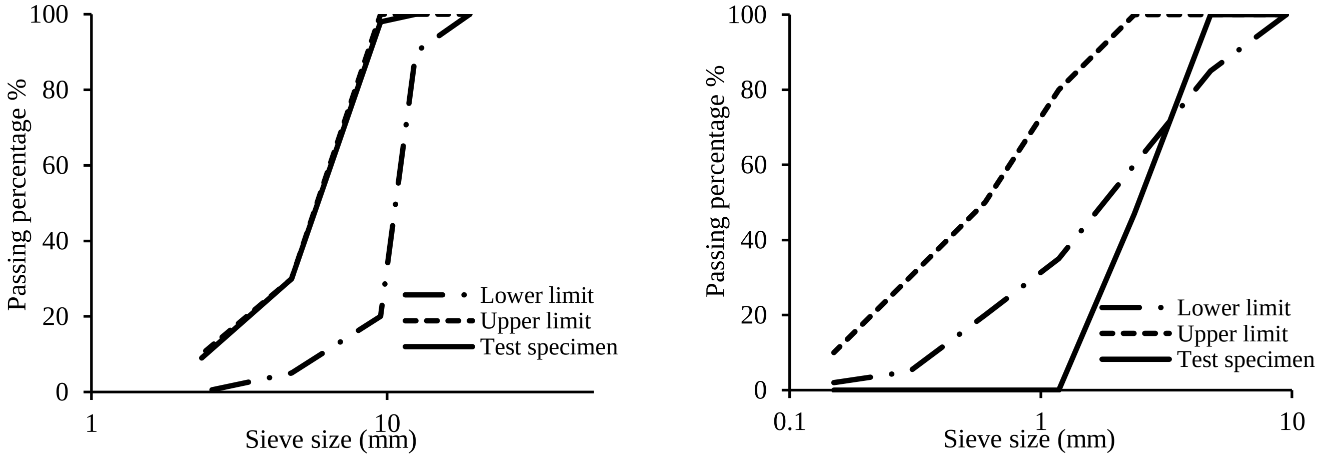

(a) **(b)**

Fig. 3. Grain size distribution chart control of PET according to ASTM C33 [24] (a) Flake PET (b) Granule PET.

Table 2. Physical properties of used PET.

Physical property of PET Results	Flake PET	Granule PET
Specific gravity ($\mathbf{gr/cm^3}$)	1.35	1.3
Chemical description ($\mathbf{gr/cm^3}$)	0.68-0.72	0.7
Color tone	Clear, light blue, blue	light green
Approx. melting point	240-250 ^{0}C	240-250 ^{0}C

2.1.3. Superplasticizer

Superplasticizers are essential for achieving adequate workability in self-compacting concrete. Polycarboxylate-based superplasticizers exhibit superior performance compared to other superplasticizer types. A polycarboxylate-based superplasticizer, with its properties listed in Table 3, was used in this study.

Table 3. Properties of superplasticizer.

Type	Modified Polycarboxylate
Color	Dark purple
State	Liquid
State Specific gravity ($\mathbf{gr/cm^3}$)	1.1
PH	5±2

2.1.4. Cement

In this study, Type II Portland cement was used. The specifications of this cement are presented in Table 4.

Table 4. Main composition of cement.

Physical characteristics	Value	Chemical composition	Cement (%)
Outlet start (min)	180	SiO2	20.35
End of the outlet (min)	225	Al2O3	4.65
2-day compressive strength (MPa)	28.1	Fe2O3	3.45
28-day compressive strength (MPa)	55.1	SO3	2.69
		CaO	63.63
		MgO	1.52
		K2O	0.73
		Na2O	0.33

2.2. Mix design

Generally, the production method of self-compacting concrete (SCC) is similar to conventional concrete, with the main difference lying in the specific rheological criteria of SCC. The SCC mixtures in this study were proportioned according to the EFNARC [25] guidelines using a conventional empirical mix design approach. The total aggregate content was initially estimated based on the framework proposed by Edamatsu et al. [26]. The water–cement ratios of 0.40 (for the target C25 strength class) and 0.36 (for the target C35 strength class) were determined through preliminary trial batches. In these trials, 7-day compressive strengths were used as a predictor to ensure that the mixtures would reach the required 28-day strengths while still maintaining adequate flowability for SCC. The initial superplasticizer dosage was selected based on values commonly reported in similar SCC studies [26]. This dosage was then refined through iterative trial mixtures using slump flow as the main control parameter until the mixtures satisfied the flowability limits recommended by EFNARC [25].

(a) **(b)**

Fig. 4. Concrete samples (a) Cylindrical samples (b) Cubic samples.

SCC with two strength classes, C25 and C35, was studied, and three groups of mixtures were examined for each class. Flake PET replaced coarse aggregates in the first group, Granule PET replaced fine aggregates in the second group, while Granule and Flake

PET replaced fine and coarse aggregates simultaneously in the third group. The replacement ratios were 5%, 10%, and 20% by the weight of the respective aggregates. Table 5 presents the mix designs used in this study for easier identification. To facilitate the identification of the mixtures, a specific naming convention was adopted. In this notation, the first part indicates the target concrete strength class (e.g., C25 or C35). The numerical value represents the replacement percentage of natural aggregates by PET waste (by weight). The letters "G" and "F" denote the type of PET used, corresponding to granules and flakes, respectively. For example, C35-10GF denotes a mixture in the C35 strength class containing a hybrid replacement of 10% PET granules and 10% PET flakes (20% total PET). The concretes were produced in accordance with the mix designs. Subsequently, tests, including slump flow, visual stability index (VSI), and V-funnel, were performed on fresh concrete. Sampling was carried out after completing the fresh concrete tests. Four standard cylindrical (150×300 mm) and six cubic (150×150×150 mm) samples were prepared for each mix design, totaling 120 cubic and 80 cylindrical samples, as illustrated in Fig. 4.

Table 5. Concrete mixture composition.

Mixture ID	PET type	PET level	PET	Coarse aggregates	Fine aggregates	Cement	Water	SP	W/C	Concrete mixture type
Unit	**-**	**%**			**kg/m^3**				**-**	**MPa**
C25	-	0	0	700	1100	370	148	1.5	0/40	**C25**
C25-05G	Granule PET	5	55	700	1045	370	148	1.5	0/40	
C25-10G		10	110	700	990	370	148	1.5	0/40	
C25-20G		20	220	700	880	370	148	1.5	0/40	
C25-05F	Flake PET	5	35	665	1100	370	148	1.5	0/40	
C25-10F		10	70	630	1100	370	148	1.5	0/40	
C25-20F		20	140	560	1100	370	148	1.5	0/40	
C25-05GF	Flake + Granule PET	5	90	665	1045	370	148	1.5	0/40	
C25-10GF		10	180	630	990	370	148	1.5	0/40	
C25-20GF		20	360	560	880	370	148	1.5	0/40	
C35	-	0	0	670	1040	460	170	3	0/36	**C35**
C35-05G	Granule PET	5	52	670	988	460	170	3	0/36	
C35-10G		10	104	670	936	460	170	3	0/36	
C35-20G		20	208	670	832	460	170	3	0/36	
C35-05F	Flake PET	5	33/5	636/5	1040	460	170	3	0/36	
C35-10F		10	67	603	1040	460	170	3	0/36	
C35-20F		20	134	536	1040	460	170	3	0/36	
C35-05GF	Flake + Granule PET	5	85.5	636/5	988	460	170	3	0/36	
C35-10GF		10	171	603	936	460	170	3	0/36	
C35-20GF		20	342	536	832	460	170	3	0/36	

The samples were demolded after 24 hours and then cured under standard conditions until testing, as depicted in Fig. 5. Furthermore, various tests were performed on hardened concrete, including density, compressive strength, and split tensile strength tests. The results of each test are presented and discussed in the following sections.

Fig. 5. Sample storage pool.

3. Experimental test results

3.1. Fresh concrete properties

The slump flow test and Visual Stability Index (VSI) are among the most vital criteria for controlling the rheological properties of SCC. These tests were used to evaluate the flowability and segregation resistance of the mixtures. According to EFNARC [25], the slump flow should be between 550 and 850 mm. The VSI ranges from 0 to 3 and indicates the degree of segregation of SCC, with values of 0 or 1 considered acceptable. Fig. 6 illustrates images of the slump test for a number of samples. Other SCC characteristics include its viscosity and filling ability, which are controlled by the V-funnel test. According to EFNARC [25], V-funnel times of up to 25 seconds are acceptable. Fig. 7 displays the V-funnel test and the experimental equipment used in this study. The results of the fresh concrete tests are summarized in Table 6.

(a) (b) (c)

Fig. 6. Slump flow test (a) C25-05F (VSI = 0) (b) C25-10G (VSI = 1) (c) C25-20F (VSI = 3).

(a) (b)

Fig. 7. The process of V-funnel test (a) Flattening the surface (b) Opening the valve.

The incorporation of PET generally reduced the flowability of SCC mixtures, as reflected by the measured slump-flow values. For both C25 and C35 mixtures, increasing the PET content led to a progressive decrease in slump flow. This reduction can be attributed to the lower specific gravity of PET compared with natural aggregates and the increased internal friction between mixture components, which restricts the movement of aggregates and reduces the ability of SCC to flow under its own weight. For example, in the C25 mixtures the slump flow decreased from 70 cm in the control mixture to about 65 cm with 10% PET flakes, whereas it dropped more considerably to around 50 cm with 10% PET granules (Table 6). These results indicate that PET granules have a stronger negative influence on the flowability of SCC than PET flakes, likely due to the higher internal friction induced by the granular particles within the fresh mixture. The results also show that mixtures with 20% PET replacement did not satisfy the rheological requirements of SCC. In contrast, mixtures with 10% replacement achieved relatively acceptable performance. Among them, the C25-10GF sample, which included 10% replacement of fine aggregate and 10% replacement of coarse aggregate with PET (corresponding to about 180 kg of PET consumption), showed satisfactory results. This finding suggests that combining two types of PET particles can increase the usable volume of PET in SCC while maintaining acceptable workability. The addition of PET weakens the results of the SCC rheological tests, an issue quite evident in Fig. 8. This situation is similarly observed in the V-funnel time improve due to the more suitable grading of PET Flake, with its grading curve falling within the ASTM C33 [24] specified range (Fig. 3a).

Table 6. Fresh SCC tests result.

Mixture ID	Slump-flow (cm)	Visual Stability Index	V-funnel time (seconds)	Viscosity class
C25	70	0	8	VS1
C25-05F	68	0	9	VS2
C25-10F	65	2	11	VS2
C25-20F	60	3	13	VS2
C25-05G	60	0	10	VS2
C25-10G	50	1	13	VS2
C25-20G	35	3	-	-
C25-05GF	60	0	10	VS2
C25-10GF	50	1	13	VS2
C25-20GF	45	3	17	VS2
C35	75	0	8	VS1
C35-05F	70	0	9	VS2
C35-10F	67	1	10	VS2
C35-20F	60	2	14	VS2
C35-05G	62	0	12	VS2
C35-10G	54	1	17	VS2
C35-20G	35	3	-	-
C35-05GF	65	0	11	VS2
C35-10GF	55	1	15	VS2
C35-20GF	45	2	25	VS2

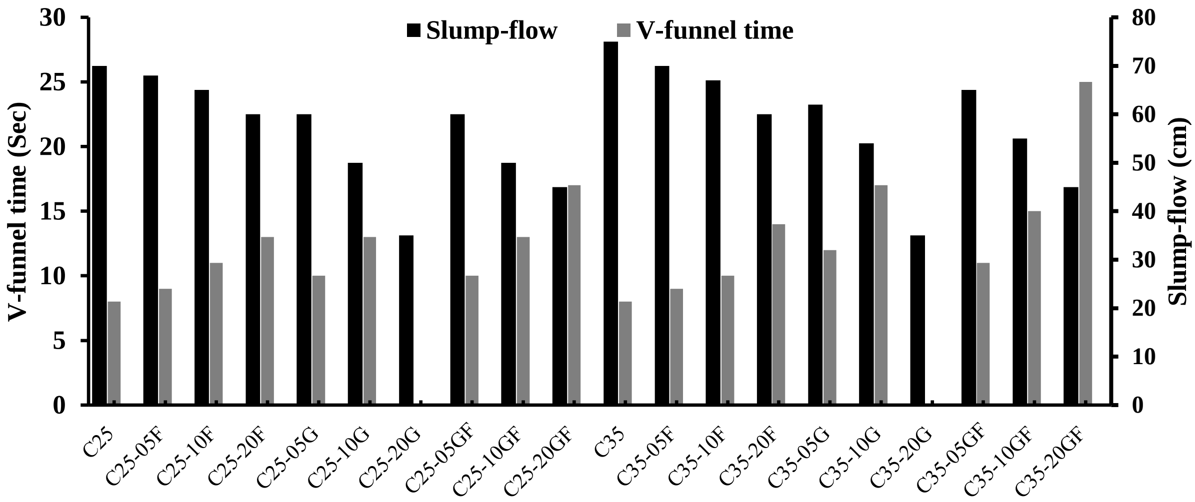

Fig. 8. Results of slump and V-Funnel tests.

A clear synergistic effect was observed when PET flakes were combined with PET granules. As shown in Table 6, mixtures with only PET granules exhibited the poorest flowability; at the 20% replacement level they even experienced complete blockage in the V-funnel. In contrast, adding PET flakes to these mixtures, despite the total PET content being higher—improved flow performance and eliminated blockage. This indicates that the beneficial influence of the flakes compensates for, and partially counteracts, the adverse effect of the granules. This synergy arises from the complementary roles of the two PET types. The flat, plate-like geometry of flakes reduces particle interlocking and helps disperse the granules, while the granules occupy part of the voids created by larger flake particles. The resulting packing condition lowers interparticle friction and prevents localized accumulation of PET granules that would otherwise hinder flow. Consequently, hybrid mixtures show superior flowability compared with mixtures containing only PET granules, particularly in the V-funnel where sensitivity to blockage is high. A comparison of the results for different concrete grades indicates that with the increased concrete grade, the slump flow and visual stability of PET-SCC improve while the V-funnel time increases. These results are due to the increased cement content and the increased viscosity of the cement paste.

3.2. Hardened concrete tests

3.2.1. Density test of hardened concrete

The density of the samples was determined using cubic samples, with 150×150×150 mm dimensions, in accordance with the ASTM C642 [27]. Three cubic specimens were tested, and the average values are reported in Table 7. The results show a clear decrease in concrete density with increasing PET content. A 20% replacement of either fine or coarse aggregates led to an approximate 7% reduction in density, whereas the combined replacement of both fine and coarse aggregates at the same level resulted in an approximate 11% reduction. Notably, the density values of mixtures containing both PET flakes and granules were slightly higher than those predicted based solely on the PET replacement level. This behavior can be attributed to improved compaction in the hybrid mixtures, which is consistent with their superior rheological performance observed in the fresh concrete tests.

3.2.3. Compressive and split tensile strength tests

Compressive strength is one of the most critical mechanical properties of SCC, as it directly influences the structural performance and durability of concrete. For each mix design, six cubic specimens (150 × 150 × 150 mm) were prepared. Three specimens were tested at 28 days, and the remaining three were tested at 90 days. Compressive strength tests were conducted in accordance with ASTM C39 [28], and the average results are presented in Table 7. Table 7 summarizes the average results for the 28-day and 90-day compressive strength samples. Split tensile strength tests were performed in accordance with ASTM C496 [29]. Four standard cylindrical specimens were prepared for each mix design and tested using a 2000 kN hydraulic testing machine (Fig. 9). Standard loading arrangements were applied to ensure failure along the loading axis, as specified by the test method.

Table 7. Results of hardened concrete tests for samples.

Mixture ID	Density kg/m^3	Average compressive strength		Average splitting tensile strength	
		28-day	90-day	28-day	90-day
C25	2350	31.2	35.2	2.8	3.2
C25-05F	2310	29.3	33.6	2.6	3.0
C25-10F	2250	25.4	30.3	2.2	2.6
C25-20F	2200	18.6	20.1	2.1	2.3
C25-05G	2310	24.7	30.9	2.4	2.8
C25-10G	2270	20.8	25.6	1.8	2.2
C25-20G	2170	9.3	10.2	1.5	1.6
C25-05GF	2320	27.3	32.6	2.3	2.6
C25-10GF	2270	23.3	29.0	2.2	2.7
C25-20GF	2100	18.0	21.6	1.7	2.1
C35	2360	41.2	45.7	3.5	3.9
C35-05F	2320	39.0	41.8	3.1	3.7
C35-10F	2260	35.7	39.5	3.1	3.5
C35-20F	2200	26.8	30.9	2.9	3.1
C35-05G	2320	24.3	26.1	3.2	3.4
C35-10G	2250	30.9	34.4	3.0	3.3
C35-20G	2150	20.4	22.5	2.5	2.7
C35-05GF	2310	32.0	36.8	3.1	.5
C35-10GF	2270	30.8	34.2	3.0	3.3
C35-20GF	2050	17.7	20.4	2.4	2.6

Table 7 presents the compressive and splitting tensile strengths at 28 and 90 days. Among all mixtures, the most favorable overall performance was obtained when 5% of the coarse aggregates was replaced with PET flakes. For the C35-05F mixture, the 28-day compressive strength decreased by only 5% relative to the control C35 mixture, while all SCC rheological criteria were fully satisfied. This indicates that low-level incorporation of flake-type PET can be tolerated without significantly compromising the mechanical properties of SCC. In contrast, the poorest mechanical performance was recorded for mixture C25-20G, with a reduction of approximately 70% in 28-day compressive strength. It must be emphasized, however, that this mixture did not satisfy the essential rheological requirements of SCC. The slump flow was only 35 cm, the Visual Stability Index reached 3, and complete blockage occurred in the V-funnel test, leading to severe compaction deficiencies. Therefore, this mixture cannot be considered a valid SCC composition, and its low strength is primarily attributed to inadequate flowability and poor consolidation rather than the intrinsic effect of PET aggregates. Beyond these two extremes, the overall trend among the remaining mixtures reveals a clear correspondence between rheological behavior (Table 6) and compressive strengths (Table 7). As expected, increasing the PET content generally reduced compressive strength; however, mixtures with improved flowability and reduced interparticle friction achieved better compaction, which effectively limited this reduction. This interpretation is further supported by Fig. 10, where the concurrent decrease in density and compressive strength across mixtures illustrates the direct influence of compaction efficiency on mechanical performance. This relationship is clearly reflected in the 10% replacement mixtures. The granule-only mixture C25-10G, which exhibited the weakest rheological performance, experienced the highest strength reduction (33%). The flake-only mixture C25-10F, benefiting from enhanced flowability, showed a smaller reduction of 19%. The hybrid mixture C25-10GF, despite containing a total of 20% PET (10% flakes + 10% granules), showed a 25% reduction—smaller than expected considering the doubled PET content and the poor behavior of granules. This confirms that improved rheology enhanced compaction and mitigated strength loss. A similar, though less pronounced, trend was observed for the C35 mixtures.

(a) (b) (c)

Fig. 9. Splitting tensile test (a) 2000 KN hydraulic jack (b) Set up for splitting tensile test (c) Sample after the test.

Table 7 presents the compressive and splitting tensile strengths at 28 and 90 days. Among all mixtures, the most favorable overall performance was obtained when 5% of the coarse aggregates was replaced with PET flakes. In this case (C35-05F), the 28-day compressive strength was only 5.4% lower than that of the C35 control mixture, while all SCC rheological criteria were fully satisfied. This result demonstrates that a low-level incorporation of flake-type PET can be accommodated without substantially compromising the mechanical properties of SCC. In contrast, the poorest mechanical performance occurred in mixture C25-20G, which experienced an approximately 70% reduction in 28-day compressive strength. It must be emphasized, however, that this mixture did not satisfy the essential rheological requirements of SCC. The slump flow was only 35 cm, the Visual Stability Index reached 3, and complete blockage occurred in the V-funnel test, leading to severe compaction deficiencies. Therefore, this mixture cannot be considered a valid SCC composition, and its low strength is primarily attributed to inadequate flowability and poor consolidation rather than the intrinsic effect of PET aggregates. Beyond these two extremes, the overall trend among the remaining mixtures reveals a clear correspondence between rheological behavior (Table 6) and compressive strengths (Table 7). As expected, increasing PET content generally reduced compressive strength. Nevertheless, mixtures with superior flowability and lower interparticle friction achieved better compaction, which effectively mitigated the strength reduction. This interpretation is supported by Fig. 10, where the concurrent decrease in density and compressive strength across mixtures highlights the governing role of compaction efficiency in the mechanical response of SCC. This relationship is especially evident in the 10% replacement mixtures. The granule-only mixture C25-10G, which exhibited the poorest rheological performance, showed the greatest strength reduction (33%). The flake-only mixture C25-10F, benefiting from improved flowability, experienced a smaller reduction of 19%. The hybrid mixture C25-10GF, despite containing a total of 20% PET (10% flakes + 10% granules), showed a 25% reduction, which is lower than expected given both the doubled PET content and the unfavorable characteristics of the granules. This confirms that enhanced rheology promoted better compaction and helped limit the strength loss. A similar, although less pronounced, trend was observed in the C35 mixtures.

Table 7 shows that the splitting tensile strength followed a trend similar to that observed for compressive strength. The largest reductions were recorded in mixtures containing 20% PET granules, reaching 48% for C25 and 27.5% for C35. In contrast, the hybrid mixtures exhibited comparatively better performance, with reductions of 38% and 31% for C25 and C35, respectively, despite containing a higher total PET content than mixtures incorporating PET granules alone. This behavior highlights the beneficial effect of combining the two PET geometries. These findings are consistent with previous studies on PET-modified concrete, which generally report a reduction in compressive strength with increasing PET content. For example, Sadrmomtazi et al. [20] observed that replacing 2.5% of aggregates with PET resulted in an 8% decrease in compressive strength, whereas a 15% replacement led to a 48.3% reduction. Several other studies have suggested that the acceptable limit of PET replacement in SCC is approximately 15%, beyond which the rheological properties deteriorate and the concrete can no longer be classified as self-compacting [7,17–20]. The present results further extend the existing literature by demonstrating that hybrid PET replacement can outperform single-type PET mixtures, an observation that has not been explicitly reported in previous studies.

Fig. 11 illustrates the percentage increase in the 90-day tensile and compressive strengths of samples compared to their 28-day conditions. As observed, in most cases, samples containing PET exhibited a higher rate of strength growth compared to conventional SCC. Thus, it can be concluded that adding PET not only has no adverse impact on the long-term strength gain of SCC but also enhances its strength following 90 days. This improvement in class C25 SCC-PET strength led to an average of 5% higher tensile and compressive strength compared to conventional SCC. However, examining the average changes in tensile and compressive strengths in class C35 reveals that the improvement in strength is not as significant. This highlights the need for further studies in this area.

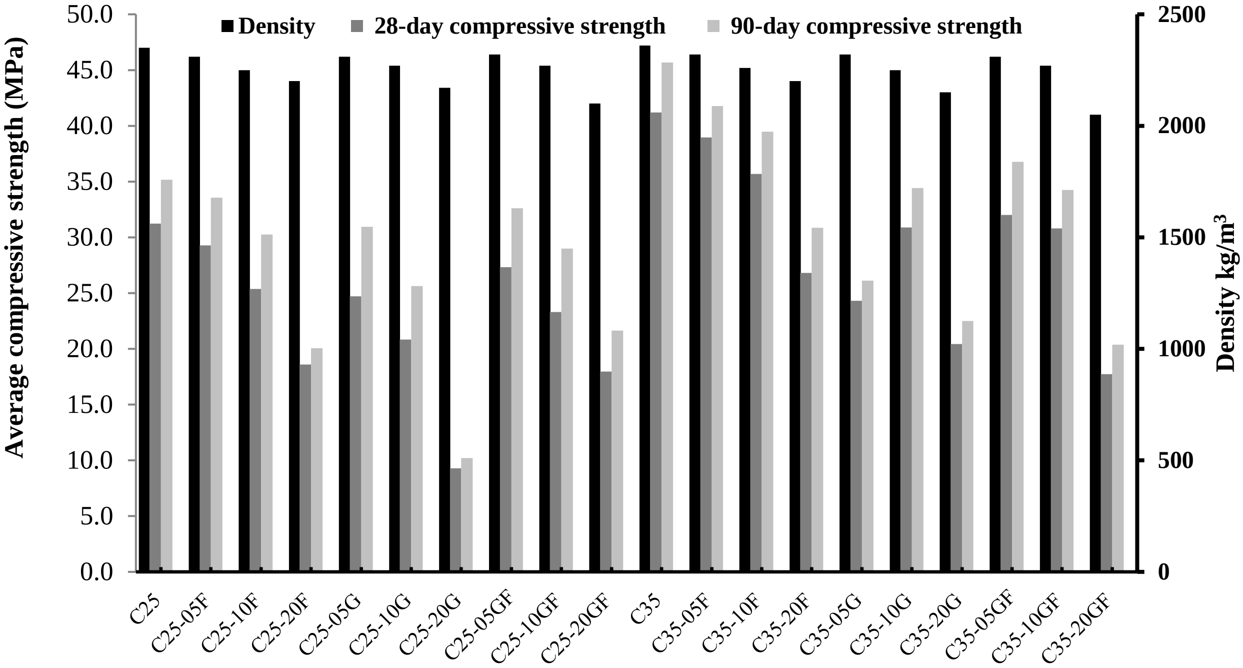

Fig. 10. Results of density and 28-Day and 90-Day compressive strength tests.

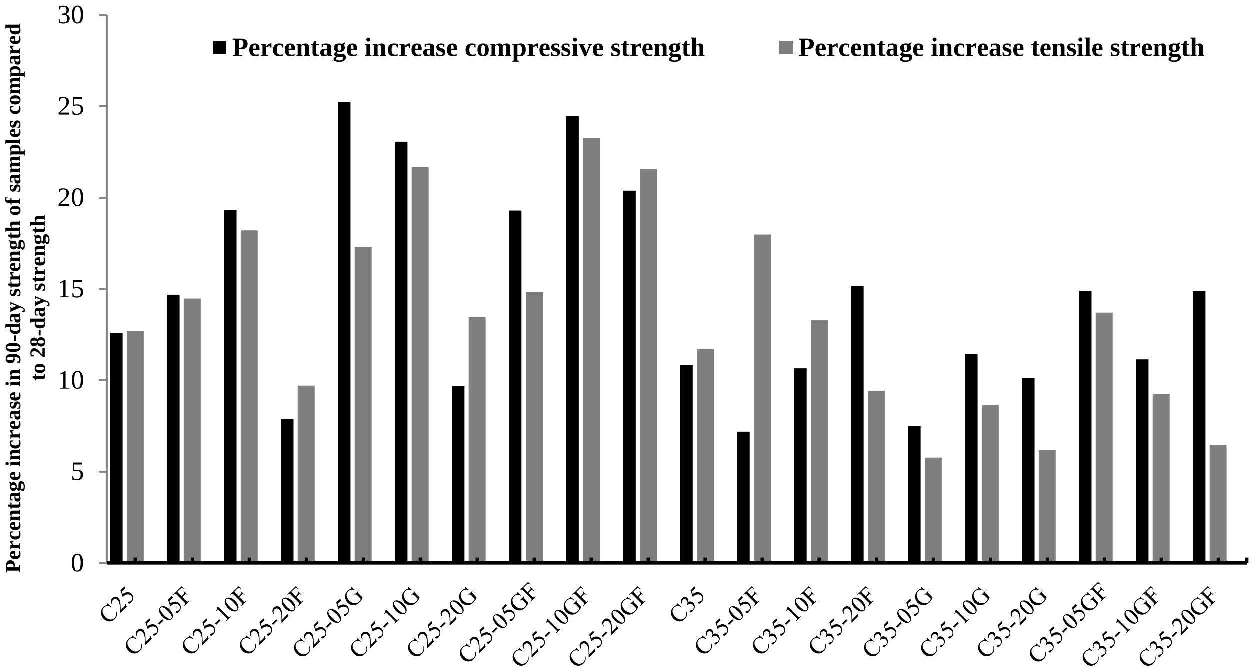

Fig. 11. The percentage increase in the 90-day tensile and compressive strengths of samples compared to their 28-day conditions.

Table 8. Images of samples after compressive strength test.

C35-20GF

C35-20G

C35-20F

C35-05GF

C35-10GF

C35-20F

C35-05GF-90

C35-10GF-90

C35-20F-90

Table 8 displays selected specimens after the compressive strength tests. As seen in the images, mixtures containing PET flakes generally exhibited better compaction compared with those containing PET granules (e.g., C35-20G). The least compacted textures were observed in granule-only mixtures, consistent with their weaker rheological performance. Moreover, the presence of PET reduced the overall cohesion of the concrete; mixtures with higher PET contents tended to lose structural integrity after loading and disintegrated more easily. The 90-day specimens displayed more brittle failure patterns, but the crack propagation remained consistent with standard compressive failure modes.

4. Conclusion

This study investigated the performance of Self-Compacting Concrete (SCC) incorporating hybrid PET waste as a replacement for natural aggregates. Based on the experimental results and the analysis of rheological and mechanical properties, the following conclusions can be drawn.

- Up to 180 kg of PET per cubic meter of SCC was successfully incorporated through hybrid aggregate replacement, exceeding the PET contents reported in most previous studies.
- A clear synergistic effect was observed in the hybrid mixtures. While the mixture containing 20% PET granules (C25-20G) failed to satisfy SCC rheological requirements due to V-funnel blockage, the hybrid mixture with 10% flakes + 10% granules (20% total PET) met all SCC criteria. This indicates that PET flakes improve the flowability and passing ability of mixtures containing PET granules.
- The best mechanical performance was achieved with 5% PET flakes (C35-05F) as a replacement for coarse aggregates, resulting in only a 5.4% reduction in 28-day compressive strength compared with the control mixture. PET incorporation did not negatively affect long-term strength development. In the C25 mixtures, PET-modified SCC showed an average 5% greater strength gain between 28 and 90 days compared with the control mixtures, whereas the improvement was less pronounced in the C35 mixtures.
- From a sustainability perspective, the optimum replacement level for maximizing waste utilization was the hybrid mixture containing 10% flakes and 10% granules (20% total PET). This mixture maintained all SCC rheological limits while limiting the compressive strength reduction to 25% (C25-10GF), which is considerably lower than expected for such a high PET content.
- A simultaneous decrease in density and compressive strength was observed, indicating that the strength reduction is mainly associated with lower compaction efficiency and the lower specific gravity of PET aggregates.
- Although the experimental results clearly showed reductions in mechanical strength with increasing PET content, the underlying microstructural mechanisms require further investigation. Future studies are therefore recommended to conduct Scanning Electron Microscopy (SEM) analysis in order to examine the interfacial transition zone (ITZ) between PET aggregates and the cementitious matrix. Such analysis would provide deeper insight into the bonding characteristics, interfacial behavior, and potential failure mechanisms responsible for the strength reduction observed in SCC containing PET.

Statements & Declarations

Author Contributions

Baitollah Badarloo: Conceptualization, Methodology, Formal analysis, Project administration, Supervision, Writing - Review & Editing.

Mahdi Moradi: Investigation, Methodology, Visualization, Validation, Formal analysis, Resources, Writing - Original Draft, Writing - Review & Editing.

Hamid Reza Koohestani: Conceptualization, Investigation, Methodology, Writing - Review & Editing.

Ali Attarzadeh: Investigation, Methodology, Visualization, Validation, Formal analysis, Resources, Writing - Original Draft, Writing - Review & Editing.

Acknowledgments

Not applicable to this research.

Funding

The authors received no financial support for the research, authorship, and/or publication of this article.

Data availability

The data presented in this study will be available on interested request from the corresponding author.

Declarations

The authors declare no conflict of interest.

References

[1] Kanchan, S., Pradhan, S., Kumar, R., Sharma, S., Bhandari, O., Priyadarshini, M., Dwivedi, S., Awwad, F., Khan, M., Ismail, E., Dhiman, R. Developing a model for waste plastic biofuels in CRDi diesel engines using FTIR, GCMS, and WASPAS synchronisations for engine analysis. Energy Exploration & Exploitation, 2024; 42: 648–684. doi:10.1177/01445987231216762.

[2] Ghosal, K., Ghosh, S. Biodegradable polymers from lignocellulosic biomass and synthetic plastic waste: An emerging alternative for biomedical applications. Materials Science and Engineering: R: Reports, 2023; 156: 100761. doi:10.1016/j.mser.2023.100761.

[3] Europe, P. An analysis of European plastics production, demand and waste data. 2020. https://plasticseurope.org.

[4] Saadullah, S. T., Haido, J. H., Al-Kamaki, Y. S. S. Mechanical properties of sustainable green self-compacting concrete incorporating recycled waste PET: A state-of-the-art review. 2023; 16: 35–57. doi:10.12989/acc.2023.16.1.035.

[5] Islam, M. A., Rahman, M., Ahmed, M. Polymer-modified Concrete: World Experience and Potential for Bangladesh. Indian Concrete Journal, 2011; 85: 1–9.

[6] Choi, Y.-W., Moon, D.-J., Chung, J.-S., Cho, S.-K. Effects of waste PET bottles aggregate on the properties of concrete. Cement and Concrete Research, 2005; 35: 776–781. doi:10.1016/j.cemconres.2004.05.014.

[7] Hasan-Ghasemi, A., Nematzadeh, M. Tensile and compressive behavior of self-compacting concrete incorporating PET as fine aggregate substitution after thermal exposure: Experiments and modeling. Construction and Building Materials, 2021; 289: 123067. doi:10.1016/j.conbuildmat.2021.123067.

[8] Abdolkhani, H., Kazeminezhad, E., Safakhah, S. Evaluating the effect of polyethylene terephthalate (PET) on the structural performance of reinforced concrete beams: experimental and numerical. Innovative Infrastructure Solutions, 2024; 9: 71. doi:10.1007/s41062-024-01380-1.

[9] Thomas, L. M., Moosvi, S. A. Hardened properties of binary cement concrete with recycled PET bottle fiber: An experimental study. Materials Today: Proceedings, 2020; 32: 632–637. doi:10.1016/j.matpr.2020.03.025.

[10] Chowdary, L., Boddepalli, K. R. Sustainable Development and Response Surface Methodology-Based Optimization of Self-Compacting Concrete Incorporating Innovative Nano Concrete Aggregate and Silica Fume. Iranian Journal of Science and Technology, Transactions of Civil Engineering, 2025; doi:10.1007/s40996-025-02082-z.

[11] Nanda, A., Panda, S., Panigrahi, S. K. Production of durable conventional concrete using recycled HDPE and PET plastic coarse aggregate. Innovative Infrastructure Solutions, 2025; 10: 74. doi:10.1007/s41062-025-01886-2.

[12] Al-Hadithi, A. I., Almawla, S. A., Mohammed, M. K. Fresh, mechanical and impact properties of self-compacting lightweight concrete containing waste PET fibers. Innovative Infrastructure Solutions, 2023; 8: 268. doi:10.1007/s41062-023-01223-5.

[13] Madandoust, R., Ranjbar, M. M., Moshiri, A. A. The effects of steel and PET fibers on the properties of fresh and hardened self-compacting concrete. Asian Journal of Civil Engineering (BHRC), 2014; 15: 671–682.

[14] Majid, M., Mohammed Al-Ani, M. Study of Some Durability Properties of Self-compacting Concrete Containing Waste Polyethylene Terephthalate. Anbar Journal of Engineering Sciences, 2023; 14: 15–30. doi:10.37649/aengs.2023.137730.1035.

[15] Oghabi, M., Khoshvatan, M. The Laboratory Experiment of the Effect of Quantity and Length of Plastic Fiber on Compressive Strength and Tensile Resistance of Self-Compacting Concrete. KSCE Journal of Civil Engineering, 2020; 24: 2477–2484. doi:10.1007/s12205-020-1578-9.

[16] Ullah Khan, S., Ayub, T. Flexure and shear behaviour of self-compacting reinforced concrete beams with polyethylene terephthalate fibres and strips. Structures, 2020; 25: 200–211. doi:10.1016/j.istruc.2020.02.023.

[17] Widodo, S., Alfirahman, R., Prawiranegara, A., Amir, M., Dewi, A. Development of Eco-friendly Self-compacting Concrete Using Fly Ash and Waste Polyethylene Terephthalate Bottle Fiber. Civil Engineering Journal, 2023; 9: 437–452. doi:10.28991/CEJ-2023-09-02-014.

[18] Aswatama, W. K., Suyoso, H., Meyfa, U. N., Tedy, P. The effect of adding PET (Polyethylene Terephthalate) plastic waste on SCC (self-compacting concrete) to fresh concrete behavior and mechanical characteristics. In: The 2nd International Joint Conference on Science and Technology (IJCST); 2018; Bali, Indonesia. p. 012023. doi:10.1088/1742-6596/953/1/012023.

[19] Jaskowska-Lemańska, J., Kucharska, M., Matuszak, J., Nowak, P., Łukaszczyk, W. Selected Properties of Self-Compacting Concrete with Recycled PET Aggregate. Materials, 2022; 15: 2566. doi:10.3390/ma15072566.

[20] Sadrmomtazi, A., Dolati-Milehsara, S., Lotfi-Omran, O., Sadeghi-Nik, A. The combined effects of waste Polyethylene Terephthalate (PET) particles and pozzolanic materials on the properties of self-compacting concrete. Journal of Cleaner Production, 2016; 112: 2363–2373. doi:10.1016/j.jclepro.2015.09.107.

[21] Odeyemi, S. O., Abdulwahab, R., Wilson, U. N., Anifowose, M. A., Ayodele, K. J. Effect of rubber crumb and polyethylene terephthalate as coarse aggregate in self-compacting concrete. Materials Today: Proceedings, 2023; 86: 14–17. doi:10.1016/j.matpr.2023.02.032.

[22] Abedi Mavaramkolaei, S., Sayarinejad, M. A., Nazari, A., Rayati Damavandi, M. Investigating the fracture behavior and ductility of self-compacting concrete containing recycled nylon granules: An experimental and modeling study. Theoretical and Applied Fracture Mechanics, 2026; 141: 105254. doi:10.1016/j.tafmec.2025.105254.

[23] Farrokh Ghatte, H., Nazari, A. Prediction of Rice Husk Ash-Based SCC Compressive Strength: Data-Driven Framework. Civil Engineering and Applied Solutions, 2025; 1: 17–28. doi:10.22080/ceas.2025.29625.1025.

[24] ASTM International. ASTM C33/C33M: Density, absorption, and voids in hardened concrete. West Conshohocken (PA): ASTM International; 2016. doi:10.1520/C0033_C0033M-16.

[25] EFNARC. Specification and guidelines for self compacting concrete. Flums, (CH): EFNARC;

[26] Edamatsu, Y., Sugamata, T., Ouchi, M. A mix-design method for self-compacting concrete based on mortar flow and funnel tests. In: 3rd International RILEM Symposium on Self-Compacting Concrete; 2003; Reykjavik (IS). p. 345–354.

[27] ASTM International. ASTM C642: Density, absorption, and voids in hardened concrete. West Conshohocken (PA): ASTM International; 2006. doi:10.1520/C0642-06.

[28] ASTM International. ASTM C39: Standard test method for compressive strength of cylindrical concrete specimens. West Conshohocken (PA): ASTM International; 2004. doi:10.1520/C0039_C0039M-04.

[29] ASTM International. ASTM C496: Standard test method for splitting tensile strength of cylindrical concrete specimens. West Conshohocken (PA): ASTM International; 2004. doi:10.1520/C0496_C0496M-04